CONF-9504160--Vol. 2

September 1995 • NREL/CP-430-20036

Proceedings of the 1995 U.S. DOE Hydrogen Program Review

Volume II

April 18-21, 1995
Coral Gables, Florida

Sponsored by the
Advanced Utility Concepts Division
Office of Energy Management
U.S. Department of Energy

National Renewable Energy Laboratory
1617 Cole Boulevard
Golden, Colorado 80401-3393
A national laboratory of the U.S. Department of Energy
Managed by Midwest Research Institute
for the U.S. Department of Energy
Under Contract No. DE-AC36-83CH10093

NREL/CP-430-20036 • UC Category: 1360 • DE95009296

Proceedings of the 1995 U.S. DOE Hydrogen Program Review

Volume II

April 18-21, 1995
Coral Gables, Florida

Sponsored by the
Advanced Utility Concepts Division
Office of Energy Management
U.S. Department of Energy

National Renewable Energy Laboratory
1617 Cole Boulevard
Golden, Colorado 80401-3393
A national laboratory of the U.S. Department of Energy
Managed by Midwest Research Institute
for the U.S. Department of Energy
Under Contract No. DE-AC36-83CH10093

Under Task No. HY511010

September 1995

TABLE OF CONTENTS

Volume I

Systems Analysis

Utilization

Production

IMPROVED METAL HYDRIDE TECHNOLOGY FOR THE STORAGE OF HYDROGEN

Krishna Sapru, L. Ming, S. Ramachandran, N.T. Stetson and S.R. Ovshinsky
Energy Conversion Devices, Inc.
Troy, MI 48084

Abstract

Low cost, high density storage of hydrogen will remove the most serious barrier to large-scale utilization of hydrogen as a non-polluting, zero-emission fuel. An important challenge for the practical use of Mg-based, high capacity hydrogen storage alloys has been the development of a low-cost, bulk production technique. Two difficulties in preparation of Mg-based alloys are the immiscibility of Mg with many transition metals and the relatively high volatility of Mg compared to many transition metals. These factors preclude the use of conventional induction melting techniques for the Mg-based alloy preparation. A mechanical alloying technique, in which Mg immiscibility and volatility do not present a problem, was developed and shows great promise for production of Mg-based alloys.

A number of Mg-based alloys were prepared via modified induction melting and mechanical alloying methods. The alloys were tested for gas phase hydrogen storage properties, composition, structure and morphology. The mechanically alloyed samples are multi-component, multi-phase, highly disordered materials in their as-prepared state. These unoptimized alloys have shown reversible H-storage capacity of more than 5 wt.% hydrogen. After 2000 absorption/desorption cycles, the alloys show no decline in storage capacity or desorption kinetics. The alloys have also demonstrated resistance to CH_4 and CO poisoning in preliminary testing. Upon annealing, with an increase in crystallinity, the H-storage capacity decreases, indicating the importance of disorder.

1. **LEVEL OF EFFORT:**

Period of contract: **One year; Nov. 8, 1993 - Nov. 8, 1994**

NO CURRENT FUNDING

Total Cost: **($) 615,920**

NREL: **($) 250,000**

ECD Cost Share: **($) 365,920**

1993	1994	1995
$ 0	$ 250,000	$?

2. PROJECT RATIONALE AND GOALS

2.1 Statement:

Large-scale introduction of hydrogen requires the development of compact, lightweight, cost-effective and safe means of storing the hydrogen. In fact the lack of a practical hydrogen storage system is one of the most serious barriers to the utilization of fuel cell technology.

2.2 PROJECT RATIONALE

POTENTIAL HYDROGEN STORAGE TECHNOLOGIES

TECHNOLOGY	kWh/M^3	(kWh/kg)	REMARKS
Compressed H_2 gas			
2400 psi	345	0.36	~1 wt.% H_2.
10000 psi	805	2.50	~6 wt.% H_2. Problem with degree of safety and cost.
Liquid H_2	701	2.38	~6 wt.% H_2. Liquification energy losses. Special handling. Boil-off losses (2-5% per day).
Carbon based Materials			
Activated Carbon	931	2.06	Under development. Cryogenic storage High cost of materials preparation.
Fullerenes $C_{60}H_{60}$			7.7 wt.% theoretical capacity (w/o container) Very early stages of development. Presently very expensive materials preparation costs.
Metal hydrides			Containers not included
TiVMn	1385	0.40	1 wt.%
FeTi	3773	0.68	1.7 wt.%
Magnesium based			
Mg_2Ni (conventional)	3192	1.24	3.2 wt.%
ECD thin films	2500	2.76	7.0 wt. %
ECD bulk alloys	~1786	2	>5.0 wt.%, (on-going work)

2.3 PROJECT RATIONALE AND GOALS

Metal Hydrides:

- **Safe**
- **Solid State**
- **Reversible**
- **Potential for high storage density**
- **Scale-up involves low cost metallurgical processes**
- **Extensively studied**
- **Problems identified**
- **Significant recent progress (ECD)**

2.4 PROJECT RATIONALE AND GOALS

A) **ECD's Previous (Thin-film) work:**

- **High Hydrogen Storage capacity (7 wt. %)**
- **Rapid Kinetics (at≥ 200°C)**
- **High tolerance to impurities**
- **Long Cycle Life**
- **Amorphous/Highly Disordered/Micro-crystalline**
- **Multi-component (3 or more selectively chosen components)**
- **Multi-phase**

B) **Problems:**

- **Thin films not suitable for many large-scale applications**
- **Desorption Temperatures too high because alloys were not optimized**

2.4 Additional Rationale- Based on ECD's Background Technology and Proprietary Position in Metal Hydrides

ECD's Thin-film hydrides prepared by vacuum sputtering (2 types):

- Transition Metal based alloys-
  Typical capacities $\leq$ 3 wt.% H
  Desorption temperatures $\approx$ 0°C

- Mg-based alloys-
  Typical capacities: 4-7 wt.% H
  Desorption temperatures $\geq$ 200°C

The thin-films were designed to have the following properties:

- Non-equilbrium, non-stoichiometric configuration
- Amorphous/Highly Disordered
- Multi-component ($\geq$3 elements selectively chosen)
- Multi-phase
- Long Cycle Life
- High Tolerance to Contaminants
- High Hydrogen Storage Capacity
- Rapid Kinetics

2.5 Program Goals

To develop superior bulk form metal hydrides having the following properties:

- **Low Cost**
- **> 4 wt. % Hydrogen Storage Capacity (delivered)**
- **High degree of reversibility**
- **Rapid Kinetics at < 150°C**
- **Ease of Scale-up**
- **High tolerance to impurities**

3. APPROACH

Development of Improved Metal Hydride Technology:

A. Process

B. Alloy Composition

C. Subsystem Engineering

D. Business Development

3.1 APPROACH A: PROCESS DEVELOPMENT

Challenge-

The overall challenge has been to develop a bulk processing technique that will allow the preparation of Mg-based, highly disordered, multi-component alloys and to reproduce ECD's thin-film work. This technique should then allow for tailoring of the alloy structure and composition to optimize for the desired properties as stated in our goals.

Problem-

- Difficult to prepare Mg/Transtion metal alloys by conventional methods
- Vapor pressure differentials between Mg and desired alloying elements
- Lack of solid solution formation

3.2 APPROACH B: ALLOY COMPOSITION

For further optimization beyond the thin-film results:

- **Low alloy cost**
- **4 wt.% hydrogen storage capacity (delivered)**
- **Lower desorption temperatures**
- **Effective pressure ~ 1 atmosphere**

3.2 APPROACH B: ALLOY COMPOSITION

General Hydride Design

$$2M + H_2 \Leftrightarrow 2MH + \text{Heat } (\Delta H)$$

Two steps: (i) $$H_2 \Rightarrow 2H$$

(ii) $$M + 2H \Rightarrow 2MH + \text{Heat } (\Delta H)$$

Need: (i) many catalytic H_2 dissociation sites

(ii) many M-H bond formation sites

For high weight percent H-storage limited choice of elements:	→	need a low weight hydride former examples- Mg; Al; C; and Si
For increased catalytic activity	→	selective incorporation of transition metals and/or rare earth metals for H_2 dissociation
For low temperature desorption	→	incorporate structural features and modifier elements to form weak **M-H** bonds

Additionally alloys should be amorphous,, multi-phase, multi-component materials with a high degree of disorder (preferably amorphous). These features have shown to increase the H-storage capacity, kinetics, resistance to impurities and cycle life.

3.3 APPROACH C: SUBSYSTEM ENGINEERING

- Storage Vessel Design for optimum cost/performance
- Heat Management
- Determine Total System Energy Density as compared to hydride (alloy) energy density

3.4 APPROACH D: BUSINESS DEVELOPMENT

- Economics of scale-up/production
- Mobile versus Stationary systems
- Partnering - Formation of Strategic Alliances
  (joint ventures, liscensing, consortiums, . . .)
- Possible Partners:
  - Auto companies
  - Fuel cell manufactures
  - Hydrogen producers
  - Chemical companies (producers of large amounts of Mg, etc.)

4. KEY RESULTS/EXPERIMENTAL TECHNIQUES

Process

a) **Induction melting/Encapsulation**

b) **Two-Zone Induction melting**

c) **Modified Mechanical Alloying**

Subsystem Engineering

4.1 KEY RESULTS: PROCESS a) Induction melting/Encapsulation

Scheme I: Sample pellet wrapped in Fe foil.

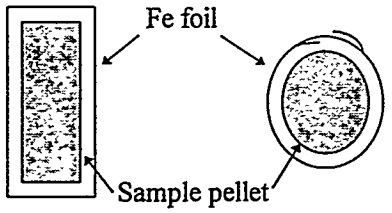

Scheme II: Fe foil wrapped granules wrapped in Ta foil

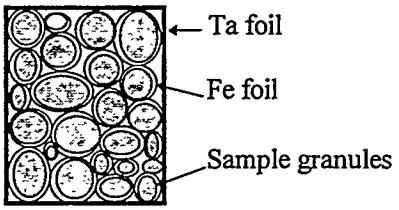

Scheme III: Mg/Mg-alloy covered with modifier powders

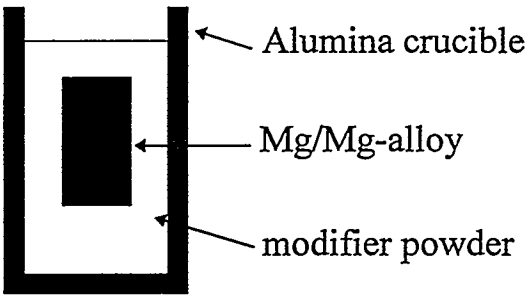

Scheme IV: Sealed stainless steel tubes

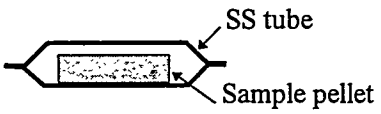

Figure 1- Encapsulation Schemes

4.2 KEY RESULTS: PROCESS b) Two-Zone Induction melting

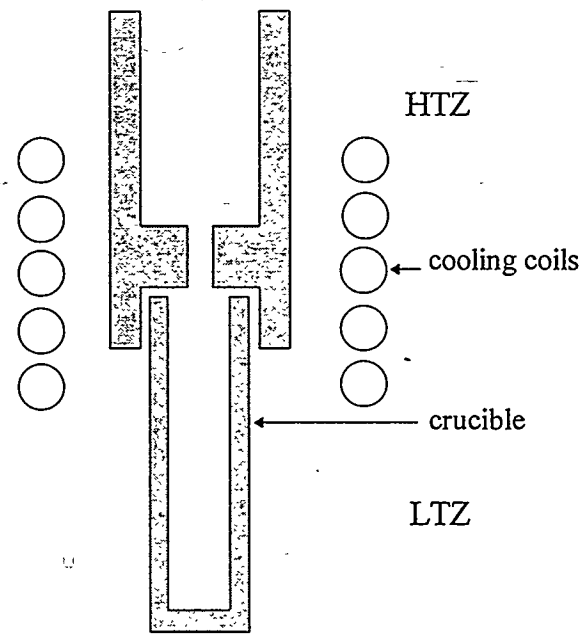

Figure 2: ECD's Novel Two-Zone induction melting

Two-zone induction melting-

- volatile reactants melted in low temperature zone (LTZ)
- non-volatile reactants melted in high temperature zone (HTZ)
- reaction between two liquid metals in LTZ

4.2 KEY RESULTS: PROCESS b) Two-Zone Induction melting

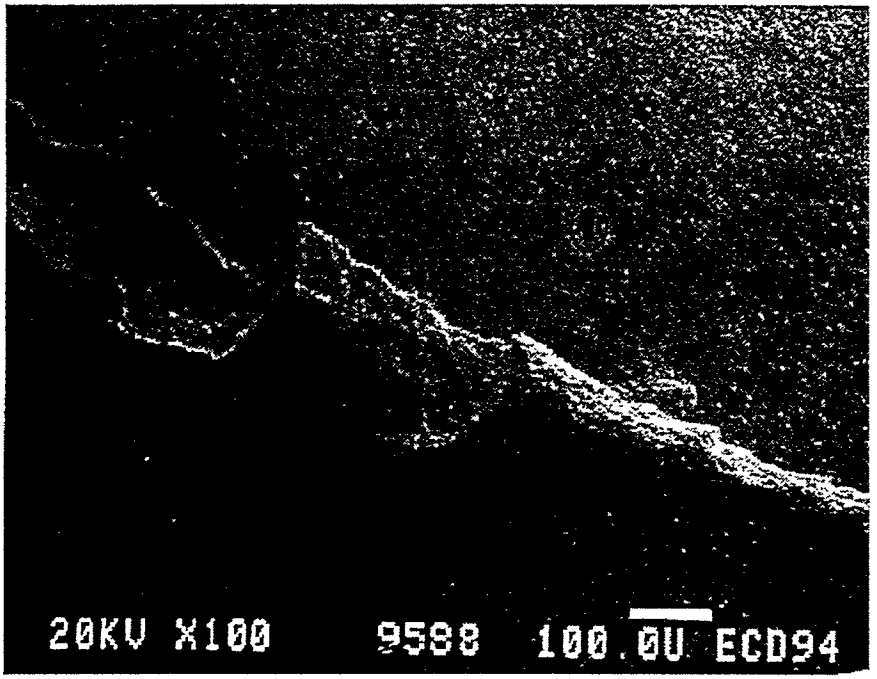

Figure 3a- Reaction interface of Two-Zone induction melt product.

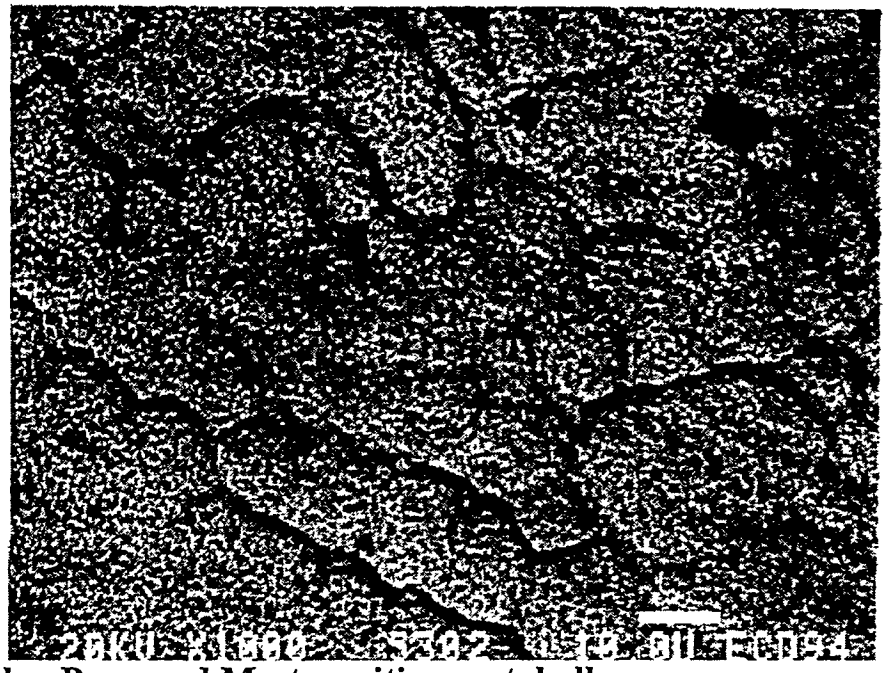

Figure 3b- Prepared Mg-transition metal alloy.

4.3 KEY RESULTS: PROCESS c) Mechanical Alloying

Mechanical Alloying is effected by the mixing, deformation and fusion of metal powders between colliding media.

Advantages:

No melting	**-**	**Vapor point differentials unimportant**
Powdered products-		**No pulverization step needed**

4.3 KEY RESULTS: PROCESS c) Effect of Processing Parameters

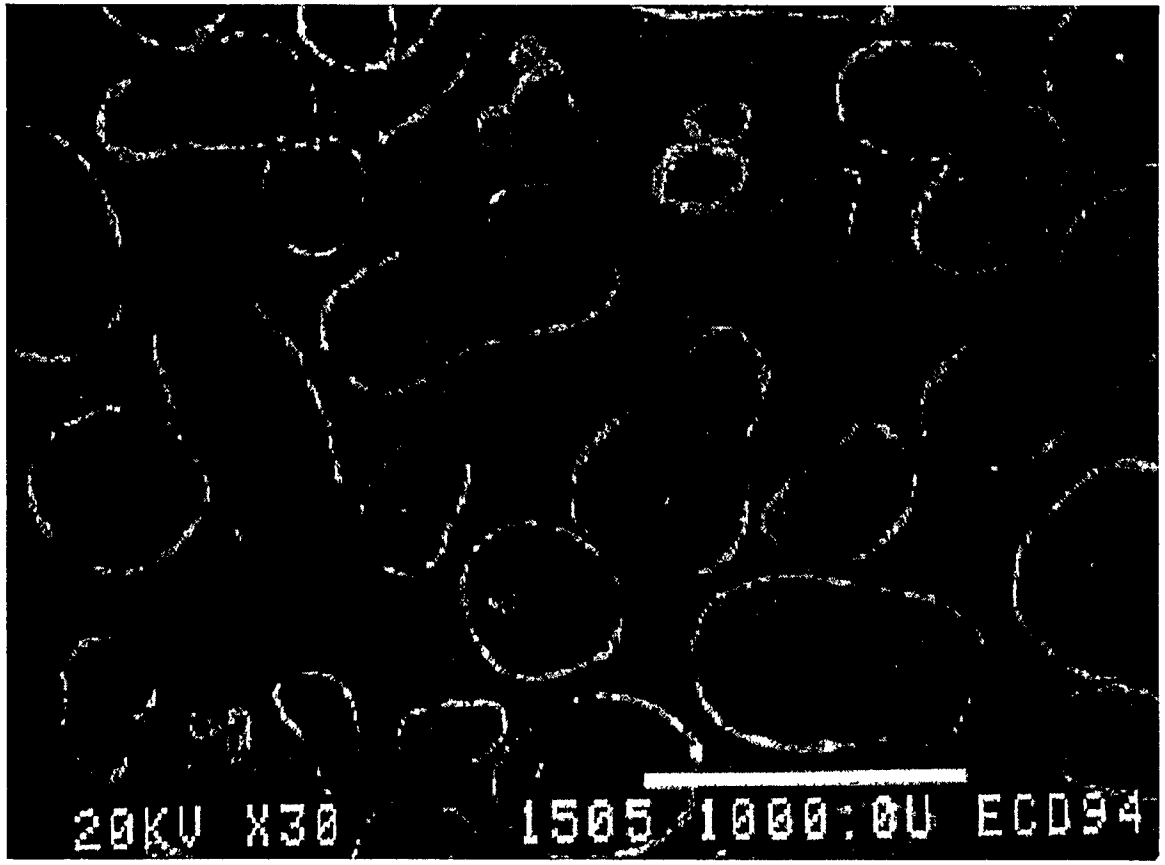

Figure 4- Mg-based storage alloy particle with a catalytic coating.

4.3 KEY RESULTS: PROCESS c) Effect of Processing Parameters

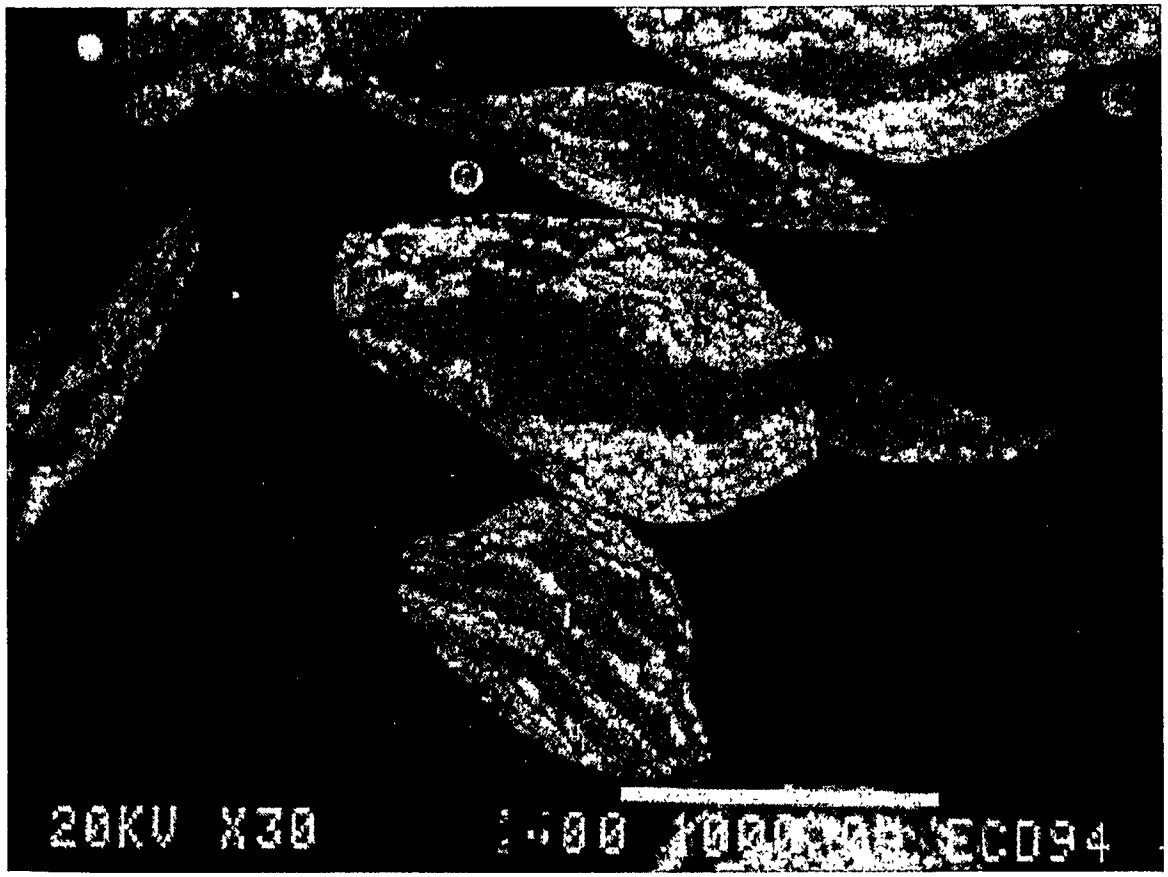

Figure 5- layered Mg-based storage alloy - catalytic phase particle

4.3 KEY RESULTS: Effect of Structure

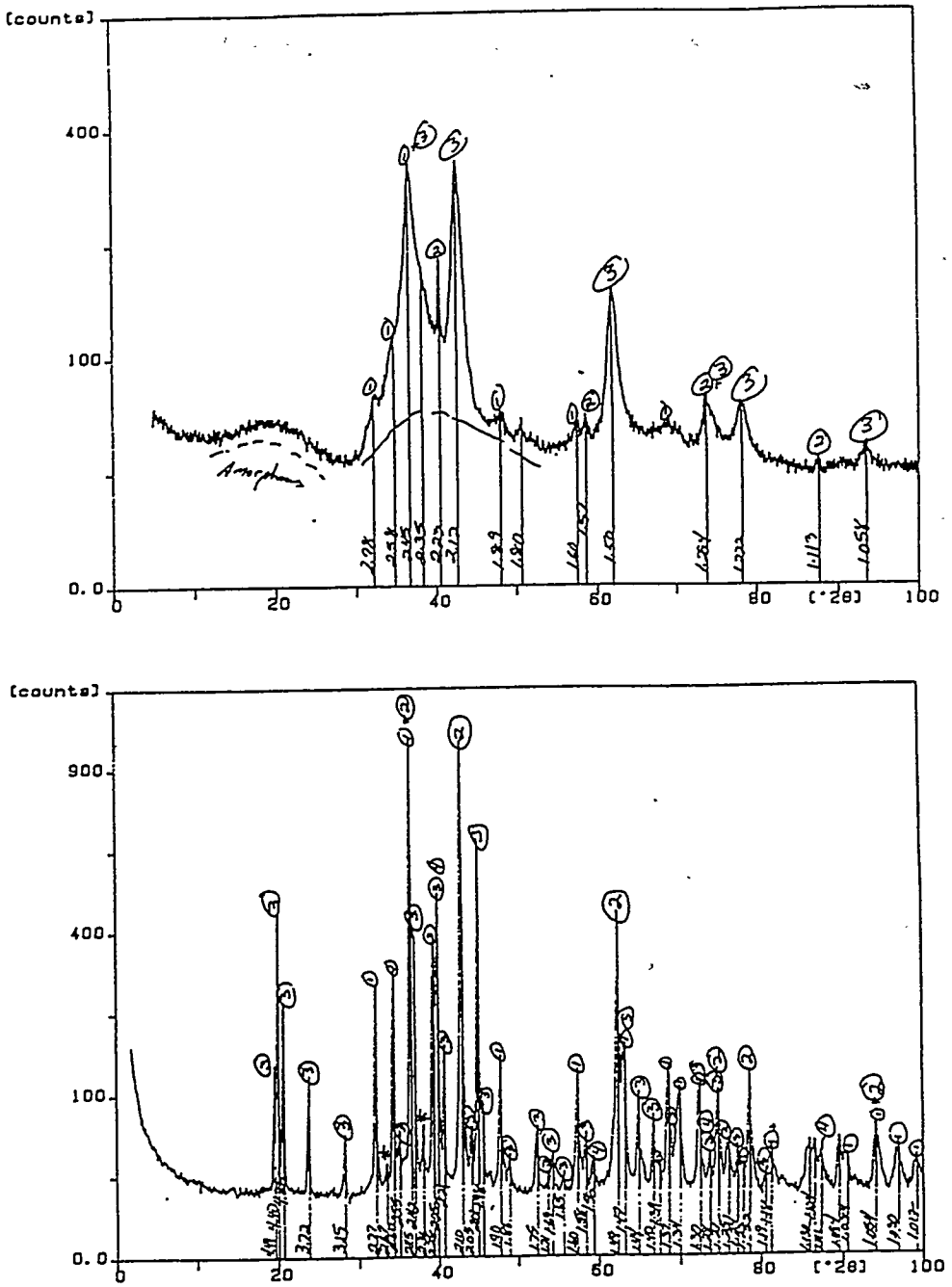

Figure 7 a & b- X-ray Diffraction patterns Mechanically alloyed sample before and after annealling.

4.3 KEY RESULTS: Effect of Processing Parameters

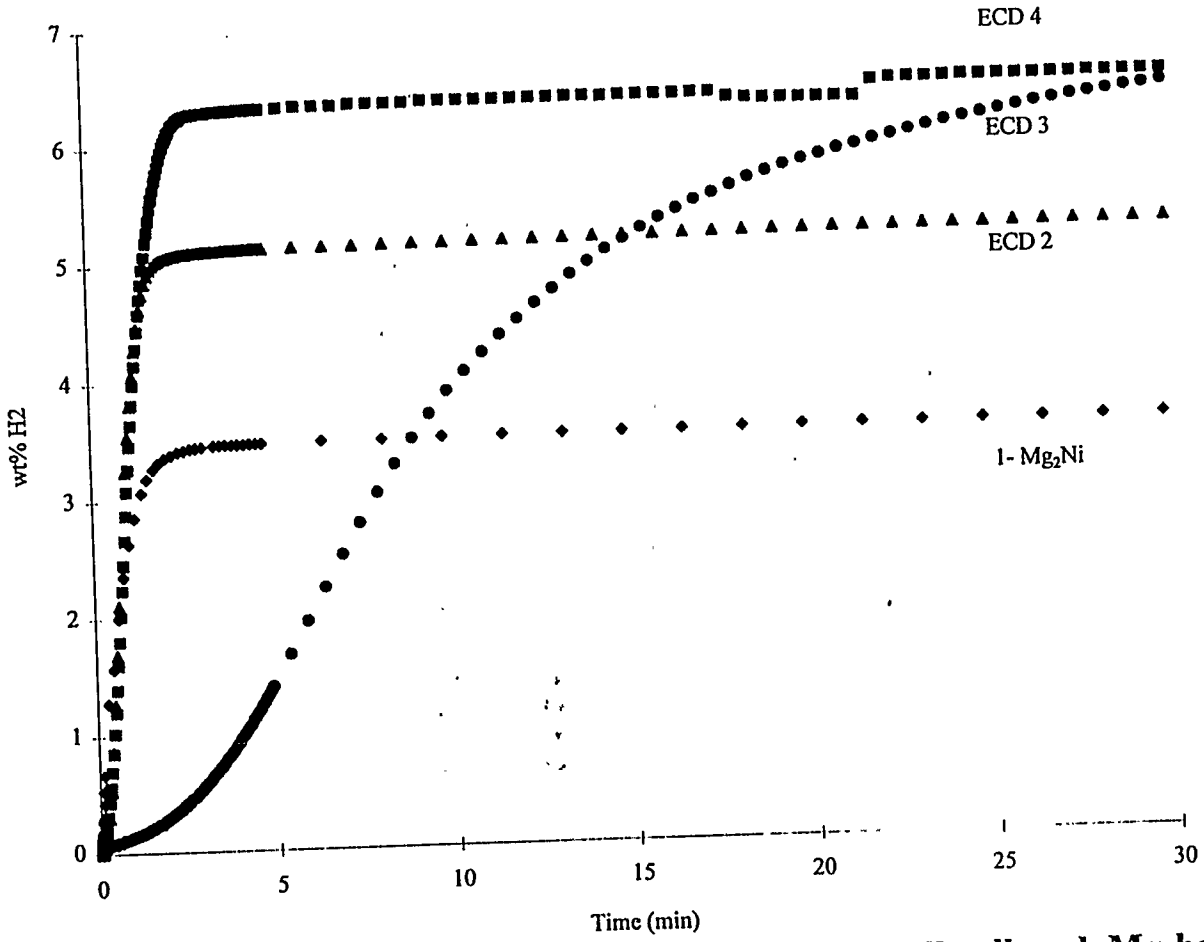

Figure 6a- Desorption kinetics of some ECD developed, mechanically alloyed, Mg-based alloys (350°C).

4.3 KEY RESULTS: Effect of Processing Parameters

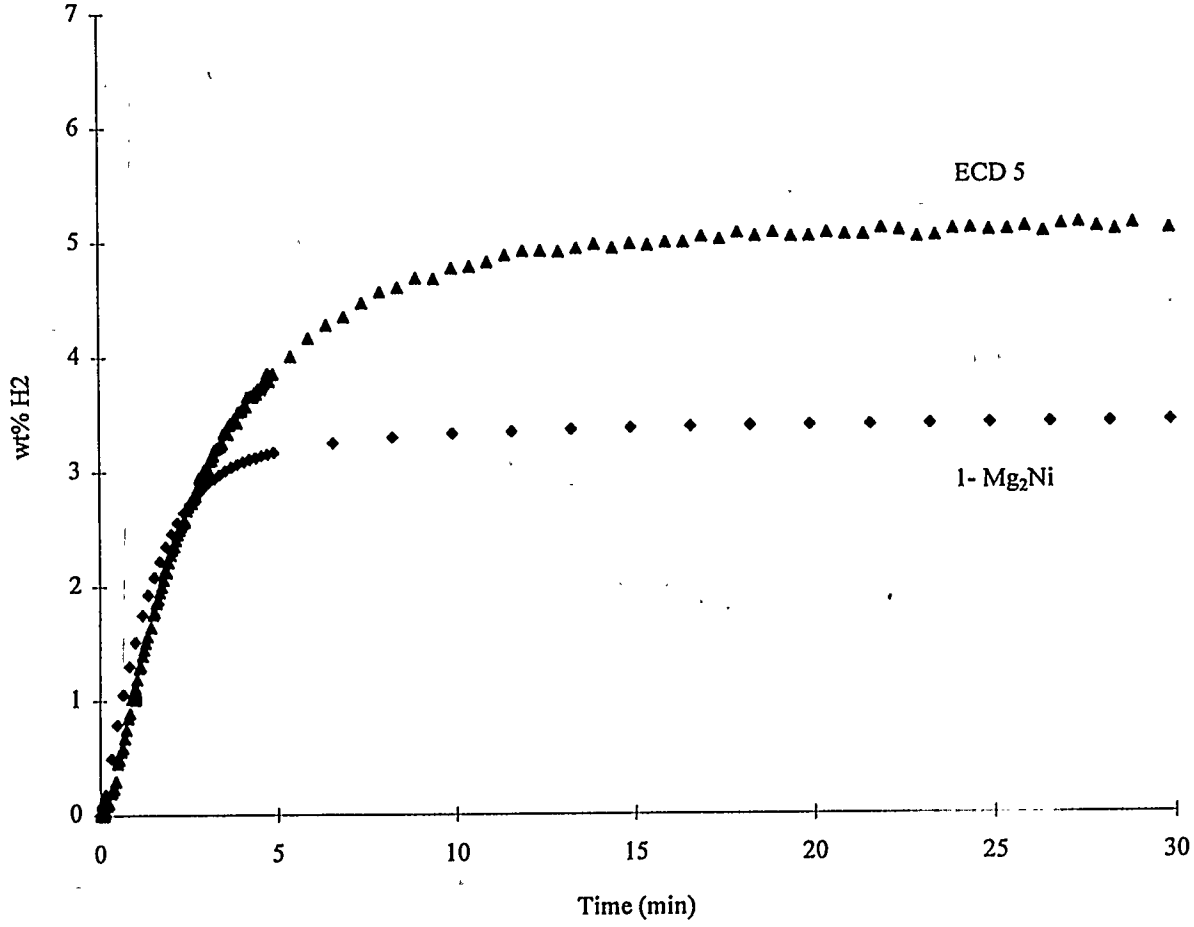

Figure 6b- Desorption kinetics of an ECD developed, mechanically alloyed, Mg-based alloy and Mg_2Ni (300°C).

4.3 KEY RESULTS: Effect of Cycling

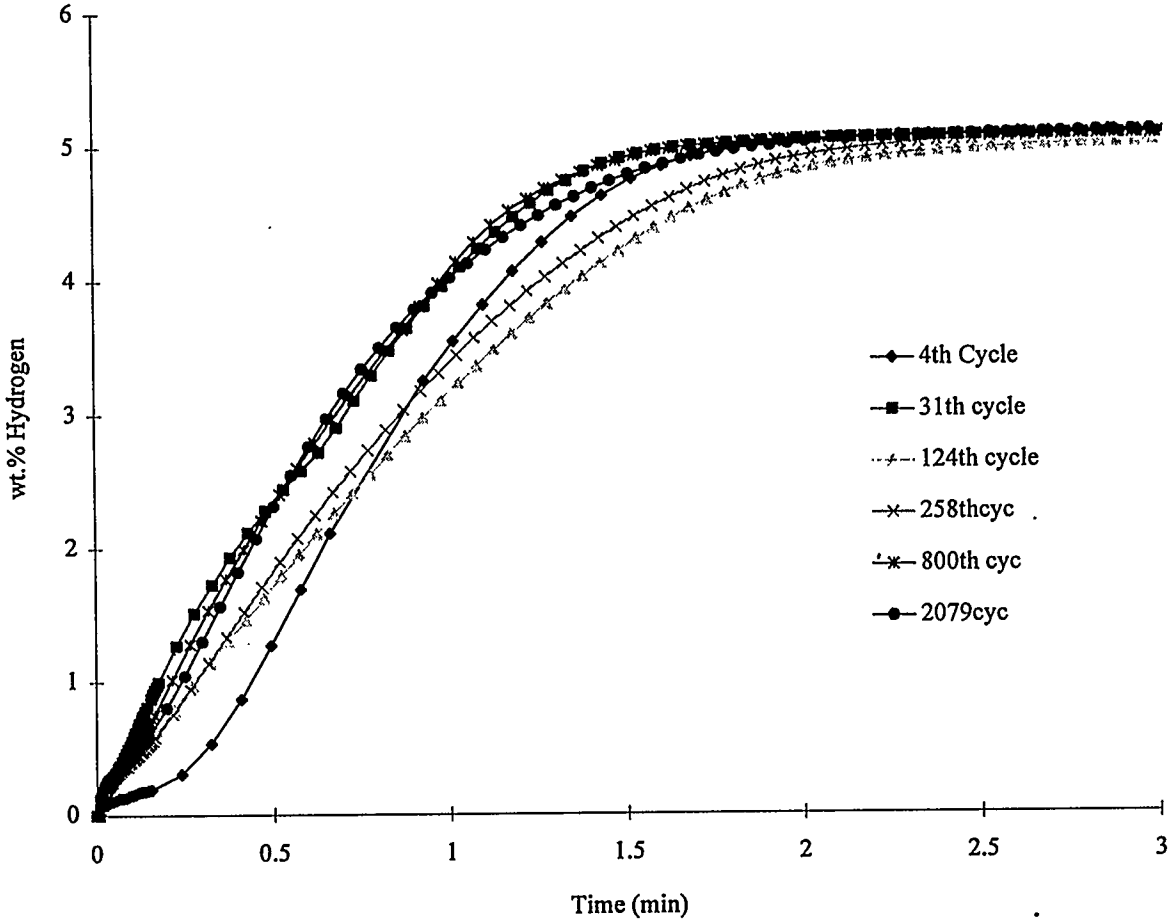

Figure 8- Desorption Kinetics of a Mechanical Alloyed sample after various numbers of cycles (350°C).

4.3 KEY RESULTS: Effect of Contaminants

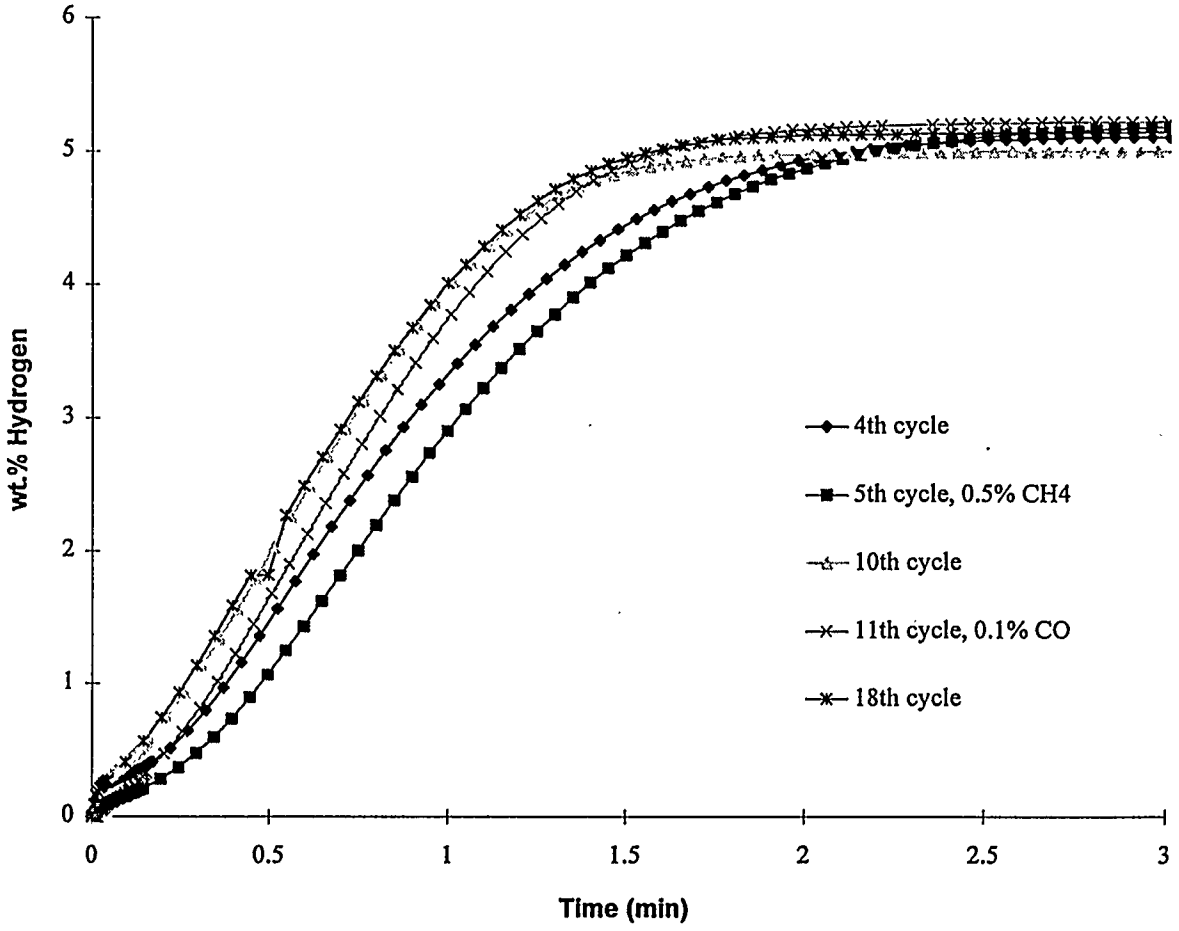

Figure 9- Desorption Kinetics of a Mechanically Alloyed sample after exposure to 0.1% CO and 0.5% CH_4 (350°C).

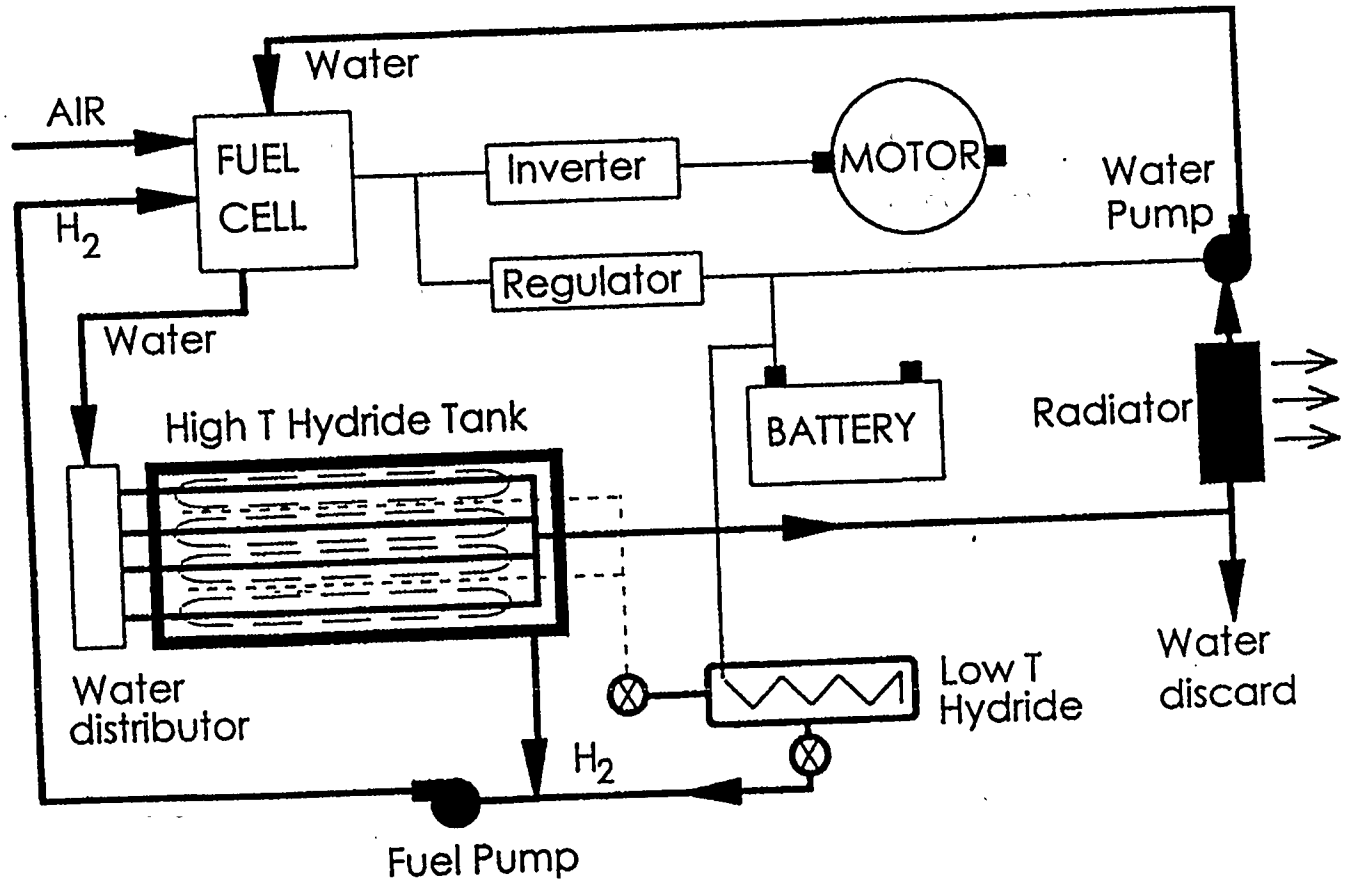

Figure 10- Preliminary design schematic developed in collaboration with the University of Michigan and Engineering Consultants of Chicago.

4.5 Summary of Key Results

We have developed a low-cost, easily scaleable process to make bulk alloys for hydrogen storage that have the following features:

- **High storage capacity- > 5 wt. % delivered**
- **Multi-component**
- **Multi-phase**
- **Amorphous / highly disordered**
- **Control of surface and bulk morphology/composition**
- **long cycle life (tested for over 2000 cycles)**
- **resistance to contaminants**
- **developed preliminary analytical model and schematic of metal hydride fuel system**
- **low alloy cost**
- **low process cost**

5. DEFINITION OF SUCCESS

The Important Challenges of "Phase I" work:

- **development of a low cost technique for the bulk production of Mg-based, high H-storage capacity alloys**
- **demonstrate feasibility of scale-up from thin-film to powders**
- **characterization of novel Mg-based alloys**

Important Milestones Achieved:

- **> 4wt. % Hydrogen storage**
- **scale-up**

5. DEFINITION OF SUCCESS

As presented at the DOE Hydrogen Program Review meeting, April, 1994:	Goal Achieved 1995
1. Can the Mg-based alloys be scaled up from thin film to bulk for mass production?	√
2. Can these alloys retain at least some of the properties obtained in thin-film form?	√
3. Can the properties be further improved upon alloy modification?	√
4. Can the alloys be prepared by low-cost (at least semi-conventional) manufacturing processes?	√
5. Can we enhance the understanding of the science and technology of metal hydrides by systematic study of the relationship between desired alloy properties and factors influencing these properties,, such as preparation methods, microstructure, composition and morphology of the alloys?	√

6. PROPOSED FUTURE WORK

- **Process Optimization:**

  Focus on mechanical alloying scale-up from 20 gram to 1 lb. batch

- **Alloy Optimization:**

  Focus on one family of alloys
  - **use selective modifiers**

- **Alloy Characterization:**

  On-going process. Helps develop the scientific basis of the results achieved

- **Analytical Modeling / Engineering Design:**

  Towards prototype, heat management

- **Fabrication & Testing of Laboratory Prototype / Storage System**

- **Economical Feasibility Study for Mobile and Stationary Utilization:**

  Identify early niche markets

  Mobile versus stationary applications

  Develop estimates of volumetric & gravimetric energy density of the total storage system

7. TECHNOLOGY TRANSFER

1. University of Michigan - modeling
2. Engineering Consultants of Chicago - engineering design
3. Visited one equipment manufacturer - discussed scale-up and equipment modification will develop complete economic model of production
4. Initial discussion with one French Automobile manufacturer interested in hydrogen storage for PEM fuel cell demonstration vehicle
5. Initiated discussion with one member of USCAR. Obtained fuel storage goals for PNGV.
6. Patent application has been filed with the US Patent office on the novel alloys.
7. Patent application for the modified MA process will be filed.

During proposed "Phase II" work, we will:

- continue previous collaborations
- develop strategic alliances for the commercialization of the technology

POLYHYDRIDE COMPLEXES FOR HYDROGEN STORAGE

Craig M. Jensen
Department of Chemistry
University of Hawaii
Honolulu, HI 96822

Abstract

Polyhydride metal complexes are being developed for application in hydrogen storage. Efforts have focused on developing complexes with improved available hydrogen weight percentages. We have explored the possibility that complexes containing aromatic hydrocarbon ligands could store hydrogen at both the metal center and in the ligands. We have synthesized novel indenyl hydride complexes and explored their reactivity with hydrogen. The reversible hydrogenation of $[IrH_3(PPh_3)(\eta^5\text{-}C_{10}H_7)]^+$ has been achieved. While attempting to prepare η^6-tetrahydronaphthalene complexes, we discovered that certain polyhydride complexes catalyze both the hydrogenation and dehydrogenation of tetrahydronaphthalene.

Introduction

A major concern in the development of hydrogen as a fuel is the problem of hydrogen storage. Solid hydrogen storage systems based on metal hydrides are safer and require far less volume than either high-pressure or cryogenic storage systems. However, hydrides of metals and alloys, which reversibly release hydrogen at adequate rates, contain too low hydrogen weight percentages for the realization of hydrogen as an energy carrier. In our laboratory, we are developing nonclassical polyhydride metal complexes as hydrogen storage materials. We have demonstrated that this class of materials can be tailored to reversibly release hydrogen over a wide range of rates and temperatures (Mediati et al. 1990, 1992; Le-Husebo and Jensen 1993). We have focused our recent efforts on developing complexes with improved available hydrogen weight percentages.

One of the most common reactions mediated by transition metal complexes is the addition of H_2 to an alkene to form an alkane as seen in Scheme 1 (Crabtree 1994).

Scheme 1.

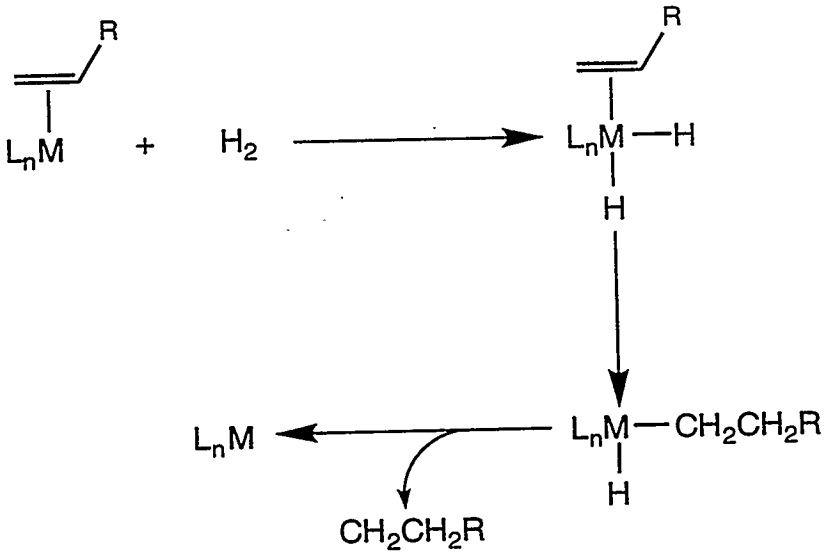

Hydrogenation of coordinated aromatic hydrocarbons is less common but has been reported for a catalytic system in which $(\eta^3\text{-}CH_2CHCH_2)Co\{P(OMe)_3\}_3$ is the catalyst precursor (Muetterties and Hirsekorn 1974; Hirsekorn et al. 1975). Recently, there have been several reports of transition metal complexes which catalyze the microreverse of Scheme 1, alkane dehydrogenation (Felkin et al. 1985; Burk and Crabtree 1987; Maguire et al. 1992; Fujii et al. 1993). The reported dehydrogenation of $[(\eta^6\text{-}C_9H_{10})Ir(PPh_3)_2]^+$ to $[(\eta^5\text{-}C_9H_7)]IrH(PPh_3)^+$ (Equation 1) provides a precedent which involves the conversion of an indan ligand into an indenyl ligand (Crabtree and Parnell 1984). Thus, it is not unreasonable to envision the reversible hydrogenation of an aromatic hydrocarbon ligand such as indenyl, C_9H_7-.

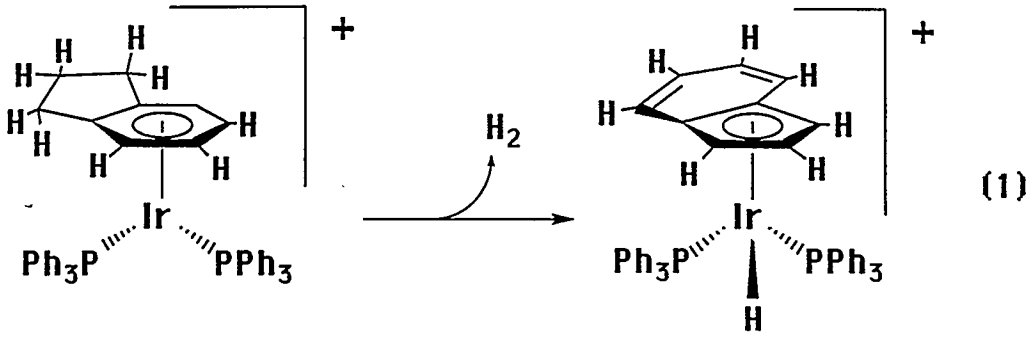

During the past year, we have explored the possibility that complexes containing aromatic hydrocarbon ligands could store hydrogen at both the metal center and in the hydrocarbon ligands. We have synthesized a variety of novel complexes containing indenyl (C_9H_7-) ligands and explored their reactivity with hydrogen.

Results

Syntheses of Indenyl Complexes

The complexes (η^5-$C_{10}H_7$)FeH(PMe_3), **1**, (Green et al. 1987); (η^5-$C_{10}H_7$)CoL_2 (L = PMe_3, **2**, PPh_3, **3**) (Huffman et al. 1992; Werner et al. 1989); and (η^5-C_9H_7)Ir(C_2H_4)$_2$, **4** (Abad 1986) were synthesized by literature methods. The iridium complexes, [(η^5-C_9H_7)$IrH_3(PPh_3)$]$^+$, **5**, and (η^5-C_9H_7)$IrH_3(PPr^{i}_3)$, **6**, (Husebo and Jensen 1995) were synthesized, as seen in Equations 2 and 3, respectively.

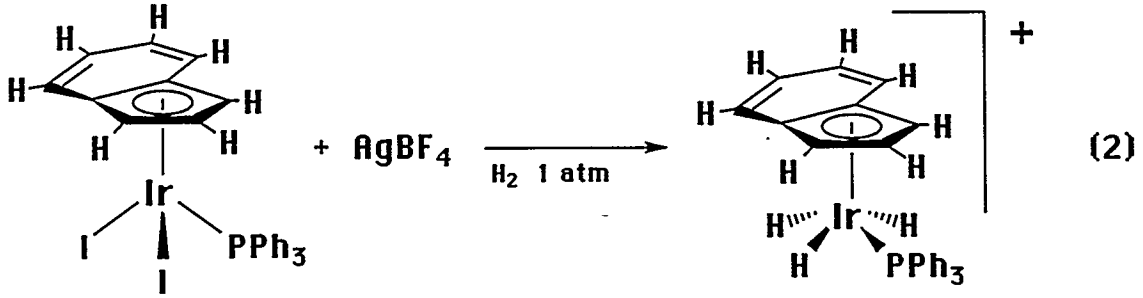

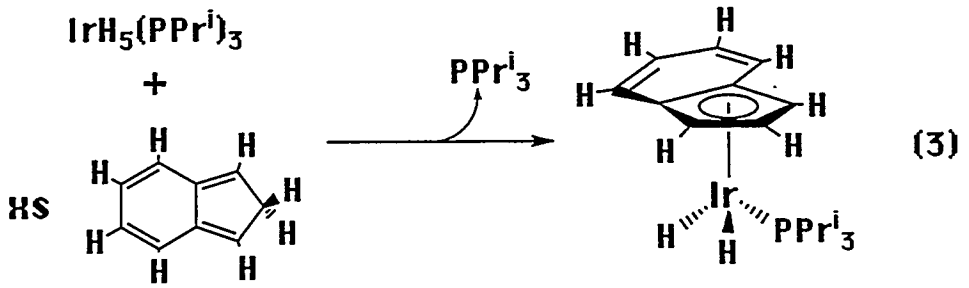

Reactivity of Iron and Cobalt Complexes with H_2

The indenyl iron complex, **1**, was unreactive with 1 atm hydrogen to its decomposition temperature of 80° C. The cobalt complexes, **2** and **3**, were found to be reactive with H_2 at very mild conditions (1.5 atm, 25° C). However, addition of H_2 to the cobalt center results in the reductive elimination of indene and subsequent production of $CoHL_3$, as seen in Equation 4.

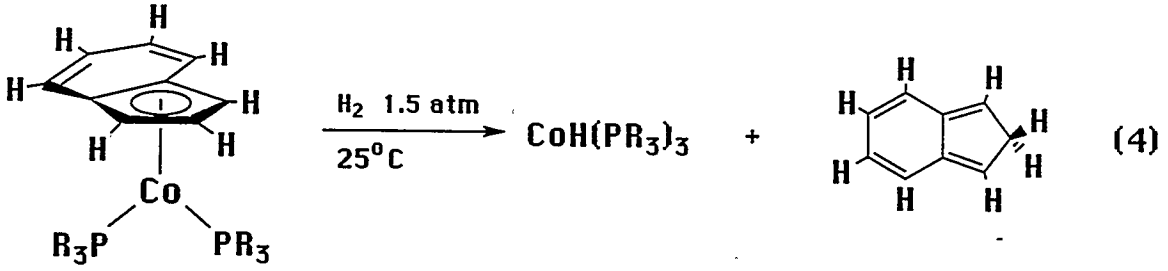

(4)

Reversible Hydrogenation Indenyl Complexes

Complex **6** reacts with H_2 to give a complicated mixture of unidentified products. This stands in contrast to **4** and **5**, which can be hydrogenated cleanly to $(\eta^5\text{-}C_9H_{11})Ir(C_2H_4)_2$ and $[(\eta^5\text{-}C_9H_{11})IrH_3(PPh_3)]^+$, respectively, as seen in Equations 5 and 6.

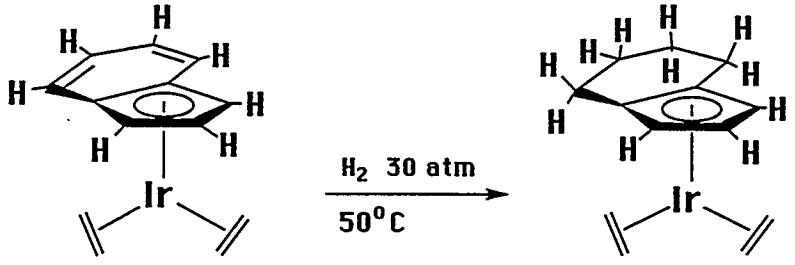

(5)

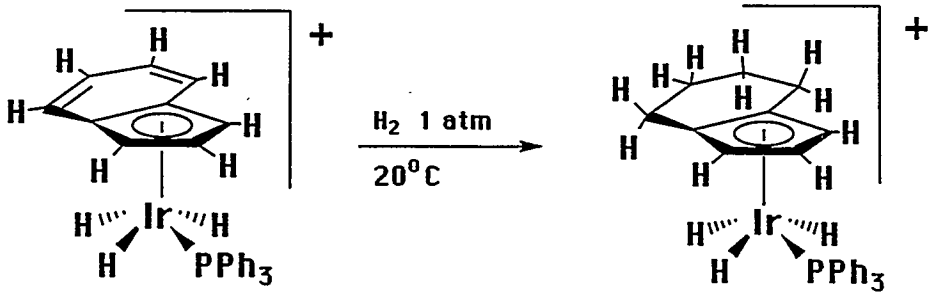

(6)

However, traces of colloidal metal were found to be responsible for the hydrogenation of the ligands in these reactions and thus H_2 does not coordinate to the complex metal center prior to ligand hydrogenation. We have subsequently found that under milder conditions, **5** is hydrogenated to an indan complex $[(\eta^6\text{-}C_9H_{10})IrH_2(PPh_3)]^+$, as seen in Equation 7. This lower temperature hydrogenation does seem to involve prior coordination of H_2 at the metal center.

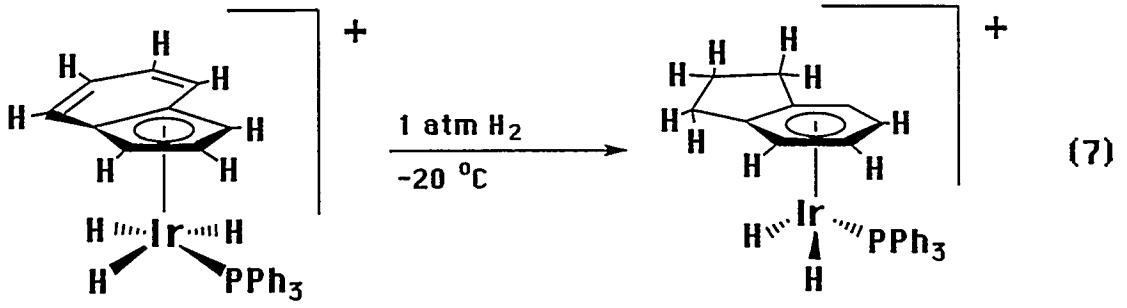

(7)

As seen in Equation 8, this process can be reversed at 60° C under 1atm of argon in the presence of the hydrogen acceptor, t-butylethylene.

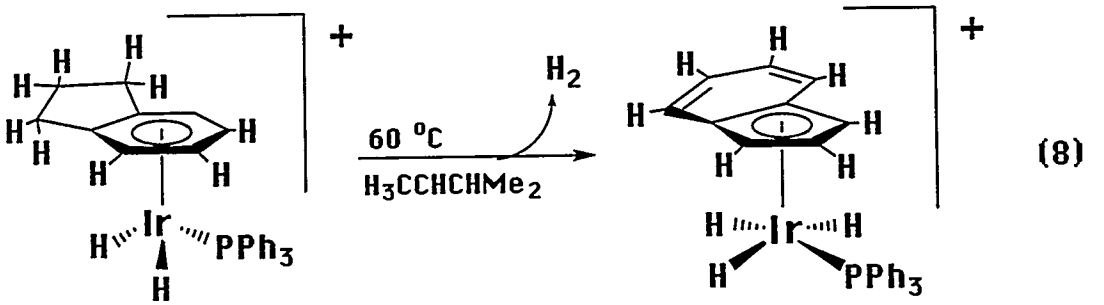

(8)

Catalytic Dehydrogenation/Hydrogenation of Tetrahydronaphthalene

We were encouraged by the discovery of an indenyl complex which can be hydrogenated and subsequently dehydrogenated. However, this system does not release free H_2. In search of a system in which ligand dehydrogenation would occur in the absence of an additional hydrogen acceptor component, we sought to explore the reactivity of related naphthalene complexes. While attempting to prepare an η^6-tetrahydronaphthalene complex from the reaction of a certain polyhydride complex and tetrahydronaphthalene, we instead obtained a mixture of naphthalene, tetrahydronaphthalene,

octahydronaphthalene, and decahydronaphthalene (decalin) along with the original complex as seen in Equation 9. This redistribution of hydrogen is apparently due to the polyhydride complex catalyzing both dehydrogenation and hydrogenation of tetrahydronaphthalene.

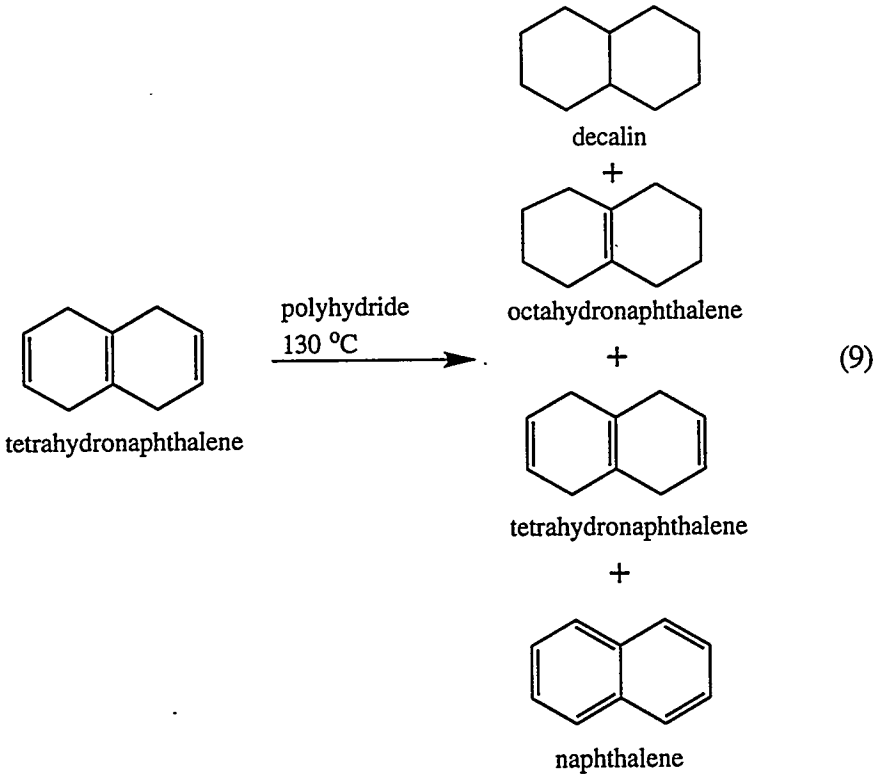

(9)

Future Directions

Reversible dehydrogenation of methylcyclohexane to toluene in the presence of platinum group metals, as seen in Equation 10, has been explored as a method of hydrogen storage.

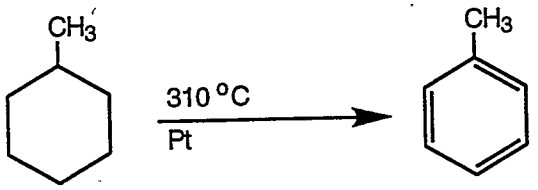

(10)

However, dehydrogenation occurs in these systems only at temperatures in excess of 300° C. This drastic energetic requirement has precluded such systems from consideration as practical methods for storing hydrogen as a fuel. We found polyhydride catalyze dehydrogenation and hydrogenation of tetrahydronaphthalene under relative mild conditions. The equilibrium distribution of naphthalene, tetrahydronaphthalene, octahydronaphthalene, and decalin should depend on the pressure of hydrogen above the system. Charging such a system with a moderate over-presssure of H_2 should shift the system greatly in favor of octahydronaphthalene and decalin. Release of H_2 from the system should shift the system to tetrahydronaphthalene and naphthalene. Thus, this system may represent the basis for a system in which >7 weight percent of hydrogen can be stored and retrieved under mild conditions.

We plan to explore the hydrogen storage potential of this system. We will first examine the equilibrium distribution of bicyclic organics which result at various partial pressures of hydrogen. We will then determine the rate of hydrogen redistribution reactions. These studies will be repeated with the polyhydride complexes showing hydrogenation/dehydrogenation activity with hydronaphthalenes.

We also plan to extend our survey of complexes containing aromatic hydrocarbon ligands. We will continue to elucidate the fundamental chemistry of their reactions with hydrogen and evaluate their hydrogen storage potential.

References

Abad, J.A. 1986. *Inorg. Chim. Acta*, 121:213.

Burk, M.J., and R.H. Crabtree. 1987. *J. Am. Chem. Soc.*, 109:8025, and references therein.

Crabtree, R.H., and C.P. Parnell. 1984. *Organometallics*, 3:1727.

Crabtree, R.H. 1994. *The Organometallic Chemistry of the Transition Metals* (2nd Edition). New York: John Wiley & Sons, p. 206-215.

Felkin, H., T. Fillebeen-Khan, R. Holmes-Smith, and Y. Lin. 1985. *Tetrahedron Letters*, 26:1999, and references therein.

Fujii, T., Y. Higashino, and Y. Saito. 1993. *J.C.S. Dalton Trans.*, 517.

Green, M.L.H., D. O'Hare, and L.L. Wong. 1987 *J.C.S. Dalton Trans.*, 2131.

Hirsekorn, F.J., M.C. Rakowski, and E.L. Muetterties. 1975. *J. Am. .Chem. Soc.*, 97:237.

Huffman, M.A., L.S. Libeskind, and W.T. Pennington. 1992.*Organometallics* , 11:255.

Husebo, T.L., and C.M. Jensen. 1995. *Organometallics*, 14:1087.

Le-Husebo, T., and C.M. Jensen. 1993. *Inorg. Chem.*, 31:3.

Maguire, J.A., A. Petrillo, and A.S. Goldman. 1992. *J. Am. Chem. Soc.*, 114:9492.

Mediati, M., G.N. Tachibana, and C.M. Jensen. 1990. *Inorg. Chem.*, 29:3.

Mediati, M., G.N. Tachibana, and C.M. Jensen. 1992. *Inorg. Chem.*, 31:1827.

Muetterties, E.L., and F.J. Hirsekorn. 1974. *J. Am. Chem. Soc.*, 96:4063.

Werner, H, J. Mahr, and G. Horlin. 1989. *Z. Anorg. Allg. Chem.*, 577:283.

HIGH EFFICIENCY STATIONARY HYDROGEN STORAGE

Scott Hynek
Ware Fuller
Sam Truslow
Arthur D. Little, Inc.
Cambridge, MA 02140

Abstract

Stationary storage of hydrogen permits one to make hydrogen now and use it later. With stationary hydrogen storage, one can use excess electrical generation capacity to power an electrolyzer, and store the resultant hydrogen for later use or transshipment. One can also use stationary hydrogen as a buffer at fueling stations to accommodate non-steady fueling demand, thus permitting the hydrogen supply system (e.g., methane reformer or electrolyzer) to be sized to meet the average, rather than the peak, demand.

We at ADL designed, built, and tested a stationary hydrogen storage device that thermally couples a high-temperature metal hydride to a phase change material (PCM). The PCM captures and stores the heat of the hydriding reaction as its own heat of fusion (that is, it melts), and subsequently returns that heat of fusion (by freezing) to facilitate the dehydriding reaction. Only a modest pressure swing is necessary to accomplish the storage/retrieval cycle. That modest pressure swing, plus another modest pressure swing to reflect the hysteresis that differentiates hydriding and dehydriding, plus thermal losses through the insulation surrounding the device, are the only energy losses suffered by this device.

A key component of this stationary hydrogen storage device is the metal hydride itself. We used nickel-coated magnesium powder (NCMP) – magnesium particles coated with a thin layer of nickel by means of chemical vapor deposition (CVD). Magnesium hydride can store a higher weight fraction of hydrogen than any other practical metal hydride, and it is less expensive than any other

metal hydride.

We designed and constructed an experimental NCMP/PCM reactor out of 310 stainless steel in the form of a shell-and-tube heat exchanger, with the tube side packed with NCMP and the shell side filled with a eutectic mixture of NaCl, KCl, and $MgCl_2$. We tested this reactor in ADL's Hydrogen Storage Test Facility, successfully, under conditions simulating a hydrogen storage/discharge cycle. Our experimental results indicate that with proper attention to limiting thermal losses, our overall efficiency will exceed 90% (DOE goal: >75%) and our overall system cost will be only 33% (DOE goal: <50%) of the value of the delivered hydrogen.

It appears that NCMP can be made to resist poisoning from impurities in the hydrogen being stored, which can be significant in hydrogen created by reforming natural gas. It further appears that NCMP can be used to purify hydrogen streams and store hydrogen at the same time. These prospects make the NCMP/PCM reactor a very attractive component in a reformer-based hydrogen fueling station.

Introduction

Need for Stationary Hydrogen Storage

Stationary storage of hydrogen permits one to make hydrogen now and use it later. With stationary hydrogen storage, one can use excess electrical generation capacity to power an electrolyzer, and store the resultant hydrogen for later use or transshipment. This excess electrical generating capacity could be intermittent in nature, as is generally the case with renewable energy sources (e.g., wind turbines, photovoltaics). The excess generating capacity could also be periodic, as is the case with central station power plants operating at off-peak hours.

One can also use stationary hydrogen storage as a buffer at fueling stations to accommodate non-steady fueling demand, thus permitting the hydrogen supply system (e.g., methane reformer or electrolyzer) to be sized to meet the average, rather than the peak, demand. It is estimated (Ogden, 1994) that the natural gas reformer for a 300 vehicle/day hydrogen fueling station, sized to meet the average fueling demand, will cost $2,200,000, and that a natural gas reformer sized to meet the peak fueling demand would cost $3,000,000. Thus, $800,000 can justifiably be spent on stationary hydrogen storage in a 300 vehicle/day fueling station.

Description of Metal Hydride/Phase Change Material Concept

Today, most stationary hydrogen is stored as liquid. If the hydrogen must be liquefied for shipment, or will be used as a liquid (e.g., the space shuttle), then the high energy cost of hydrogen liquefaction (roughly 30% of its higher heating value) can be justified - it has already been paid. However, liquefying a gaseous hydrogen feedstream to store that hydrogen in order to satisfy an eventual demand for gaseous hydrogen is needlessly expensive and inefficient.

Storing hydrogen as a compressed gas requires substantial work of compression, unless the pressure is kept low; but low-pressure tankage is voluminous indeed. Higher storage pressures reduce the volume of tankage, but at the cost of greater work of compression.

There is one other technology currently used to store hydrogen: metal hydrides. Figure 1 presents a van't Hoff plot that serves to

1. Describe the equilibrium pressure-temperature characteristics of certain metal hydrides,

2. Distinguish between high-temperature metal hydrides (those grouped on the left-hand side) and low-temperature metal hydrides (those grouped on the right-hand side), and

3. Indicate why magnesium hydride has been dismissed by developers of vehicular storage systems: the discharging of high-temperature metal hydrides requires higher-temperature heat than vehicular fuel cells generate, and one cannot afford to use anything but "free" heat to discharge the hydrogen (the heat required represents 30% of the hydrogen's higher heating value).

However, if one can store the heat given off during the charging (hydriding) of a high-temperature metal hydride, and re-use that energy during discharging (dehydriding), then one can take advantage of the relatively higher gravimetric and volumetric densities of high-temperature metal hydrides (relative to low-temperature metal hydrides) and of the relatively low cost of the metals from which high-temperature metal hydrides are made. Figure 2 suggests how this heat can be stored, using a bed of phase change material (PCM).

The PCM could be any of a number of salts, or mixtures of salts, that melt at the temperature corresponding to the pressure at which one wants to operate the hydride storage bed. For our experimental demonstration system, we selected as our PCM the tertiary eutectic mixture of 24% (by weight) NaCl, 20% KCl, and 55% $MgCl_2$, which melts at 385°C, because of its relatively high latent heat of fusion and its relatively low cost. Figure 3 indicates that if

a) The temperature difference between the metal hydride bed and the PCM bed is 10°C, and if

b) There were no difference between the equilibrium pressures associated with absorption and desorption at a given temperature and composition;

then a magnesium hydride bed in thermal contact with this PCM would operate at 14 atm while charging, and at 9 atm while discharging, for a pressure swing of 5 atm. In fact, there is a difference (or hysteresis) between the equilibrium pressures associated with absorption and desorption at a given temperature and composition, which adds to the pressure swing, as is indicated in Figure 4.

Aside from heat lost through the thermal insulation surrounding the metal hydride/PCM reactor, the work of compression associated with this modest pressure swing represents the only energy loss from both charging and discharging.

Figure 5 shows a simple, yet effective, means by which the hydride bed and the PCM bed can be kept chemically distinct yet thermally intimate: a shell-and-tube heat exchanger. Only the tube side need withstand high pressure, but both the shell and tube sides must be made of stainless steel 310 to withstand the corrosive attack of this PCM.

Applications for Metal Hydride/Phase Change Material Concept

This concept is applicable to short-term stationary hydrogen storage. The thermal losses from the reactor that occur in a day represent only a small fraction of the HHV of a single charge of hydrogen. Thus, any stationary hydrogen storage application that "turns over" at least once per day would be viable.

A hydrogen fueling station that uses hydrogen made by electrolysis with off-peak electricity (that is, hydrogen made at night) will turn over once per day. A hydrogen fueling station that uses hydrogen made by locally reforming natural gas will turn over at least once per day, for hydrogen can be made continually and a smaller storage capacity can serve a given average fueling demand.

This concept is not applicable to long-term stationary hydrogen storage. One should not expect to store hydrogen in a NCMP/PCM reactor (and the heat of hydriding as heat of fusion) for more than a few days, unless the reactor is extremely well insulated. The thermal losses from the reactor that occur in a week can be a significant fraction of the higher heating value (HHV) of a single charge of hydrogen.

The NCMP/PCM concept might be suited to short-range transport applications. Should a hydrogen source and a hydrogen customer be located too far apart for a pipeline, yet not so far apart that a truck or barge would take more than a day in transit; and should the amount of hydrogen to be shipped be insufficient to justify locating a liquefaction plant at the hydrogen source; this concept could be the least expensive way to transport hydrogen from source to customer. However, it is not suited to vehicular applications, for the weight and bulk of the PCM would be excessive.

Description of Nickel-Coated Magnesium Powder

Magnesium, because of its double valence and its low molecular weight, forms a metal hydride that is 7.7 percent (by weight) hydrogen, a greater hydrogen fraction than any other practical metal hydride. Still, it is not generally used because of

1. The high temperatures associated with its dehydriding,

2. Its slow reaction kinetics, and

3. The tendency for magnesium to poison (that is, form irreducible oxides when exposed to, for example, water vapor).

The heat exchange between the metal hydride and the PCM removes the problems of high-temperature dehydriding. The reaction kinetics of powdered magnesium hydride can be improved by the addition of a small amount (1-2%) of powdered nickel, which serves as a catalyst. Poisoning can be avoided by ensuring that the hydrogen being stored is free of water vapor, carbon dioxide, and the like.

However, the hydrogen available from natural gas fuel processors is hardly free of water vapor and CO_2, and purifying it sufficiently to avoid poisoning magnesium could be costly. Our system uses magnesium in the form of fine powder (maximum particle diameter roughly 40μ), with each particle coated with a very thin (less than 1μ) layer of nickel by means of a chemical vapor deposition process; this nickel layer is meant to protect the magnesium from poisoning by serving as a barrier to oxygen-containing molecules.

The nickel coating does not appear to diffuse appreciably into the magnesium, thus permitting a thin coating of nickel to remain at the surface in its original concentration.

Applications for Nickel-Coated Magnesium Powder

Inclusion in a NCMP/PCM reactor is one application for NCMP, but there are others. It could be used anywhere that powdered magnesium is used to store hydrogen, wherever improved reaction kinetics or resistance to poisoning is desired.

NCMP could be an effective medium for pressure swing absorption if it can be made to resist poisoning of the magnesium by such species as water vapor, carbon monoxide, and carbon dioxide. These are the species found in reformate, and if NCMP can be made to tolerate these, then the NCMP/PCM reactor concept could find use as a high-efficiency pressure swing absorber in hydrogen fueling stations supplied by reforming of natural gas.

Discussion

NCMP/PCM Reactor Construction

We designed and fabricated a laboratory prototype NCMP/PCM reactor (shown in Figure 6), and tested it in ADL's Hydrogen Storage Test Facility (shown in Figure 7). This reactor took the form of a shell-and-tube heat exchanger (see Figure 5), with the NCMP on the tube side and the PCM on the shell side. This configuration offers adequate heat transfer surface area (that is, the area of the tubes), so as to minimize the temperature difference that might otherwise build up between the NCMP and the PCM.

This shell-and-tube heat exchanger was made with U-tubes and a single tube sheet, to minimize

capital cost. It was also made with a high aspect ratio, both to minimize the number of holes in the tube sheet (as is done in industrial practice), and to exacerbate any pressure difference that might develop along the length of the tubes.

Electrical resistance heating was provided, both to heat the reactor to operating temperature and to make up for thermal losses through the insulating jacket. This electrical resistance heating could have been incorporated within the shell (in place of one of the U-tubes), but instead was accomplished by wrapping heating tapes around the shell, under the insulating jacket, primarily for convenience.

To our knowledge, this was the first such physical implementation of thermally coupling metal hydrides and PCMs, though the concept has been suggested before (Sandrock, 1982). The reactor performed as expected; that is, it accepted and rejected hydrogen essentially isothermally and isobarically.

The primary design goals for the test-scale NCMP/PCM reactor were that it:

- Be representative of a full-scale system design in terms of material used, construction geometry and methods (e.g. welded shell-and-tube), tube lengths, and surface-to-volume ratio.

- Be sized to store a large enough quantity of hydrogen so as to be representative of a full-scale system, yet small enough to allow low-cost construction and testing.

NCMP/PCM Reactor Efficiency

NREL defines (NREL, 1993) the storage efficiency of a stationary hydrogen storage system to be

$$\frac{\textit{Delivered Hydrogen}}{\textit{Delivered Hydrogen} + \textit{Process Total Primary Energy}}$$

The DOE goal is "75% round-trip energy efficiency" for "stationary bulk hydrogen storage systems" (DOE, 1992).

Two factors bear upon the efficiency of a NCMP/PCM reactor:

1. the pressure swing the reactor exhibits in operation, and

2. the thermal losses through the shell of the reactor pressure vessel.

Pressure Swing

The pressure swing of a reactor represents an energy loss, because the difference in charging and discharging pressure (that is, the pressure swing) represents irrecoverable work of compression. We

observed pressure swings greater than those which could be attributed to heat transfer between the NCMP bed and the PCM bed (see Figure 3) and to the difference between the absorption and desorption isotherms (see Figure 4). Moreover, the total pressure swings we observed depended greatly on the hydrogen content within the NCMP bed, as is demonstrated by Figure 8.

The total pressure swing is due to the sum of

1. the thermal pressure swing, due to heat transfer between the NCMP bed and the PCM bed;

2. the hysteresis pressure swing, due to the difference between the absorption and desorption isotherms; and

3. the friction pressure swing, due to the pressure drop between the point at which hydrogen enters/leaves the NCMP bed (that is, the tubesheet end) and the point within the bed at which the hydriding/dehydriding reaction occurs.

At the beginning of the hydriding cycle, the hydrogen entering the NCMP bed reacts with the NCMP nearest the tubesheet, and the hydriding pressure (determined by heat transfer to the PCM bed and by the absorption isotherm) is essentially the hydrogen pressure entering the bed. Similarly, at the beginning of the dehydriding cycle, the hydrogen exiting the NCMP bed comes from the NCMP nearest the tubesheet, and the dehydriding pressure (determined by heat transfer from the PCM bed and by the desorption isotherm) is essentially the hydrogen pressure exiting the bed. Thus, the total pressure swing is little more than the sum of the thermal pressure swing and the hysteresis pressure swing.

During hydriding, as the reaction front proceeds away from the tubesheet (that is, as the NCMP nearest the tubesheet becomes fully hydrided), the friction pressure drop (that is, the pressure drop due to flow through the NCMP bed) increases; the hydrogen pressure entering the bed must be increased to compensate for that pressure drop in order to maintain the hydriding pressure. Similarly, during dehydriding, as the reaction front proceeds away from the tubesheet (that is, as the NCMP nearest the tubesheet becomes fully dehydrided), the friction pressure drop (that is, the pressure drop due to flow through the NCMP bed) also increases; the hydrogen pressure exiting the bed must be decreased to compensate for that pressure drop in order to maintain the hydriding pressure.

If the tubes containing the NCMP are long enough, or narrow enough; and if the NCMP is tightly packed (due, perhaps, to the swelling caused by hydriding), then this pressure drop due to flow through the NCMP bed can dominate. Figure 8 shows that this is indeed the case as the reaction front becomes distant from the tubesheet; that is, when the NCMP is almost fully hydrided or almost fully dehydrided.

This friction pressure swing can be greatly reduced by providing a flow path for hydrogen through the NCMP bed, a path that cannot be blocked by the swelling NCMP. We had hoped that the horizontal orientation of our tubes, plus our not-too-tightly packed NCMP, would leave such a flow path, but such was evidently not the case. One means of providing such a flow path, the likes of

which we would recommend for any subsequent NCMP bed, is to insert a "hydrogen artery," such as the 300 mesh stainless steel screen rolled into 5-mm tubes used in a recent metal hydride heat pump (Lee, 1995), into each tube.

Even without a "hydrogen artery," the friction pressure swing (and thus the total pressure swing) can be rendered manageable by simply reducing the rate of fill and discharge. The leftmost point on Figure 9 represents the asymptotes of Figure 8, and the other points represent asymptotes of similar curves for data taken at lower fill/discharge rates.

Thermal Losses

Figure 9 might lead one to think that by decreasing the fill/discharge rates, and thus decreasing the pressure swing, one will increase the efficiency of the NCMP/PCM reactor. If thermal losses were of no consequence, this would be so.

However, our test-scale NCMP/PCM reactor did have significant thermal losses (though a well-designed, scaled-up reactor need not), because the increased fill/discharge time that inevitably accompanies a decreased fill/discharge rate allowed these thermal losses more time to dominate the efficiency equation. Table 1 shows just how badly increased fill time can decrease efficiency if thermal losses are allowed to dominate.

Table 1. Effect of Thermal Losses (which are proportional to the Fill/Discharge Time) on Efficiency

Flow Rate (g/m)	Fill/Discharge Time (hours)	Pressure Swing (psi)	Storage Efficiency
0.5	3	260	64%
0.25	5	120	51%
0.1	13	55	30%

However, thermal losses need not dominate at all. Indeed, by simply using a greater shell diameter and by applying 4" of insulation, one can raise the efficiency to 86%. Also, by taking three additional steps, one can increase the storage efficiency to 93%:

1. Use a larger tube diameter to decrease the friction pressure swing (see the preceding section), thus decreasing the total pressure swing to 130 psi.

2. Use better insulation; that is, use insulation with 0.025 W/m/°C conductivity instead of the 0.036 W/m/°C Fibrefrax that we used.

3. Site multiple reactor shells close together, so that they insulate each other.

Phenomena Exhibited by NCMP

Nickel-coated magnesium powder (NCMP) is a compellingly interesting material. It can serve as a useful substitute for pure magnesium powder as a hydridable material for storing pure hydrogen, but its potential for resistance to poisoning is what sets NCMP apart from pure magnesium powder. With not too much further study, NCMP could be demonstrated to be capable of separating hydrogen from hydrogen-rich streams such as reformate, even while acting as a storage medium.

Reduction of Nickel Oxide

Reduction of a nickel oxide catalyst by hydrogen is a known practice when starting up a process that involves a nickel catalyst. If the nickel layer on NCMP is oxidized, and if that nickel oxide layer is to be reduced, it is important that any water vapor thus formed be removed from the vessel (as with evacuation), lest it poison any exposed magnesium surface.

Accordingly, we pressurized with ambient-temperature hydrogen a small pressure vessel half-filled with a sample of NCMP, thus causing a small amount of hydrogen to be stored as a metal hydride. We then heated the pressure vessel while evacuating the NCMP bed, and provided a means to detect water vapor (condensation on a cold mirror) in the vessel effluent, the presence of which water vapor would indicate that the reduction of nickel oxide (with hydrogen) had taken place in the vessel. Because the partial pressure of this water vapor was on the order of a few microns of mercury (that is, no more than the observed total pressure), we needed a very cold surface to condense it; we used a polished metal tube through which flowed liquid nitrogen. Surrounding the polished metal tube was a transparent tube, and the vessel effluent passed through the annular region between the transparent tube and the polished metal tube enroute to the vacuum pump.

We did indeed detect water vapor in this fashion, and thus proved the existence of the nickel oxide reduction reaction. We thus considered it necessary to encourage such a reduction reaction in our NCMP/PCM reactor, and the elimination of the resulting water vapor from that reactor, before using the reactor to store hydrogen. We did use this same technique to reduce the nickel oxide in the NCMP/PCM reactor, and did again encounter water vapor, which constitutes further evidence that the nickel oxide was indeed there to be reduced.

Chemical Analysis of NCMP

We determined the weight fraction of nickel in our NCMP to 1.6% by dissolving a sample of our NCMP in dilute nitric acid, and by having this solution analyzed by means of atomic absorption spectroscopy.

Optical Analysis of NCMP

We examined a number of samples with ADL's scanning electron microscope (SEM) at various levels of magnification. These samples included

- NCMP as received
- NCMP after 2-3 hydriding/dehydriding cycles with 99.95% pure hydrogen
- NCMP after 100 hydriding/dehydriding cycles with hydrogen laced with 2.5% by volume carbon dioxide and saturated with water vapor at room temperature (by means of passing it through a high-pressure bubbler)
- Pure magnesium powder
- Pure magnesium powder after 2 hydriding/dehydriding cycles with 99.95% pure hydrogen
- Mixture of magnesium and nickel powders
- Mixture of magnesium and nickel powders after 2 hydriding/dehydriding cycles with 99.95% pure hydrogen

Figures 10 through 12 are scanning electron micrographs that show the as-received NCMP. Figure 10 (204x) shows that there is a range of particle sizes present, but nothing that wouldn't fit through a 40μ sieve opening. Figure 11 (499x) shows that the particles are generally shaped like platelets; there is more than one way to make magnesium powder, and this powder was (presumably) mechanically brushed off of solid magnesium. Figure 12 (2050x) shows that the surface is relatively smooth; even the features are flat.

Figure 13 is a scanning electron micrograph taken by Ultramet (all other scanning electron micrographs presented are taken by ADL) of the as-received NCMP powder that has been embedded in Bakelite, ground flat so as to section certain particles with a 6-μ diamond wheel, and etched with oxalic acid to distinguish the magnesium (which etches when exposed to oxalic acid) from the nickel (which does not etch when exposed to oxalic acid). Arrow A points to the magnesium interior, and arrow B to the nickel coating. This picture does suggest a distinct interface (that is, no diffusion or alloying) between the nickel and the magnesium.

Figures 14 through 17 are scanning electron micrographs that show the NCMP after several hydriding/dehydriding cycles. Figure 14 (204x) shows slightly more features than does Figure 10 (204x). Figure 15 (499x) suggests that some particles have grown features, while others have not. Figure 16 (1530x) focusses on feature-less particles, whereas Figure 17 (1530x) focusses on a particle that looks like a cauliflower ready to be picked. The magnesium in Figure 17's central particle seems to have burst open the nickel layer.

Figure 18 (504x) is a scanning electron micrograph that shows the NCMP after eight hydriding/dehydriding cycles. Note that the fractal-like surface features are quite pronounced.

Figures 19 is a backscatter electron image, generated by an electron microprobe under the direction of Dr. George Thomas of Sandia National Laboratory, of NCMP after several cycles that has been

embedded and sectioned, but not etched. The brightness of this image is proportional to the atomic number of the atoms, and the nickel coating is readily distinguishable from the magnesium interior. This electron micrograph seems to suggest that the nickel coating is not as continuous as it appears in Figure 13 (which, it should be repeated, shows the as-received NCMP).

Figure 20, also taken under the direction of Dr. Thomas, shows three separate images of the same portion of the same particle (several-cycled NCMP powder that has been embedded and sectioned, but not etched). The right-hand image is similar to Figure 19; the left-hand image (red) shows the response solely to magnesium, and the center image the response solely to nickel.

Dr. Thomas interprets these images as showing that the magnesium has diffused into (alloyed with) the nickel coating to some extent. Additional analysis on his part shows that this diffusion of magnesium into nickel is more extensive than is suggested by Figure 20. It also shows that where both Mg and Ni are present, they are present in the ratio of Mg_2Ni. It is worth noting that no nickel appears to have diffused into the magnesium interior of the particles.

Figures 21 and 22 are scanning electron micrographs of pure magnesium powder, supplied to us by Dr. Borislav Bogdanovic of the Max-Planck-Institut für Kohlenforschung (Germany). Figure 21 (504x) is of the as-received powder, and Figure 22 is of that same powder after only one cycle of hydriding/dehydriding. Note that after only one cycle, there has been substantial formation of fractal-like surface features.

Figures 23 and 24 are scanning electron micrographs of a mixture of magnesium powder and nickel powder, also supplied to us by Dr. Bogdanovic. Figure 23 (504x) is of the as-received powder, and Figure 24 is of that same powder after two cycles of hydriding/dehydriding. Note that after only two cycles, there has been substantial formation of fractal-like surface features.

Magnesium Transport

The appearance of fractal-like surface features on both magnesium particles and on NCMP particles suggests that magnesium, once exposed, has a certain mobility within the packed bed. Even before we documented this mobility with the scanning electron micrographs shown in the preceding section, we observed a phenomenon that is at once unexpected and intriguing: the growth of magnesium crystals within the pressure vessels in which we were testing early samples of NCMP.

Figure 25 indicates the locations within the vessel where these crystals were observed to have been formed:

1. On the upper portion of the vessel's inner surface,

2. On that portion of the vessel's inner surface near the top of the packed bed of NCMP, and

3. On the thermocouple sheath, with the heaviest concentration near the top of the packed bed of NCMP.

Figures 26 and 27 presents scanning electron micrographs of the deposits found in the third location (T/C sheath, near NCMP surface) after testing our first sample of NCMP.

Analysis shows these crystals to be almost pure magnesium, and their high quality suggests that they grew slowly. It is unknown whether they grew during the evacuation and heating process, or during the hydriding/dehydriding process during which we measured the pressure-composition isotherms (PCIs).

So far, we can only speculate as to their cause(s). Two insights:

- The lower bound of the first crystal region (upper portion of vessel's inner surface) seems to correspond with the upper bound of the vessel's heater, which region could be expected to be cooler than the rest of the vessel's inner surface.

- The region near the surface of the packed bed of NCMPs (the level of which may vary as the particles swell/shrink while hydriding/dehydriding) is where the flux of hydrogen vapor would be highest.

Preliminary Model to Explain the Behavior of the NCMP

In this section we will describe a hypothetical, physical model that explains the behavior of the NCMP. There are insufficient data to prove this hypothesis, but none of the data that we do have are contradicted by it. We present it as a means of applying direction to further investigation.

1. First of all, there seems to be some mechanism by which magnesium is transported either along surfaces or through the vapor phase of the NCMP test vessels. That mechanism is probably not the vapor pressure of magnesium, which we calculate to be only 2×10^{-6} atm at 385°C. However, it could be surface diffusion of either magnesium atoms or magnesium hydride molecules.

2. This transport mechanism would seem to account for the anomalous crystal formation within the vessels discussed in the preceding section, but it does not account for the distinct locations in which the crystals form. It would seem to account for the growth of "features" on the NCMP particles (see Figures 14 through 16). It may even account for the "activation" phenomenon often encountered with metal hydrides; if, before the initial hydriding/dehydriding cycle, the surfaces of the metal particles are as smooth as those of Figure 10; and if, after the initial few hydriding/dehydriding cycles, the surfaces are as fractal-like as those of Figure 18, then the reaction kinetics (which are often considered to be surface-limited) could be expected to improve.

3. The nickel coating on NCMP improves the kinetics to the point where additional surface area is not needed; this could be why we measure the same performance on the first hydriding/dehydriding cycle as we do on subsequent cycles with NCMP.

4. However, this transport phenomenon requires exposed magnesium surface. Unless and until the nickel coating can be breached (as in the particle shown in Figure 17), there will be no transport of magnesium; that is, no anomalous crystal growth, and no growth of fractal-like features on top of the nickel layer.

5. The growth of these fractal-like magnesium features on the nickel layer has no appreciable effect on the reaction kinetics. Either the fractal-like features or the nickel layer itself speeds the reaction kinetics to the point where other phenomena (such as hydrogen diffusion down the tube to the particle in question) limit the overall reaction rate.

6. However, fractal-like magnesium features outside the nickel layer are subject to poisoning, forming a blanket of magnesium oxide or magnesium carbonate that limits the reaction kinetics.

7. Not all of the NCMP particles need to crumble, or burst, to effect this magnesium transport and its concomitant susceptibility to poisoning. Those particles that do burst have magnesium surfaces that can be poisoned, and those particles that receive a fractal-like magnesium coating atop the nickel coating can also be poisoned.

According to this model, if all particles are thoroughly coated when installed and stay coated throughout operation, then there will be no magnesium transport and no susceptibility to poisoning.

The possibility that this model could be substantially correct, and its prediction that smaller NCMP particles are invulnerable to poisoning, indicates strongly that it should be investigated.

NCMP Potential

The potential of NCMP extends beyond hydrogen storage applications. The nickel coating, if made to stay intact (as it well may with smaller particles of NCMP), could render NCMP useful in purifying contaminated hydrogen streams, because

1. the permeability of the nickel coating to hydrogen, and only hydrogen, permits pure hydrogen to leave the contaminated hydrogen stream and enter the magnesium (as magnesium hydride), to be returned later to the process stream once the contaminants have been purged/flushed/evacuated from the interstices between the NCMP particles; and

2. the impermeability of the nickel coating to species other than hydrogen prevents the contaminants from reacting with the magnesium.

Figure 28 shows how an NCMP/PCM reactor could be used in conjunction with a stationary fuel processor, performing the critical function of separating the hydrogen from the nitrogen, carbon dioxide, and carbon monoxide that contaminate the hydrogen-rich product stream from the low-temperature shift reactor.

Those who have studied PEM fuel cells know that PEM fuel cells are even less tolerant to CO than is the human body (which can at least metabolize *some* CO), that CO_2 can be transformed into CO at the anode by the reverse water gas shift reaction, and that both CO and CO_2 must be removed from the hydrogen before it enters the fuel cell's anode. Thus, a technology (such as NCMP) that can remove CO and CO_2 from the eventual anode reactant stream should be of interest to students/proponents of PEM fuel cells.

Those who have studied stationary fuel processors (which supply hydrogen to storage, and not directly to fuel cells) may recognize that the ability to separate hydrogen from nitrogen makes possible the use of relatively inexpensive partial oxidation (POX) reactors without air separation plants. They will also recognize that small-scale stationary fuel processors using steam reformers are capital-intensive, not fuel-intensive, and that a large decrease in reformer capital cost can easily justify a small decrease in efficiency. Thus, a technology (such as NCMP) that can permit the much-less-expensive, but slightly-less-efficient (though perhaps not in a stationary configuration), POX reformer (as compared with a steam reformer) to function upsteam of a fueling station storage system (rather than in front of an integrated fuel cell) should be of interest to students/proponents of stationary fuel processors.

Those who have studied both PEM fuel cells and stationary fuel processors have good cause to follow closely the further development of NCMP, for NCMP constitutes an enabling technology for fuel cell vehicles.

Conclusions

From the results of our efforts over the past year, we conclude the following:

1. The NCMP/PCM Reactor Concept Works.

Our laboratory prototype NCMP/PCM did what we said it would do. We were able to charge it with hydrogen, and retrieve that hydrogen from it, essentially isothermally. The pressure swing was somewhat greater than we thought it would be, but for reasons that we understand and can counter. We have successfully experimentally demonstrated the concept that we described in our technical proposal, and have solved the technical challenges we faced with respect to salt containment, corrosion, and hydrogen leakage.

2. The NCMP/PCM Reactor Can Be Made To Work Better.

Thermal losses could be reduced by reducing the surface-to-volume ratio and by improving the insulation. The energy efficiency could be improved by eliminating (or greatly reducing) the pressure swing associated with the hydrogen pressure difference along the tubes. This could easily be accomplished by modifying the prototype to include a "hydrogen artery," as discussed previously.

3. Our NCMP Has Almost the Hydrogen Capacity of Pure Magnesium Powder.

It may have better reaction kinetics; however, the limited thermal and mass diffusion within our NCMP/PCM reactor (and in our test vessels) effectively mask differences in reaction kinetics. NCMP's capacity for hydrogen (weight percentage hydrogen) is consistent with its (high) magnesium percentage.

4. Our NCMP Can Be Improved.

Repeated cycling in the presence of poisoning agents (water vapor, carbon dioxide) caused eventual deterioration of performance. We suspect that smaller particles of NCMP might, and hope to soon confirm experimentally that they can, avoid this deterioration by virtue of resisting the crumbling inherent in large metal hydride particles.

5. NCMP Offers Great Promise.

If the nickel coating can be made to remain intact; and if by remaining intact it does permit the magnesium to resist poisoning even in the presence of the water vapor, carbon monoxide, and carbon dioxide to be found in reformate; then an NCMP/PCM reactor could serve as a high-efficiency pressure swing absorber. Such a device could meet the purification needs, as well as the storage needs, of hydrogen fueling stations that create hydrogen by means of reforming natural gas.

Future Work

The NCMP/PCM reactor concept should be investigated further, in the context of using it as a high-efficiency pressure swing absorber as well as a high-efficiency stationary hydrogen storage system. Its performance in both contexts could be improved by

a. Developing an improved NCMP to increase its durability and resistance to poisoning;

b. Including "hydrogen arteries" in each of the tubes, to eliminate the pressure differences that arise along the length of these tubes as hydrogen is stored and discharged; and

c. Improving the insulation surrounding the reactor to minimize thermal losses.

Our recommended approach to improving NCMP durability and resistance to poisoning is to identify the cause of the crumbling and to adjust either NCMP structure or reactor operating conditions accordingly. Specifically,

1. Determine how small particles of NCMP must be in order to resist crumbling (at 385°C) better than do the 40μ particles used in the present effort. This should be done by characterizing these particles optically (using ADL's scanning electron

microscope, or SEM) and metallurgically (by grinding embedded particles to section them) before testing and after various numbers of cycles of hydriding/dehydriding.

2. Determine if thicker nickel coatings can enable NCMP to resist crumbling. If indeed it is the magnesium (and not the nickel) that swells/shrinks during hydriding/dehydriding, then the particles can only crumble when the nickel coating is ruptured by the swelling magnesium. A thicker nickel coating could offer sufficient tensile strength to resist crumbling.

3. Determine if operating at lower temperatures can eliminate crumbling. Differential thermal expansion may be contributing to the crumbling; magnesium has roughly twice the thermal expansion coefficient of nickel.

Once the effects of particle size, coating thickness, and temperature on crumbling are known (from steps 1-3), it will be possible to select the appropriate combination of smaller particle size, thicker coatings, and lower operating temperatures to resist crumbling. This will make it possible to perform steps 4-6.

4. Determine the relationship, if any, between the crumbling of NCMP particles (with its concomitant exposure of magnesium surface) and the appearance of magnesium crystals on the vessel walls and the apparent growth of magnesium crystals on the NCMP particles. That is, determine if the absence of crumbling is accompanied by the absence of anomalous crystal growth.

5. Determine the relationship, if any, between the crumbling of NCMP particles (with its concomitant exposure of magnesium surface) and the deterioration of their performance as a metal hydride, with no deliberate exposure of the NCMP to poisoning agents.

6. Determine the relationship, if any, between the crumbling of NCMP particles (with its concomitant exposure of magnesium surface) and the deterioration of their performance as a metal hydride, with deliberate exposure of the NCMP to one or more poisoning agents.

If steps 4-6 demonstrate that avoiding crumbling does indeed prevent anomalous crystal growth; prevent deterioration of hydrogen storage performance; and prevent deterioration due to poisoning; then it would be appropriate to experiment with various charge, purge, and discharge times to determine those combinations that most effectively purify hydrogen with known concentrations of magnesium-poisoning agents such as water vapor, carbon monoxide, and carbon dioxide.

Once the appropriate form of NCMP has been demonstrated to be an effective pressure swing absorbent (and, by default, an effective hydrogen storage medium), then we would recommend modifying the NCMP reactor with hydrogen arteries and improved insulation.

Acknowledgements

We wish to acknowledge the technical contributions made by Dr. Borislav Bogdanovic of the Max-Planck-Institut für Kohlenforschung (Germany), who helped us to determine the nickel content of the NCMP and who furnished us with samples of magnesium and nickel powders; Dr. Thomas Cawthon of NREL, who helped us to understand some of the phenomena we observed in our initial tests; and Dr. George Thomas of Sandia National Laboratory, who helped us to characterize the NCMP. And, of course, we wish to thank those at NREL and DOE who exercised the consummate wisdom of selecting this project for funding.

References

Ogden, J.M., E. Dennis, and J.W. Strohbehn. "A Technical and Economic Assessment of the Role of Natural Gas in a Transition to Hydrogen Transportation Fuel." 10th World Hydrogen Energy Conference, June, 1994.

Sandrock, G.D., and E. Snape. "Reaction Heat Storage Method for Hydride Tanks." U.S. Patent No. 4,566,281, January 28, 1986.

NREL. Amendment No. 1 to "Hydrogen Storage: Planning, Analysis and Research and Development." Letter of Interest (LOI) No. RAR-3-13294, May 28, 1993.

DOE. "Hydrogen Program Plan: FY 1997." DOE/CH 10093-147, June, 1992.

Lee, S.-G., Y.-K. Kim, and J.-Y. Lee. "Operating Characteristics of Metal Hydride Heat Pump Using Zr-Based Laves Phases." *Int. J. Hydrogen Energy*, Vol. 20, No. 1, pp. 77-85, 1995.

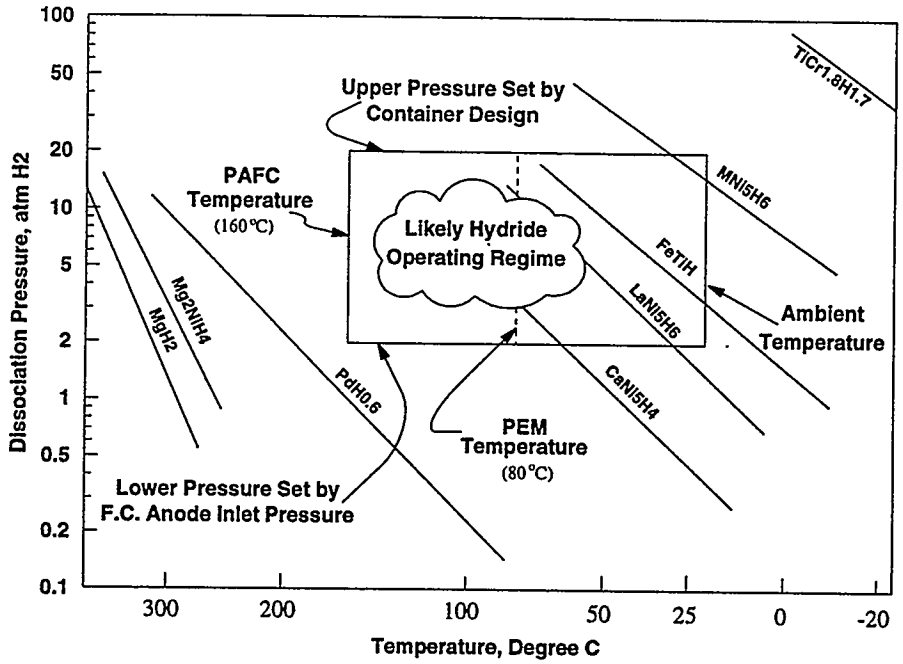

Figure 1: High-temperature Metal Hydrides are Inappropriate for On-Board Storage

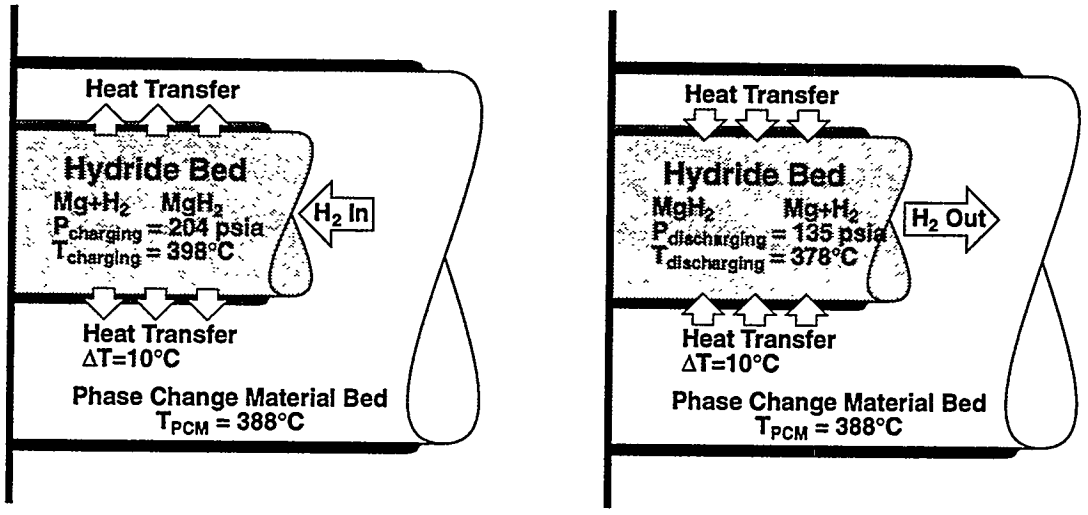

Figure 2: PCMs Can Store the Heat Given Off During Hydriding and Return it for Dehydriding

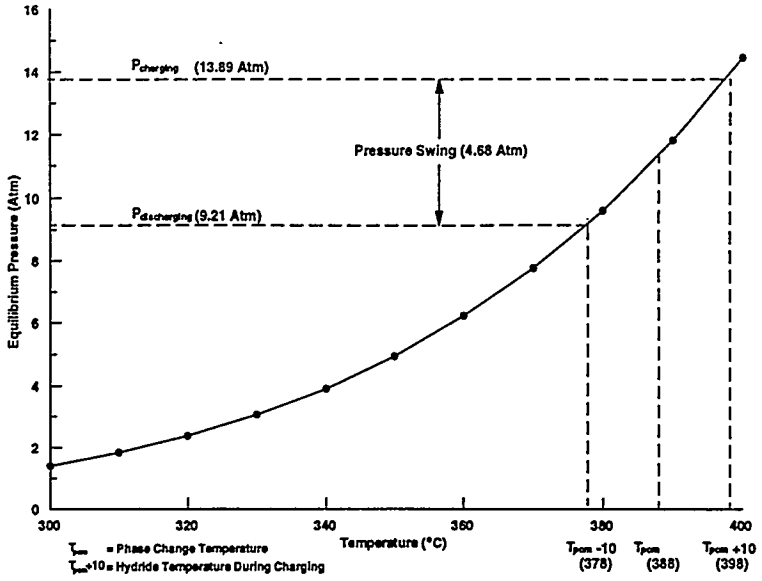

Figure 3: **Heat-Transfer-Based Pressure Swing Associated with MgH_2 and $24NaCl{\cdot}20KCl{\cdot}55MgCl_2$**

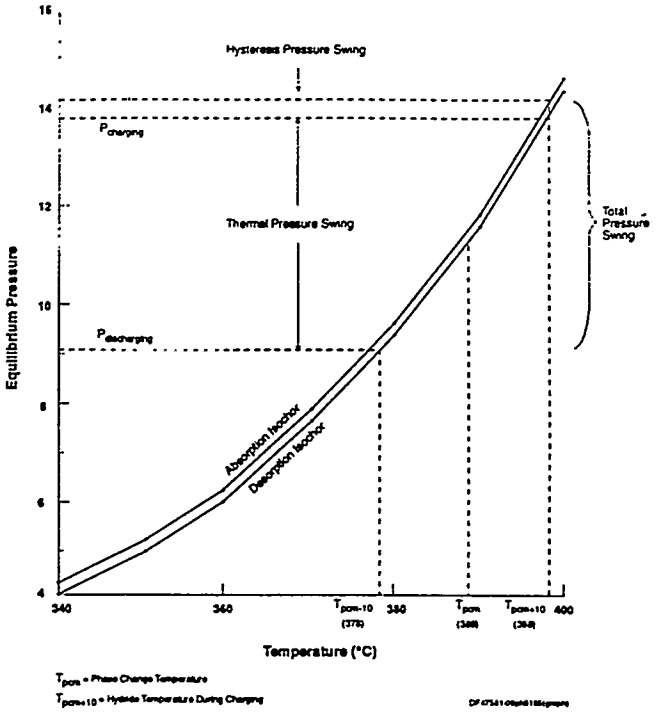

Figure 4: **Heat Transfer Plus Hysteresis-based Pressure Swing Associated With MgH_2 and $24NaCl{\cdot}20KCl{\cdot}55MgCl_2$**

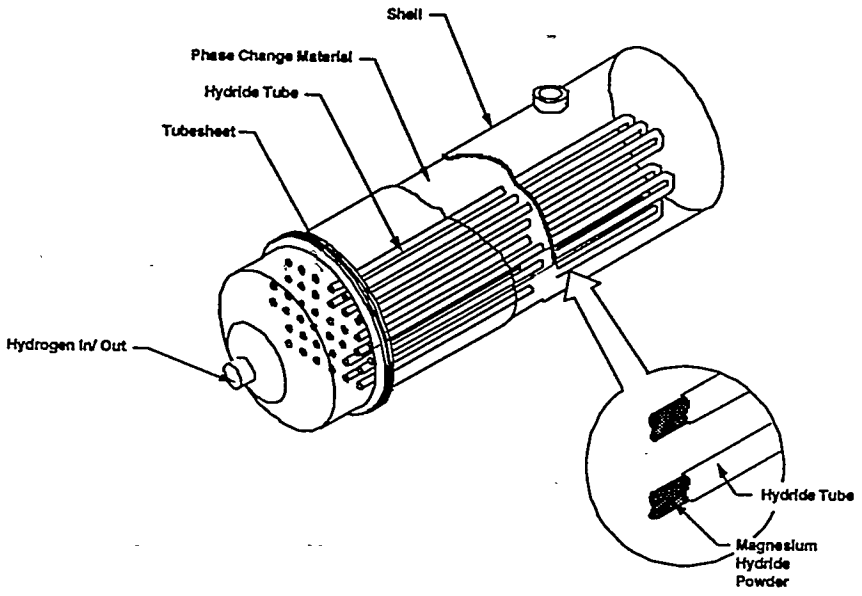

Figure 5: **Thermally and Physically Integrated Metal Hydride and Phase Change Material**

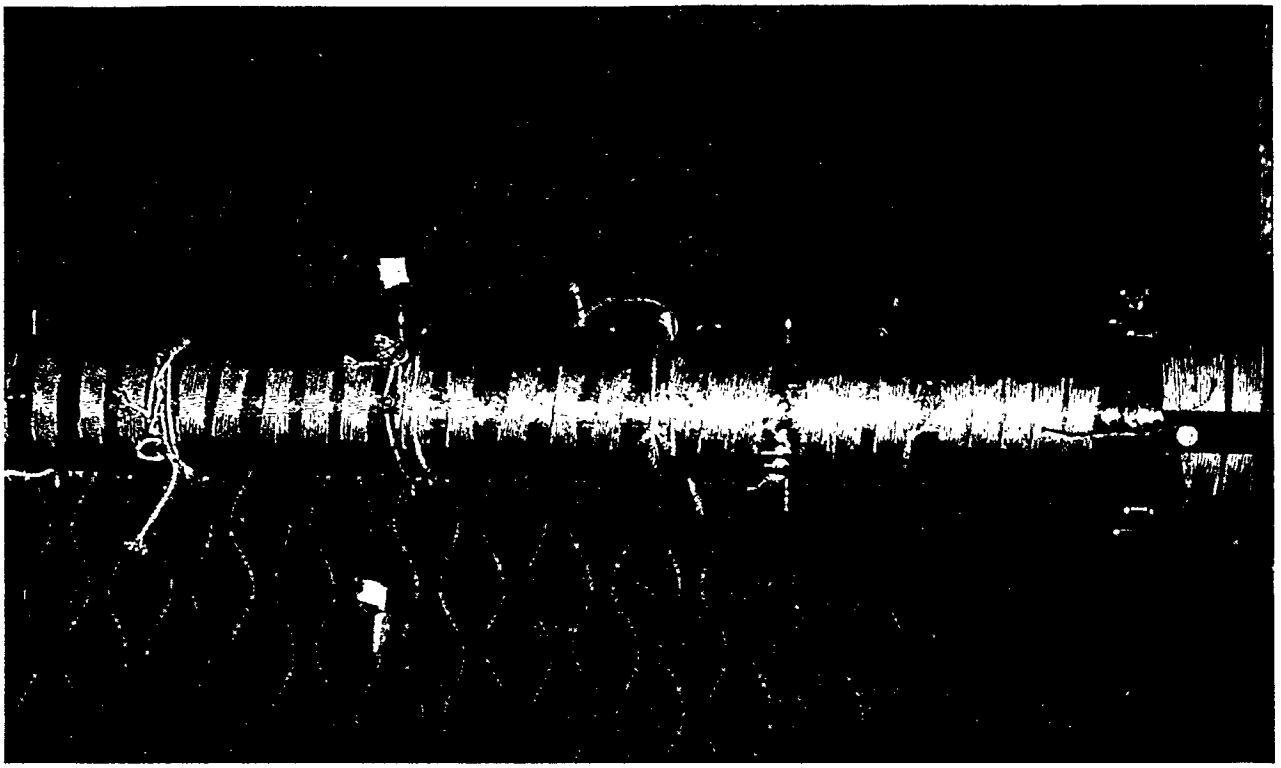

Figure 6: **Test-scale NCMP/PCM Reactor (Reactor)**

Figure 7: ADL's Hydrogen Storage Test Facility (HSTF)

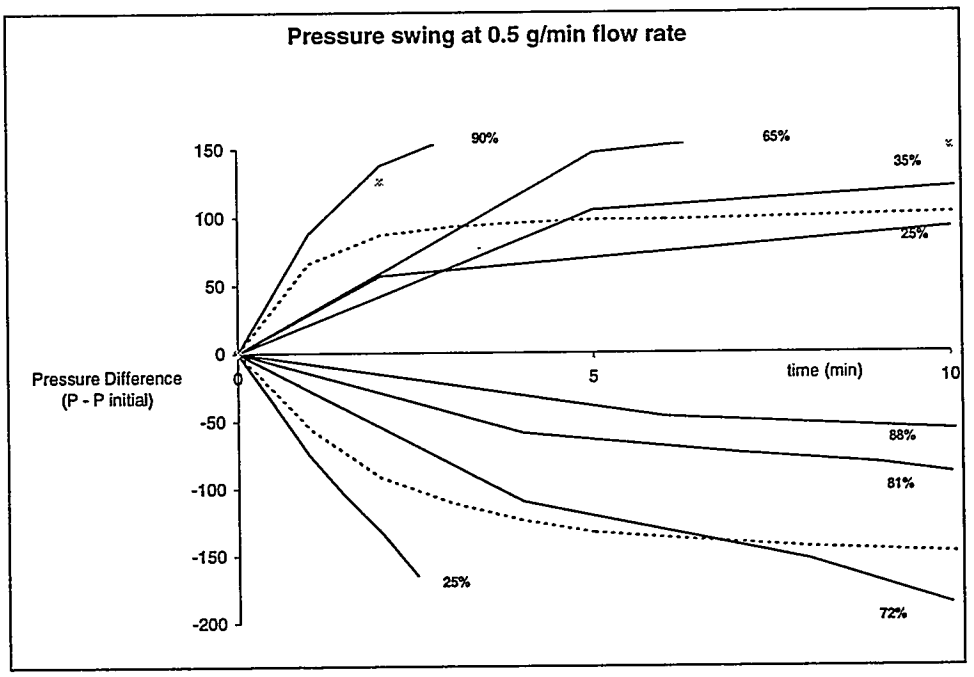

Figure 8: Reactor Pressure Swing as a Function of Reactor Hydrogen Content

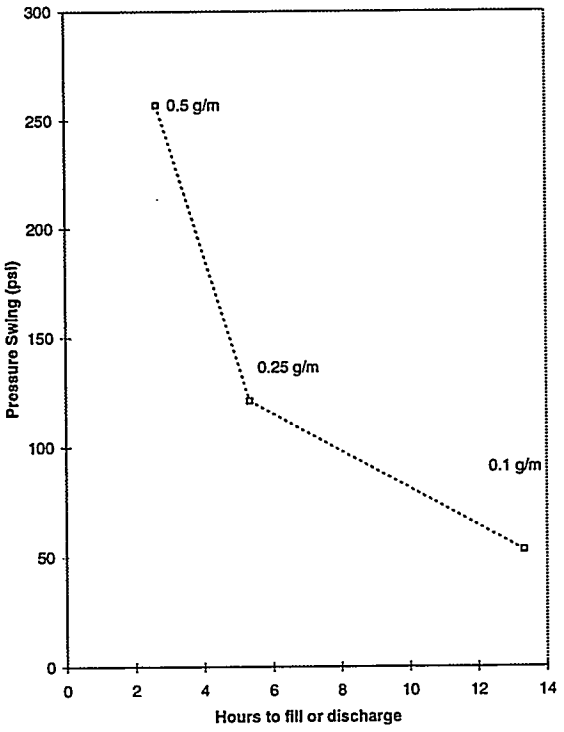

Figure 9: Pressure Swing Depends on Fill Rate

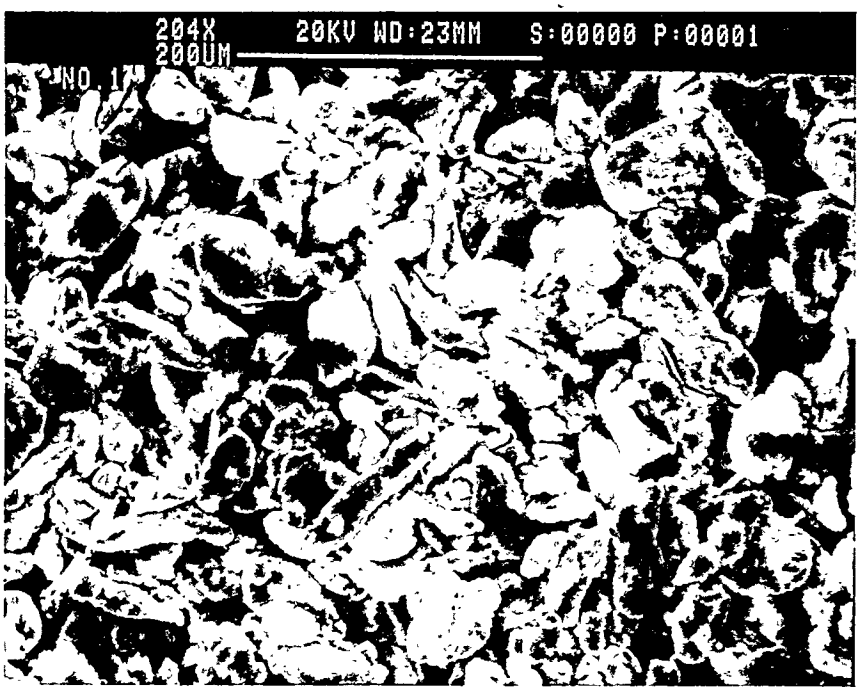

Figure 10: As-received NCMP, 204x

Figure 11: As-received NCMP, 499x

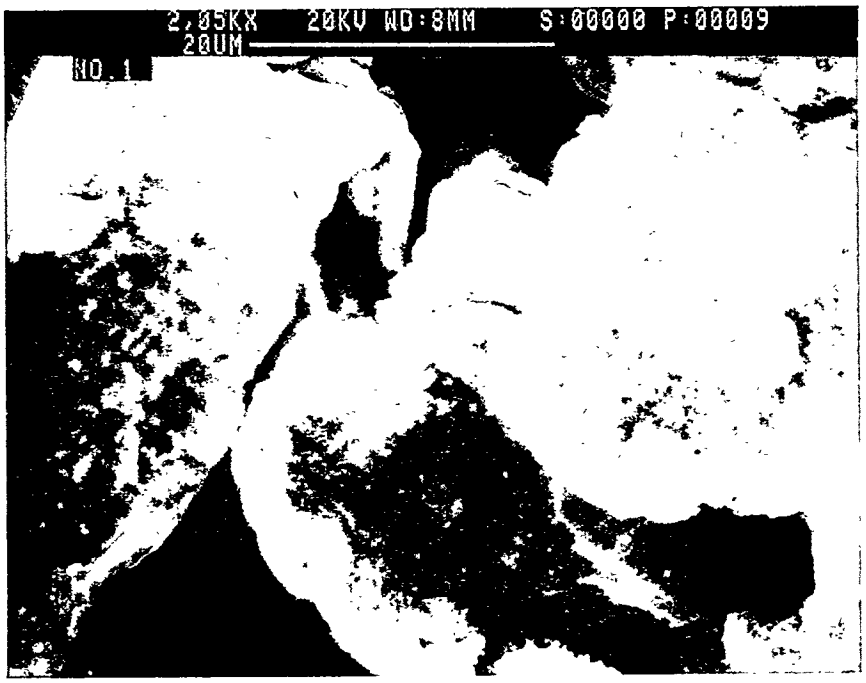

Figure 12: As-received NCMP, 2050x

Figure 13: As-received NCMP, Sectioned, 10,000x

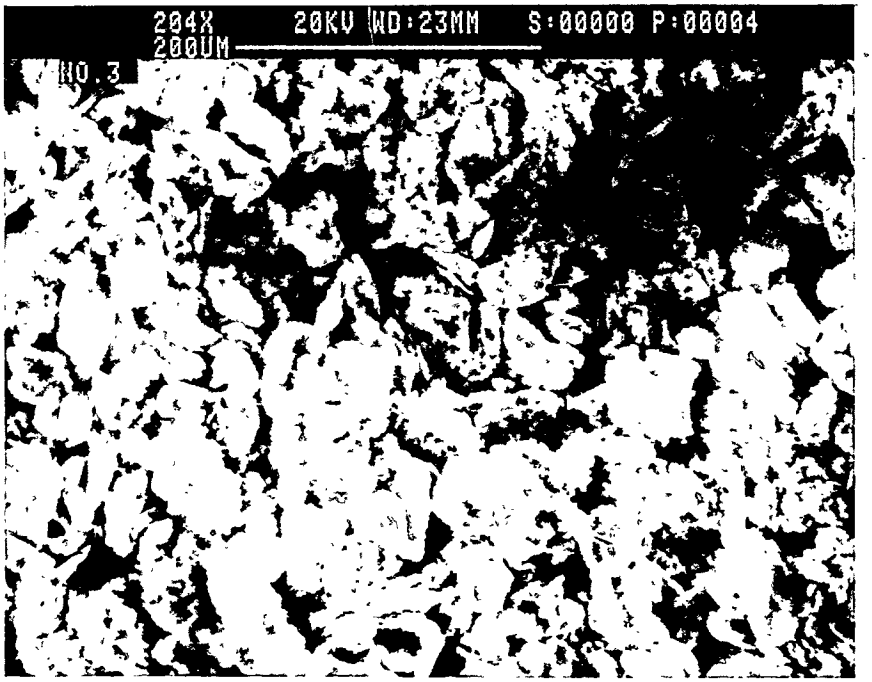

Figure 14: NCMP After Several Cycles, 204x

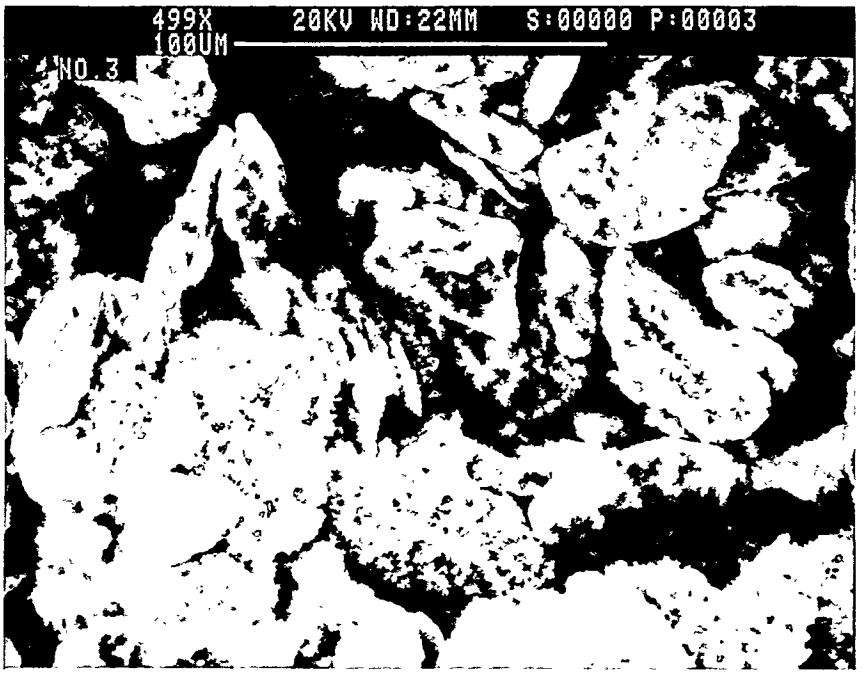

Figure 15: NCMP After Several Cycles, 499x

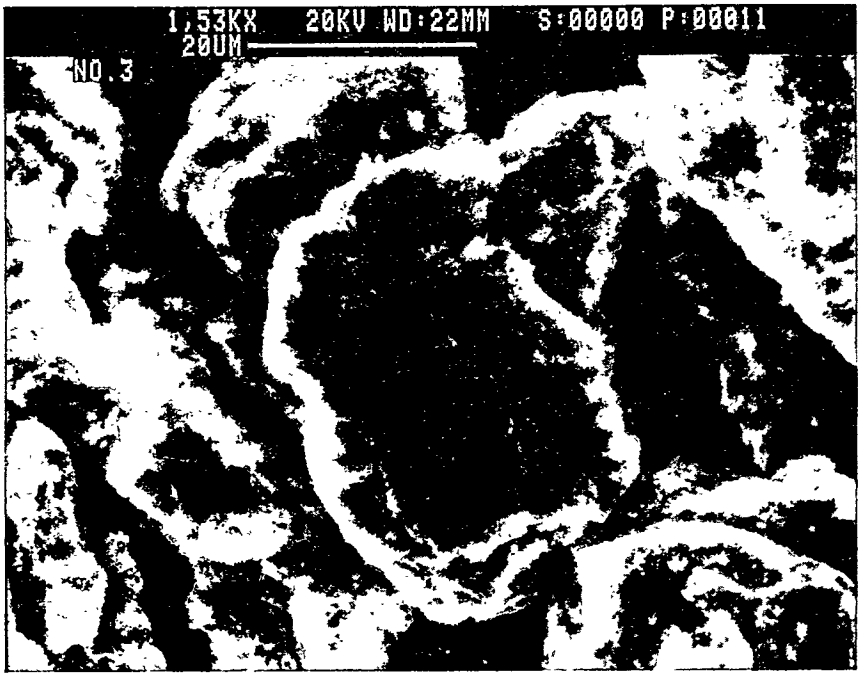

Figure 16: NCMP After Several Cycles, 1530x

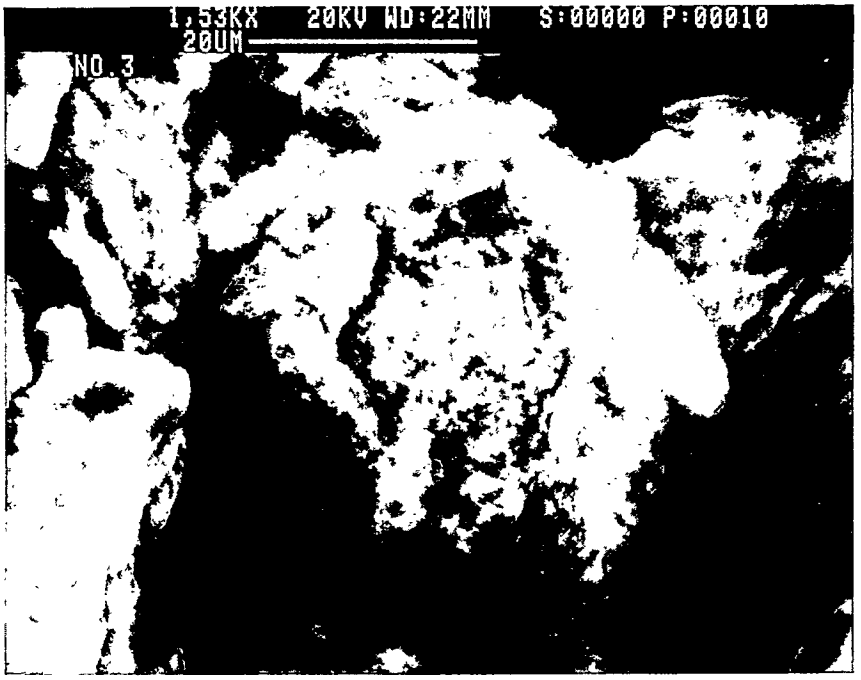

Figure 17: NCMP After Several Cycles, 1530x

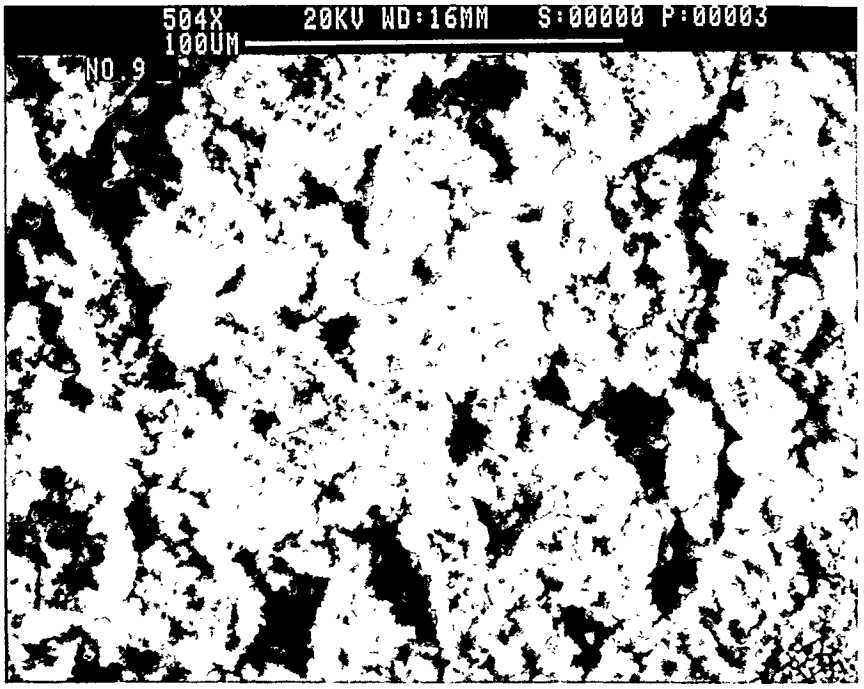

Figure 18: NCMP After Eight Cycles, 504x

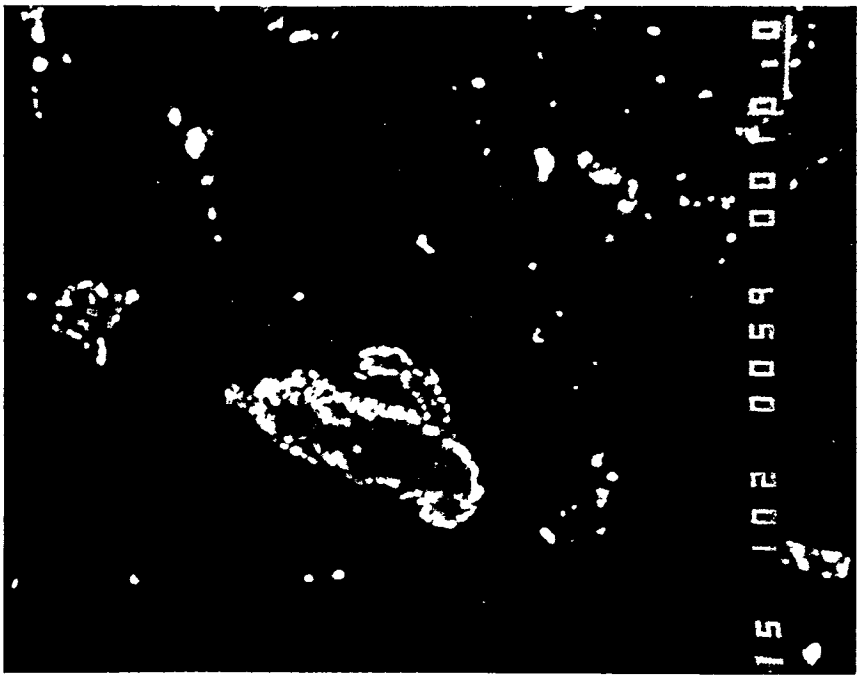

Figure 19: NCMP After Several Cycles, Sectioned

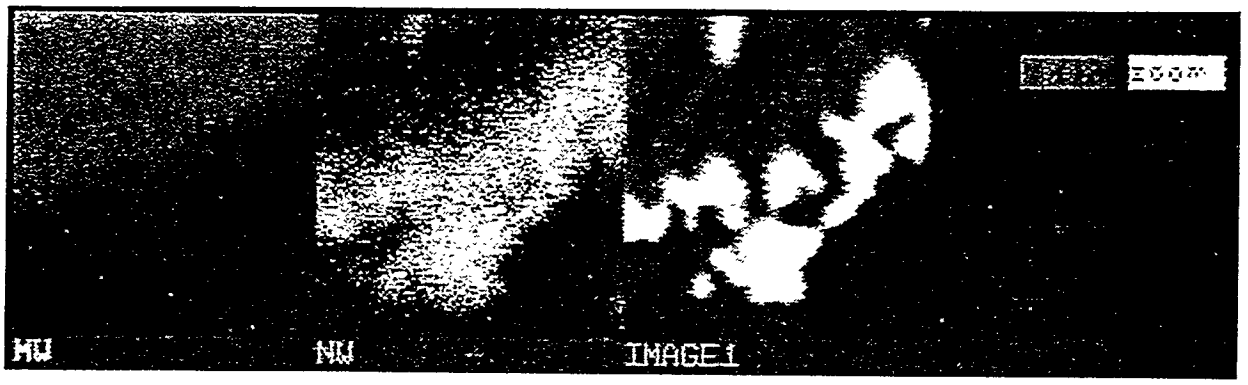

Figure 20: NCMP After Several Cycles, Sectioned, 7800x

Figure 21: Pure Magnesium Powder, as Received, 504x

Figure 22: Pure Magnesium Powder After One Cycle, 504x

Figure 23: Mixture of Magnesium and Nickel Powders, as Received, 504x

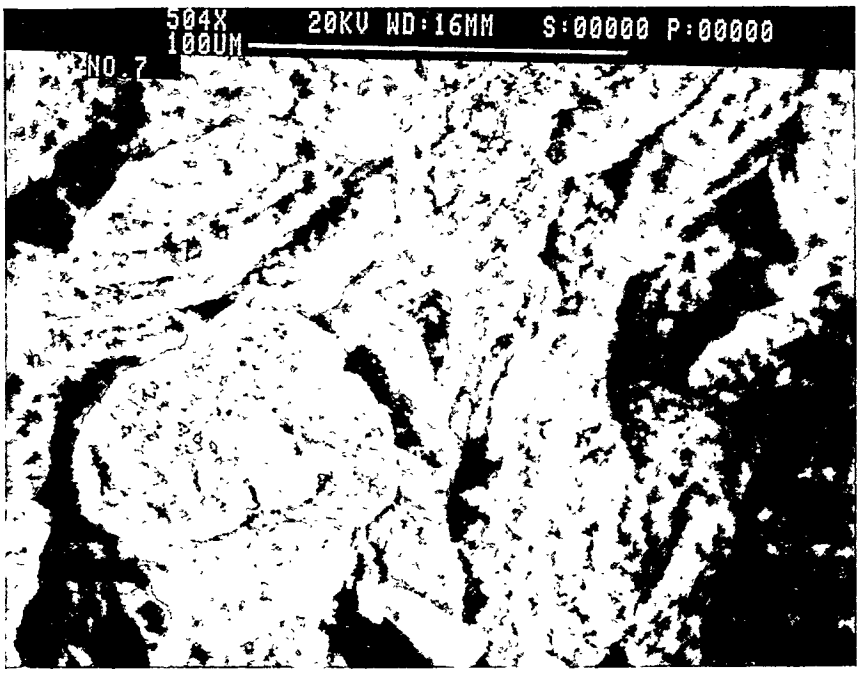

Figure 24: Mixture of Magnesium and Nickel Powders After Two Cycles, 504x

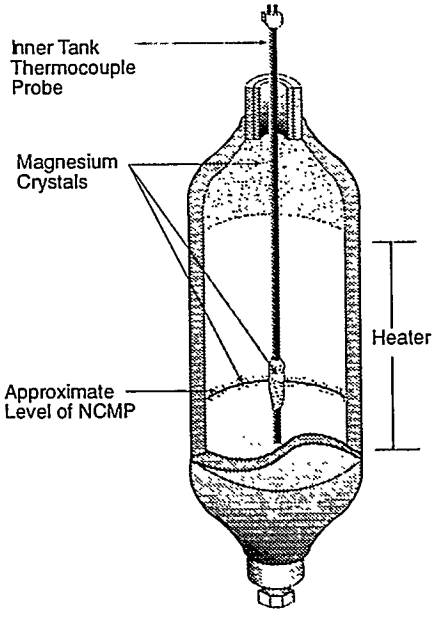

Figure 25: Locations of Magnesium Crystal Growth in #2 Sample Vessel

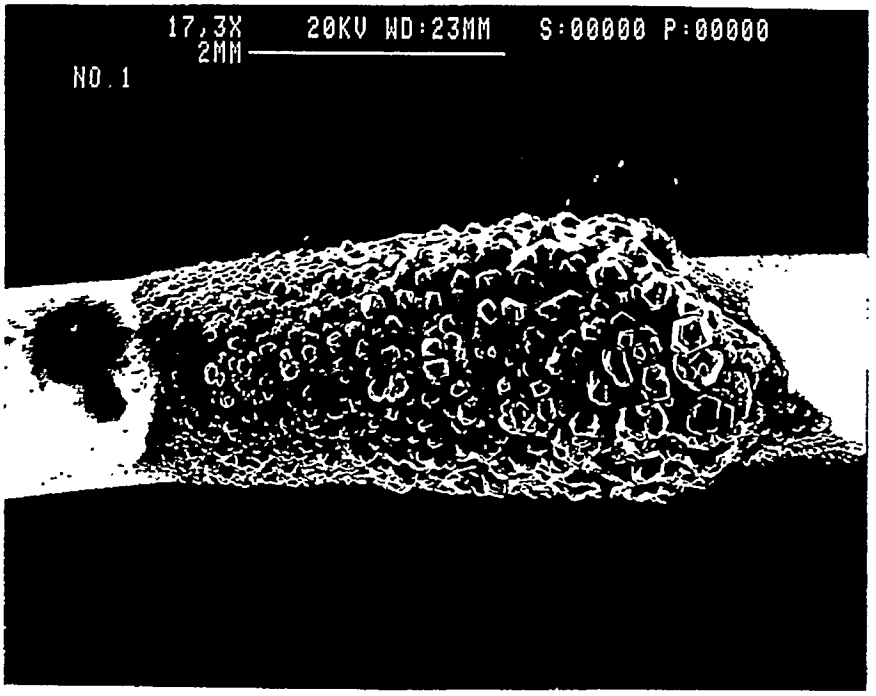

Figure 26: Magnesium Crystal Formations on Thermocouple Sheath in Sample Vessel #1

Figure 27: Magnesium Crystal Formations on Thermocouple Sheath in Sample Vessel #1

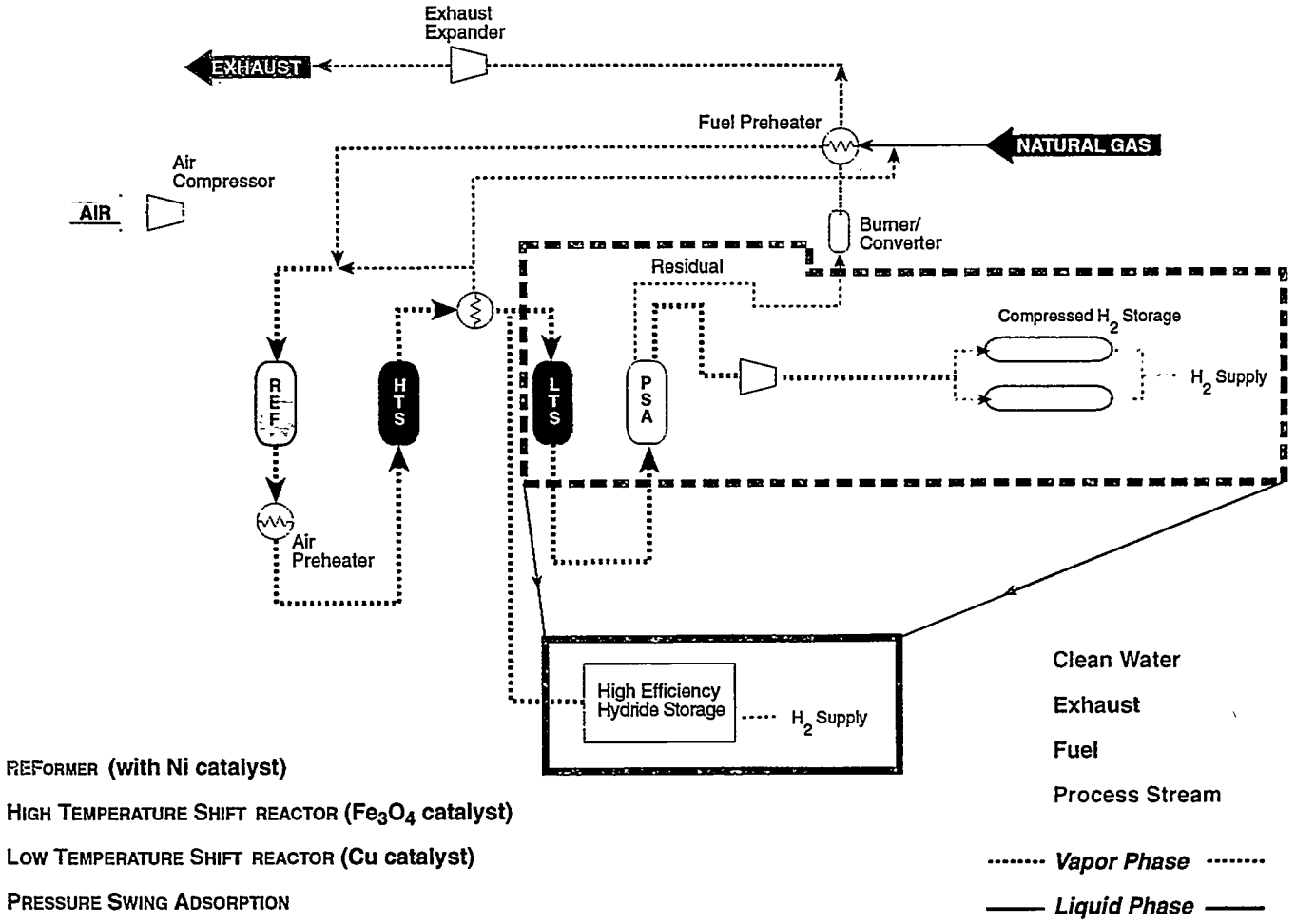

Figure 28: The NCMP/PCM Reactor is a Natural Adjunct to a Fuel Processor

HYDROGEN STORAGE AND DELIVERY SYSTEM DEVELOPMENT

J. L. Handrock, K. Wally, and T. N. Raber
Sandia National Laboratories
Livermore, CA 94550

Abstract

Hydrogen storage and delivery is an important element in effective hydrogen utilization for energy applications and is an important part of the FY1994-1998 Hydrogen Program Implementation Plan. The purpose of this project is to develop a platform for the engineering evaluation of hydrogen storage and delivery systems with an added focus on lightweight hydride utilization. Hybrid vehicles represent the primary application area of interest, with secondary interests including such items as existing vehicles and stationary uses. The near term goal is the demonstration of an internal combustion engine/storage/delivery subsystem. The long term goal is optimization of storage technologies for both vehicular and industrial stationary uses.

In this project an integrated approach is being used to couple system operating characteristics to hardware development. A model has been developed which integrates engine and storage material characteristics into the design of hydride storage and delivery systems. By specifying engine operating parameters, as well as a variety of storage/delivery design features, hydride bed sizing calculations are completed. The model allows engineering trade-off studies to be completed on various hydride material/delivery system configurations.

A more generalized model is also being developed to allow the performance characteristics of various hydrogen storage and delivery systems to be compared (liquid, activated carbon, etc.). Many of the basic features of the hydride storage model are applicable to the development of this more generalized model.

Model results will be presented relating various lightweight hydride material property characteristics to storage and delivery system performance. Preliminary results suggest that modest system weight savings are likely when utilizing current hydride materials with proposed high efficiency engines. Additional analyses have also been completed to examine what future hydride material property improvements are necessary to make lightweight hydride utilization feasible. The engineering implications of these results on the utilization of lightweight hydrides in vehicular applications will be discussed.

Introduction

Project Rationale

Hydrogen storage and delivery is an important element in effective hydrogen utilization for energy applications and is an important part of the FY1994-1998 Hydrogen Program Implementation Plan. This project is part of the Field Work Proposal entitled Hydrogen Utilization in Internal Combustion Engines (ICE). (See related DOE Hydrogen Program Review papers for additional programmatic activity discussions.) The near term goal of the ICE program is the demonstration of an internal combustion engine/storage/delivery subsystem. The long term goal of the program is the introduction of a hydrogen engine into fleet or industrial stationary source use. Within this framework, this project has three primary goals for expanding the current state of the art of hydrogen storage and delivery system technology. These three goals are:

1. Develop an analytical and experimental platform for performing engineering evaluations on hydrogen storage and delivery systems.

2. Investigate the utilization of lightweight hydrides.

3. Provide a hydrogen storage and delivery system for the Internal Combustion Engine Hydrogen Utilization Program Illustration.

These three separate, but related, goals provide the basis for an integrated approach for coupling hydrogen storage and delivery technology to the operating characteristics of potential hydrogen energy use applications. This integrated approach is crucial to the effective utilization of hydrogen in energy applications.

Approach

The initial focus of this program has been centered at investigating the utilization of lightweight hydrides (Goal 2). This activity is being pursued in parallel with the lightweight hydride material development work being conducted as part of the ICE Hydrogen Utilization program (Thomas 1994). An analytical model has been developed to evaluate the utilization of lightweight hydrides for hybrid vehicle applications. Using the insights gained from this model conceptual designs have been

developed for both a hybrid vehicle storage system and a reduced scale prototype storage system. This work (hydride storage model and prototype demonstration) will provide the foundation for development of an expanded analytical and experimental platform for performing engineering evaluations of storage and delivery systems (Goal 1). The general storage system evaluation capability, coupled with the evaluation of lightweight hydride utilization, will assist in the selection of a hydrogen storage and delivery system for the ICE Hydrogen Utilization illustration activity (Goal 3).

The approach taken in this program is intended not only to expand the current understanding of lightweight hydride utilization but the design, development and fabrication of hydrogen storage and delivery systems.

Discussion

During the current program year four key activities have been completed.

1. Conceptual design of lightweight hydride storage and delivery system for hybrid vehicle illustration.

2. Development of hydride storage and delivery system model.

3. Preliminary analysis of hydride storage and delivery system design and operational characteristics

4. Conceptual design of prototype lightweight hydride storage and delivery system (test bed).

In the following sections these four activities will be discussed in terms of the three primary programmatic goals.

Generalized Storage and Delivery System Evaluation Capability

A steady state model has been developed which integrates engine and storage material characteristics into the design of hydride storage and delivery systems. This work is the foundation for the development of a more generalized storage and delivery system model. The analytical representation of items such as burners and heat exchangers will be improved. Additional capabilities will also be added to the model, such as the representation of cold starts, bed modularity and electric heaters. In addition, the model will be generalized to allow the analysis of different types of storage and delivery system technologies, such as liquid and activated carbon. Many of the basic features of the hydride storage model are applicable to the development of this more generalized model.

Utilization of Lightweight Hydrides

Hydrides have the potential for storing hydrogen in a safe, efficient, and economical manner for a

variety of applications (Robinson 1994). The most commonly used hydrides are those which operate at or near room temperature. These materials have a relatively low heat of formation. Chemical bond characteristics of stable lightweight hydrides (> 3 wt % hydrogen) are typically accompanied by elevated operating temperatures and large heats of reaction. These energy needs are in conflict with traditional operating characteristics of proposed high efficiency engines. Therefore, successful utilization of lightweight hydrides requires an integration of engine performance, hydride material properties and storage and delivery system design. In the following two sections analytical and experimental activities focused on investigating the utilization of lightweight hydrides is discussed.

Hydride Storage and Delivery System Model

A steady state model has been developed which integrates engine and storage material characteristics in the design of hydride storage and delivery systems. A schematic of the model is shown in Figure 1. The model includes individual modules representing the engine, startup and primary hydride beds, heat exchangers, and a burner. Energy and hydrogen mass flow balance were used as the means by which individual components in the model were linked together analytically. Each module includes an energy exchange efficiency (power output versus power input) as well as component weight and volume calculations. Modeling of the hydride material includes representation of such items as hydrogen/hydride weight fraction, reaction enthalpy, operating temperature, pressure-composition-temperature (PCT) hydrogen availability, packing density and specific heat. Material properties of the hydride container were also included to allow modeling of the hydride bed as an integral unit. Table 1 contains a listing of sample model parameters.

Table 1. Sample Model Parameters

Input	Results
Engine	Engine hydrogen use, kg
Engine coolant efficiency	System operating duration, sec
Engine exhaust efficiency	System total energy output, J
Engine drive power efficiency	System weight, kg
Engine drive power output, W	System energy use efficiency
Energy Transfer	Bed operating fraction (primary/total)
Heat exchanger (1) efficiency	Primary bed hydrogen availability, kg
Heat exchanger (2) efficiency 1	Primary bed hydrogen fill, kg
Heat exchanger (2) efficiency 2	Primary bed mass heating time, sec
Burner efficiency	Primary bed operating duration, sec
	Primary energy output, J
Primary Bed	
Hydrogen/hydride weight fraction	Bed operating temperature, C
Hydride efficiency	Bed container material 100% density, kg/m3
Hydride 100% packed density, kg/m3	Bed container material fractional density
Hydride fractional density	Bed container material specific heat, J/kg-C
Hydride specific heat, J/kg-C	Bed container/hydride weight fraction
Hydride heat of formation, J/kg-H2	Bed efficiency
Heating value of hydrogen used, J/kg	Ambient temperature (for bed heating), C

Sizing of the startup and primary hydride beds is accomplished by assuming two modes of operation. In the first mode the vehicle operates off the startup bed while the primary bed is heated to its operating temperature. Energy from the engine exhaust is used to heat the primary bed. Also, if needed, the startup bed provides hydrogen to the burner to provide supplemental heating of the primary bed. In the second operational mode the primary bed is used to supply hydrogen to operate the engine, replenish the startup bed and operate the burner as a supplemental heating source.

The structure of the model was developed so as to be consistent with the hybrid vehicle model developed by Lawrence Livermore National Laboratory (Aceves 1994). Given a particular vehicle design the LLNL model can be used to determine the engine energy output and operating duration

required to obtain a particular vehicle range. In the current model this information (operating duration and energy output) is used as input to size the hydride beds (weight, volume, hydrogen fill, etc.) and evaluate overall storage and delivery system performance.

This model has been used to investigate the effects of various system characteristics on the design of vehicular hydride storage systems. In particular the effects of hydride operating temperature and heat of formation on system weight and energy use efficiency will be discussed. Hydride materials such as LaNi and FeTi are the most commonly used hydrides for vehicular applications (DeLuchi 1989). The advantages of these materials are that the operating temperature and heat of formation requirements can typically be satisfied by utilizing engine waste heat, either from the exhaust or coolant systems. The disadvantage of these materials is their relatively low hydrogen weight density ($\approx$ 2%) (Robinson 1994). Hydride materials such as Mg2Ni offer the potential for higher hydrogen weight densities, but typically the heat of formation energy requirements can not be satisfied by utilizing waste engine heat. Some form of supplemental heating is therefore required to allow continued operation of the bed (Hoffman 1976). If the additional heating requirements are minimal the overall system performance may be improved by utilizing a lightweight hydride. However, substantial supplemental heating requirements, both in terms of total energy and elevated operating temperatures, may offset advantages of utilizing a lightweight hydride. The current model assists in performing a systems level evaluation on the feasibility of utilizing various hydride materials for vehicular applications. Table 2 provides a summary of results in the analysis of various hydride materials. Calculations were completed to provide a vehicle operating range of 380 miles at 80 mpg. Such conditions require an engine hydrogen delivery of 4.75 kg (Smith 1994).

Table 2. Hydride Storage and Delivery System Weight and Energy Use Efficiency

Weight, kg	Benchmk FeTi	Current Mg2Ni	Alloy SNL	Alloy A	Alloy B	Current Mg
Startup Bed	318	67	51	38	35	67
Primary Bed		168	162	159	148	94
Burner		4	4	4	4	4
H Exch (1)	3	3	3	3	3	3
H Exch (2)		12	12	12	12	12
System wt	321	254	232	216	202	180
System eff	1.00	0.80	0.87	0.91	0.98	0.70
Prim/Total Op.		0.79	0.84	0.88	0.89	0.79
Op. Temp., C	4	250	200	150	150	300
Heat of Form. (J/kg-H2 E7)	1.42	3.05	2.74	2.74	2.04	3.89

The first column of Table 2 contains performance characteristics for an FeTi hydride storage and delivery system. For comparison purposes this configuration is considered the benchmark case. A system weight of 321 kg and a system energy efficiency of 1.00 were calculated. System energy use is the fraction of the total amount of hydrogen used which is delivered to the engine. At the bottom of the table the operating temperature and heat of formation of the FeTi bed is indicated. The second column provides performance characteristics for a Mg2Ni (lightweight) hydride system. The startup

bed in this instance (as is true for the remaining cases) is the same FeTi hydride used in the benchmark case. The increased hydrogen weight density of the Mg2Ni yields a modest reduction in system weight, even though a burner and additional heat exchanger are required. This decrease in system weight, however, is accompanied by a decrease in system energy use efficiency. This decrease results from the need to burn hydrogen to accommodate increased reaction enthalpy energy requirements.

The modest weight savings predicted from using currently available Mg2Ni hydride versus FeTi is likely not enough to warrant utilization in a hybrid vehicle, especially when one considers the increase in system complexity. The logical question is, therefore, what improvements in material properties are required to achieve substantial weight savings and acceptable energy use efficiencies. In the third, fourth, and fifth columns of Table 2 the effects of improved hydride operating temperatures and heats of formation are presented. Alloy SNL is representative of a material under development at Sandia as part of the ICE Hydrogen Utilization Program (Thomas 1994). The decrease in operating temperature of 50°C and decrease in heat of formation of 10% yielded a 9% decrease in system weight. Likely more important, though, is a corresponding increase of 9% in energy use efficiency. The table columns titled Alloy A and Alloy B are further examples of the changes in performance characteristics which can be expected from improvements in material properties.

The last column of Table 2 gives performance characteristics for a Mg hydride system. The apparent advantage of this material is a hydrogen storage density by weight which is approximately twice that of current Mg2Ni materials. This benefit is seen in the significant decrease in system weight which can be achieved. However, this material has a significantly higher heat of formation. As a result the energy use efficiency of the Mg system is only 70%, more than 12% less than Mg2Ni. The tradeoff between system weight and energy use efficiency is a current topic under study.

An important part of designing a lightweight hydride storage and delivery system is the selection of the startup and primary bed sizes. Using the hydride storage model the effect of bed operating ratio on system weight and energy use was investigated. (Bed operating ratio is defined as the fraction of the total system operating duration in which the primary bed is operating. For example, a bed operating ratio of 0.7 indicates that the primary bed operates for 70% of the time and the startup bed operates 30% of the time.) Figure 2 contains a plot of system weight versus bed operating ratio for Mg2Ni, Alloy SNL and Alloy B. Note that for the Mg2Ni material there is a steady decrease in system weight up to an operating ratio of about 0.80, after which little reduction in weight is achieved. This break in the weight - operating ratio relation marks the point at which the startup bed no longer operates long enough to allow the primary bed to reach operating temperature without the benefit of supplemental heating. The same behavior is seen for the Alloy SNL and Alloy B, though the effect is slightly less pronounced because of the improved material properties.

Figure 3 contains a plot of system energy use efficiency versus bed operating ratio for the same materials presented in Figure 2. Once again the energy use versus bed operating curve is bilinear, with a break at the point where the startup bed no longer operates long enough to allow the primary bed to reach operating temperature without the benefit of supplemental heating. A further increase in operating ratio results in a marked decrease in energy use efficiency. These results, along with those presented from Figure 2, suggest that the ideal relative sizing of the hydride storage beds is

such that the startup bed operates just long enough to get the primary bed up to operating temperature.

Model results have been presented relating various lightweight hydride material property characteristics to storage and delivery system performance. Preliminary results suggest that only modest system weight savings are likely when utilizing current hydride materials with proposed high efficiency engines. Furthermore, these weight savings are accompanied by a decrease in energy use efficiency. These results confirm the need for additional material property improvements and continued focus on system design integration.

Prototype Hydride Storage and Delivery System Development

A prototype hydrogen storage and delivery system conceptual design has been completed. The purpose of this system is to provide a test bed for the evaluation of lightweight hydrides and to serve as a foundation for the development of a generalized hydrogen storage and delivery system experimental capability. The ultimate design will be modularized so as to allow evaluation of a variety of system configurations. Bed design and construction will be integrated with hydride material properties to reduce weight and volume, and therefore enhance system performance. Hydride properties, such as thermal conductivity and hydrogen kinetics, will be measured.

Collaboration with industrial partners will be an important part of the development of this experimental facility. This is particularly true in the areas of hydride material/bed fabrication, elevated temperature component design and fabrication (heat exchangers, pumps, valves, etc.), hydrogen sensor technology and hydrogen safety. The goal is to complete fabrication of the prototype test bed by the end of FY1995, allowing testing to commence early in FY1996.

Hybrid Vehicle Storage and Delivery System

The near term goal of the ICE Hydrogen Utilization Program is the demonstration of an internal combustion engine/storage/delivery subsystem. As part of this program the Hydrogen Storage and Delivery System Development project will provide a hydrogen storage and delivery system. The insights gained from the generalized storage system evaluation platform and the investigation of the utilization of lightweight hydrides will guide the selection of the storage technology to be utilized. This selection will occur early in FY1996.

Future Work

Activities in the near term will be focused on two areas in particular:

1. Expanded system modeling capabilities.

2. Prototype system hardware development.

The current hydride storage and delivery model will be expanded both in breadth and depth. The analytical representation of items such as burners and heat exchangers will be improved. Additional capabilities will also be added to the model, such as the representation of cold starts, bed modularity and electric heaters. In addition, the model will be generalized to allow the analysis of different types of storage and delivery system technologies, such as liquid and activated carbon.

The second near term activity is the design, development, fabrication and construction of a prototype storage and delivery system test bed. The purpose of this test bed is to support the investigation of the utilization of lightweight hydride storage systems and to be the foundation for a generalized storage and delivery system experimental platform. The goal is to complete the fabrication of the prototype system by the end of FY1995.

Long term activities will be focused on the following three areas:

1. Development of a generalized experimental storage and delivery system platform.

2. Investigation of alternative lightweight hydride storage applications.

3. Hybrid vehicle storage system selection and development.

As mentioned previously the prototype test bed will serve as the foundation for development of a more generalized evaluation capability. Investigation of alternate lightweight hydride storage applications will also be conducted. Systems which operate at elevated temperatures are prime candidates since supplemental heating penalties can be minimized. The third far term activity is the selection and development of an ICE hybrid vehicle storage system. Selection of the storage technology will be made early in FY1996 based upon experimental and analytical evaluations.

References

Aceves, S. M. and Smith, R. J. 1994. *A Hybrid Vehicle Evaluation Code and Its Application to Vehicle Design*, LLNL Technical Report UCRL-JC-117918 Rev 1. Livermore, CA: Lawrence Livermore National Laboratory.

DeLuchi, M. A. 1989. "Hydrogen Vehicles: An Evaluation of Fuel Storage, Performance, Safety, Environmental Impacts, and Cost." *Int. J. of Hydrogen*, Vol. 14, No. 2, pp. 81-130.

Hoffman, K. C., Reilly, J. J., Salzano, F. J., Waide, C. H., Wiswall, R. H., and Winsche, W. E. 1976. "Metal Hydride Storage for Mobile and Stationary Applications, " In *Proceedings of the Society of Automotive Engineers, Fuels and Lubricants Meeting*, 760569. St. Louis, MO: Brookhaven National Laboratory.

Robinson, S. L. and Handrock, J. L. 1994. *Hydrogen Storage for Vehicular Applications: Technology Status and Key Development Areas*, Sandia Report SAND94-8229, Livermore, CA: Sandia National Laboratories.

Smith, R. J. and Aceves, S. M. 1994. "Hydrogen Storage and Vehicle Studies, " In *Proceedings of DOE Hydrogen Program Review,* Coral Gables, FL: Lawrence Livermore National Laboratory.

Thomas, G. J. and Guthrie, S. E. 1994. "Lightweight Hydride Storage Materials, " In *Proceedings of DOE Hydrogen Program Review,* Coral Gables, FL: Sandia National Laboratories.

Figure Captions

Figure 1. Hydride storage model schematic.

Figure 2. System weight versus hydride bed operating ratio for a hybrid vehicle application.

Figure 3. System energy use efficiency versus hydride bed operating ratio for a hybrid vehicle application.

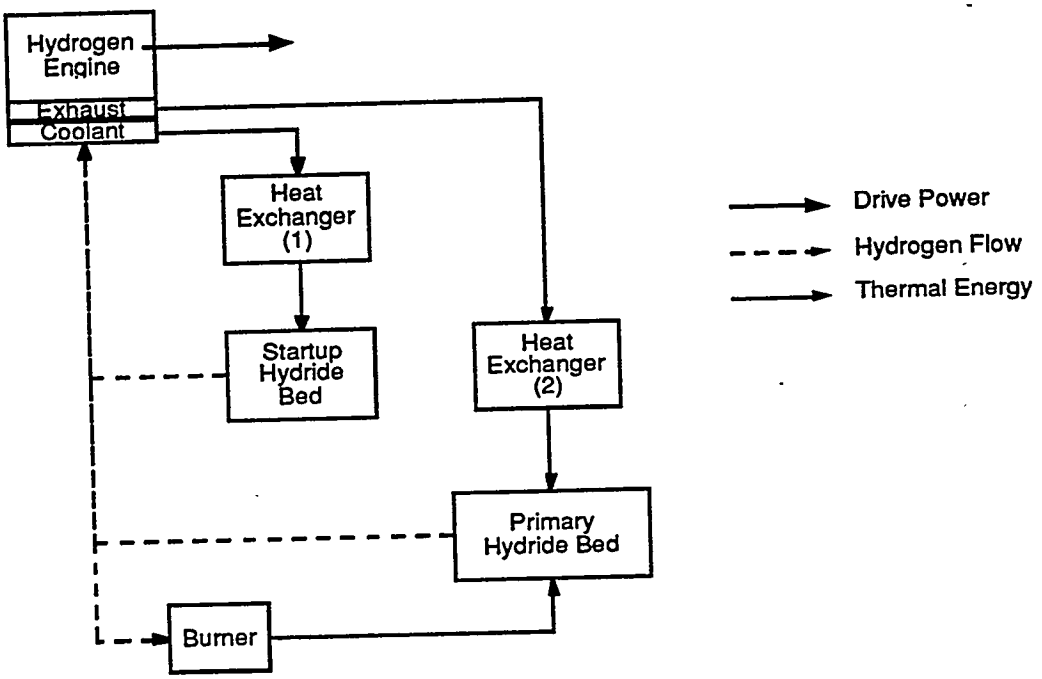

Figure 1. Hydride storage model schematic.

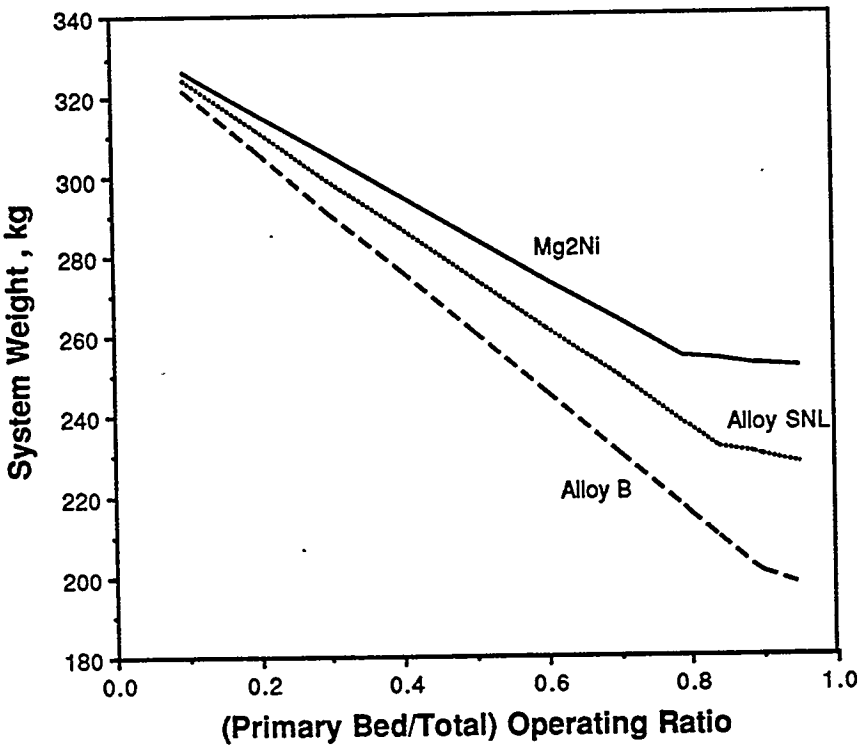

Figure 2. System weight versus hydride bed operating ratio for a hybrid vehicle application.

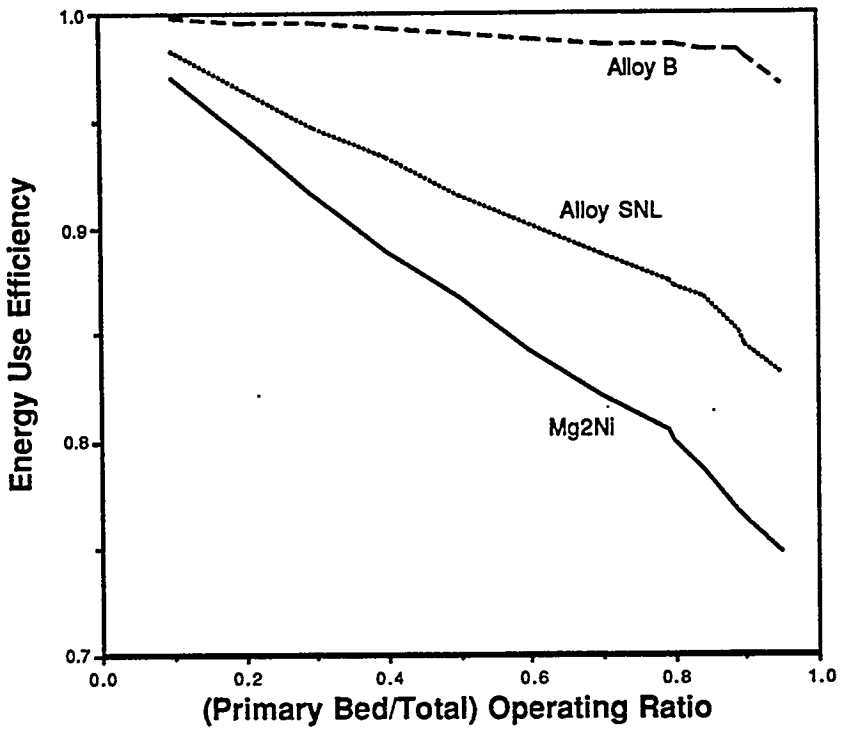

Figure 3. System energy use efficiency versus hydride bed operating ratio for a hybrid vehicle application.

SYNTHESIS, CHARACTERIZATION, AND MODELING OF HYDROGEN STORAGE IN CARBON AEROGELS

R.W. Pekala, P.R. Coronado, and D.F. Calef
Chemistry & Materials Science Department
Lawrence Livermore National Laboratory
Livermore, CA 94550

Abstract

Carbon aerogels are a special class of open-cell foams with an ultrafine cell/pore size (<50 nm), high surface area (600-800 m^2/g), and a solid matrix composed of interconnected colloidal-like particles or fibers with characteristic diameters of 10 nm. These materials are usually synthesized from the sol-gel polymerization of resorcinol-formaldehyde or phenolic-furfural, followed by supercritical extraction of the solvent and pyrolysis in an inert atmosphere. The resultant aerogel has a nanocrystalline structure with micropores (<2 nm diameter) located within the solid matrix. Carbon aerogel monoliths can be prepared at densities ranging from 0.05-1.0 g/cm^3, leading to volumetric surface areas (> 500 m^2/cm^3) that are much larger than commercially available materials. This research program is directed at optimization of the aerogel structure for maximum hydrogen adsorption over a wide range of temperatures and pressures. Computer modeling of hydrogen adsorption at carbon surfaces was also examined.

Introduction

Aerogels have a unique morphology in that *both* the covalently-bonded particles of the solid phase and the interconnected pores of the gas phase have nanometer-sized dimensions. This structure leads to extremely high surface areas (400-1100 m^2/g) with a large fraction of the atoms covering the surface of the interconnected particles. Sol-gel polymerization conditions

can be used to engineer the particle size, particle interconnectivity, and pore size in these materials.

The polycondensation of (1) melamine with formaldehyde, (2) resorcinol with formaldehyde, and (3) phenolic with furfural are three proven synthetic routes for the formation of organic aerogels. The latter two materials can also be pyrolyzed in an inert atmosphere to give carbon aerogels. Carbon aerogels are the first electrically conductive aerogels to be synthesized, and they are finding applications as electrodes in energy storage devices. In this paper, we discuss the chemistry-structure-property relationships of carbon aerogels as they relate to hydrogen adsorption under cryogenic conditions.

Technical Approach

Synthesis

The preparation of resorcinol-formaldehyde (RF) aerogels and their carbonized derivatives has been described previously [Pekala 1992]. Briefly, resorcinol (1,3 dihydroxybenzene) and formaldehyde were mixed in a 1:2 molar ratio, respectively. Deionized/distilled water was added as the diluent and sodium carbonate as the base catalyst. After stirring to form a homogeneous solution, the mixture was poured into glass vials, sealed, and cured at elevated temperature (50-85°C). Upon completion of the cure cycle, the crosslinked gels were exchanged with acetone and subsequently dried from supercritical carbon dioxide (T_c = 31°C; P_c = 7.4 MPa). This procedure resulted in the formation of monolithic RF aerogels in cylindrical form (25 mm diameter x 60-85 mm long). The monoliths were then pyrolyzed (600-1100°C) in flowing nitrogen to form carbon aerogels.

Phenolic-furfural (PF) gels were prepared from a commercially available polymer solution (FurCarb UP520; QO Chemicals, Inc., West Lafayette, IN) [Pekala, in press]. This solution was composed of approximately a 50:50 mixture of a phenolic novolak resin dissolved in furfural. The Furcarb UP520 was diluted with 1-propanol and 10 phr catalyst (a mixture of aromatic acid chlorides; Q2001; QO Chemicals, Inc., West Lafayette, IN) was added. Solutions prepared with different amounts of diluent were then poured into glass vials, sealed, and cured for 7 days at 85°C. A small amount of syneresis was observed during the cure cycle, allowing the gels to be easily removed. PF gels were supercritically dried and pyrolyzed in the same manner as RF gels.

Adsorption Measurements

Hydrogen adsorption measurements were performed in an apparatus similar to that shown in Figure 1. Carbon aerogels were heated at ~250°C and resorcinol-formaldehyde aerogels at ~150°C under vacuum in sample holder "A" to remove surface contaminants (e.g., water). The sample holder was then submerged in liquid nitrogen (77 K), and hydrogen (99.999 %) was bled slowly through a set of control valves from reservoir "B" into "A". The pressure

in "A" was monitored as a function of the hydrogen delivered. The total volume of the carbon aerogel was calculated from the skeletal density measured by helium pycnometry. Next, a stainless steel "plug" of the proper volume was inserted into "A" and the run was repeated. The difference in the adsorption curves allowed us to calculate the amount of hydrogen adsorbed as a function of pressure.

Modeling

Two modeling projects were performed to help understand the storage capability of modified graphites and nanostructured carbons. A semi-empirical quantum chemical study of hydrogen intercalation into modified graphites was performed along with molecular dynamic studies of hydrogen transport through carbon nanotubes.

Results and Discussion

Aerogel Structure-Property Relationships

The structure and properties of RF-derived carbon aerogels are largely controlled by the [Resorcinol]/[Catalyst] (R/C) ratio of the starting solution. At R/C=50, carbon aerogels have particle diameters on the order of 7-9 nm with specific surface areas of ~800 m^2/g. In this type of aerogel, the particles are well-interconnected with the neck size approaching the particle diameter. In contrast, carbon aerogels synthesized at R/C=200, have lower surface areas (~600 m^2/g) and smaller necks between spherical particles of ~12 nm diameter. Interestingly, the specific surface area of these carbon aerogels is practically independent of the bulk density for samples prepared *at the same R/C ratio* [Pekala 1995]. Thus, RF-derived carbon aerogels with a higher bulk density simply have more interconnected particles per unit volume than their low density counterparts. In the case of the PF-derived carbon aerogels, specific surface area (~500 m^2/g) is also found to be largely independent of density at a given catalyst level [Pekala, in press].

Transmission electron micrographs of RF-derived carbon aerogels reveal an interconnected fibrous structure at R/C=50 whereas distinct spherical particles are observed at R/C=200. These structures have been explained in terms of the initial sol-gel chemistry and solution thermodynamics [Gebert 1994; Pekala 1992]. The PF-derived carbon aerogels reveal interconnected platelets of irregular shape with characteristic sizes of 10-15 nm. Figure 2 shows representative TEMs for the carbon aerogels derived from different precursors.

Raman spectroscopy was performed on carbon aerogels to probe the internal structure of the interconnected particles or platelets. In both cases, a Raman-allowed E_{2g2} peak was observed near 1580 cm^{-1} (designated as the*G* band) while a Raman line attributable to in-plane disorder was observed near 1360 cm^{-1} (the *D* band). The in-plane microcrystallite size L_a was estimated from Knight's empirical formula, $L_a = 44\ (I_G/I_D)$. For RF-based carbon aerogels pyrolyzed at 1050°C, L_a is approximately 25 Å, independent of the bulk density or R/C ratio.

For PF-based carbon aerogels pyrolyzed under the same conditions, L_a ranges from 25-35 Å with a slight density dependence. In both cases, the Raman data suggest that 25-35 Å wide graphene sheets are the underlying units in the carbon aerogel structure. The size of these units is largely independent of the sol-gel polymerization conditions and precursor chemistry; however, L_a is sensitive to heat treatment temperature [Fung 1993; Reynolds 1994].

Table 1. Hydrogen Adsorption at 77K

Aerogel Composition	Aerogel density (g/cm^3)	Pyrolysis Temp (°C)	H_2(wt.%)	H_2(kg/m^3)
RF-derived CARBON	0.149	1050	5.87	9.3
RF-derived CARBON	0.284	1050	3.56	10.5
RF-derived CARBON	0.637	1050	3.19	21.0
PF-derived CARBON	0.422	1050	2.12	9.1
PF-derived CARBON	0.547	1050	2.25	12.6
PF-derived CARBON	0.742	1050	1.46	11.0
RF	0.106	—	16.75	21.3
RF	0.193	—	4.5	9.1
RF	0.411	—	4.4	19.0

Because of the *high volumetric surface areas* that can be achieved in aerogels, it was hoped that they would enable us to meet the DOE volumetric energy density requirement for hydrogen storage (62 kg H_2/m^3). In our previous report, we found that hydrogen was quickly adsorbed onto aerogels at relatively low pressures. A plateau value was reached for carbon aerogels by 500 psi. In some resorcinol-formaldehyde (RF) aerogels, hydrogen adsorption continued to increase with pressure. Figure 3 shows the adsorption profile for an RF aerogel having a bulk density of 0.106 g/cm^3. This samples adsorbs 16.8 wt % hydrogen at 77 K and 1000 psi. The highest value achieved in carbon aerogels was 5.9 wt. % under similar conditions. Based upon these results, we investigated the dependence of hydrogen adsorption upon aerogel density. Table 1 outlines the data for RF and carbon aerogels. In general, the specific hydrogen adsorption decreases as the aerogel density increases. Our original

hypothesis assumed that the high *volumetric surface areas* achievable in aerogels would enable us to approach the DOE volumetric energy density requirement of 62 kg H_2/m^3. To date, the highest volumetric adsorption values that we have achieved are only 20-24 kg H_2/m^3 at 77 K. These data suggest that aerogels have limited utility for hydrogen storage.

Modeling

For the quantum chemical study two parallel coronene molecules (Figure 4) were used as a model of graphite. These are polyaromatic rings with twenty four carbons each.. This molecule was chosen as the largest molecular cluster model that could be handled with existing computer power. In order to create different environments, the coronene's hydrogens were replaced by the series F, Cl, Br, I, OH, NH_2, CH_3, SH, PH_2. This provides a data set of ten molecules . On each of these molecules, the geometry of the complex was varied to find the configuration with the lowest energy. A hydrogen molecule was placed in the center directly between the two substituted coronenes and the geometry optimized again. In the simplest cases, these calculations can be thought of as giving us three pieces of information - the initial preferred interplanar distance, the preferred interplanar distance with the H_2 in between and the energy change. The calculations were performed using the MOPAC semi-empirical quantum chemical package.

The results of these calculations yield information on several aspects of the nature of hydrogen intercalation. One question that is answered immediately is that the hydrogen molecule does not dissociate into atomic hydrogen in any of the modified graphitic environments. The way the substituents effect the system seems to depend mostly on their size and the degree to which they cause distortion of the planarity of the coronene. For H, F, Br, OH, SH, and PH_2 substituents the coronenes essentially remained planar and the effect of substitution was to change the preferred initial separation. Introduction of a H_2 molecule always led to an increase in the separation and some increase in the total energy of the complex. This is shown in Figures 4 for unsubstituted coronenes. The trend in this set was that the larger the initial separation, the larger the change in the distance but at a smaller energy cost. For Cl, I, CH_3, and NH_2 substituents, considerable distortion occurs in the coronene. The CH_3 systems, with and without the H_2, are shown in Figure 5. The major cause of distortion was steric interaction between bulky substituents, although in the case of the halogens the interplay between electronic interactions (weakening ring bond strength) and steric interactions is important. For these compounds introducing the interplanar hydrogen can have unusual effects, even allowing the highly distorted molecules to find lower energy structures.

The second set of calculations are ongoing and they are classical molecular dynamics calculations of H_2 diffusing through carbon clusters of various forms. The intention is to calculate the diffusion constants for H_2 in amorphous and nanostructured environments. We have written programs to construct carbon nanotubes (Figure 6) and have modified existing molecular dynamics packages to allow the carbon to be either a rigid matrix or to have thermal vibrations. As the rigid calculations are orders of magnitude faster, they are being

used to get longtime diffusivities while the thermal calculations are used to understand the short time dynamics in greater detail.

Future Work

The aerogel synthesis and characterization efforts have been terminated; however, a modest level of computer modeling will continue into the future.

Acknowledgments

This work was performed under the auspices of the U.S. Department of Energy by Lawrence Livermore National Laboratory under contract #W-7405-ENG-48.

References

Gebert, M.S. and R.W. Pekala, 1994. "Fluorescence and Light Scattering Studies of Organic Sol-Gel Reactions," *Chem. Mater.*, **6**(2), 220-226.

Fung, A.W.P., Z.H. Wang, K. Lu, M.S. Dresselhaus, and R.W. Pekala, 1993. "Characterization of Carbon Aerogels by Transport Measurements," *J. Mat. Res.*, **8**(8), 1875-1885.

Pekala, R.W. and C.T. Alviso, 1992. "Carbon Aerogels and Xerogels" in *Novel Forms of Carbon*, C.L. Renschler, J.J. Pouch, and D.M Cox, eds., MRS Symp. Proc. 270, 3-14.

Pekala, R.W., S.T. Mayer, J.L. Kaschmitter, and F.M. Kong, 1995. "Carbon Aerogels: An Update on Structure, Properties, and Applications," in *Sol-Gel Processing and Applications*, Y.A. Attia, ed., (New York: Plenum Press), pp. 369-377.

Pekala, R.W., C.T. Alviso, X. Lu, J. Gro, and J. Fricke, in press. "New Organic Aerogels based upon a Phenolic-Furfural Reaction," *J. Non-Crystalline Solids*.

Pekala, R.W., C.T. Alviso, and J.D. LeMay, 1992. "Organic Aerogels: A New Type of Ultrastructured Polymer," in *Chemical Processing of Advanced Materials*, L.L. Hench and J.K. West, eds., (New York: John Wiley & Sons, Inc.), pp. 671-683.

Reynolds, G.A.M., A.W.P. Fung, Z.H. Wang, M.S. Dresselhaus, and R.W. Pekala, 1994. "Morphological Effects on the Transport and Magnetic Properties of Polymerica and Colloidal Carbon Aerogels," *Phys. Rev. B*, **50**(24), 18 590-18 600.

Figure Captions

Figure 1. Schematic diagram of hydrogen adsorption apparatus.

Figure 2. Transmission electron micrographs of carbon aerogels derived from (a) resorcinol-formaldehyde [R/C=200] precursor and (b) phenolic-furfural precursor. Both samples were pyrolyzed at 1050°C under flowing nitrogen.

Figure 3. Adsorption isotherm (77 K) for resorcinol-formaldehyde aerogel having a bulk density of 0.106 g/cm^3. The sample was synthesized at R/C=200.

Figure 4. Depiction of two coronene molecules (a) before and (b) after hydrogen insertion.

Figure 5. Depiction of two methyl-substituted coronene molecules (a) before and (b) after hydrogen insertion.

Figure 6. Computer model of a carbon nanotube.

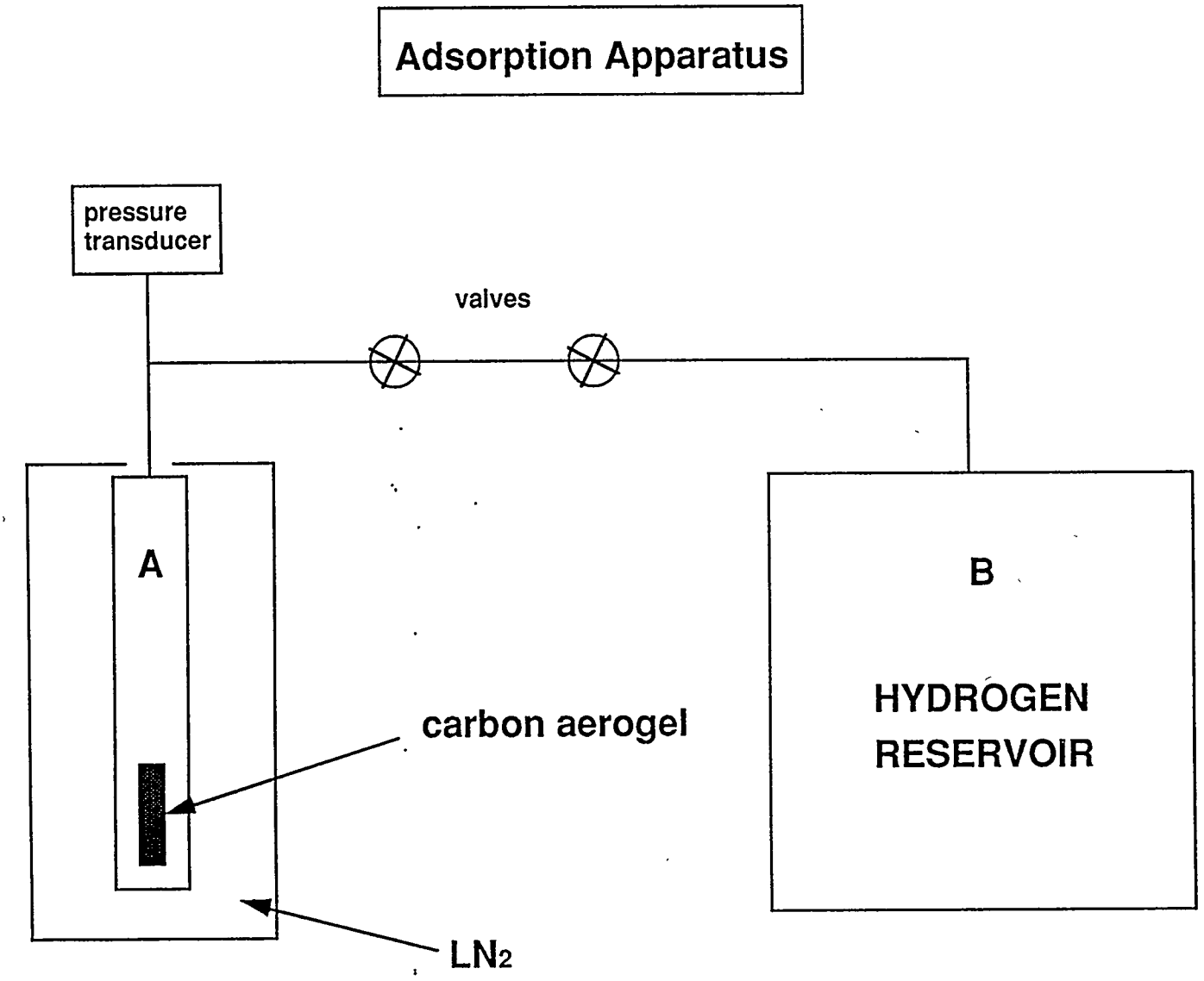
Adsorption Apparatus
pressure transducer
valves
A
B
HYDROGEN RESERVOIR
carbon aerogel
LN2

Figure 1

Figure 2(a)

Figure 2(b)

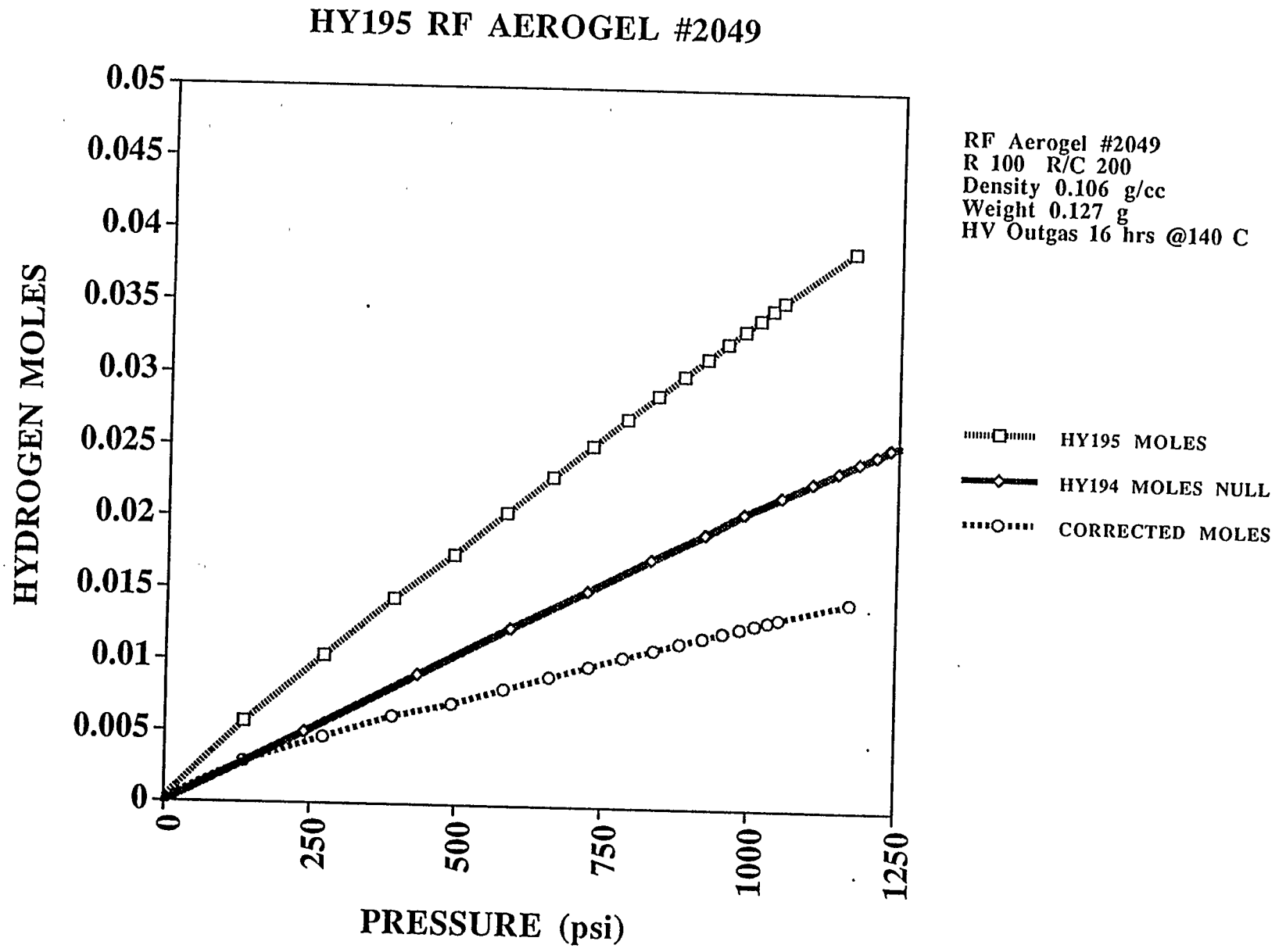
HY195 RF AEROGEL #2049
HYDROGEN MOLES
0.05
0.045
0.04
0.035
0.03
0.025
0.02
0.015
0.01
0.005
0
0
250
500
750
1000
1250
PRESSURE (psi)
RF Aerogel #2049
R 100 R/C 200
Density 0.106 g/cc
Weight 0.127 g
HV Outgas 16 hrs @140 C
HY195 MOLES
HY194 MOLES NULL
CORRECTED MOLES

Figure 3

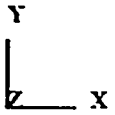

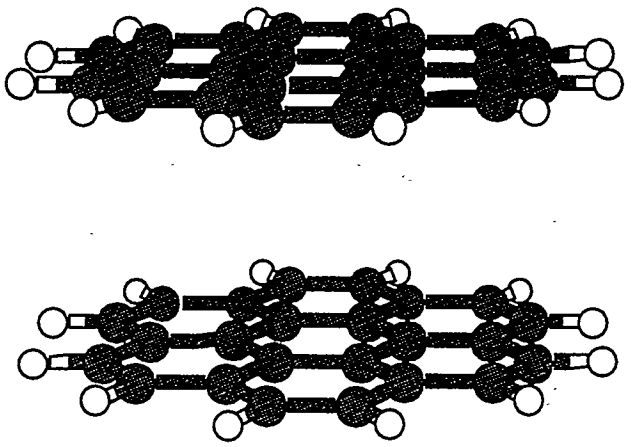

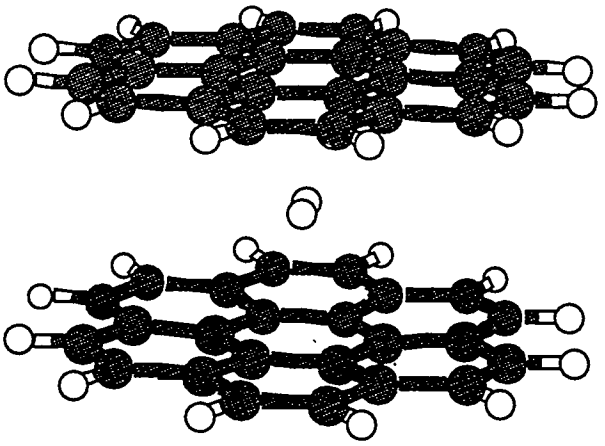

Figure 4

Active

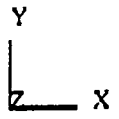

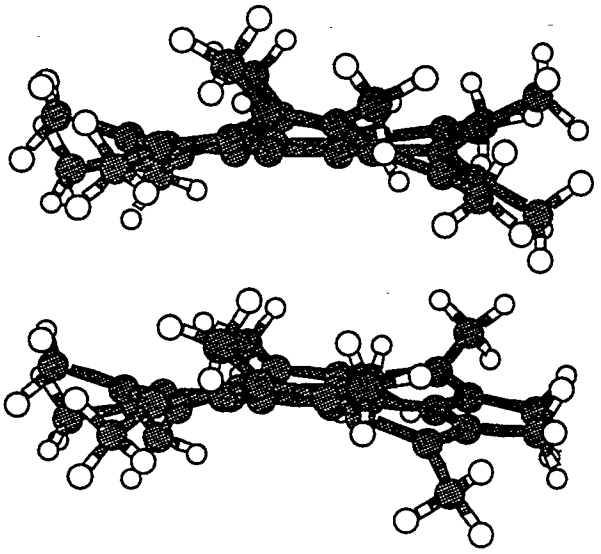

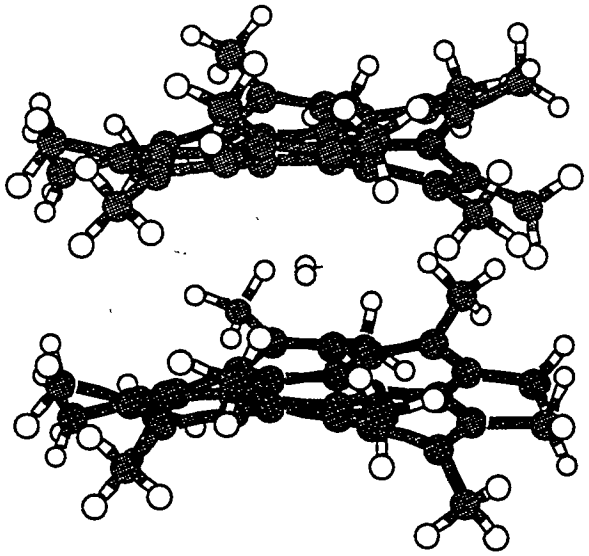

Figure 5

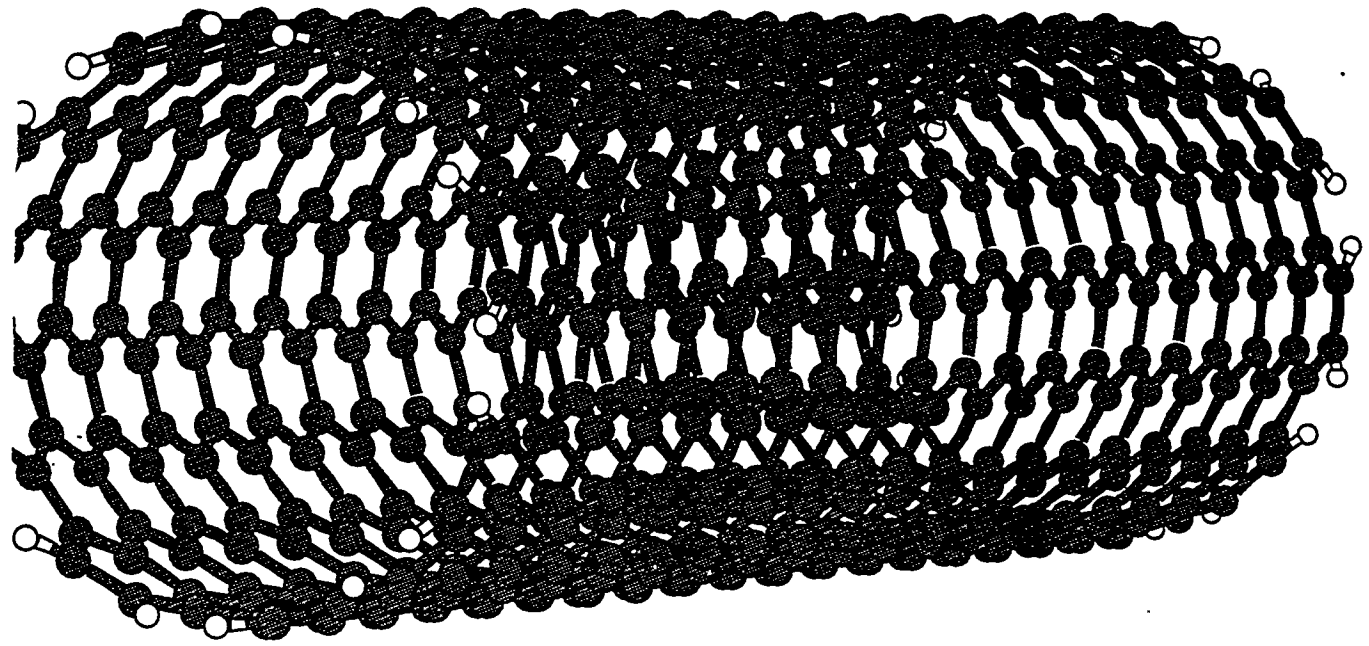

Figure 6

HYDROGEN TRANSPORT AND STORAGE IN ENGINEERED GLASS MICROSPHERES

Glenn D. Rambach
Lawrence Livermore National Laboratory
Livermore, CA 94550
510-423-6208, Fax 510-423-0618

Abstract

New, high strength glass microspheres filled with pressurized hydrogen exhibit densities which make them attractive for bulk hydrogen storage and transport. The membrane tensile stress at failure for our engineered glass microspheres is about 150,000 psi, permitting a three- fold increase in pressure limit and storage capacity above commercial microspheres, which have been studied a decade ago and have been shown to fail at membrane stresses of 50,000 psi. Our analysis relating glass microspheres for hydrogen transport with infrastructure and economics, indicate that pressurized microspheres can be economically competitive with other forms of bulk rail and truck transport such as pressurized tube transports and liquid hydrogen trailers.

Introduction

Commercially produced glass microspheres were studied in the late 1970s for their application to storage of hydrogen (Teitel, 1981). These spheres, shown in Fig. 1, have diameters of 25 to 200 μm and membrane thicknesses of approximately 1 to 20 μm. At elevated temperatures of 150 - 400°C the glass exhibits an increased permeability to hydrogen which permits the microspheres to be pressurized by immersion in high pressure hydrogen for a period of time. The hydrogen diffuses through the microsphere membranes, equilibrating the internal and external pressures and filling the spheres. Once filled, cooling the spheres to room temperature reduces the permeability trapping the hydrogen within the spheres.

Microspheres can be handled in packed beds (Figure 2.). If a large bed of microspheres is filled in the above manor, it can be used as a hydrogen transport container. After transport and storage at room temperature, the hydrogen is released from the microspheres by reheating the bed to increase the permeability. The empty microspheres can then be cycled and refilled. Fill rate is a function of glass properties, permeating gas, temperature and pressure differential.

The commercial spheres described above were usually made by spraying glass frits or gels into a furnace. Because this manufacturing process resulted in defects in the sphere geometry and material defects in the membrane, the membrane's biaxial tensile stress at failure (burst) for the commercial microspheres was limited to about 50,000 psi. Because LLNL's Laser Fusion Program had need for glass microspheres made under much more controlled conditions, a method of microsphere production was developed which resulted in defect-free microspheres. All microspheres produced from this method have diameters that fall within a few-micron band and can be treated as a monodispersion. A key distinction of this new process is the absence of membrane or geometric defects, which raises the biaxial tensile stress at failure of the engineered microspheres to about 150,000 psi, and permits a three-fold increase in pressure limit for microspheres having the same dimensions and materials as the commercial ones. Further improvements in the microsphere process should significantly increase the failure strength of glass microspheres above 150,000 psi, enabling an increase in mass fraction and bed density while decreasing fill times.

Considering glass microspheres which are currently possible to produce, a bed of 50-μm- diameter engineered microspheres with 1.1-μm-thick membranes and 150,000 psi failure stress, containing hydrogen at 9000 psi with a 1.5 safety factor, could exhibit a hydrogen mass fraction of 10% and a hydrogen bed density of 20 kg_{H2}/m^3. A comparison of glass microspheres to conventional pressure vessels and liquid hydrogen is shown in Figure 3.

A safety factor of 1.5 is reasonable because a bed of 50-μm diameter microspheres would have a number density of $10^7/cm^3$. A failure of the primary container holding the spheres or a failure of any spheres themselves will not result in the propagation of a failure through the rest of the bed. Also, since a large bed of microspheres represents the subdivision of a pressure container, and its PV energy into individual pressure vessels with volumes less than .01 mm^3, it is possible for the pressure safety limit for transporting hydrogen to be several times greater than it is today for conventional pressurized transport vessels.

Background

The key intrinsic properties that are relevant to hydrogen storage in glass microspheres fall into two categories. First are those related to the gravimetric and volumetric hydrogen capacities, and second are those related to the energy and time required to fill and release hydrogen. Our current understanding of all these parameters for high-strength glass microspheres is based on semi-empirical expressions developed early in the 1970s for laser fusion targets (Woerner, Weinstein, Moen, and Rittman, 1979). In the Laser Fusion Program, a single microsphere would be assembled into a target after being filled with the hydrogen isotopes, deuterium and tritium. Since the fill process for laser

fusion applications was done on single microspheres, the heat supplied to raise the glass temperature and the time used to fill the spheres were both much greater than the minimum necessary to do the job. For large beds of microspheres to be used in economic transport and storage of hydrogen, it will be necessary to use as little fill energy and time as possible.

Storage Capacity

As in any pressure vessel, the storage capacity of a microsphere is limited by the burst pressure of the container and an applied safety factor. The burst pressure of the sphere (P_b) is given by:

$$P_b = 4\sigma_{max}\Delta r/D \qquad (1)$$

where σ_{max} is the biaxial tensile (hoop) stress in the sphere membrane at failure, Δr is the membrane thickness and D is the sphere outer diameter. Figs. 4 and 5 show the mass fraction of hydrogen and the volumetric density of hydrogen that can be stored in a bed of 50-μm diameter microspheres with a safety factor of 1.5. These figures only consider the mass and volume of the hydrogen and sphere bed, and exclude the mass and volume of any external container.

In Fig. 4, it can be seen that high-strength, glass microsphere beds can offer hydrogen mass fractions greater than 12% at internal pressures of 3600 psi and greater than 10% at 9000 psi. Fig. 5 illustrates the fact that the property that limits glass microsphere applications for on-board vehicle storage is the volumetric density. The packing fraction considered here is 63%, which is reasonable for beds of monodisperse spheres. Even at internal pressures of 9000 psi, the hydrogen density in the bed is about 20 kg_{H2}/m^3. A very efficient piston-engine or fuel-cell hybrid, hydrogen-fueled vehicle may require 3 - 5 kg of hydrogen on board for approximately 480 km, which, at 9000 psi, would require a bed volume of loaded spheres of 150 - 250 liters (39 - 66 gallons). In addition to the volume of charged spheres, more volume would be taken up on a vehicle for storage of discharged spheres and for heat exchangers and other processing equipment, making the volume too great for practical use on a light duty vehicle.

When considering bulk transport of hydrogen, such as by truck or rail car, the heat exchangers and other processing equipment can be located at the end points of the transport lines. The truck trailer or rail car need only provide containment for the charged spheres and a small blanket pressure of hydrogen. As in both pressure-vessel or liquid hydrogen transport, the discharged microspheres must be returned to the hydrogen charging facility for recharging.

A 12-tube trailer truck pressurized to 2640 psi, will hold 335.6 kg of hydrogen, which would constitute about 1% of the trailer weight. A trailer designed to carry a bed of glass microspheres having inside dimensions of 2.5m x 2.5m x 12m, and a volume of 75 m^3 would carry 1500 kg of hydrogen (~4.5 times the capacity of a 12-tube trailer) if the spheres were loaded at 20 kg_{H2}/m^3, or 750kg of hydrogen (~2.25 times the capacity of a 12-tube trailer) if the spheres were loaded at 10 kg_{H2}/m^3. The mass fraction of hydrogen in the trailer would be greater than the 1% of the tube trailer.

A liquid hydrogen trailer with the capacity of 49.2m^3 (13,000 gallons) could carry 3500 kg of

hydrogen (~2.3 times the capacity of the above microsphere trailer at 20 kg_{H2}/m^3), but the trailer capital cost is approximately $500,000. The capital cost per kg of hydrogen carrying capacity is $142.85/$kg_{LH2}$. The cost of mass produced glass microspheres is expected to be significantly less than $4.00/kg, however even at that price, a trailer and bed of spheres is estimated to be about $66.00/$kg_{LH2}$.

Energy and Time Required for Loading and Unloading

The energy needed to fill a bed of microspheres is the sum of the energy used to pressurize the hydrogen to the overpressure for filling and the heat used to raise the bed temperature for a suitable increase in permeability. For glasses, the permeability (K) can be expressed as (Souers, 1986, Woerner, Weinstein, Moen, and Rittman, 1979)

$$K = K_o T \exp(-\theta/T) \tag{2}$$

where T is the temperature of the glass and K_o and are constants that are functions of the mole percent of network modifiers (M) in the glass. For silicate glasses

$$K_o \approx \{3.4 + (8 \times 10^{-4}) M^3\} \times 10^{-17} \tag{3}$$

and

$$\theta \approx 3600 + 165M \tag{4}$$

For a given pressure differential (ΔP) across the glass microsphere membrane, the internal pressure (P_i) at any time during fill or release of hydrogen is

$$P_i = P_{io} \pm \Delta P\{1-\exp(-t/\tau)\} \tag{5}$$

where P_{io} is the original internal pressure and t is time. The + sign applies to filling and the - sign applies to releasing. The term τ is the fill or release time constant, which can be expressed as

$$\tau = r_i^2 \Delta r/(3RTKr_o) \tag{6}$$

where r_i and r_o are the inside and outside radii, respectively of the microspheres, and R is the gas constant. For a step function in temperature, 63% of the hydrogen would transfer in one time constant, and 86% would transfer in two time constants.

Figs. 6 through 9 are related to the energy needed to fill and release the microspheres with hydrogen. Fig. 6 shows the heat required, as a fraction of the lower heating value of the hydrogen stored, to raise the temperature of the combined masses of microspheres and hydrogen. The increase in heat required for increases in pressure is primarily due to the increased mass of glass needed to maintain the same safety factor.

For pressurization, the energy required is a function of, among other parameters, the compressor efficiency and the number of stages. In Fig. 7 the compression energy for a 75% efficient, three-stage

compressor is added to twice the value for heat from Fig. 6, to give a total energy required for a fill and release cycle of hydrogen. The figure shows that the "round trip" energy for reasonable pressures and temperatures ranges from 10% and 20% of the lower heating value of the hydrogen stored. This total energy requirement is less than that needed to liquify hydrogen for shipment.

Fig. 8 shows the variation in hydrogen permeability with temperature, for silicate glass. The resulting fill and release time constant is given in Fig. 9 for 30-μm-diameter microspheres with a 0.675-μm-thick membrane made with a glass containing 15% network modifiers. An increase of 200°C in temperature results in a decrease of the time constant by four orders of magnitude. However, the fill, release time constant is still about one hour, which means it would take three hours at 220°C to fill or release the microsphere by 95%. An increase in temperature to 370°C would give the same result in 15 minutes.

Conclusions

The performance of glass microspheres appears to be sufficient for applications to bulk storage and transport of hydrogen based on the analysis using semi-empirical modeling. To date there is still some uncertainty in the behavior of hydrogen-permeable glasses with regard to the effect of network modifiers, and to strengths. Also, the behavior of large beds of high-strength microspheres has not been studied. Truck trailers using glass microspheres can transport several times the mass of hydrogen than a large pressure tube trailer. Also, hydrogen transporters employing glass microspheres can require significantly less capital cost than liquid hydrogen transporters, and the cycle energy required for transport in microspheres is less than for liquid hydrogen transport.

Acknowledgments

This work performed under the auspices of the U. S. Department of Energy by the Lawrence Livermore National Laboratory under contract No. W-7405-ENG-48. The author wishes to thank Charles Hendricks of W. J. Schafer Associates, Incorporated for his help in this project.

References

Shelby, J. E. 1973. A Comprehensive Review of Gas Permeation, Diffusion, and Solubility in Inorganic Glasses, Technical Report SLL-73-0259, Livermore, CA, Sandia National Laboratory.

Souers, P. Clark 1986, Hydrogen Properties for Fusion Energy, Berkeley: University of California Press.

Souers, P. C., Moen, I., Lindahl, R. O., and Tsugawa, R. T. 1978. "Permeation Eccentricities of He, Ne, and D-T from Soda-Lime Glass Microbubbles." J. American Ceramic Soc., Vol. 61, No.1-2.

Teitel, Robert J. 1981. Microcavity Hydrogen Storage - Final Progress Report, Technical Report BNL 51439, New York, Brookhaven National Laboratory.

Woerner, R. L., Weinstein, B. W., Moen, I. M., and Rittman, J. G. 1979. Working Strengths and D-T Fill Procedures for Glass Microsphere Laser Fusion Targets, Technical Report UCRL-82728, Livermore, CA, Lawrence National Laboratory.

Figure Captions

Figure 1. Geometry and dimensions of glass microspheres for hydrogen storage.

Figure 2. Microspheres will be handled in packed beds for use as a hydrogen transport medium.

Figure 3. Comparisons of hydrogen storage density and mass fraction for different hydrogen storage systems and media.

Figure 4. Mass fraction of hydrogen stored in a bed of high-strength glass microspheres.

Figure 5. Volumetric density of hydrogen stored in a bed of high-strength, glass microspheres.

Figure 6. Fraction of hydrogen lower heating value needed for one heating cycle to raise the temperature of a microsphere bed and hydrogen.

Figure 7. Fraction of hydrogen lower heating value needed for one pressure cycle and two heating cycles to load and unload a bed of microspheres with hydrogen.

Figure 8. Permeability constant vs. temperature increase above 20C, for hydrogen in glass microspheres with 15% of network modifiers.

Figure 9. Time constant vs. temperature increase above 20C, for exponential fill or release of hydrogen using above glass microspheres with diameters of 30 μm and 0.675 μm-thick walls. These microspheres could contain hydrogen at 9000 psi with a safety factor of 1.5.

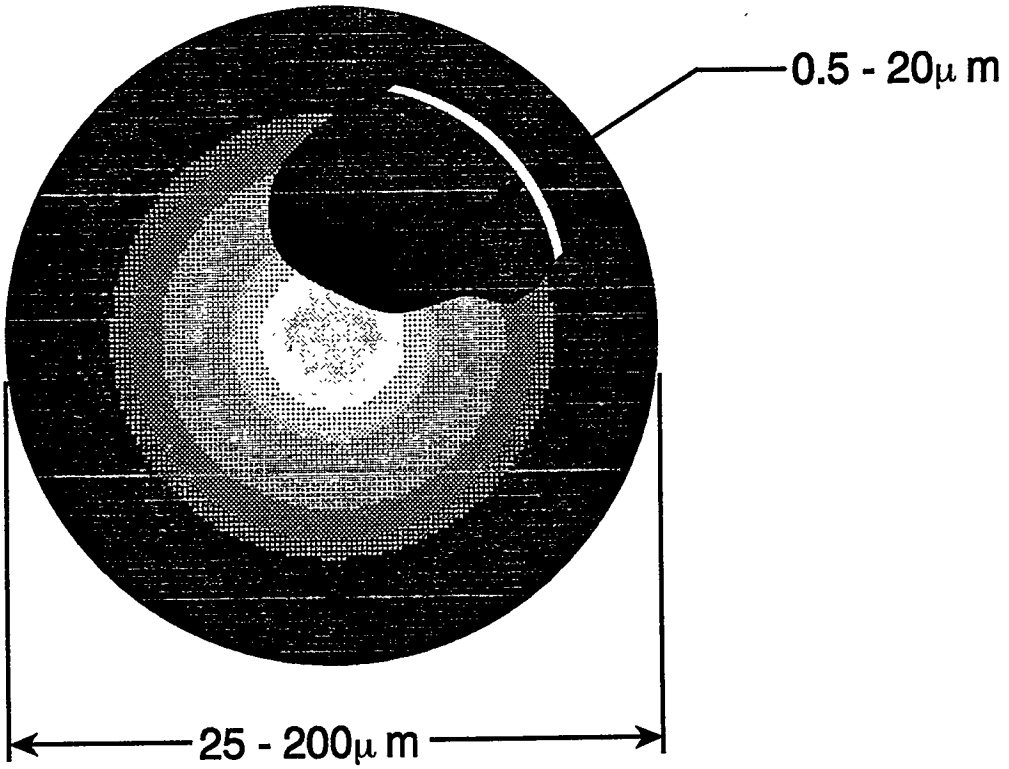

Figure 1.

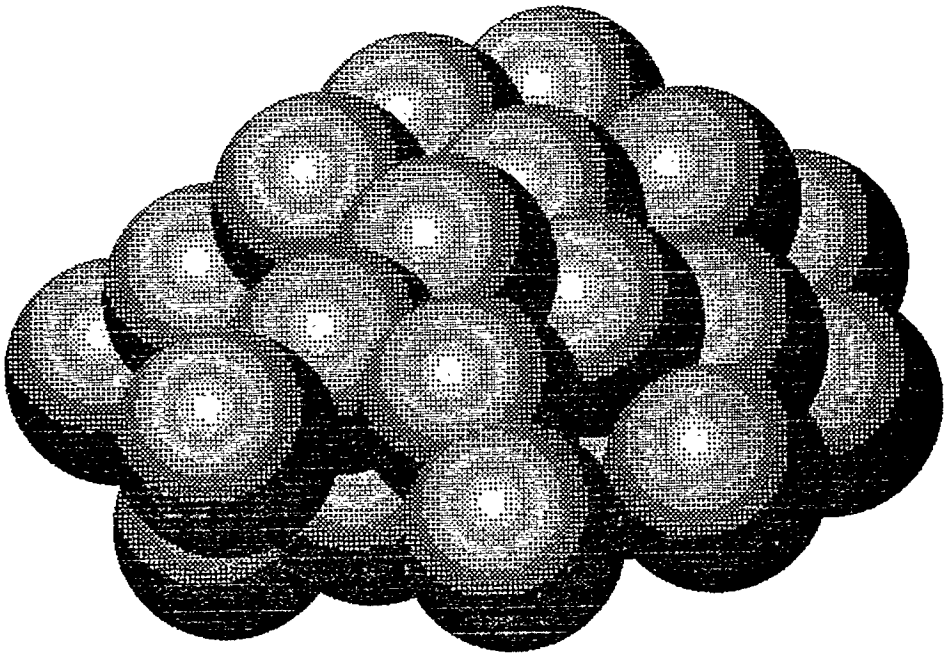

Figure 2.

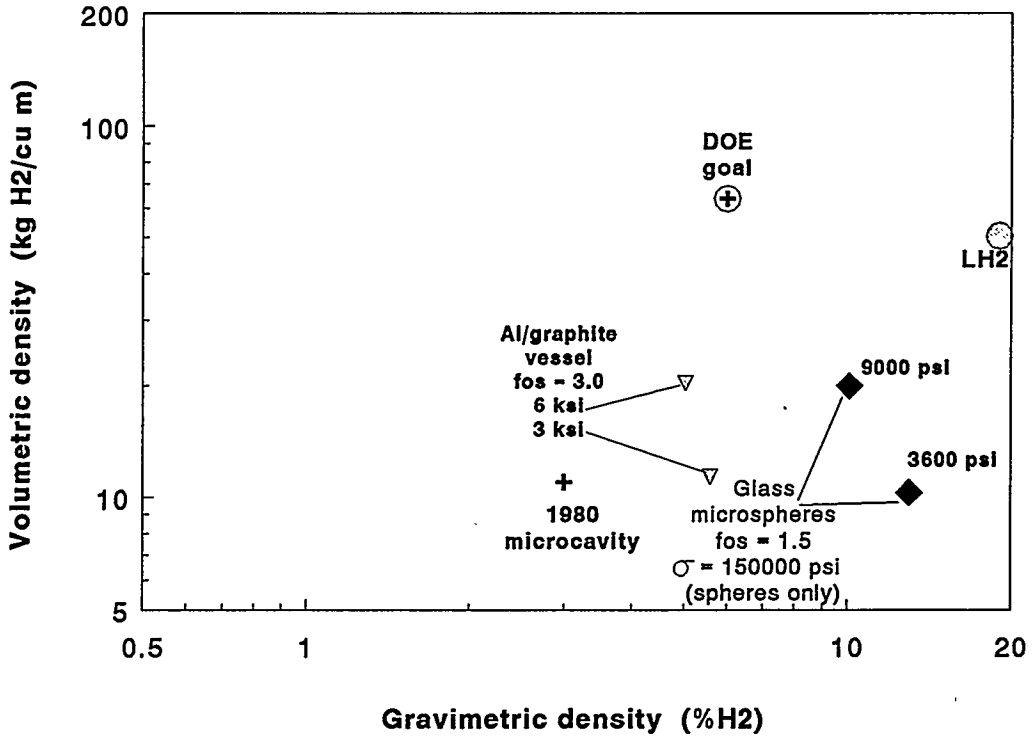
200
100
10
5
0.5
1
10
20
Volumetric density (kg H2/cu m)
Gravimetric density (%H2)
DOE
goal
LH2
Al/graphite
vessel
fos = 3.0
6 ksi
3 ksi
1980
microcavity
Glass
microspheres
fos = 1.5
σ = 150000 psi
(spheres only)
9000 psi
3600 psi

Figure 3.

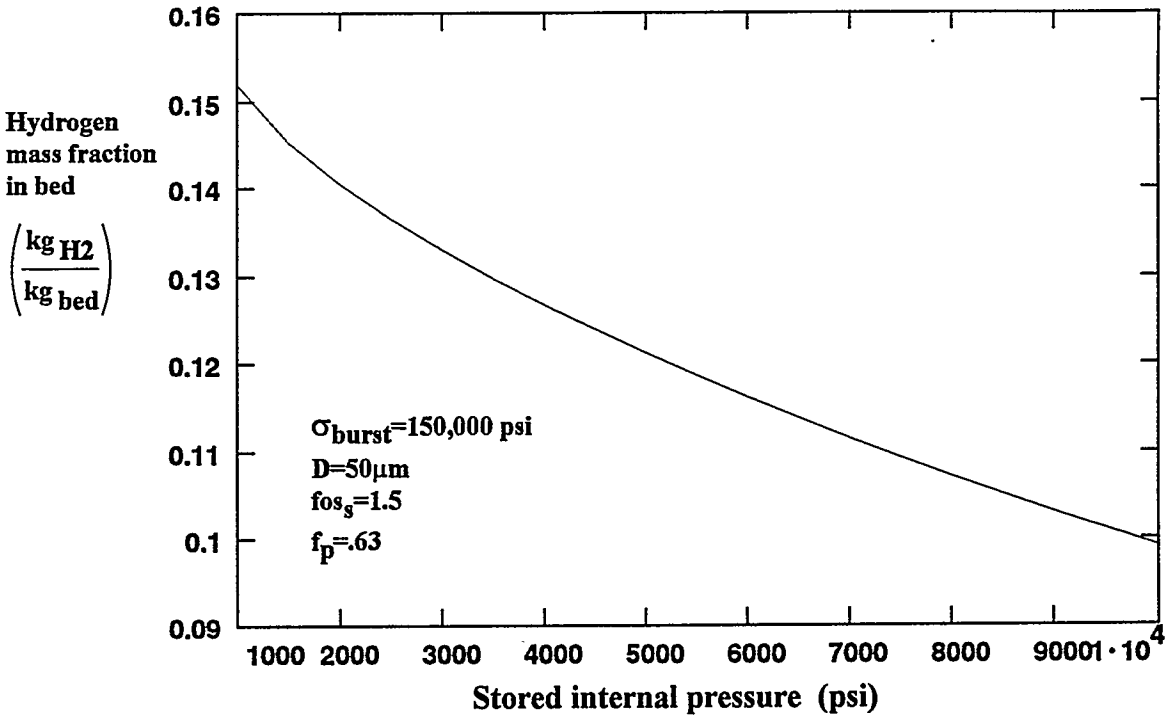

Figure 4.

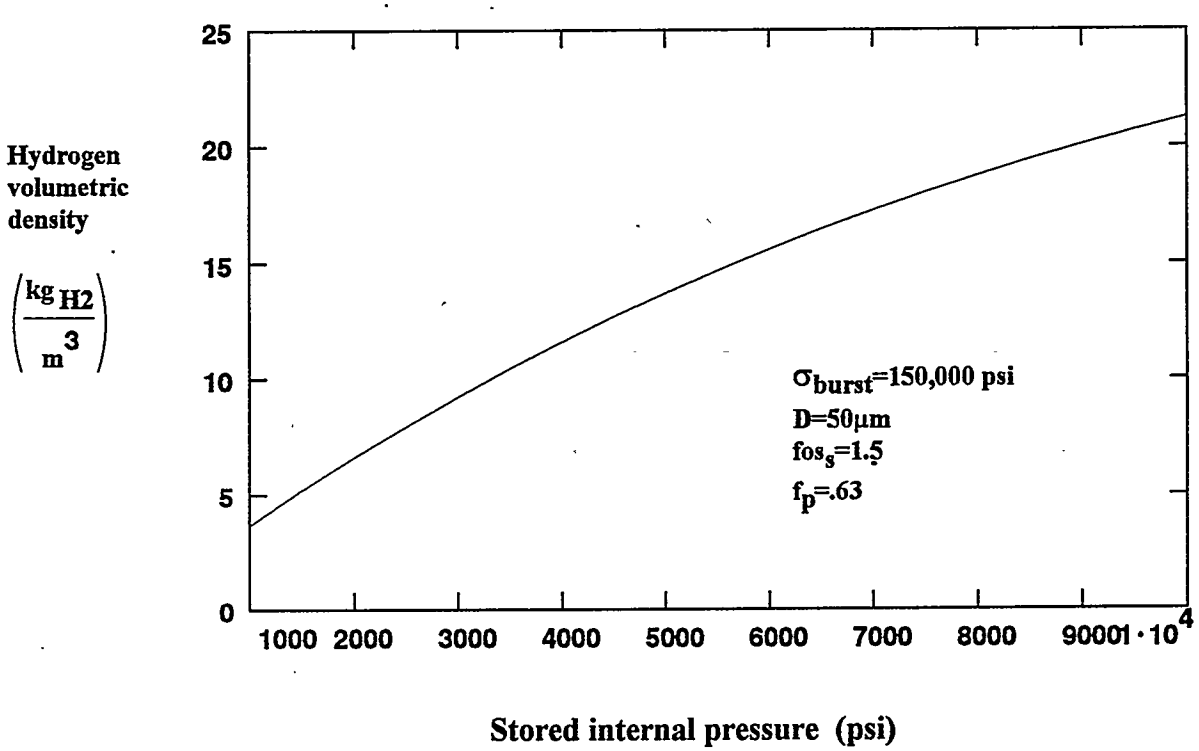

Figure 5.

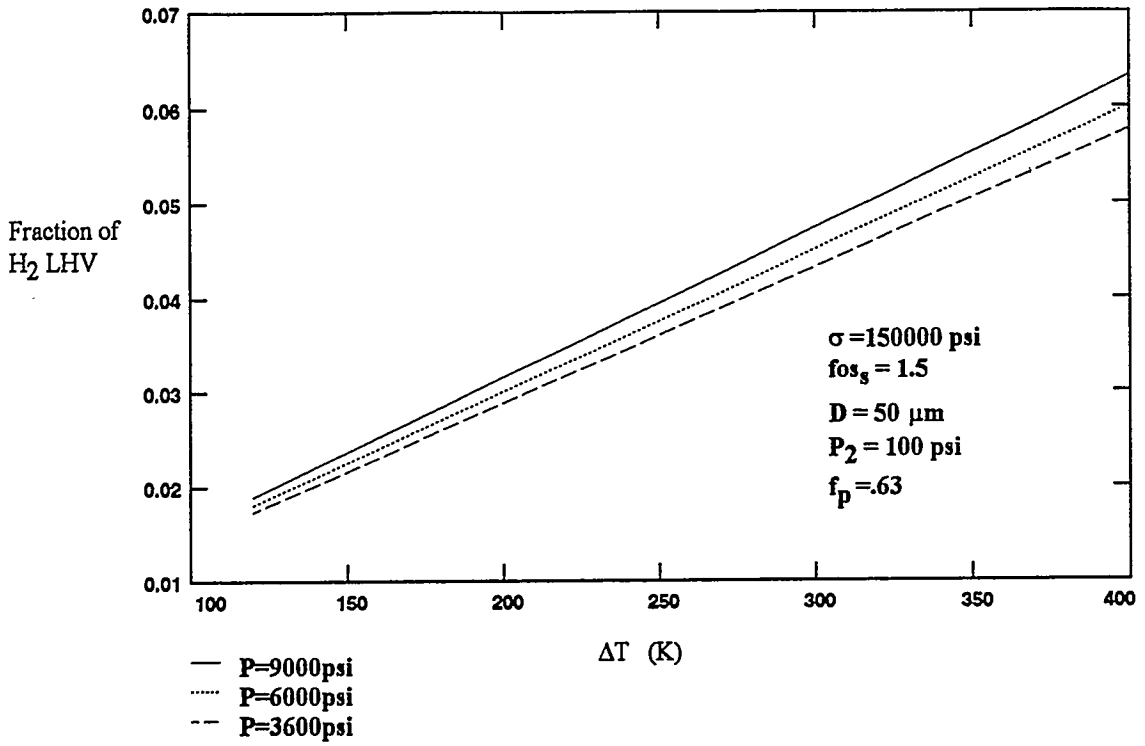

Figure 6.

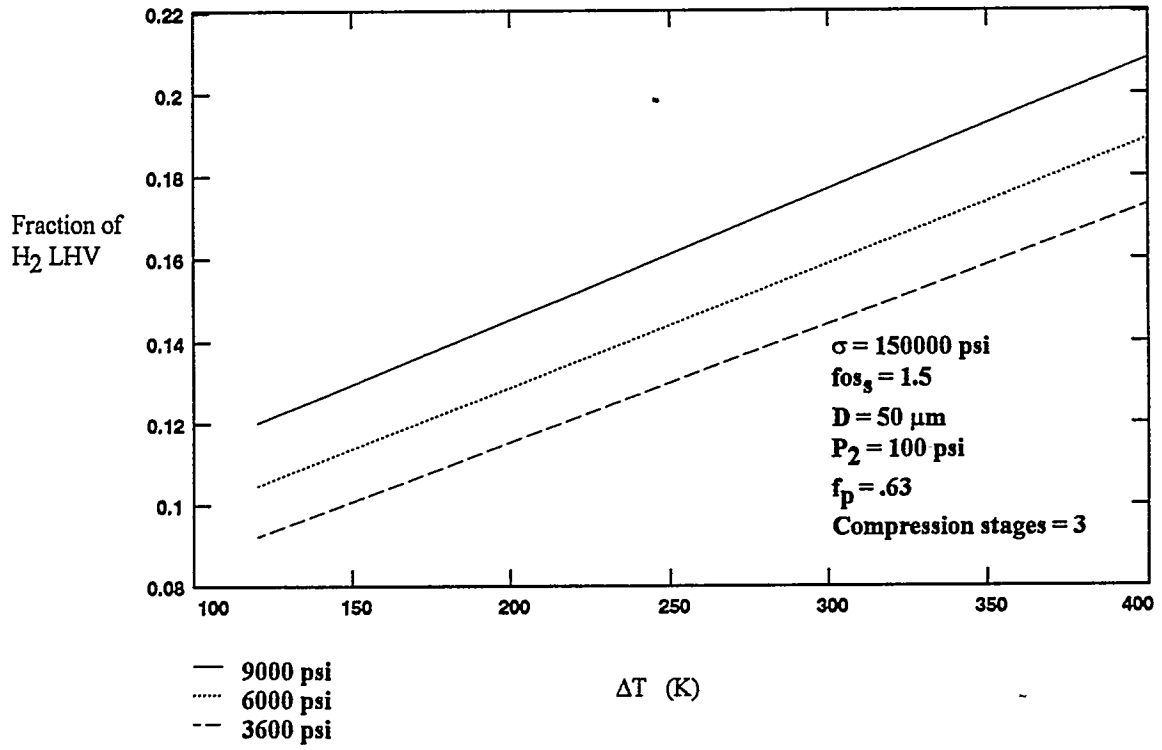

Figure 7.

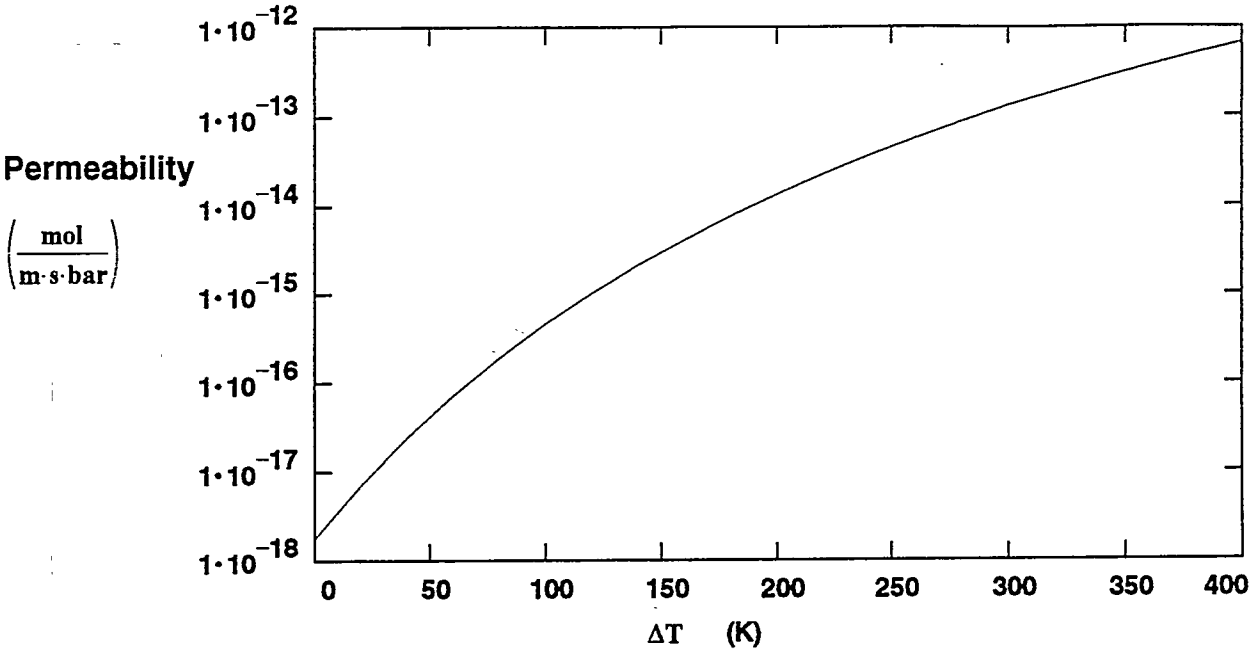

Figure 8.

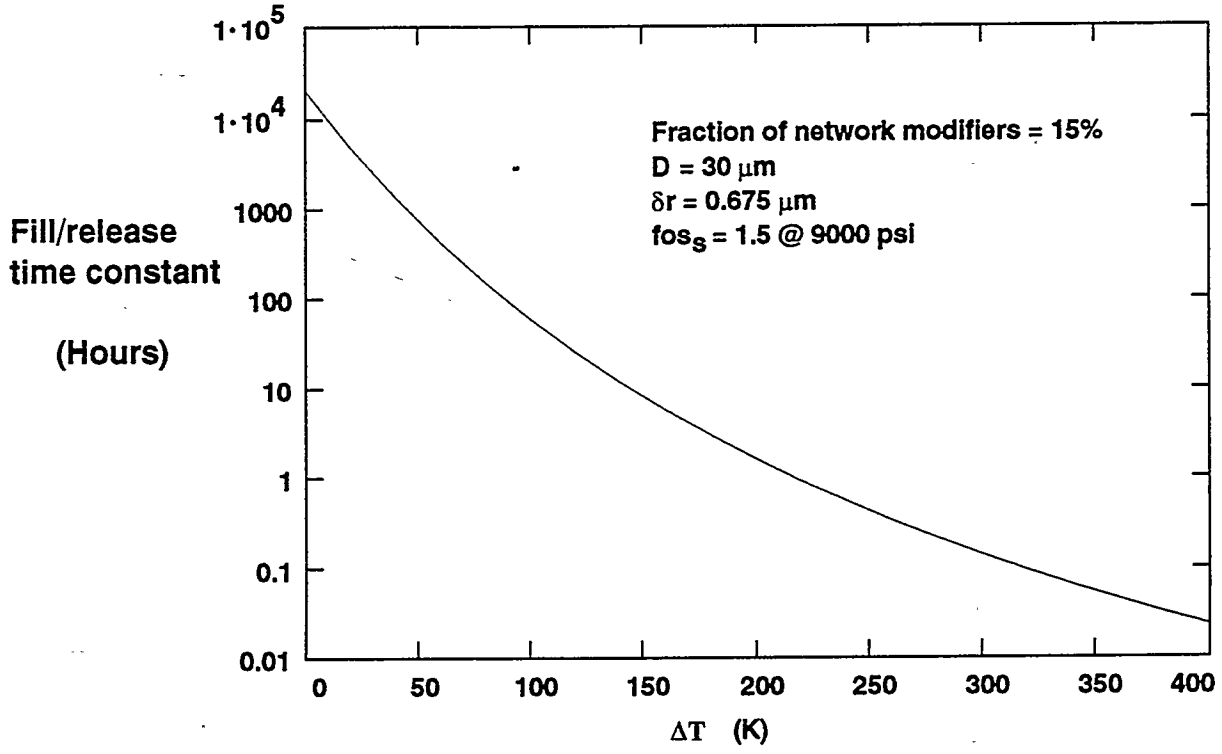

Figure 9.

CARBON NANOTUBE MATERIALS FOR HYDROGEN STORAGE

A.C. Dillon, T.A. Bekkedahl, A.F. Cahill, K.M. Jones, and M.J. Heben
National Renewable Energy Laboratory
Golden,CO 80401-3393

Abstract

The lack of convenient and cost-effective hydrogen storage is a major impediment to wide scale use of hydrogen in the United States energy economy. Improvements in the energy densities of hydrogen storage systems, reductions in cost, and increased compatibility with available and forecasted systems are required before viable hydrogen energy use pathways can be established. Possible approaches to hydrogen storage include: physical storage via compression or liquefaction; chemical storage in, for example, methanol, ammonia, or diborane; metal hydrides; and gas-on-solid adsorption. Although each storage method possesses desirable attributes, no approach satisfies all of the efficiency, size, weight, cost and safety requirements for transportation or utility use. Carbon-based hydrogen adsorption materials hold particular promise for meeting and exceeding the U.S. Department of Energy hydrogen storage energy density targets for transportation if concurrent increases in hydrogen storage capacity and carbon density can be achieved. These two goals are normally in conflict for conventional porous materials, but may be reconciled by the design and synthesis of new adsorbent materials with tailored pore size distributions and minimal macroporosity. Carbon nanotubes offer the possibility to explore new designs for adsorbents because they can be fabricated with small size distributions, and naturally tend to self-assemble by van der Waals forces. In last year's Proceedings of the Hydrogen Program we presented the result that nanotube-containing materials could store 8.4 wt% hydrogen at 82 K and 11 psi. This year we report heats of adsorption for hydrogen on nanotube materials that are 2 and 3 times greater than for hydrogen on activated carbon. The hydrogen which is most strongly bound to these materials remains on the carbon surface to temperatures greater than 285 K. These results suggest that nanocapillary forces are active in stabilizing hydrogen on the surfaces of carbon nanotubes, and that optimization of the adsorbent will lead to effective storage at higher temperatures. In this paper we will also report on our activities which are targeted at

understanding and optimizing the nucleation and growth of single wall nanotubes. In particular, we have performed extensive transmission electron microscope imaging to correlate single wall nanotube yield with location within our reactor as a function of carbon rod translation rate. These experiments were made possible by the development of a unique feedback control circuit which stabilized the plasma-arc during a synthesis run.

Statement of the Problem / Relevance of the Work

Background

Implementation of a domestic renewable hydrogen energy economy would reduce all forms of pollution associated with the use of fossil and nuclear fuels, and decouple the United States from volatile and unmanageable foreign energy markets. Development of an environmentally benign and domestically available energy source such as hydrogen may well become a matter of national economic security as the United States continues to increase the fraction of imported petroleum beyond 50% of total consumption.

Hydrogen *storage* is a key enabling technology that must be significantly advanced in performance and cost effectiveness if the U.S. is to establish a hydrogen energy economy. As described in the U.S. DOE Hydrogen Program Plan for FY 1993 - FY 1997, compact and lightweight hydrogen storage systems for transportation do not exist, and low-cost low-loss stationary storage for industrial or utility use is unavailable.

Nearly 50% of the total oil used by the U.S., a fraction which is roughly equivalent to the amount which is imported, is consumed by the transportation sector (NES 1992). This fraction could be supplanted by using hydrogen to power either a fuel cell or an advanced internal combustion engine in vehicular applications. However, even with advances in hydrogen production and utilization technologies, the development of hydrogen powered vehicles will be impeded by the lack of suitable storage options. Currently, there are no hydrogen storage technologies that provide high gravimetric and volumetric energy density storage in a cost effective and safe manner. The requirements for on-board hydrogen storage are difficult to meet because of the lower energy content of stored hydrogen as compared to either gasoline or diesel fuels. New approaches to hydrogen storage with drastically improved performance characteristics are critically needed if the wide-spread use of hydrogen powered vehicles is to become a reality.

Research and development geared towards implementation of a national hydrogen energy economy will have many indirect benefits to the U.S. economy. With almost 600 million vehicles in the world in 1992 - double the number in 1973 - the conflict between energy requirements, power generation, and environmental concerns is felt on a world-wide basis (Flavin & Lenssen 1994). Thus, there is a need for hydrogen-related technologies overseas, and the advancement of a national hydrogen energy economy will create opportunities for the sale of U.S. hydrogen-related technologies abroad.

Currently Available Hydrogen Storage Technologies

Possible approaches to hydrogen storage include: physical storage via compression or liquefaction; chemical storage in hydrogen carriers (e.g. methanol, ammonia); metal hydrides; and gas-on-solid adsorption. Although each storage method possesses desirable attributes, no approach satisfies all of the efficiency, size, weight, cost and safety requirements for transportation or utility use. Table 1 displays a compilation of the advantages and disadvantages associated with the various H_2 storage technologies.

Gas-on-solid adsorption and metal hydride storage are inherently safer than physical hydrogen storage methods. In addition, these two methods of hydrogen storage avoid the use of toxic chemicals (a concern normally associated with chemical carriers), and both have the potential to be more energy efficient than physical storage methods. Figure 1 compares the performance of systems based on physical, metal hydride, and adsorption storage in terms of volumetric and gravimetric energy densities. The figure also displays the DOE energy density target value for vehicular hydrogen storage systems. This latter value assumes fuel cell use and a 350 mile range, and represents the storage of ~400 kBtu of hydrogen (~2.9 kg) in the weight and volume of the gasoline tank in a conventional internal combustion engine vehicle with the same range. Clearly, the DOE storage density goals can only be met with significant advances in hydrogen storage technologies.

Table 1. Advantages and Disadvantages of Storage Technologies.

Compressed H_2	Ad:	Well-developed technology base, good gravimetric performance, good dormancy characteristics.
	Dis:	Large volume, compression costs, safety.
Liquid H_2	Ad:	Excellent volumetric and gravimetric energy density for large containers.
	Dis:	Liquefaction costs, boil-off losses, poor performance in small systems.
Gas-on-Solid	Ad:	Fair volumetric and gravimetric energy densities, potentially inexpensive.
	Dis:	Requires compression and cooling. Complexity.
Metal Hydrides	Ad:	High volumetric energy density. Safe.
	Dis:	Poor gravimetric performance. Trade-off between high wt% and high dissociation temperature.
Chemical Storage	Ad:	High gravimetric storage density.
	Dis:	Toxicity, impure hydrogen stream, re-hydrogenation reaction.

The hydrogen storage properties of high-surface-area "activated" carbons have been extensively studied (Carpetis & Peshka 1980; Schwarz 1; Agarwal et al. 1987; Schwarz 1993). These materials are normally prepared from a variety of biological or mineralogical carbonaceous materials by

processing that includes: chemical activation to produce dehydration or decomposition of organic constituents; low-temperature carbonization (400-500°C) to remove volatile organics; and high-temperature oxidation (800-1000°C to develop porosity and surface area (Kirk et al. 1978). These methods produce microcrystalline, non-graphitic carbon materials with specific surface areas of 300-2500 m^2/gm. One of the best currently available activated carbons adsorbs ~4.8 wt% H_2 at a temperature of 87 K and a pressure of 870 psi. Under the same conditions, a carbon fiber-wrapped pressure vessel containing this activated carbon stores an additional 4.3 wt% (carbon basis) as compressed gas in the voids within the container. Taking into account the weight of the pressure vessel and vacuum jacket, the total system stores H_2 at 4.2 wt% and 16.8 kg/m^3 (Schwarz 1993).

Unfortunately, the aforementioned storage system does not significantly benefit from the incorporation of carbon under the chosen operating conditions. A simple calculation using the parameters specified by Schwarz (1993) reveals that hydrogen could be stored at 4.8 wt% and 16.5 kg/m^3 at the same pressure and temperature *without* carbon.

Activated carbons are ineffective in hydrogen storage systems because only a small fraction of the pores in the typically wide pore-size distribution are small enough to interact strongly with gas phase hydrogen molecules. For this reason adsorption isotherms are typically drawn-out and become linear at higher pressures. A semi-empirical model which describes pore growth during pyrolysis and/or gasification of coal shows that pore number densities vary with $1/r^3$, where r is the pore radius (Simons & Finson 1979). Thus, although the number of micropores is relatively large, the small number of larger pores comprise a large fraction of the total pore volume. In fact, porous carbons synthesized by conventional thermal processing generally exhibit more than 50% of total pore volume as macroporosity with pore dimensions greater than ~40 Å (Quinn & MacDonald 1992). Macropores only participate in monolayer adsorption, and are therefore relatively ineffective in adsorption storage.

The performance of all activated carbon adsorption systems falls short of the DOE Hydrogen Program Plan storage goals (6.5 wt % H_2 and 62 kg H_2/m^3). Researchers at A.D. Little (Hynek et al. 1992) have predicted that both Hydrogen Program Plan storage goals could be met if a gravimetric energy density of 8 wt% could be achieved while carbon density was increased from ~0.4 to 0.8 gm/cc. This is a technically challenging task since the surface area and density of porous materials are generally inversely related.

To date, most research on hydrogen adsorption storage materials has been empirical in nature and has relied on simply reporting the hydrogen adsorption/desorption properties of commercially available carbons and zeolites. The parameters which are critical for hydrogen adsorption system performance (surface area, pore size distribution, micropore volume, heat of adsorption, thermal conductivity, material integrity, kinetics, etc.) are typically *measured* but not *controlled.* A complete understanding and optimization of hydrogen adsorption mechanisms will only be achieved when critical material parameters can be controllably varied to establish relationships between properties and performance. Our research is targeted at the proper design and engineering of materials in the nanometer-size regime to produce high performance adsorbents for hydrogen storage. We believe our approach will meet the challenge for carbon adsorbents outlined by Hynek et al. (1992).

Technical Approach

The gas adsorption performance of a porous solid is maximized when all the pores are not larger than a few molecular diameters (Gregg & Sing, 1982). Under these conditions the potential fields from the walls of the so-called micropores overlap to produce a stronger interaction than would be possible for adsorption on a semi-infinite plane. At sufficiently low temperatures, where the escaping tendency of the gas is much less than the adsorption potential, the entire micropore may be filled with a condensed adsorbate phase by nanocapillary filling. For the case of hydrogen, with a van der Waals diameter of ~4.4 Å (CRC 1975), pores would be required to be smaller than ~40 Å to access this nanocapillary filling regime. Sufficiently small pores would exhibit an adsorption potential strong enough to localize H_2 at relatively higher temperatures. Ideally, the entire porous volume of an adsorbent would be of the microporous variety, and the volume and mass of the adsorbent skeleton would be the minimum necessary to develop the adsorption potential and provide sufficient thermal conductivity for management of heat fluxes associated with adsorption and desorption. Such a material would meet the technical challenge described above by providing increased material density while also increasing gravimetric storage density.

In FY 1993, we initiated a research program to identify and investigate new solid-state hydrogen storage options possessing the potential for dramatic improvements over currently available technologies. Our conceptual model indicated that single-wall carbon nanotube assemblies could be fabricated to behave as nearly ideal adsorbents (Bekkedahl & Heben, 1994). Simple calculations indicated that a close-packed assembly of 20Å diameter tubules would have a surface area close to the theoretical maximum for graphite (~5000 m^2/gm) and a density of ~1 gm/cc. Further calculations indicated that a single isolated 20 Å tube could meet both DOE energy density targets by storing H_2 at densities of 7.8 wt% and 65 kg/m^3. This latter calculation considered a close-packed arrangement of H_2 molecules as a first monolayer on the interior of the nanotube, with subsequent volume filling by liquid H_2. Additional storage in the interstitial spaces between assembled tubes would also be possible. Furthermore, if nanocapillary forces are active in ensembles of carbon nanotubes, these H_2 storage capacities could be obtained at higher temperatures and lower pressures than those that are required for activated carbons.

In the Proceedings of the 1994 Hydrogen Program Review, we presented microbalance measurements which demonstrated gravimetric hydrogen storage densities of up to 8.4 wt% at 82 K and 11 psi on carbon nanotube samples. This substantial hydrogen uptake at low pressures demonstrated a strong interaction between hydrogen and these materials. Such behavior indicated that nanotube materials provide environments with higher heats of adsorption than can be found with activated carbons, and suggested that these materials could be optimized for use as efficient hydrogen storage materials.

During the past year, we performed temperature programmed desorption (TPD) measurements to directly determine if the unique nanostructures in nanotube materials can adsorb hydrogen more strongly than is possible with currently available adsorbents. In this paper we present the results from our measurements which demonstrate that hydrogen adsorption energies on nanotube materials are indeed factors of 2-3 times higher than the maximum that has been observed for hydrogen adsorption on conventional activated carbons. These results strongly indicate that nanocapillary filling

mechanisms are operative in carbon nanotube materials. Optimization of material design to fully utilize nanocapillary forces in these materials should enable a nanotube-based hydrogen storage system to operate at temperatures considerably above those needed for activated carbon-based systems, thus reducing, and possibly eliminating, refrigeration and insulation requirements.

If single-wall carbon nanotube materials are to become a viable hydrogen storage option, the materials must be synthesized in a cost effective manner. A rough analysis of the data presented by Ebbessen & Ajayan (1992) estimated a cost of $1500/kg of multi-wall tubule material. This estimate was derived from data published by the first researchers who were able to synthesize milligram quantities of multi-wall tubules, and the cost is essentially that for serendipitous production with only minimal optimization. Dramatic improvements in the synthesis of multi-walled tubules have already been reported (Hausslein 1995). However, the yields and costs expected for formation of nanotube materials optimized for hydrogen storage have not yet been determined. Clearly, as the governing parameters which control tubule synthesis are identified, the efficiency of the synthesis will be improved with accompanying reductions in cost. In this paper we will also present results of our efforts to understand, control, and optimize the production of single wall carbon nanotubes.

Results and Discussion

Our approach to developing engineered carbon nanotubules for hydrogen storage applications has involved two closely coupled tasks. In the first task, we analyze the hydrogen storage properties of nanotube-containing samples under a variety of temperature and pressure conditions. Samples used for the uptake measurements presented in this paper were obtained through our collaboration with D.S. Bethune and his research group at IBM. Task 2 is focused on the synthesis of carbon nanotubes and nanotubule assemblies. Our objectives for this task are to produce research quantities for analysis in Task 1, and to develop an understanding of the nucleation and growth of carbon nanotubules so that mass production of optimal materials may be achieved.

Temperature Programmed Desorption

In order to develop carbon nanotube materials for hydrogen storage, it is critical to obtain a better understanding of the interactions between hydrogen and the various types of carbon surfaces and structures present in nanotube materials. Specifically, we have been interested in determining if hydrogen molecules are stabilized by adsorption on nanotube materials to a greater extent than on activated carbons. This result has been theoretically predicted by others (Pederson & Broughten 1992), and serves as a basis for our experimental investigations. TPD is a versatile technique for measuring the thermal stabilities of adsorbates on surfaces. Proper application of the technique yields thermodynamic information about the available binding sites, and elucidates the kinetic parameters associated with desorption. A typical TPD experiment consists of controllably dosing a molecule (or atom) onto a surface to prepare an adsorbed amount, linearly increasing the temperature of the surface with a predetermined heating program, while monitoring the species which desorb into the gas phase with a mass spectrometer as a function of time and temperature.

Experimental Procedure

A schematic of the ultra high vacuum (UHV) chamber we have used for TPD studies is shown in Figure 2. The UHV chamber was pumped both by a 60 l/s Balzers turbomolecular pump, and a liquid nitrogen cooled cryostat mounted on a differentially pumped feedthrough (George 1986). The latter also served as sample mount. The turbomolecular and cryo pumps enabled operating pressures of 1-2 x 10^{-8} Torr to be obtained without baking. The UHV chamber was equipped with a mass spectrometer for line-of-site measurement of desorbing species. An ion gauge and a capacitance manometer were employed to monitor the pressure of the chamber. Gas admission was controlled with a variable conductance valve.

Approximately one milligram of carbon nanotube material was placed in a packet formed from strips of .025 mm thick platinum foil. The platinum strips had a length of 17 mm and a width narrowing from 11 mm to 5 mm at the point where the nanotube material was located. A spot welder was used to secure the platinum foil packet around the nanotube material. Several pin holes were sufficient to provide for diffusion of gas phase species in and out of the platinum packet. The platinum foil was clamped to a copper block at the bottom of the liquid nitrogen cooled cryostat. Plates of 2 mm thick sapphire provided electrical isolation between the copper block and the cryostat.

A sample mounted on the end of the liquid nitrogen cooled cryostat could be cooled to 100 K and heated to 1000 K using resistive heating. Temperatures were measured using a .005 in diameter chromel/alumel thermocouple which was inserted through a 0.5 mm diameter hole in the top of the platinum foil and subsequently secured using ceramic glue. The temperature was maintained by a temperature controller which drove the DC current output of a programmable power supply. A laboratory computer was used to record both the sample temperature and the mass spectra of the desorbing species as a function of time.

Pre-adsorbed species on the surfaces of the carbon nanotube materials were removed prior to each TPD experiment by annealing the sample in vacuum to 870 K. The sample was then exposed to hydrogen at 300 Torr for 10 minutes at 273 K, and subsequently cooled to 100 K prior to evacuation of the chamber. When a pressure of 1-3 x 10^{-8} Torr was obtained, the sample temperature was increased using a linear heating rate of ~ 2°/s. Line of sight TPD spectra were recorded every 2 s up to temperatures of 870 K using the mass spectrometer.

Experimental Results

A typical H_2 temperature programmed desorption spectrum for carbon nanotube material is shown in Figure 3. The figure displays two peaks for hydrogen desorption into high vacuum at 146 and 285 K. Qualitatively, the presence of hydrogen after the sample has been evacuated indicates a strong interaction between H_2 and the sample. Moreover, the two peaks suggest the existence of two distinctly different sites which can store hydrogen.

Using the methods of Chan et al. (1980), activation energies for hydrogen desorbing from each of the two distinct sites can be obtained. Assuming first order desorption and negligible readsorption, the

following equation may be used to estimate the desorption activation barrier E_d:

$$E_d/RT_M = -1 + (1 + 5.832T_M^2/W_{1/2}^2)^{1/2}$$

In the expression, T_M and $W_{1/2}$ correspond to the maximum temperature of the TPD peak, and to the full width of the peak at half of the maximum intensity, respectively. R is the universal gas constant. For the desorption peaks at 146 and 285 K, the calculated desorption activation barriers using this expression are 13 kJ/mol and 18 kJ/mol, respectively. For these nanotube materials, the activation energy for desorption should be approximately equal to the heat of adsorption since hydrogen adsorption is expected to be non-dissociative. Thus, one can make a direct comparison between our measurements and the value of 6.5 kJ/mol that has been obtained previously for activated carbon (Schwarz 1992). Our results demonstrate that hydrogen can be bonded more strongly to nanotube materials than activated carbons, and that nanocapillary filling mechanisms may indeed be operative in our samples. Moreover, these results indicate that the isolation or efficient synthesis of the material fraction responsible for the peak at 285 K would offer the possibility for hydrogen storage by adsorption at ambient temperatures.

In addition to the hydrogen desorption signal, a desorption signal for N_2 was measured at 153 K. This latter signal indicates a strong interaction between the sample and nitrogen since the hydrogen we used for dosing was typically 99.9% pure. In a worse case scenario, if the one part per 1000 impurity in the H_2 was N_2, the 200 Torr H_2 dose would be accompanied by a 200 mTorr N_2 dose. To probe the degree of competition between H_2 and N_2 for the available sites, TPD experiments were performed in which the sample was first exposed to N_2, and then to high purity H_2. Interestingly, the amount of hydrogen adsorbed was not greatly affected by the N_2 dose for N_2 dose pressures as high as 50 mTorr. These results suggest that nanotube materials will not be significantly affected by nitrogen contamination in a working hydrogen storage system, and that the sites responsible for H_2 adsorption are largely inaccessible to larger molecules. Interactions with other possible contaminants have not yet been explored.

Nanotube Synthesis

The parameters which control the nucleation and growth of single-wall carbon nanotubes in the spark-gap process are unclear at the present time. There is considerable activity around the world which is directed toward developing a more detailed understanding of the relevant processes. Our activity has focused on developing techniques to stabilize the plasma-arc during production to allow investigation of the interdependence of key experimental parameters.

Experimental Procedures

The growth of single-wall carbon nanotubes is achieved by co-evaporating cobalt/carbon mixtures in a spark-gap evaporator (SGE) (Bethune et al. 1993). Figure 4 is a schematic diagram of the SGE we have constructed for studying and optimizing the synthesis of single-wall tubes (SWTs). In the instrument, two graphite electrodes of differing diameters (6 & 13 mm) are mounted onto the baseplate of the evaporator by electrically isolated positioners. Electrical feedthroughs connect the

graphite rods to a multi-tapped transformer capable of supplying more than 5 kW. The two graphite rods are held co-axially, and a rotational feedthrough imparts linear motion to the small rod via a pinion/rack gear arrangement. The pumping system consisting of a liquid nitrogen cold-trap, a diffusion pump, and a roughing pump, is used to evacuate the bell jar to less than 10^{-6} torr. While the system is being pumped the two graphite rods are contacted and resistively heated to liberate any adsorbed gases. The synthesis run is performed once the rods have been cooled and separated and the chamber has been back-filled with helium to a pressure of ~500 Torr.

The 6 mm graphite rod is doped with cobalt by drilling-out and re-filling a 2.9 mm hole with a 52 wt% cobalt/carbon mixture. The 6 mm rod is thus the source for both carbon and cobalt in the SGE, with a cobalt density averaged across the rod diameter of ~14 wt%. The co-evaporation occurs from the 6 mm rod due to the higher current density and temperature in this rod relative to the 13 mm rod.

The spark-gap can be initiated by manually advancing the 6 mm rod towards the 13 mm rod at a rate of ~1 mm/min with 15-20 volts between the rods. When the rods are close enough to ionize He gas molecules within the gap, electrical current flow is established which sputters and evaporates material from the smaller rod. Two distinctly different modes of operation were noted in early experiments with arc currents of ~150 AC amps. One mode was characterized by a gap spacing of ~1 mm and a blue plasma extending 1-2 cm above the rods. In contrast, the second mode operated with a ~1/2 mm gap between the rods without a well defined plasma. The operating mode was dependent on the rate of translation, the gap size, and the arc current for a particular applied voltage, and could not be manually stabilized due to the dynamic nature of the plasma-arc. Although SWTs could be fabricated by these methods, the poor control during these initial experiments made it impossible to quantify the tubule production yields in terms of the run parameters or the deposit location.

In an effort to improve the controllability of the synthesis process, an electronic feedback circuit was constructed to stabilize the arc with respect to either the arc-current, the gap voltage, or the feed rate (Fig. 4). A computer data acquisition system was employed to monitor the arc current, voltage, and feed rate, and allowed the interdependency of the arc parameters to be analyzed.

The electronic feedback circuitry was used to perform three different 10 minute runs with a potential of 16.2 volts and translation rates of 1.5, 2.5 and 4.5 mm/min. The nanostructures produced in each of the different runs were analyzed by transmission electron microscopy (TEM) in order to ascertain optimal conditions for single-wall tubule production. Samples were prepared for TEM investigations by suspending 1 mg of sample in 86 ml of acetone. The solutions were ultrasonicated for 5 mins, and 1 cc was charged into a 1.5 - 1.8 x 100 mm micro-capillary and atomized onto carbon-coated Cu grids from a fixed distance of 8-9 cm. The Cu grid was sprayed with the solutions three separate times resulting in a consistent amount of material on the grids.

TEM images were obtained with a Philips CM-30 TEM/STEM instrument operating at 200 kV with a 50 μm objective aperture for improved contrast. The images were taken at magnifications from 4.4k to 340k and recorded on a 1024 x 1024 CCD camera. Each sample was surveyed for approximately 35-45 mins and four to five images were recorded to ensure a true representation of

the suspended material. Individual images were analyzed to determine the relative concentrations of SWTs, multi-wall tubes, and graphitic platelettes. A scoring scheme was developed to allow data obtained from different images pertaining to the same run to be normalized and displayed on a common scale. These comparisons were made possible by the consistent and reproducible sample preparation techniques described above.

Experimental Results

Our SGE has enabled the routine production of SWTs under a variety of conditions. Figure 5 shows a TEM image of a sample with a particularly high SWT content. The features within the micrograph represent several of the different types of nanostructures that are produced in the SGE process. The image shows bundles of SWTs arranged like spaghetti, and cobalt nanoparticles with diameters from ~5 to 30 nm. The image also shows the fine non-crystalline carbon layer which coats the nanostructures. Two other types of nanostructured carbons that are often observed, multi-wall tubes and graphitic platelettes, are not shown in this image.

The runs performed at the three different translation rates each produced four macroscopically different types of soot in specific locations within the reactor. The soot types were classified as: soot from the reactor walls (soot-walls); soot from the columnar deposit which forms on the 13 mm rod (nub); "cobweb"-like soot which forms on and drapes over the water cooling lines, mechanical positioners, and electrical leads within the chamber (web); and the soft, spongy deposit which forms on the cylindrical end surfaces of the 13 mm rod (soft-nub). The locations of the different types of soot are schematically depicted in Figure 4.

Figure 6 shows the compiled TEM data for the three different runs. The figure depicts the distribution of the various carbon nanostructures within the macroscopically different types of soot, as a function of translation rate. The data displayed in figure 6 leads to several important conclusions regarding the synthesis of SWTs in the SGE. Firstly, no SWTs were synthesized in the 4.5 mm/min run (a relative content < 0.2 on the scale of Fig. 6 indicates zero content). Instead, the yields of graphitic platelettes and multi-walled tubes were relatively high in all soot types. The gap spacing during the 4.5 mm/min run is extremely small and indiscernible to the unaided eye (<0.5 mm). Thus it appears that the feedback control circuitry stablizes the 4.5 mm/min production in the second mode of operation which was described earlier. Under these conditions it appears that the current in the gap is predominantly carried by an arc with a high current density, rather than by a lower temperature, uniform plasma. The local temperature on the small rod can be significantly higher than would be found at slower translation speeds. Thus, the sputtering and evaporation rates of material from the small rod are expected to be locally enhanced with higher translation speeds. In fact, measurement of the rod length after the run revealed that the 6 mm rod was consumed at a rate of ~5.3 mm/min, while the small rod was consumed at a rate of 3.5 mm/min in the 2.5 mm/min run .

The density of gas phase carbon atoms should be quite high near the origination point for the electric arc on the small graphite electrode. Because the higher temperatures persist for some length into the small rod, cobalt is released either by evaporation or splashing, and the carbon species are generated in the absence of gas phase cobalt. This view is supported by the absence of cobalt nanoparticles in

the TEM images of the soots produced in the 4.5 mm/min run. Rapid cooling occurs as buoyancy forces eject carbonaceous fragments from the high temperature zone near the electrode gap. We believe that the combination of sputtering, high temperatures, loss of cobalt, and rapid cooling give rise to the absence of SWTs and the relatively high concentrations of graphitic platelettes and multi-wall tubes in the soots produced by the 4.5 mm/min run.

Figure 6 also demonstrates that SWTs were not found in the nub material in any run. In addition, SWTs were only found in soot from the reactor walls in the case of the 1.5 mm/min run. In general, the SWT yield was highest in the soft nub and web fractions produced at the slower translation speeds. Cobalt and graphite are presumably dispersed into the gas phase at comparable rates under these conditions, and have more time to interact before being quenched. Consequently, the growth of SWTs is effectively catalyzed. The location at which the soft nub grows has a temperature which is between that of the plasma zone and the reactor walls/floor. This location is in line-of-site of the flux of material leaving the spark-gap, and provides an environment for maximum SWT production in the reactor.

Summary and Conclusions

We have employed TPD studies to monitor the stability of physisorbed hydrogen on carbon nanotube material as a function of temperature. These studies have monitored the desorption of H_2 at 146 and 285 K indicating the presence of two unique H_2 adsorption sites. The desorption activation barriers for these two sites are 13 kJ/mol and 18 kJ/mol, respectively, and can be equated to the heats for adsorption into the two sites. These values are factors of 2 and 3 times greater, respectively, than the maximum value reported for an activated carbon material (6.5 kJ/mol). It is likely that these two adsorption sites occur on two unique carbon structures, and that nanocapillary forces are responsible for producing the enhanced heats of adsorption. If the carbon structures which strongly interact with hydrogen can be isolated or produced in high yield, then the development of an ambient temperature carbon adsorbent with high energy densities will be possible.

We have developed methods for the synthesis of single-wall carbon nanotube materials using a spark-gap evaporation system that features feedback control of critical operating parameters. The instrument has enabled a series of experiments in which the rate of carbon rod translation was controllably varied. TEM was utilized to image the nanostructures that were produced in the different types of materials that were made. A comparative analysis for the different translation rates allowed the SGE process to be understood on a more detailed level. In particular, it was found that a balance between cobalt particle and graphite fragment generation is required for high SWT yield. Data obtained from these investigations will provide guidance in the design of strategies for the efficient, cost-effective production of nanotube materials.

Future Work

Much work needs to be done in order to determine and perhaps achieve the full promise of carbon

nanotubes in hydrogen storage applications. We will continue our efforts (not discussed here) to separate and purify the various volume fractions in soots formed by the co-evaporation of Co and C so that uptake and TPD data may be obtained from the individual components. Several possible purification routes exist such as chromatography, ultracentrifugation, train sublimation, and chemical etching schemes. We will rely heavily on atomic force microscopy and TEM to correlate adsorption behaviors with structural features. We will also extend our measurement capabilities to access H_2 adsorption at higher pressures and temperatures Adsorption measurements on compacted materials and plugs produced by spark-gap evaporation will determine achievable volumetric energy densities.

Our in-house tubule synthesis capabilities will continue to be directed towards synthesis of small, single-wall nanotubules via the co-evaporation of carbon and metals. Attempts to control the geometry of the deposit will involve choices in electrode spacing, starting materials, deposition conditions (i.e. pulsed or AC currents), and ambient gas composition (e.g. other inert gases, or perhaps a carbon containing gas to provide a carbon source (CH_4)). We are particularly interested in using H_2 as a background gas, rather than He, to produce SWTs that are free of amorphous carbon. We will also employ new strategies employing organometallic molecules for the introduction of transition metal dopants that should provide more control than is presently available with the current doping method. We will also attempt to control the packing density and the size distribution of the tubules by establishing nucleation sites for tubule growth.

References

Agarwal, R.K., .J.S. Noh, J.A. Schwarz, and P. Davini. 1987. "Effect of Surface Acidity of Activated Carbon on Hydrogen Storage." *Carbon*, 25:219-226.

Bekkedahl, T.A., and M.J. Heben. 1994. "Advanced Materials for Hydrogen Strorage: Carbon Nanotubules." *Proceedings of the 1994 DOE/NREL Hydrogen Program Review*, 149-163. Livermore, CA.

Bethune, D.S., C.H. Kiang, M.S. de Vries, G. Gorman, R. Savoy, J. Vazquez and R. Beyers. 1993. "Cobalt-catalyzed Growth of carbon Nanotubes with Single-layer Walls." *Nature*, 363: 605-607.

Carpetis, C., and W. Peshka. 1980. "A Study on Hydrogen Storage by Use of Cryoadsorbents." *Int. J. Hydrogen Energy*, 5:539-554.

CRC, 1975. Handbook of Chemistry and Physics.

Ebbesen, T.W., H. Hiura, J. Fujita, Y. Ochiai, S. Matsui, and K. Tanigaki. 1993. "Patterns in the Bulk Growth of Nanotubes." *Chem. Phys. Lett.*, 209 (1,2): 83-90.

Flavin, C. and N. Lessen , 1994. *Power Surge.* New York: W.W. Norton & Co.

George, S.M., 1986. "A Simple and Versatile Liquid Nitrogen Cooled Cryostat on a Differentially Pumped Rotary Feedthrough." *J. Vac. Sci. Technol. A* , 4:2394-2404.

Gregg, S.J., and K.S.W. Sing. 1982. *Adsorption, Surface Area and Porosity*, New York: Academic Press.

Hausslein, R.W. 1995. "Commercial Manufacture and Uses of Carbon Nanotubules." Abstract #790 at the 187th Meeting of the Electrochemical Society. Reno, NV

Hynek, S., J. Bentley, B. Barnett, E. Shanley, and G. Melhem. 1992. Hydrogen Storage Technologies: Present and Future.", presentation to the Hydrogen Energy Council, December 9, Montreal, Quebec.

Kirk, R.E., D.F. Othmer, M. Grayson, and D. Eckroth. 1978. *Kirk-Othmer Encyclopedia of Chemical Technology.* New York: John Wiley & Sons.

National Energy Strategy,. 1992.

Pedersen, M.R., and J.Q. Broughten. 1992. "Nanocapillarity in Fullerene Tubules." *Phys. Rev. Lett.* 69:2689-2692.

Quinn, D.F., and J.A. MacDonald. 1992. "Natural Gas Storage." *Carbon*, 30:1097-1103.

Quinn, D.F., and J.A. MacDonald. 1992. "Natural Gas Storage." *Carbon*, 30:1097-1103.

Schwarz, J.A., 1. "Modification Assisted Cold Storage (MACS)." contract report to Brookhaven National Laboratories, contract # 186193-S.

Schwarz, J.A., 1992. "Activated Carbon Based Storage System." in *Proceedings of the 1992 DOE/NREL Hydrogen Program Review*, 271-278. Honolulu, HI.

Schwarz, J.A., 1993. "Activated Carbon Based Storage System." in *Proceedings of the 1993 DOE/NREL Hydrogen Program Review*, 89-102. Cocoa Beach, FL.

Flavin, C. and N. Lessen , 1994. *Power Surge*. New York: W.W. Norton & Co.

Simons, G.A., and M.L. Finson. 1992. "The Structure of Coal Char: Part I. Pore Branching." *Comb. Sci. Techn.*, 19: 217-225.

C.M. Chan, R. Aris and W.H. Weinberg. "An Exact Single-Curve Analysis Technique for TPD Spectra" *Appl. Surf. Sci.* 4 (1980) 234.

Figure Captions

Figure 1. Comparison of hydrogen storage systems. The solid line at 8.4 wt% represents this work on a material weight basis. The volumetric energy density for nanotube materials has not yet been evaluated.

Figure 2. Temperature programmed desorption experimental apparatus.

Figure 3. Hydrogen TPD spectrum following a 200 Torr H_2 exposure on carbon nanotube material at 113 K.

Figure 4. Spark gap evaporator for synthesis of single-walled carbon nanotubes.

Figure 5. TEM image of single-walled carbon nanotubes.

Figure 6. Comparison of carbon nanotube yield versus rod translation rate

Existing Hydrogen Storage Options

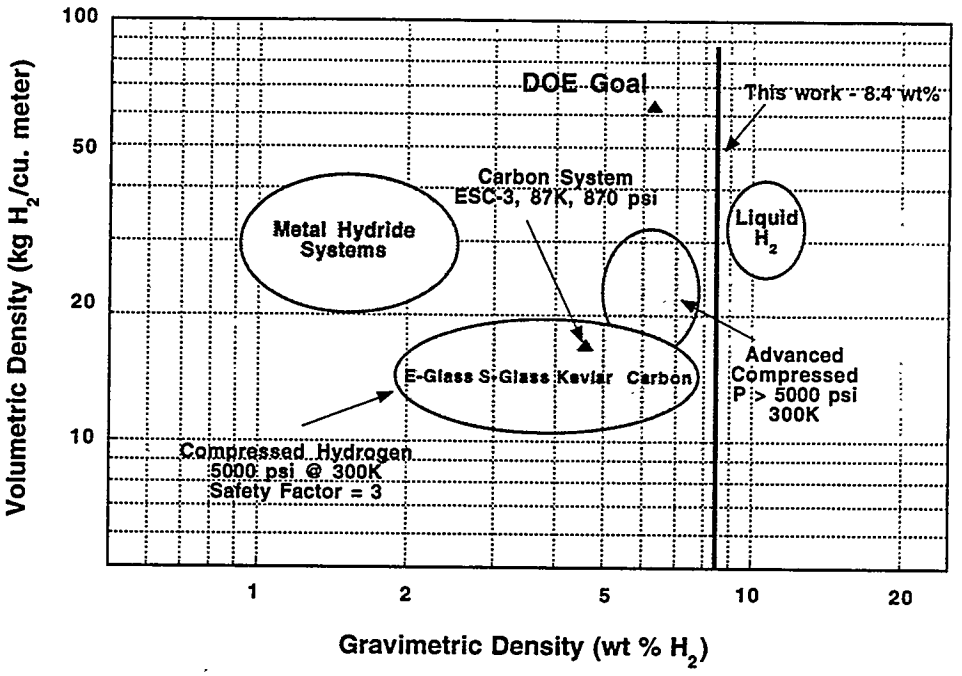

After S. Hynek et al.,"Hydrogen Storage Technologies:Present and Future"
with data from I. Kuhn presented at Workshop on Hydrogen Storage Technogies, Nov. 11, 1993, Golden , CO,
from J.A. Schwarz, 1993 DOE/NREL Hydrogen Program Review, and from M. Deluchi,
"Hydrogen Fuel-Cell Vehicles", Research Report UCD-ITS-RR-92-14, University of California, Davis.

Figure1

Temperature Programmed Desorption (TPD)

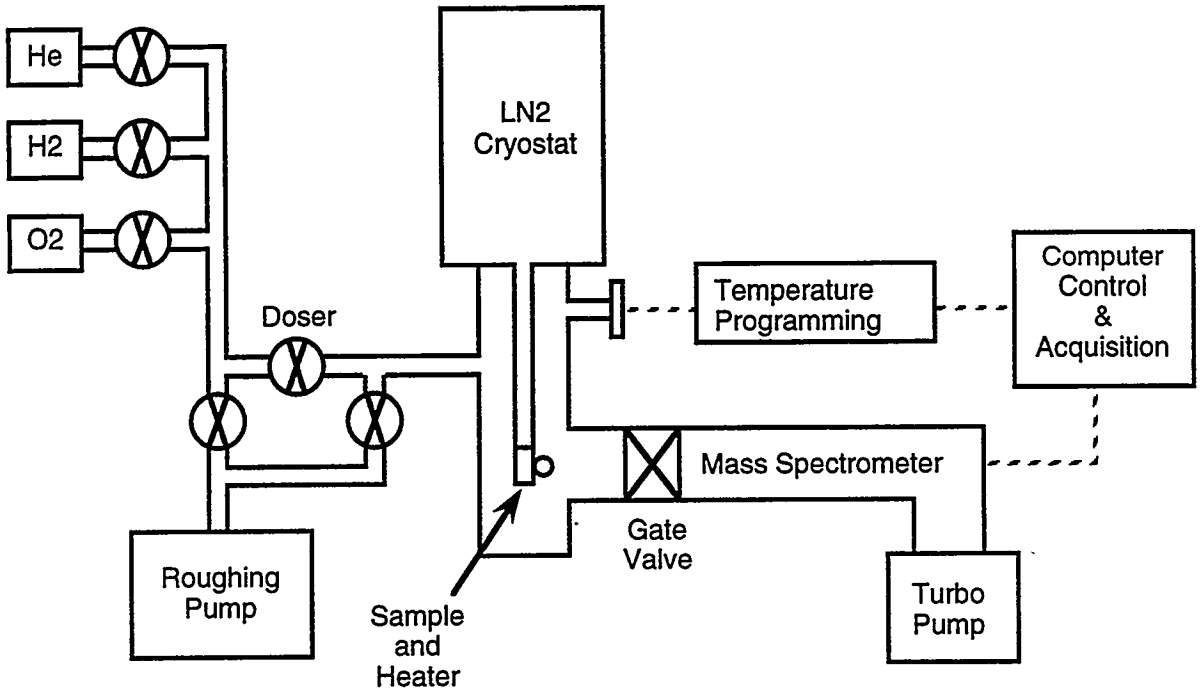

Figure 2

TPD of H_2 from Carbon Nanotube Sample

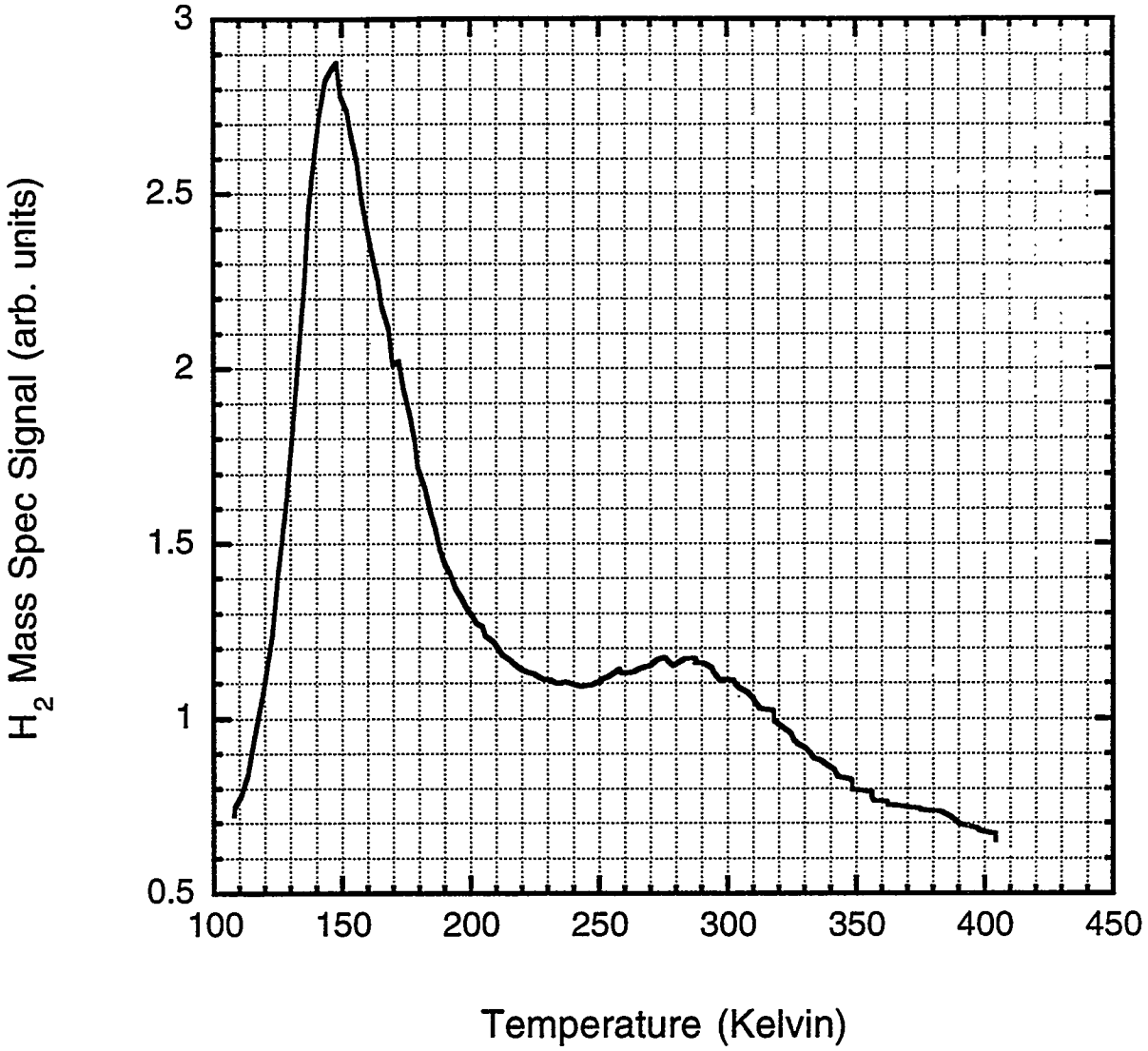

Figure 3

Feedback-Stabilized Spark-Gap Evaporation

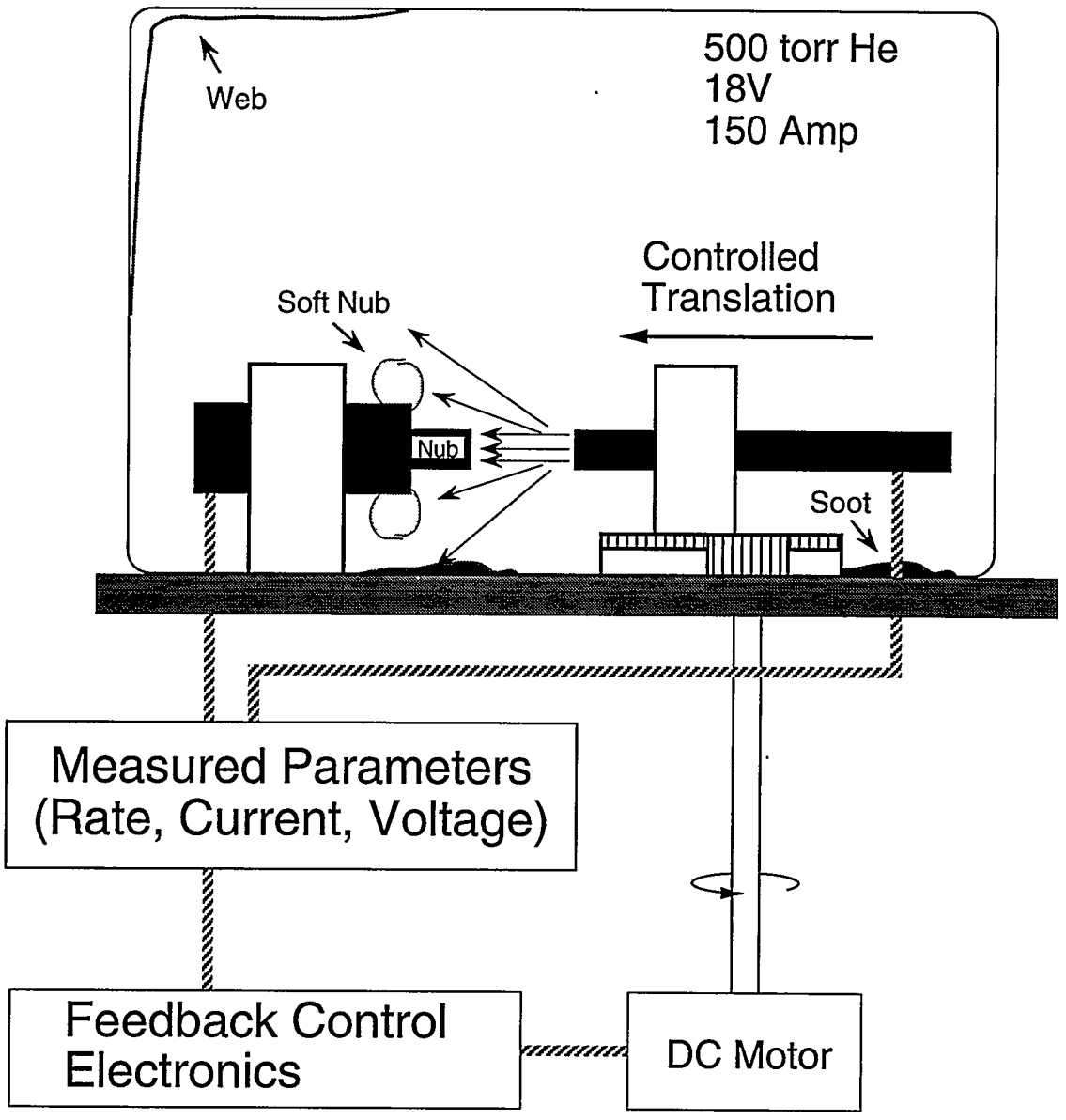

Figure 4

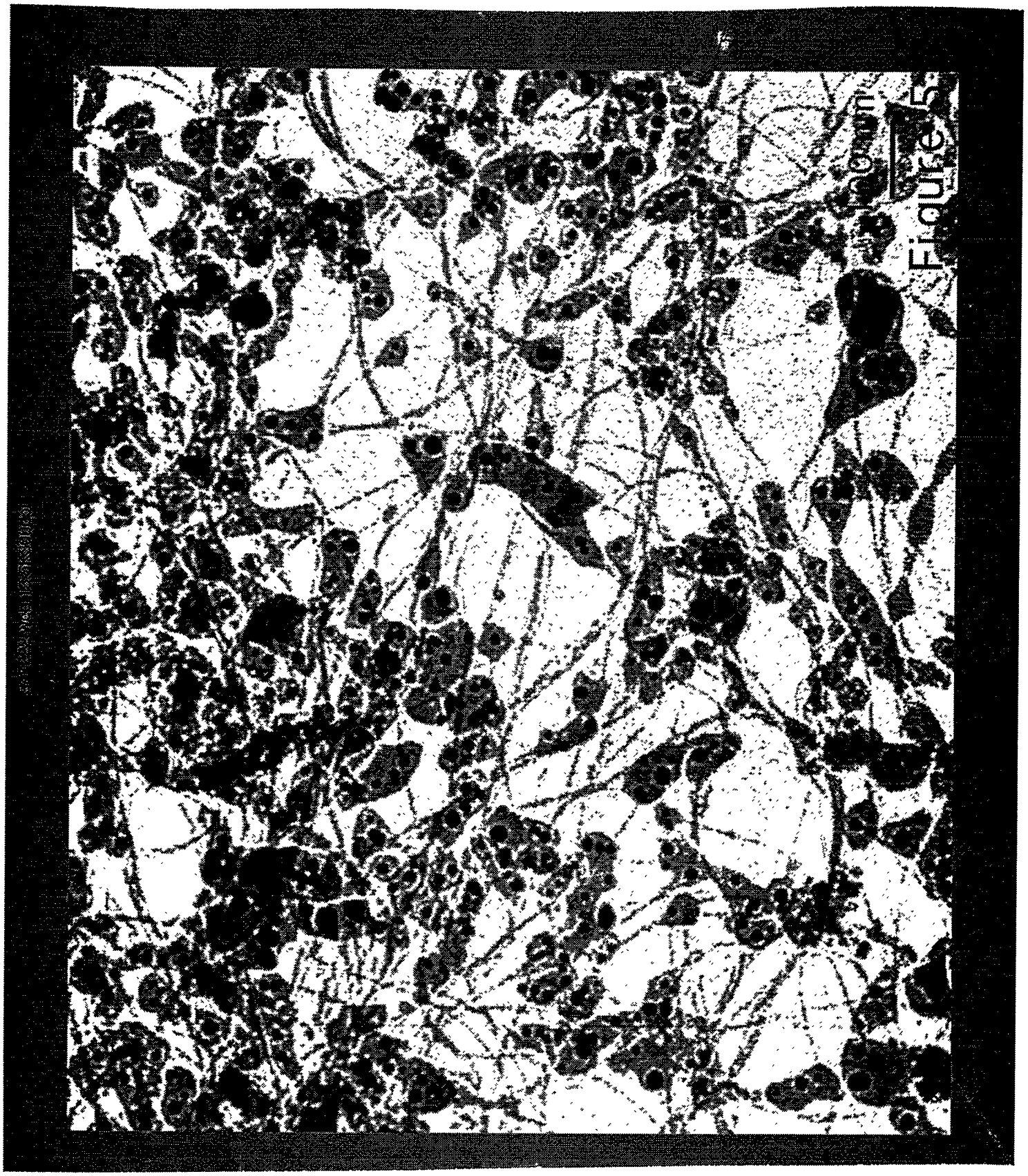
Figure 5

TEM Analysis of Materials Synthesized at Different Rates

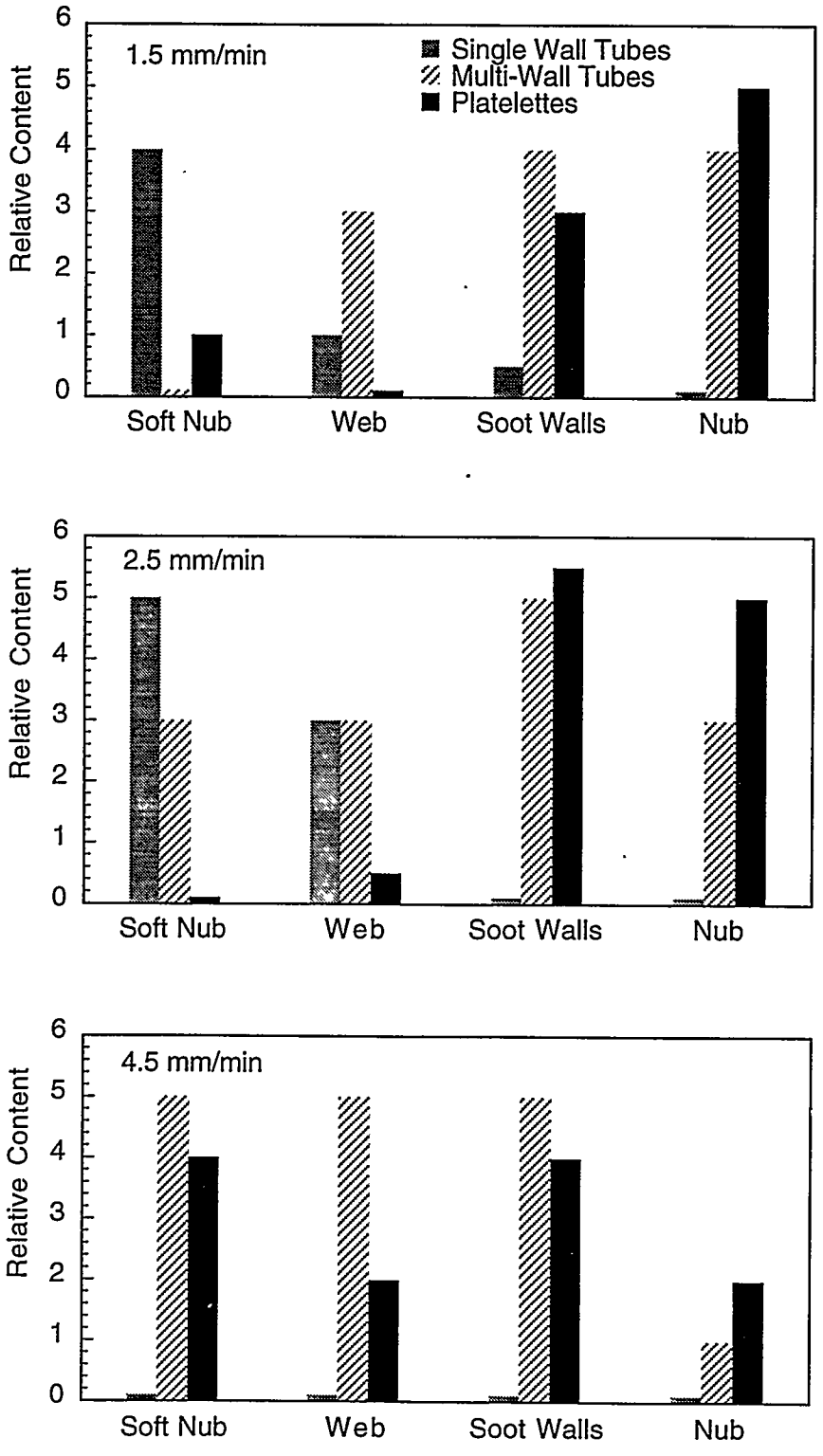

Figure 6

Lightweight Hydride Storage Materials

G. J. Thomas, S. E. Guthrie and W. Bauer
Sandia National Laboratories
Livermore, CA 94550

Abstract

The need for lightweight hydrides in vehicular applications has prompted considerable research into the use of magnesium and its alloys. Although this earlier work has provided some improved performance in operating temperature and pressure, substantial improvements are needed before these materials will significantly enhance the performance of an engineered system on a vehicle. We are extending the work of previous investigators on Mg alloys to reduce the operating temperature and hydride heat of formation in light weight materials.

Two important results will be discussed in this paper: (1) a promising new alloy hydride was found which has better pressure-temperature characteristics than any previous Mg alloy and, (2) a new fabrication process for existing Mg alloys was developed and demonstrated.

The new alloy hydride is composed of magnesium, aluminum and nickel. It has an equilibrium hydrogen overpressure of 1.3 atm. at 200°C and a storage capacity between 3 and 4 wt.% hydrogen. A hydrogen release rate of approximately 5×10^{-4} moles-H_2/gm-min was measured at 200°C. The hydride heat of formation was found to be 13.5 - 14 kcal/mole-H_2, somewhat lower than Mg_2Ni.

The new fabrication method takes advantage of the high vapor transport of magnesium. It was found that Mg_2Ni produced by our low temperature process was better than conventional materials because it was single phase (no Mg phase) and could be fabricated with very small particle sizes. Hydride measurements on this material showed faster kinetic response than conventional material. The technique could potentially be applied to in-situ hydride bed fabrication with improved packing density, release kinetics, thermal properties and mechanical stability.

Introduction

Hydrogen storage remains an important factor in effective hydrogen utilization for energy applications and is a major element of the FY 1994-1998 Hydrogen Program Implementation Plan. The objective of this project is to investigate light weight hydrides for the storage of hydrogen with emphasis on improved weight efficiency and hydride bed properties. It is integrated into our overall hydrogen utilization program which includes internal combustion engine optimization and storage system engineering projects.

The development of a light weight reversible hydride would be a significant factor in enabling hydrogen utilization as a vehicular fuel. Magnesium hydride, with a storage capacity of 7.6 wt.% hydrogen, is considerably lighter than AB_5 or AB_2 alloy hydrides and would appear to be a suitable candidate. However, pure Mg requires a high temperature for hydriding and dehydriding, and suffers from poor hydrogen uptake and release kinetics. This is due to two factors: (1), a large covalent binding energy of Mg with hydrogen and (2), poor molecular dissociation and recombination of hydrogen on the surface of this metal.

There have been many studies which have attempted to modify this behavior in Mg by alloy additions (see, for example, the review by Selvam[1]) or by modifying the surface[2-5]. Surface modifications have been shown to enhance the uptake kinetics; however, they do not affect the thermodynamic stability of the Mg-H bond and, hence, the desorption properties are not necessarily improved. Similarly, alloys with higher equilibrium overpressures compared to Mg, in particular Mg-Al alloys[6], have relatively slow kinetics at temperatures below 300° C. In order to impact transportation applications, a Mg alloy must demonstrate improved behavior in all of the desired properties; that is, lighter weight, better kinetics and a higher equilibrium pressure at lower temperatures.

The present work has focussed on the Mg-Ni and Mg-Al alloy systems. Various fabrication methods, including ingot metallurgy, rapid solidification and mechanical alloying, have been employed. We have also examined the use of surface coatings for improving the kinetic behavior of hydrides. Mechanical, physical vapor deposition and chemical vapor deposition coating techniques were employed. By using equilibrium pressure-composition-temperature (PCT) measurements, kinetic measurements and detailed microscopic analyses of these materials, a detailed understanding of composition, microstructure and hydride performance can be achieved.

Two important results have been obtained which will be discussed in this paper: (1) a promising new alloy hydride was found which has better pressure-temperature characteristics than any previous Mg alloy and, (2) a new fabrication process for existing Mg alloys was developed and demonstrated.

Previous Results in Mg-Al

Figure 1 is a composite showing both the equilibrium phase diagram of the Mg-Al alloy

system, on the left-hand side, and plots of the measured pressure-temperature behavior for different Mg-Al alloys on the right. Consider, first of all, the phase diagram on the left. It shows, in addition to the pure metal phases and solid solutions, three intermetallic phases - $Al_{12}Mg_{17}$, Al_3Mg_2 and an R phase with a composition of 42 at.% Mg. On the right-hand side of the figure is a semilog plot of the equilibrium hydride pressure as a function of reciprocal temperature for various Mg-Al mixtures. These data by Reilly and Wiswall[6] were taken for Al contents ranging from 15 to 60 at. % in the temperature range from about 300 to 380° C. They show that the pressure initially increases with increasing Al content, but then decreases. A composition of 55 at.% Al had the highest pressure.

The arrows pointing from the pressure-temperature data to the phase diagram show the composition and temperature corresponding to the hydride measurements. The lowest Al compositions, 15 and 23 at.%, are seen to consist of a mixture of Mg and $Al_{12}Mg_{17}$, with the predominant phase Mg (about 70% at the higher Al content). Since the observed equilibrium pressures shown in the plot correspond very closely to that of Mg, it is likely that this phase dominated the hydride measurements. In contrast, the 44 at.% alloy is seen to lie within the $Al_{12}Mg_{17}$ intermetallic phase and exhibits a higher overpressure in the same temperature range. Similarly, the 60 at.% alloy, Al_3Mg_2, also is a single intermetallic phase and has an even higher hydride pressure.

The alloy containing 55 at.% Al, with a composition very close to the indicated R phase, was found to have the highest equilibrium overpressure. It is interesting to note that the hydride pressure at 300° C for this alloy lies somewhat below the expected exponential behavior (linear on the log plot) and, also, is outside of the indicated stable temperature range for the R phase.

These results have been described because, first of all, they indicate significantly higher hydrogen overpressures for Mg-Al alloys. Secondly, they clearly show that one has to consider the intermetallic phases present for a given composition when interpreting hydride behavior. In particular, hydride measurements in mixed phase materials can be dominated by one of the phases and require the full range of hydrogen content to be explored.

Mg-Ni-Al

We have studied the addition of Ni to Mg and Al in an effort to enhance the hydrogen kinetic behavior of the Mg-Al alloys while retaining some of the high overpressure properties found previously. A new alloy hydride composed of magnesium, aluminum and nickel has been found which has many desirable properties. It has an equilibrium hydrogen overpressure of 1.3 atm. at 200°C and a storage capacity between 3 and 4 wt.% hydrogen. The kinetic behavior is also very good, allowing equilibrium measurements to be made as low as 150°C. At 200°C, the hydrogen release rate was found to be about 5×10^{-4} moles-H_2/gm-min. This rate would meet calculated hybrid vehicle delivery requirements.

A plot of log pressure versus reciprocal temperature is shown in figure 2. Temperatures in

degree C are indicated at the top of the graph. The new alloy data are plotted along with the previous Mg-Al results as well as some results due to Nachman and Rohy[7]. Note, first of all, that the temperature range of the measurements is extended much lower than any previous data. Also, it is interesting that the present results at 300° C are close to the highest overpressure behavior found by Reilly and Wiswall. Indeed, the data appear to be an extension of the earlier results down to lower temperatures. However, the new alloy does not have an Al or Al+Ni content equivalent to the R-phase Al composition.

It is not clear at this time whether the lower equilibrium pressures at lower temperatures, particularly at 150° C, accurately reflect the material properties or are simply due to experimental uncertainty in determining the true equilibrium behavior. The results shown in Figure 2 are measured in desorption and, hence, non-equilibrium results would indicate pressures lower than expected. The heat of formation of the hydride, estimated from these data, is believed to be between 13.5 and 14 kcal/mole H_2. This value is somewhat lower than that for Mg_2Ni.

Vapor Phase Formation of Alloys

A property of Mg often overlooked during hydride studies is the relatively high vapor pressure of this metal at typical hydride operating temperatures. For example, at 400° C, the vapor pressure is about a millitorr, whereas Al, which has a melting temperature close to that of Mg, has a vapor pressure about 12 orders of magnitude lower. Other properties of Mg which can affect hydride measurements include rapid solid state interdiffusion with other metals, particularly Ni, which can alter samples during the course of a measurement.

We have found, however, that these properties can be exploited to fabricate more stable alloys and have demonstrated the process by forming Mg_2Ni from the vapor phase. The technique is described in Figure 3. A mixture of Ni particles and Mg is first evacuated, then heated to a temperature above 300° C with a hydrogen overpressure. Mg vaporized from the Mg particles is transported to the Ni particles where Mg_2Ni is formed. The vapor pressure of the alloy is lower than Mg and, hence, the particles act as sinks for the vaporized Mg. Interdiffusion in the particles is sufficiently rapid at these temperatures to allow the process to proceed rapidly.

The backscattered electron image of a cross-sectioned sample following this procedure is shown in Figure 3. The different phases are identified. The brightest areas are pure Ni which remains after the Mg has been used up. The schematic in the lower left depicts the process for the indicated particle. The light gray in the image is the Mg-Ni phase formed as a shell from the outer surface and surrounds the remaining Ni core. The darker gray regions are shells of MgO which are remnants of the original Mg particles. This oxide was formed on the Mg particles by normal handling prior to the experiment.

The alloy formed by this method has properties which are desirable for hydride applications. A major advantage of the technique is that a pure single phase alloy can be fabricated; that

is, no eutectics are formed as in conventional melting and solidification processes. Furthermore, the final alloy reflects the shape of the starting Ni material. By using readily available Ni powder, small, uniform alloy hydride material can be produced. Measurements of hydrogen release from vapor phase synthesised material show significantly better kinetic behavior than alloy material produced by conventional methods. These small, single phase hydride particles would also be expected to have good stability over many cycles of operation. The technique could potentially be applied to in-situ hydride bed fabrication with improved packing density, release kinetics, thermal properties and mechanical stability.

References

1. P. Selvam, B. Viswanathan, C.S. Swamy, V Srinivasan: Int. J. Hydrogen energy, 11 (1986) 169.
2. B. Bogdanovic, T.H. Hartwig, B. Spliethoff: Int. J. Hydrogen Energy, 18 (1993) 575.
3. R. Zidan, D.K. Slattery, J. Burns: Int. J. Hydrogen Energy, 16 (1991) 821.
4. F.J. Liu, G Sandrock, S. Suda: J. Alloys and Compounds, 190 (1992) 57.
5. F.J. Liu, G. Sandrock, S. Suda: Z. Phys. Chem., 183 (1994) 163.
6. J.J. Reilly and R.H. Wiswall, Jr.: BNL 19436, August 1, 1974.
7. J.F. Nachman and D.A. Rohy:DOE/CS0016-T1.

Figure Captions

Figure 1. Composite figure of the Mg-Al phase diagram and pressure-temperature hydride measurements in Mg-Al alloys. The arrows show the position of each of the alloys on the phase diagram.

Figure 2. Plot of the log pressure versus reciprocal temperature for the Mg-Al-Ni hydride. Previous data from references 6 and 7 are included.

Figure 3. Backscattered electron micrograph showing the formation of Mg_2Ni by vapor transport of Mg onto Ni particles. The schematic at lower left shows the structure of the indicated particle. each of the phases are identified.

- 15-25% Al content yields Mg overpressure 2 phase region – Mg + $Al_{12}Mg_{17}$
- R phase has highest overpressure stable between 320–370°C

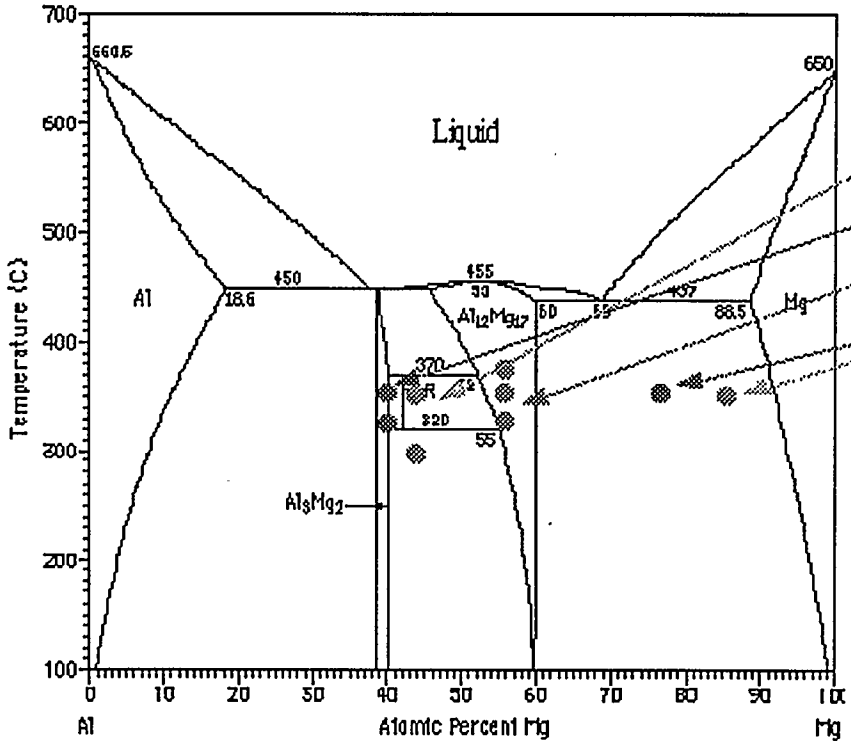

Reilly-Wiswall data for Mg-Al alloys

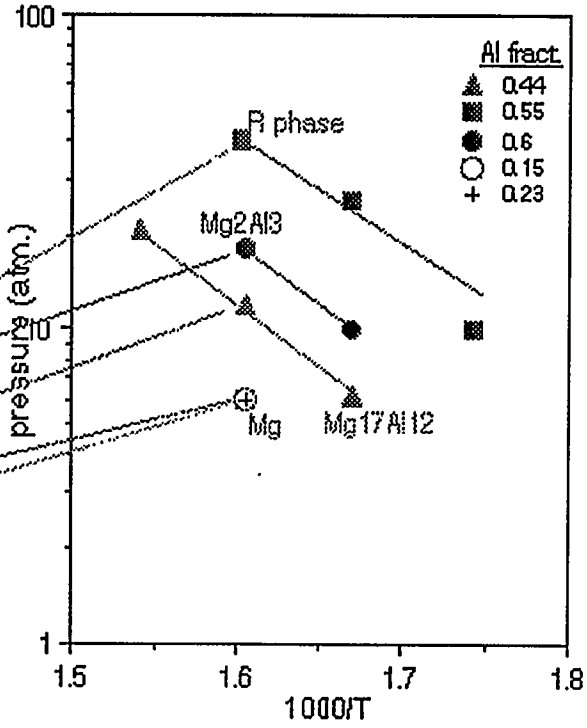

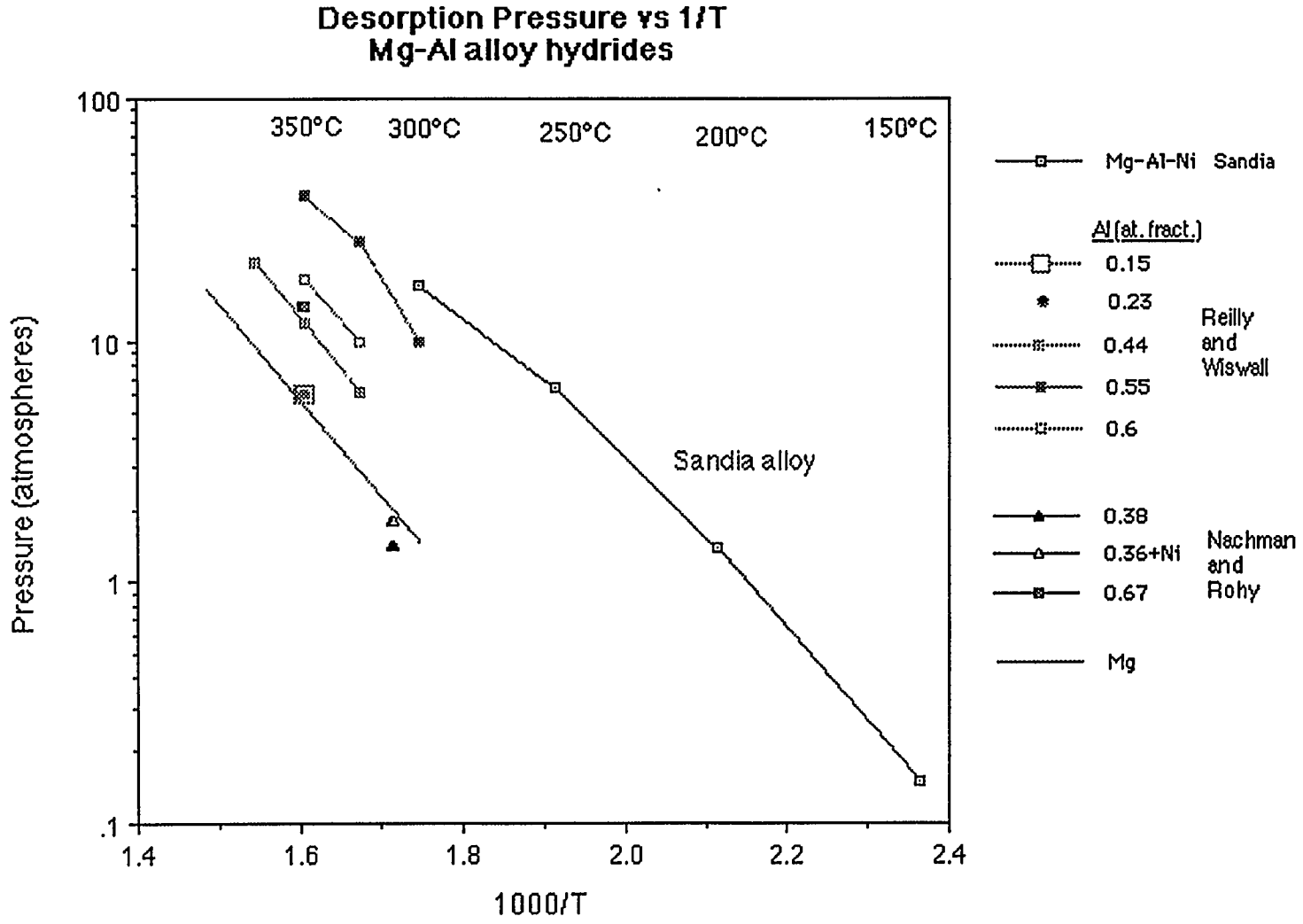
Desorption Pressure vs 1/T
Mg-Al alloy hydrides
100
10
1
.1
Pressure (atmospheres)
350°C
300°C
250°C
200°C
150°C
Sandia alloy
1.4
1.6
1.8
2.0
2.2
2.4
1000/T
Mg-Al-Ni Sandia
Al (at. fract.)
0.15
0.23
0.44
0.55
0.6
Reilly and Wiswall
0.38
0.36+Ni
0.67
Nachman and Rohy
Mg

- **starting material**
  mix of Ni powder and chemically extracted Mg particles
- **heat treatment**
  300-320° C with hydrogen overpressure

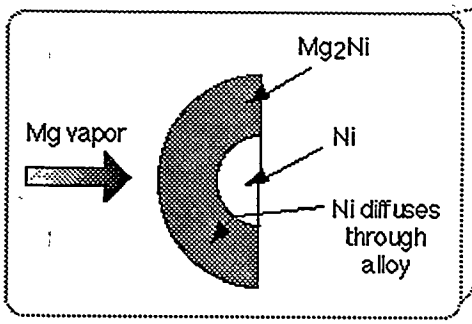

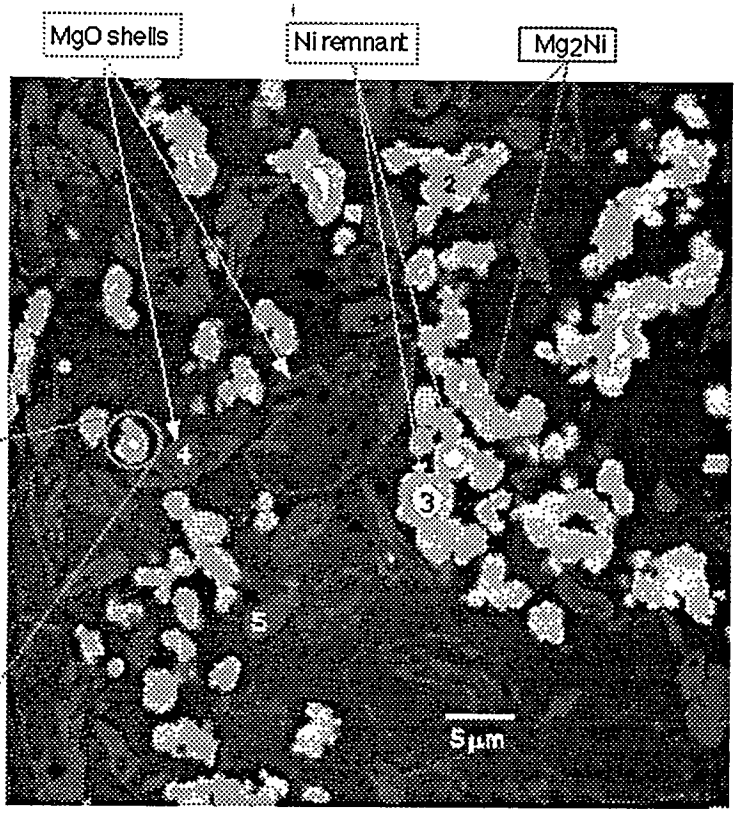

PRODUCTION OF HBR FROM BROMINE AND STEAM FOR OFF-PEAK ELECTROLYTIC HYDROGEN GENERATION

R.E. Schlief,[a] R.J. Hanrahan,[a] and M.A. Stoy[a]
and
P W. Langhoff[b]
Solar Reactor Technologies, Inc.
3250 Mary Street, Suite 407
Miami, FL 33133

ABSTRACT

Progress is reported on the development of a renewable energy source based solar-electrolytic system for production of hydrogen and oxygen. It employs water, bromine, solar energy and supplemental electrical power. The concept is being developed by Solar Reactor Technologies, Inc., (SRT) under the auspices of Cooperative Agreement No. DE-FC36-95GO10049, A002, with the U.S. Department of Energy (DoE). An overview of the nature and objectives of this program is provided here, and technical progress made during the first (three-month) performance period of the Phase I work effort is reported.

The SRT concept entails (i) absorption of concentrated solar radiation by bromine vapor $Br_{2(g)}$ in a high-temperature reactor producing $Br_{(g)}$ atoms, (ii) reaction of $Br_{(g)}$ with water yielding hydrogen bromide (HBr), and (iii) electrolysis of stored hydrogen bromide for production of $H_{2(g)}$ and recovery of $Br_{2(l)}$. Incorporation of solar radiation in the primary photochemical step (i) reduces by 50 - 70% the electrical power required to split water. The SRT concept is very attractive from an economic viewpoint as well. The reversible fuel cell employed in the SRT electrolysis concept is capitalized via

---

[a]Department of Chemistry, University of Florida, Gainesville, FL 32611
[b]Department of Chemistry, Indiana University, Bloomington, IN 47405

its use in load leveling by the utility. The price of SRT-produced hydrogen would essentially only reflect the cost of the solar components and off-peak electrical power.

A 1 kW solar reactor was designed and constructed during the first three-month performance period by SRT personnel at the University of Florida, Gainesville. It was employed in taking survey data of the reaction between bromine and steam at temperatures between 900 and 1300 K. This reaction was run under purely thermal conditions, i.e. in the absence of solar photons. The experimental data are reported and interpreted employing concomitant thermodynamic calculations.

Reactor thermal efficiency can be significantly improved by the incorporation of a heat exchanger. The anticipated improvement is discussed briefly as well as the effect of a photochemical boost to the reaction. The amount of this enhancement will be studied in the next three month performance period.

INTRODUCTION

Hydrogen is a valuable chemical feedstock and processing agent (Heydorn, *et al.*, 1990), and a potential energy carrier for a hydrogen-based economy (Winter, *et al.*, 1990). Inexpensive and efficient production of hydrogen would provide significant motivation for its adoption in the latter context. Although steam reforming of methane can provide cheap and plentiful hydrogen under appropriate conditions (Wendt and Bauer, 1988), production methods based on renewable resources are more desirable from a sustainable longer-term perspective. Accordingly, Solar Reactor Technologies, Inc., (SRT) has entered into a cooperative agreement with the U.S. Department of Energy (DoE) to develop a renewables-based hydrogen production system employing solar energy and supplemental electrical power. An overview of the nature and objectives of this venture is provided here, and technical progress made during the first (three-month) performance period of the Phase I work effort is reported.

Solar-Electrolytic Hydrogen Concept

The envisioned SRT renewables-based hydrogen production system is represented schematically in Figure 1 (Antolovic, *et al.*, 1990; Gupta and Hanrahan, 1992; Schlief, 1994). On the left of the figure is depicted a photochemical reactor driven by concentrated solar radiation. The reactor operates in conjunction with an associated reversible fuel cell (Beaufrere, *et al.*, 1979), shown on the right, which is connected to the electric utility grid. Water and liquid bromine $Br_{2(l)}$ are converted in a solar reactor into oxygen $O_{2(g)}$ and hydrogen bromide, which can be stored in gaseous $HBr_{(g)}$, liquid $HBr_{(l)}$, or aqueous $HBr_{(aq)}$ form. Hydrogen bromide is subsequently decomposed electrolytically in a fuel cell during off-peak periods into hydrogen $H_{2(g)}$ and liquid bromine $Br_{2(l)}$. Hydrogen and bromine are stored for on-peak electrical power generation employing the fuel cell, the system operating in this mode as a load-leveling device. Alternatively, hydrogen can be taken off for sale and bromine recycled to the photochemical reactor for continuing hydrogen bromide production, the system operating in its hydrogen production mode. Capital cost benefits are derive from the synergistic combination of the two operating modes of the envisioned SRT system (DiPietro and Badin, 1995).

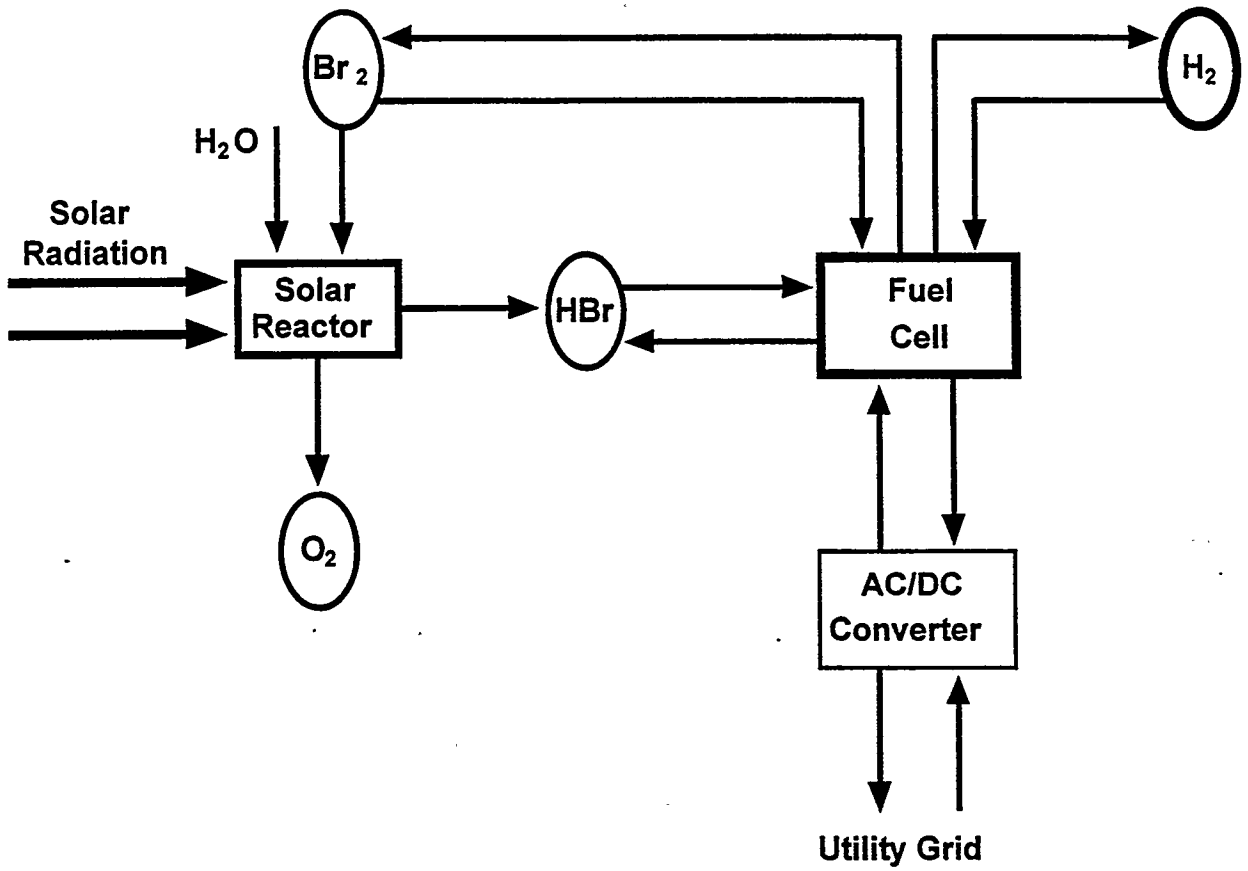

Figure 1. Schematic representation of a bromine-based system for solar-electrolytic hydrogen production combining a chemical reactor driven by concentrated solar radiation (left) with a reversible fuel cell (right). Storage of HBr, H_2 and B_2 along with a grid interface completes the energy storage concept.

System Energetics

The chemical energetics of the envisioned system are shown in simplified form in Figure 2. In the first step of the chemical cycle, absorption of solar photons in the photochemical reactor initiates the reaction of bromine with water

$$Br_{2(l)} + H_2O_{(l)} + h\nu \rightarrow 2HBr_{(g)} + \tfrac{1}{2}\, O_{2(g)}, \quad \Delta H^\circ_{298} = +213.0 \text{ kJ/mole}, \qquad (1)$$

producing oxygen and hydrogen bromide. Electrolysis of product hydrogen bromide

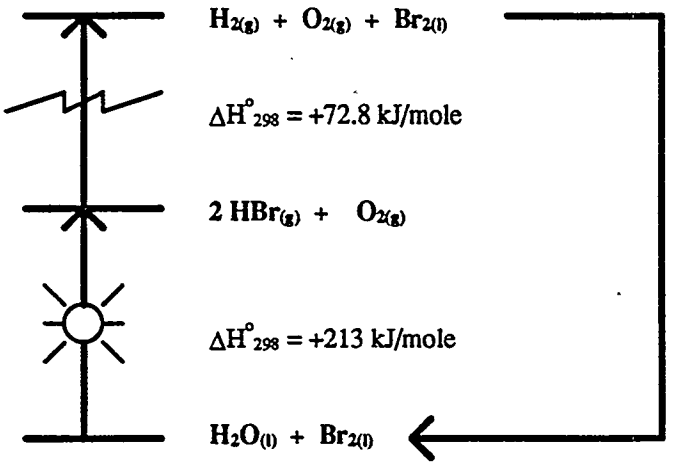

Figure 2. Schematic energy diagram for the solar-assisted electrolytic hydrogen production concept depicting the photochemical and electrolytic steps. Note that approximately three-quarters of the total energy required to split water into H_2 and O_2 is supplied by solar energy. One-third (74.9 kJ/mole) of the 213 kJ/mole solar step contributes to the vaporization of $H_2O_{(l)}$ and $Br_{2(g)}$.

produces hydrogen and recovers bromine in the second step

$$2HBr_{(g)} \rightarrow Br_{2(l)} + H_{2(g)},\ \Delta H^{\circ}_{298} = +72.8\ \text{kJ/mole}. \qquad (2)$$

The net result of the two-step cycle is the water splitting reaction

$$Br_{2(l)} + H_2O_{(l)} + h\nu \rightarrow Br_{2(l)} + H_{2(g)} + \tfrac{1}{2}\,O_{2(g)},\ \Delta H^{0}_{298} = +285.8\ \text{kJ/mole}, \qquad (3)$$

producing hydrogen and oxygen, with bromine returned to its initial state.

Incorporation of solar radiation in the primary photochemical step of Equation (1) above is seen to provide approximately three-quarters of the energy cost of the overall water splitting reaction, Equation (3). Moreover, separation of oxygen from water in the initial step, and production of hydrogen in a second physically distinct electrolytic step, provides technical advantages not shared by other solar-driven water splitting methods, such as direct thermal decomposition (Scholl and Fields, 1994).

Solar Reaction Efficiency

Elemental bromine plays a central role in the concept depicted in Figures 1 and 2 and Equations (1) to (3). This compound is an efficient solar absorber (Seery and Britton, 1964), yielding very chemically reactive $Br_{(g)}$ radicals upon absorption of wavelengths between 350 and 570 nm (Calvert and Pitts, 1966). Reaction with water vapor yields a storable hydrogen carrier in the form of hydrogen bromide. Since the mean energy per mole of solar photons *hv* absorbed is ~ 270 kJ/mole, the circumstances are favorable for photochemically driving the thermally unfavorable (ΔG^0_{298} = +130.1 kJ/mole) reaction of Equation (1). Preliminary calculations indicate approximately one-third of the concentrated solar power, largely the UV and short wavelength visible portion of the spectrum, can be absorbed directly by $Br_{2(g)}$ under anticipated reactor operating conditions. The remainder, predominantly the visible and infrared portion, is available to supply process heat for driving the liquid-to-vapor phase change of the reactants and bringing them to temperatures exceeding 1,000 K.

In order to proceed with development of the envisioned hydrogen production system on a commercial scale, it is necessary to first fully quantify the reaction between bromine and steam in the absence of solar photons in Equation (1). The chemical yield and overall power conversion efficiency need to be determined as functions of thermal and input flow conditions in a laboratory-scale reactor. These performance data will be employed in the design and construction of a larger-scale reactor for field-testing.

Status of Phase I Project

Progress is reported here of work performed largely during the first three-month performance period of the Phase I FY-95 effort. It involves studies of the thermal reaction between bromine and steam at elevated temperatures.

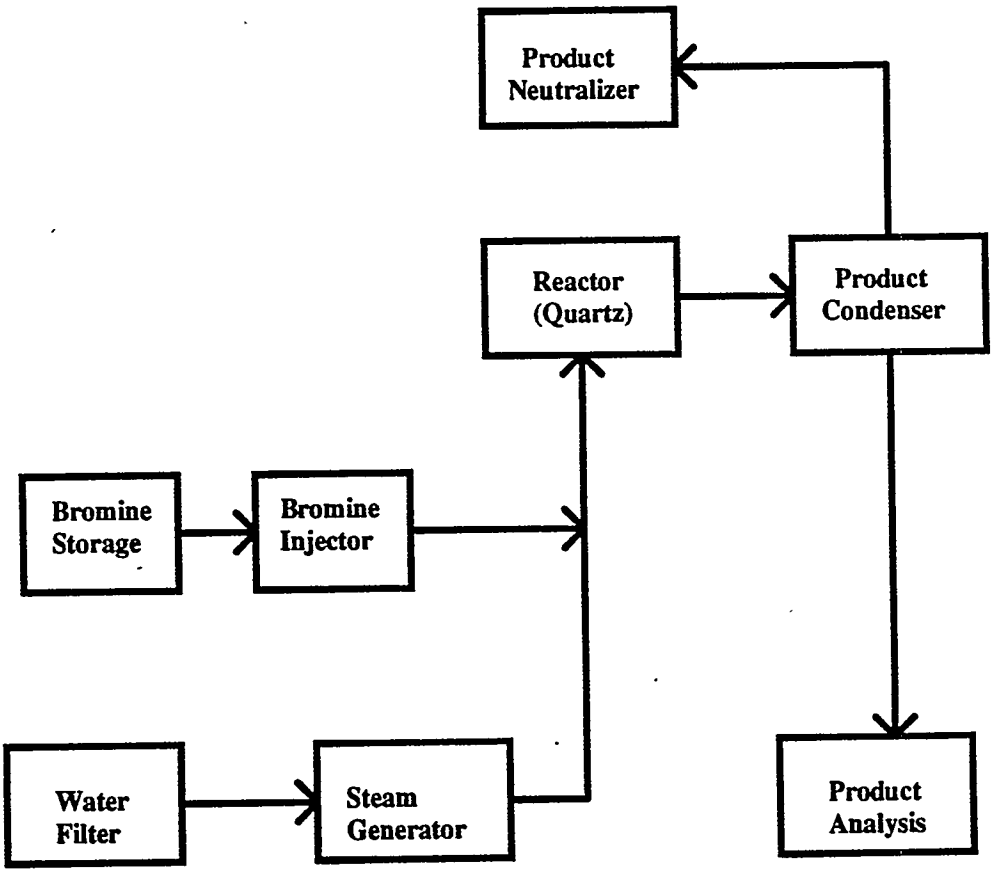

Figure 3. Block diagram of SRT's 1 kW solar reactor system, used in purely thermal reactions.

1 kW Reactor System (Task A)

The 1 kW system is comprised of an overall safety protocol, based on an extensive review of the chemical literature on bromine and hydrogen bromide safety, and nine other technical components:

1. Safety protocol.
2. Heliostat and tracker with control system and base.
3. Solar dish concentrator (1 m diam.) and mount.
4. Quartz reactor and assembly with heater and temperature controller.
5. Steam generator with flow control.
6. Bromine injector with flow control.
7. Product condenser.
8. System flow connections.
9. Product analysis techniques.
10. Thermal experimental protocols.

Progress has been made at the University of Florida, Gainesville, in the construction of the 1 kW reactor system during this period of performance. A schematic block diagram of the system is shown in Figure 3. All material components of the 1 kW system have been constructed at this date (April 95) and the system tested and operated as a thermal reactor. Detailed descriptions of each of the above components follows.

1. Safety Protocol - Literature from the chemical industry on bromine and HBr safety has been assembled in a safety notebook. Specific questions regarding SRT's research program have been directed to Albemarle Corp., one of the two largest U.S. bromine producers, and satisfactory replies were obtained. An initial protocol for neutralizing bromine and HBr spills has been developed and a spill kit assembled. Preliminary tests have satisfactorily demonstrated the efficacy of aqueous neutralizing solutions containing sodium hydroxide, sodium carbonate, and sodium thiosulfate. Additional safety equipment has been ordered and received, including safety aprons, goggles, respirators, cartridges, gloves, and boots.

2. Heliostat and Tracker - American Sunco, Inc. has constructed and delivered a 1.5 m x 1.5 m heliostat unit with two-axis tracking. It tracks automatically once the sun has been acquired via manual adjustment.

3. Solar Dish Concentrator and Mount - A Bausch & Lomb Model 486 concave mirror with a 1 meter (37.5") diameter, high quality aluminized front surface, and f/d = 0.40 has been acquired. Laser ray tracing was used to characterize the focus.

4. Quartz Reactor and Assembly - Figure 4 depicts the reactor used in these experimental studies. Reactor dimensions were chosen to match a corresponding tube heater (2" i.d., 4" o.d., 12" length). Steam and bromine vapors were mixed in a Pyrex tube external to the reactor. Reactant gases flowed into the reaction region through a ring of heat exchange tubes and exited through a central tube.

Calculations indicated that a series of 1 cm i.d. quartz tubes (40 cm length) will bring reactant gases at chosen flow rates to operating temperature (900 to 1300 K). A series of 6 thermocouple wells were used to measure reactor temperatures. A metal flange supported both ends of the tube. The quartz reactor was mounted in a chemical hood for the preliminary thermal experiments. In the solar experiments, it will be mounted on a platform to allow X, Y, and Z adjustment. The steam generator, sampling system, and bromine delivery system will be mounted adjacent to this platform. Suitable ventilation, spill trays, and an enclosure will be provided.

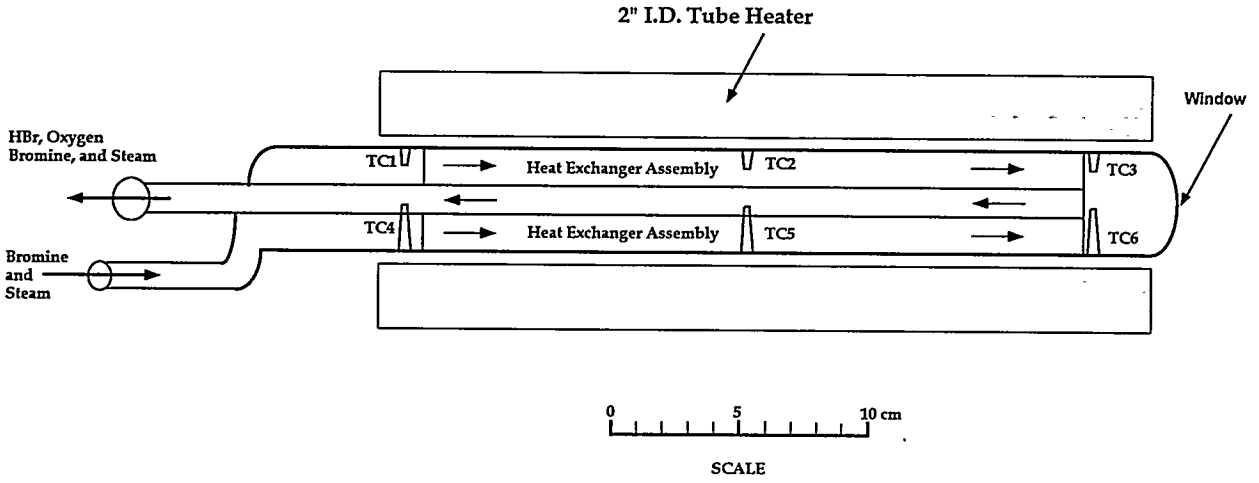

Figure 4. Scale drawing of quartz photochemical reactor used in the study of the bromine-steam chemical reaction. Thermocouple wells (TC1 - TC6), heat exchanger tubes, central product exit flow tube, window, and jacketing heater unit are depicted.

5. Steam Generator - A Sussman 3 kW steam generator was ordered and tested. The unit provides up to 3.6 moles/min of steam at up to 90 psi. A metering valve, other valves and fittings completed the steam delivery assembly.

6. Bromine Injector - A glass burette with Teflon valve was used to meter bromine via gravity flow through a fine Pyrex injection tip (0.3 mm i.d.). PFA (Perfluoralkoxy) and PVDF (Polyvinylidene) tubing and fittings were used. Steam flowing past the tip vaporizes the bromine and carries it into the reactor.

7. Product Condenser - The condensing and sampling system was comprised of a quartz pre-condenser and Pyrex condenser. The pre-condenser was cooled with a constant air flow. Its role was to prevent thermal shock in the Pyrex condenser by the hot reactor exit gases. The Pyrex condenser had a minimal number coil turns for low hold-up volume. Erlenmeyer flasks with ground glass joints were used as sample and waste bottles.

8. System Flow Connections - System flow connectors, valves, fittings, and tubing were chosen from quartz, Pyrex, Kynar (PVDF), Perfluoralkoxy (PFA), and Teflon (PTFE), all bromine-resistant materials, as appropriate. Quartz and Pyrex were used in the high temperature applications.

9. Product Analysis - Aqueous hydrogen ion concentration was determined by NaOH titration. Aqueous bromide ion concentration was determined by a titration involving silver nitrate and an indicator dye. A scheme for analyzing HOBr(aq) and bromate was located in the chemical literature.

10. Thermal Experimental Protocols - This item will be refined as work progresses with the operational 1 kW reactor system during the second three-month performance period of Phase I. Valuable operating experience has already been obtained in the first three-month period. This involved choosing suitable steam and bromine flow rates, sampling methods, reactor insulation, and heating rates. Safe bromine and HBr handling, spill neutralization, and safety equipment tests were demonstrated as well.

The 1 kW reactor assembly (Item 4) is an essential component of the system. Figure 4 depicts the quartz reactor used in this study. Referring to the figure, steam and bromine vapor (Items 5 and 6) enter the reactor through an annular ring of heat exchanger tubes brought to temperature by an external heater. The reactants enter the photochemical reaction zone at the far end of the reactor, shown as a convex window. The product mixture consisting of product HBr, oxygen, unreacted bromine, and exits through the central tube. It is quenched by a condenser (Item 7) and sampled for analysis (Item 9).

In the thermal studies described in this report, i.e. conducted in the absence of solar radiation, the window was thermally insulated. In the up-coming solar studies, a significant portion (~10%) of the reactor heating power will be supplied by solar photons. Key results obtained to date employing the 1 kW system are reported in the following section.

KEY RESULTS TO DATE

Reaction (1) between bromine and steam in the absence of solar photons has been studied between 900 and 1300 K. The lower range of experimental reactor temperatures was chosen such that HBr yields would be sufficient to measure. The upper range was set by the material properties of the quartz reactor. Quartz undergoes devitrification above about 1300 K, making it much more brittle. Reactor temperatures were chosen in 50 and 100 K increments between these two limits. Input bromine mole fractions $\chi_{Br2(in)}$ ranged between 0.01 and 0.2, readily achievable conditions. The

reactor was operated at atmospheric pressure.

Thermal Yield Data - Experiment and Thermodynamics

Published data were used in thermodynamic and kinetic rate constant calculations (Atkinson, *et al.*, 1992). Supporting quantum mechanical energy-surface calculations clarified the critical rate determining step, Equation 7. Table 1 enumerates many of the single-step chemical reactions thought to play an important role in HBr production. This compilation is by no means exhaustive. These are seen to include H_2O, Br_2, HBr, O_2, H_2, OH, Br, O, H, HOBr, BrO, and HO_2.

In Figure 5 are shown thermodynamic calculations of equilibrium hydrogen bromide yields for the purely thermal reaction. The effect of bromine thermal dissociation into Br atoms, which reduces equilibrium [Br_2] values, was included. Significant conversion yields of HBr and O_2 are predicted over the ranges of temperature and mole fraction experimentally studied, particularly in the limit of low bromine mole fraction (χ_{Br2}). Also shown in Figure 5 are survey experimental data, some approaching 50% conversion, over a range of χ_{Br2} values for five different temperatures in the 1 kW system acting as a thermal reactor.

The HBr yield Y of Equation (1) for a given time interval is defined in this report as

$$Y = n_{HBr(out)}/(2\ n_{Br2(in)}) \qquad (4),$$

where $n_{HBr(out)}$ is the number of moles HBr produced and $n_{Br2(in)}$ the moles Br_2 input. Sufficiently slow reactant flow rates and correspondingly long reactor residence times would improve heat transfer to the reactant gases. This in turn would promote bromine conversion yields reaching the thermodynamic equilibrium limit.

Reaction			ΔH^0_{298} (kcal/mole)
1.	$Br_2 + h\nu$	→ Br + Br	-15.5
2.	$Br_2 + M$	→ Br + Br + M	46.1
3.	Br + Br + M	→ Br_2 + M	-46.1
4.	Br + H_2O	→ HBr + OH	31.8
5.	HBr + OH	→ Br + H_2O	-31.8
6.	Br_2 + OH	→ Br + HOBr	-9.9
7.	HOBr + OH	→ BrO + H_2O	-17.3
8.	BrO + OH	→ HBr + O_2	48.2
9.	BrO + BrO	→ Br_2 + O_2	-52.8
10.	HBr + BrO	→ Br + HOBr	-14.4
11.	O + HOBr	→ Br + HO_2	-9.5
12.	HO_2 + O	→ OH + O_2	-53.6
13.	HO_2 + H	→ H_2O + O	-53.8
14.	HO_2 + Br	→ HBr + O_2	-38.9
15.	BrO + OH	→ HOBr + O	0.2
16.	O + Br_2	→ Br + BrO	-10.1
17.	O + HBr	→ Br + OH	-14.7
18.	O + HBr	→ BrO + O_2	-20.8
19.	O + HOBr	→ BrO + OH	-0.2
20.	O + BrO	→ Br + O_2	-62.9
21.	OH + O	→ 0_2 + H	-16.9
22.	H + Br_2	→ Br + HBr	-41.5
23.	H + BrO	→ HBr + O	-31.4
24.	HBr + O_2	→ Br + HO_2	38.9
25.	HBr + O_2	→ HOBr + O	48.5
26.	HBr + O_2	→ BrO + OH	48.2
27.	Br_2 + O_2	→ BrO + BrO	52.8
28.	Br + HBr	→ Br_2 + H	41.5
29.	Br + HOBr	→ Br_2 + OH	9.9
30.	Br + BrO	→ Br_2 + O	10.1
31.	Br + OH	→ HBr + O	14.7
32.	Br + O_2	→ BrO + O	62.9
33.	BrO + H_2O	→ HOBr + OH	17.3
34.	H_20 + O	→ $H0_2$ + H	53.8
35.	0_2 + H	→ OH + O	16.9

Table 1. Bromine-Water Chemical Reaction Set. Reactions are for the gas phase.

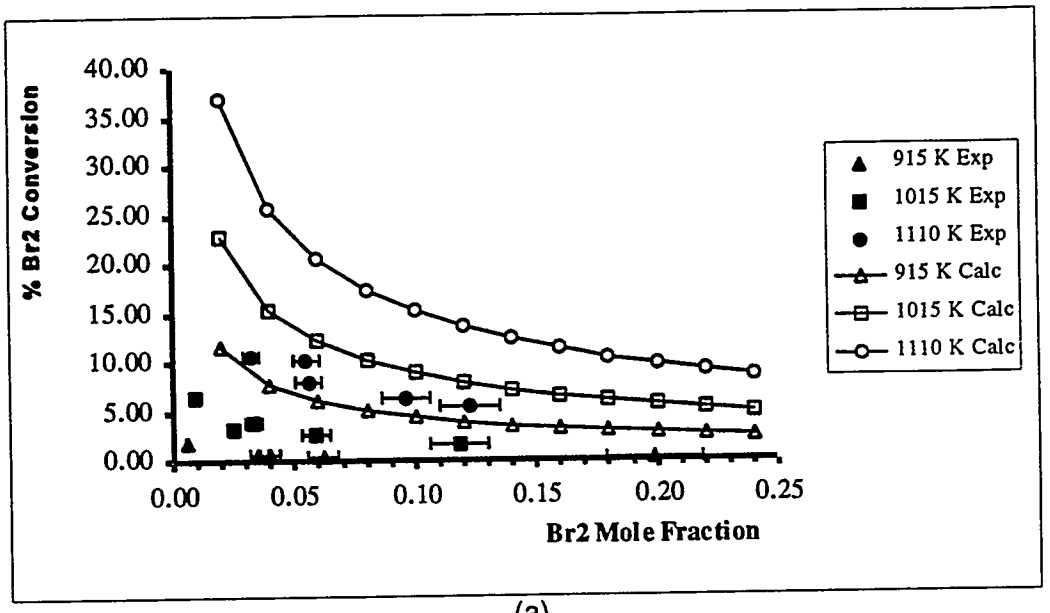

(a)

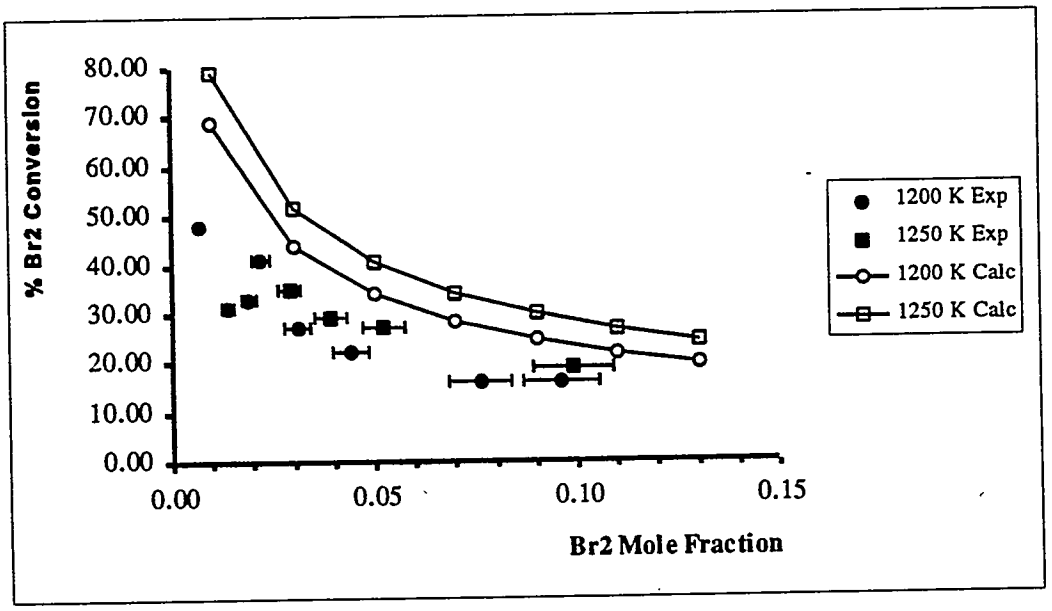

(b)

Figure 5. Calculated thermodynamic and experimental yields for the bromine-steam reaction as a function of bromine mole fraction χ_{Br2} and reaction temperature. The solid points refer to experimental data, which always lie below the calculated points (hollow). Both predicted and experimental yields increase with temperature and decrease with χ_{Br2}.

It was assumed, in agreement with preliminary analytical tests, that HBr was the major aqueous product. Yields reported here are based on acid molarity [H^+] of the condensed product mixture determined by sodium hydroxide titration. Bromide ion titration is currently being perfected. An upper limit to the presence of bromine oxyacids in the product mixture will be inferred from a thorough mass balance for bromine and oxygen in future work. If present in significant quantities, which is not anticipated, their effect upon hydrogen bromide electrolysis will be determined in consultation with electrochemical experts.

Experimental data are compared in Table 2 with the calculated thermodynamic predictions of Figure 5 corresponding to mean experimental temperatures and bromine mole fractions. Reagent throughput is denoted by the total molar flow rate in moles per minute. Two trends in experimental HBr yields are in good agreement with those predicted by the thermodynamic calculations. Specifically, *yield increases with temperature and decreases with bromine mole fraction.*

However, it is readily apparent that the degree of agreement between experimental and calculated yields is better at higher reactor temperatures. This suggests a combination of two factors. (1) Radiative heat transfer to reactants was improved, resulting in gas temperatures closer to those registered by the thermocouples. Heat transfer can be improved by prolonging residence times and boosting heat transfer surface area. A simple means of increasing the surface area would involve placing quartz wool in the reactor. Residence times, which follow from reactor volume and total molar flow rate, varied between 0.1 and 1 second. (2) Reaction kinetics were much faster at higher temperatures, resulting in a closer approach to steady-state conditions. As residence times exceed the steady-state time-constant, yields approach the thermodynamic value, which defines an upper limit. Reaction kinetics are dictated by temperature, and cannot be changed appreciably without introduction of a catalyst or operating at much higher temperatures. In the current scope of this project, testing of catalytic materials will not be undertaken.

The experimental temperatures cited in Table 2 refer to the mean values of four thermocouples (TC2, TC3, TC5, and TC6) along the reactor length (Figure 4). Their variation was no more than approximately ± 15 K, suggesting the temperature in the hottest half of the reactor was largely uniform. There was an appreciable temperature gradient between the reactor inlet/exit and the middle of the reactor. For the 1250 K studies, the inlet gradient (TC1- TC2) was 390 K over a 13 cm length and the outlet gradient (TC4 - TC5) 275 K. For the 915 K studies, inlet and outlet gradients were slightly lower at 335 K and 220 K, respectively.

T(K)	χ_{Br2}	Y_{exp}	Y_{calc}	Reactant flow (mol/min)
915	0.199	0.3%	3.1%	0.34
915	0.062	0.5	6.0	0.34
915	0.040	0.7	7.7	0.35
915	0.035	0.7	8.4	0.33
915	0.006	1.8	23.4	0.34
1015	0.118	1.6	8.4	0.35
1015	0.059	2.6	12.3	0.34
1015	0.033	3.8	17.0	0.32
1015	0.025	3.2	19.8	0.33
1015	0.009	6.5	34.1	0.34
1110	0.120	5.6	14.1	0.38
1110	0.096	6.3	15.9	0.35
1110	0.056	7.9	21.2	0.34
1110	0.055	10.2	21.4	0.35
1110	0.032	10.6	28.3	0.32
1200	0.096	16	23.5	0.41
1200	0.044	22	34.5	0.34
1200	0.031	27	40.4	0.38
1200	0.022	41	46.8	0.33
1200	0.007	48	68.8	0.36
1250	0.099	19	27.6	0.45
1250	0.052	27	37.4	0.45
1250	0.039	29	42.4	0.41
1250	0.029	35	47.9	0.40

Table 2. Thermal HBr Yield Data. T is mean reactor temperature, χ_{Br2} bromine mole fraction, Y_{exp} experimental HBr yield, Y_{calc} calculated thermal yield, and the total reactant molar flow rate.

The error bars associated with the experimentally determined HBr yields are due to those in product analysis (± 5%) and reagent flow rates (± 10%). Experimental improvements will be implemented in future experiments. Another uncertainty is in the temperatures measured by the thermocouples residing in reactor thermocouple wells. Further studies will determine the radiative, conductive, and convective heat transfer contributions to those values.

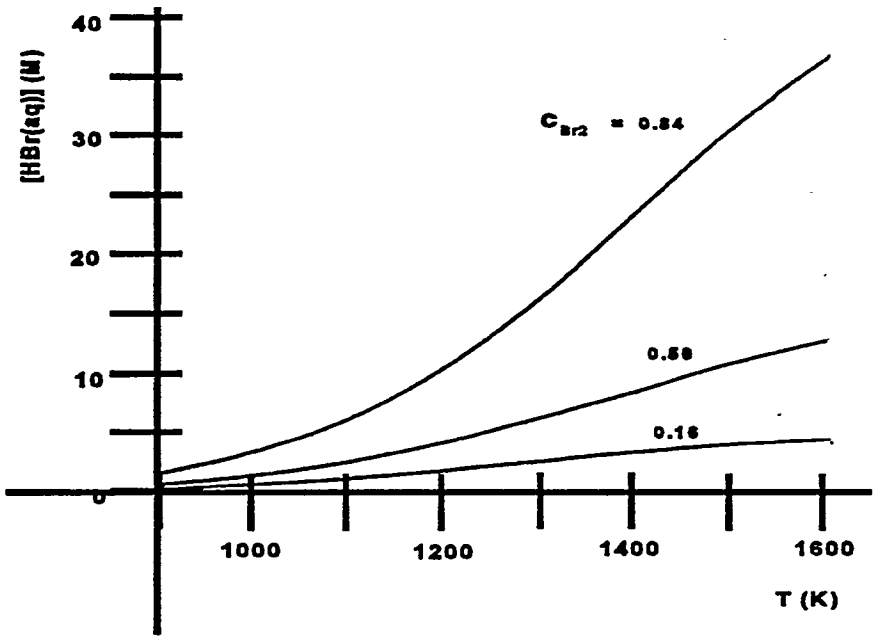

Figure 6. Calculated HBr molarity for the condensed product mixture of the bromine-steam reaction as a function of reaction temperature for the indicated input reagent stream compositions, $\chi_{Br2} = 0.167$, 0.50, and 0.833.

It should be noted that the high yields under conditions of excess water, i.e., $\chi_{Br2} < 0.5$, predicted in Figure 5 are not directly suitable for electrolysis, where the [HBr] should exceed 5 M. The concentration of the resulting solutions is quite low due to excess unreacted water. This point is illustrated in Figure 6, which depicts the molarity [H^+] of the condensed product mixture as a function of temperature and input reactant composition. Here it is assumed that theoretically calculated HBr yields are achieved. It is seen that bromine mole fractions $\chi_{Br2} = 0.833$ and 0.5 are expected to yield [HBr] > 5 M for reactor temperatures above 1200 K. On the contrary, for $\chi_{Br2} < 0.5$, HBr concentrations are lower at all temperatures.

In order to achieve sufficiently high HBr concentrations, high reactor temperatures and high χ_{Br2} fractions are requisite. This observation has important consequences for the power conversion efficiency of the solar-electrolytic process, as discussed below.

FUTURE WORK: PHOTOCHEMICAL ENHANCEMENT

The previously discussed thermal experiments and accompanying calculations serve to quantify chemical conditions in the reactor prior to its reaching the photochemical reaction zone of the solar studies. In the latter region, the kinetics of the photochemical reaction determine the solar enhancement. This is the boost in yield due to solar photons over and above that realized in the purely thermally driven reaction. It is useful to understand a simplified model of the photochemical reaction in order to identify conditions leading to acceptable power conversion efficiencies, which also involves the thermal reaction.

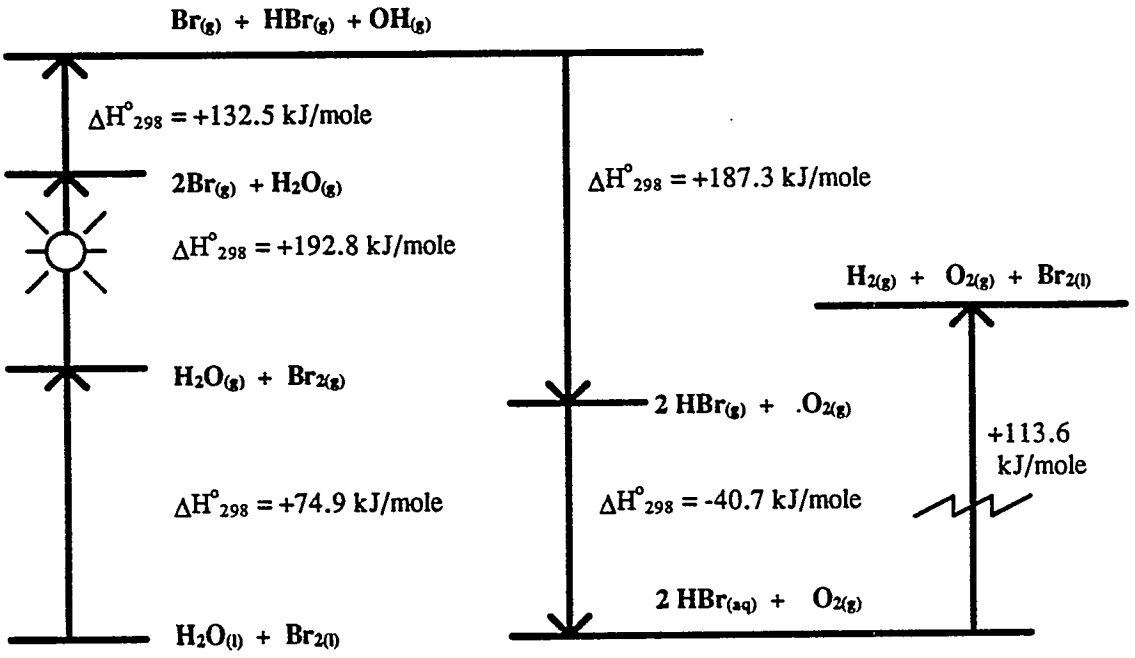

Figure 7. Schematic representation of the energetics of the bromine-water photochemical reaction kinetics and the presence of a rate-determining reaction barrier.

The role of solar photons in increasing HBr yield is clarified by Figure 7, which provides an overview of the energetics of the photochemical reaction. Liquid bromine and water are vaporized and the gases heated to ~ 1,000 K. This is accomplished in the experiments described in this report by a steam generator and reactor tube heater. In the larger field test reactors, the infrared and visible components of the terrestrial solar spectrum not absorbed by bromine (See Figure 8), about two-thirds of the total power, will be used to heat the reactant gas stream and facilitate the liquid-to-gas phase change. The implementation of an efficient heat exchanger will greatly boost the amount of heat recovered from the product flow stream and hence overall thermal efficiency (See next section).

Bromine atoms and molecules reach equilibrium concentrations at high reactor temperatures and in the absence of solar photons in accordance to the dissociation-recombination equations

$$Br_{2(g)} + M^* \rightarrow 2Br_{(g)} + M, \qquad \Delta H^\circ_{298} = +192.8 \text{ kJ/mole} \tag{5}$$

$$2Br_{(g)} + M \rightarrow Br_{2(g)} + M^*, \tag{6}$$

where M is any of the species present (Br, Br_2, H_20, HBr, O_2, etc.). In the photochemical

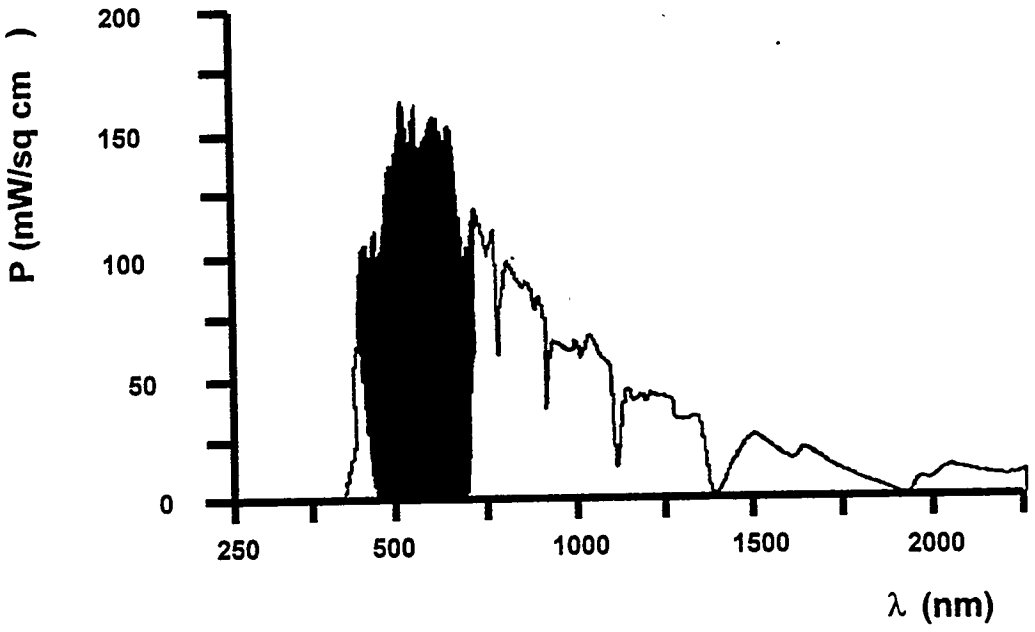

Figure 8. Portion of the terrestrial solar spectrum (AM 1) absorbed by bromine vapor, about 33%, indicated by the dark segment.

reaction region near the reactor window, visible photons are strongly absorbed by bromine vapor $Br_{2(g)}$, producing bromine atoms $Br_{(g)}$ in accordance with the expression

$$Br_{2(g)} + h\nu \rightarrow 2Br_{(g)}. \quad (7)$$

Bromine atoms remove hydrogen from water vapor in the critical rate determining step

$$Br_{(g)} + H_2O_{(g)} \rightarrow HBr_{(g)} + OH_{(g)}, \Delta H^0_{298} = +176.5 \text{ kJ/mole}. \quad (8)$$

This mechanism provides additional hydrogen bromide yield over and above the thermal yields shown in Figure 5. Subsequent faster radical reaction steps remove intermediate $OH_{(g)}$ (See Table 1) and diminish the extent of bromine atom recombination, the reverse of Equation (7). The reaction sequence terminates with the final production of $O_{2(g)}$ with high exothermicity, as indicated on the right of Figure 7. Once $O_{2(g)}$ is formed, there is little contribution from the back reaction to Equation (1) due to the high energy barrier. Accordingly, the four steps of Equations (5) to (8) are approximately rate determining in the overall proposed reaction scheme. A high efficiency for solar-to-chemical conversion can be achieved if the chemical conversion step of Equation (8) is made to dominate the thermal dissociative and recombination reactions of Equations (5) and (6). Subsequent solar photochemical studies of Equations (7) and (8) employing the 1 kW reactor will ascertain their importance to the overall yield.

FUTURE WORK: HEAT EXCHANGER

Heating the reactant gases in SRT's larger Phase II (10 kW Pioneer and 35 kW Pilgrim) and III (100 kW pre-commercial demonstration) reactors will be achieved solely by solar means. As mentioned before, bromine absorbs up to one-third of the terrestrial solar spectrum, dissociating via Equation 7. The bromine atoms thus formed have a high kinetic energy, which translates into significant local heating in the irradiated reactor volume (Antolovic, *et al.*, 1989). This can also lead to high HBr yields (See Figure 5) and thermal-to-chemical conversion efficiencies.

Since reagents are brought to high temperature prior to undergoing reaction, high conversion efficiencies can be achieved additionally by recovering thermal energy from the product flow stream. The overall solar-to-chemical power conversion efficiency ϵ of such a thermally driven reactor can be written in the form

$$\epsilon = \epsilon_{rec}\epsilon_{reac}/(1 - \epsilon_{exch}(1 - \epsilon_{reac})). \quad (9)$$

Here, ϵ_{rec} is the solar-to-thermal power conversion efficiency of the receiver unit, ϵ_{exch} is the thermal efficiency of the heat exchanger, and ϵ_{reac} is the thermal-to-chemical power conversion efficiency of Equation (1). An upper limit to the last efficiency can be determined by the chemical yield shown in Figure 5. Equation (9) follows from an energy balance applied to a thermal reactor operating with heat recovery from the product stream.

In Figure 9 are shown overall solar-to-chemical conversion efficiencies calculated using Equation (9). They are plotted as a function of reaction ϵ_{reac} efficiency. Multiple curves refer to varying receiver ϵ_{rec} efficiencies. Here it was assumed that $\epsilon_{rec} = \epsilon_{exch}$. High overall efficiencies are predicted for modest thermal conversion yields with sufficiently high ϵ_{rec} and ϵ_{exch} values. The thermal yields reported in Figure 5 and Table 2, when employed in conjunction with Figure 9, indicate that high overall solar-to-chemical conversion efficiencies can be obtained for the purely thermally driven reaction, Equation (1). The solar photochemical enhancement would be an added boost.

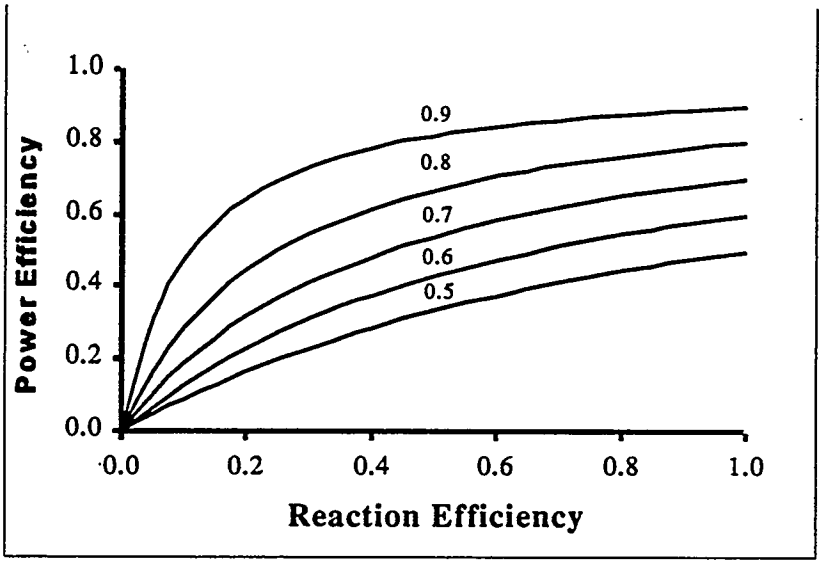

Figure 9. Solar-to-chemical conversion efficiencies ϵ as a function of reaction efficiency ϵ_{reac} for different heat exchanger efficiencies ϵ_{exch}. Here it is assumed that the receiver and heat exchanger efficiencies are equal, $\epsilon_{rec} = \epsilon_{exch}$.

It should be noted that the addition of a porous black body absorber inside the solar reactor will enhance heat transfer to the inflowing reactant gases. This would effectively increase ϵ_{rec} and hence the overall efficiency. Since only about one-third of the terrestrial solar spectrum is absorbed by bromine, it is imperative that the remainder be used in bringing reactants to temperature. This concept may be included in SRT's 10 kW Pioneer design. Further, low quality heat ($T < 500$ K) will be used in facilitating reactant liquid-to-vapor phase change and product separation.

PROPOSED APPROACH FOR FURTHER DEVELOPMENT OF THE CONCEPT

The SRT project is presently being amended so that it will be comprised of three phases as shown in the following timeline. The reason for the amendment is to provide for commercialization and demonstration of the concept, due to the success of the present experimental effort. The first phase, which has been partially completed with this report encompasses background research on the

bromine-steam reaction, both in the absence and presence of solar photons, on a bench-top scale (1 kW). The design, fabrication, and testing of a larger 10 kW solar reactor at NREL follows. This work will be completed as defined in the present contract. In the second phase (proposed), a second 10 kW and a 35 kW reactor system will be designed, fabricated, and tested. Electrochemical studies of a hydrogen-bromine fuel cell will be undertaken. Finally, the proposed third phase involves construction, and demonstration of a 100 kW_{solar} pre-commercial reactor/fuel-cell unit.

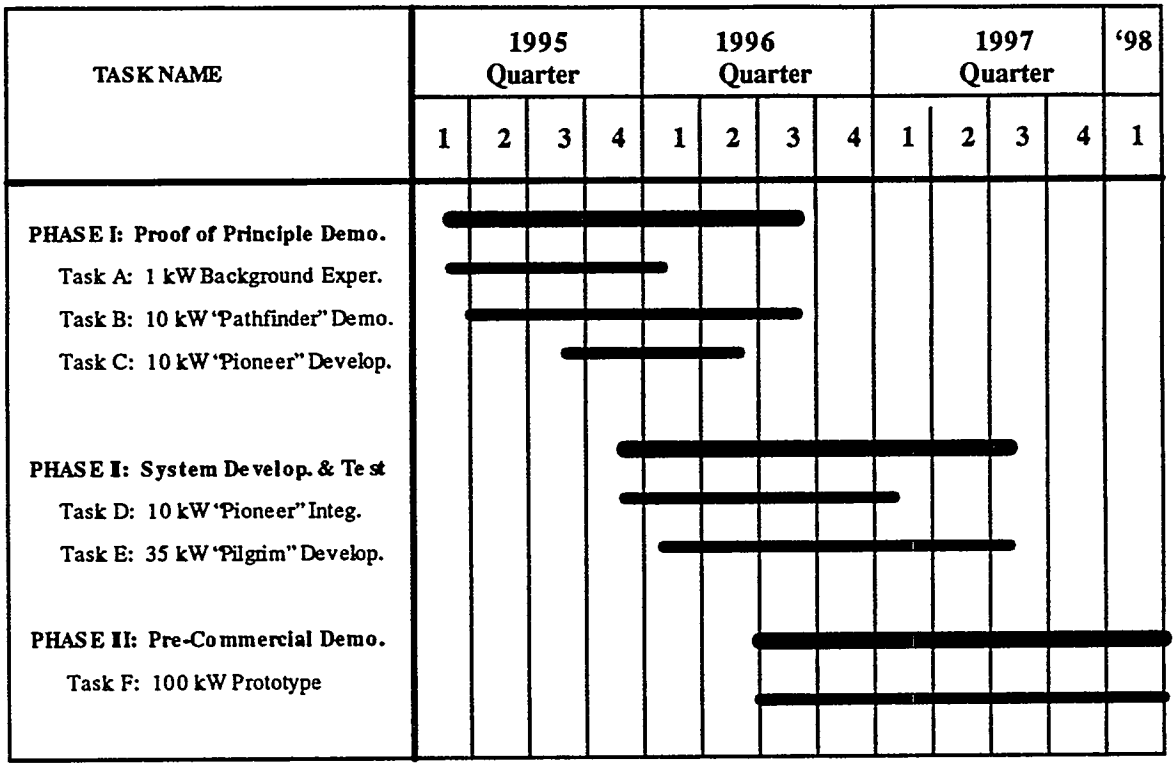

Technical and management support will be provided by collaborating groups working under contract to DoE. These groups include the Florida Solar Energy Center (photochemistry support), the University of Miami Clean Energy Research Institute (safety analysis), Energetics, Inc. (system analysis), R. K. Sen and Associates, Inc. (economic analysis, the National Renewable Energy Laboratory (High-Flux Furnace), Hamilton Standard Inc. (electrochemistry) and Sandia National Laboratories (engineering and materials support). The Phase I FY-95 activities are performed largely at the University of Florida, Gainesville, and Indiana University, Bloomington, operating under support from SRT. A synopsis of the three phases follows.

Phase I, Proof-of -Principle Demonstrations (Presently Ongoing)

Studies of the bromine-water photochemical reaction Equation (1) are being performed (Task A) under the auspices of this first phase of this work. A 1 kW system was designed, constructed and operated as a thermal reactor during the first four months of the contract period. It will be modified

for use as a solar reactor in the next stage of this project. Theoretical studies of the thermodynamics and kinetics of the most relevant contributing reactions will be undertaken to interpret the experimental data.

A reactor to be used with a 10 kW dish (Pathfinder) will be designed (Task B) and demonstrated at NREL in collaboration with the participating groups identified above. The emphasis will be on reactor design optimization. Bromine and steam will be delivered to the reactor, the effluent products condensed, analyzed and neutralized. Integration of bromine and water recycling, a heat exchanger, and a fuel cell will be included in a second generation 10 kW reactor named Pioneer. It will be designed (Task C) for integration into a complete system demonstration in Phase II.

Phase II, System Development and Testing

Components of the 10 kW Pioneer system (reactor, heat exchanger, product separation, fuel cell, and reactant and product storage) shall be fabricated by several vendors (SRT, Hamilton Standard, Sandia, NREL, and others), integrated, and tested at the NREL facility (Task D). The complete SRT energy-storage/load leveling concept will be tested and demonstrated. In the energy storage mode, HBr will be produced by the solar reactor for subsequent electrolysis and hydrogen production, while in the load leveling mode, hydrogen and bromine will combine to produce electricity and HBr in the fuel cell. An extensive safety and operating protocol will be implemented before, during, and after this testing.

Based on the results of the Pioneer demonstration, a larger version of the Pioneer system matched to a 35 kW dish (Pilgrim) will be designed (Task E). Commercial vendors will fabricate components and the unit will be tested at Sandia National Laboratories. The goal will be to demonstrate a unit that is one-third as large as the Phase III 100 kW pre-commercial demonstration system.

Phase III, Pre-Commercial Demonstration

During the Phase III work effort, three 35 kW_{solar} Pilgrim units will be integrated into a 100 kW pre-commercial demonstration system. This modular approach is advantageous to system cost, maintenance, and future upgrading. The envisioned system will be operated at the proposed DoE integrated hydrogen facility in Palm Desert, CA.

CONCLUSION

Initial data on the thermal reaction between bromine and steam at elevated temperatures (900 - 1300 K) were discussed. It is seen for all temperatures that the experimental yields are lower than the theoretical ones. This is surmised as due to either (1) reactant gas temperatures lower than those recorded by reactor thermocouples, or (2) reactor residence times shorter than the time-scale required to reach equilibration of the reaction kinetics. Further work is required to determine the contribution of each.

The experimental data do agree well with two important trends predicted by thermodynamics: (1) increasing HBr yield with increasing temperature, and (2) decreasing yield with increasing bromine reactant mole fraction. These two competing trends are discussed in the context of achieving a desirably high HBr concentration in the condensed product mixture for subsequent electrolysis.

The importance of efficient heat transfer between inflowing reactants and outflowing products has been determined and reviewed. Overall thermal-to-chemical efficiencies in excess of 50% are anticipated for realistic operating conditions. The contribution of solar photons in enhancing the photochemical bromine-steam reaction is under investigation and will be demonstrated with the 1 kW system. The effect of the solar-assisted reaction would be a boost to an already efficient purely thermal reaction.

REFERENCES

D. Antolovic, E.J. Bair, and P.W. Langhoff. 1989. "Radiation Augmented Fluids Technology," Final Report prepared by SRT for Wright-Patterson AFB, WRDC-TR-89-2036.

D. Antolovic, E.J. Bair, A.K. Gupta, R.J. Hanrahan, and P.W. Langhoff. 1990. "Halogen-Based Photoproduction of Hydrogen." Honolulu, HI: *Eighth World Hydrogen Energy Conference.*

R. Atkinson, D.L. Baulich, R.A. Cox, R.F. Hampson, Jr., J.A. Kerr, and J. Troe. 1992. "Evaluated Kinetic and Photochemical Data for Atmospheric Chemistry". *J. Phys. Chem Ref. Data* **21**: 1125.

A. Beaufrere, R.S. Yeo, S. Srinivasan, J. McElroy, and G. Hart. 1990. "A Hydrogen-Halogen Energy Storage System for Electric Utility Applications". Washington, DC: *Proceedings of the 11th Inter-Society Conversion Engineering Conference.*

J.G. Calvert and J.N. Pitts. 1966. *Photochemistry.* New York: Wily, p. 184.

T. Cawthon and N. Rossmeissl. "FY 1995 Hydrogen Program Annual Operating Plan". U.S. DoE Office of Utility Technology, Advanced Utility Concepts Division. Maryland: Energetics, Inc.

J.P. DiPietro and J.S. Badin. 1995. "Integrated Systems Analysis of the HBr-Based Hydrogen Production and Electricity Generation System Developed by Solar Reactor Technologies". DoE Hydrogen Program Technical Review Meeting. Coral Gables: Energetics, Inc.

A.K. Gupta and R.J. Hanrahan. 1992. "Gas Phase/Liquid Phase Photochemical Reaction Between Bromine-Water for the Formation of Hydrogen Bromide Solution". Miami: SRT, Inc., Technical Report.

B. Heydorn, H. Schwendener, and M. Tashiro. 1990. *Chemical Economics Handbook, Production Review of Hydrogen.* Palo Alto: SRI International.

R.E. Schlief. 1994. "Solar Photochemical Production of HBr from Bromine and Steam for Off-Peak Electrolytic Hydrogen Production." Unsolicited Proposal Submitted to the Department of Energy. Miami: Solar Reactor Technologies, Inc.

K. Scholl and C. Fields. 1994. "Solar Thermal Hydrogen." DoE Hydrogen Program Technical Review Meeting. Coral Gables: NREL.

D.J. Seery and D. Britton. 1964 "The Continuous Absorption Spectra of Chlorine, Bromine, Iodine, Bromine Chloride, Iodine Chloride, and Iodine Bromide." *J. Phys. Chem.* **68**: 2263.

H. Wendt and G.H. Bauer. 1988. "Water Splitting Methods," in C.J. Winter and J. Nitsch, Eds., *Hydrogen as an Energy Carrier: Technologies, Systems, Economy.* Berlin: Springer-Verlag, p. 166.

C.J. Winter, H. Klaiss, and J. Nitsch. 1990. *Int. J. Hydrogen Energy*, **15**: 79.

PHOTOELECTROCHEMICAL BASED DIRECT CONVERSION SYSTEMS

Shyam Kocha, Doug Arent, Mark Peterson, Brent MacQueen, Art Frank, and
John A. Turner
National Renewable Energy Laboratory
Golden, CO 80401-3393

Abstract

The goal of this research is to develop a stable, cost effective, photoelectrochemical based system that will split water upon illumination, producing hydrogen and oxygen directly, using sunlight as the only energy input. This type of direct conversion system combines a photovoltaic material and an electrolyzer into a single monolithic device. We report on our studies of two multijunction multiphoton photoelectrochemical devices, one based on the ternary semiconductor gallium indium phosphide, ($GaInP_2$), and the other one based on amorphous silicon carbide. We also report on our studies of the solid state surface treatment of $GaInP_2$ as well as our continuing effort to develop synthetic techniques for the attachment of transition metal complexes to the surface of semiconductor electrodes. All our surface studies are directed at controlling the interface energetics and forming stable catalytic surfaces.

Introduction

The production and storage of hydrogen via renewable resources represents a key part of a sustainable energy system. Photovoltaic systems coupled to electrolyzers exemplify such a system and are commercially available. However, since current commercial electrolyzers suffer from high capital costs, they are a major contributor to the cost of electrolytically produced hydrogen. Photoelectrochemical (PEC) water splitting, also known as photoelectrolysis, represents an advanced alternative to a PV/electrolysis system. The incident light, absorbed in a semiconductor electrode, splits water directly. A one-step monolithic system such as this eliminates the need to generate electricity externally and subsequently feed it to an electrolyzer. This type of monolithic system also reduces semiconductor processing since surface contacts, interconnects and wiring are no longer necessary.

Energetically, at 25°C, splitting water into hydrogen and oxygen requires a voltage of 1.229 V. At current densities for solar applications, typical values of the overvoltage for the hydrogen evolving and oxygen evolving reactions are 50 mV and 275 mV respectively. [1-6] A potential then, of at least 1.6 V, is required for a water splitting system. For a single gap semiconductor based direct conversion water splitting system, the requirement of at least 1.6 V added to the internal losses from the semiconductor, indicates a minimum bandgap of 1.8 electron volts is required.[7,8] This means that the entire spectrum of visible light can be used for water splitting. Additionally, the system must be stable in an aqueous environment. Metal based catalysts are required on both the hydrogen and oxygen evolving surfaces to speed up the redox reactions and stabilize the semiconductor. A further requirement is that the semiconductor band edges span both redox potentials of the hydrogen and oxygen evolution reactions.

Splitting up the solar spectra by using two or more absorbers with different bandgaps increases the maximum theoretical efficiency of the total system.[6,7] Tandem cell technology connects photovoltaic layers (pn junctions) with different bandgaps in series, one behind the other, in a single monolithic cascade device. The wide bandgap material is placed on top towards the sun and the second cell with a smaller bandgap is placed behind the top layer. The smaller bandgap then absorbs the photons that are not absorbed by the top layer. This configuration offers a greater utilization of the solar spectra, resulting in higher solar conversion efficiencies. The monolithic structure also minimizes the amount of active area needed for specific power applications.

Discussion

Gallium Indium Phosphide Studies

While the band gap of $GaInP_2$ is nearly ideal for the photoelectrochemical production of H_2 and O_2, surface modification is required to move the band edges to more positive potentials in order to provide adequate overlap with the redox potentials of the water splitting reactions. Previously, we have showed that 8-Quinolinol effectively moves the band edges toward more positive potentials. This movement places the valence band of $GaInP_2$ at ~1V vs. normal hydrogen electrode (NHE), which provides ~0.2V overpotential for the evolution of O_2 from a pH 7 buffer solution. However, this is still not sufficient to accomplish water splitting. The following surface studies are directed at controlling the interfacial energetics as well as forming stable catalytic surfaces.

Heterojunction surface layers

Part of our early work on $GaInP_2$ indicated that the band edges were sensitive to the growth conditions at the end of the deposition process. We have under taken a study of the effect that changes in the growth conditions have on the surface characteristics. In addition to achieving appropriate band edge positions, surface layers may be effective passivators of surface states, thereby reducing the number of nonradiative recombination centers and improving the overall conversion efficiency of the device. Surface modification is typically achieved by either continuous epitaxial deposition of appropriate materials or post deposition treatments, which may include transformation of the surface via an exchange type reaction or chemically treating the surface. For our $GaInP_2$ based photoconversion system, we have explored three major experimental solid state avenues in attempting

to achieve controllable flat band potential variations: (1) exploitation of the naturally occurring CuPt ordering phenomena in $GaInP_2$, whereby monolayer superlattices are formed on the Group III sublattice and the effective bandgap of the macroscopic sample is reduced; (2) systematic variation of the surface chemical potential through use of substrates with various miscuts. In this approach, the base GaAs substrate is accurately polished to reveal a known surface bonding structure. The bonding structure affects the growth of the $GaInP_2$ in terms of composition, the occurrence of ordering, and doping levels; and (3) epilayer surface modification with lattice matched and mismatched high bandgap material. Here, materials were selected from the entire range of (Al,Ga,In-As,P) binary, ternary, and quartenary combinations to provide full experimental investigation of the possible passivating and band edge movement compounds.

Heterojunction surface layers - Results:

In these experiments, we used photoluminescence (PL) and capacity data to determine the effect, if any, of the surface treatment on the energetic at the interface. The magnitude of the PL peak intensity and the (PL) can be used as an indicator of the non-radiative surface recombination rate. A low surface recombination rate indicates a good surface and typically results in higher efficiencies and faster charge transfer rates. Capacitance data is used to measure the energetic position of the band edges. Any displacement of the flatband potential produced by a change in the surface composition or surface alloy ratio is determined by capacitance measurements.

Approach #1) Five samples were prepared of GaAs substrates of crystal face (100), miscut 2° toward the (110) plane. The samples displayed bandgaps of 1.85 to 1.89 eV at room temperature. This 40 meV change is approximately one-third of the maximum observed bandgap reduction (110 meV) for $GaInP_2$. Mott-Schottky experiments revealed essentially no variation (+ 10 meV) in the flat band potential among the different samples indicating that the bandgap of the resultant CuPt ordered $GaInP_2$ has little if any effect on the flat band potential.

Approach #2) Samples of $GaInP_2$ were epitaxially deposited on (100) GaAs with misorientations of 2°, 4°, 6°, 9°, and 15.8° toward (111)B under identical conditions in a single run of the reactor. Under identical conditions, the resultant $GaInP_2$ is expected to display variations in the bandgap energy and doping density (the amount of spontaneous ordering and impurity incorporation depend on the growth conditions and substrate misorientation). For samples with variations in band gap energy of ~30 meV, we observe 150 meV shifts in the flat band potentials. Samples grown on 6°(111)B misoriented substrates displayed the most positive flat band potential, 0.65 V vs. the standard calomel electrode (SCE). These results suggest that the surface chemistry of the photoelectrode can be exploited via this approach to improve the energetics of the water splitting reaction. However, the flat band movement is not sufficient to eliminate additional post-deposition treatments.

Approach #3) The study of solid state surface layer modification was broken down into three subsections to individually address the effect of composition variations when changing either Group V or Group III constituent elements.

(a) $[Al_xGa_{(1-x)}]_{0.52}In_{0.48}P$ layers of 50 and 100Å and x = {0.1, 0.2, and 0.3} were deposited as potential passivation reagents. We observed strong shifts in the flat band potentials, although, these

changes were nonsystematic with Al concentration and did not represent any improvement over the bare $GaInP_2$ surface. Additionally, increasing Al concentrations deteriorated the ideality of the Mott-Schottky response, indicative of increased surface states due to Al oxidation.

(b) $Ga_xIn_{(1-x)}P$ layers of 50 and 100Å and x = {0, 0.25, 0.75, and 1} were deposited as potential passivating surface layers. These layers are lattice mismatched and thus are strained relative to the $Ga_{0.52}In_{0.48}P$ active layer. Transmission electron microscopy of samples with GaP overlayers revealed that misfit dislocations onset above 50Å thereby reducing the passivating effects. For both In and Ga rich $Ga_xIn_{(1-x)}P$ overlayers, we observed little or slightly negative shifts in the flat band potential in comparison to freshly etched $GaInP_2$ (Fig. 1 & 2). Some improvement in the linearity of the Mott-Schottky response was observed with In rich samples (Fig. 2). This improvement is indicative of a reduction in the number of electrochemically active surface states and most probably results from the formation of a stable InO_x surface species.

(c) $GaAs_xP_{(1-x)}$ layers of 50 and 100Å and x = {0, 0.1, 0.4, 0.96. and 1} were deposited. Similar to (b) above, these layers are also lattice mismatched with the onset of dislocations occurring above thicknesses of 50Å. Mott-Schottky analysis revealed a monotonic decrease in the flat band potential, as well as increasing non-ideality, with increasing P content in the surface layer. These results are consistent with theoretical understandings that predict relatively large shifts in the valence band energies as the Group V element varies. However, previous photoelectrochemical measurements of the valance band edge of GaP placed it more positive than that of GaAs, however, for these experiments we observed movement in the opposite direction (Fig. 3).

Directed Modification for Control of Surface Energetics

Another approach to the problem of interfacial energetics is the directed modification of $GaInP_2$ with the goal of permanently shifting the energetics of the $GaInP_2$ solution interphase. Moving the band edges to more positive potentials requires the permanent addition of positive charge to the interface. One of the promising surface modification systems we have focused on is the use of a highly active ruthenium based water oxidation catalyst. This is the ruthenium dimer $L_2(H_2O)Ru\text{-}O\text{-}Ru(H_2O)L_2^{4+}$ where L = 5,5'-dicarboxylate-2,2'-bipyridine. This catalyst was developed under an OER/BES research program, and a patent was recently issued on this catalyst. The combination of the +4 positive charge and the catalytic activity represents an important area to study. We have accomplished the first step in the path towards the directed modification of $GaInP_2$ with this ruthenium water oxidation catalyst.

In this study the ruthenium catalyst was covalently attached to indium doped tin oxide (ITO). ITO is used in the initial investigation because it allows for a more complete investigation of the attachment scheme and the nature and amount of coverage. Investigation of the $GaInP_2$ surface by X-ray photoelectron spectroscopy (XPS) reveals the presence of indium oxides, indicating that the same attachment scheme developed for ITO can be used. The similarity of the surface of ITO with the surface of $GaInP_2$ (both have similar oxide surfaces) should facilitate the transfer of the modification techniques. The covalent attachment of the ruthenium catalysts to ITO was accomplished via amide bond formation with a silylamine linking agent, specifically N-(2-aminoethyl)-3-aminopropyltrimethoxysilane bound to ITO via Si-O bonds formed with surface oxides. The modified ITO was characterized by XPS, Raman spectroscopy, cyclic voltammetry (CV) and

coulometry. XPS analysis clearly indicates the presence of ruthenium on the surface. Raman spectra and electrochemical data further indicate that the ruthenium catalyst has been attached to the ITO without any significant chemical changes.

A current voltage curve, using a glassy carbon electrode, of the ruthenium catalyst dissolved in an aqueous solution of 0.5 M H_2SO_4, showed a reversible wave at +1.19 volts (vs. NHE) corresponding to ruthenium (III-IV) couple and a catalytic water oxidation wave at +1.49 volts. The peak separation for the ruthenium wave was 100mV. A current voltage curve under the same conditions on an ITO electrode derivatized with the ruthenium catalyst, showed the III-IV ruthenium oxidation wave at +1.14v and the water oxidation wave at +1.6 volts. In this case, the peak separation for the ruthenium wave was 25mV. The narrowing of the peak potential separation for bound complex relative to the unbound complex is indicative of a surface attached species and was expected. By integrating the charge passed when the bound complex is oxidized, the surface coverage can be determined. These coulometry experiments indicated that the surface concentration of the ruthenium catalyst in ITO was 2.0×10^{-10} moles/cm^2. This result is consistent with other work in the literature on surface modification using similar ruthenium complexes. Our preliminary work also indicates that the surface attached complex is far more stable that the unbound complex in homogeneous solution. Work to be completed on the ruthenium derivatized ITO involves the determination of the catalytic rate, lifetime of the catalyst, and the pH dependence of the oxidation of water.

Tandem Cell Studies - $GaInP_2$/GaAs

We have continued to study the process whereby the $GaInP_2$/GaAs tandem cells evolve oxygen and hydrogen simultaneously from the same surface. A possible explanation involves the formation of a Schottky barrier at the semiconductor/electrolyte interface. This barrier may change the solid state band energetics causing the co-evolution of H_2 and O_2 at the illuminated surface of the tandem cells.

Modeling of GaAs/GaInP and InP/InGaAs Tandem Solar Cells

Model calculations were performed on prototype tandem cell structures consisting of $GaInP_2$/GaAs and InP/InGaAs systems to determine the possible effect a Schottky barrier would have on the internal band structure. These cells operate with emphasis on two different regions of the solar spectrum. The GaAs/$GaInP_2$ is a high voltage-low current system optimized for space applications with its lowest turn on energy of 1.4 eV; the InP/GaInAs cell is a higher current-lower voltage system that is more active in the near IR due to the low (0.75 eV) band gap of the InGaAs. We have modeled the steady-state dark band equilibrium conditions of these cells using the program HETMOD, previously obtained from IBM, in which both the Poisson and Schroedinger equations are solved simultaneously.

We used the following test structure (illustrated for the InGaAs/InP cell), with limited thicknesses in both the top and bottom pn regions in order to elucidate the band bending within the tunnel junction. The HETMOD program can be model the test structure as a function of structure, bandgap, doping level and type, and surface bias (Schottky Barrier height).

Structure	Material	Doping/Level	Thickness
Surface			
Top Cell	InP	n, $1x10^{17}$	1000
	InP	p, $1 x10^{17}$	7000
Tunnel Junction	InGaAs	p, $7 x10^{18}$	200
	InGaAs	n, $7 x10^{18}$	200
Window	InP	n, $2 x10^{17}$	1000
Bottom Cell	InGaAs	n, $1 x10^{17}$	1000
	InGaAs	p, $1 x10^{17}$	7000
Buffer	InP	p, $1 x10^{19}$	1000
Substrate	InP	p, $1 x10^{19}$	

For the GaAs/GaInP tandem cell (Fig.4), we find: (1) a smaller calculated value of the expected open circuit voltage (~ 1.85-1.9 V vs. 2.29 V for the actual device), (2) an extremely functional tunnel junction in terms of band overlap and tunneling probability, and (3) extreme surface band bending, which even at 1V bias displays a reversal in electric field within the first few thousand Å of the surface. The difference in the open circuit voltages may arise for some discrepancies in the known band offsets in this system as well as the doping levels at which degeneracy occurs. The overall underlying cell characteristics are as expected, including the small interface discontinuity at the epilayer/substrate interface (small spikes at ~ 12000Å in Fig. 4).

The surface band bending is somewhat surprising, and we speculate that this may account for some of the unexpected behavior of the tandem cell/PEC devices. Because of the complexity of this device, we are unsure as to the nature of the Schottky barrier height and therefore the band bending at the surface. We have accordingly applied various surface voltages to simulate different Schottky barrier heights at the cell/solution interface.

Traditionally, for n-type material, surface band bending develops to promote hole diffusion to the surface. This arises from the equilibration of the Fermi levels of the n-type material and the redox level of the couple solution. The bulk bands remain below the surface band edges, and thus only one carrier is influenced by the electric field at the surface. For the tandem structure the near-surface band bending is more complicated, due to the thin n-type emitter layer on top of the p-type base. Within the first 1000Å of the surface, the electric field displays both a positive and negative slope. Hence, a driving force exists for both electrons and holes to diffuse to the surface. Electrons from the top-most n-type layer are readily available to migrate to the surface under the influence of the electric field within the last 500Å. Holes must either thermionically emit over the barrier or ballistically transport (tunnel) through the bent-band region to the surface.

In the dark, under steady-state conditions, we expect a band bending diagram as calculated above. Under illumination, however, we expect the surface voltage-induced band bending to flatten. If charge then dissipates and a quasi-dark condition is reestablished, the sign of the surface field will oscillate. Under such oscillatory E-field changes, either holes or electrons will be energetically favored to diffuse to the surface and perform chemistry. Other mechanisms may also apply, and it

is unclear at the present what critical factors in the tandem cell itself or the surface treatments could induce oscillatory behavior.

Equivalent results have been found for a p-InP terminated device. Again, we find significant surface band bending, which under moderate applied bias displays a reversal in the electric field. In this case, we find (1) fairly accurate calculation of the expected open circuit voltage (~ 1.2 V vs. 1.19); (2) an extremely functional tunnel junction in terms of band overlap and tunneling probability; and (3) extreme surface band bending, which displays a reversal in electric field within the first few thousand Å of the surface.

These results suggest that an interesting experiment would be to contact the surface of the device with an ohmic contact and measure the surface photovoltage. Electrochemical impedance spectroscopy may also help elucidate the nature of the surface field.

Fig. 5 shows a schematic of a surface contacted tandem cell device. The actual fabrication of the front contacts and the attachment of Cu wires in these small electrodes is difficult and our success rate has been disappointing. However some data has been obtained, an example of which is shown in Fig. 6. Note the time variations of the surface photovoltage. This may be due to local oscillations of the surface voltage. Oscillation of this type are typical of chaotic behavior and are not unknown in photoelectrochemical systems.[9,10] There are a number of ways to control chaotic behavior, one possible approach is to modify the structure of the semiconductor device. Figure 7 shows the transient current behavior for a tandem cell in which the thickness of the p-$GaInP_2$ layer has been increased from 0.7μm to 1.2μm. Note that now the current transient behaves as expected. Our study of these type of cells has shown that even when the cell appears to be operating properly, some oxygen is still being produced at the illuminated surface. This indicates that additional modifications need to be made in order to fully control the surface energetics.

Tandem Cell Studies - α-Si/α-SiC cells

While the $GaInP_2$/GaAs tandem cells represent a high efficiency system, it will likely be a relatively expensive one. A less expensive alternative system currently being studied is one based on amorphous silicon (α-Si). There are two main technological problems that must be solved before an α-Si based system could operate as a photoelectrolysis device. (1) Its bandgap is insufficient to effect the decomposition of water and (2) α-Si is not stable in contact with aqueous electrolytes, (it decomposes within a few minutes). Current state-of-the art α-Si based devices address both of these problems. Triple junction α-Si devices can have voltages greater than 1.8 volts, which is sufficient for water splitting, and cells are being developed which have a surface coating of amorphous silicon carbide (α-SiC). Figure 8 shows the structure of an α-SiC/α-Si device currently being tested in our laboratories. Preliminary work in our laboratory has shown that α-SiC provides a stable surface layer and is effective at protecting the underlying photovoltaic layers. We are initiating a contract with Materials Research Group (MRG) to design and grow α-Si/α-SiC triple junctin and tandem cells specifically for water splitting. We are also collaborating with Prof. Cameron Moore from the University of Denver on the modification and optimization of these tandem cells for direct conversion hydrogen producing systems.

In reviewing the literature on α-SiC, we have found very little research reported on the photoelectrochemisty of α-SiC. We have therefore initiated a collaborative effort with Professor Jan

Augustynski of the University of Geneva (Geneva, Switzerland) to study α-SiC in aqueous solution. MRG will grow various α-SiC samples for us and we will send them to Prof. Augustynski's group for study. This joint work is part of an IEA collaborative research effort.

Conclusions

Good progress has been made in our understanding of the area of surface modification and the control of the interfacial energetics of $GaInP_2$. Advancement has been made towards the control of the co-evolution of H_2 and O_2 from the $GaInP_2$ based tandem cell system. Promising results have been obtained from α-SiC tandem cells. The α-SiC has shown an ability to protect the underlying α-Si layers.

Future Work

We plan to investigate new tandem cell structures and catalytic coatings for increased efficiency and proper operation (separated oxygen and hydrogen evolution reactions). We intend to explore new semiconducting materials. We will increase our efforts in the design and testing of α-Si/α-SiC based semiconductor systems for water splitting. We will also continue to work on the surface modification of $GaInP_2$ focusing on its application as a single bandgap water splitting system.

Acknowledgments

The XPS work was performed by Art Nelson.

References

1) S. Horowitz, J. M. Longo and H. H. Horowitz, *J. Electrochem. Soc.*, 130, 1851 (1983)
2) Damjanovic, A. Dey, and J. O'M Bockris, *Electrochim. Acta*, 11, 791 (1966)
3) W. Boer, *Sol. Energy*, 19, 525 (1977)
4) Rasiyah and A. C. C. Tseung, Electrochemical Society Extended Abstracts, Vol. 81-1, Minneapolis, MN, # 530, p.1305, May 10-15, 1981.
5) Ottagawa and J. O'M Bockris, *J. Electrochem. Soc.*, 129, 2391 (1982).
6) Gerischer, in *Topic in Applied Physics*, B. O. Seraphin ed., Vol 31, p 115-172 (1979).
7) R. Bolton, S. J. Strickler, and J. S. Connolly, *Nature*, 316, 495 (1985).
8) F Weber and M. J. Dignam, *Int. J. Hydrogen Energy*. 11, 225 (1986).
9) T. M. Koper, E. A. Meulenkamp, and D. Vanmaekelbergh, *J. Phys. Chem.*,97, 7337 (1993).
10) Pohlmann, G. Neher, and H. Tributsch, *J. Phys. Chem.*,98, 11007, (1994).

Figure Captions

Figure 1 *Gallium Rich Surfaces* (a) Mott-Schottky plots of ~ 1 μm thick p-type $Ga_{0.52}In_{0.48}P$ with 50 or 100Å Ga rich surface layers of either GaP or $Ga_{0.75}In_{0.25}P$. (b) Time resolved photoluminescence (TRPL) decay traces for p-type $Ga_{0.52}In_{0.48}P$ with 100Å GaP (K942), 100Å $Ga_{0.75}In_{0.25}P$ (K945) and freshly etched $Ga_{0.52}In_{0.48}P$.

Figure 2 *Indium Rich Surfaces* (a) Mott-Schottky plots of ~ 1 μm thick p-type $Ga_{0.52}In_{0.48}P$ with 50 or 100Å In rich surface layers of either InP or $Ga_{0.25}In_{0.75}P$. (b) TRPL decay traces for p-type $Ga_{0.52}In_{0.48}P$ with and without 50Å of $Ga_{0.25}In_{0.75}P$ surface layer, before and after etching.

Figure 3 *GaAsP surface epilayer modification* (a) Mott-Schottky plots of ~ 1 μm thick p-type $Ga_{0.52}In_{0.48}P$ with 50 or 100Å GaAsP surface layers grown at gas phase ratios PH_3:AsH_3 of 2:1, 50:1, 100:1. (b) TRPL decay traces for p-type $Ga_{0.52}In_{0.48}P$ with 100Å $GaAs_{0.96}P_{0.04}$ compaired to freshly etched $Ga_{0.52}In_{0.48}P$. The epitaxially modified surfaces show shorter radiative lifetimes.

Figure 4 Simulation of the internal band structure of a $GaInP_2$/GaAs tandem cell with variable surface schottky barrier heights.

Figure 5 Tandem cell configuration for surface photovoltage measurement.

Figure 6 Transient surface photovoltage measurements at different illumination intensities.

Figure 7 Transient photoresponse of two tandem cells with different p-layer thicknesses. K430 has a p-$GaInP_2$ layer of 0.7 μm, K462 has a p-layer of 1.2 μm. The photocurrent now flows in the proper direction.

Figure 8 Tandem cell configuration for amorphorous silicon based water splitting system.

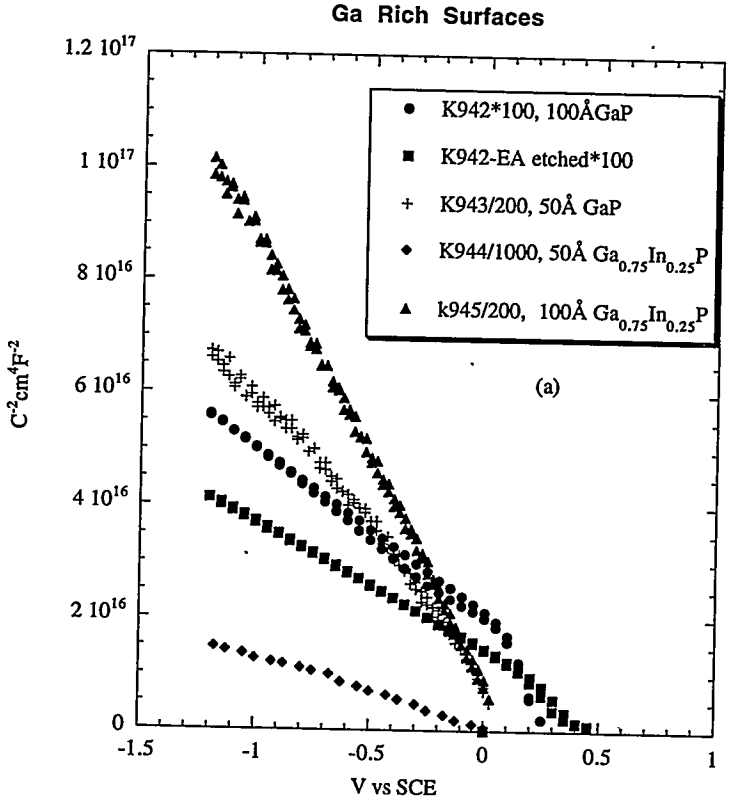
Ga Rich Surfaces
1.2 10^17
1 10^17
8 10^16
6 10^16
4 10^16
2 10^16
0
C^-2cm^4F^-2
-1.5
-1
-0.5
0
0.5
1
V vs SCE
K942*100, 100ÅGaP
K942-EA etched*100
K943/200, 50Å GaP
K944/1000, 50Å Ga0.75In0.25P
k945/200, 100Å Ga0.75In0.25P
(a)

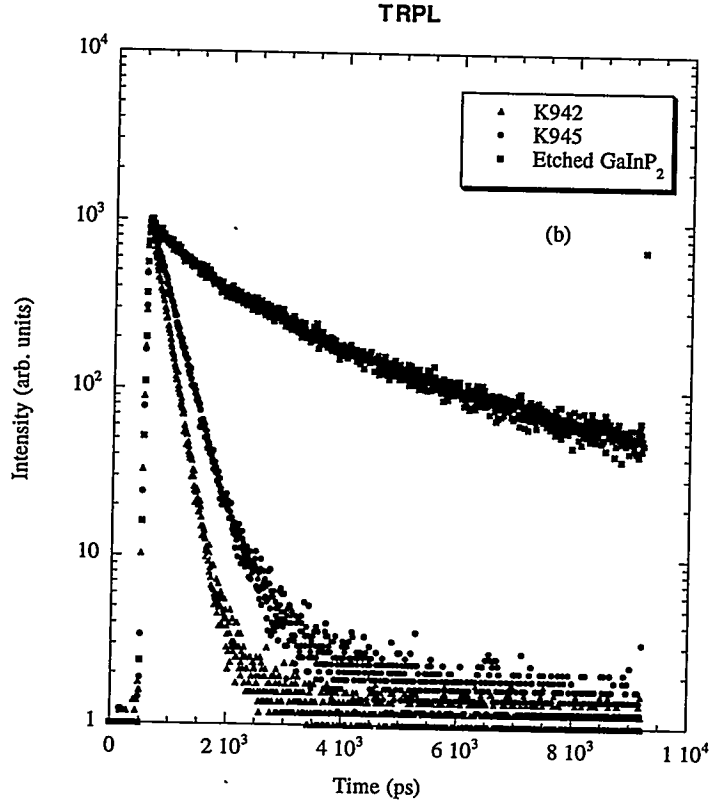
TRPL
10^4
10^3
10^2
10
1
Intensity (arb. units)
0
2 10^3
4 10^3
6 10^3
8 10^3
1 10^4
Time (ps)
K942
K945
Etched GaInP2
(b)

In Rich Surfaces

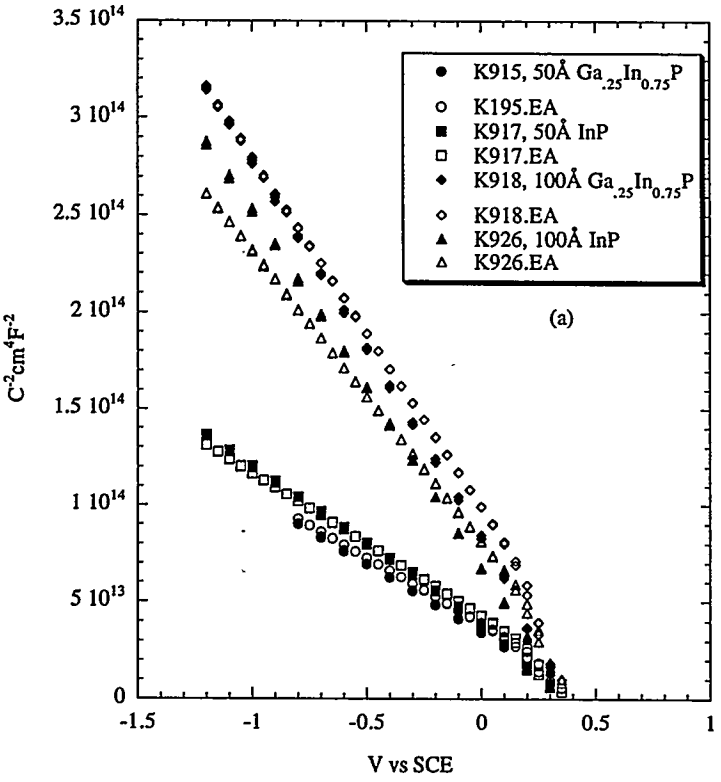

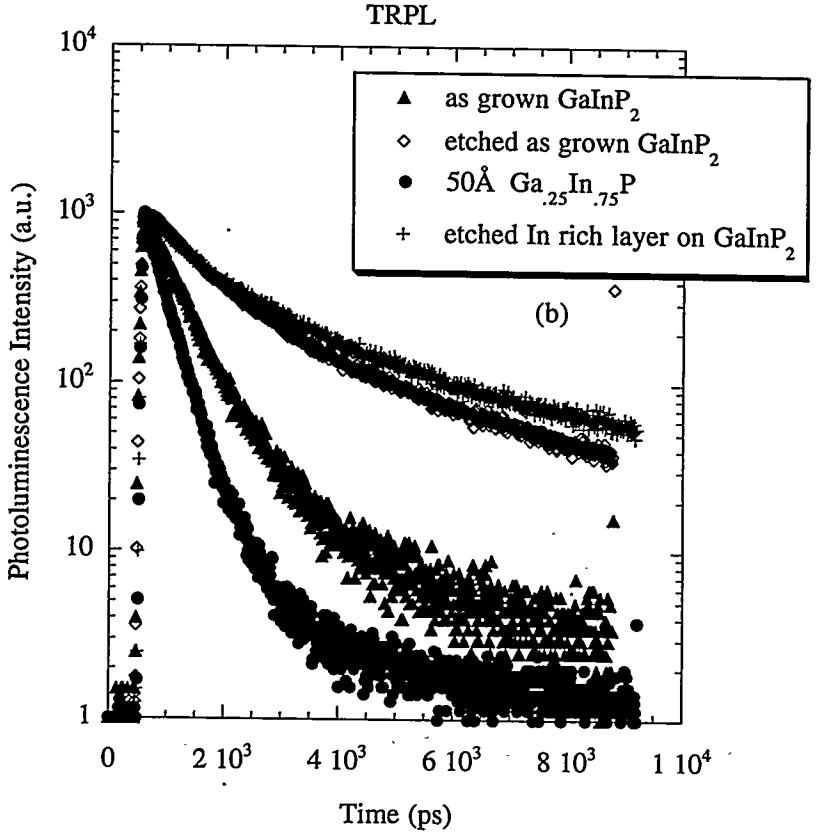

• Same for 100Å $Ga_{0.25}In_{0.75}P$, and 50, 100Å InP

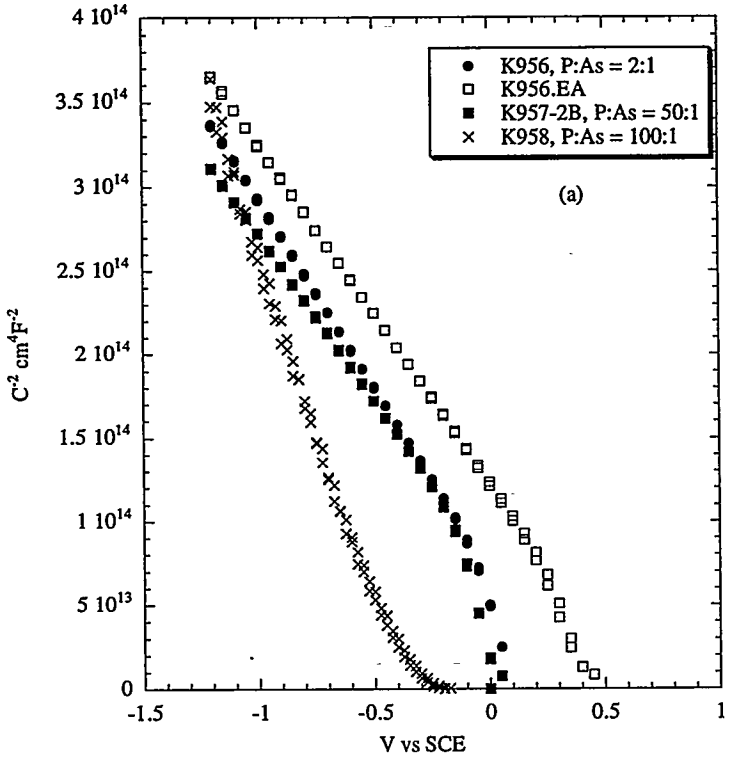
K956, P:As = 2:1
K956.EA
K957-2B, P:As = 50:1
K958, P:As = 100:1
(a)
C^{-2} cm^{4}F^{-2}
V vs SCE

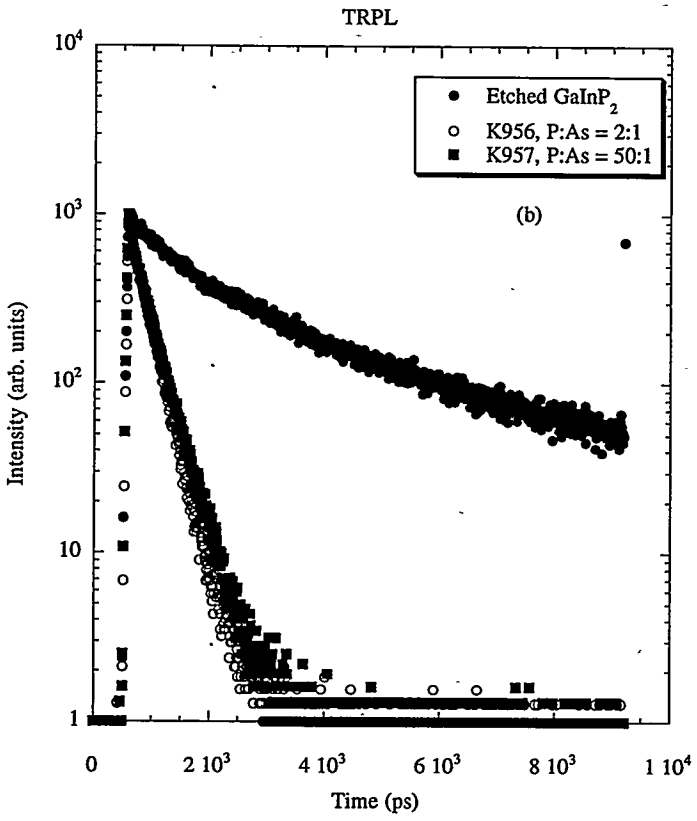
TRPL
Etched GaInP$_2$
K956, P:As = 2:1
K957, P:As = 50:1
(b)
Intensity (arb. units)
Time (ps)

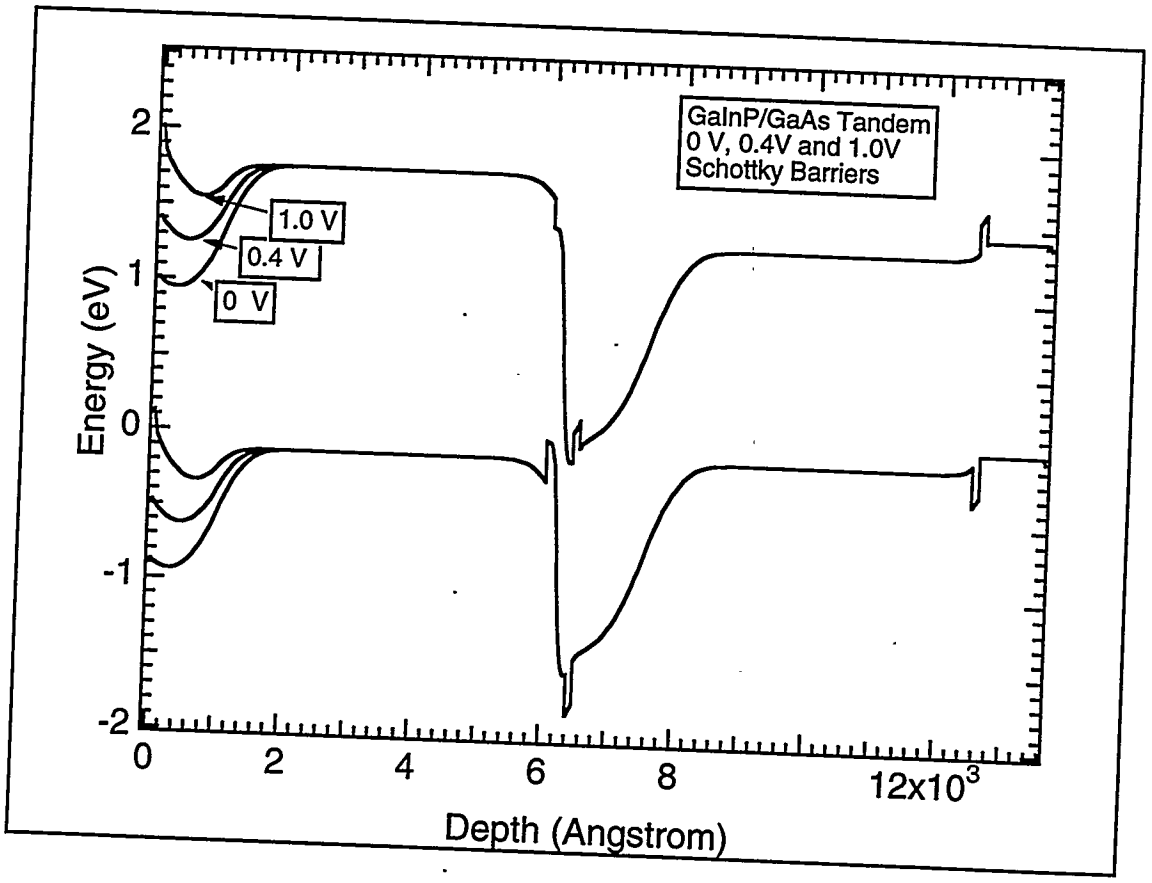
GaInP/GaAs Tandem
0 V, 0.4V and 1.0V
Schottky Barriers
1.0 V
0.4 V
0 V
Energy (eV)
2
1
0
-1
-2
0
2
4
6
8
12x10^3
Depth (Angstrom)

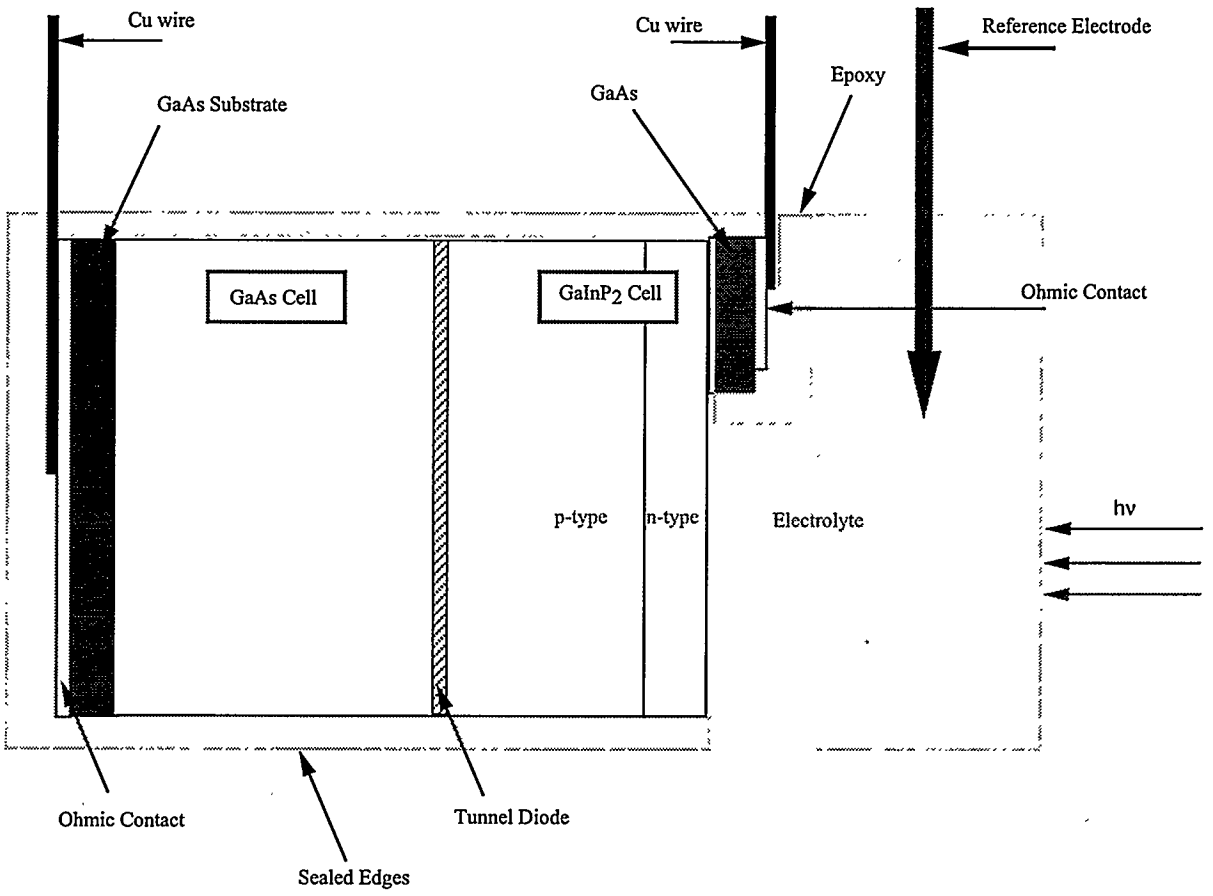

Tandem Cell Configuration for Surface Photovoltage Measurement

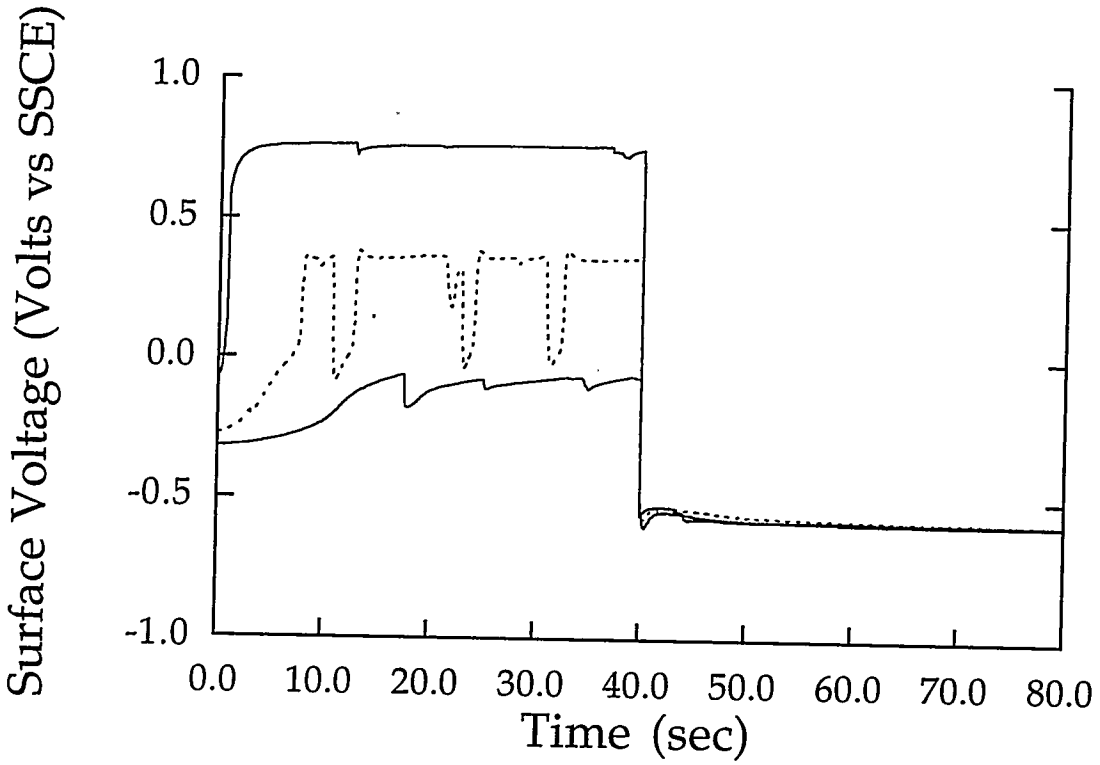
Surface Voltage (Volts vs SSCE)
1.0
0.5
0.0
-0.5
-1.0
0.0
10.0
20.0
30.0
40.0
50.0
60.0
70.0
80.0
Time (sec)

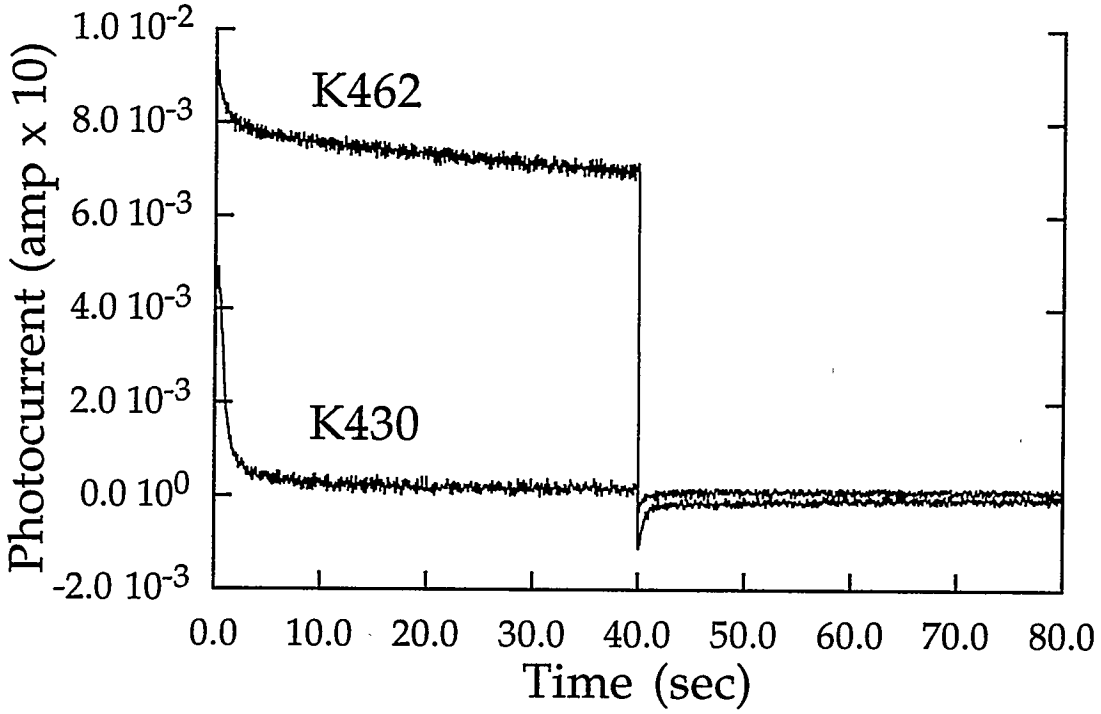
1.0 10-2
8.0 10-3
6.0 10-3
4.0 10-3
2.0 10-3
0.0 100
-2.0 10-3
Photocurrent (amp x 10)
K462
K430
0.0
10.0
20.0
30.0
40.0
50.0
60.0
70.0
80.0
Time (sec)

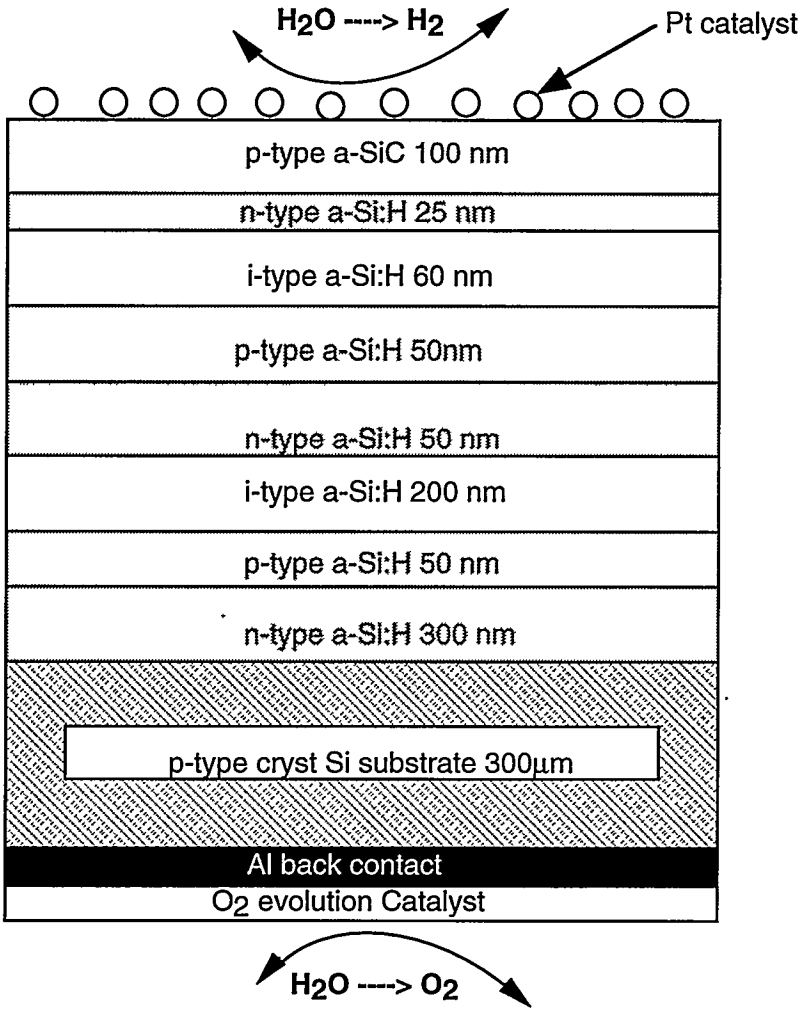

α-Si Triple Junction Cell for Photoelectrochemical Based Direct Conversion System

CARBON DIOXIDE FIXATION AND PHOTOEVOLUTION OF HYDROGEN AND OXYGEN IN A MUTANT OF *CHLAMYDOMONAS* LACKING PHOTOSYSTEM I

E. Greenbaum,[1] J. W. Lee,[1] C. V. Tevault,[1] S. L. Blankinship,[1] and L. J. Mets[2]

[1]Chemical Technology Division
Oak Ridge National Laboratory
Oak Ridge, TN 37831-6194

[2]Department of Molecular Genetics and Cell Biology
University of Chicago
1103 E. 57th Street
Chicago, IL 60637

ABSTRACT

Sustained photoassimilation of atmospheric CO_2 and simultaneous photoevolution of molecular hydrogen and oxygen has been observed in a Photosystem I deficient mutant B4 of *Chlamydomonas reinhardtii* that contains only Photosystem II. The data indicate that Photosystem II alone is capable of spanning the potential difference between water oxidation/oxygen evolution and ferredoxin reduction. The rates of both CO_2 fixation and hydrogen and oxygen evolution are similar in the mutant to that of the wild-type *C. reinhardtii* 137c containing both photosystems. The wild-type had stable photosynthetic activity, measured as CO_2 fixation, under both air and anaerobic conditions, while the mutant was stable only under anaerobic conditions. The results are discussed in terms of the fundamental mechanisms and energetics of photosynthesis and possible implications for the evolution of oxygenic photosynthesis.

INTRODUCTION

In the fundamental biological process of photosynthesis, atmospheric carbon dioxide is reduced to carbohydrate using water as the source of electrons with simultaneous evolution of molecular oxygen: $H_2O + CO_2 + \text{light} \rightarrow O_2 + (CH_2O)$ (Deisenhofer and Norris 1993). It is well established that two light reactions, Photosystems I and II (PSI and PSII) working in series, are required to perform oxygenic photosynthesis. Experimental data supporting the two-light reaction model are based on the quantum requirement for complete photosynthesis, spectroscopy, and direct biochemical analysis (Ley and Mauzerall 1982; Gaffron 1960; Clayton 1980; Warburg et al. 1950; Warburg and Burk 1950; Emerson 1958; Emerson and Lewis 1943; Hill and Bendall 1960; Duysens et al. 1961; Frank 1957; Latimer 1952; Greenbaum 1980; Hiyama 1985; Lee 1993). Some algae also have the capability to evolve molecular hydrogen in a reaction energized by the light reactions of photosynthesis. This process, now known as biophotolysis (Lien and San Pietro 1975), can use water as electron donor and lead to simultaneous evolution of molecular hydrogen and oxygen (Greenbaum 1980). In green algae, hydrogen evolution requires prior incubation under anaerobic conditions and atmospheric oxygen inhibits hydrogen evolution and also represses the synthesis of hydrogenase enzyme (Gaffron and Rubin 1942). CO_2 fixation competes with proton reduction for electrons released from the photosystems (Graves et al. 1989). Interest in biophotolysis arises from both the questions that it raises concerning photosynthesis and its potential practical application as a process for converting solar energy to a non-carbon-based fuel (Gaffron and Rubin 1942). Prior data supported the requirement for both Photosystem I and Photosystem II in spanning the energy gap necessary for biophotolysis of water to oxygen and hydrogen (Bishop et al. 1977; Greenbaum 1980). In this paper we report that PSII alone is capable of driving sustained simultaneous photoevolution of molecular hydrogen and oxygen in an anaerobically adapted PSI-deficient strain of *Chlamydomonas reinhardtii*, mutant B4, and that CO_2 competes as an electron acceptor. Light-dependent photoassimilation of CO_2 is sustained in the mutant at rates and quantum yields that are comparable to those of wild-type alga, both under anaerobic and initial aerobic conditions. Taken together, the results imply that these algae have efficient biochemical mechanisms for spanning the energy gap between oxygen evolution and H_2 evolution or CO_2 reduction with only PSII acting as a light trap.

MATERIALS AND METHODS

Mutant B4 of *Chlamydomonas reinhardtii*, deposited with the Duke University *Chlamydomonas* Genetics Center and available as Stock No. CC2933, was obtained following metronidazole enrichment described in detail elsewhere (Roitgrund and Mets 1990). Analysis of the algal cultures before and after our experiments indicated that this mutant had a chlorophyll fluorescence induction transient characteristic of PSI-deficient strains (Bennoun and Chua 1976) and lacked the reaction center core (CPI) complex in LDS electrophoresis at 4°C. P700 signals were undetectable as was the G = 2.007 EPR signal characteristic of PSI (Thurnauer and Zhang 1994). Genetic analysis indicated that the B4 mutation is carried in a nuclear gene and is unable to assemble the functional message for the psaA gene encoding one of the two major apoproteins of the PSI complex. This property has been described previously for several other nuclear gene mutants of *C. reinhardtii* that evidently encode components essential for the trans-splicing of this tripartite message (Choquet

1988). In the absence of the psaA message, the cells were unable to synthesize any PSI complexes. Experiments using Schott 730-nm cut-off filters discussed below (Fig. 1A and 1C) demonstrate the expected photoresponse for absence of PSI in mutant B4 and its presence in wild-type *Chlamydomonas*.

Figure 1A demonstrates simultaneous photoevolution of molecular hydrogen and oxygen from mutant B4 in an atmosphere of 363 ppm CO_2 in helium; Figure 1B contains data for the simultaneous photoevolution of hydrogen and oxygen in pure helium. Figures 1C and 1D contain corresponding data on simultaneous photoevolution of hydrogen and oxygen from the wild-type *Chlamydomonas* 137c. Mutant B4 was grown photoheterotrophically using minimal growth medium with acetate. The reaction itself was performed in minimal growth medium by successive washings to eliminate all soluble acetate. Data for mutant B4 and the control wild-type 137c were obtained simultaneously in a dual-photoreaction chamber flow system. To maintain anaerobiosis, even during photosynthetic oxygen production, the algal suspension was continuously purged with O_2-free carrier gas. Therefore, regular respiration or chloroplast respiration play no role in the experiments performed under anaerobiosis, either in helium or CO_2 in helium. The experimental technique for measuring the simultaneous photoevolution of oxygen and hydrogen has been previously described (Greenbaum 1984). Even though it totally lacks Photosystem I, sustained simultaneous photoevolution of hydrogen and oxygen was observed, demonstrating that a Photosystem II-driven reaction can span the potential difference between water oxidation/oxygen evolution and proton reduction/hydrogen evolution. The reversible equilibrium thermodynamic potential for these two reactions is 1.23 V. Of course, since the reactions do not occur reversibly at thermodynamic equilibrium, the actual potential must be higher, about 1.4-1.6 V (Bouges-Boquet 1980).

In Figs. 1A (mutant) and 1C (wild-type), with CO_2 present in the carrier gas, it can be seen that there is an initial surge of hydrogen which peaks and then declines to zero while the light is still on. This hydrogen photoevolution pattern for wild-type *Chlamydomonas* has been previously analyzed and reported (Graves et al. 1989). Briefly, when the algae have been dark-adapted, the Calvin-Benson cycle is shut off. Consequently, upon illumination all reducing equivalents are shunted through the ferredoxin/hydrogenase pathway. As the Calvin-Benson cycle is activated by light, it becomes the exclusive sink for reducing equivalents. The monotonic decrease in the rate of hydrogen production from its peak value represents the real-time activation of the CO_2 reduction cycle. When the light is turned off, thermally-activated hydrogen evolution is observed. This pattern repeats itself when the light is turned on again. The source of thermally-activated hydrogen is reduced carbon, identified by Klein and Betz as primarily starch, that has been stored during previous photosynthesis (Klein and Beta 1978). *C. reinhardtii* grows quite well in an anaerobic atmosphere consisting of CO_2 and helium (Graves et al. 1990). In a pure helium atmosphere, illustrated by the data of Figs. 1B and 1D, the hydrogen time profiles are qualitatively different. They climb monotonically to an approximate steady state production rate with the light turned on and return to zero when it is turned off. Since CO_2 is not present in this atmosphere, the Calvin cycle is not activated and does not serve as a sink for reducing equivalents. Oxygen activity is less in helium, presumably due to the absence of CO_2 and the Photosystem II bicarbonate requirement (Stemler and Govindjee 1973). Irradiation with $\lambda > 700$ nm light (which supports PSI but not PSII) in the wild-type alga (Fig. 1C insert) results in a low, but significant, rate of hydrogen evolution. For B4, (also shown in the Fig. 1C insert)

$\lambda > 700$-nm light naturally does not stimulate H_2 production; it actually suppressed residual dark hydrogen evolution.

Perhaps the most remarkable aspect of the data for mutant B4 for CO_2 in helium (Fig. 1A) is that the Calvin cycle is evidently activated in this system and serves as an electron sink. This is positively demonstrated by the data of Fig. 2 in which the photoassimilation of CO_2 by both mutant and wild-type as illustrated. It therefore follows that mutant B4 can perform complete oxygenic photosynthesis using a single Photosystem II reaction. As seen in Fig. 2A, CO_2 photoassimilation is stable for both mutant B4 and wild-type *Chlamydomonas* in an anaerobic atmosphere. However, only the wild-type alga, containing both Photosystems I and II, is stable in air. Within 24 hours, mutant B4 lost 90% of its photosynthetic activity. Figure 3 illustrates the postirradiated algae, cultures of wild-type and mutant B4 in air, with the latter completely bleached. Thus we conclude that PSI is required for oxygenic photosynthesis in aerobic environments (the normal condition in nature) but not under anaerobic conditions. Since the oxidant generated in Photosystem II must be more oxidizing than +0.8 V, it follows that a single Photosystem II reaction center has the thermodynamic potential to perform complete photosynthesis. Thus, although our findings are novel and unexpected, they do not violate known thermodynamic properties of the photosynthetic system.

A number of observations in the literature have possibly suggested that PSII alone could reduce ferredoxin and thus NADP. Working with *Chlamydomonas* ACC-1, a mutant that lacked Photosystem I, Klimov et al. (Klimov et al. 1986) observed the photoreduction of $NADP^+$. However, oxygen evolution was not demonstrated, and this was interpreted as a non-physiological reaction, an alternative electron pathway occurring only at high light intensities. Boychenko et al. (1986), utilizing a polarographic technique, were able to observe transient evolution of both hydrogen and oxygen from a mutant of *Chlamydomonas* that was deficient in PSI. Arnon and Barber (1990) reported the photoreduction of $NADP^+$ by isolated reaction centers of Photosystem II with 1,5-diphenylcarbazide as the electron source. However, the reaction centers of this work were not functional oxygen evolution preparations, possible PSI contamination was not excluded, and the key emphasis of the Arnon-Barber paper was the requirement for plastocyanin. More recently, Allakhverdiev and Klimov (1992) demonstrated the requirement of manganese for anaerobic photoreduction of $NADP^+$ by Photosystem II of higher plants. The primary electron acceptor of Photosystem II is pheophytin, which has an E_m of -0.61 V (Klimov et al. 1977; Klimov and Krasnovsky 1981; Klimov et al. 1979).

Irrespective of specific molecular mechanisms, our data clearly illustrate a new type of photosynthesis being performed by the Photosystem II light reaction. These experiments also have implications for the evolution and origin of water-splitting photosynthesis. Anoxic photosynthetic bacteria exhibit two different mechanisms characterized by either pheophytin-quinone or Fe-S type reaction centers. Blankenship (1992) proposed that "some sort of genetic fusion event took place between two bacteria" producing a chimeric organism. Subsequently, the two systems were linked, and the oxygen evolution system was added. However, no examples of the intermediate stages have been observed. Our data support an alternative hypothesis: a bacterium containing the pheophytin-quinone reaction center developed into the oxygen-evolving PSII type of photosynthesis, with

photosystem I being added later for survival when molecular oxygen became a major component of the earth's atmosphere. Data which support this theory are presented in Figs. 2A and 2B.

From a practical point of view, a single-light reaction implies that the maximum thermodynamic conversion efficiency of light energy into chemical energy, as represented by the Gibbs free energy of molecular hydrogen or reduced carbon, can be potentially doubled, from about 10% to 20% since a single photon rather than two is now required to span the potential difference between water oxidation/oxygen evolution and proton reduction/hydrogen evolution. This is obviously not the case for the data of Figs. 1 and 2 where, under identical conditions, B4 and wild-type have similar quantum efficiencies. However, further studies on algal mutants, with perhaps closer coupling to the reducing site of Photosystem II, may achieve the desired result of increased light conversion efficiency.

ACKNOWLEDGMENTS

The authors thank J. R. Benemann for critically reading the manuscript and making valuable comments, suggestions, and criticisms. We also thank M. Seibert, D. Tiede, J. Woodward, and M. E. Reeves for comments and suggestions on this work, and D. J. Weaver for secretarial support. We also thank E. Harris and the staff of the Duke University *Chlamydomonas* Genetics Center for providing the initial samples of Photosystem I-deficient *Chlamydomonas* mutants that were used for the initial experiments in this work. This work was supported by the U.S. Department of Energy, Pittsburgh Energy Technology Center, and the National Science Foundation. Oak Ridge National Laboratory is managed by Martin Marietta Energy Systems, Inc., for the U.S. Department of Energy under contract DE-AC05-84OR21400.

REFERENCES

Allakhverdiev, S. I., and V. V. Klimov. 1992. *Z. Naturforsch.*, 47c:57-62.

Arnon, D. K., and J. Barber. 1990. *Proc. Natl. Acad. Sci. USA*, 87:5930-5934.

Bennoun, P., and N.-H. Chua. 1976. In *Genetics and Biogenesis of Chloroplasts and Mitochondria*, 33-39.

Bishop, N. I., M. Fricke, and L. W. Jones. 1977. In *Biological Solar Energy Production*, 13-22. New York: Academic Press.

Blankenship, R. E. 1992. *Photosyn. Res.*, 33:91-111.

Bouges-Boquet, B. 1980. *Biochim. Biophys. Acta*, 594:85-103.

Boychenko, V. A., S. I. Allakhverdiev, V. G. Ladygin, and V. V. Klimov. 1986. *Doklady Akad. Nauk*, 995-998.

Clayton, R. K. 1980. *Photosynthesis: Physical Mechanism and Chemical Patterns.* Chapter 3. Cambridge: Cambridge Univ. Press.

Choquet, Y., M. Goldschmidt-Clermont, J. Girard-Bascou, U., Kok, P. Bennoun, and J.-D. Rochaix. 1988. *Cell*, 52:903-913.

Deisenhofer, J. and J. R. Norris (eds.) 1993. *The Photosynthetic Reaction Center*, Vols. I and II, San Diego: Academic Press.

Duysens, L. N. M., J. Amesz, and B. M. Kamp. 1961. *Nature*, 190:510-511.

Emerson, R. J., and C. M. Lewis. 1943. *Am. J. Bot.*, 30:165-178.

Emerson, R. 1958. *Ann. Rev. Plant Physiol.*, 9:1-24.

Franck, J. 1957. In *Research in Photosynthesis.* 142-146. New York: Interscience.

Gaffron, H., and Rubin, J. 1942. *J. Gen. Physiol.*, 26: 219-240.

Gaffron, H. 1960. In *Plant Physiology: A Treatise*, Vol. IB, 3-277. New York: Academic Press.

Graves, D. A., C. V. Tevault, and E. Greenbaum. 1989. *Photochem. Photobiol.*, 50:571-576.

Graves, D. A., G. M. Spradlin, and E. Greenbaum. 1990. *Photochem. Photobiol.* 51.

Greenbaum, E. 1980. *Biotechnol. Bioeng. Symp.*, 10:1-13.

Greenbaum, E. 1984. *Photobiochem. Photobiophys.*, 8:323.

It is comprised of a flow system using a Hersch electrogalvanic cell as the oxygen sensor and a tin-oxide semiconductor as the hydrogen sensor. Absolute calibration of both sensors was achieved with an in-line electrolysis and Faraday's Law of Electrochemical Equivalence. A Model 220 Keithley Instruments constant current source was used to electrolyze water to generate calibration steps of hydrogen and oxygen spanning the range of gases produced by the algae. Carbon dioxide photoassimilation was measured with a LiCor Model LI-6252 infrared CO_2 analyzer. For anaerobic CO_2 uptake experiments, the electrogalvanic oxygen analyzer could be placed in the flow stream to measure simultaneous O_2 evolution and CO_2 assimilation. The oxygen production rates (not shown in the data with this paper) were numerically equal to the CO_2 uptake. Using this system it was also demonstrated that respiration is not involved in any of the processes occurring under anaerobiosis. Control experiments in which steady levels of oxygen were titrated both up-and down-stream from the algal reactor chamber indicated that oxygen levels that were numerically equal to the rate of oxygen produced by the algae passed through the chamber without being respired by the algae. This is not surprising since the helium flow purge maintains the concentration of oxygen below 10 ppm at all stages of the experiment.

Hill, R., and F. Bendall. 1960. *Nature*, 186:136-137.

Hiyama, T. 1985. *Physiol. Veg.*, 23:605-610.

Klein, U., and A. Betz. 1978. *Plant Physiol.*, 61:953-956.

Klimov, V. V., A. V. Klevanik, V. A. Shuvalov, and A. A. Krasnovsky. 1977. *FEBS Lett.*, 82: 183-186.

Klimov, V. V., S. I. Allakhverdiev, S. Demeter, and A. A. Krasnovsky. 1979. *Dokl. Akad. Nauk SSSR*, 249:227-230.

Klimov, V. V., and A. A. Krasnovsky. 1981. *Photosynthetica*, 15:592-609.

Klimov, V. V., S. I. Allakhverdiev, and V. G. Ladygin. 1986. *Photosyn. Res.*, 10:355-361.

Latimer, W. M. 1952. *The Oxidation States of the Elements and Their Potentials in Aqueous Solutions*, 2nd Edition. 29-50. New York: Prentice-Hall.

Lee, J. W. 1993. Ph.D. Dissertation, Cornell University, p. 131.

Ley, A. C. and D. C. Mauzerall. 1982. *Biochem. Biophys. Acta*, 680: 95-106.

Lien, S., and A. San Pietro. 1975. *An Inquiry into Biophotolysis of Water to Produce Hydrogen*, NSF RANN GI 40253.

Roitgrund, C., and L. Mets. 1990. *Curr. Genet.*, 17:147-153.

Stemler, A., and Govindjee. 1973. *Plant Physiol.*, 52:119-123.

Thurnauer, M., and D. Zhang. 1994. Personal communication.

Warburg, O., and D. Burk. 1950. *Arch. Biochem. Biophys.*, 25:410-443.

Warburg, O., D. Burk, V. Schocken, and S. B. Hendricks. 1950. *Biochim. Biophys. Acta*, 4:335-346.

FIGURE LEGENDS

Fig. 1 Simultaneous photoevolution of molecular hydrogen and oxygen by *Chlamydomonas* mutant B4 and wild-type *Chlamydomonas* 137c. (A) mutant B4, 363 ppm CO_2 in helium; (B) mutant B4, helium; (C) wild-type, 363 ppm CO_2 in helium; (D) wild-type, helium. As indicated in Figs. 1A and 1C, irradiation with light of wavelength $\lambda > 700$ nm generated Photosystem I-dependent hydrogen evolution in 137c, whereas no such hydrogen evolution was observed in mutant B4. In B4 thermally-activated hydrogen production was slightly suppressed with far-red light, whereas PSI-dependent hydrogen production was observed with wild-type 137c. As also indicated in Figs. 1A and 1C, the peak and decline of hydrogen evolution while the light is still on represents the real-time activation of the Calvin-Benson cycle following a period of darkness. The chlorophyll concentration for the experiments of Figs. 1A and 1C was 15 µg/ml; for Figs. 1B and 1D it was 3 µg/ml. The simultaneous photoevolution of hydrogen and oxygen was measured in a tandem flow system containing a tin-oxide gas-sensitive semiconductor for the hydrogen measurement and a Hersch electrogalvanic cell for the oxygen measurement. Absolute calibration of both sensors was achieved using an in-line electrolysis cell, a constant current source, and Faraday's Law of Electrochemical Equivalence.

Fig. 2 A comparative study of photosynthesis between mutant B4 and wild-type 137c in anaerobic and aerobic atmospheres. (A) 363 ppm CO_2 in helium; (B) 363 ppm CO_2 in air. The loss of photosynthetic activity by mutant B4 indicated in Fig. 2B was accompanied by a bleaching of its chlorophyll. See Fig. 3 for a visual comparison. Continuous measurement of CO_2 was achieved with an in-line infra-red spectrophotometer. The CO_2 detector was calibrated using an electronic gas blender with primary standard gas mixtures of CO_2 in helium.

Fig. 3 Photograph of postirradiated algae in air with 500 W/m^2 white light. Left: wild-type *Chlamydomonas* 137c; Right: *Chlamydomonas* mutant B4. Whereas the initial chlorophyll concentration of each sample was the same at the start of the experiment, the final concentration of the wild-type alga increased following irradiation while B4's chlorophyll diminished. The algae were illuminated for 23 hours at 20°C. The algal chamber on the right containing the bleached sample of B4 appears larger in diameter due to the lens effect of the water jacket surrounding both identical chambers.

ORNL DWG 94A-605R

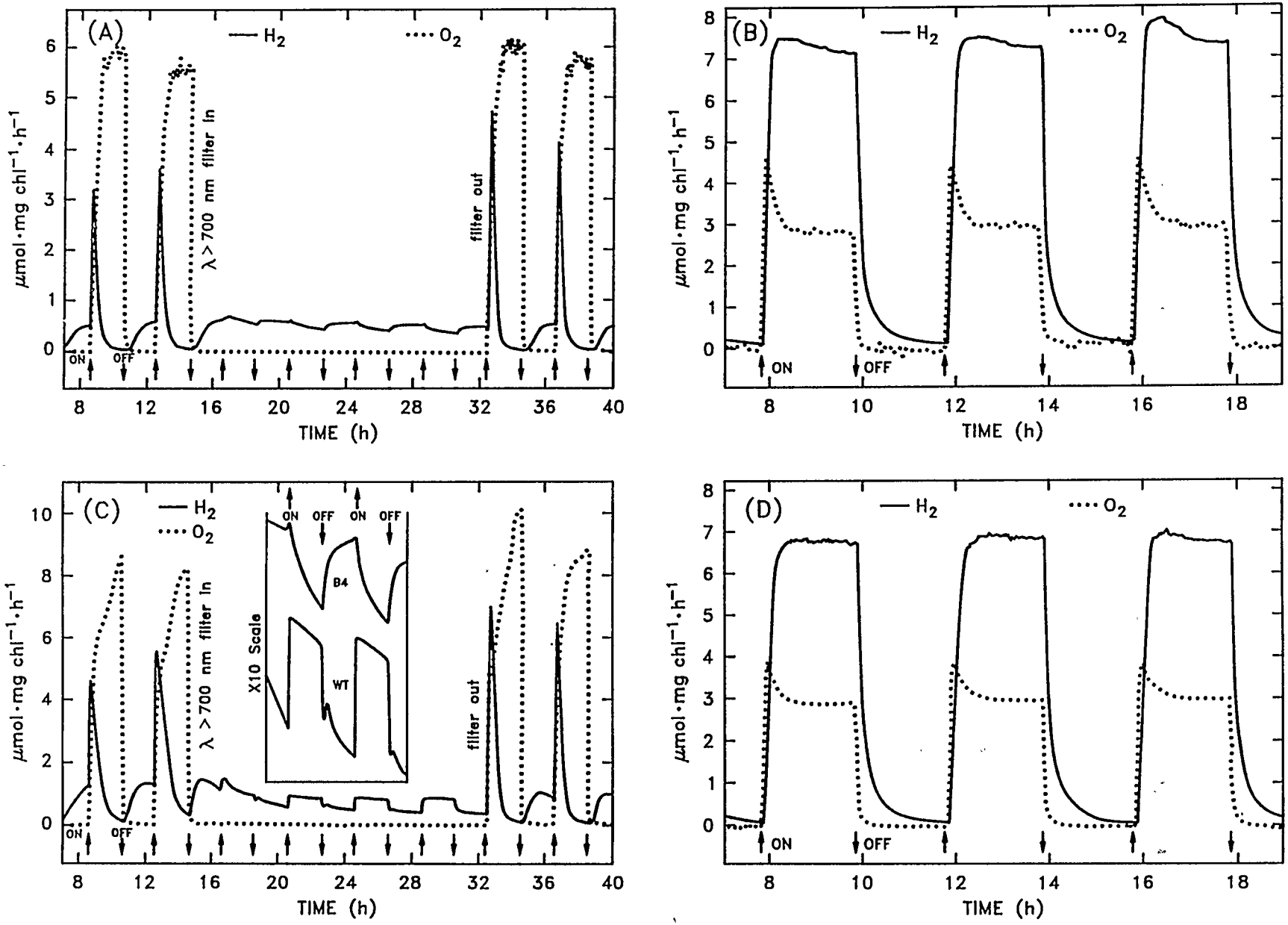

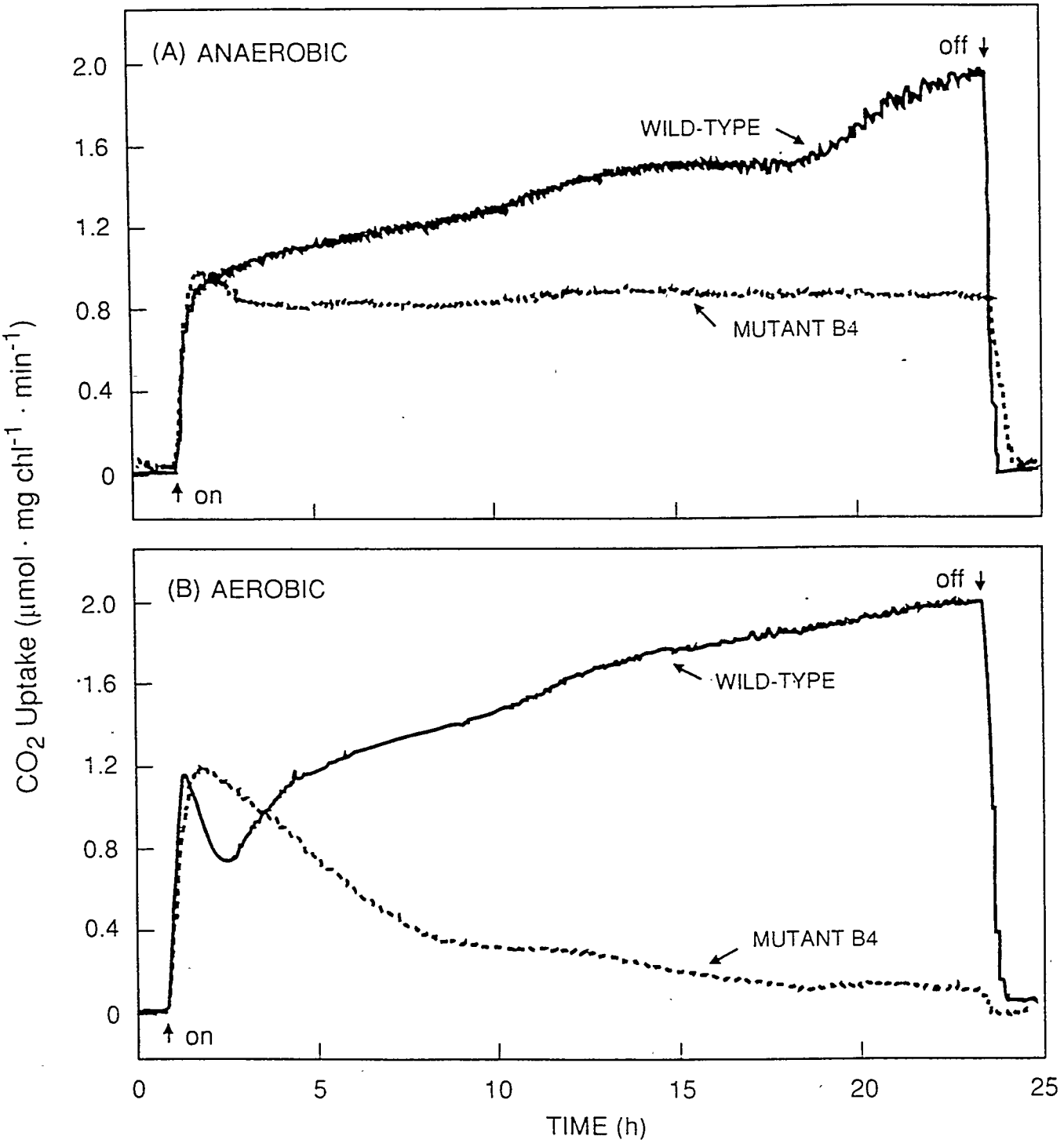

FIG. 2

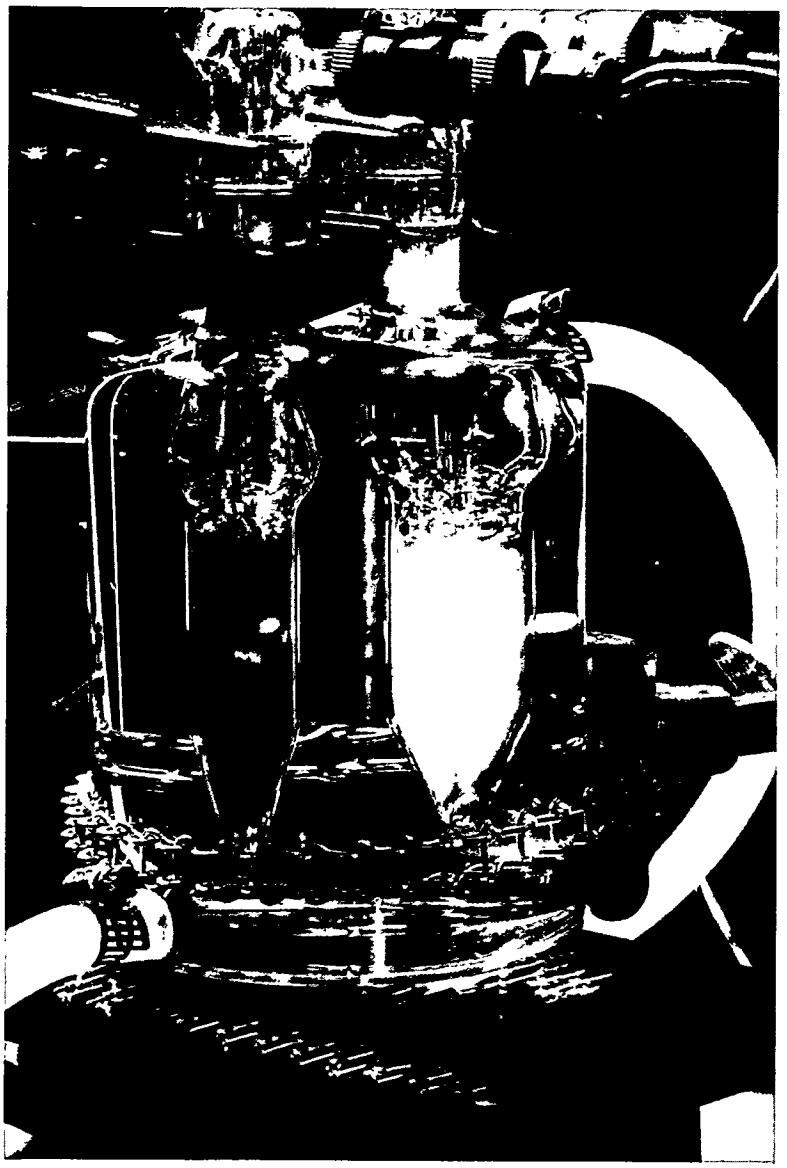

PHOTOELECTROCHEMICAL HYDROGEN PRODUCTION

Richard E. Rocheleau, Eric Miller, and Zhe Zhang
Hawaii Natural Energy Institute
School of Ocean and Earth Science and Technology
University of Hawaii
Honolulu, HI 96822

Abstract

The large-scale production of hydrogen utilizing energy provided by a renewable source to split water is one of the most ambitious long-term goals of the U.S. Department of Energy's Hydrogen Program. Photoelectrochemical devices—direct photoconversion systems utilizing a photovoltaic-type structure coated with water-splitting catalysts—represent a promising option to meet this goal. Direct solar-to-chemical conversion efficiencies greater than 7% and photoelectrode lifetimes of up to 30 hours in 1 molar KOH have been demonstrated in our laboratory using low-cost, amorphous-silicon-based photoelectrodes. Loss analysis models indicate that the DOE's goal of 10% solar-to-chemical conversion can be met with amorphous-silicon-based structures optimized for hydrogen production. In this report, we describe recent progress in the development of thin-film catalytic/protective coatings, improvements in photoelectrode efficiency and stability, and designs for higher efficiency and greater stability.

Introduction

The Department of Energy's goal for the direct production of hydrogen from renewable resources is likely to be met using photoelectrochemical hydrogen production systems, with water as the feedstock and sunlight as the energy source . The feasibility of producing hydrogen in such systems, based on a light-absorbing semiconductor or photovoltaic device coated with water-splitting catalysts, has been demonstrated in several laboratories, including ours. The DOE's goal requires additional improvements in efficiency, lower materials costs, and development of a prototype system capable

of sustained operation. The past several years have seen steady progress in each of these areas.

The goal of this work is to demonstrate sustained operation of a direct photoelectrolysis system which splits water into H_2 and O_2 with sunlight as the only energy source. Specific objectives include: (1) identification of optimal system and photoelectrode designs, (2) development of stable electrode/electrolyte interfaces, and (3) demonstration of high-efficiency photoelectrodes. We anticipate development of a small area modular system capable of sustained operation under moderate solar concentration within two years.

In this report, we describe the development of sputter-deposited, thin-film metal oxide and intermetallic catalysts for the oxygen and hydrogen evolutions reactions, respectively, and progress in the development of high-efficiency, amorphous silicon photoelectrodes. Research needs and plans for the future are also discussed.

Background

The search for high-efficiency processes for the photoelectrochemical (PEC) production of hydrogen from water increased dramatically following reports that n-TiO_2 photoanodes could provide a significant fraction of the energy needed to split water (Fujishima and Honda 1972). The "classic" photoelectrochemical cell utilizes a semiconductor in contact with an electrolyte to generate an electric field. The semiconductor is often treated with catalytic coatings to reduce over-voltages and provide some protection against corrosion. Although high solar conversion efficiencies were demonstrated in the early stages with reversible redox couples (e.g., Heller et al. 1981; Rosenbluth and Lewis 1986), progress in the development of an efficient system for direct hydrogen production from an aqueous electrolyte was hampered by the high voltage required to dissociate water and the corrosive nature of the aqueous electrolytes. The only photon processes demonstrated to split water without external bias have employed very wide bandgap materials such as $SrTiO_3$ and KTaQ (Wrighton et al. 1977; Kraeutler and Bard 1978). Unfortunately, these materials utilize only the UV part of the solar spectrum, resulting in very low solar-to-chemical efficiencies.

The lack of progress in resolving these issues has led to a new approach: the use of solid state multijunction devices which can deliver the required voltage while accessing a large fraction of the solar spectrum. Because the electrical field in such systems is generated by junctions within the solid state rather than at the solid-electrolyte interface, there is greater flexibility in the photoelectrode design and a wider choice of semiconductor materials and protective coatings that may be used. In recent years, direct hydrogen production has been demonstrated using multijunction amorphous-silicon-based photoelectrodes (Lin et al. 1989; Matsumura et al. 1986; Rocheleau et al. 1994), hybrid crystalline-amorphous silicon systems (Sakai et al. 1988), and crystalline III-V multijunction devices (Koch et al. 1994).

During the past year, we have demonstrated solar-to-hydrogen conversion efficiencies (LHV of H_2 produced/incident sunlight) greater than 7% under 1-sun illumination, greater then 6% under 3 suns, and stabilized efficiencies over 5% for 30 hours using photoelectrodes fabricated from multijunction

amorphous silicon solar cells provided by the Solarex Thin Film Division. Analyses of losses and systems performance indicate the potential for significantly higher efficiencies and longer lifetimes.

Scope/Technical Approach

Loss analyses based on widely accepted models for photovoltaic cells have been combined with models of the electrolysis reactions to determine the hydrogen production potential (efficiency) of a variety of single and multiphoton systems using semiconductor materials ranging from low-cost amorphous silicon to the high-cost, high-performance crystalline III-V materials. We have concluded that multijunction amorphous silicon and amorphous silicon/crystalline silicon hybrid devices have the greatest potential for achieving direct solar-to-hydrogen production efficiencies above 10%, while meeting the requirement of reasonable cost. Research efforts are focused on solving the critical materials issues required for stable performance of the high-efficiency amorphous silicon photoelectrodes. Research activities include synthesis of thin film catalytic coatings, special semiconductor/catalyst test structures, and photoelectrodes. Materials and photoelectrodes are performance-tested using potentiodynamic and potentiostatic measurements. Surface analysis techniques are used to examine chemical and structural characteristics of the materials, identify failure modes, and identify new materials options. All semiconductor systems considered for use in photoelectrode fabrications are commercially available or determined to be compatible with the manufacturing processes currently under development by the photovoltaics industry.

Results

Loss Analysis

Our focus on multijunction amorphous silicon structures was argued in a paper presented at the Tenth World Hydrogen Energy Conference (Rocheleau et al. 1994). A significant result of this analysis was that single-junction photoelectrodes which require semiconductor bandgaps equal or greater than approximately 2.0 eV to generate the required operating voltage (1.5 to 1.7 volts) are limited by their absorption spectra, yielding maximum hydrogen production rates which are only about half that of the highest performance multiphoton devices. While photoelectrodes based on high cost III-V multijunction devices are predicted to perform best, tandem- or triple-junction amorphous silicon with high-quality, thin-film catalysts are expected to produce hydrogen at up to 50% of the maximum hydrogen production rate of the III-Vs at much lower cost, while crystalline/a-Si hybrid cells could achieve as much as 75% of the maximum. Based on these preliminary performance models, expected low cost, and commercial availability, a detailed phenomenological model for the a-Si devices, which accounts for real performance losses due to optical and carrier transport limitations, has been developed (Rocheleau and Vierthaler 1994) for design of optimal a-Si:H photoelectrodes.

Catalyst Development

The development of high-activity, thin-film catalysts for both oxygen- and hydrogen-producing

reactions optimized specifically for application to our amorphous silicon photoelectrodes has been identified as a critical materials need. Last year, we reported the development of electrodeposited NiO_x thin-film catalysts alloyed with a variety of transitions and rare-earth metals which exhibited very low overpotentials and reasonable stability in 1N KOH, our standard test electrolyte.

Efforts during the past year have focused on development of magnetron-sputtering deposition processes for synthesis of these doped metal-oxides with similarly low overpotentials for application as anodic catalysts and Group VI-VIII intermetallics as cathodic catalysts. The sputtering facilities and procedures have been described in detail in earlier reports. Figures 1 and 2 show the potentiodynamic scans and optical properties of NiO_x films from a Ni target in a 20% O_2/argon mixture. Oxygen overpotentials of the best sputtered NiO_x films are nearly identical to those reported for electrochemically deposited films of the same composition but exhibit significantly better uniformity, adherence, and stability in the KOH. SEM micrographs show an apparently amorphous structure (a-NiO_x) at 30,000X magnification for the films deposited with background pressures below 3 mTorr, while clearly defined well-faceted submicron structures are visible in the films deposited at pressures greater than 4 mTorr (mcr-NiO_x). As shown in Figures 1 and 2, there was a trade-off between transparency and catalytic activity consistent with the observed changes in morphology. Both types of films exhibit good stability in the 1N KOH electrolyte during extended potentiostatic testing. Current work is directed toward decreasing the overpotentials of the sputtered films even further by the addition of the transition and rare-earth metal impurities used so successfully in the electrodeposited samples.

Two different a-Si multijunction cell configurations are produced commercially, one utilizing a glass substrate coated with a transparent conducting oxide (TCO) by the Solarex Thin Film Division (glass/TCO/pin-pin-pin) in which light enters through the glass, and one utilizing an opaque stainless steel substrate by ECD (SS/nip-nip-nip/CTO), in which light enters through a top coating of conductive oxide. In both structures, the incident light enters through the p-layer, a requirement for high carrier collection efficiency imposed by the transport properties of the amorphous silicon. The cathodic (hydrogen) catalyst which is deposited on the n-side of the devices must be stable and exhibit low overpotentials but is not required to be transparent. Last year, electrodeposited Co-Mo films with very low overpotentials were reported. Figure 3 shows the potentiodynamic scans of a number of recently synthesized sputtered Co-Mo films, the best of which exhibit overpotentials comparable to the best electrodeposited films. As was the case for our NiO_x, the sputtered Co-Mo films exhibit superior uniformity, adherence, and stability compared to the electrodeposited samples.

Practical systems using the SS/nip-nip-nip/CTO cells require overcoating of the p-layer or the CTO with a chemically stable, highly transparent, high-activity catalyst. While progress has been made in the development of a transparent NiO_x (Figures 1 and 2), further increases in activity and stability of the p-silicon/catalyst interface in alkaline electrolytes are required to achieve the sustained operation required for success. Amorphous SiC:H films are being grown in our Plasma Enhanced Chemical Vapor Deposition system using silane, methane, diborane, and hydrogen mixtures to allow complete electrochemical characterization of the a-SiC:H/catalyst interface. Carbon content, bandgap, and electrical properties of the a-SiC:H can be modified by changing the gas mix and process parameters. The a-SiC:H films have exhibited excellent corrosion resistance in both acidic and alkaline electrolytes

in our initial stability tests. The ability to deposit pinhole-free films will be critical as pinholes can lead to corrosion of the underlying unalloyed silicon films.

Amorphous Silicon Photoelectrodes

Photoelectrodes have been fabricated from high-efficiency, triple-junction, amorphous silicon solar cells provided by the Solarex Thin Film Division and ECD. The Solarex glass/CTO/pin-pin-pin cells were approximately 10.3% efficient in the solid state under 1 sun conditions with an open-circuit voltage of 2.4V, a short-circuit current of 6.1 mA/cm^2, and fill factor of 70. The test cells were provided as an array of 16 square devices, each 0.27 cm^2 in area. Photoelectrodes were fabricated from individual cells cut from the array with a border of several mm allowing access to the underlying CTO. The cathodic (exposed) surface was protected with a thin Ni foil catalyzed with approximately one micron of sputter-deposited Co-Mo. An electrical lead was attached to the CTO for connection to an independent anodic counterelectrode and saturated calomel reference electrode for half-cell characterization. The counterelectrode consisted of a thin Ni foil with sputter-deposited μcr-NiO_x catalyst. The edges of the photoelectrode were encapsulated in epoxy to prevent shorts to the electrolyte.

The photoelectrode performance in 1N KOH was characterized using a standard three-terminal apparatus previously described (HNEI 1991, 1992). This set-up includes a Keithley Model 236 source-measurement unit interfaced to a Macintosh LC computer running Labview software. Data were acquired every 20 to 50 mV at a rate of 2 seconds per step. Evolved hydrogen and oxygen were collected in inverted funnels attached to calibrated burettes. Following the dynamic characterization, current and gas evolution rates were measured continuously for up to 30 hours without external bias at both 1- and 3-sun illumination intensities.

Figure 4 shows the current density at different bias conditions under 1- and 3-sun illumination. The current density at 1 sun with no external bias is consistent with the short circuit current density of the solid-state cell, indicating that we are operating in the flat portion of the solid-state J-V curve. The current density scaled linearly with illumination as expected. The slightly greater slope at reverse bias for the 3-sun curve may be indicative of some additional shunting effects at the higher current density.

Figure 5 shows the current density with no external bias conditions as a function of time. There was no observable degradation during the first 5 hours. The current decreased approximately 20% between hours 5 and 15, remaining relatively constant at the lower value until 30 hours, at which time there was a fairly sudden failure of the system. Examination of the device indicated failure of the epoxy used to isolate the device from the electrolyte. Work has been initiated to develop photoelectrode designs which will not be subject to this mode of failure, such as the use of Teflon seals.

Figure 6 shows the calculated hydrogen evolution based on the current density shown in Figure 5 and the total volumes of gas collected above the cathode (hydrogen) and anode(oxygen). The agreement between the calculated and measured hydrogen evolution is considered to be within the accuracy of

our present gas collection system. The volume of oxygen collected is only 40% that of hydrogen (50% is expected). The difference is attributed to difficulty collecting all of the very small oxygen bubbles and possible dissolution of oxygen into the solution, although these effects require independent confirmation.

Summary and Plans

Demonstration of direct hydrogen production with a solar-to-chemical conversion efficiency greater than 5% for over 30 hours at 3 suns illumination is a very positive result. We will initiate efforts to build a prototype system capable of sustained operation. Our newly developed phenomenological model of amorphous silicon cell behavior will be used to assess optimal cell designs focusing on tandem designs which have the potential for even higher hydrogen production rates.

Further optimization of the catalytic coatings with improved transparency and affording greater protection to the underlying semiconductor will be necessary for sustained operation of the SS/pin-pin-pin-based structures available from ECD. Full characterization of the electrochemical behavior of the a-SiC:H/catalyst interfaces will be conducted. It is our intent to continue our collaborations with our industrial partners.

Acknowledgments

We wish to thank the National Renewable Energy Laboratory for its support of this project under Subcontract XAR-3-13514-01 and the U.S. Department of Energy under Grant DE-FG04-94AL85804. We also wish to thank Dr. Liu Yang and Dr. Robert Oswald of the Solarex Thin Film Division and Dr. Xunming Deng of Energy Conversion Devices for the amorphous silicon samples used in this work.

References

Fujishima, A., and K. Honda. 1972. *Nature*, 238:37.

Kocha, S., M. Peterson, H. HJilal, D. Arent, and J. Turner. 1994. *Proceedings of the 1994 U.S. Department of Energy/National Renewable Energy Laboratory Hydrogen Program Review*, 301. Livermore, CA: U.S. Department of Energy and National Renewable Energy Laboratory.

Kraeutler, B. and A.J. Bard. 1978. *Journal of the American Chemical Society*, 100:4317.

Lin, G.H., M. Kapur, R.C. Kainthla, and J. O'M. Bockris. 1989. *Applied Physics Letter*, 55(4):386.

Matsumura, A.J., Y. Sakai, S. Sugahara, Y. Nakato, and H. Tsubomura. 1986. *Solar Energy*

Materials, 12:57.

Rocheleau, R.E. , Z. Zhang, E. Miller, and Q. Gao. 1994. *Proceedings of the 1994 U.S. Department of Energy/National Renewable Energy Laboratory Hydrogen Program Review*, 335. Livermore, CA: U.S. Department of Energy and National Renewable Energy Laboratory.

Rocheleau, R.E., Z. Zhang, E. Miller, and M. Vierthaler. 1994. "Photoelectrochemical Production of Hydrogen: Engineering Loss Analysis." *Hydrogen Energy Progress X*, 2:737-746, D.L. Block and T. Veziroglu (eds.) Pergammon Press.

Rocheleau, R.E., and M. Vierthaler. 1994. "Optimization of Multijunction a-Si:H Solar Cells Using an Integrated Optical/Electrical Model." *Proceedings of the 21st World Conference on Photovoltaic Energy Conversion* (in press). New York: IEEE.

Rosenbluth, M., and N.S. Lewis. 1986. *Journal of the American Chemical Society*, 108:4689.

Sakai, Y., S. Sugahara, M. Matsumura, Y. Nakato, and H. Tsubomura. 1988. *Canadian Journal of Chemistry*, 66:1853.

Wrighton, M.S., P.T. Wolczanski, and A.B. Ellis. 1977. *Journal of Solid State Chemistry*, 22:17.

Figures

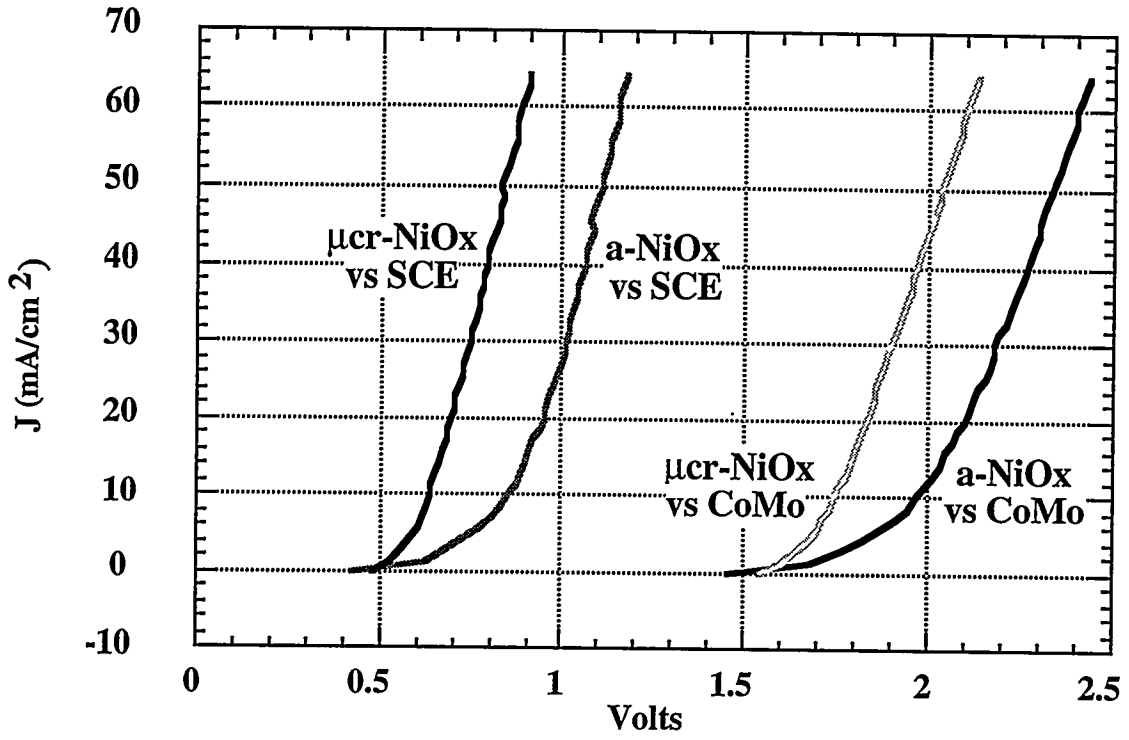

Figure 1. Half-Cell and System Current Voltage Behavior for Amorphous (a-NiO_x) and Microcrystalline (µcr-NiO_x) Sputter-Deposited Nickel Oxide Thin-Film Catalysts.

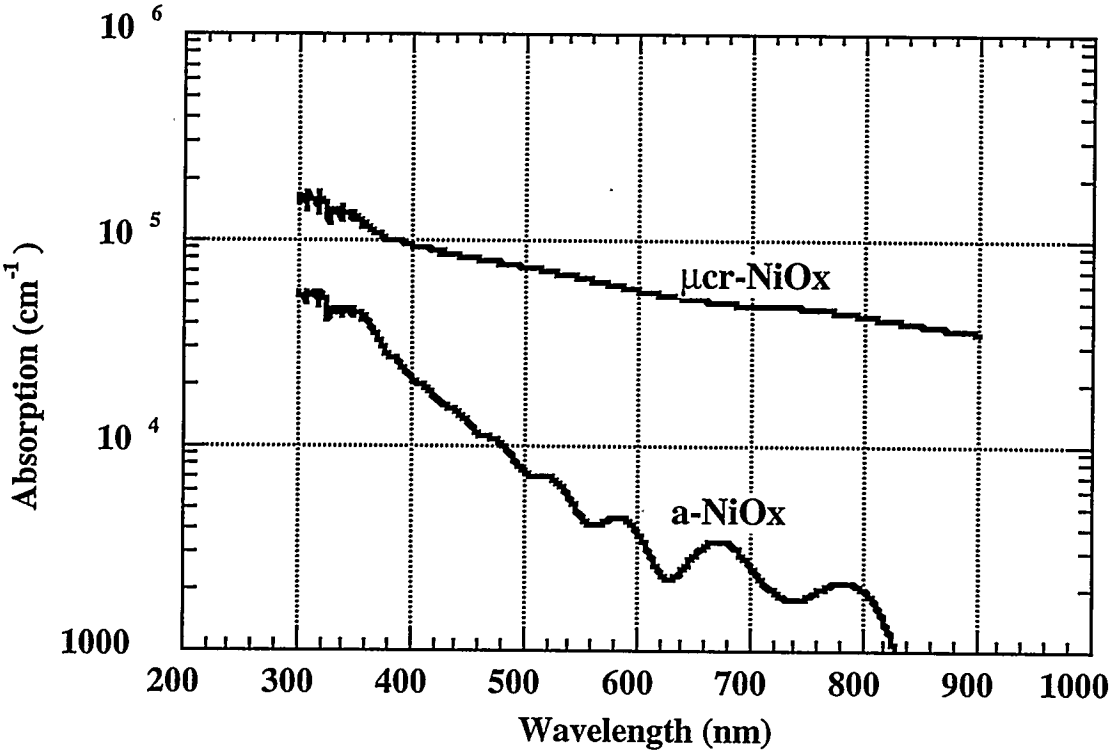

Figure 2. Absorption Coefficient of Amorphous (a-NiO_x) and Microcrystalline (µcr-NiO_x) Sputter-Deposited Nickel Oxide Thin-Film Catalysts.

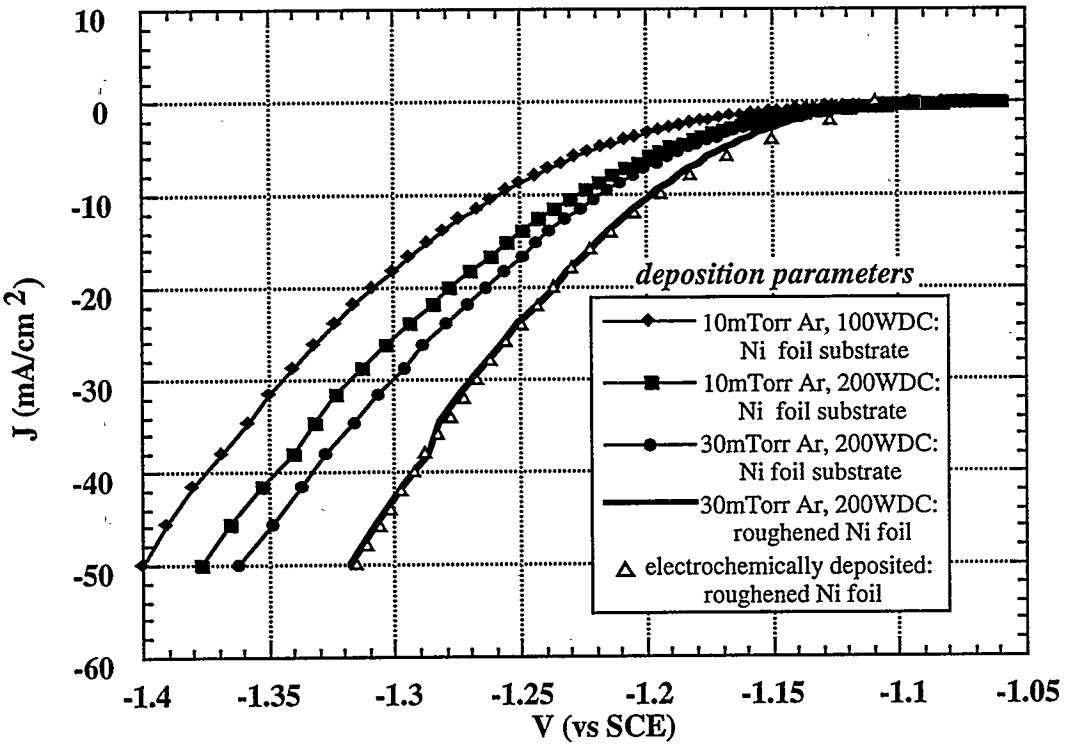

Figure 3. Half-Cell Current-Voltage Behavior of Sputter-Deposited and Electrochemically-Deposited Co-Mo Thin-Film Catalysts.

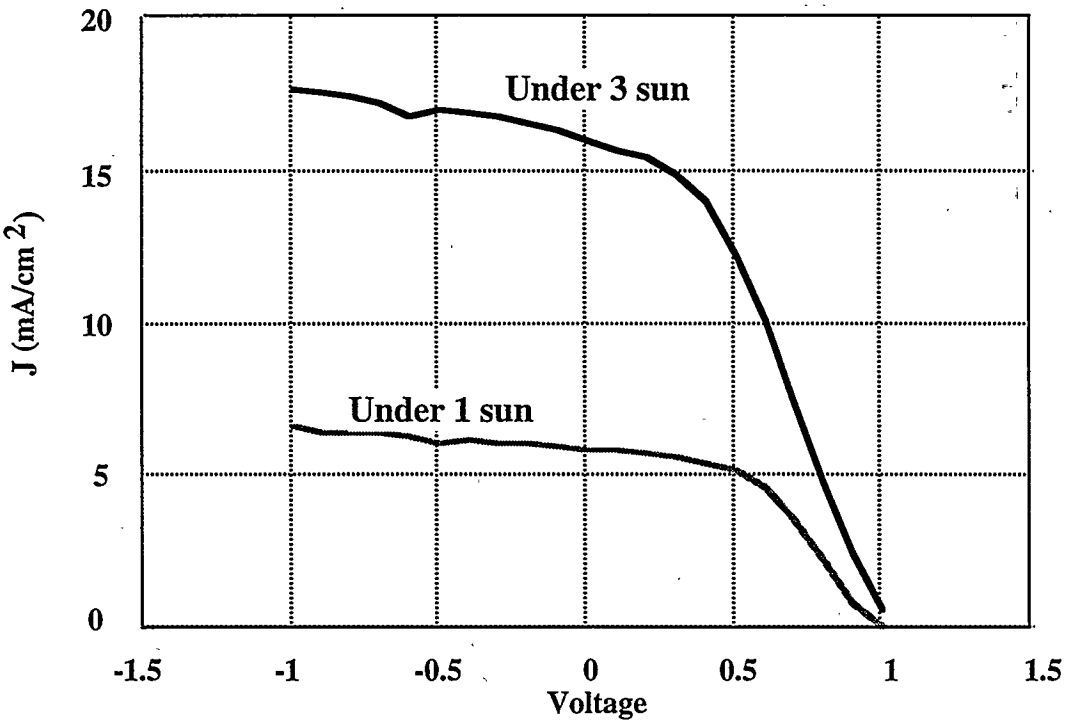

Figure 4. Current-Voltage Behavior of a Glass/CTO/Pin-Pin-Pin Photoelectrode at 1- and 3- Sun Illumination in 1N KOH (Sputtered NiO_x Anode, Sputtered Co-Mo Cathode).

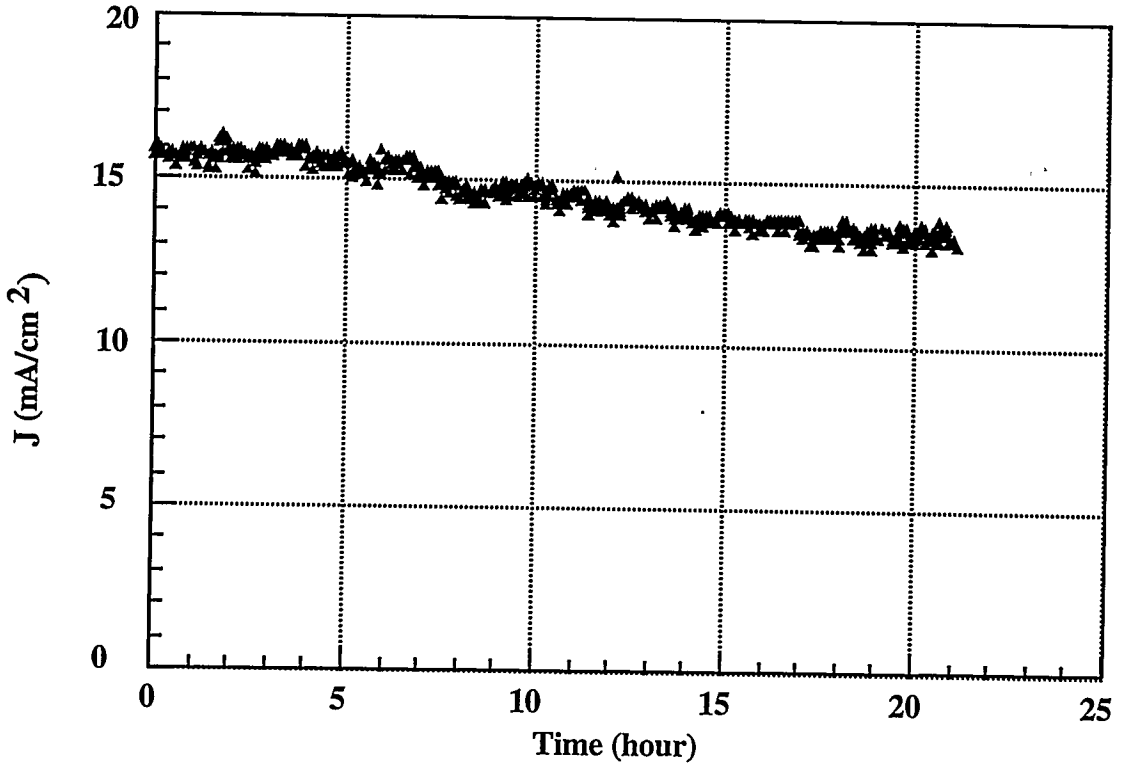

Figure 5. Performance of a Glass/CTO/Pin-Pin-Pin Photoelectrode Held at 3-Sun Illumination with No External Bias for 21 Hours (Sputtered NiO_X Anode, Sputtered Co-Mo Cathode).

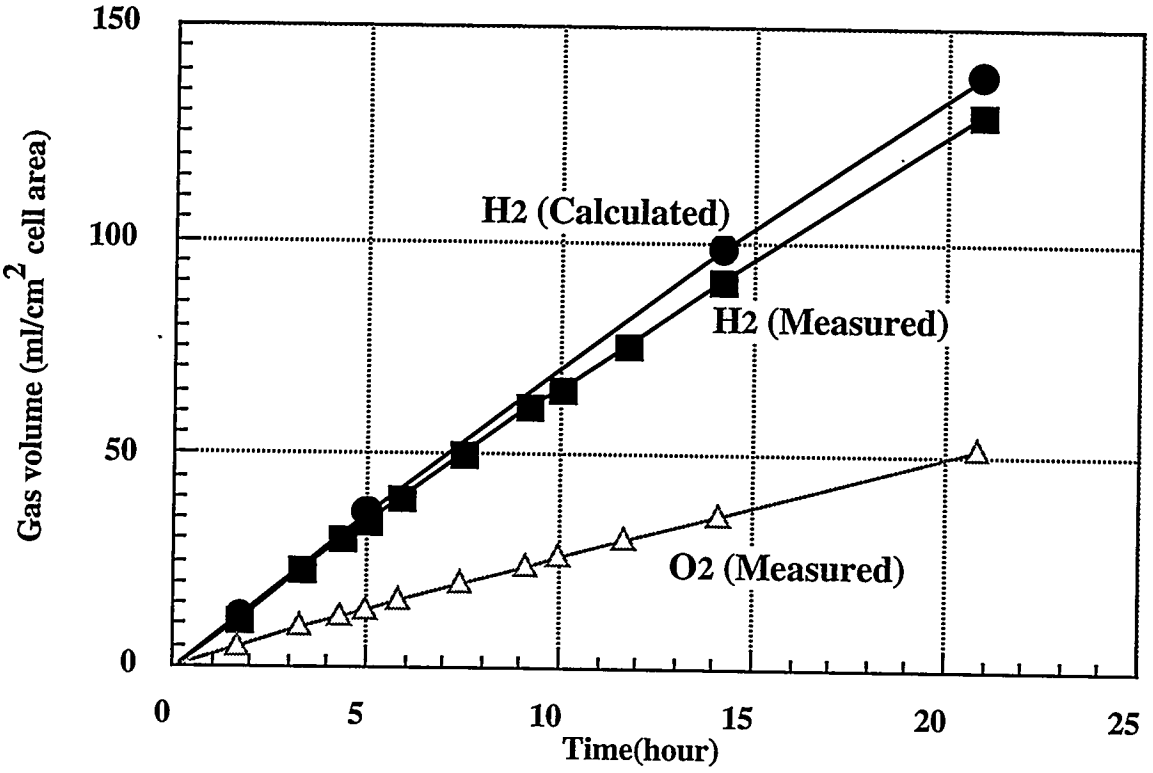

Figure 6. Comparison of the Calculated Hydrogen Production (From Current Density, Figure 5) with Collected Gas (Glass/CTO/Pin-pin-pin Operated at 3-Sun Illumination with No External Basis).

BIOLOGICAL HYDROGEN PHOTOPRODUCTION

Yasuyuki Nemoto
International Research Center for Biological Hydrogen Photoproduction,
Rosenstiel School of Marine and Atmospheric Sciences,
University of Miami
4600 Rickenbacker Causeway, Miami, FL 33149

Abstract

Following are the major accomplishments of the 6th year's study of biological hydrogen photoproduction which were supported by DOE/NREL.

1) We have been characterizing a biological hydrogen production system using synchronously growing aerobically nitrogen-fixing unicellular cyanobacterium, *Synechococcus* sp. Miami BG 043511. So far it was necessary to irradiate the cells to produce hydrogen. Under darkness they did not produce hydrogen. However, we found that, if the cells are incubated with oxygen, they produce hydrogen under the dark. Under 80% argon + 20% oxygen condition, the hydrogen production activity under the dark was about one third of that under the light + argon condition.

2) Also it was necessary so far to incubate the cells under argon atmosphere to produce hydrogen in this system. Argon treatment is very expensive and should be avoided in an actual hydrogen production system. We found that, if the cells are incubated at a high cell density and in a container with minimum headspace, it is not necessary to use argon for the hydrogen production.

3) Calcium ion was found to play an important role in the mechanisms of protection of nitrogenase from external oxygen. This will be a clue to understand the reason why the hydrogen production is so resistant to oxygen in this strain.

4) In this strain, sulfide can be used as electron donor for the hydrogen production. This result shows that waste water can be used for the hydrogen production system using this strain.

Introduction

Advantages of biological hydrogen production system using marine nitrogen-fixing cyanobacteria are:

1) Basically, only air, seawater and sunlight are necessary to maintain the system. They are freely obtained in the tropical and subtropical area. Microorganisms replicate by themselves. Therefore, the cost for the set-up and maintenance of this system would be minimum as compared with other non-biological system.

2) This system does not produce any harmful by-products nor pollute the air and sea, and therefore, it is environmentally friendly.

3) Biomass produced concomitantly with hydrogen production can be used to produce other useful materials, such as foods, chemicals and medicine.

4) Efficiency of a biological system can be improved by genetic engineering.

However, living organisms have very complex systems in their physiology, biochemistry and genetics, and controlling the complex metabolism to enhance hydrogen photoproduction is generally difficult. Therefore, projects dealing with living organisms need more time and more laborious efforts than those of non-living systems.

In previous intensive efforts and long years of research for photosynthetic microorganisms which have high hydrogen producing capabilities from marine environments, we found a very unique, aerobic, nitrogen-fixing, unicellular cyanobacterial strain *Synechococcus* sp. strain Miami BG 043511, which has an exceptionally high hydrogen production capability. Since this strain is a single celled organism, it is amenable to synchronous culture under nitrogen-fixing conditions. The studies of synchronous culture of this strain revealed that hydrogen production from water consists of two processes; (1) photosynthetic process which involves water photolysis and CO_2 fixation, produces O_2, and finally accumulates carbohydrate (glycogen), and (2) hydrogen production process that utilizes glycogen synthesized during the former process and produces H_2 and CO_2 using light and nitrogenase. CO_2 can be recycled between the two processes. Therefore, the overall reaction of both processes is as follows:

$$H_2O + \text{light} - H_2 + \frac{1}{2} O_2$$

It is well known that nitrogenase and hydrogenase, which catalyze hydrogen photoproduction, are extremely oxygen sensitive enzymes. A small amount of oxygen inhibits hydrogen photoproduction. Therefore, it was previously believed that these two seemingly incompatible reactions, oxygen producing photosynthesis and anoxygenic hydrogen photoproduction, could not coexist within the same cell. However, we found that these two reactions are temporally separated within the cell cycle in the unicellular cyanobacterium, *Synechococcus* sp. strain Miami BG 043511. We also found this same phenomenon during the incubation of non-growing cells which were harvested from well synchronized cultures of the strain.

However, so far, the reaction of the hydrogen production was absolutely light-dependent, and therefore, continuous light conditions were necessary for the biological hydrogen production system, because both photosynthetic phase and hydrogen production phase required concurrent light irradiation. Also, so far, argon treatment was necessary for the hydrogen production because both nitrogen and oxygen inhibit the hydrogen production although the inhibition mechanisms are different. These conditions, namely continuous light and argon treatment, are unfavorable for an actual application of biological hydrogen production.

In this year, we concentrated on the circumvention of these conditions and found a possible way for the hydrogen production system which does not require continuous light conditions nor argon treatment.

Also, although the protection mechanisms of nitrogenase form internally evolved oxygen was elucidated by the finding that the photosynthetic phase and hydrogen production phase are temporally separated within a cell cycle, it is completely unknown why the hydrogen production in this strain is resistant to external oxygen. We found that calcium ion has an important role in the protection of nitrogenase from external oxygen.

At last, we found that hydrogen sulfide can be used as electron donor in this strain as is in many photosynthetic bacterial strains, and therefore, this cyanobacterial strain can be used to make waste-water clean and to produce hydrogen at the same time.

I. Hydrogen Production and Nitrogenase Activity under the Dark in *Synechococcus* sp. strain Miami BG 043511

Introduction

Biological hydrogen production by photosynthetic microorganisms has been studied as one of the ways to produce clean renewable energy source (Mitsui and Kumazawa 1977, Mitsui 1992, 1993). This method is cheaper than other methods, because the organisms grow by themselves in seawater under solar energy and no expensive material is required.

Among photosynthetic microorganisms, nitrogen-fixing cyanobacteria are the most desirable in order to keep clean environment, because they can not fix CO2 to produce organic material using solar

energy but also fix nitrogen to produce combined-nitrogen such as nitrate and ammonia, which can cause pollution in the environment.

Mitsui et al. found an aerobically nitrogen-fixing unicellular marine cyanobacterium, *Synechococcus* sp. strain Miami BG 043511 (Leon et al. 1986). This strain is very unique because it can grow diazotrophically under aerobic conditions. It was found that the cell cycle in this strain is composed of photosynthetic phase and nitrogen-fixing phase (Mitsui et al. 1986, 1987, 1993). Therefore, oxygen produced during the photosynthesis does not inhibit, at least directly, the extremely oxygen-sensitive nitrogenase activity, because the two processes are temporally separated within one cell cycle. This explains the reason way this strain can grow both photosynthetically and diazotrophically (Mitsui et al. 1986).

When the cells with high nitrogenase activity are incubated under light and argon condition, the nitrogenase cannot fix nitrogen because of the absence of nitrogen and, instead, it reduces proton to produce hydrogen. Hydrogen production activity in this strain is the highest among photoautotrophically growing microorganisms. Using a dense cell suspension, it is possible to produce 7 ml H_2/ml culture during a 12-hr period (Yih et al. unpublished data).

However, so far, not only the photosynthetic process but also the hydrogen production reaction was completely light-dependent in this strain (Suda et al 1992, Kumazawa and Mitsui 1994, Mitsui and Suda 1995), which means that the continuous irradiation of light is necessary for a biological hydrogen production system based on this cyanobacterial strain.

In this study, we examined the possibility of hydrogen production under the darkness, and found that hydrogen can be produced under the darkness if oxygen is provided to the system.

Methods

Strain and culture conditions

A marine unicellular cyanobacterium, *Synechococcus* sp. strain Miami BG 043511, was grown under batch culture conditions for 5 to 7 days i a combined-nitrogen free medium (A-N medium) as described in Mitsui and Cao (1988). Fifty milliliters of batch culture was inoculated into a water-jacketed glass cylinder (8.5 cm in diameter) containing 3.3 liter of A-N medium with 2.5 g/l $NaHCO_3$, and cultured at 30°C under a light intensity of 150 $\mu E/m^2/sec$ (Mitsui and Cao 1988). Air containing ca. 4% CO_2 was bubbled in through the bottom of the culture cylinder. The pH of the medium was maintained at 7.6 ± 0.1 by slight adjustment of the CO_2 concentration. After 72 hr of culture under the light, the cells were subjected to 16-h dark, 16-h light and 16-h dark periods sequentially to synchronize the cell cycle (Suda et al. 1992). After this pretreatment, the synchronized cells were cultured under continuous light irradiation. The beginning of this last light period is designated as 0 hr of the synchronous culture.

Assay for nitrogenase activity

Nitrogenase activity was determined as described by Leon et al. (1986). Five-milliliter aliquot was put in a 25-ml Fernbach flask fitted with a butyl-rubber stopper. The inner atmosphere was air or substituted by argon gas by repeated evacuation and gassing. Various amounts of oxygen was injected into the flask containing argon using a syringe through the stopper. After the addition of oxygen, inner pressure was equalized to the ambient atmosphere by pricking a needle into the stopper for a second. Then, 2 ml of acetylene was added to these various treated flasks. The flasks were incubated for 30 min in a shaker bath at 30°C under a light intensity of 150 $\mu E/m^2/sec$, or covered with two sheets of aluminum foil and incubated under the darkness in the shaker. The reaction was terminated by injection 1 ml of 20% trichloroacetic acid through the rubber stopper. A 0.5-ml gas sample was taken from the flask, and the amount of ethylene was determined using a gas chromatograph (Hewlett Packard, model 5710A) fitted with a flame ionization detector and dual columns (Porapak R).

Assay for hydrogen production

Five-milliliter sample was put in a 25-ml Fernbach flask and treated under various kinds of atmosphere and light conditions in the same way as described in the nitrogenase assay. At various intervals, a syringe filled with 0.1-ml argon was pricked through the rubber stopper into the flask, and the internal atmosphere was well mixed using the plunger. The, 0.1-ml gas sample was taken by the syringe from the flask, and injected into a gas chromatograph (Shimadzu, GC-8A) with a thermal conductivity detector to measure the amounts of hydrogen, oxygen and nitrogen.

Determination of dry weight and cellular carbohydrate content

Fifty-ml of cell suspension was collected on a preweighed glass microfiber filter (Whatman, 934AH) and washed twice with distilled water. Cellular dry weight was measured after the filer was dried at 90°C for 24 hr.

The phenol/sulfuric acid method (Dubois et al. 1956) was used to measure the carbohydrate content of cell suspensions which had first been centrifuged at 5,000 x g for 10 min, washed once with fresh culture medium and resuspended in distilled water.

Results

Characteristics of conventional hydrogen production system using Synechococcus *sp strain Miami BG 043511*

So far, we studied hydrogen production in *Synechococcus* sp. Miami BG 043511 under argon atmosphere and with light irradiation. When the portions of cell suspension were taken from the synchronous culture at 12 hr of the synchronous culture and incubated under air or argon atmosphere with or without light irradiation, a significant amount of hydrogen was produced only under argon + light condition (Fig. 1-1). This condition was best for the hydrogen production so far, and the final

yield of the hydrogen production is around 20 to 25 μmol H_2/mg dry weight/12 hr. There is no significant hydrogen production under argon + dark condition. Therefore, this reaction of hydrogen production under the argon condition is absolutely light-dependent.

On the other hand, in the presence of air, there was no significant amount of hydrogen production both under the light and the dark conditions. This is because the nitrogenase used the available energy to fix nitrogen.

Effects of light intensity on the hydrogen production

Using the same experimental system, the light intensity was changed during the period of the hydrogen production under argon atmosphere. As is shown in Fig. 1-2, again, with no irradiation, no hydrogen was produced, and the activity of hydrogen production was saturated at the light intensity of 150 $\mu E/m^2/sec$, which is a relatively dim light. The hydrogen production was slightly inhibited by increasing the light intensity to more than 150 $\mu E/m^2/sec$.

Oxygen-sensitive hydrogen production under the light

Hydrogen production was measured at various concentrations (0% to 20%) of oxygen in argon atmosphere under the light conditions (Fig. 1-3). In the absence of oxygen, hydrogen production activity was maximum, and ca. 25 μmol H_2/mg dry weight/12 hr. The curve of hydrogen accumulation was almost linear up to 26 hr from the onset of the reaction. Although the initial rate of hydrogen production seemed not to be affected by the oxygen concentration, the final yield of hydrogen production decreased as the oxygen concentration increased.

As shown in Fig. 1-4, the activity of hydrogen production under the light was inhibited by increasing the oxygen concentration within a range of 0% to 10%. At 10% of oxygen concentration, ca. 60% of the activity remained. There was no more inhibition of hydrogen production even at the oxygen concentration of 20%.

Oxygen-dependent hydrogen production under the dark

Under the same conditions with respect to the atmosphere, hydrogen production was measured under the dark. As shown in Fig. 1-3, in the absence of oxygen, there was no hydrogen production. However, when the oxygen concentration increased, a significant amount of hydrogen was produced. Maximum yield of hydrogen produced under the darkness was 7 μmol H_2/mg dry weight/12 hr.

As shown in Fig. 1-4, at the oxygen concentration below 2%, the amount of hydrogen produced increased with a linear relationship to the oxygen concentration. However, there was no more increase nor decrease in hydrogen production even when the oxygen concentration increased up to 20%.

Nitrogenase activity during the hydrogen production period

Since the hydrogen production is catalyzed by nitrogenase in this strain, nitrogenase activity was measured under the same conditions as for the measurement of hydrogen production. The incubation time for nitrogenase activity was always 30 min to avoid the artificial effects of acetylene itself on the activity. During the incubation for the nitrogenase assay, the conditions were the same as for the hydrogen production assay. The conditions were under air, argon and 80% argon + 20% oxygen and under the light or dark.

Fig. 1-5 shows the results. Under the air conditions, no hydrogen was produced no matter whether light was given or not. However, under these conditions, nitrogenase activity was observed form 9 hr to 12 hr after the onset of synchronous culture. After 12 hr, nitrogenase activity decreased to zero under both the light and dark conditions. This is because the cells fixed nitrogen which is contained in the air during that period. After the sufficient amount of nitrogen was fixed, the nitrogenase activity was repressed. Under these conditions, nitrogenase reduced dinitrogen to make ammonium, and did not reduce protons to produce hydrogen.

Under argon + light conditions the hydrogen production was maximum. Under the same conditions, nitrogenase activity was found to be high (ca. 1.6 μmol C_2H_2/mg dry weight/hr), and this high activity was maintained for more than 12 hr, and then decreased. The maintenance of high activity of nitrogenase was well correlated with the high hydrogen production activity under these conditions with a linear increase for more than 12 hr. Under argon + dark conditions, no hydrogen was produced as in Fig. 1-1 but no nitrogenase activity was detected either.

Under 80% argon + 20% oxygen + light conditions, the hydrogen production was inhibited by half in this experiment as compared with that under argon + light conditions. Nitrogenase activity under this condition was very interesting, because the activity during the initial 4-hr period was almost the same as that under the best conditions (argon + light), but after 6 hr, it was declined to ca. 0.4 μmol C_2H_2/mg dry weight/hr, and low activity was somehow maintained from 16 hr to 24 hr after the onset of synchronous culture. Under 80% argon + 20% oxygen + dark conditions, hydrogen was produced even if the amount was very low. Nitrogenase activity was similar to that under 80% argon + 20% oxygen + light, but the activity came to almost zero at 18 hr after the onset of synchronous culture.

Potential nitrogenase activity during the hydrogen production period

Since the carbohydrate which is synthesized during the photosynthetic period preceding the period of high nitrogenase activity is used as energy during the nitrogenase reaction, the change of carbohydrate content was examined.

As shown in Fig. 1-7, under argon + light condition, carbohydrate content decreased approximately half, that is from 0.4 to 0.2 mg/mg dry weight, during the hydrogen production. In contrast to this result, under 80% argon + 20% oxygen + dark condition, carbohydrate content decreased very quickly and at 16 hr after the onset of synchronous culture, it came to 0.1 mg/mg dry weight. This value is actually the minimum value of carbohydrate content in the strain using the current assay

method (data not shown). The hydrogen production ceased quickly under this condition and the curves of the decrease of carbohydrate and the accumulation of hydrogen were correlated with each other with a mirror relationship.

From these results, it is suggested that the amount of hydrogen produced under the argon + oxygen + dark condition is determined by the carbohydrate content at the start of dark treatment.

Effects of light intensity during the photosynthetic period on the hydrogen production

In order to increase the hydrogen production activity, it seems to be important to increase the carbohydrate content at the beginning of the dark period. So, the light intensities of 150μE/m^2/sec (control) and 1,500 μE/m^2/sec were used for the preceding photosynthetic period. In this experiment, 500-ml portions of culture were taken from the cylinder for the synchronous culture at 0 hr of the synchronous culture and incubated in a 1-liter Fernbach flask with bubbling with air + 4% CO_2, under light illumination of 150 and 1,500μE/m^2/sec. At 12 hr of the culture, samples were taken and incubated for hydrogen production under various conditions.

Fig. 1-8 shows the results. Under the light of 150μE/m^2/sec, the profiles of hydrogen production were the same as before. Under the light intensity of 1,500μE/m^2/sec, the hydrogen production activity on a basis of μmol H_2/mg dry weight was almost the same as under low light intensity even if there is a slight increase of hydrogen production under the conditions except for dark + argon condition (Fig. 1-8A). However, the dry weight of cells under the high light intensity was almost three times higher than under the low light intensity at 12 hr of the synchronous culture. Fig. 1-8B shows the results of hydrogen production in a basis of μmol H_2/ml culture. On a per ml culture basis, which is equal to a per cell basis, hydrogen production was enhanced almost three times as a result of the increase of cellular dry weight. Since the increase in dry weight is supposed to be mainly due to the increase in glycogen content, this suggests that the final yield of the hydrogen production is dependent upon the glycogen content at the start of the reaction of hydrogen production.

Discussion

Hydrogen production under the dark

So far, Mitsui et al. have examined the physiological characteristics of hydrogen production in Synechococcus sp. strain Miami BG 043511. However, these studies mainly used argon conditions for hydrogen production to avoid the inactivation of nitrogenase by oxygen. Under the darkness, no hydrogen is produced if the atmosphere is 100% argon, and the hydrogen production is a completely light-dependent reaction.

However, in this strain light is necessary for the photosynthesis, and its cell cycle is composed of photosynthetic phase and high nitrogenase activity phase. If light were absolutely necessary not only for the photosynthesis but also for the hydrogen production process which is catalyzed by nitrogenase, then continuous light conditions would be necessary even for an actual application of biological hydrogen production using this strain. However, continuous light conditions are not

welcome for an actual application because the natural light conditions on the earth is light and dark cycles.

However, if oxygen is supplemented to the system under the darkness, the cells produce hydrogen. Although the final yield is about one-third of that under the best conditions, which is light and 100% argon. From the results described above, the smaller yield is not due to the adverse effects of oxygen, but it is suggested that, in darkness, the amount of hydrogen produced is determined by the amount of glycogen at the start of the reaction of hydrogen production. In other words, although the light and argon conditions are the best conditions for the hydrogen production, light energy itself provided during the reaction supports, even if partially, the hydrogen production. So it is reasonable that the hydrogen production is the highest under this condition. However, if an actual applied biological hydrogen production system should be operated under natural conditions, the dark hydrogen production seems to be the only way for us to seek.

Enhancement of hydrogen production under the dark

Since the yield of hydrogen production under the dark is determined by the carbohydrate content at the start of the hydrogen production reaction, it is now important to optimize the conditions for the photosynthesis during the period preceding the hydrogen production. As is shown in Fig. 1-8, it is possible to enhance the hydrogen production by increasing the light intensity during the photosynthetic phase.

Reference

Dubois, M., K. A. Gilles, K. Hamilton, P. A. Rebers and F. Smith (1956) Colorimetric method for determination of sugars and related substances. *Anal. Chem.* 28:350-356.

Kumazawa S. and A. Mitsui (1994) Efficient hydrogen photoproduction by synchronously grown cells of a marine cyanobacterium, Synechococcus sp. Miami BG 043511, under high cell density conditions. *Biotech. Bioeng.* 44:854-858.

Leon, C., S. Kumazawa and A. Mitsui (1986) Cyclic Appearance of Aerobic Nitrogenase Activity during Synchronous Growth of Unicellular Cynaobacteria. *Current Microbiol*, 13:149-153.

Mitsui, A. (1992) Hydrogen Photoproduction by Marine Cyanobacteria for Alternating the Carbon Energy Sources.. In J.C. Hunter-Cevera (ed.) *Short communications of the 1991 International Marine Biotechnology Conference*, Volume II, 710-723. Wm C. Brown Publishers, Dubuque, Iowa.

Mitsui, A. (1993) Recent Research Development on Biological Hydrogen Photoproduction. In T. Ohta and T. Homma (ed.) *Energy System and Conversion*, S11-S24. Universal Academy Inc., Tokyo.

Mitsui, A. and S. Cao. (1988) Isolation and Culture of Marine Nitrogen-Fixing Unicellular Cyanobacteria, *Synechococcus. Methods Enzymol*, 167:105-113.

Mitsui, A., S. Cao, A. Takahashi and T. Arai (1987) Growth Synchrony and Cellular Parameters of the Unicellular Nitrogen -Fixing Marine Cyanobacterium, *Synechococcus* sp. strain Miami BG 043511 under Continuous Illumination. *Physiol. Plant*, 69:1-8.

Mitsui, A and S. Kumazawa (1977) Hydrogen Production by Marine Photosynthetic Organisms as a Potential Energy Source. *In*: A. Mitsui, S. Miyachi, A. San Pietro and S. Tamura (ed) *Biological solar energy conversion*, 23-51. Academic Press, New York.

Mitsui, A., S. Kumazawa, A. Takahashi, H. Ikemoto, S. Cao and T. Arai (1986) Strategy by which Nitrogen-Fixing Unicellular Cyanobacteria Grow Photoautotrophically. *Nature*, 323:720-722.

Mitsui, A. and S. Suda (1995) Alternative and cyclic appearance of H_2 and O_2 photoproduction activities under non-growing conditions in an aerobic nitrogen-fixing unicellular cyanobacterium *Synechococcus* sp *Curr. Microbiol*, 30:1-6.

Mitsui, A., S. Suda and N. Hanagata (1993) Cell Cycle Events at Different Temperatures in Aerobic Nitrogen-Fixing Marine Unicellular Cyanobaterium *Synechococcus* sp. Miami BG 043511. J. *Mar Biotechnol*, 1:89-91.

Suda, S., S. Kumazawa and A. Mitsui (1992) Change in the H_2 Photoproduction Capability in a Synchronously Grown Aerobic Nitrogen-Fixing Cyanobacterium, *Synechococcus* sp. Miami BG 043511. *Arch Microbiol*, 158:1-4.

II. Hydrogen Production without Argon Treatment

Introduction

So far, repeated treatments of argon gassing and evacuation were necessary to produce hydrogen in our biological hydrogen production system (Suda et al 1992, Kumazawa and Mitsui 1994, Mitsui and Suda 1995). This is because the cells do not produce hydrogen in the presence of nitrogen. However, the treatments with argon and evacuation are very expensive and should be avoided in an actual application of biological hydrogen production.

In this experiment, we designed a new hydrogen production system, which can be operated without any argon treatment or evacuation.

Materials and methods

Strain and culture conditions

The strain used in this study and the method for the synchronization of the cell cycle were the same as in the previous section. The beginning of this last light period is designated as 0 hr of the synchronous culture. At 8 hr of the synchronous culture, the cells were harvested by centrifugation at 3,000 x g for 10 min and resuspended in a fresh A-N medium at the cell density of 3 mg/ml dry weight. Twenty-two milliliters of the suspension were put in a square-shaped glass bottle (25 ml volume). This glass bottle was fitted with butyl-rubber stopper and the cell suspension was stirred by a stirrer. The inner atmosphere was connected to ambient atmosphere by a combination of two needles connected with each other by a short glass rod (Fig. 2-1).

The glass bottles were put in a water bath at 30°C and the cell suspension in them was stirred with a stirrer. The cells were irradiated with an Xenon lump from a lateral position with the light intensity of 1,500 $\mu E/m^2/sec$. At 11.5 hr after the onset of the synchronous culture, only one of the glass bottles was bubbled with argon for 20 min.

Measurement of hydrogen production

The needles of both bottles (one with argon treatment and the other without it) which extend to the ambient atmosphere were connected to an inverted flask which is filled with water and fitted with butyl-rubber stopper and another needle for the drain of water. The gas produced was trapped in this water-filled flask (Fig. 2-1). The flask was exchanged with a new one at intervals. The internal atmosphere of these flasks were analyzed by a gas chromatograph. In this experiment, the rates of production of gases were measured and the accumulation of the gases was calculated from the rates.

Results

Hydrogen production without argon or evacuation

Fig. 2-2 shows the results. In the case with argon treatment, hydrogen production was observed from 15 hr to 25 hr of the synchronous culture, with its maximum activity at 18 hr (Fig. 2-2A, left). Final yield of the hydrogen production was ca. 11 ml/bottle (Fig. 2-2A, right). Oxygen was also detected but only after 24 hr of the synchronous culture. This shows the beginning of the second photosynthetic phase.

On the other hand, in the case without any argon treatment, hydrogen production was also observed from 18 hr to 25 hr of the synchronous culture (Fig. 2-2B, left). There was a lag period in the beginning, during which no hydrogen was produced, with contrast to the case with argon treatment. During this initial period, nitrogen appeared to be produced. Oxygen was also detected under the is condition only after 24 hr of the synchronous culture. Final yield of hydrogen production was ca. 9 ml/bottle (Fig. 2-2B, right), which was comparable to yield with argon treatment.

Discussion

From this experiment, it was shown that the argon treatment is not necessary to produce hydrogen. In the experimental design, the inner headspace of the culture bottles was made minimum, and the cell density was relatively high. During the photosynthetic phase (actually 8 hr to 12 hr of the synchronous culture), oxygen was evolved and it was expected that the nitrogen naturally dissolved i the medium will be purged with the oxygen production. Although it is unknown how much nitrogen remained at the 12 hr of the synchronous culture in the bottle without any argon treatment, it is suggested that the amount of nitrogen in the cell suspension was almost minimum because the comparable amount of hydrogen was actually produced from this bottle.

There seem to be two factors which repress the activity of nitrogen fixation and enhance the hydrogen production in this experiment. One is the effects of the oxygen evolution during the photosynthetic phase which will purge the nitrogen dissolved in the medium, as mentioned above. Another is the cell concentration in the bottle. If the cell concentration is higher, the available nitrogen for each cell will be limited so that more hydrogen is produced.

References

Kumazawa S. and Akira Mitsui (1994) Efficient hydrogen photoproduction by synchronously grown cells of a marine cyanobacterium, Synechococcus sp. Miami BG 043511, under high cell density conditions. *Biotech. Bioeng.* 44:854-858.

Mitsui, A. and S. Suda (1995) Alternative and cyclic appearance of H2 and O2 photoproduction activities under non-growing conditions in an aerobic nitrogen-fixing unicellular cyanobacterium *Synechococcus* sp. *Curr. Microbiol*, 30:1-6.

Suda, S., S. Kumazawa and A. Mitsui (1992) Change in the H2 Photoproduction Capability in a Synchronously Grown Aerobic Nitrogen-Fixing Cyanobacterium, *Synechococcus* sp. Miami BG 043511. *Arch Microbiol*, 158:1-4.

III. Effects of Calcium Ions on Nitrogenase Activity.

Introduction

Nitrogenase is known to be an extremely sensitive enzyme to oxygen (Smith and Evans 1971, Gallon et al. 1974). In spite of this fact, several strains of unicellular cyanobacteria are capable of growing diazotrophically under an aerobic condition (Fay 1992). It has been of a great interest to learn how they protect the brittle enzyme from the attach of oxygen molecules. Mitsui et al. reported that *Synechococcus* sp. strain Miami BG 043511 separates photosynthesis and nitrogen fixation in different phases, and a high respiratory activity keeps the intracellular oxygen level low during the nitrogen fixation (1986). In this report, using the same strain, the role of calcium ions in the protection mechanism of nitrogenase was investigated.

Materials and methods

Microorganism and cultivation.

A marine unicellular cyanobacterium, *Synechococcus* sp. strain Miami BG043511, was maintained by batch cultivation in a combined nitrogen-free medium (A-N medium) as described by Mitsui and Cao (1988). Twenty-five milliliter of batch culture was inoculated into a water jacketed glass cylinder (85 mm diameter) with 3.31of sterilized A-N medium containing 29 mM sodium bicarbonate, and was cultivated at 30°C under a light intensity of 150 $\mu E/m^2/sec$. Carbon dioxide gas mixed with air at concentration of 4% (V/V) was bubbled through tubing attached to the bottom of the cylinder at a rate of 400 ml/min. The medium pH was kept at 7.7 by slight adjustments of the carbon dioxide content throughout the cultivation. Synchronous growth was established by 16 hr cultivation in the dark followed by 16 hr in the light and another 16 hr in the dark after a 72 hr pre-cultivation in the light. Synchronity was maintained for about seventy-two hours under the subsequent continuous illumination.

Nitrogenase activity.

5-ml aliquots of culture or cell suspension were taken and transferred into 25 ml Fernbach flasks fitted with a butyl-rubber stopper. The inner atmosphere was replaced with pure argon gas before 2 ml of acetylene was injected with a syringe through the stopper. Incubation was carried out in a water bath at 30°C under a light intensity of 150 $\mu E/m^2/sec$ for 30 min unless otherwise indicated. The reaction was terminated by injecting 1 ml of 4N sulfuric acid. A 0.5 ml of gas sample was taken from the flask to quantitate ethylene formed by reduction of acetylene using a gas chromatograph (Hewlett Packerd, Model 5710A) equipped with a dual column (Porapak R) and a flame ionization detector.

Photosynthesis and respiration.

The activities of photosynthesis and respiration were determined by measuring the rate of oxygen production and consumption. A 1-ml sample was withdrawn from the culture and placed in an airtight glass cell fitted with Clark type oxygen electrode (Yellow Springs Instruments, Model 5331).

The sample suspension was stirred with a small magnetic bar, being kept at 30°C by recirculating water in a jacket. Photosynthetic activity was measured under an incident light intensity of 150 $\mu E/m^2/sec$. Respiratory activity was determined under a complete darkness after saturating the suspension with oxygen by bubbling air.

Cell concentration.

Cell dry weight was measured by collecting cells on a glass fiber filter from 100 ml of culture or suspension, followed by washing twice with the same volume of distilled water. The dried cell pellet was weighed after an incubation in an oven at 90°C for no less than sixteen hours.

Results

Inactivation of nitrogenase in calcium-free suspensions.

Synchronously grown cells were harvested at 14 hr after the final onset of light, when their nitrogenase activity was about 60% of the highest at around 12 hr. Those cells lost nitrogenase activity quite quickly when suspended in solutions lacking sodium or calcium ions. IN the medium without calcium chloride or sodium chloride, there was not acetylene reduction observed, but in A-N medium lacking other compounds there was no significant decrease of activity (Fig. 3-1). The same results were obtained in a simplified experiment using TAPS buffer (Fig. 3-2). Nitrogenase activity appeared only when both of calcium chloride and sodium chloride were added to the suspension.

Activities under various concentrations of sodium chloride and calcium chloride were measured. The optimum concentration for sodium chloride was determined as 400 mM (Fig. 3-3), however, a concentration of 200 mM was enough for a normal activity. 600 mM sucrose of the same concentration of sorbitol was able to substitute for it, so the effect of sodium chloride was thought to be an osmotic one. For calcium chloride, 5mM was required for the maximum activity (Fig. 3-4), while its original concentration was 2.5 mM in A-N medium. There was not a remarkable difference between activities at the concentration above 5 mM. Once the activity disappeared after a treatment with a solution lacking calcium ions, it was never restored even if cells were resuspended in a complete solution containing excess calcium chloride (Fig. 3-5). This result suggests that the disappearance is not inhibition but inactivation.

Changes of calcium dependency during synchronous cultivation.

Changes in nitrogenase activity were monitored with or without calcium ions throughout the synchronous cultivation from 8 hr to 18 hr after the final onset of light. Measured with calcium chloride, nitrogenase activity started to rise at 8 hr and disappeared at around 16 hr, having its peak at 13 hr (Fig. 3-6). Calcium ions had no effect during the former half of the active period (8-12 hr). During the latter half (12-18 hr), on the contrary, the activity without calcium was significantly suppressed, compared to that with calcium. The highest activity without calcium was 75% of that with calcium. Time courses of inactivation showed a remarkable difference of characteristics between

cells harvested at 10 hr and those at 14 hr. 10 hr cells were resistant to the absence of calcium ions, while 14 hr cells were quite sensitive to it (Fig. 3-7).

Anaerobic cell washing and measurement.

Synchronously grown cells were harvested at 14 hr after the final onset of light, then were washed with an incubated in the buffers with or without calcium chloride under completely anaerobic condition using sodium thioglycolate as an oxygen absorbent. There was no inactivation observed even without calcium if cells were treated anaerobically, while they lost all activity simply by being washing and incubated without calcium chloride under normal aerobic condition (Fig. 3-8).

Photosynthetic activity and respiratory activity.

Rates of respiration and photosynthesis were measured during synchronous growth period (Fig. 3-9). A tight correlation between respiration and nitrogenase activity was observed. Respiration was remarkably enhanced when the nitrogenase activity was high. The profiles of those two time courses gave a completely identical shape except that there was a low level of basal respiration when cells had no nitrogenase activity. Without calcium ions, respiratory activity was suppressed only in the latter half (12-15 hr) of the active period as was the nitrogenase activity.

Net oxygen evolution increased from 12 hr through 15 hr, in an inverse relation to the nitrogenase and respiratory activities, in measurements both with and without calcium chloride. Photosynthetic oxygen production rates, calculated from values of dark respiration rate and net evolution rate, showed no difference between cells with and without calcium ions. It is suggesting that the absence of calcium ions did not affect the photosynthesis system at all, and that other cellular functions were kept quite normal. The response to the elimination of calcium ions was quite fast in 13 hr cells (Fig. 3-10). Five minutes after the addition of enough EGTA to chelate all calcium ions, respiration dropped to a low rate that was comparable to the rate at the time when cells had not nitrogenase activity. Lost respiratory activity was not recovered by addition of excess calcium chloride. 10 hr cells, being resistant to the absence of calcium ions, showed no response to EGTA. Respiration was suppressed by EGTA in 16 hr cells to almost zero, and it was slightly restored by addition of calcium ions.

Discussion

It has been demonstrated that calcium ion has an important role in maintenance of nitrogenase activity in cells of Synechococcus sp. strain Miami BG 043511. A quick, irreversible inactivation of nitrogenase occurred when cells are exposed to a calcium-free atmosphere. On the other hand, it did not affect their photosynthetic activity at all, which suggests that the inactivation is not a whole cell event such as a collapse of cell walls, but specific to nitrogenase and related mechanisms.

The inactivation caused by the absence of calcium ions was not observed under anaerobic conditions. This fact indicates that the calcium ion is closely related to the protection mechanism of nitrogen fixation from external oxygen. The rapidity of inactivation also suggests that the effect is an oxygen-

related one. Oxygenic respiration has been regarded as a possible mechanism from protecting nitrogenase (Yates et al. 1974, Gallon et al. 1984). A considerably high respiration rate has been reported for unicellular cyanobacteria which are capable of fixing nitrogen under aerobic conditions (Mitsui et al. 1986, Grobbelaar et al. 1987). In this study, the elimination of calcium ions caused a significant suppression on dark respiration, which shows that calcium ion is able to increase the respiratory rate. This understanding is in agreement with the reports on *Azotobacter* (Yates et al. 1974), *Gloeocapsa* (Hamadi et al. 1981) and another species of *Synechococcus* (Chen et al. 1988).

However, it is interesting that such inactivation does not occur at a stage when nitrogenase activity is increasing in the cells from 8 hr through 12 hr after the final onset of light. I this period, respiration is not affected by the elimination of calcium ions either. These results suggest that there is another mechanism that enhances respiration during this period. Cells might abandon some of their protective reactions when nitrogenase activity is not essential for them (12-16 hr), which would allow the effects of calcium ions to appear distinctly.

It is quite likely that respiration is functioning as an effective ATP supply for nitrogenase as well as a protection mechanism (Maryan et al. 1986). Since nitrogen fixation is a highly ATP-consuming reaction, respiration must be contributing to the regeneration of ATP together with photophosphorylation. From this point of view, there could be another interpretation for the effect of calcium. It possibly enhances nitrogen fixation itself directly, therefore observed high respiration rates are just the simple results of the high ATP requirement. Net oxygen evolution is never dramatically negative but remains slightly negative or even positive when nitrogenase is highly active (Fig. 4-9B). This fact supports that the idea more or less, since such a low oxygen consuming activity seems unable to solely keep the intracellular atmosphere strictly anaerobic. As photosynthetic oxygen production is still alive at a rate which is not negligible, the cell should be almost saturated with oxygen when the net evolution rate is near zero. The fact that the respiratory activity lost on a treatment with EGTA cannot be restored by excess calcium ions, also suggests the existence of another protection mechanism.

Our broad conclusion is that calcium ion has a protective effect on nitrogenase from external oxygen by enhancing respiration, but it cannot be the only protection system in this microorganism. Some questions still remain waiting to be investigated in future studies.

References

Chen, T. H., Huang, T. C. and Chow, T. J. (1989) Calcium is required for the increase of dark respiration during diurnal nitrogen fixation by Synechococcus RF-1. *Plant Science 60*, 195-198

Fay. P. (1992) Oxygen relations of nitrogen fixation in cyanobacteria. *Microbiol. Rev.* 56, 340-373

Hamadi, A. F. and Gallon, J. R. (1981) Calcium ions, oxygen and acetylene reduction (nitrogen fixation) in the unicellular cyanobacterium *Gloeocapsa* sp. 143/3. *J, Gen, Microbiol.* 125, 391-398

Gallon, J. R. and Hamadi, A. F. (1984) Studies on the effect of oxygen on acetylene reduction (nitrogen fixation) in *Gloeocapsa* sp. ATCC 27152. *J. Gen. Microbiol.* 130, 495-503

Gallon, J. R., La Rue, T. A. and Kurz, W. G. W. (1974) Photosynthesis and nitrogenase activity in the blue-green alga *Gloeocapsa*. *Can. J. Microbiol.* 20,1633-1637

Grobbelaar, N., Lin, H. Y. and Huang, T. C. (1987) Induction of a nitrogenase activity rhythm in *Synechococcus* and the protection of its nitrogenase against photosynthetic oxygen. *Curr. Microbiol.* 15, 29-33

Maryan, P., Eady, R. R., Chaplin, A.E. and Gallon, J. R. (1986) Nitrogen fixation by *Gloeothece* sp. PCC 6909: Respiration and not photosynthesis supports nitrogenase activity in the light. *J. Gen. Microbiol.* 132, 789-796

Mitsui, A. and Cao, S. (1988) Isolation and culture of marine nitrogen-fixing unicellular cyanobacteria, *Synechococcus*. *Methods. Enzymol.* 167, 105-113

Mitsui, A. Kumazawa, S., Takahashi, A., Ikemoto, H., Cao, S. and Arai, T. (1986) Strategy by which nitrogen-fixing unicellular cyanobacteria grow photoautotrophically. *Nature* 323, 720-722

Smith, R. V. and Evans, M. C. W. (1971) Nitrogenase activity in cell-free extracts of the blue-green alga *Anabaena cylindrica J. Bacteriol.* 105,913-917

Yates, M. G. and Jones, C. W. (1974) Respiration and nitrogen fixation in *Azotobacter*. *Adv. Microbiol. Physiol.* 11,97-135

IV. Sulfide as electron source for H_2 photoproduction

Introduction

Sulfide is one of the major pollutants in the environment and can be found in sewage, industrial and agricultural wastes, polluted rivers, marine water, and sediments. Obviously, its removal via biological processes is of high significance. It is known well that sulfide can be consumed by photosynthetic bacteria such as Chlorobiaceae. Chromatiacae (Imhoff, 1982), and Rhodospirillaceae (Hansen and van Gemerden 1972). Some strains of *Chromatium* sp. (Mitsui et al. 1980) and in some strain of *Ectothiorhodospira vacuolata* (Imhoff, 1982) have been found to use sulfide to increase both growth and H_2 production.

These photosynthetic bacteria contain photosystem I only can use sulfide instead of H_2O as electron source. Sulfide is known to support also anoygenic photosynthesis in some strains of cyanobacteria and to stimulate H_2 production in N_2 fixing filaments of *Nostoc muscorum* (Fry et al. 1984). Cyanobacteria have both photosystems, generally using water as electron donor and thus evolving O_2. Recently, we used *Synechococcus* sp strain Miami BG 043511, a facultative aerobically nitrogen fixing unicellular cyanobacterium, to study the utilization of added substrates other than water for H_2 photoproduction (Luo and Mitsui 1994). The loss of nitrogenase activity and H_2 photoproduction with cell ageing could be restored by adding substrates such as pyruvate, glucose, sucrose, and glycerol to the cell suspension. However, H_2 production occurs only in the light and increases with light intensity (Luo and Sternberg, unpublished data). Therefore, we assume that at least photosystem I is involved in this recovery of nitrogenase activity and H_2 production after the addition of these substrates. These processes may thus be similar to those in photosynthetic bacteria.

Under these assumptions we investigated the capacity of Synechococcus sp. strain Miami BG 043511 to use sulfide as potential electron source for H_2 photoproduction.

Methods

Special treatment

Batch cultures with normal A-N medium was used for this studies. In the incubation medium, however, sulfur containing chemicals were replaced by sulfur free chemicals: $CuCl_1 \cdot 2H_2O$, $FeCl_2 \cdot 4H_2O$, and $MgCl_2 \cdot 6H_2O$ to obtain an only sulfide containing medium. The pH of the solutions was adjusted to about 7.6 with HCl solution. The stock solutions of sodium sulfide were 2M in sulfide. Immobilized batch culture samples were prepared according to the procedure described by Matsunaga and Mitsui (1982).

Growth and stress conditions

The time course of growth of a random batch culture of Synechococcus sp. strain Miami BG 043511 is shown in Fig.4-1. The samples taken on the 3rd, 7th, and 15th days represent different growth stages of these cells. In addition to physiological changes by the age of the culture, the stationary

phase (15 days) represents severe stress conditions, since light became limited by the density of the culture and some nutritional elements became deficient.

Results

The effect of sulfide mixture with suspension on the H_2 production

Hydrogen accumulation during the incubation of batch cultures during growth and ageing is shown in Fig. 4-2. It can be clearly seen from the data that H_2 production capability of the cells declines from 3 to 15 days culture (open circles). The amount H_2 accumulations to 3 to 5 times higher in 3-day old cells than in 7-day old cells, and 5 to 8 times higher than in 15-day old cells. The incubation of cells with sodium sulfide up to 1 mM did not show significant changes in H_2 photoproduction (data not shown). All suspensions treated wit 5 mM (sold triangles) and 25 mM (open triangles) sodium sulfide solution, respectively, demonstrated different results. In 3 days old cells H_2 photoproduction was strongly suppressed by 5 and 25 mM sodium sulfide. The suppression was much less in 7 day old cells. In cells of the stationary phase 5 mM sodium sulfide enhanced H_2 photoproduction by about 30%, where as 25 mM sodium sulfide still inhibited H_2 photoproduction.

As H_2 accumulation reached a constant level under various concentration of sodium sulfide added, the amounts of H_2 accumulations were compared to the controls. The H_2 values expressed in percent of the untreated control are shown in Fig. 4-3. It is obvious that the tolerance to the positive effect of sodium sulfide on H_2 photoproduction increases with age of the culture and concentrations up to 5mM. Higher concentrations were only inhibiting.

The effect of sulfide separation from suspension on H_2 production

In analogy to photosynthetic bacteria, we could assume that the cells take up H_2S, which might derive from sodium sulfide according to the following equation:

$$Na_2S + H_2O + CO_2 \text{ ------> } Na_2CO_3 + H_2S$$

In order to test this hypothesis and to separate the possible direct physiological effect of the sodium sulfide and its dissociates on the cells the following experiments were designed.

A vial (volume 1.5 cm^3) was fixed at the bottom of the flask, a piece of filter paper was inserted and the sodium sulfide solution injected into the vial. By this setup the sulfide uptake could only occur via the gas phase. Again, low concentrations of sodium sulfide had no significant effect (data not shown). The results are shown in Fig. 4-4 demonstrate that the changes in H_2 production with incubation time show patterns similar to those of direct sodium sulfide solution administration. However, the inhibiting and the stimulating effect of the sulfide evaporating from filter paper on H_2 production was stronger than that caused by the corresponding concentrations of sodium sulfide at direct cell contact. It has thus to be concluded that the inhibiting effect on H_2 production is not due to the direct contact of sodium sulfide with the cells. The stimulating effect of sulfide on H_2

production is identical with that of its direct administration and appears in the resting cells under stress conditions, only.

When sodium sulfide was indirectly administrated to the cells on filter paper, both, the inhibiting and the stimulating effect on H_2 production at all age of the cells were slightly higher than those caused by the solution in direct contact with the cells. This may be related to higher sulfide concentration in the incubation flasks with separated sulfide compared to those when sulfide was mixed with the cells. In accordance with these results we have to assume that H_2S, deriving from the dissociation of sodium sulfide and its reaction wit CO_2 serves as electron source for H_2 photoproduction.

Responses of immobilized cells to sulfide

When sodium sulfide solution was stepwise injected into suspensions cells immobilized in agar during incubation, the inhibiting effect of sulfide on H_2 production was found to be much less pronounced at all ages of the cultures (Figs. 4-5 and 4-6). The concentrations of the sodium sulfide solutions injections indicated by arrows were 0.2 and 1mM (Fig. 4-5) and 2.5 mM in Fig. 4-6., respectively. A significant stimulating effect of the addition of sodium sulfide solution on H2 evolution was observed only for 15-days old cells at final sulfide concentrations higher than 10 mM (Fig. 4-6).

The changes in pH

The pH-changes in the suspension media before and after incubation are compared in Table 1. There is an identical tendency of a slight pH-change at all ages of the cells. It can thus be concluded that the inhibiting effect of sodium sulfide on H_2 photoproduction in batch cultures is independent of changes in pH of the medium.

Discussion

There are two major types of photosynthetic bacteria, non-sulfur and sulfur strains. Photosynthetic non-sulfur bacteria (Rhodospirillaceae) have the capability to use a wide range of organic substances, such as carbohydrates, organic acids, and fatty acids for growth and H_2 production (Kumazawa and Mitsui 1981; Mitsui et al. 1980). Photosynthetic sulfur bacteria (Chromatiaceae and Chlorobiaceae) have the unique ability to use sulfide as an electron donor for growth and H_2 production (Mitsui 1994) like photosynthetic nonsulfur bacteria and also sulfide as electron donor for H_2 production like the photosynthetic sulfur bacteria. With cell getting age under stress conditions in aged cultures our cyanobacterium can use higher concentrations of sulfur for H_2 production. This may be due to a partly loss in photosystem II activity. At present, however, the exact mechanism is yet not clear, as the ratio of evolved oxygen to hydrogen (data not shown) did not decline sufficiently for this explanation.

The presented data, however, suggest a possible mechanism for cyanobacteria to survive under stress as well as under pollution conditions. This result seems to be practical implication, as cyanobacteria thus could not only be used to remove sulfide and other organic substrates from waste water, but at the same time use the electrons made available for H_2 photoproduction.

References

Fry, -I., Robinson., A. E., Sath, S., Packer, L. 1984. The role of Na2S in anoxygenic photosynthesis and H2 production in the cyanobacterium Nostoc muscorum: Biochem. Biophys. Res. Commun. 23:1138-1143.

Hansen, T. A. 1974. Sulfide als electronendonor voor Rhodospirillaeae, Doctoral thesis, University of Groningen, The Netherlands. Hansen, T. D., van Gemerden, H. 1972. Sulfide utilization by purple nonsulfur bacteria, Arch Mikrobiol. 86:49.

Holm-Hansen, O., Riemann, B. 1978/ Chlorophyll a determination: improvements in methodology. OIKOS 30:438-447.

Imhoff, J. F. 1982. Response of photosynthetic bacteria to mineral nutrients. In: Handbook of biosolar resources. (Ed.) O. R. Zaborsky, A. Mitsui, and C. C. Black, Jr. p. 135-146. CRC Press, Inc. Boca Raton, Florida.

Kumazawa, S., Mitsui, A. 1981. Characterization and optimization of hydrogen photoproductionby a saltwater blue-green alga, *Oscillatoria* sp. Miami BG 7. I. Enhancement through limiting the supply of nitrogen nutrients. Int. J. Hydrogen Energy 6:339-348.

Leon, C., Kumazawa, S., Mitsui, A. 1986. Cycle appearance of aerobic nitrogenase activity during synchronous growth of unicellular cyanobacterium, *Synechococcus*. Current Microbiol. 13:149-153.

Luo, Y. -H., Mitsui, A. 1994. Hydrogen production from organic substrates in an aerobic nitrogen-fixing marine unicellular cyanobacterium *Synechococcus* sp. strain Miami BG 043511. J. Biotech. Bioeng. 44:1255-1260.

Matsunaga, T., and Karube, I., Suzuki, S. 1980. Some observations on immobilized hydrogen-producing bacteria: Behavior of hydrogen in gel membrane. Biotechnol. Bioeng. 22:2607-2615.

Matsunaga, T., Mitsui, A. 1982. Sea water based hydrogen production by immobilization marine photosynthetic bacteria. Biotechnol. Bioeng. 12:411-450.

Mitsui, A. 1992. Hydrogen photoproduction by marine cyanobacteria for alternating the carbon energy sources. In: Short communications of the 1991 International Marine Biotechnology Conference. J.C. Hunter -Cevera (Ed), Wm C. Brown Publishers, Dubuque, Iowa, Volume II. p. 710-723.

Mitsui, A., Cao, S. 1988. Isolation and culture of marine nitrogen-fixing unicellular cyanobacterium. *Synechococcus*. *Method. Enzymol.* 167:105-113.

Mitsui, A., Kumazawa, S., Philips, E.J., Reddy, K.J., Gill, K., Matsunaga, T., Renuka, B.R., Kusumi, T., Reyes-Vasquez, G., Miyazawa, K., Haynes, Ikemoto, H., Duerr, E., Leon, C.B., Rosner, D., Sesco, R., Moffat, E.. 1984. Mass cultivation of algae and photosynthetic bacteria: Concepts and Application. In: Biotech. and Biopro. Engin. T.K. Ghose (ed.). International Union of Pure and Appl., Chemi. and Indian N. S. A. United India Press, New Delhi. pp. 119-155.

Mitsui, A., Ohta, Y., Frank, J., Kumazawa, S., Hill, C., Rosner, D., Barciela, S., Greenbaum, J., Hayes, L., Oliva, L., Dalton, P., Radway, J., and Giffard, P., 1980. "Photosynthetic bacteria as alternative energy sources: Overview on hydrogen production research," in T. N. Veziroglu (ed.), Alternative Energy Sources II. Vol. 8 Hydrogen Energy, Hemisphere Publ. Co., Washington, DC. pp. 3483-3510.

Mitsui, A., Matsunaga, T., Ikemoto, H., Renuka, B. R. 1985. Organic and Inorganic waste treatment and simultaneous photoproduction of hydrogen by immobilized photosynthetic bacteria. Develop. in Indust. Microbiol. 26:209-222.

Table 1. Changes in the pH-values before and after incubation of batch cultures with and without sodium sulfide (5 mM).

Age of cells (Days)	pH (before incubation) pH	ph (after incubation Control	5mM
3	7.6	8.67±0.02	8.56±0.03
7	7.6	8.59±0.05	8.49±0.23
15	7.6	8.25±0.08	8.10±0.19

Conclusion and perspective

[1] Biological hydrogen production system operable under the natural conditions

As was described above, two major problems for an applied system of biological hydrogen production can be solved; hydrogen can be produced under the darkness if a small amount of oxygen is supplied to the system, and it is not necessary to use argon if the concentration of available nitrogen in the medium is reduced to almost zero.

Fig. 5-1 shows a rough idea of an applied biological hydrogen production system based on the results which were obtained in this year's study.

During the day time, the cells produce a lot of oxygen by photosynthesis and the produced oxygen is stored in a container whose volume can change freely following the change of internal pressure. At the end of day time, the oxygen produced during the day time is removed partially from the system. During the night time, the cells consume oxygen and produce hydrogen. At the end of the night time, it will be ideal that all of the oxygen has been used up and only the produced hydrogen remains in the system. At the dawn, the produced hydrogen is taken, part of the cell suspension is drained, and the system is filled with fresh seawater. Waste water can be mixed in the medium. The dilution ratio will determine the growth rate of the cells. To get the highest efficiency of the hydrogen production, the growth rate of the cells should be minimum.

Factors which can affect the efficiency of the hydrogen production in this system will be the cell concentration, the thickness of the cell layer, the dilution rate of the cells, concentration of CO_2 and N_2 in the fresh medium which is supplied to the system. In the future, these factors should be optimized.

[2] Protection mechanisms of nitrogenase activity from externally derived oxygen

Calcium ion was found to have role in the protection mechanisms of nitrogenase from externally derived oxygen. To understand the mechanisms further, it will be necessary to measure both nitrogenase activity and hydrogen production activity *in vitro*. It is possible that some structure exists in the cells which surround the nitrogenase and protect it from external oxygen. Although biochemical nature of the protection mechanisms is unknown at present, it is likely that some idea can be obtained from *in vitro* experiments.

Elucidation of the protection mechanisms of nitrogenase from oxygen will be also very helpful to establish in the future an *in vitro* hydrogen production system using isolated enzymes and artificial photosystems which can be operated with the highest efficiency.

Acknowledgments

The principal investigator, Y. Nemoto, expresses many thanks to the late Prof. Dr. Akira Mitsui, who taught us about the originality in science and the mission of scientists in the research field of hydrogen production. Also he thanks Dr. Y-H. Luo, Dr. T. Tsuzuki, Dr. W. Yih, Ms. K. A. Song, Ms. Sigal and Ms. C. Campbell for their excellent participation in this project and very hard work, including many overnight experiments. Last but not least, Dr. T. Matsunaga, Dr. H. Senger, Dr. D. Dörnemann, Dr. E. Tel-Or and Dr. N. Veziroglu kindly helped us continue this project.

Legend to Figures

Fig. 1-1 Hydrogen production in *Synechococcus* sp. strain Miami BG 043511. Cells were taken from the synchronous culture at the 12 hr after the onset of light and incubated under argon or air and under light or dark. Open circle, argon + light; closed circle, argon + dark; open square, air + light; closed square, air + dark.

Fig. 1-2 Effects of light intensities on the hydrogen production *Synechococcus* sp. strain Miami BG 043511. Cells were taken from the synchronous culture at the 12 hr of the synchronous culture and hydrogen production was measured after the incubation under argon atmosphere at various intensities of light for 12 hr.

Fig. 1-3 Hydrogen production in *Synechococcus* sp. strain Miami BG 043511 at various s concentrations (0% to 20%) of oxygen under argon atmosphere under the light (150 $\mu E/m^2/sec$) or under the dark. 5-ml of cell suspension was taken from the synchronous culture at 8 hr from the onset of the synchronous culture and treated under various conditions as described in the Materials and Methods. Open symbols, light; closed symbols, dark.

Fig. 1-4 Effects of oxygen concentration on the hydrogen production under the light or dark. The cell suspension was treated under various concentrations of oxygen under the light or dark as in Fig. 1-3. At 23 hr after the onset of synchronous culture, hydrogen production was measured. Open circle, light; closed circle, dark.

Fig. 1-5 Hydrogen production activity and nitrogenase activity measured under the same conditions. Cells were harvested from the synchronous culture at 9 hr from the onset of synchronous culture, and then incubated under various atmospheres (air, 100% argon and 80% argon + 20% oxygen) under light or dark conditions. [A] and [B] show hydrogen production and nitrogenase activity, respectively, under the air. Open square, light + air; closed square, dark + air. [C] and [D] show hydrogen production and nitrogenase activity, respectively, under argon or 80% argon + 20% oxygen. Open circle, light + argon; closed circle, dark + argon; open triangle, light + 80% argon + 20% oxygen. Open circle, light + argon; closed circle, dark + argon; open triangle, light + 80% argon + 20% oxygen; closed triangle, dark + 80% argon +20% oxygen.

Fig. 1-6 Hydrogen production activity and potential nitrogenase activity. Nitrogenase activity was always measured under light + 100% argon conditions. [A], light + argon; [B] light + 80% argon + 20% oxygen; [C] dark + argon; [D] dark +

80% argon + 20% oxygen. Circle shows hydrogen production and square shows nitrogenase activity.

Fig. 1-7 Changes in hydrogen production activity and cellular carbohydrate content. [A] shows the result under light + argon; [B] shows the result under dark + 80% argon + 20% oxygen. Inlets show the change in cellular carbohydrate content.

Fig. 1-8 Effects of light intensity during the photosynthetic phase on the subsequent hydrogen production. During the period from 0 hr to 12 hr of synchronous culture, the cells are irradiated with light whose intensities are 150 $\mu E/m^2/sec$ ([A] and [B]) or 1,500 $\mu E/m^2/sec$ ([C] and [D]). At 12 hr of the synchronous culture, the cells are incubated under argon or 80% argon + 20% oxygen under light or dark conditions. Hydrogen produced is expresses as μmol H_2/mg dry weight ([A] and [C]) and μmol H_2/ml culture ([B] and [D]). Open circle, light + argon; closed circle, dark + argon; open triangle, light + 80% argon + 20% oxygen; closed triangle, dark + 80% argon + 20% oxygen. Dry weight at 12 hr of the synchronous culture is shown in the figures.

Fig. 2-1 Schematic representation of the hydrogen collecting system used for the experiment.

Fig. 2-2 Hydrogen production under the conditions with and without argon treatment. [A] shows the results with argon treatment and [B] shows the results without argon treatment. Figures in the left column show the rate of gas production, and figures in the right column show the amount of gas accumulation.

Fig. 3-2 Effects of calcium chloride, sodium chloride, potassium chloride and magnesium sulfate on nitrogenase activity. 40 ml aliquots of culture were harvested at 14 hr after the final onset of light. Cells were collected by centrifugation and resuspended in the same volume of fresh A—N medium, centrifugal supernatant or 20 mM TAPS buffer (pH 8.0) containing 300 mM sodium chloride, 5 mM calcium chloride, 20 mM potassium chloride and/or 20 mM magnesium sulfate for measurements of nitrogenase activity. The cell concentration in the reaction mixture was 115 µg cdw/ml.

Fig. 3-3 Dependency of nitrogenase activity on the concentration of sodium chloride, 40 ml aliquots of culture were harvested at 14 hr after the final onset of light. Cells were collected by centrifugation and resuspended in the same volume of centrifugal supernatant 20 mM magnesium sulfate for measurements of nitrogenase activity. The cell concentration in the reaction mixture was 119 µg cdw/ml.

Fig. 3-4 Dependency of nitrogenase activity on the concentration of calcium chloride, 40 ml aliquots of culture were harvested at 14 hr after the final onset of light. Cells were collected by centrifugation and resuspended in the same volume of centrifugal supernatant or 20 mM TAPS buffer (pH 8.0) containing 300 mM sodium chloride and various concentrations of calcium chloride for measurements of nitrogenase activity. The cell concentration in the reaction mixture was 135 µg cdw/ml.

Fig. 3-5 Effects of washing with various solutions on nitrogenase activity. 40 ml aliquots of culture were harvested at 14 hr after the final onset of light. Cells were collected by centrifugation and resuspended in the same volume of centrifugal supernatant or 20 mM TAPS buffer (pH 8.0) containing 300 mM sodium chloride, various concentrations of calcium chloride, 5 mM EDTA and/or 2 µM calcium ionophore A23187. Measurements of nitrogenase activity were carried out after an incubation in each solution for four hours at 0°C. The cells were again collected by centrifugation and resuspended in 20 mM TAPS buffer (pH 8.0) containing 300 mM sodium chloride and 5 mM calcium chloride before the measurements. The cell concentration in the reaction mixture was 155 µg cdw/ml.

Fig. 3-6 Changes of dependency of nitrogenase activity on calcium ions during a synchronous cultivation. Nitrogenase activity was measured in 20 mM TAPS buffer (pH 8.0) containing 300 mM sodium chloride with or without 5 mM calcium chloride, every two hours during the synchronous cultivation. The cell concentration in the culture was 115 µm cdw/ml at the final onset of light. Activities (A) and the ratio (Ca-/Ca+) of activities (B) are plotted.

Fig. 3-7 Time courses of inactivation of nitrogenase in the presence or absence of calcium ions. Cells were collected by centrifugation at 10 hr or 14 hr after the final onset of light, and suspended in 20 mM TAPS buffer (pH 8.0) containing 300 mM sodium chloride with or without 5 mM calcium chloride. The cell concentrations in the reaction mixture were 125µg cdw/ml for 10 hr cells and 138 µg cdw/ml for 14 hr cells.

Fig. 3-8 Inactivation under an aerobic or anaerobic condition. Four 50 ml aliquots of culture were harvested at 14 hr after the final onset of light. Cells were collected by centrifugation and resuspended in the same volume of 20 mM TAPS buffer (pH 8.0) containing 300 mM sodium chloride with or without 5 mM calcium chloride. For anaerobic treatments and measurements, solutions were degassed by aspiration and 4 mM sodium thioglycolate was added to remove remaining oxygen. Immediately after suspended in the solutions, the cells were transferred into 100 ml Fernbach flasks fitted with a rubber stopper, and the gas phase was replaced with argon. 5 ml of each suspension was taken with a syringe every thirty minutes during an incubation

at 0°C for two hours, and transferred into a 25 ml Fernbach flask filled with argon before a measurement of the remaining nitrogenase activity. For aerobic experiments, the whole procedure except the measurement was carried out in open air without the oxygen absorbent. The cell concentration was 167 µg cdw/ml in the measurement.

Fig. 3-9 Changes of respiratory activity, nitrogenase activity and net oxygen evolution. Rates of respiration (A), nitrogenase activity (B) and net oxygen release or uptake in the light (B) were measured in 20 mM TAPS buffer (pH 8.0) containing 300 mM sodium chloride and 5 mM calcium chloride or 5 mM EGTA, every two hours during the synchronous cultivation. The cell concentration in the medium was 136 µg cdw/ml at 12 hr after the final onset of light.

Fig. 3-10 Responses of respiration to elimination of calcium ions. Culture was withdrawn from the cylinder at 10 hr (B), 13 hr (A) or 16 hr (B) after the final onset of light. The rates of respiration were measured on addition of 5-10 mM EGTA or 5-20 mM calcium chloride at the indicated timings. The cell concentrations were as follows; 10 hr cell, 144 µg cdw/ml; 13 hr cell, 133 µg cdw/ml; 166 hr cell, 129 µg cdw/ml.

Fig. 4-1 Changes in cell density during growth in a batch culture of *Synechococcus* sp. strain Miami BG043511. Cells were grown in inorganic medium and illuminated with 150 $\mu E/m^2/sec$. Cell density was measured by counting the cells under the microscope with a Thoma hemacytometer.

Fig. 4-2 Time course of H_2 accumulation during incubation of 3-days, 7-days, and 15-days old cells. Controls without sulfide addition are indicated by open circles. Final sulfide concentrations were 5 mM (solid triangles) and 25 mM (open triangles). Notice that the scale of ordinate changes.

Fig. 4-3 Relative H_2 production (the amount of H_2 at the highest accumulation in the sulfide-treated samples relative to that in control) as a function of the sulfide concentration. The solid circles, squares, and triangles represent 3-days, 5-days and 15-days old cells in batch cultures. Values above 100% indicate a stimulating effect of sulfide on H_2 production, those below 100% an inhibiting effect.

Fig. 4-4 Time course of H_2 accumulation in 3-days, 7-days, and 15-days old cells during incubation. Sodium sulfide was injected into a vial (1.5 cm^3) on the bottom of each flask equipped with a piece of filter paper, the sulfide solution thus being separated from the suspension medium. Control (open circles) and 5 (solid triangles) and 25 mM (open triangles) show a similar course or curves in Fig. 4-2.

Fig. 4-5 Time course of H_2 accumulation in 3-day and 7-day old immobilized cells. Sodium sulfide solution was gradually (every other day) injected into flask with immobilized cells. Open circles represent controls. Arrows indicate the time of 0.2 mM (solid triangles) and 1 mM (solid squares) of sodium sulfide addition.

Fig. 4-6 Time course of H_2 accumulation in 3-day, 7-day, and 15-day old immobilized cells during incubation. 2.5 mM (solid triangles) of sodium sulfide solution was gradually (every other day) injected into the flasks. Open circles represent the control.

Fig. 5-1 Schematic representation of the future plan of biological hydrogen production system using *Synechococcus* sp. Miami BG 043511.

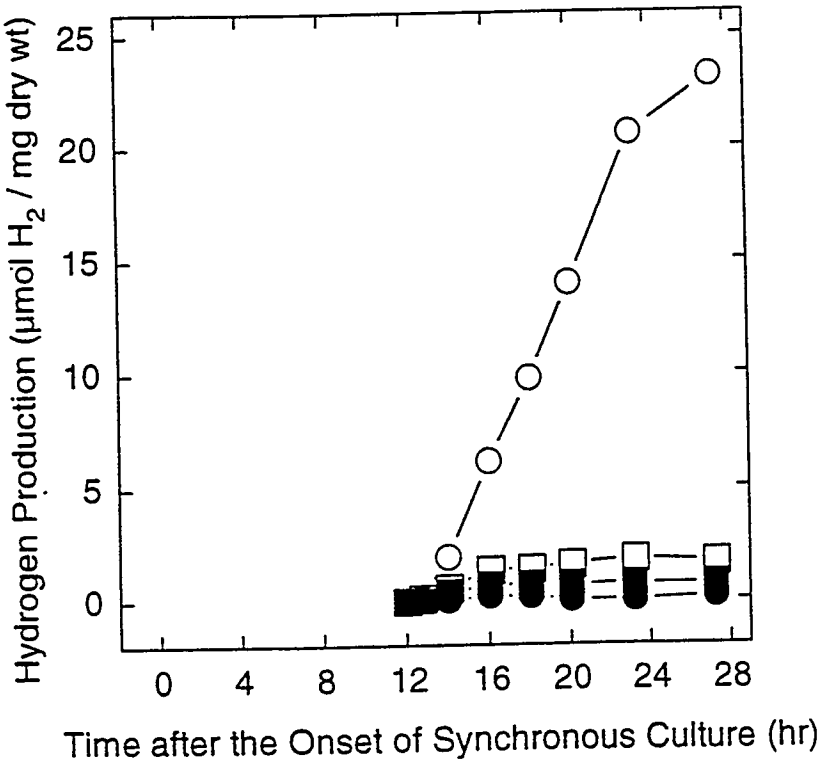

Fig. 1-1 Hydrogen production in *Synechococcus* sp. strain Miami BG 043511. Cells were taken from the synchronous culture at the 12 hr after the onset of light and incubated under argon or air and under light or dark. Open circle, argon + light; closed circle, argon + dark; open square. air + light; closed square, air + dark.

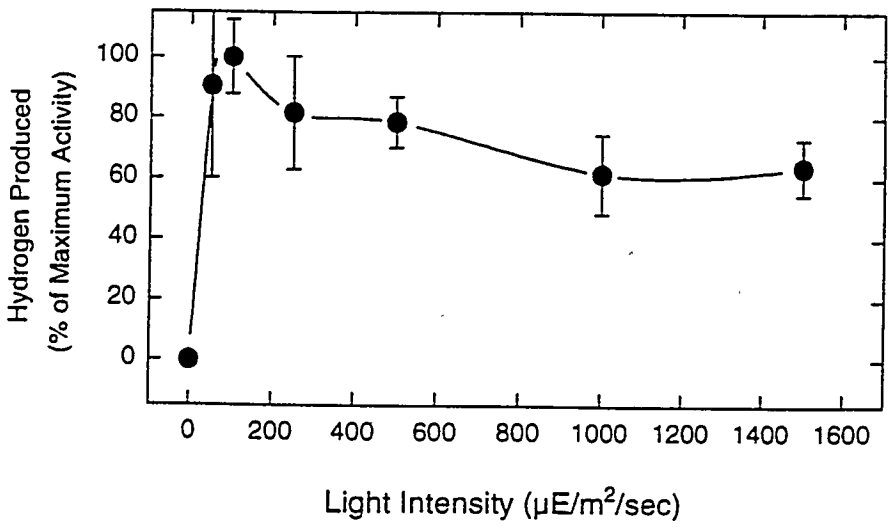

Fig. 1-2 Effects of light intensities on the hydrogen production in *Synechococcus* sp. strain Miami BG 043511. Cells were taken from the synchronous culture at the 12 hr of the synchronous culture and hydrogen production was measured after the incubation under argon atmosphere at various intensities of light for 12 hr.

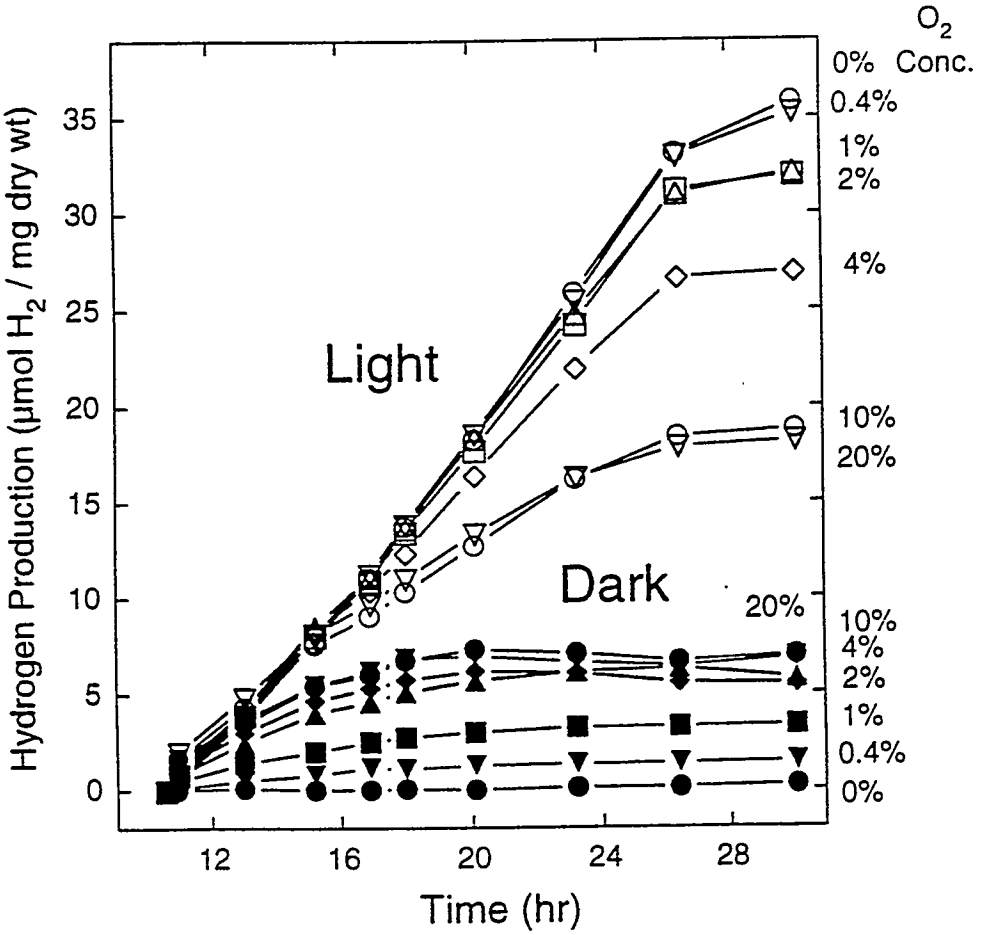

Fig. 1-3 Hydrogen production in *Synechococcus* sp. strain Miami BG 043511 at various concentrations (0% to 20%) of oxygen under argon atmosphere under the light (150 µE/m²/sec) or under the dark. 5-ml of cell suspension was taken from the synchronous culture at 8 hr from the onset of the synchronous culture and treated under various conditions as described in the Materials and Methods. Open symbols, light; closed symbols, dark.

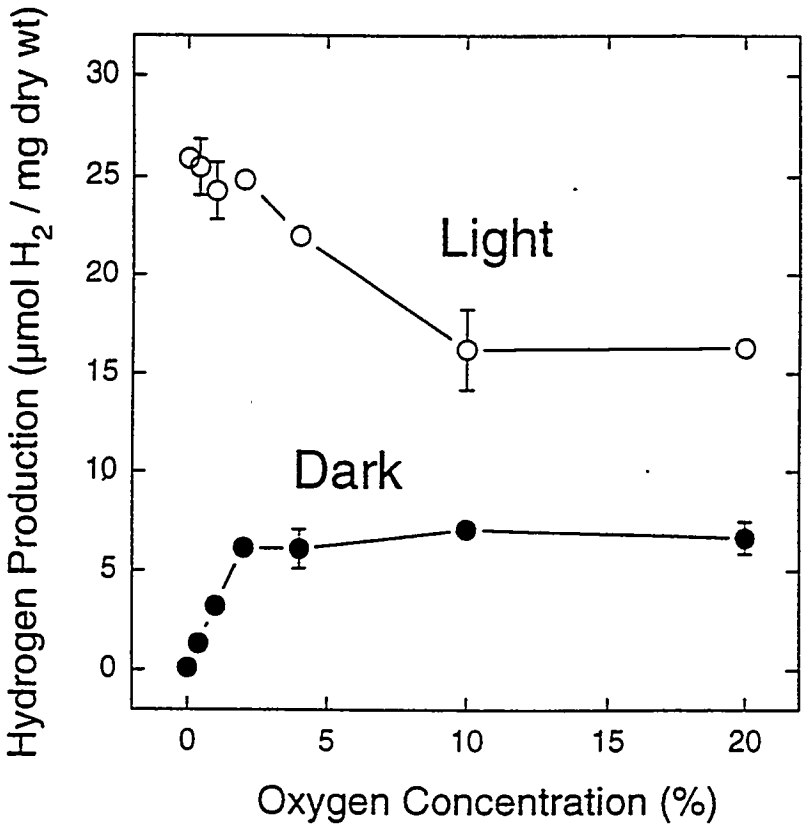

Fig. 1-4 Effects of oxygen concentration on the hydrogen production under the light or dark. The cell suspension was treated under various concentrations of oxygen under the light or dark as in Fig. 1-3. At 23 hr after the onset of synchronous culture, hydrogen production was measured. Open circle, light: closed circle, dark.

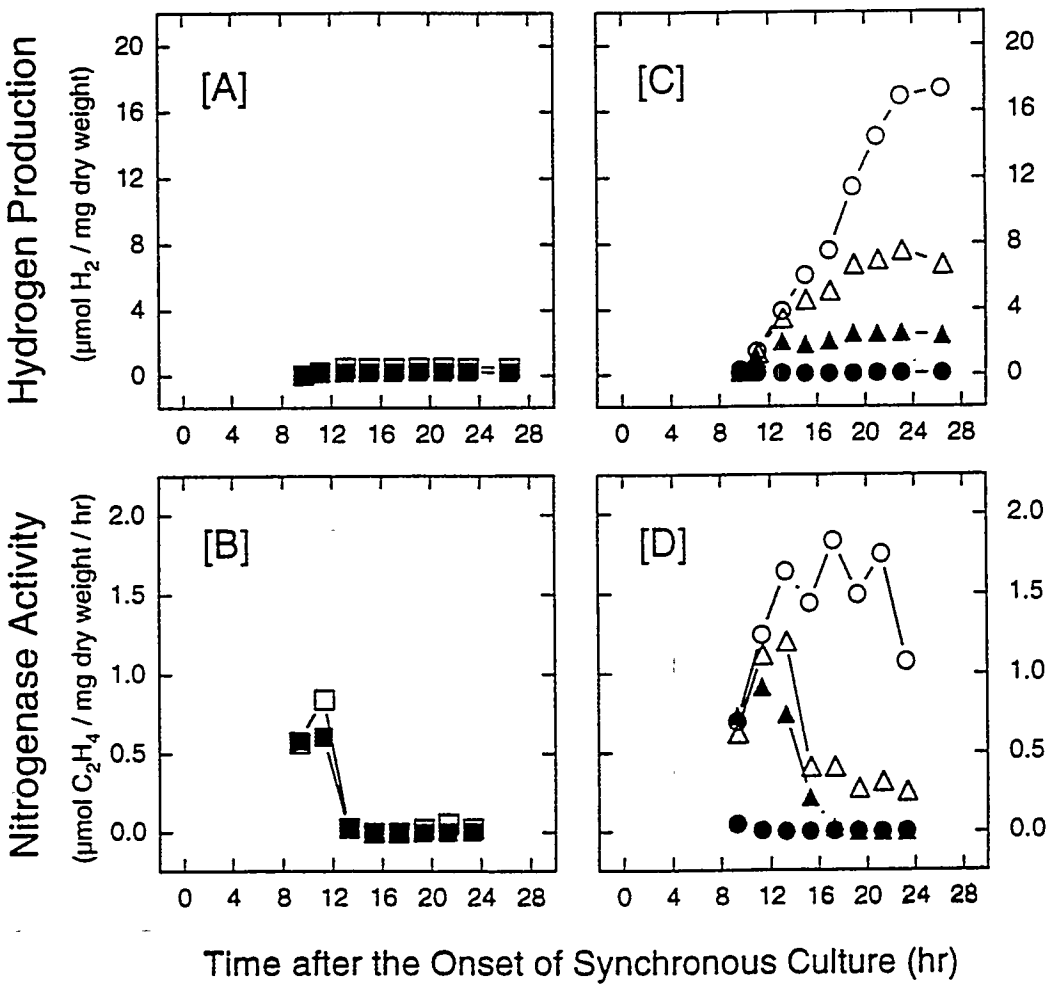

Fig. 1-5 Hydrogen production activity and nitrogenase activity measured under the same conditions. Cells were harvested from the synchronous culture at 9 hr from the onset of synchronous culture, and then incubated under various atmospheres (air, 100% argon and 80% argon + 20% oxygen) under light or dark conditions. [A] and [B] show hydrogen production and nitrogenase activity, respectively, under the air. Open square, light + air; closed square, dark+ air. [C] and [D] show hydrogen production and nitrogenase activity, respectively, under argon or 80% argon + 20% oxygen. Open circle, light + argon; closed circle, dark + argon; open triangle, light + 80% argon + 20% oxygen; closed triangle, dark + 80% argon + 20% oxygen.

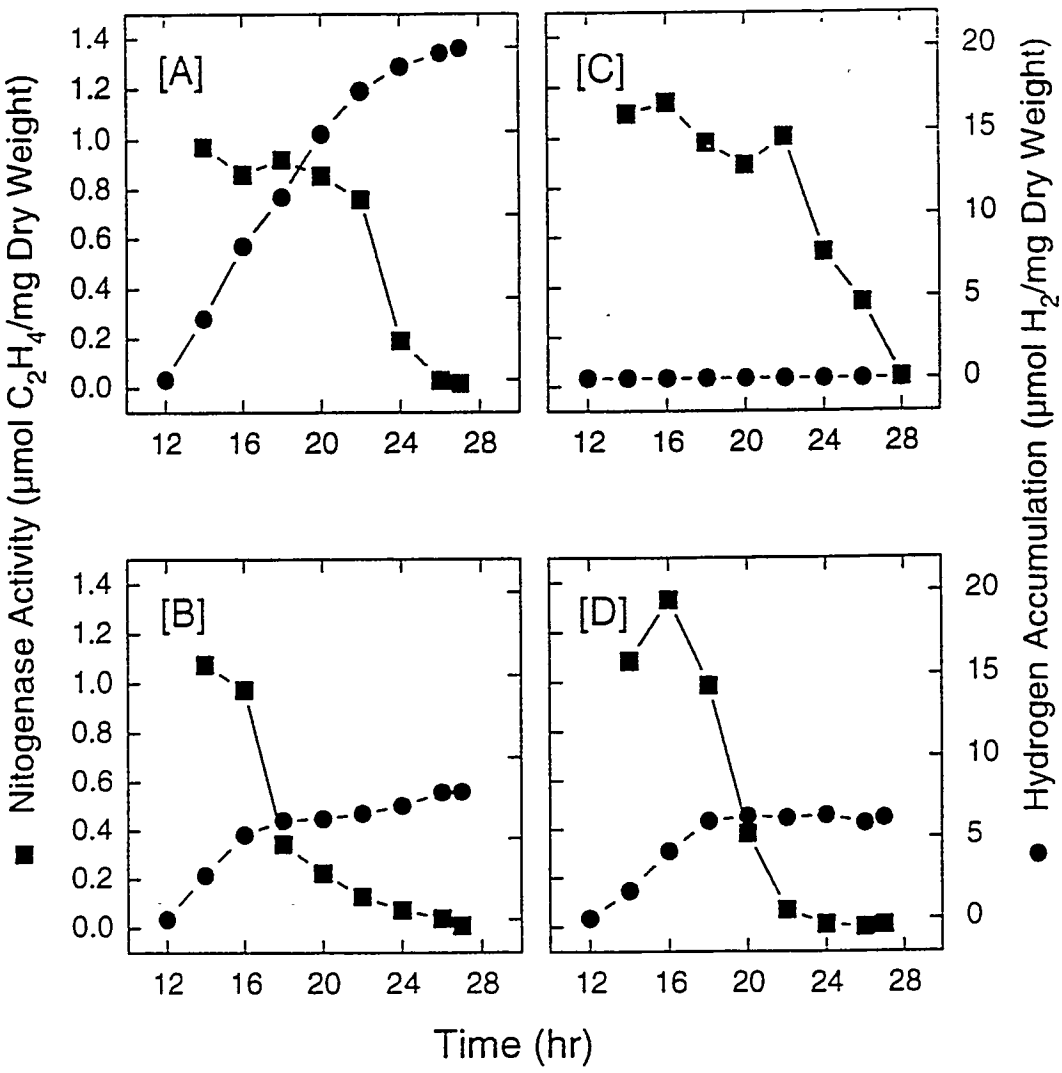

Fig. 1-6 Hydrogen production activity and potential nitrogenase activity. Nitrogenase activity was always measured under light + 100% argon conditions. [A], light + argon; [B] light + 80% argon + 20% oxygen; [C] dark + argon; [D] dark + 80% argon + 20% oxygen. Circle shows hydrogen production and square shows nitrogenase activity.

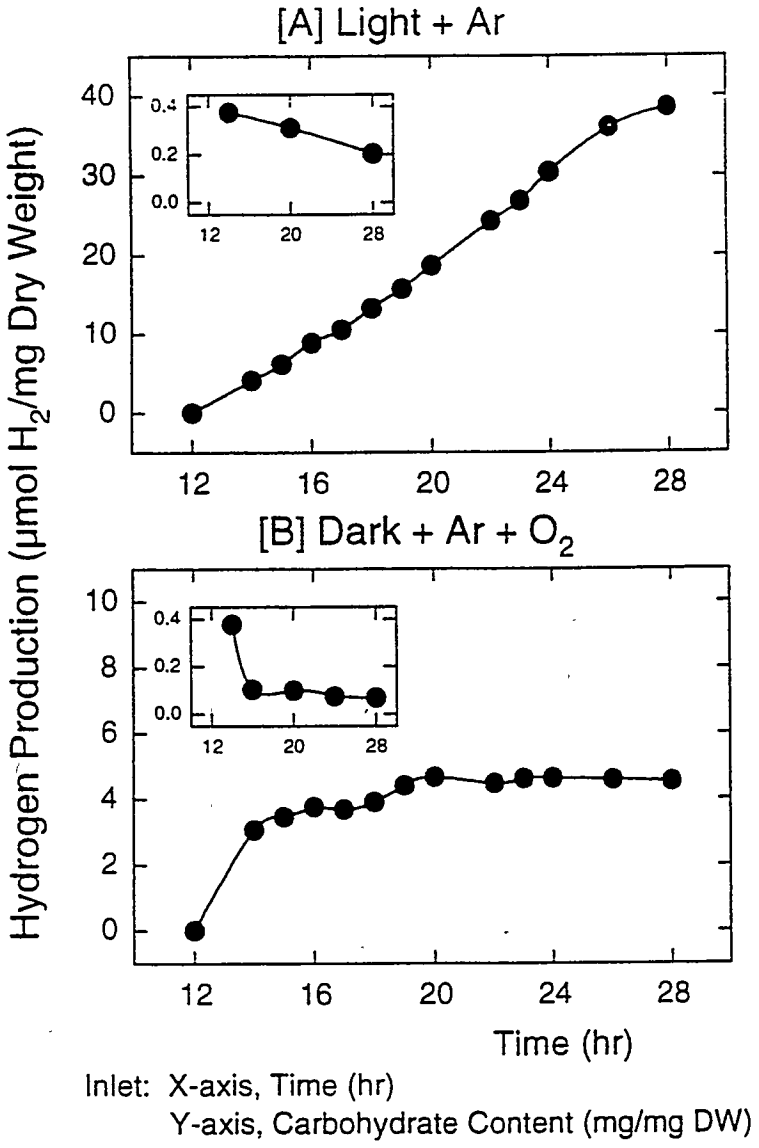

Fig. 1-7 Changes in hydrogen production activity and cellular carbohydrate content. [A] shows the result under light + argon; [B] shows the result under dark + 80% argon + 20% oxygen. Inlets show the change in cellular carbohydrate content.

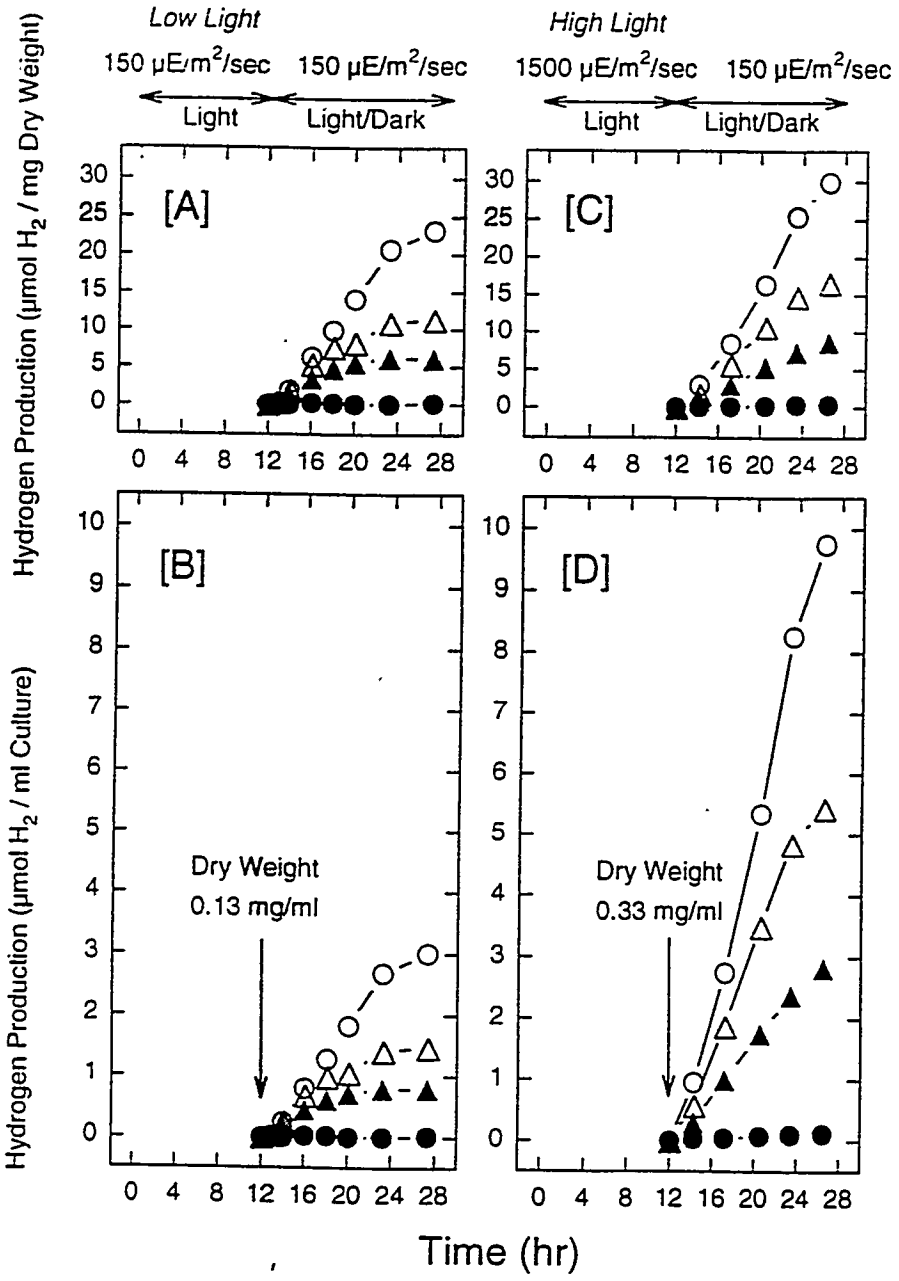

Fig. 1-8 Effects of light intensity during the photosynthetic phase on the subsequent hydrogen production. During the period from 0 hr to 12 hr of synchronous culture, the cells were irradiated with light whose intensities are 150 μE/m²/sec ([A] and [B]) or 1,500 μE/m²/sec ([C] and [D]). At 12 hr of the synchronous culture, the cells were incubated under argon or 80% argon + 20% oxygen under light or dark conditions. Hydrogen produced is expressed as μmol H_2/mg dry weight ([A] and [C]) and μmol H_2/ml culture ([B] and [D]). Open circle, light + argon; closed circle, dark + argon; open triangle, light + 80% argon + 20% oxygen; closed triangle, dark + 80% argon + 20% oxygen. Dry weight at 12 hr of the synchronous culture is shown in the figures.

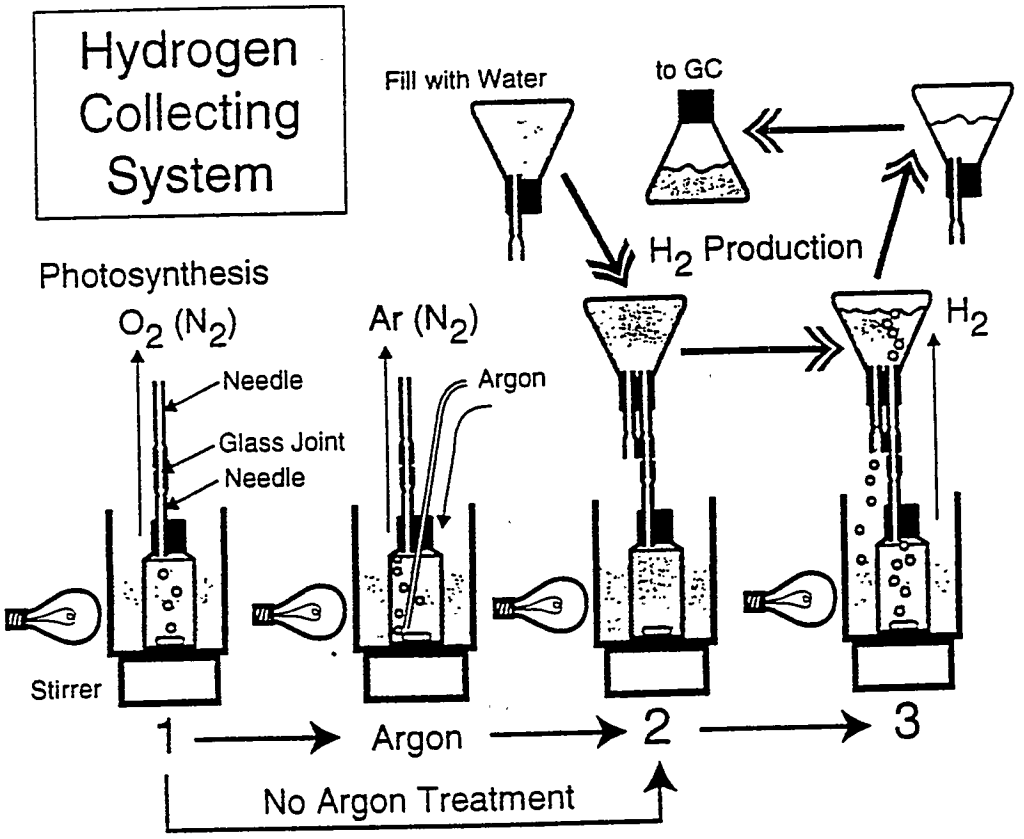

Fig. 2-1 Schematic representation of the hydrogen collecting system used for the experiment.

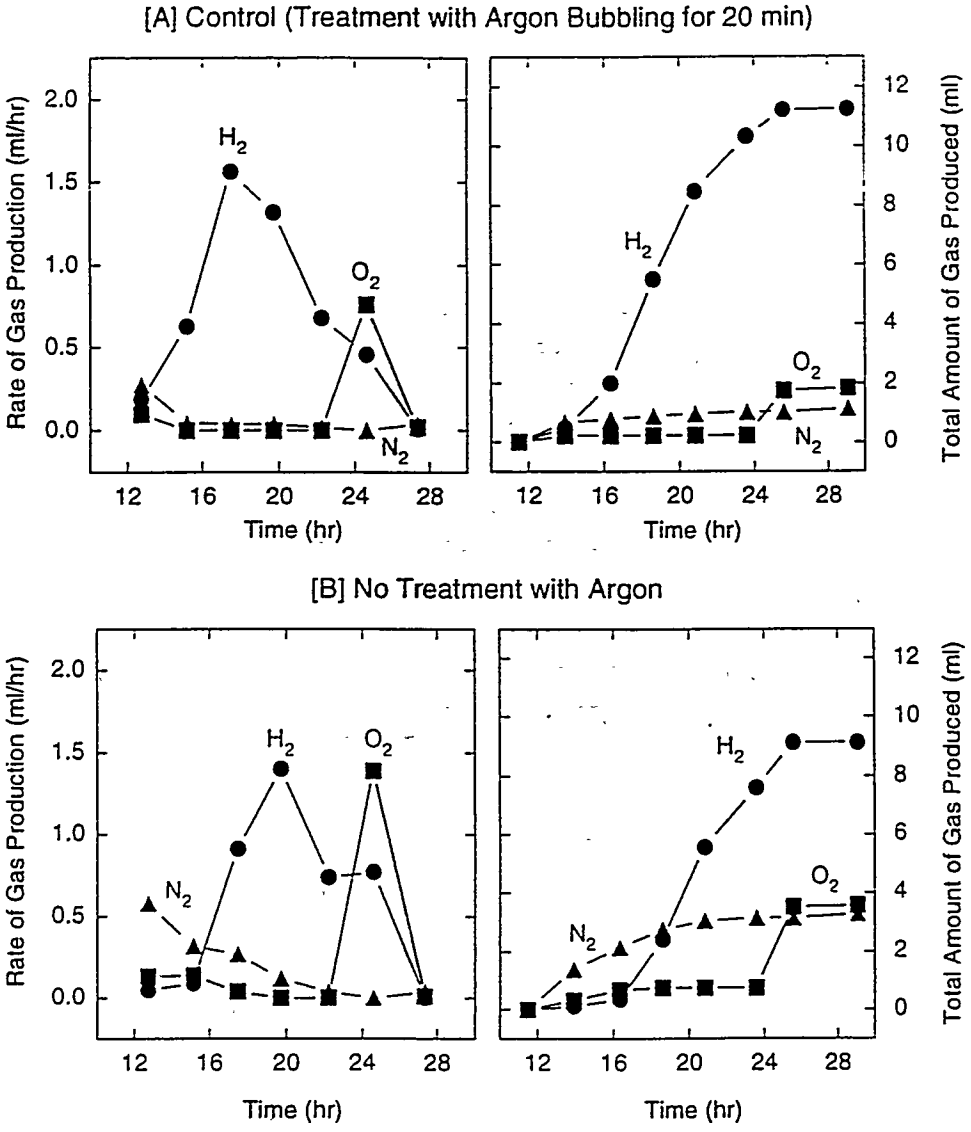

Fig. 2-2 Hydrogen production under the conditions with and without argon treatment. [A] shows the results with argon treatment and [B] shows the results without argon treatment. Figures in the left column show the rate of gas production, and figures in the right column show the amount of gas accumulation.

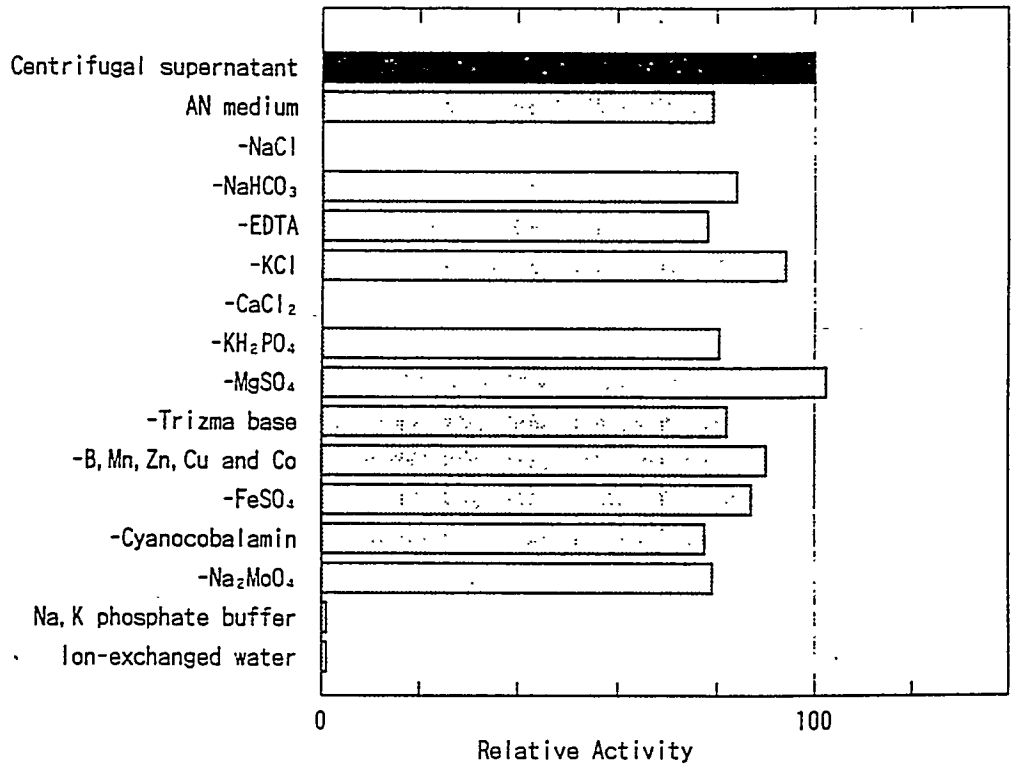

Fig. 3-1 Nitrogenase activities in A-N medium or media which lack one or several components of A–N. 40 ml aliquots of culture were harvested at 14 hr after the final onset of light. Cells were collected by centrifugation and resuspended in the same volume of centrifugal supernatant, each fresh media. 50 mM sodium, potassium phosphate buffer (pH 8.0) or ion exchanged water for measurements of nitrogenase activity. The cell concentration in the reaction mixture was 123 μg cell dry weight (cdw)/ml. Original concentrations for each component in A–N medium are as follows; NaCl, 300 mM; $NaHCO_3$, 29 mM; EDTA, 80 μM; KCl. 8 mM; $CaCl_2$, 2.5 mM; KH_2PO_4, 370 μM; $MgSO_4$, 20 mM; trizma base, 80 μM; H_3BO_3, 560 μM; $MnCl_2$, 22 μM; $ZnCl_2$, 2 μM; $CuSO_4$, 20 nM; $CoCl_2$, 60 nM; $FeSO_4$, 144 μM; cyanocobalamine, 14 nM; Na_2MoO_4, 5 μM. Reactions were carried out for 45 min.

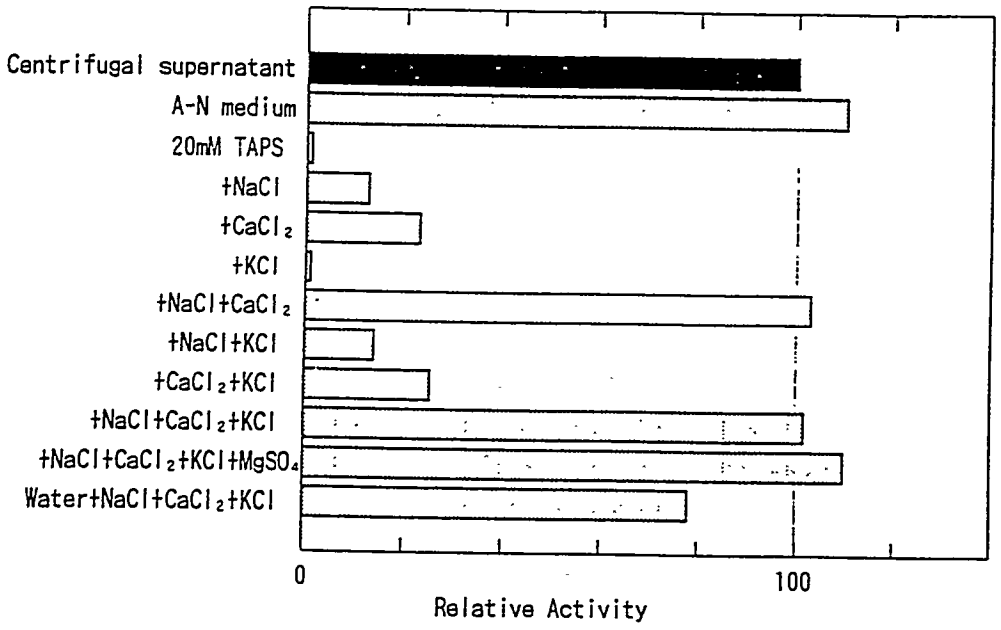

Fig. 3-2 Effects of calcium chloride, sodium chloride, potassium chloride and magnesium sulfate on nitrogenase activity. 40 ml aliquots of culture were harvested at 14 hr after the final onset of light. Cells were collected by centrifugation and resuspended in the same volume of fresh A–N medium, centrifugal supernatant or 20 mM TAPS buffer (pH 8.0) containing 300 mM sodium chloride. 5 mM calcium chloride, 20 mM potassium chloride and/or 20 mM magnesium sulfate for measurements of nitrogenase activity. The cell concentration in the reaction mixture was 115 μg cdw/ml.

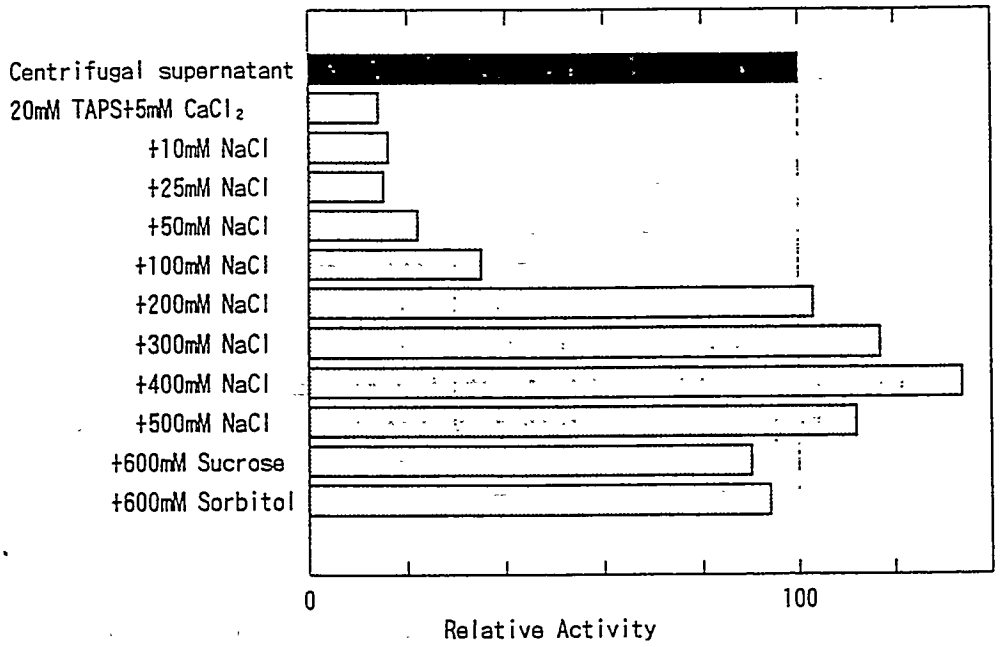

Fig. 3-3 Dependency of nitrogenase activity on the concentration of sodium chloride. 40 ml aliquots of culture were harvested at 14 hr after the final onset of light. Cells were collected by centrifugation and resuspended in the same volume of centrifugal supernatant, 20 mM TAPS buffer (pH 8.0) containing 5 mM calcium chloride and various concentrations of sodium chloride. 60 mM sucrose or 600 mM sorbitol for measurements of nitrogenase activity. The cell concentration in the reaction mixture was 118 μg cdw/ml.

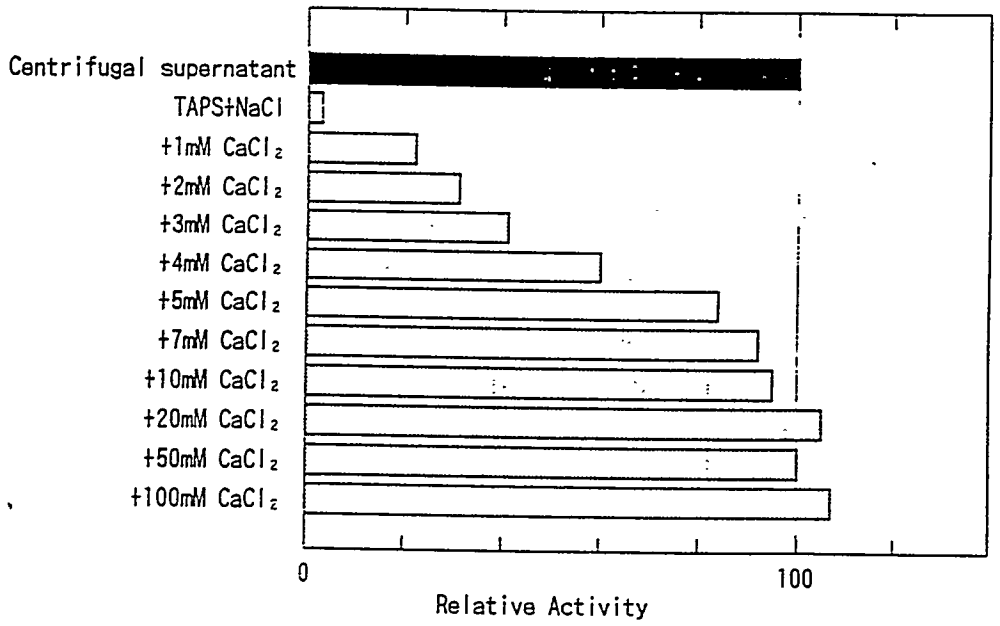

Fig. 3-4 Dependency of nitrogenase activity on the concentration of calcium chloride. 40 ml aliquots of culture were harvested at 14 hr after the final onset of light. Cells were collected by centrifugation and resuspended in the same volume of centrifugal supernatant or 20 mM TAPS buffer (pH 8.0) containing 300 mM sodium chloride and various concentrations of calcium chloride for measurements of nitrogenase activity. The cell concentration in the reaction mixture was 135 μg cdw/ml.

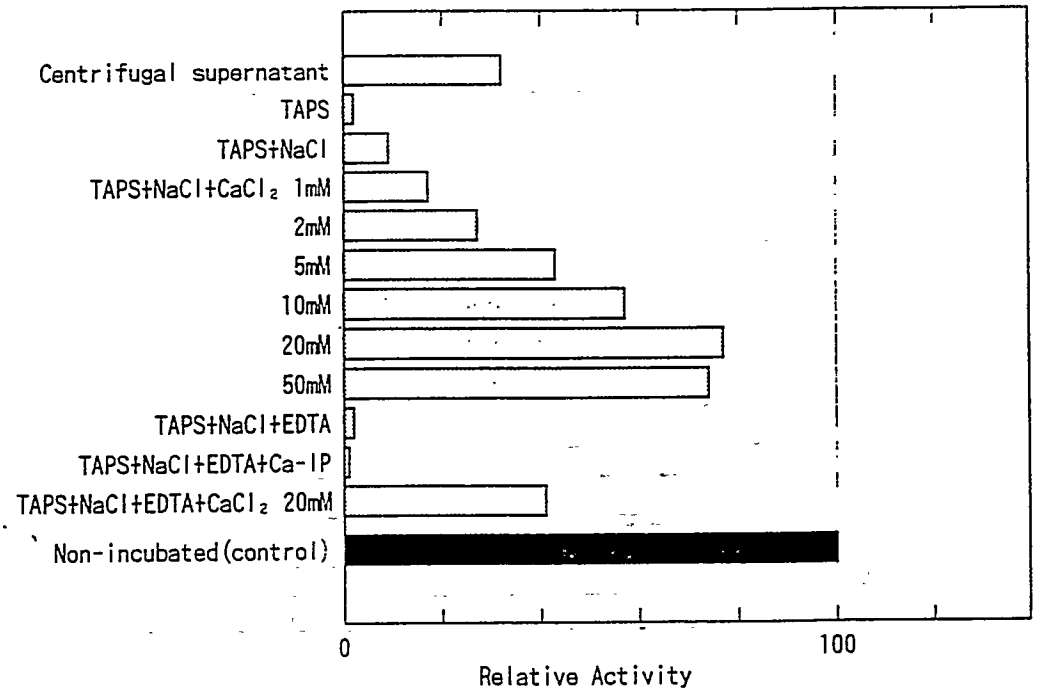

Fig. 3-5 Effects of washing with various solutions on nitrogenase activity. 40 ml aliquots of culture were harvested at 14 hr after the final onset of light. Cells were collected by centrifugation and resuspended in the same volume of centrifugal supernatant or 20 mM TAPS buffer (pH 8.0) containing 300 mM sodium chloride. various concentrations of calcium chloride. 5 mM EDTA and/or 2 μM calcium ionophore A23187. Measurements of nitrogenase activity were carried out after an incubation in each solution for four hours at 0°C. The cells were again collected by centrifugation and resuspended in 20 mM TAPS buffer (pH 8.0) containing 300 mM sodium chloride and 5 mM calcium chloride before the measurements. The cell concentration in the reaction mixture was 155 μg cdw/ml.

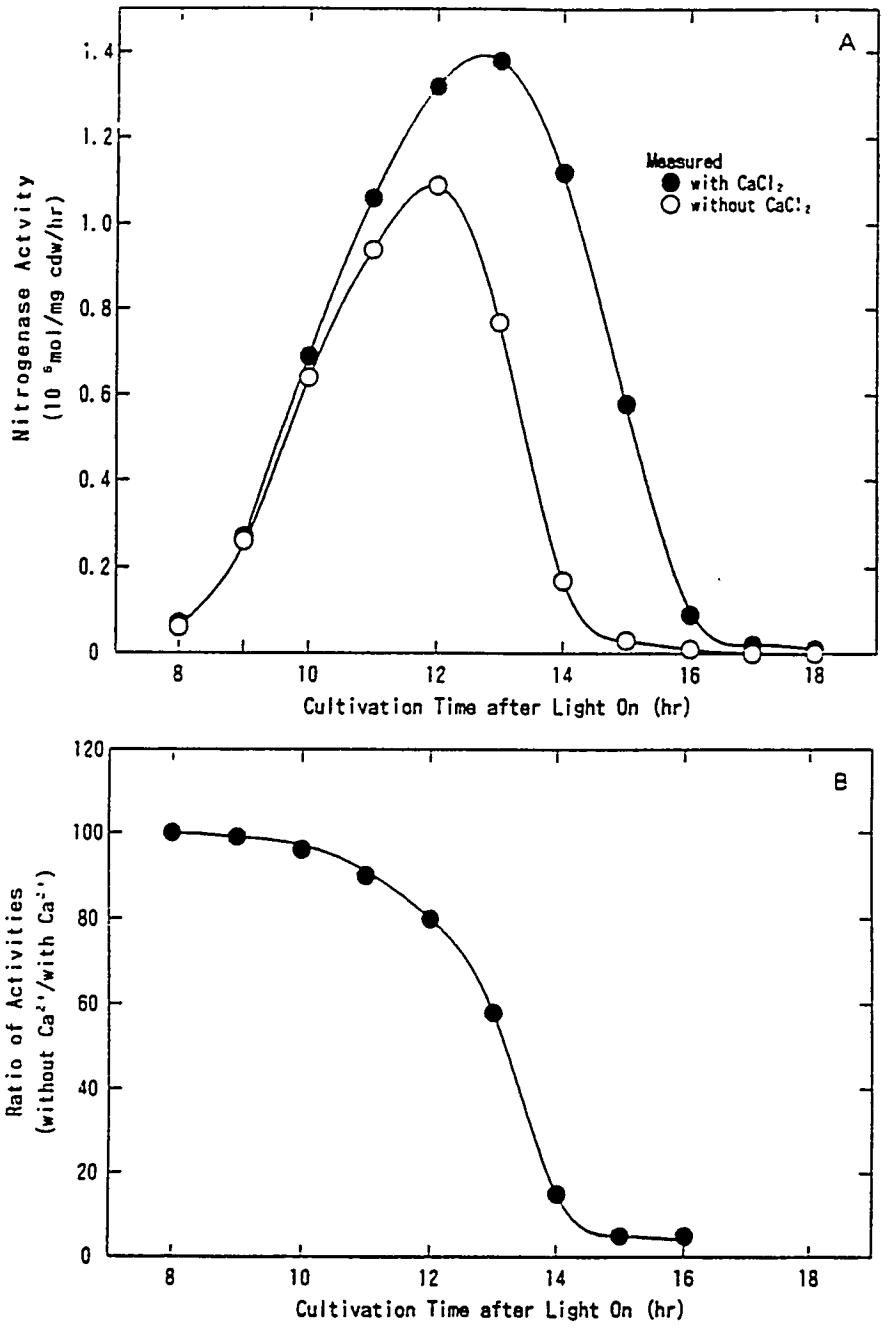

Fig. 3-6 Changes of dependency of nitrogenase activity on calcium ions during a synchronous cultivation. Nitrogenase activity was measured in 20 mM TAPS buffer (pH 8.0) containing 300 mM sodium chloride with or without 5 mM calcium chloride, every two hours during the synchronous cultivation. The cell concentration in the culture was 115 μg cdw/ml at the final onset of light. Activities (A) and the ratio (Ca-/Ca+) of activities (B) are plotted.

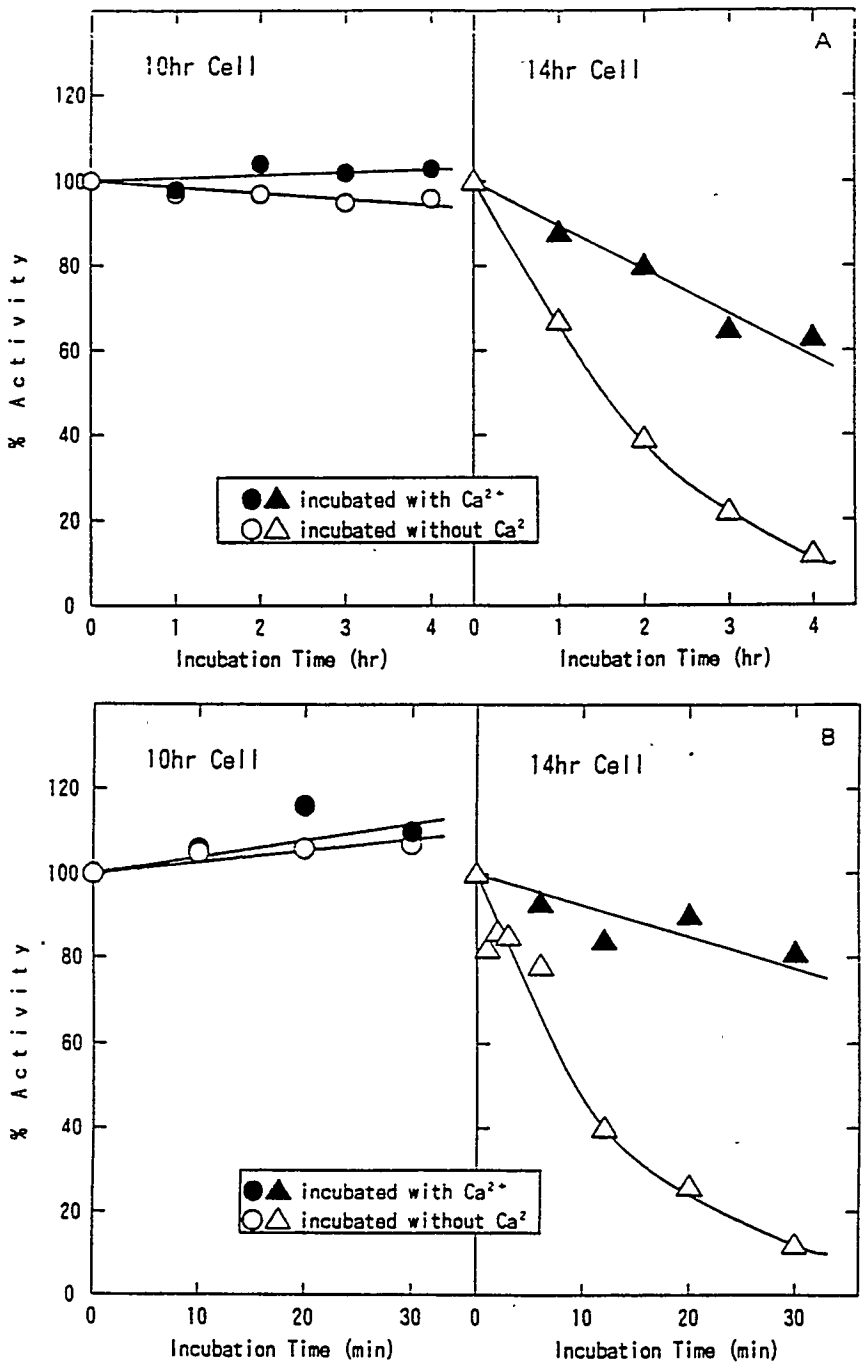

Fig. 3-7 Time courses of inactivation of nitrogenase in the presence or absence of calcium ions. Cells were collected by centrifugation at 10 hr or 14 hr after the final onset of light, and suspended in 20 mM TAPS buffer (pH 8.0) containing 300 mM sodium chloride with or without 5 mM calcium chloride. Incubation was carried out at 0°C (A) or 30°C (B) before measurements of remaining activity in the buffer containing 300 mM sodium chloride and 5 mM calcium chloride. The cell concentrations in the reaction mixture were 125 μg cdw/ml for 10 hr cells and 138 μg cdw/ml for 14 hr cells.

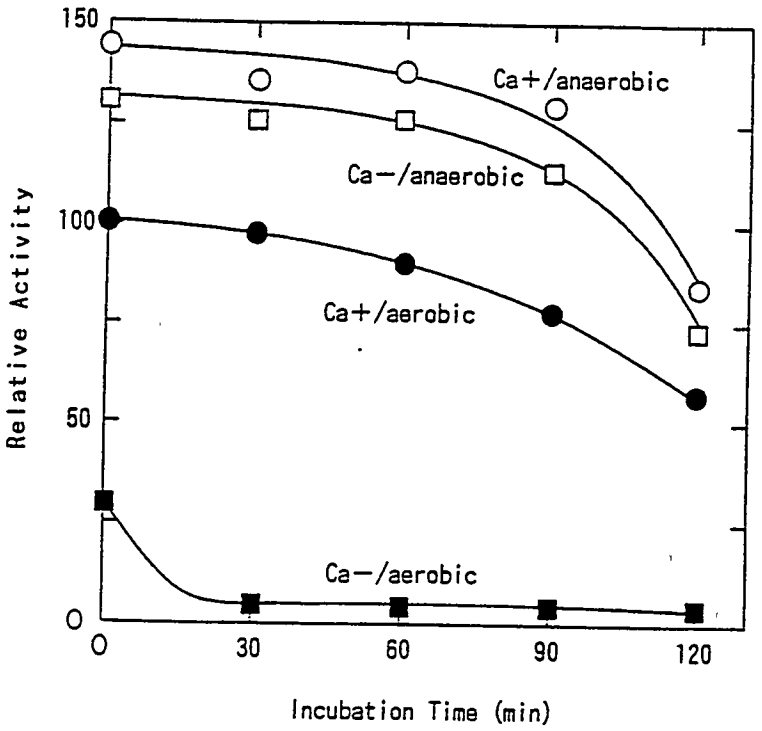

Fig. 3-8 Inactivation under an aerobic or anaerobic condition. Four 50 ml aliquots of culture were harvested at 14 hr after the final onset of light. Cells were collected by centrifugation and resuspended in the same volume of 20 mM TAPS buffer (pH 8.0) containing 300 mM sodium chloride with or without 5 mM calcium chloride. For anaerobic treatments and measurements. solutions were degassed by aspiration and 4 mM sodium thioglycolate was added to remove remaining oxygen. Immediately after suspended in the solutions. the cells were transferred into 100 ml Fernbach flasks fitted with a rubber stopper, and the gas phase was replaced with argon. 5 ml of each suspension was taken with a syringe every thirty minutes during an incubation at 0°C for two hours, and transferred into a 25 ml Fernbach flask filled with argon before a measurement of the remaining nitrogenase activity. For aerobic experiments, the whole procedure except the measurement was carried out in open air without the oxygen absorbent. The cell concentration was 167μg cdw/ml in the measurement.

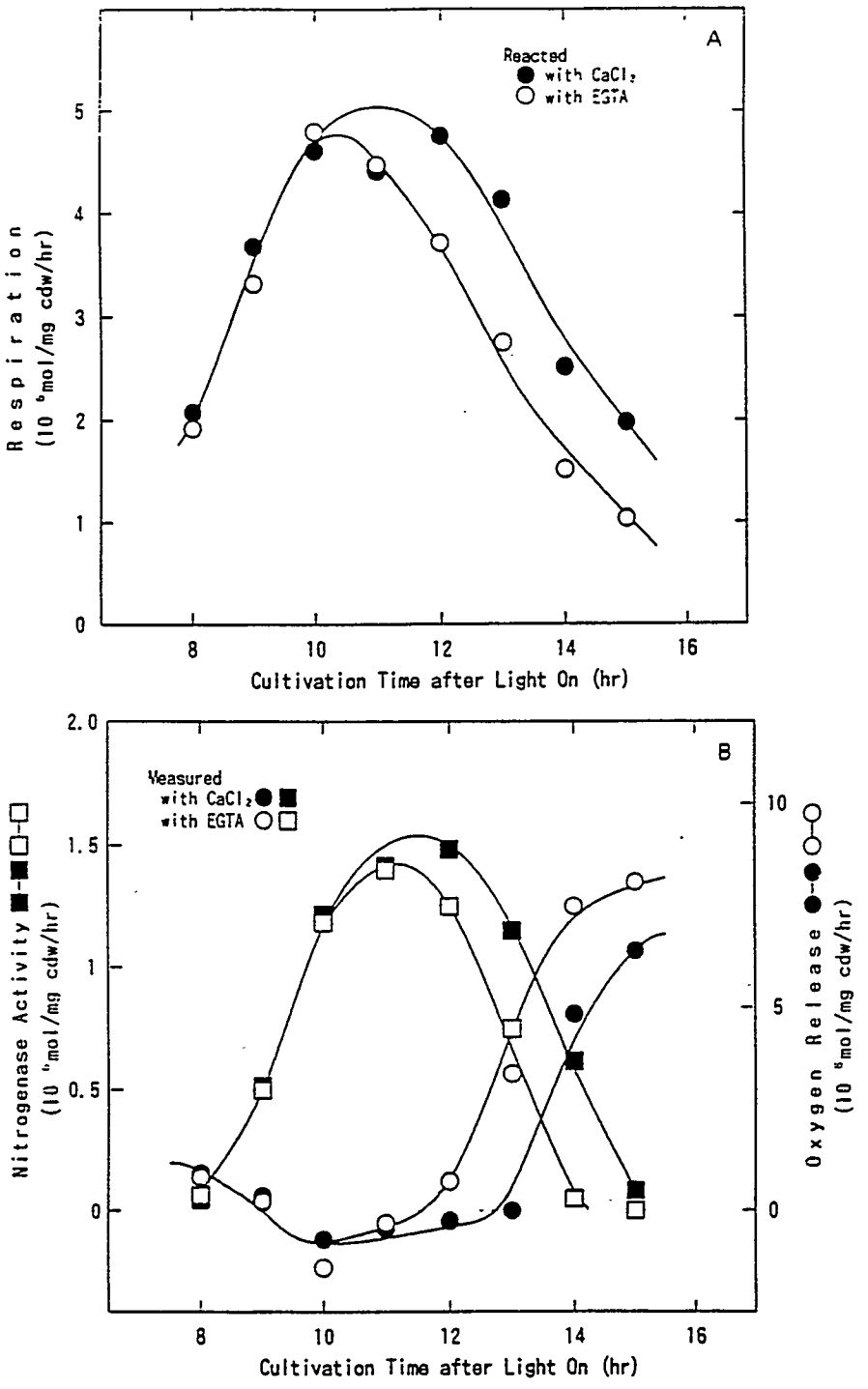

Fig. 3-9 Changes of respiratory activity , nitrogenase activity and net oxygen evolution. Rates of respiration (A), nitrogenase activity (B) and net oxygen release or uptake in the light (B) were measured in 20 mM TAPS buffer (pH 8.0) containing 300 mM sodium chloride and 5 mM calcium chloride or 5 mM EGTA, every two hours during the synchronous cultivation. The cell concentration in the medium was 136μg cdw/ml at 12 hr after the final onset of light.

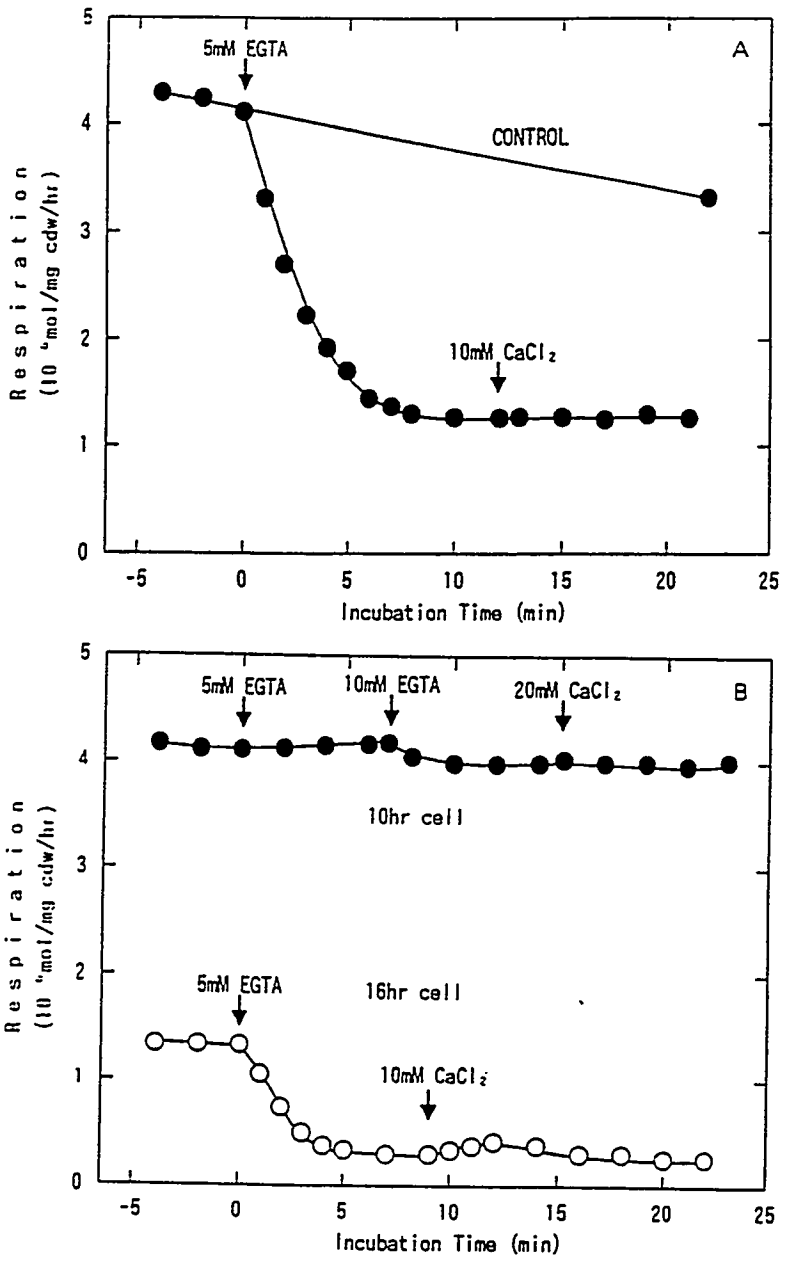

Fig. 3-10 Responses of respiration to elimination of calcium ions. Culture was withdrawn from the cylinder at 10 hr (B), 13 hr (A) or 16 hr (B) after the final onset of light. The rates of respiration were measured on addition of 5-10 mM EGTA or 5-20 mM calcium chloride at the indicated timings. The cell concentrations were as follows; 10 hr cell, 144 μg cdw/ml ; 13 hr cell, 133 μg cdw/ml; 16 hr cell, 129 μg cdw/ml.

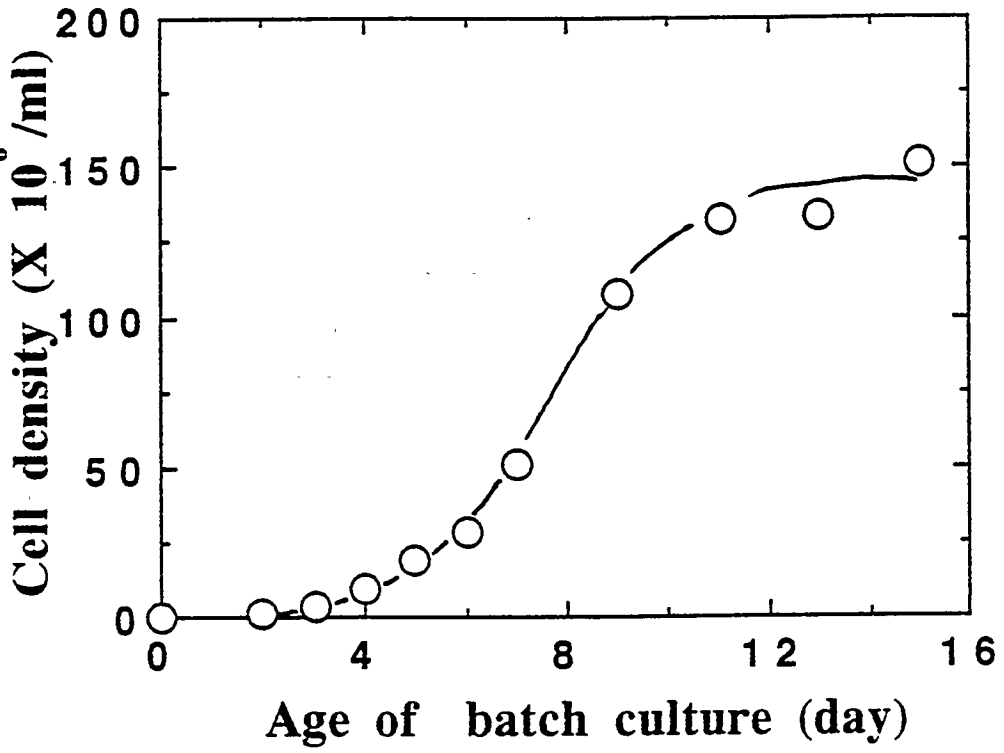

Fig. 4-1 Changes in cell density during growth in a batch culture of *Synechococcus* sp. strain Miami BG 043511. Cells were grown in inorganic medium and illuminated with 150 μE/m²/sec. Cell density was measured by counting the cells under the microscope with a Thoma hemacytometer.

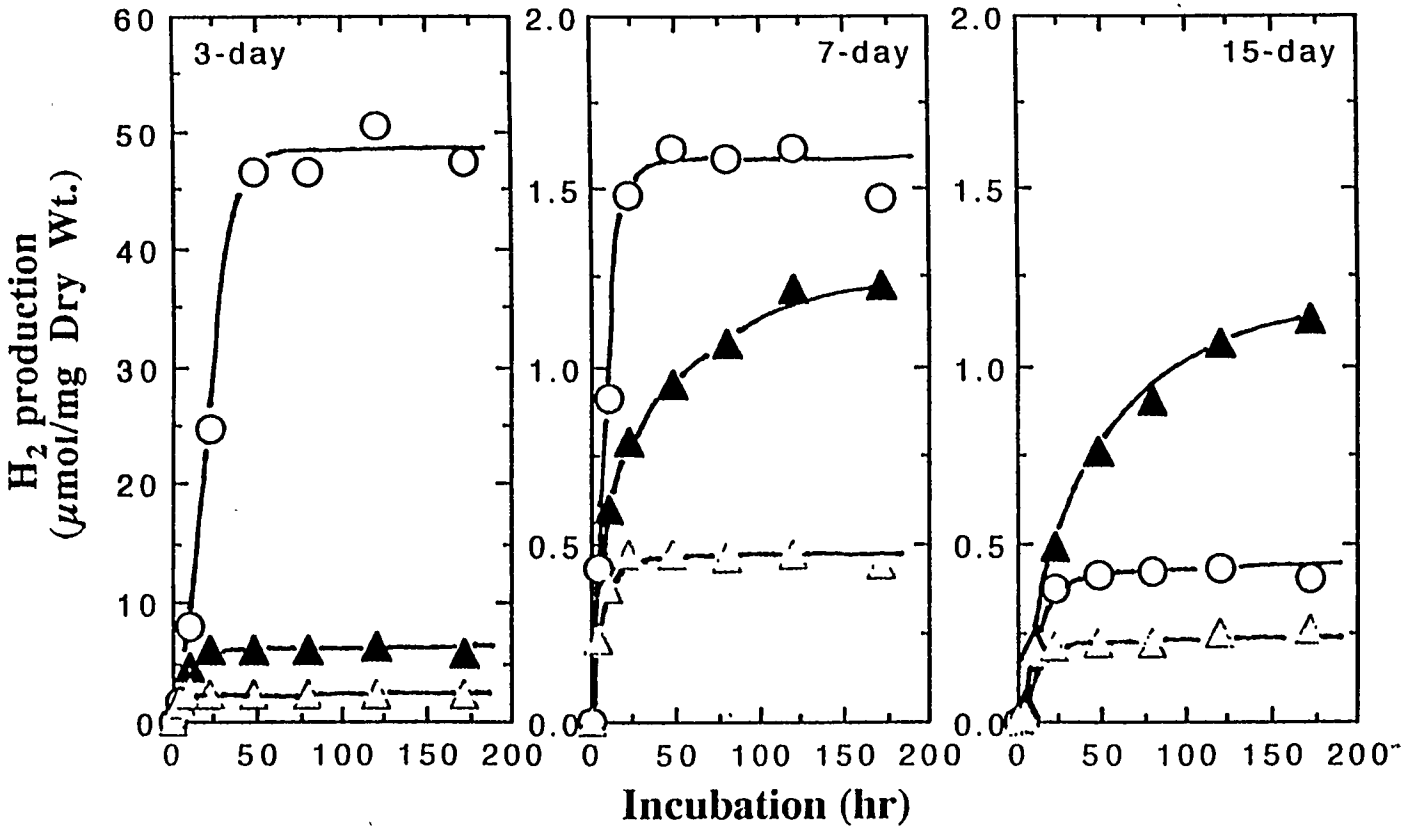

Fig. 4-2 Time course of H_2 accumulation during incubation of 3-days, 7-days, and 15-days old cells. Controls without sulfide addition are indicated by open circles. Final sulfide concentrations were 5 mM (solid triangles) and 25 mM (open triangles). Notice that the scale of ordinate changes.

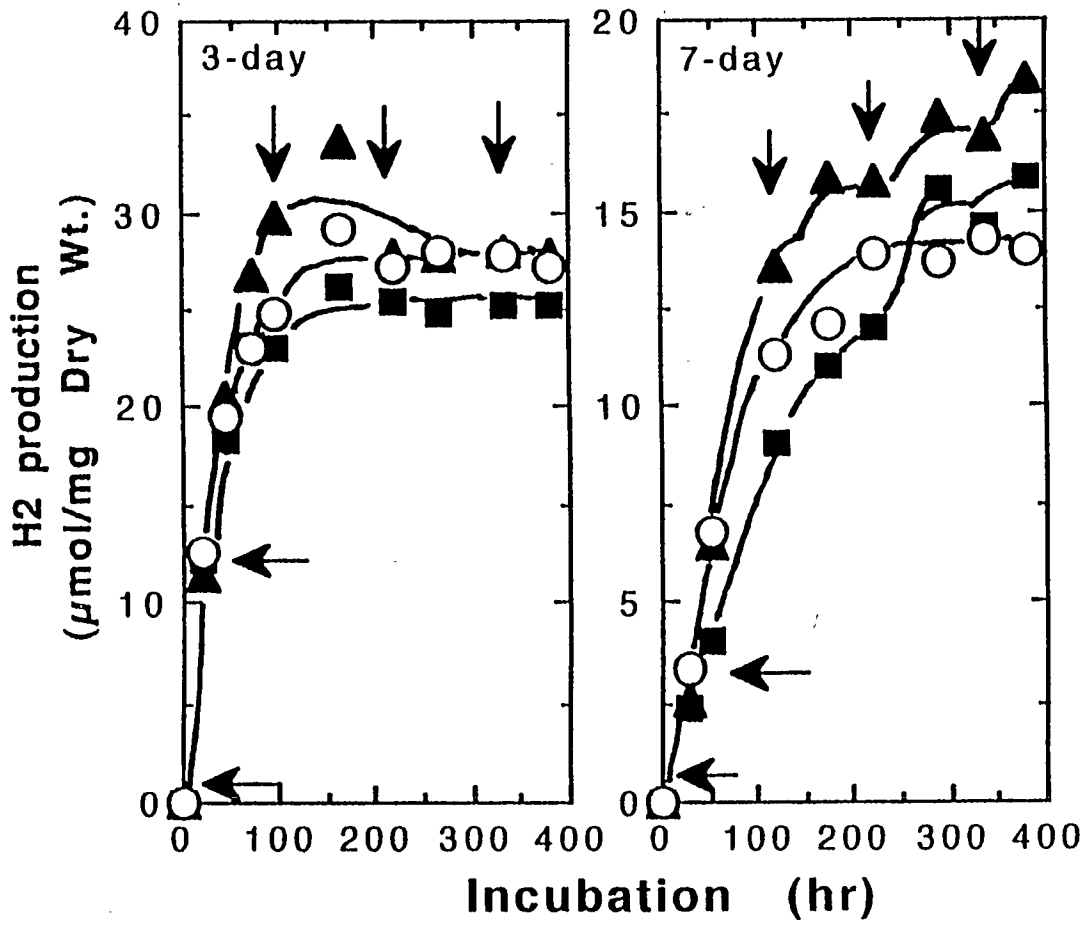

Fig. 4-5 Time course of H_2 accumulation in 3-day and 7-day old immobilized cells. Sodium sulfide solution was gradually (every other day) injected into flask with immobilized cells. Open circles represent controls. Arrows indicate the time of 0.2 mM (solid triangles) and 1 mM (solid squares) of sodium sulfide addition.

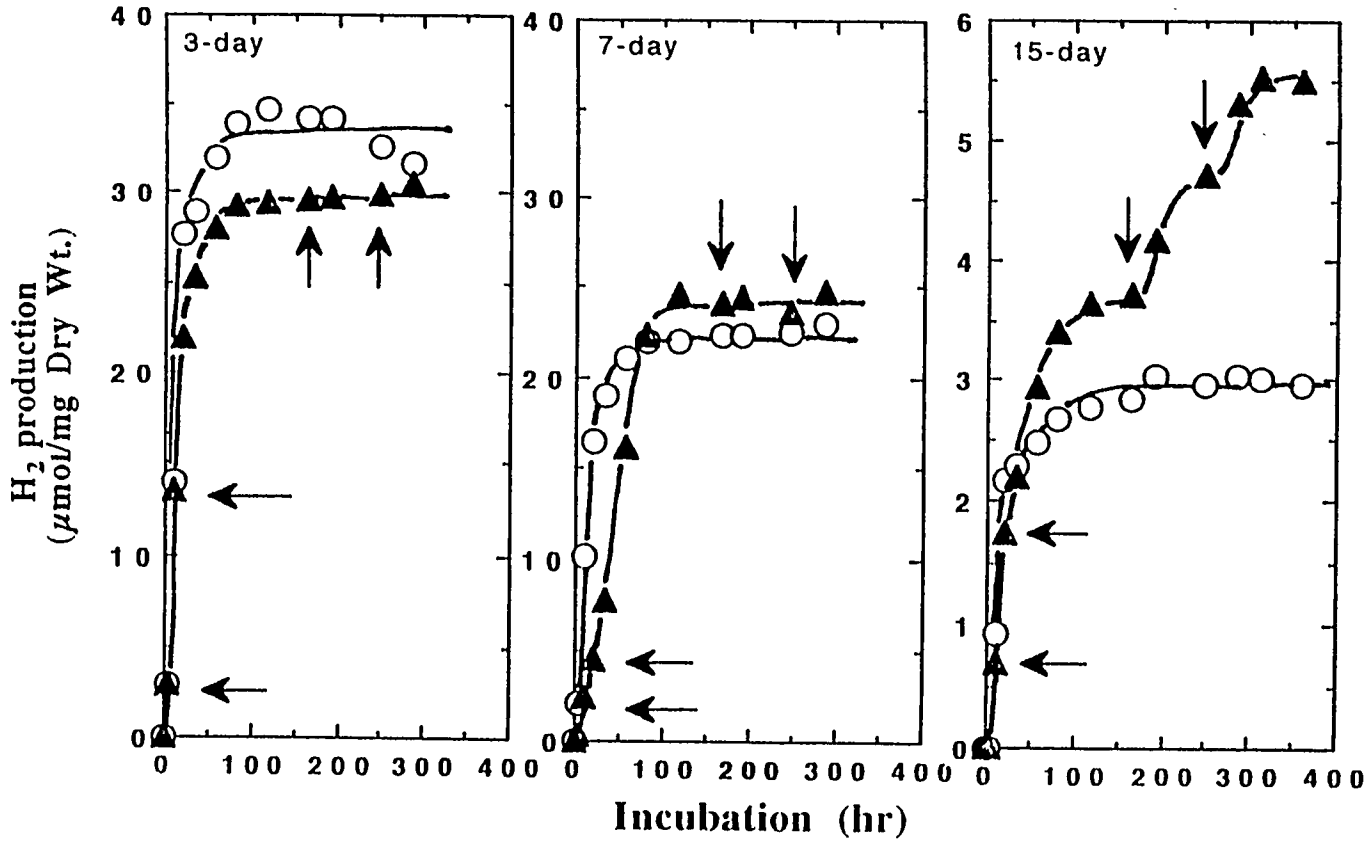

Fig. 4-6 Time course of H_2 accumulation in 3-day, 7-day, and 15-day old immobilized cells during incubation. 2.5 mM (solid triangles) of sodium sulfide solution was gradually (every other day) injected into the flasks. Open circles represent the control.

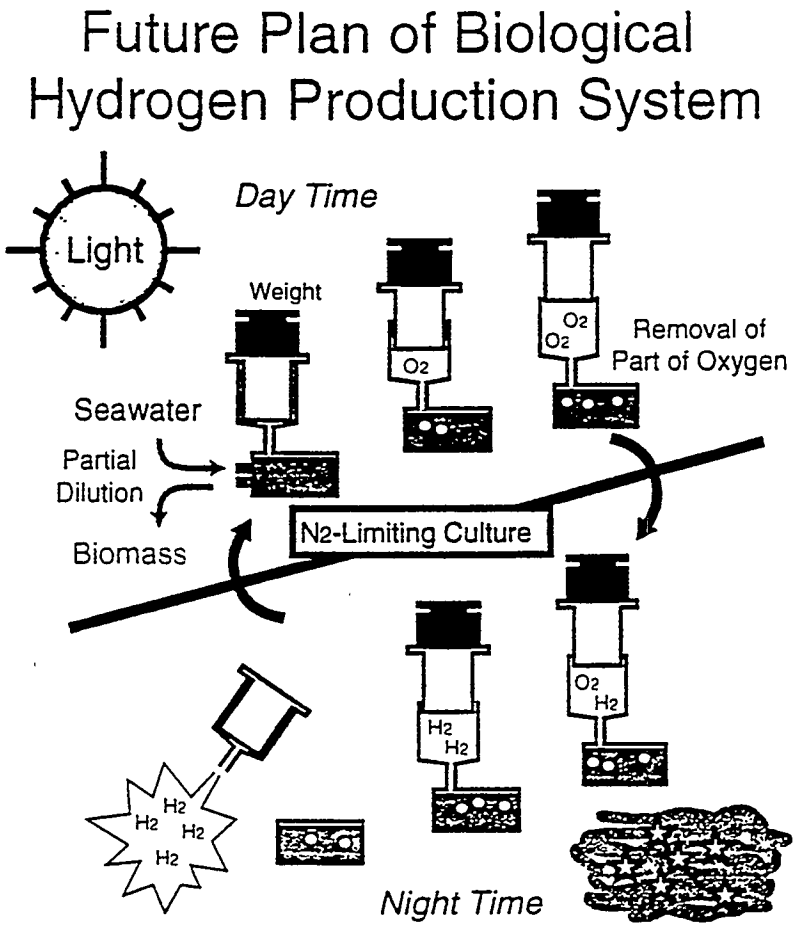

Fig. 5-1 Schematic representation of the future plan of biological hydrogen production system using *Synechococcus* sp. Miami BG 043511.

MICROBIAL HYDROGEN PRODUCTION

P. F. Weaver, P.-C. Maness, S. Martin, S. Muralidharan, and A. J. Frank
National Renewable Energy Laboratory
Golden, CO 80401

Abstract

Photosynthetic bacteria inhabit an anaerobic or microaerophilic world where H_2 is produced and consumed as a shared intermediary metabolite. Within a given bacterial isolate there are as many as 4 to 6 distinct enzymes that function to evolve or consume H_2. Three of the H_2-evolving physiologies involving three different enzymes from photosynthetic bacteria have been examined in detail for commercial viability. Nitrogenase-mediated H_2 production completely dissimilates many soluble organic compounds to H_2 and CO_2 at rates up to 131 μmol $H_2 \cdot min^{-1} \cdot g\ cdw^{-1}$ and can remain active for up to 20 days. This metabolism is very energy intensive, however, which limits solar conversion efficiencies. Fermentative hydrogenase can produce H_2 at rates of 440 $\mu mol \cdot min^{-1} \cdot g\ cdw^{-1}$ at low levels of irradiation over indefinite periods. The equilibrium for this activity is low (<0.15 atmospheres), thereby requiring gas sparging, vacuuming, or microbial scavenging to retain prolonged activity. Microbial H_2 production from the CO component of synthesis or producer gases maximally reaches activities of 1.5 $mmol \cdot min^{-1} \cdot g\ cdw^{-1}$. Mass transport of gaseous CO into an aqueous bacterial suspension is the rate-limiting step. Increased gas pressure strongly accelerates these rates. Immobilized bacteria on solid supports at ambient pressures also show enhanced shift activity when the bulk water is drained away. Scaled-up bioreactors with 100-200 cc bed volume have been constructed and tested. The near-term goal of this portion of the project is to engineer and economically evaluate a prototype system for the biological production of H_2 from biomass.

The CO shift reaction enables a positive selection technique for O_2-resistant, H_2-evolving bacterial enzymes from nature. Twelve photosynthetic bacterial strains have been isolated which exhibit H_2-producing activity even in the presence of full air. The membrane-bound hydrogenase enzyme has been extracted from membranes and purified extensively. The purified enzyme retains its O_2-

resistance. When added to a thylakoid preparation from spinach along with a redox mediator, electrons generated from water-splitting photoreactions were linked to a photoevolution of H_2. An indigenous electron mediator linking water-splitting to O_2-resistant H_2 evolution is being sought. Genetic constructs of cyanobacterial or green algal hosts with the bacterial hydrogenase and redox mediator will be pursued. The mid-term goal of this aspect of the project is to photobiologically evolve H_2 from H_2O in an economically viable process.

Three patents have been issued (a fourth is pending) on research supported by the Program. Many applications to biological fuel cells and biosensors have been identified. Four follow-on proposals have been written for spin-off applications. Industrial interest has been obtained for possible leveraged efforts on these applications.

Introduction

An economic process for producing hydrogen, whether biologically or chemically based, would ideally be H_2O derived, solar driven, highly efficient, durable, insensitive to hydrogen partial pressure, and inexpensive to build and operate. A complete system fulfilling all of these goals is not currently available. Of the biological options, systems employing intact cells of photosynthetic bacteria are the most advanced. Unlike cyanobacteria or algae, however, photosynthetic bacteria do not oxidize water and therefore do not directly fulfill the first criterion. They do, however, evolve H_2 from biomass (previously generated from H_2O and CO_2). These bacteria employ several different enzymatic mechanisms that may have commercial potential for possible near term applications of H_2 production from biomass. One mechanism that incorporates thermal and biological processes appears particularly promising.

The desired criterion for sustained hydrogen production based on the direct photooxidation of water is the most difficult to achieve. Oxygen production is inherent in the oxidation of water, and the hydrogen-evolving enzymes of cyanobacteria and algae are usually rapidly inactivated by oxygen. A number of newly isolated photosynthetic bacterial strains contain an O_2-resistant, evolving hydrogenase enzyme. This hydrogenase has been partially purified from two strains of bacteria, where it is found tightly bound to membrane fractions. The enzymes utilize a ferredoxin-like electron donor for H_2 production. Genetic transfer and expression of the oxygen-resistant, bacterial hydrogenase enzyme and cofactor in a cyanobacterial or algal host could provide a method for the linkage of photoreduced ferredoxin to an evolving hydrogenase, even in the simultaneous presence of photoevolved oxygen. This type of genetic construct could grow naturally when CO_2 was present, but would concomitantly photoevolve H_2 and O_2 from water in the absence of CO_2. Creation of a recombinant microbe to fulfill all of the ideal criteria listed above is considered an early mid-term goal.

Results and Discussion

Many photosynthetic bacterial strains have at least four, and possibly six, different metabolic pathways with unique terminal enzymes for the production and consumption of H_2. Three *in vivo* metabolisms leading to the production of H_2 from biomass have been examined in considerable detail. A fourth metabolism linking H_2 production to water oxidation has been demonstrated in mixed cell-free extracts and indicates the feasibility of a genetically engineered microbial strain performing the same activity in intact cells.

Biomass-to-Hydrogen via Nitrogenase

Of the intact cell metabolisms of phototrophs that evolve hydrogen, the nitrogenase-mediated reactions have been the most studied. Nearly all isolates of photosynthetic bacteria have a nitrogenase enzyme complex (Weaver et al. 1975), which, in the absence of ammonium ion or dinitrogen gas and in the presence of oxidizable organic materials, functions to reduce protons and evolve hydrogen. A large variety of soluble organic acids, alcohols, and sugars can be nearly totally photoconverted into H_2 and CO_2 by this metabolism. Rates of 131 μmol H_2 evolved·min^{-1}·g cdw^{-1} have been obtained in saturating light. Hydrogen evolution is largely light dependent (Schultz et al. 1985) and strongly exergonic. The hydrolysis of about 4 ATP (largely synthesized in light) is required to generate each H_2 and can drive the gas production to equilibrium pressures in excess of 100 atmospheres. Radiant energy conversion efficiencies (ignoring the chemical energy of the organic substrate) are about 5.3% for the most active strains of photosynthetic bacteria. The best outdoor, solar-driven efficiency is 3.4%. Cultures grown on glutamate as the nitrogen source produced H_2 at linear rates for 7-10 days before *nif*$^-$ strains began to dominate the cultures. Experiments with weekly feedings of N_2 maintained the *nif*$^+$ wild-type genotype dominant and active H_2 production could be observed for more than 30 days. Even with the assumption that the best strains and conditions could be maintained, the maximum solar conversion efficiencies that could be expected are probably less than 10%, however, due to the large energy expenditure of the bacteria in performing this H_2-evolving metabolism. Non-sterile, solar-driven cultures (200-300 liter scale) were susceptible to contamination by sulfate-reducing and methanogenic bacteria growing on the evolved H_2 plus CO_2. Limiting the available fixed nitrogen, including that present in sedimented photosynthetic bacteria, is necessary to limit H_2S and CH_4 evolution by the contaminants. Algal growth is similarly inhibited by this method and also by the strongly reducing conditions. An in-house cost analysis of the process has been performed (Herlevich and Karpuk1982). First year costs for H_2 production, clean-up, and compression are estimated at $24.40 per 10^6 Btu at 5% solar energy conversion and $15.70 per 10^6 Btu at 10% conversion efficiency.

Biomass-to-Hydrogen via Fermentative Hydrogenase

Many strains of photosynthetic bacteria also produce hydrogen from organic substrates by way of a fermentative hydrogenase enzyme when grown in intermittent or low, continuous light (Schultz and Weaver 1982). High, continuous light represses synthesis of the enzyme. The enzyme does not require ATP. It can mediate hydrogen production at rates more than 3-fold those of nitrogenase, or

about 440 µmol H_2/min·g cells. However, it equilibrates at low partial pressures of about 0.1 atmospheres of H_2. The active rates of hydrogen production can thus only be maintained by sparging with inert gas, by vacuuming, or by scavenging with a hydrogen-consuming process. Sparging or vacuuming are considered prohibitively expensive, although closed-loop, spared systems connected to fuel cells may be effective. Methanogenic bacteria strongly contaminate non-sterile cultures. In fact, methanogenic bacteria naturally scavenge the H_2 to such low levels that they are extremely effective in maintaining the H_2 partial pressure considerably below the equilibrium pressure, which functions to "pull" the conversion of organic materials into H_2 and CO_2 and then into CH_4. This apparently natural process is the basis for an NREL patent on solar-enhanced anaerobic digestion (Weaver, 1990).

Biomass-to-Hydrogen via CO-linked Hydrogenase

A unique type of hydrogen producing activity was found in a strain of photosynthetic bacteria (Uffen 1976) that functioned only in darkness to shift CO (and H_2O) into H_2 (and CO_2). We have isolated more than 400 strains of photosynthetic bacteria from local sites that perform this shift reaction in darkness, as does the Uffen strain, but will also quantitatively assimilate CO into new cell mass in light, which makes them easy to grow. We have tested many of our strains for CO shift activity and growth with crude (water-scrubbed only) synthesis gas (primarily CO and H_2) generated from thermally gasified wood chips. In light, the novel photosynthetic bacteria assimilate the CO and H_2 components and a portion of the trace gases. In darkness, all of the isolates respond similarly by shifting the CO component of synthesis gas into additional H_2, thereby leaving a product gas highly enriched in H_2 (with CO_2 and trace pyrolysis gases). No inhibitory effects of synthesis gas on long-term photosynthetic growth were noted. At ambient temperature and pressure conditions and starting from 200,000 ppm of CO in the gas phase, less than 18 ppm of CO remained at equilibrium. The product gas could be fed directly into a phosphoric acid fuel cell with generation of electrical power. No harmful effects to the fuel cell were noted.

Free energy calculations indicate that the shift conversion of CO into H_2 should release about 9.7 kcal per mol. This may be barely sufficient to generate ATP in an energy conserved reaction, depending on the biochemical mechanism employed by the bacteria. Anaerobic, dark growth on CO as the sole source of both carbon and energy is not readily apparent as an increase in cell mass, although slight increases are observed when CO and low levels of non-fermentable yeast extract are simultaneously present. Molar growth yield determinations under the latter condition indicate that 60 mg of new cell material was synthesized per mol of CO shifted into H_2. Assuming a standard Y_{ATP} of 10.5 g cells per mol of ATP, it can be calculated that only one molecule of ATP is synthesized for every 175 molecules of CO shifted. A biochemical mechanism for such a stoichiometry is difficult to envision. Experiments measuring the incorporation of radioactively labeled CO and the effects of phosphorylation uncouplers are inconclusive. Whether energy is conserved or not is important to know for cell replenishment considerations in the design of bioreactors for long-term CO shift activity.

Bacterial catalyzed rates as high as 1.5 mmol H_2 produced from CO per min per g cell dry weight were obtained from vigorously agitated cultures at low cell density. Less actively stirred cells at more

normal cell densities (2-6 g cells per liter) exhibit H_2 production rates of 10-100 μmol per min per g cells, reflecting a limiting mass transfer of CO into solution. Gas pressures of more than 12 atmospheres strongly increased shift rates but were still limiting.

A simple, low energy method to enhance mass transfer of the gaseous substrate has proven to be at least partially effective. Six-mm polyethylene beads were coated with mussel hold-fast protein. About 25% of the amino acid residues of the protein are lysines, which present positively charged quaternary amines to the surrounding environment. Since microbes in solution at neutral pH have an excess number of negative charges on their surfaces, they electrostatically bind to the coated bead surfaces at high concentrations in monolayer films. When the immobilized bacteria on beads are stacked in a column and the bulk water drained away, passage of gaseous CO through the interstitial zone of the column results in its effective shift into H_2. Rates of 0.1-0.5 mmol CO shifted per min per g cells were estimated (bound cells were difficult to quantitate) for a period of about 70 days before the bacterial sorption to the beads was degraded.

Depending on the functional lifetimes of reactor designs using immobilized bacterial cells, we will probably have to replace the bacteria periodically. We are developing electrochemically controlled, ion exchange surfaces to accomplish this. Small conducting particles (e.g., graphite) are being derivatized with electroactive groups (e.g., ferrocenes, quinones, or viologens) that in the oxidized state give the surface positive charge that will electrostatically bind negatively charged bacterial cells. Upon reduction of the electroactive groups to a net neutral or negative charge, the bacteria should be released into an aqueous void volume and washed away. Reoxidation of the surface presents a clean surface for the binding of fresh bacteria to regenerate the water-gas shift activity.

Bacteria readily bind to the positively charged surfaces but are sloughed off after a relatively short period. Preliminary speculation is that the charged groups are degrading in an aqueous environment, perhaps due to hydrolysis of the silanol linkage.

H_2 from Water via Oxygen-resistant Hydrogenase

The photosynthetic bacterial strains that perform the water-gas shift reaction were normally isolated under strictly anaerobic conditions since hydrogen is an essential intermediate in their growth and evolving hydrogenase enzymes are normally rapidly inactivated by oxygen. By intentionally adding oxygen to the enrichment cultures, however, conditions are established that positively select only bacterial strains from nature that have an oxygen-resistant hydrogenase. As a result, far fewer bacterial isolates occur in enrichment cultures under aerobic conditions, but about 12 strains have been isolated by this method. Subsequent testing of these isolates showed relatively small losses in evolving hydrogenase activity over a one or two hour exposure to full air. If the O_2-tolerant hydrogenase enzymes from bacteria could be genetically transferred into cyanobacteria or algae, expressed, integrated into their membranes, and linked to photoreduced ferredoxin in the absence or limitation of CO_2, then a new whole-cell method for the photoproduction of H_2 from H_2O becomes feasible.

The O_2-resistant, CO-linked hydrogenase has been examined in extracts of three different strains of photosynthetic bacteria. It is strongly bound to membrane fractions in all three. Several attempts at hydrogenase extraction with ionic or non-ionic detergents resulted in partial release of the enzyme, which degraded relatively rapidly with time. CHAPS was effective at solubilizing hydrogenase activity without causing degradation. The CHAPS-extracted enzyme has been purified 830-fold on a bacteriochlorophyll basis and 17-fold on a protein basis. Its molecular weight is 58,000 daltons based on gel exclusion chromatography. The oxygen-sensitivity of the purified protein is approximately the same as it is in membranes, retaining more than 50% activity after two hours exposure to full air. Of critical importance to its potential for genetic transfer into an oxygenic phototroph, the enzyme exhibits no direct oxyhydrogenase activity, i.e., H_2 and O_2 do not recombine into H_2O on the enzyme surface. The first X-ray structure of a hydrogenase enzyme was recently reported (Volbeda, et al.1995). It could be very informative to obtain similar primary and quaternary structures for the O_2-resistant hydrogenase to glean information on the mechanism of its resistance.

Before attempting genetic exchange of the O_2-resistant hydrogenase, it is first necessary to determine whether the hydrogenase will couple to photoreductants generated from H_2O photolysis. Adding the bacterial hydrogenase to a thylakoid preparation from a spinach extraction produced very little coupling until methyl viologen, a redox mediator, was also added. Purified samples of two of the six known ferredoxins from photosynthetic bacteria would not replace the methyl viologen. Nevertheless, these data indicate that water-splitting linked to O_2-resistant H_2 production is possible with an appropriate native cofactor. Hydrogen production ceases when oxidized $NADP^+$ is added to the mixed cell-free extracts, thereby implying that normal electron transfer in the phototroph would dominate when CO_2 was present, but H_2 production would commence when CO_2 becomes limiting.

Future Work

Bioreactor designs for enhanced mass transfer of CO from synthesis gas will have a major impact on the economics of the potential technology. Contact times of a few minutes or seconds would dramatically affect costs. Developing stable films of bacteria on high surface area supports in the absence of a bulk water phase and using pressurized gas should increase mass transfer rates to the point where they are no longer limiting. At this point, the bacteria themselves can be genetically enhanced up to 100-fold by overproducing the enzymes responsible for the CO shift into H_2. Dr. S. Markov, who has extensive expertise in immobilized microbial bioreactors, will be joining NREL near the end of April 1995 to aid in achieving these goals.

The now-purified O_2-resistant hydrogenase and carbon monoxide dehydrogenase enzymes can be used in an assay for the natural redox cofactor, which will be purified and characterized. Direct linkage of H_2 production to H_2O-derived photoreductants should then be possible. Attempts at genetic exchange and expression of the bacterial proteins in a cyanobacterial host will follow.

References

Herlevich, A., and M. Karpuk. 1982. SERI/TP-235-1548, 12 pp.

Schultz, J.E., and P.F. Weaver. 1982. *J. Bacteriol.*, 149:181-190.

Schultz, J.E., J.W. Gotto, P.F. Weaver, and D.C. Yoch. 1985. *J. Bacteriol.*, 162:1322-1324.

Uffen, R.L. 1976. *Proc. Nat. Acad. Sci.*, 73:3298-3302.

Volbeda, A., M.-H. Charon, C. Piras, E.C. Hatchikian, M. Frey, and J.C. Fontecilla-Camps. 1995. *Nature*, 373:580-87.

Weaver, P.F. U.S. Patent #4,919,813, issued April 24, 1990.

Weaver, P.F., J.D. Wall, and H. Gest. 1975. *Arch. Microbiol.*, 105:207-216.

Weaver, P.F., S. Lien, and M. Seibert. 1980. *Solar Energy*, 24:3-45.

Weaver, P.F., and A.J. Frank. U.S. Patent #5,208,154, issued May 4, 1993.

Weaver, P.F., and P.-C. Maness. U.S. Patent #5,250,427, issued Oct. 5, 1993.

DEVELOPMENT OF AN EFFICIENT ALGAL H_2-PRODUCING SYSTEM

Maria L. Ghirardi, Stephen P. Toon, and Michael Seibert
National Renewable Energy Laboratory, Golden, CO 80401

Abstract

The objectives of this effort are to generate O_2-tolerant, H_2-producing mutants from the green alga *Chlamydomonas reinhardtii*; test them in a laboratory-scale system for the continuous photoproduction of H_2 under aerobic conditions; and collaborate with Dr. Greenbaum at Oak Ridge National Laboratory (ORNL) to improve the efficiency of H_2 production in intact and cell-free systems. Hydrogen production by green algae has the following significant advantages over other biological systems: ATP production is not required; high theoretical efficiencies are possible; and water is used as the source of reductant with no stored intermediary metabolites. The current practical limitations to using green algae in a photobiological H_2-producing system include the sensitivity of hydrogenases to O_2; the occurrence of a dark back reaction between O_2 and H_2 (i.e., the oxy-hydrogen reaction); competition between the CO_2 reduction and the H_2-producing pathways for electrons from H_2O; the low equilibrium pressure of H_2 release; and saturation of H_2-production at low light intensity. ORNL has been working extensively on the last issue. In this new initiative, we will address the hydrogenase O_2-sensitivity problem in *Chlamydomonas reinhardtii* by generating and selecting for O_2-tolerant, H_2-producing mutants. Our approach will involve treating cell suspensions of *Chlamydomonas* with a mutagen, followed by selection for growth under photoreducing conditions (which favor a functional, O_2-tolerant H_2-consuming hydrogenase), as well as for survival under conditions that favor a functional O_2-tolerant H_2-producing hydrogenase under increasing O_2 stress. The dual approach will allow us to select for mutants that not only show increased O_2 tolerance but may also exhibit decreased levels of the oxy-hydrogen back reaction. Any mutant strain isolated will be characterized in detail and tested for the continuous production of H_2 under aerobic conditions in a bioreactor also to be developed under this project. Finally, we will attempt to transfer the O_2-tolerance trait to organisms being developed at ORNL, either by sexual

reproduction or by molecular genetic techniques. This last approach will be facilitated by using cell wall-less (cw) strains of *Chlamydomonas*, which are more amenable to genetic transformation techniques.

Our efforts to date have included setting up optimal growth conditions for the cw15 strain of *Chlamydomonas*, preliminary measurements of simultaneous O_2 and H_2 evolution in these cells, and studies on the level of O_2 required to completely inhibit H_2 production. Having established these baseline parameters, we will initiate the mutagenesis studies this coming year.

Introduction

This is a new project that was initiated in December 1994. The work done on the project over the last 3 ½ months included project planning, staffing, ordering and setting up of equipment, establishing cultures, and running some preliminary experiments to determine baseline parameters of hydrogen production by oxygen-sensitive, wild-type organisms.

Project Rationale

The desired characteristics of a photobiological H_2 production system are: use of water as the source of reductant; solar-driven; highly efficient; durable/self-replicating; H_2 produced at high equilibrium pressure; and cost-competitive (Weaver et al. 1980). There are three major classes of H_2-producing organisms: photosynthetic bacteria, cyanobacteria, and green algae. Photosynthetic bacteria utilize reductants other than water to produce H_2, in a reaction catalyzed by the enzyme nitrogenase. This reaction is quite energy intensive, requiring at least 4 ATP H_2 produced (Weaver et al. 1979; however, see Weaver et al. in these proceedings). Cyanobacteria also produce H_2 via nitrogenase. However, in this case the source of reductant is H_2O, and the reaction involves the formation of a metabolic intermediate. As a result, the efficiency of H_2 production is at least 9-10 quanta/H_2 (Benneman 1994). Green algae do not contain a nitrogenase, and H_2 production in these organisms is catalyzed by the enzyme hydrogenase. This reaction does not require ATP input, nor the generation of metabolic intermediates. Consequently, higher theoretical conversion efficiencies of 4 quanta/H_2 produced can be achieved.

The Workshop on Photobiological Production of Hydrogen (San Pietro 1994), held prior to the April, 1994 DOE Hydrogen Program Review, identified the following main practical limitations to using green algae as H_2-producers: the sensitivity of the hydrogenase enzyme(s) to O_2 (which is a co-product of water oxidation in photosynthesis); and saturation of H_2-production at low light intensity. Dr. Greenbaum at Oak Ridge National Laboratory (ORNL) has been working extensively on this second issue. Other problems associated with H_2 production by green algae are: the occurrence of a back reaction between O_2 and H_2 (the oxy-hydrogen reaction); and competition between the CO_2 reducing and H_2-producing pathways for electrons from H_2O.

The objectives of this project are to generate O_2-tolerant, H_2-producing mutants from the green alga *Chlamydomonas reinhardtii*; test them in a laboratory-scale system for the continuous

photoproduction of H_2 under aerobic conditions; and collaborate with ORNL to improve the overall efficiency of H_2 production in intact and cell-free systems. This work will ultimately result in the development of a cost effective photobiological system for the direct renewable production of H_2 from water.

Background

The conversion of light energy into chemical energy by photosynthetic green algae occurs through the following steps: light absorption by antenna pigments and subsequent transfer of the excitation energy to special pairs of chlorophyll molecules, the reaction centers of photosystems II (PSII) and I (PSI); charge separation at the reaction centers, followed by linear transfer of electrons through a chain of redox carriers from H_2O to ferredoxin, concomitant with the formation of a H^+-gradient across the photosynthetic membrane; utilization of the H^+-gradient to drive ATP synthesis; and dark fixation of CO_2 by the enzymes of the Benson-Calvin cycle, using the reduced ferredoxin and ATP generated as above.

Ferredoxin plays a key role in chloroplast metabolism, since it is involved in supplying reducing equivalents to a number of metabolic pathways other than carbon fixation, such as sulfate reduction, nitrate reduction, cyclic electron transport around PSI, and H_2-production. Under normal photosynthetic conditions, the H_2-producing pathway is inoperative, due to rapid and complete inactivation of the hydrogenase by photosynthetically-produced O_2 (Erbes et al. 1979). Many of the other pathways can be controlled by the availability of substrates. On the other hand, H_2 production by green algae requires induction of the hydrogenase, accomplished by anaerobic treatment of algal cells in the dark for up to several hours (Weaver et al. 1979; Roessler & Lien 1984).

Hydrogenases in green algae catalyze the reversible H_2-production reaction,

$$2H^+ + 2e^- \rightleftharpoons H_2.$$

The forward reaction is driven by reduced ferredoxin, as discussed above. The back "H_2 uptake reaction" can also take place. The free energy change ($\Delta G°'$) associated with H_2 production by hydrogenase is close to zero, which makes it readily reversible. Unfortunately, hydrogenases can also catalyze the wasteful oxy-hydrogen back reaction,

$$2H_2 + O_2 \rightarrow 2H_2O.$$

As a consequence, H_2 produced in the presence of O_2 can be lost.

A biological approach to solve the hydrogenase O_2-sensitivity was developed about 18 years ago (McBride et al. 1977). The approach uses a genetic selection technique based on the reversible H_2 uptake reaction catalyzed by hydrogenase. Selection of mutants was done under photoreductive conditions and increasing concentrations of O_2. Oxygen-tolerant mutants of *Chlamydomonas reinhardtii* obtained by this technique could withstand up to 8% O_2. Unfortunately, the mutants exhibited the oxy-hydrogen reaction and were not maintained in culture for further study.

Approach

(a) Generation and Selection of Mutants

It is clear that novel approaches are required to develop an O_2-stable hydrogenase in green algae. We will address the O_2-sensitivity problem by generating and selecting for O_2-tolerant mutants of *Chlamydomonas reinhardtii* both under H_2-uptake (as above) and H_2-producing selective pressure. This latter approach may help eliminate the high rates of oxy-hydrogen reaction observed previously.

Our work involves the following steps: growth of *Chlamydomonas* cells under photoautotrophic (photosynthetic) conditions; generation of mutants by treatment of cells with the mutagen nitrosoguanidine (Harris 1989); selection of survivors under H_2 production pressure; and concomitant selection of mutants under photoreductive conditions, as described above (H_2 uptake pressure). Repetitive selection cycles will be done at increasing concentrations of O_2, in order to ultimately select for organisms that can photoproduce H_2 at ambient O_2 concentrations.

(b) Development of a Laboratory-Scale Bioreactor

Once we have successfully isolated an O_2-tolerant, H_2-producing strain of *Chlamydomonas*, we will engineer a laboratory-scale system to test the feasibility of producing H_2 from that mutant on a continuous basis. The system will consist of two compartments: a large, closed H_2-production chamber under low CO_2 partial pressure engineered to favor the hydrogenase pathway from reduced ferredoxin (Cinco et al. 1993); and a smaller open-air regenerative chamber under ambient or high CO_2 partial pressure that allows the culture to rejuvenate. The culture will slowly circulate between the two chambers. Both O_2 and H_2 will be produced concomitantly in the production chamber. Among the technical issues that we will address are: optimal design and scaling of the reaction; potential for immobilization of the cells; collection of gases evolved by the cultures; maintenance of the O_2-tolerance trait, if necessary, by submitting the culture to selective pressure on a regular basis (this particular problem may or may not be significant, depending on whether or not the selected mutant is the result of a readily reversible single point mutation); and separation of O_2 and H_2 produced by the culture. Dr. Greenbaum at ORNL is currently working on the last issue.

© Isolation of the Mutant Hydrogenase Gene and Characterization of the Enzyme

The third step of our work will involve a collaborative effort with ORNL. As discussed above, Dr. Greenbaum has been working on optimizing *Chlamydomonas* H_2 production by addressing the problem of saturation of the reaction at low light intensity. Our objective is to transfer the O_2-tolerance trait that we will develop to the ORNL organisms (or vice-versa), in order to obtain a commercially viable organism. This will require us either to identify and isolate the hydrogenase gene from the O_2-tolerant mutant of *Chlamydomonas* and transform wild-type cells, or use genetic methods to transfer the trait to wild-type cells by sexual reproduction. In order to accomplish successful transformation in *Chlamydomonas*, we have selected a cell wall-less (cw) strain with which to work. The lack of a cell wall facilitates the introduction of foreign DNA (Kindle 1990).

(d) Development of Cell-free H_2 producing Systems

Recent work in Dr. Greenbaum's laboratory has shown that algal mutants lacking PSI can photoproduce H_2 using only PSII (see Greenbaum's paper in these proceedings). We have the capability of isolating PSII membrane fragments, core PSII particles, and PSII reaction centers, all of which lack PSI. These materials differ in their association with a membrane, the size of their light-harvesting antennae, their ability to photooxidize H_2O, and the presence of a stable quinone electron acceptor on the reducing side. Furthermore, ORNL has developed a platinization process that deposits Pt H_2-producing catalyst on photosynthetic membranes (Greenbaum 1985). We are working with ORNL in an attempt to isolate PSII material for bioplatinization. The objective of this task is to investigate the possibility of developing a hybrid artificial water-splitting, H_2-producing system, equivalent to a photochemical diode with an expected efficiency of around 20%.

Results and Discussion

Growth of cells

The first step in our project has been to measure baseline parameters for H_2 photoproduction by wild-type *Chlamydomonas*. To initiate our research, we obtained a cell wall-less strain of *Chlamydomonas reinhardtii* (cw15) from the Chlamydomonas Center at Duke University. Cells are grown photoautotrophically in a high salt liquid medium (Sueoka's medium), modified according to Vladimirova & Markelova (1980). Cell cultures are maintained on agar plates, containing 0.8% agar (Davies & Plaskitt, 1971).

To rapidly initiate this project, we first grew cells on a shaker table, under 3.2 $W \cdot m^{-2}$ cool white fluorescent light at ambient temperature (about 25°C), without any CO_2 supplement. The measured doubling times were about 36 h for the first 4 days following inoculation, using the optical density at 660 nm to monitor cell density (Fig. 1). Since doubling times of as little as 8 h for the cw15 *Chlamydomonas* mutant have been reported (Thompson & Mosig 1984), we transferred the cultures to a controlled temperature (24-25°C) growth chamber, at a light intensity of 11 $W \cdot m^{-2}$. Cell cultures were supplemented with air (0.035% CO_2) throughout the growth cycle. Figure 2 shows a characteristic growth curve under these conditions. Since we observed decreased doubling times of 17.5 hs for the first 4 days after inoculation, it is clear that air supplement increases growth rates. We will next bubble the cell cultures with 1.7% CO_2 to sustain even faster growth rates.

Simultaneous H_2/O_2 production

We have used a 2-electrode (Clark-type) system to simultaneously measure light-induced H_2 and O_2 production by *Chlamydomonas* cells. The detection of H_2 production requires anaerobic induction of the hydrogenase. The procedure that we have developed for activating the enzyme requires: resuspending the cells in a buffer containing 50 mM potassium phosphate and 3 mM $MgCl_2$ at pH 7.2 (Happe et al. 1994) at a final concentration of about 175 µg Chl $.ml^{-1}$ (Roessler & Lien 1982); bubbling the cell suspension with argon for about 30 min in the dark; adding dithiothreitol (DTT) to

a final concentration of about 40 mM in order to maintain reducing conditions (Weaver et al. 1979); incubating the samples in the dark at room temperature for 4-5 hs; and transferring the samples to 4°C for the convenience of overnight storage.

In order to measure H_2 production from the induced samples, we added 12 µg Chl/ml to a small aliquot (2.3 ml) of anaerobic assay buffer (50 mM MOPS, pH 6.8) in the electrode chamber (Roessler & Lien 1982). Immediate H_2 production is detected upon illumination (Fig. 3), but it lasts for only 3-4 min. No substantial H_2 consumption is observed when the light is turned off. Oxygen evolution, on the other hand, is preceded by a 1-2 min lag period upon illumination. It starts slowly and then accelerates gradually to a maximum rate. The rate of O_2 evolution starts to slow after about 10 min. Oxygen is consumed when the lights are turned off. The sample shown in Fig. 3 was not treated with DTT during the incubation period. Addition of DTT affects the rates of O_2 evolution (but not the initial rates of H_2 evolution). However, the presence of DTT allows us to take more than one aliquot from each sample without inactivating the enzyme by exposure to air.

Rates of up to 100 µmoles $H_2 \cdot mg\ Chl^{-1} \cdot h^{-1}$ in *Chlamydomonas* have been reported (Weaver et al. 1979, Weaver et al. 1980). The maximum rates of H_2 evolution that we have measured thus far are of the order of 35-42 µmoles $H_2 \cdot mg\ Chl^{-1} \cdot h^{-1}$. However, our assay conditions have not as yet resulted in completely anaerobic conditions. In order to investigate the effect of O_2 on hydrogenase activity, we measured rates of H_2 evolution in the presence of different initial concentrations of O_2 down to about 0.3% (Fig. 4). These values were taken after a 2-minute exposure of the sample to each O_2 concentration. The data were fitted to a single exponential decay curve. From that curve we estimated both V_0, the initial rate of H_2 evolution in the complete absence of O_2, and the I_{50} for O_2, the initial concentration of O_2 that inactivates half of the enzyme activity after a 2-minute exposure. These values were of the order of 70-90 µmoles $H_2 \cdot mg\ Chl^{-1} \cdot h^{-1}$ and 0.3-0.46% O_2, respectively. Figure 4 also indicates that complete inactivation of wild-type hydrogenase occurs when cells are exposed to about 2.5-3% O_2 for 2 min. These values agree with previous reports (Erbes et al. 1979; McBride et al. 1979; Weaver et al. 1979), and allow us to establish 3% O_2 as the concentration to be used in our initial mutagenesis selection cycle. The I_{50} for O_2 in selected mutants will be determined and compared to that of wild-type cells.

Platinization of isolated PSII materials

Based on the redox midpoint potential of pheophytin, the primary electron acceptor of PSII, it is possible, from a thermodynamic perspective, for PSII alone to both oxidize water to O_2 and to reduce protons to molecular H_2. In collaboration with ORNL, we demonstrated that PSII core particles can evolve O_2 using positively charged and negatively charged platinum complexes as Hill acceptors. As of yet we have not demonstrated binding of metallic platinum to PSII, a requirement for cell-free H_2 evolution. Fortunately the platinization procedures that we have tried do not destroy water splitting function in PSII core particles, nor affect charge separation in isolated PSII reaction center complexes. We surmise that charged Pt complexes are not suitable for platinization of PSII, and will next attempt to use a hydrophobic Pt compound that can diffuse into the proteinaceous PSII structure, close to the low potential acceptor where the platinization process can be completed.

Conclusion and Future Work

Having established the required baseline parameters for H_2 photoproduction by wild-type *Chlamydomonas* cells, we will proceed with the mutagenesis studies. During our first selection step, O_2-tolerant mutants will be selected under an initial $_2O$ concentration of about 3%, using both approaches described above. The O_2 concentration will gradually be increased in subsequent steps up to 21% (O_2 partial pressure in air). We will determine the kinetic parameters for H_2 production by selected mutants at each step, and compare them to values obtained with wild-type cells, in order

to ensure the selection of a true O_2-tolerant mutant. Finally, we will start to design and build a laboratory scale H_2 production bioreactor to test our mutants.

Acknowledgments

The authors would like to thank Dr. Robert Togasaki of Indiana University, Bloomington, Indiana for helpful discussions.

References

Benneman, J.R. 1994. *Feasibility Analysis of Photobiological Hydrogen Production.* 10th World Hydrogen Energy Conference, Cocoa Beach, FL.

Cinco, R.M., J.M. MacInnis, and E. Greenbaum. 1993. "The Role of Carbon Dioxide in Light-Activated Hydrogen Production by *Chlamydomonas Reinhardtii.*" *Photosynth. Res.* 38:27-33.

Davies, D.R., and A. Plaskitt. 1971. "Genetical and Structural Analyses of Cell-wall Formation in *Chlamydomonas reinhardi.*" *Genet. Res.* 17:33-43.

Erbes, D.L., D. King, and M. Gibbs. 1979. "Inactivation of Hydrogenase in Cell-free Extracts and Whole Cells of *Chlamydomonas reinhardi* by Oxygen." *Plant Physiol.* 63:1138-1142.

Greenbaum, E. 1985. "Platinized Chloroplasts: A Novel Photocatalytic Material." *Science* 230:1373-1375.

Happe, T., B. Mosler, and J.D. Naber. 1994. "Induction, Localization and Metal Content of Hydrogenase in the Green Alga *Chlamydomonas reinhardtii.*" *Eur. J. Biochem.* 222:769-774.

Harris, E.H. 1989. *The Chlamydomonas Sourcebook.* New York: Academic Press.

Kindle, K.L. 1990. "High-frequency nuclear transformation of *Chlamydomonas reinhardtii*". *Proc. Natl. Acad. Sci. USA* 87:1228-1232.

McBride, A.C., S. Lien, R.K. Togasaki, and A. San Pietro. 1977. "Mutational Analysis of *Chlamydomonas reinhardi*: Application to Biological Solar Energy Conversion." In *Biological Solar Energy Conversion.* New York: Academic Press.

Roessler, P., and S. Lien. 1982. "Anionic Modulation of the Catalytic Activity of Hydrogenase from *Chlamydomonas reinhardtii.*" *Arch. Biochem. Biophys.* 213:37-44.

Roessler, P.G., and S. Lien. 1984. "Activation and *De Novo* Synthesis of Hydrogenase in *Chlamydomonas.*" *Plant Physiol.* 76: 1086-1089.

San Pietro, A. 1994. *Photobiological Production of Hydrogen*, Workshop for photobiological H_2 production: Report to the Department of Energy. Livermore, CA.

Thompson,R.J., and G. Mosig. 1984. "Light and Genetic Determinants in the Control of Specific Chloroplast Transcripts in *Chlamydomonas reinhardtii*." *Plant Physiol.* 76:1-6.

Vladimirova, M.G., and A.G. Markelova. 1980. "Autotrophic Growth of the Cell-wall-free Mutant *Chlamydomonas reinhardii* CW-15 under Conditions of Intensive Culture." *Sov. Plant Physiol.* 27:878-889.

Weaver, P.F., S. Lien, and M. Seibert. 1979. "Improved Hydrogen Photoproduction from Photosynthetic Bacteria and Green Algae." In *Proceedings of the Fifth Joint US/USSR Conference of the Microbial Enzyme Reactions Project*, 461-479. Jurmala, Latvia, USSR.

Weaver, P.F., S. Lien, and M. Seibert. 1980. "Photobiological Production of Hydrogen." *Solar Energy* 24:3-45.

Figure Legends

FIGURE 1. Growth curve for *Chlamydomonas reinhardtii*. Cells were grown on a shaker table, under 3.2 $W \cdot m^{-2}$ cool white fluorescent light and ambient temperature (about 25°C). (A) Optical density at 660nm as a function of time following inoculation of liquid medium with cells. (B) Semi-logarithmic plot of the data shown in (A). The slope of the line is a measure of the first-order rate constant for exponential growth, from which a doubling time of 36 h was calculated.

FIGURE 2. Same as Fig. 1, except that cells were grown in a growth chamber, under 11 $W \cdot m^{-2}$ fluorescent light, at controlled temperature of 24-25°C. The culture was bubbled with air. The estimated doubling time during log phase was 17.5 h.

FIGURE 3. Simultaneous light-induced H_2 and Q evolution. *Chlamydomonas* cells were harvested during the late log phase of growth and concentrated to 175 µg Chl/ml in 3 mM $MgCl_2$ 50 mM potassium phosphate buffer at pH 7.2. The samples were made anaerobic by bubbling with argon for 5 h in the dark. Hydrogen and O_2 evolution were measured in a 2-electrode chamber, by diluting the cell suspension in 50 mM MOPS pH 6.8, to a final concentration of 12 µg Chl/ml. The initial O_2 concentration in the chamber was 0.53%. The arrows indicate when the light was turned ON and OFF. The estimated rates are, respectively 27.5 µmoles $H_2 \cdot mg\ Chl^{-1} \cdot h^{-1}$ and 58.6 µmoles $O_2 \cdot mg\ Chl^{-1} \cdot h^{-1}$.

FIGURE 4. Effect of initial O_2 concentration on the rate of H_2 evolution by *Chlamydomonas* cells. The data were fitted to a single exponential decay equation, from which we extracted V_0 and a first-order constant, k. The rate of H_2 evolution in a completely anaerobic medium (V_0) is 87.22 µmoles $H_2 \cdot mg\ Chl^{-1} \cdot h^{-1}$. The I_{50} for Q, corresponding to the Q concentration which inhibits half of the reaction was, calculated from k and equaled 0.30% O_2.

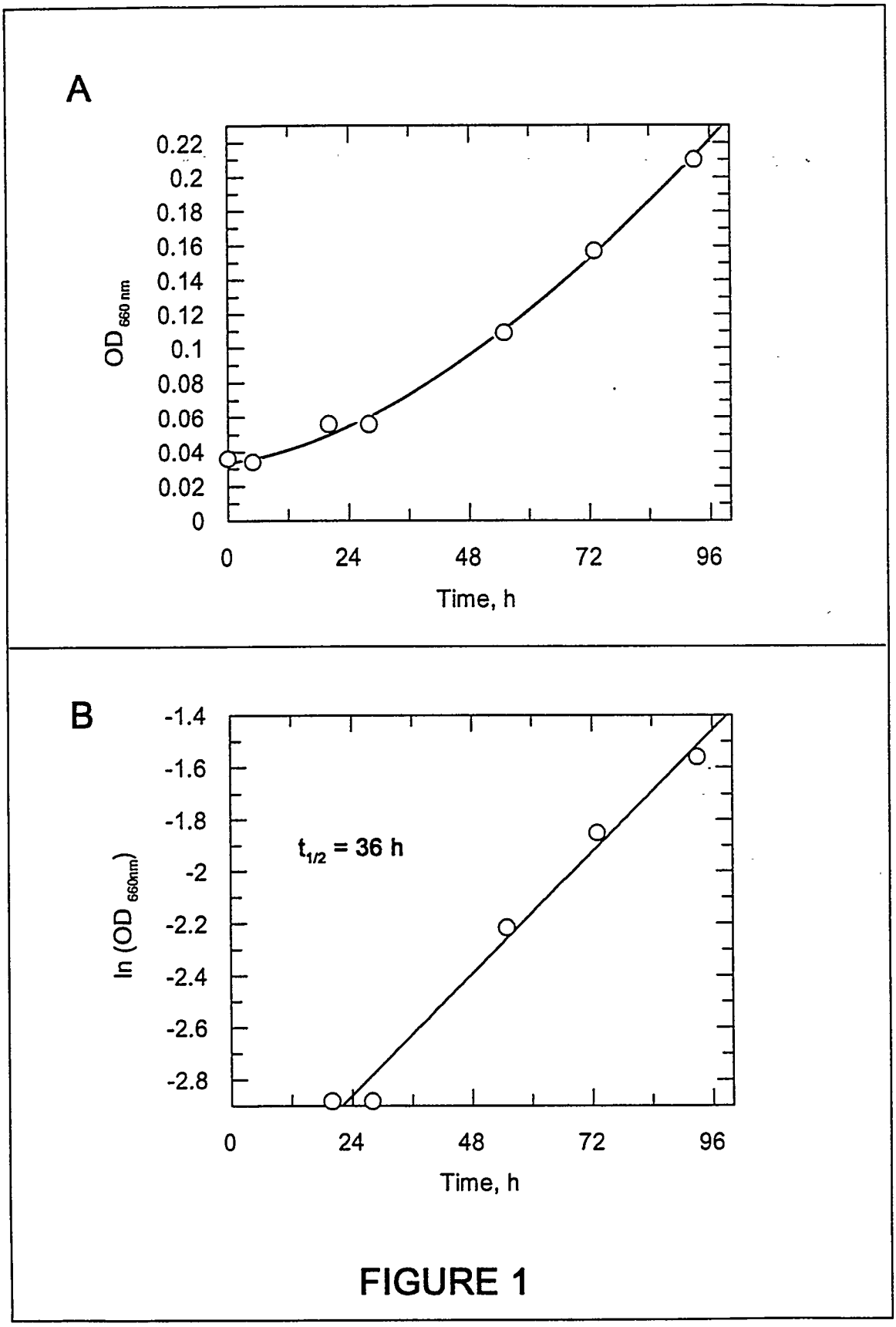
A
0.22
0.2
0.18
0.16
0.14
0.12
0.1
0.08
0.06
0.04
0.02
0
OD 660 nm
0
24
48
72
96
Time, h
B
-1.4
-1.6
-1.8
-2
-2.2
-2.4
-2.6
-2.8
ln (OD 660nm)
t1/2 = 36 h
0
24
48
72
96
Time, h

FIGURE 1

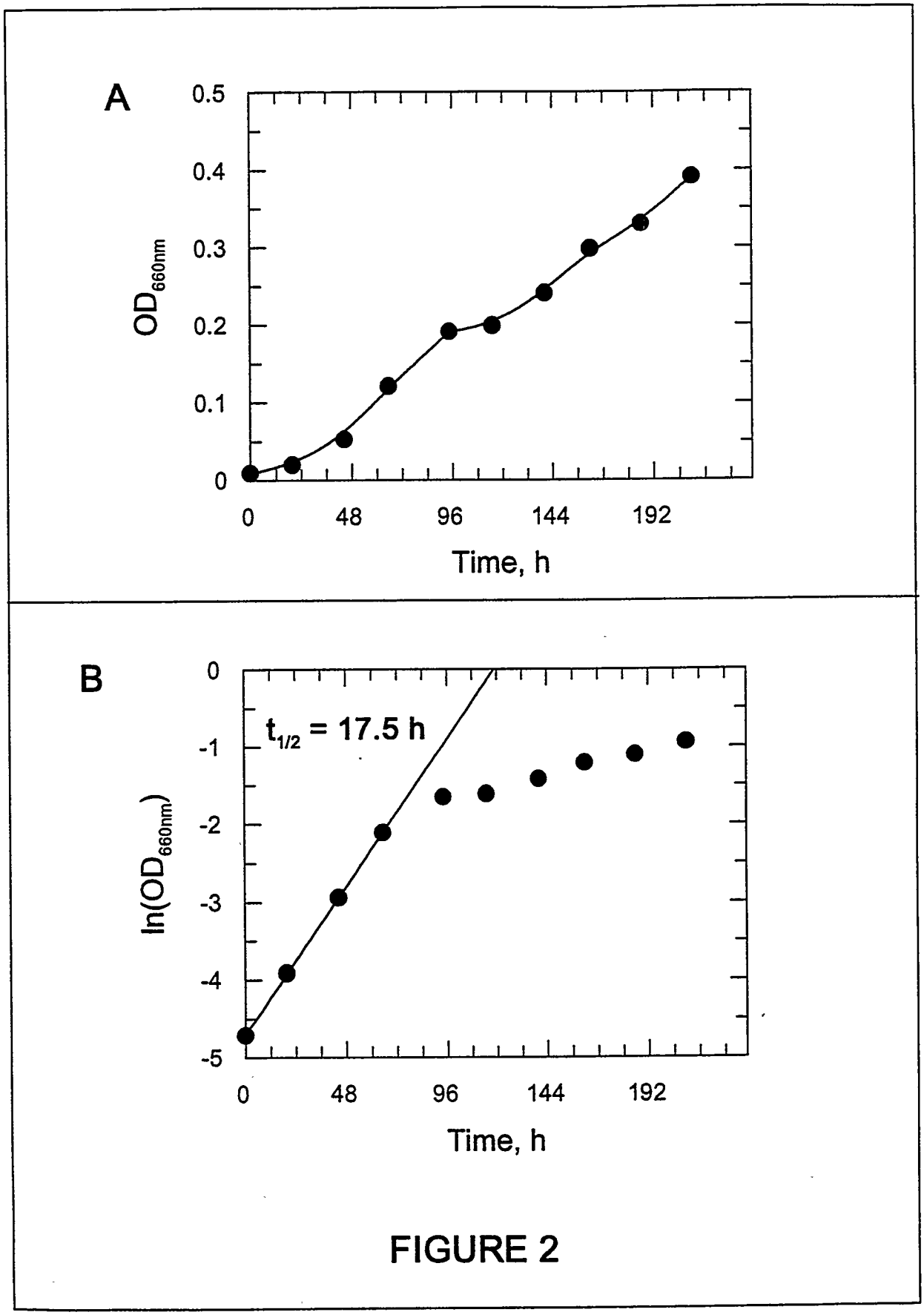
A
0.5
0.4
0.3
0.2
0.1
0
OD660nm
0
48
96
144
192
Time, h
B
0
-1
-2
-3
-4
-5
t1/2 = 17.5 h
ln(OD660nm)
0
48
96
144
192
Time, h

FIGURE 2

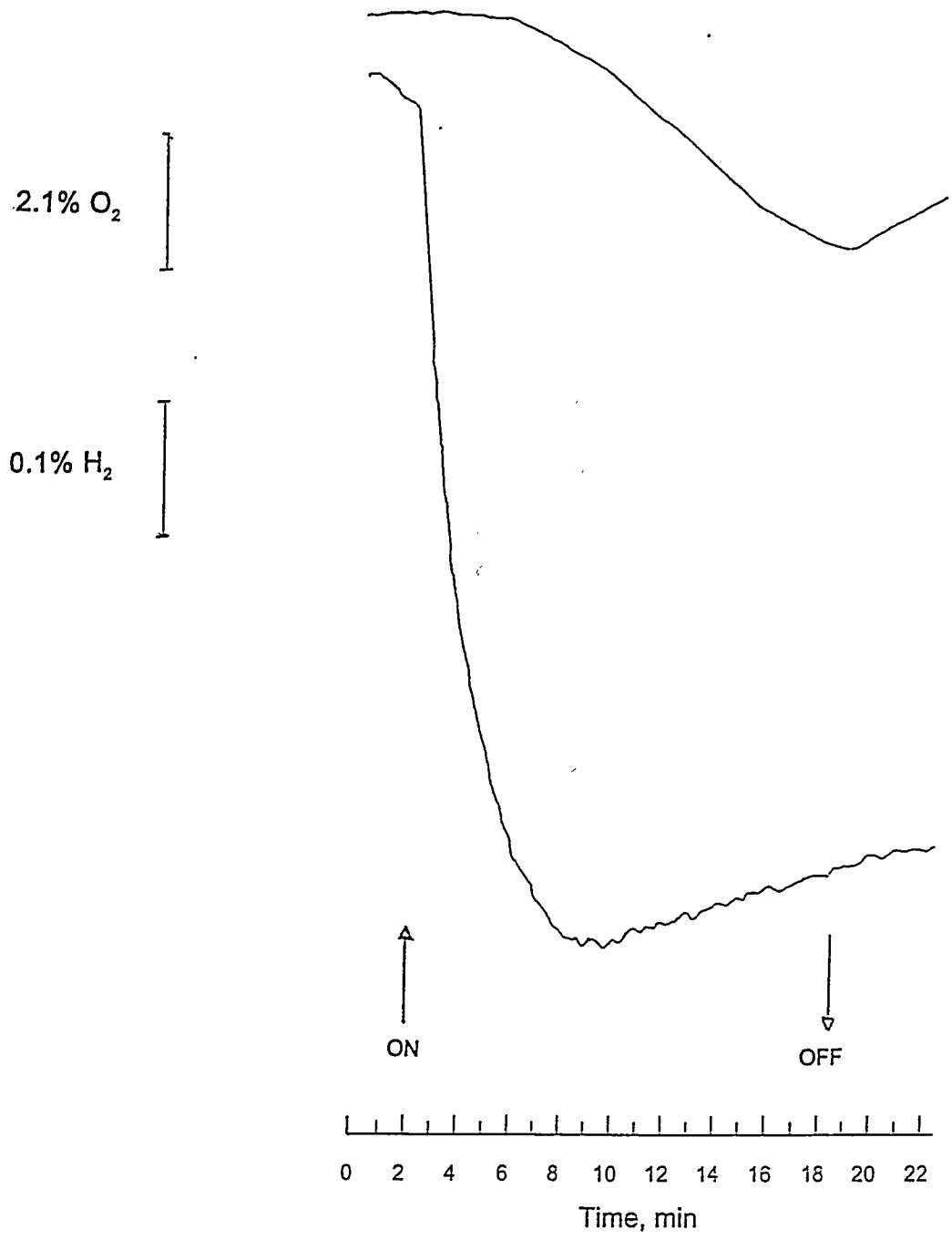

FIGURE 3

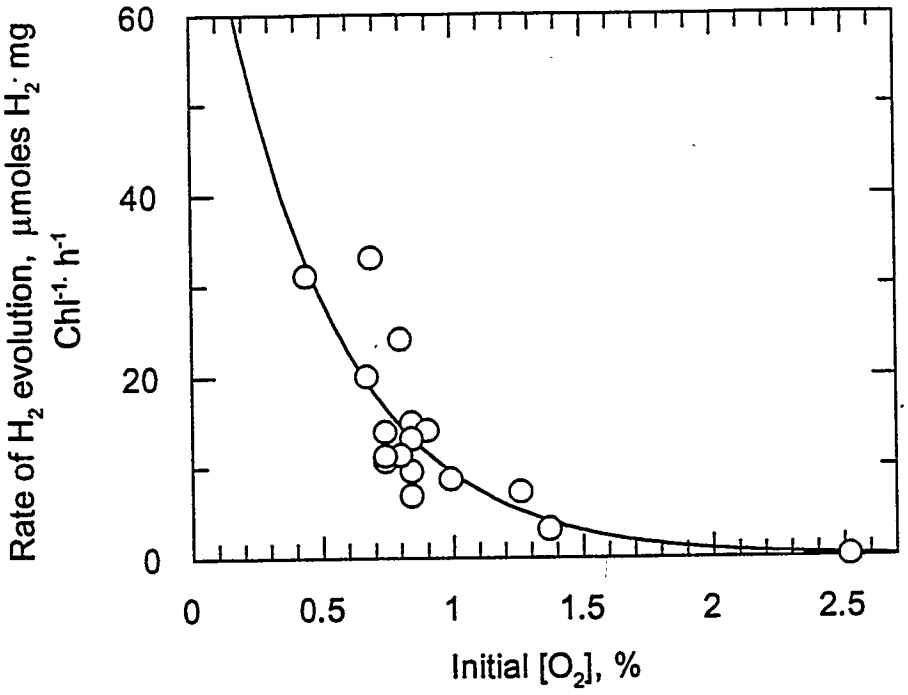

V_0 = 87.22 µmoles H_2 · mg Chl^{-1} · h^{-1}

I_{50} = 0.30% O_2

FIGURE 4

DEVELOPMENT OF SOLID ELECTROLYTES FOR WATER ELECTROLYSIS AT INTERMEDIATE TEMPERATURES

Clovis A. Linkous
Robert W. Kopitzke
Florida Solar Energy Center
Cape Canaveral, FL 32920

Background

Advantages in Performing Water Electrolysis at Elevated Temperature

If an electrolyzer could operate at higher temperatures, several benefits would accrue. The first is that the thermodynamic electrical energy requirement to drive the reaction would be reduced. As shown in figure 1, supplying the total enthalpy of reaction at any temperature involves a combination of electrical and thermal energy inputs. Because of the positive entropy associated with water decomposition, the thermal contribution increases as temperature rises, allowing the free energy requirement to decrease.

Thus the open circuit voltage, V_{oc}, for water splitting drops as temperature rises. At room temperature, V_{oc} for water decomposition is 1.229 V. At 400° C, voltage requirement has dropped to 1.1 V; at 1000° C, it is only 0.92 V. Since electricity is a more expensive form of energy on a btu basis, the more energy taken from the thermal surroundings the better. Moreover, this thermal energy content could be solar-derived. While the cost of solar thermal energy varies in the range of $360-900/peak kilowatt, the installed cost of photovoltaic electricity is in the range of $4,000-5,000/peak kilowatt. Thus if one is compelled to erect an array of photovoltaic panels to generate the e.m.f. necessary to split water, substituting as much area with thermal collectors as possible represents a substantial cost savings.

A second benefit is that activation barriers for the various electrode surface chemical reactions are

more easily surmounted as temperature increases. As it stands now, expensive noble metals are frequently required in electrolyzers to keep cell voltages acceptably close to the thermodynamic value. For a unit operating at higher temperature one may be able to substitute cheaper, less catalytic metals with higher intrinsic activation energies toward O_2 and H_2 evolution.

This same consideration may likely be applicable to the electrolyte itself. Ionic motion in solids is frequently modeled as a hopping process, where the mobile ionic species, in our case H^+ or H_3O^+, makes activation-limited jumps from one binding site to an adjacent one. Thus one could anticipate reduced ohmic overpotential loss from the electrolyte as well.

Current Proton Exchange Membrane Technology

In principle, this type of electrolyzer would include any electrolyte consisting of a polymeric material that could be fabricated into a gas impermeable membrane that could transport ions necessary to support water electrolysis. In practice, proton exchange membrane technology, or PEM, has come to mean those cells employing a perfluorinated hydrocarbon sulfonate ionomer, such as Du Pont's Nafion™. Originally developed as a substitute for other types of cell separators utilized in the chlor-alkali industry, it has come to occupy a place of prominence in the search for more efficient, less expensive ways to electrolytically produce H_2.

To exhibit protonic conductivity, Nafion must be pre-swelled with water, usually by boiling it. In this state it has a conductivity on order of 0.01 $(ohm\text{-}cm)^{-1}$. In comparison to a 1 M HCl solution (0.1 $(ohm\text{-}cm)^{-1}$), it is a factor of 10 too resistive, but can be fabricated and mounted in a cell with much closer tolerances, so that the absolute resistance is comparable. The uptake of water can amount to 28% by weight (Lu 1979).

The water uptaken into Nafion is for the most part free and unbound, since it is quickly lost once temperature exceeds 100° C. By pressurizing the system, one can increase operating temperature; however, by the time temperature has been raised to 150° C, the thermal stability of the perfluorinated ionomer itself is brought into question. The normally light brown or clear membrane irreversibly becomes dark and brittle. Thus currently one cannot operate PEM electrolysis cells at temperatures above 150° C.

The sulfonated ionomer is acidic in nature, and so other components, especially the anode and its external electrical contacts, must have some corrosion resistance. To date this has required that the anode be either a noble metal such as Pt or a transition metal alloy based on Ir or Ru (IEA, 1987).

Development of Intermediate Temperature Solid Electrolytes

At the current level of water electrolysis technology, there exists an 800-900 degree gap, between zirconia-based ceramic membranes at the high end and PEM cells at the low end, in which there are no electrolytic systems suitable for water electrolysis. Even if one includes all of the fuel cell technologies that could possibly be run in reverse, such as phosphoric acid at up to 200° C and molten carbonate as low as 600° C, there still exists a 400 degree gap. In terms of striking a balance between

faster kinetics and lower open circuit voltage by raising temperature, and reducing corrosion and materials compatibility problems by lowering it, operation in the 200-400° C range appears to be desirable.

Most efforts to develop high temperature proton conductors have involved hydrated inorganic oxides (Glasser 1975; Kreuer 1988). A less explored avenue would be to consider engineering polymers, those specialized polymers whose structures allow them to be used in applications requiring extremes of temperature and corrosivity. However, since they were developed for other applications such as flame retardant materials, seals for electronic components in hostile environments, and autoclavable medical supplies (Reisch 1989), their behavior in an electrolytic situation at elevated temperature has not been well characterized.

Previous Work

To date, over 40 different polymeric materials, each known for their thermal and chemical resistance, were examined under steam/O_2 and steam/H_2 conditions. This was done to simulate conditions that would be observed in the anode and cathode compartments of a steam electrolysis cell (Linkous 1992). Of these, several polymer families showed good stability: liquid crystal aromatic polyesters, polybenzimidazoles, and some of the polyimides were stable at 200° C. The polyphenylene sulfides, polysulfones, polyethersulfones, the various polyketones, and some of the polyimides were stable at 300° C. None of the polymers tested could withstand the combination of steam and O_2 at 400° C; however, some of the polyketones did survive at 400° C under the reducing environment.

Mostly recently, emphasis has been placed on selecting a few of the most promising candidates and trying to make ionomers (polymers containing ionic groups) out of them. Performance of some of the more promising base polymer materials is shown below:

Table 1. Thermohydrolytic Stability of Selected Polymers
24 hour exposure to 1:1 H_2/H_2O or O_2/H_2O

Percent Weight Loss

	200° C		300° C		400° C	
sample *	H_2/H_2O	O_2/H_2O	H_2/H_2O	O_2/H_2O	H_2/H_2O	O_2/H_2O
PEEK	-0.5	-0.2	0.5	-15.7	-	-
PES	0.1	0.3	-1.0	-1.1	-12.2	-24.6
PBI	1.8	-3.2	-2.8	-34.4	-	-
FPI	0.2	-0.1	0.6	0.1	-59.9	-79.0
PPQ	0.0	0.1	-1.9	-0.5	-6.2	-87.3

* PEEK=polyetheretherketone; PES=polyethersulfone; PBI=poly(benzimidazole); FPI=fluorinated polyimide; PPQ=polyphenylquinoxaline

The above short list of polymers makes a fair representation of those families that are most likely to succeed as high temperature solid electrolytes. Some of the polymers of interest consisted of 1,4-disubstituted phenyl groups separated by any of a number of linkages:

$$-[X\text{-(phenyl)-}Y\text{-(phenyl)-}Z\text{-(phenyl)}]_n ,$$

where X,Y,Z = -O-, -C(O)-, $-C(CH_3)_2-$, $-SO_2-$, -S-, etc.

for PEEK, X = Y = -O-, Z = -C(O)-;

for PES, X = $-SO_2-$, Y = -O-, etc.

In the present work, our task has been to sulfonate these materials, converting them to ionomers, and then characterize their thermohydrolytic and proton-conducting behavior.

Experimental

H_2O uptake by the ionomer membranes was determined by soaking the films in distilled water for one hour. It is uncertain whether the degree of water uptake so obtained truly constituted saturation - certainly the recommended procedure for swelling Nafion is more severe, involving boiling for several hours. Many of the test membranes, however, were not stable under boiling conditions, and so milder water uptake conditions had to be used.

Degree of sulfonation was determined via a combination of acid/base titrimetry and gravimetry. A dry sample of the test material would be weighed and then thoroughly soaked in 1 M HCl(aq) to completely protonate all of the sulfonic acid moieties contained within. It would then be rinsed with distilled water to remove excess acid and placed in a 3 M NaCl solution. This action would displace all of the labile protons and release them to the surrounding salt solution. The acidified salt solution would then be titrated with standardized NaOH solution. The results were used to calculate either degree of sulfonation (%), with 100% meaning 1 sulfonic acid group per repeating unit, or acid density (milliequivalents/g).

Resistance measurements were made using an a.c. bridge at 1000 Hz. The membrane conductivity cell was patterned after the work done at Los Alamos (Zawodzinski 1991). Sample membranes were suspended in a holder and clamped with platinum contacts at opposite edges. Resistance values so obtained would be corrected by the dimensions of the sample membrane to yield conductivity.

It was decided that since conductivity was a valid parameter in assessing the viability of a candidate membrane, we could use the conductivity bridge in a type of thermal analysis. To perform the "thermoconductimetric" analysis, the conductivity cell was suspended inside a Parr reactor that was

equipped with electrical feedthroughs to enable connection with the a.c. bridge. Temperature was slowly ramped while measuring conductivity. An exponential rise in conductivity was obtained, consistent with Arrhenius-type behavior, as shown for SPEEK in figure 2. In each case, temperature was raised until failure of the membrane occurred. This would be noted by a precipitous drop in conductivity.

Results and Discussion

Ionomer Synthesis and Membrane Fabrication

PEEK

PEEK was sulfonated at various levels between 20%-75% by varying either reaction time or temperature. Typical values of time and temperature employed and the resulting degree of sulfonation are shown in figure 3. The sulfonation was performed by dissolving a sample (10g) of PEEK in concentrated sulfuric acid. Once the reaction time was completed, the reaction was quenched by adding the viscous acid solution dropwise to cold, rapidly stirring water.

Once the polymer had been sulfonated and obtained as solid white strands and droplets, it was usually necessary to convert it into thin sheets for characterization. Films were cast by dissolving the polymer in DMF, casting the solutions in a crystallizing dish, and evaporating the solvent to dryness. Films were hot-pressed to uniform thickness at 100°C and several thousand psi.

PES

Sulfonated PES was prepared using the concentrated sulfuric acid method. The levels of sulfonation obtained were 7%, 17.5% and 29.5%. All attempts to cast films from solvent resulted in cracked films. The suspicion was that the concentrated sulfuric acid used in the reaction was causing some decomposition of the polymer and resulting in shorter chain length. Attempts to sulfonate at greater than 29.5% resulted in H_2O soluble polymers (actually the 29.5% sample was soluble in hot water).

Blends of SPES with commercial PES were made to try and form a non-brittle film. A 1:1 blend of 29.5% SPES and PES gave a film that did not crack. This obviously limits the degree of sulfonation.

Higher degrees of sulfonation were finally achieved using a literature procedure with dissolved sulfur trioxide, SO_3, as the sulfonating agent. By varying the molar ratio of SO_3 to base polymer, 10% and 70% sulfonation levels were obtained.

PBI

Sulfonation of PBI was attempted using the concentrated sulfuric acid method, but was not successful. The polymer simply dissolved and re-precipitated after water dilution without reaction. Sulfonation was subsequently accomplished by soaking membranes, which were cast from a DMF

solution doped with LiCl, in a 10% H_2SO_4 solution and then heating the swollen membrane at 300°C. This was based on a procedure obtained from Hoechst-Celanese (Powers 1986). Initially, the swollen membranes were heated for one hour; this gave very brittle films that were not useful. Shortening the heating period to 1-2 minutes seems to improve the characteristics of these membranes. Attempts to make a membrane pliable enough for trials in the Parr reactor are still underway.

PPQ

Sulfonation of PPQ was also unsuccessful using the sulfuric acid method, but the soak and bake method using 35% H_2SO_4 has produced flexible membranes. The PPQ membranes used in this procedure are obtained from Cemota (Centre d'Études des Matériaux Organiques pour Technologies Avancées). The percent sulfonation (as determined by weight) can be controlled by varying the soaking period.

FPI

EYMYD films were cast from the supplied resin from the Ethyl Corporation and cured according to the prescribed procedure to give the polyimide film. Curing of a free film (not coated on any substrate) caused a crumpling of the membrane.

Attempts to sulfonate the polyimide were made using concentrated H_2SO_4, concentrated H_2SO_4 at elevated temperature, and 30% oleum. In all cases some discoloring of the solution occurred, but no significant dissolution or reaction was observed. The problem seemed to be the resistance of these films to any moisture uptake.

Attempts to sulfonate the diamine portion of the monomer were made using simple dissolution in concentrated H_2SO_4. The diamine dissolved readily and was apparently sulfonated based on ^1H NMR at almost 200% after overnight reaction (one SO_3H group on each of the amine bearing aromatic rings). This sulfonated material would not dissolve in NMP (N-methyl pyrrolidone), however, when an attempt was made to do the polymerization reaction. Reducing the sulfonation reaction time from overnight to 6 hours gave a solid that was soluble in NMP. However, the polymerization reaction run under the hood with dry solvent and dry materials resulted in a brittle film when the reaction mixture was solvent cast. The assumption is that the polymerization reaction is producing low molecular weight polymer which forms a brittle film.

The polymerization reaction was performed using non-sulfonated diamine as a test of the polymerization reaction procedure. Attempts made in both the glove box and in the fume hood did not result in a usable film. Further consultation with the literature will be made before continuing this particular synthetic effort.

Thermoconductimetric Results

SPEEK showed substantial water uptake. At first glance this would be considered a positive attribute, but the moisture uptake also brought on the loss of mechanical properties. At 80°C in the

Parr reactor, a 32% degree of sulfonation SPEEK sample showed a resistance of 75 kΩ at 81°C. At saturation its H_2O uptake was 47% by weight of the original dried film. This corresponds to 25.6 H_2O molecules/sulfonic acid. Upon examination, the membrane had swollen into a gel-like state, and was unusable for further testing. H_2O absorbance was also tested on 20% SPEEK at 80°C to see if it possessed the rigidity to act as a good membrane; this too swelled to a gel-like state and was unusable.

A thick film cast with 10% SPES showed only 3% H_2O uptake and was highly non-conductive (> 1100 kΩ). Films using 70% SPES gave measurable results.

A resistance experiment was done with an SPPQ sample (% sulfonation unknown) which had an H_2O uptake of 23.2%. At 80°C the resistance was in the range of 30-35 kΩ. A second piece of SPPQ (no H_2O uptake information-but it had a longer soaking period) gave a resistance of 1.3 kΩ at 80°C. At elevated temperatures the membrane gave a minimum resistance of 525 Ω at 119°C. The membrane subjected to the higher temperatures (up to 165°C) had completely dissolved (or decomposed) when the reactor was opened up.

A resistance experiment was performed using SPPQ sulfonated at 100% degree of sulfonation (one SO_3H unit/monomer). The H_2O absorbance at this level of sulfonation is 13.8%. This is a rather resistive system, since at 80°C the resistance is 200 kΩ.

A resistance experiment on Nafion 117 was run using the Parr reactor setup; it gave a value of 850 Ω at 81°C and a minimum of 400 Ω at 167°C. The stability of the Nafion in high temperature steam was better than the other sulfonic acid polymers. The temperature reached a maximum of 270°C, and after cooling the reactor down, the membrane remained intact, although discoloration of the membrane had occurred.

A summary of the performance data for the ionomer membranes is shown in Table 2. As was discussed in the synthetic section above, degrees of sulfonation well in excess of the commercial product were achieved. In terms of thermal stability, only the SPPQ compared favorably with Nafion. Activation energies, as determined from the slope of their respective $\ln(\sigma_{H+})$ vs T^{-1} plots, were decidedly higher than that for Nafion, indicating some difficulty in the proton transfer process.

Table 2. Thermoconductimetric Data for Candidate Polymers

Sample	% SO_3H	n (meq/g)	T_{max}	E_{act} (kcal/mol)	σ_{H+} $(\Omega\text{-cm})^{-1}$ 100° C
Nafion	13	0.83	150	0.9	0.18
SPEEK	32,xl	1.02	98	8.1	0.025
SPES	70	2.42	121	6.2	0.022
SPPQ	107	1.87	153	3.9	0.005

Proton conductivities were compared at 100° C. Since the SPEEK membranes were typically unstable at that temperature, a cross-linking reaction using 1,1'-carbonyl diimidazole followed by reaction with bis-(4-aminophenyl) sulfone (Nolte 1993) was performed on a 32% sulfonated sample. Nevertheless, conductivities were below that of Nafion.

The combination of high degree of sulfonation and low conductivity with respect to Nafion points to a difference in conductivity mechanism. Water uptake measurements, while not given for all the samples, were generally quite substantial, commensurate with the high degree of sulfonation. Nafion is a perfluorinated hydrocarbon sulfonic acid ether; the acid is attached to the end of a 6-atom (on average) side chain. The aryl sulfonic acid polymers prepared in this work have sulfonic acid groups attached directly to the phenylene backbone, thus removing that degree of freedom. The base polymers typically have large glass transition temperatures, a good attribute as far as mechanical stability is concerned, but possibly detrimental with respect to proton conduction. Tertiary structure, i.e., how the polymer strands bind to one another, is another attribute that may be important to ionic conduction.

Acknowledgements

The authors would like to thank Dr. Gordon Nelson of the Florida Institute of Technology Chemistry Department for his guidance on this work. Financial support from the U.S. Department of Energy, Office of Advanced Utility Concepts is gratefully acknowledged.

References

Glasser, L. 1975. "Proton Conduction and Injection in Solids." *Chem. Rev.*, 75:21-65.

International Energy Agency Program of Cooperative Research and Development. 1987. *Task IV. Electrolytic Hydrogen Production*, 1986 Annual Progress Report, U.S. Department of Energy.

Kreuer, K. 1988. *J. Molecular Structure*, 177:265.

Linkous, C.A. 1992. "Development of solid electrolytes for water electrolysis at intermediate temperatures," in vol I of *Hydrogen Energy Progress IX. Proceedings of the 9th World Hydrogen Energy Conference*, 419-427. T.N. Veziroglu, et al, eds., Paris, France, June 22-25, 1992, M.C.I., Paris.

Lu, P.W.T., and S. Srinivasan. 1979. *J. Appl. Electrochem.*, 9:269-283.

Nolte, R., K. Ledjeff, M. Bauer, and R. Mülhaupt. 1993. "Partially sulfonated poly(arylene ether sulfone) - A versatile proton conducting membrane material for modern energy conversion technologies." *Journal of Membrane Science*, 83:211-220.

Powers, E.J., G.A. Serad. 1986. "History and Development of Polybenzimidazoles." In *High Performance Polymers: Their Origin and Development*, 355-373. R.B. Seymour and G.S. Kirshenbaum, eds., New York.

Reisch, M.S. 1989. "Electronic Uses Spur Growth of High-Performance Plastics." *Chem. and Eng. News*, 67:21-49.

Zawodzinski, Jr., T.A., M. Neeman, L.O. Sillerud, and S. Gottesfeld. 1991. "Determination of Water Diffusion Coefficients in Perfluorosulfonate Ionomeric Membranes." *J. Phys. Chem.*, 95:6040-6044.

Figure Captions

Figure 1. Energy relationships in water electrolysis.

Figure 2. SPEEK conductivity versus temperature.

Figure 3. Effect of temperature and reaction time on degree of PEEK sulfonation.

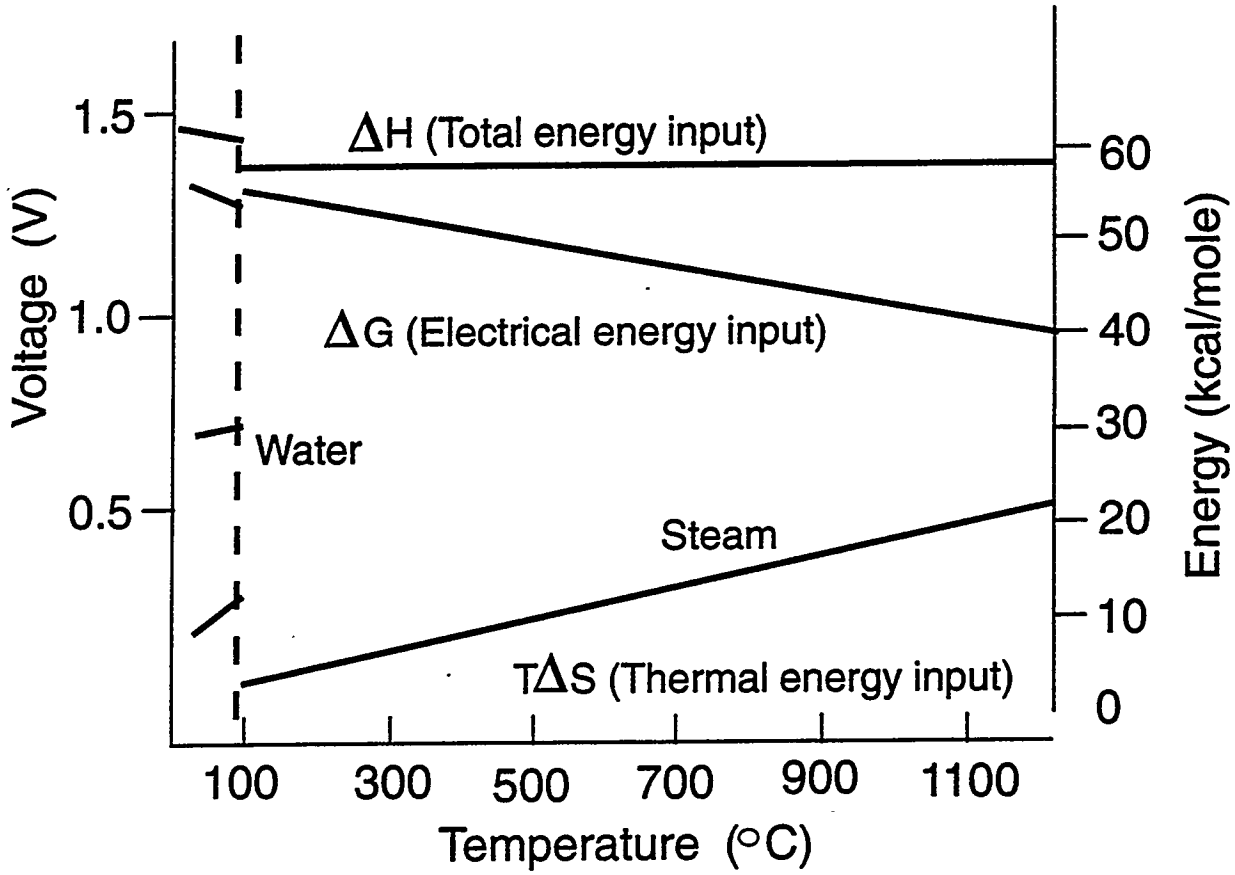
1.5
1.0
0.5
Voltage (V)
ΔH (Total energy input)
ΔG (Electrical energy input)
Water
Steam
TΔS (Thermal energy input)
60
50
40
30
20
10
0
Energy (kcal/mole)
100
300
500
700
900
1100
Temperature (°C)

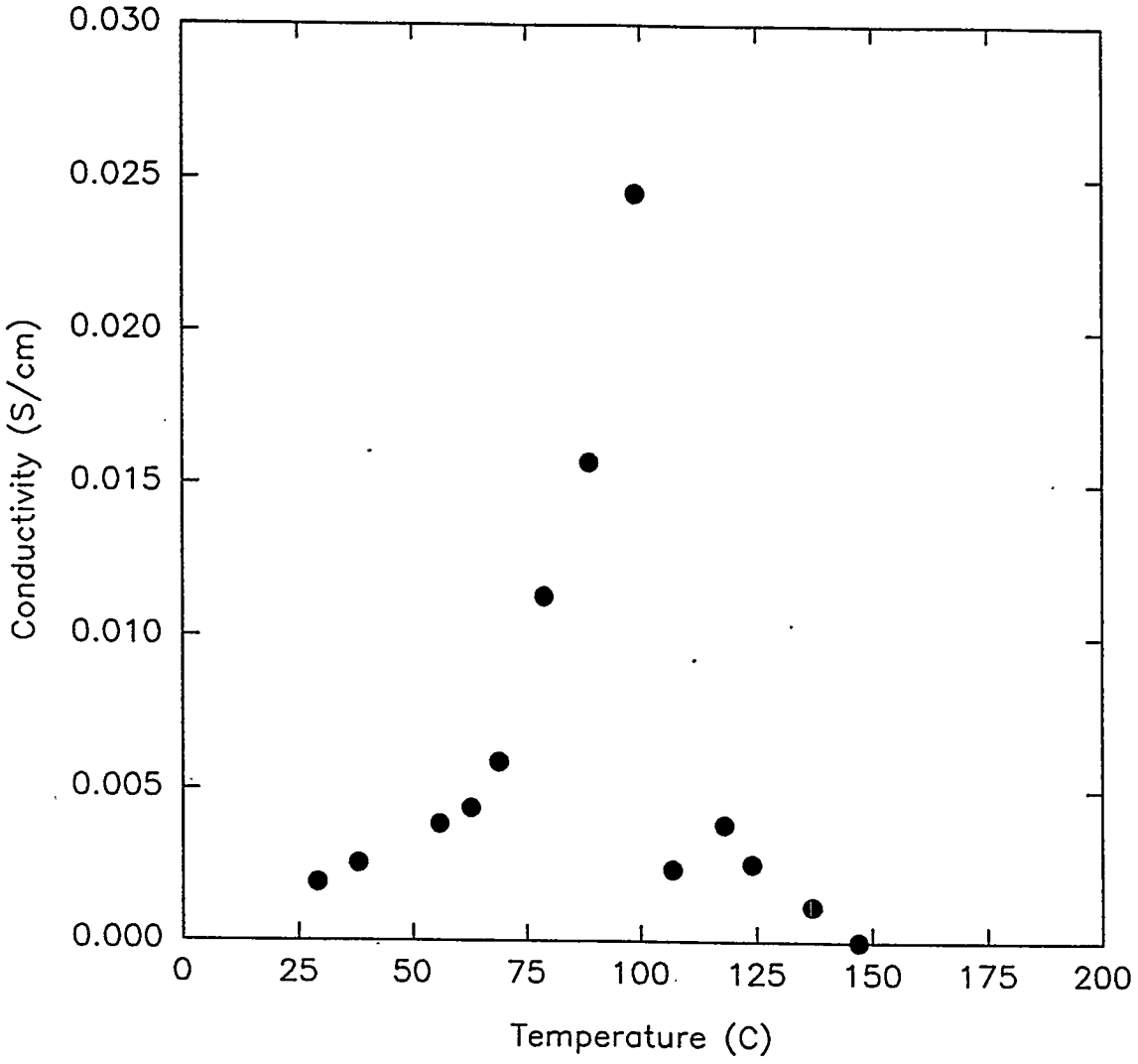
0.030
0.025
0.020
0.015
0.010
0.005
0.000
Conductivity (S/cm)
0
25
50
75
100
125
150
175
200
Temperature (C)

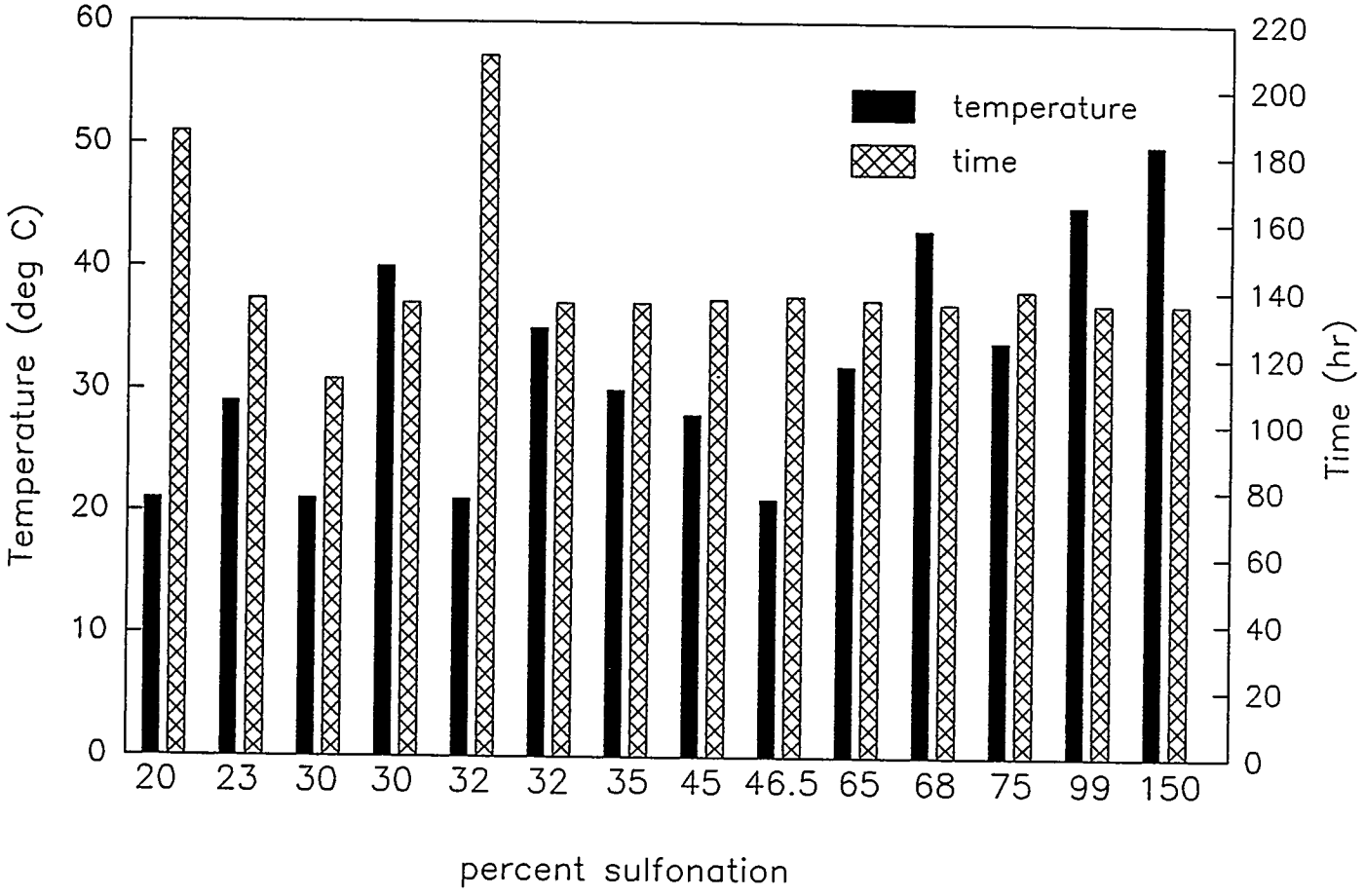
60
50
40
30
20
10
0
Temperature (deg C)
220
200
180
160
140
120
100
80
60
40
20
0
Time (hr)
temperature
time
20
23
30
30
32
32
35
45
46.5
65
68
75
99
150
percent sulfonation

BIOMASS TO HYDROGEN VIA FAST PYROLYSIS AND CATALYTIC STEAM REFORMING

E. Chornet, D. Wang, D. Montané, S. Czernik, D. Johnson and M. Mann
National Renewable Energy laboratory (NREL)
1617 Cole Boulevard
Golden, CO 80401-3303

Abstract

Fast pyrolysis of biomass results in a pyrolytic oil which is a mixture of (a) carbohydrate-derived acids, aldehydes and polyols, (b) lignin-derived substituted phenolics, and (c) extractives-derived terpenoids and fatty acids. The conversion of this pyrolysis oil into H_2 and CO_2 is thermodynamically favored under appropriate steam reforming conditions. Our efforts have focussed in understanding the catalysis of steam reforming which will lead to a successful process at reasonable steam/carbon ratios and process severities. The experimental work, carried out at the laboratory and bench scale levels, has centered on the performance of Ni-based catalysts using model compounds as prototypes of the oxygenates present in the pyrolysis oil. Steam reforming of acetic acid, hydroxyacetaldehyde, furfural and syringol has been proven to proceed rapidly within a reasonable range of severities. Time-on-stream studies are now underway using a fixed bed barometric pressure reactor to ascertain the durability of the catalysts and thus substantiate the scientific and technical feasibility of the catalytic reforming option. Economic analyses are being carried out in parallel to determine the opportunity zones for the combined fast pyrolysis/steam reforming approach. A discussion on the current state of the project is presented.

Introduction

Gasification of carbonaceous materials to yield syngas (a mixture of H_2 and CO once CO_2 and H_2O are removed), followed by shift conversion to convert the CO into H_2 and CO_2, is a well established

process. As well, catalytic steam reforming of hydrocarbons, particularly methane, LPG and naphthas is the traditional way of commercially producing hydrogen.

Recent advances in fast pyrolysis of biomass have prompted us to examine this route as an alternative to gasification. The interest lies in developing a small size technology that would convert residual or dedicated biomass into a "pyrolytic oil" or "biocrude" in high yields (typically 75 wt% of the dry biomass). The biocrude can be transported to a centralized hydrogen production system where catalytic steam reforming will be used to convert the biocrude into H_2. This approach, if technically and economically feasible, will lead to a regionalized system of production of biocrude using relatively small fast pyrolysis units.

The biocrude produced via fast pyrolysis of lignocellulosic biomass is comprised (Elliott, 1988) of about 85 wt% of oxygenated organic compounds and 15 wt% water (dispersed in the organic medium). The organic fraction is a mixture of acids, aldehydes, alcohols, ketones, furans, substituted phenolics and oligomers derived from the carbohydrate and lignin fractions of the biomass. Very little ash and residual carbon (i.e., char) are present in the biocrude when appropriate filtration technology is used in the pyrolysis process.

Results from fluid bed fast pyrolysis of poplar (Piskorz *et al*, 1988; Radlein *et al*, 1991) have shown a 76 wt% yield of biocrude. The organic fraction (~85 wt% of the biocrude) has an elemental composition of $CH_{1.33}O_{0.53}$.

The hydrogen potential of the biocrude, if an adequate reforming technology is developed, will amount to 12.6 wt% of the initial biomass. (Poplar, $CH_{1.47}\ O_{0.67}$, is used as the substrate for this determination).

In order to address the technical feasibility of converting the biocrude into H_2 and CO_2 via catalytic steam reforming, we have initiated a research project with the following objectives:

- determine, using thermodynamic simulations, the conditions under which the components of the pyrolytic oils can be steam reformed to H_2 and CO_2.
- select suitable catalysts to convert the oxygen rich pyrolytic oil into H_2 and CO_2.
- assess, via bench scale experiments, the yields of H_2 (and CO_2) as a function of treatment severity, catalyst type and catalyst time-on-stream
- develop a process flow diagram based on the results obtained
- carry out economic forecasts as a function of feedstocks costs, plant configuration and plant capacity.

In the first year of the project, FY 1994, we addressed the first two objectives (Chornet, *et al*, 1994). The current report covers the work conducted in FY 1995 centered on the mechanistic aspects of the

second objective and the assessment of the results obtained in the newly constructed bench scale catalytic system as part of the third objective. The fourth and fifth objectives are covered as part of a separate effort reported as a distinct paper (Mann, 1995).

Gasification Versus Pyrolysis for Production of Hydrogen

There are two competitive methods for the production of hydrogen from biomass by thermoconversion:

- gasification followed by water-gas shift (WGS) reaction
- pyrolysis, followed by steam reforming of the pyrolysis oils or biocrude.

Gasification is a partial oxidation process that converts biomass into a syngas mixture. The "ideal case" process can be represented as:

$$\text{biomass} + \text{oxygen} \rightarrow \text{carbon monoxide} + \textit{hydrogen} + \text{energy}$$

Additional hydrogen can be generated by a catalytic steam treatment, known as water-gas shift process, of the product gas. Stoichiometry of these reactions is presented as follows:

Gasification: $$CH_{1.47}O_{0.67} + 0.165\,O_2 \rightarrow CO + 0.735\,H_2$$

WGS: $$CO + H_2O \rightarrow CO_2 + H_2$$

$$CH_{1.47}O_{0.67} + 0.165\,O_2 + H_2O \rightarrow CO_2 + 1.735\,H_2$$

Theoretically, the yield of hydrogen produced by gasification is 14.3% (of the weight of biomass). However, the practical yield is lower. Substantial amount of biomass carbon is converted to carbon dioxide by combustion during the gasification step and there is less amount of CO to generate hydrogen through the water-gas shift step. For example, the Renugas process developed by Institute of Gas Technology (IGT) (Evans *et al*, 1988), which is one of the most efficient gasification technologies, generates 0.31 Nm^3 of hydrogen from 1 kg of wood. Assuming that other gas components such as carbon monoxide, methane, and other hydrocarbons could be stoichiometrically converted to carbon dioxide and hydrogen, the hydrogen production would increase by 0.88 Nm^3. This would result in a total hydrogen yield from biomass of 10.7 wt%.

Pyrolysis is a thermal decomposition process occurring in an inert atmosphere in the following way:

$$\text{biomass} + \text{energy} \rightarrow \text{liquid} + \text{gas} + \text{char}$$

The chemical reactions for this method can be summarized as follows:

Pyrolysis: $CH_{1.47}O_{0.67} \rightarrow 0.73\ CH_{1.33}O_{0.53} + 0.16\ H_2O + 0.09\ CH_{0.4}O_{1.25} + 0.18\ CH_{0.8}O_{0.06}$
(wood) (pyrolysis oil) (gas) (char)

Steam reforming: $0.73\ CH_{1.33}O_{0.53} + 1.07\ H_2O \rightarrow 0.73\ CO_2 + 1.56\ H_2$

$$CH_{1.47}O_{0.67} + 0.91\ H_2O \rightarrow 0.73\ CO_2 + 1.56\ H_2 + 0.09\ CH_{0.4}O_{1.25} + 0.18\ CH_{0.8}O_{0.06}$$

Assuming that the steam reforming of the pyrolysis oil is complete the production of hydrogen would be equal to 12.9% of the biomass weight. In reality, the hydrogen yields from both gasification and pyrolysis technologies will be lower than the reported values. Thermodynamics of the water-gas shift or steam reforming reactions does not allow for total conversion of carbon monoxide, hydrocarbons, or pyrolysis oil components to carbon dioxide and hydrogen, unless high amounts of steam are used. With reasonable amounts of steam/carbon (molar ratio per carbon atom of about 5) the expected yield will be around 80% of theoretical.

Advantages and Drawbacks of the Methods. Each of the above methods for generation of hydrogen has its advantages and drawbacks.

Gasification is a more mature technology that has been developed to the stage of demonstration plant and is close to commercialization. Its advantage is that it does not require any external source of energy. Air gasification, especially, is a simple and inexpensive process. However, its application for the production of hydrogen is not very likely because it provides gas highly diluted with nitrogen. Oxygen gasification generates product gas of more favorable composition but is much more expensive than air process because of the cost of pure oxygen which has to be brought to the plant. Steam gasification is highly endothermic and requires an external source of steam via a boiler.

Gasification is a high temperature process carried at 850-950°C. In addition to the gas, it also produces 1.5-3.5 wt% of tars. These tars are mostly comprised of naphthalene, anthracene, and other polycyclic aromatic hydrocarbons (PAH) that pose a serious environmental concern. In contrast to aliphatic hydrocarbons and oxygenated organic compounds, they are very difficult to convert by steam treatment.

Fast Pyrolysis has not yet been developed to the same stage of commercial demonstration as gasification, though several pilot plant units have been constructed and operated in recent years (Ensyn-Red Arrow, Union Fenosa). Pyrolysis is more complex than gasification because it generates a more diversified product and requires an external heat supply. However, it also has several important advantages:

- Potentially it can yield more hydrogen per unit of biomass than gasification if high efficiency in the subsequent steam reforming step is achieved.

- Fast pyrolysis is carried at lower temperatures than gasification (450-550°C) and generates

highly oxygenated liquids. These liquids can be easily converted to hydrogen and carbon oxides in contrast to gasification tars that pose a serious environmental problem.

- The pyrolysis process is actually energetically neutral. Though it requires external heat, this heat can be supplied by combustion of the process byproducts (char and gas).

- Because pyrolysis oils, in contrast to producer gas, are easily transportable, the combined process of pyrolysis and catalytic reforming can be carried independently at different locations allowing to minimize costs of feedstock, its transportation, and product (hydrogen) distribution.

Pyrolysis can also be carried at a high temperature (750-850°C). In such a case, especially if it occurs in a steam environment, most of biomass is directly converted to gases containing a substantial amount of hydrogen. However, as in gasification, this approach also generates highly refractory polycyclic aromatic tars. Because of that, we favor a two step approach with pyrolysis conditions optimized for the generation of oils free of polycyclic aromatic tars. The second step is the catalytic steam reforming of the oils to hydrogen.

Fast Pyrolysis Technologies

Conventional pyrolysis of biomass has been known for several millennia as a method for charcoal production. However, the oil crisis of the 1970s stimulated development of new pyrolysis technologies directed to converting biomass into liquid fuels. In the 1980s, several so-called fast pyrolysis processes have been developed. The common features for all these processes are high rates of heat transfer, moderate temperatures (450-550°C), and short (less than 1 second) vapor residence time in the reactor. These reaction conditions result in a high conversion of biomass (up to 75 wt%) into a liquid product, i.e., the pyrolysis oil or biocrude.

The most important fast pyrolysis technologies are:

- Waterloo Fast Pyrolysis Process (Scott *et al*, 1985). This fluidizing bed technology was developed at the University of Waterloo, Canada. Pyrolysis of biomass occurs in a sand bed with process gases used for fluidization. The 4 kg/h unit consistently generates pyrolysis oils at the 72-76 wt% yield (on dry wood basis); this oil contains 85 wt% of organic compounds and 15 wt% of water. The process has been scaled up to 200 kg/h of biomass by Union Fenosa in Spain.

- Rapid Thermal Processing (Graham *et al*, 1988). Originally developed at the University of Western Ontario, Canada. Ensyn Engineering constructed a 10 kg/h reactor that generated up to 68 wt% of liquids (unknown water content) from biomass. Ensyn then constructed several larger transport reactors: 30 and 80 kg/h in Ottawa and 25 t/day at Red Arrow in Wisconsin. Currently, they are designing a 15 t/day plant in Umbria, Italy. These large units operate using transport reactor principles and data on their performance has not been published.

- Entrained Flow Pyrolysis (Kovac *et al*, 1988). The process has been developed at the Georgia Technical Research Institute. Pyrolysis of biomass takes place in a stream of up flowing hot combustion gases. The oil yields reported were up to 60 wt% of biomass. A 200 kg/h unit based on this technology was constructed by Egemin in Belgium. However, it has never achieved the expected performance; at a feed rate of 50 kg/h only 45 wt% of biomass was converted into liquids.

- Vortex Ablative Pyrolysis (Diebold and Scahill, 1988). The technology has been developed at the National Renewable Energy Laboratory. Biomass pyrolyzes on the hot reactor wall where heat transfer rate is very high because of the centrifugal force effect. The highest liquid yields obtained from a 25 kg/h reactor are 65-70 wt%.

- Vacuum Pyrolysis developed at the Université Laval, Canada (Roy *et al*, 1987). Though, considering the criteria of heat transfer and residence time, this is not a "fast pyrolysis process", its products are similar to those obtained by the above discussed processes. A reactor operating at 250-450°C, 30 mm Hg, and with a biomass feed rate of 0.8 kg/h provided 64 wt% of liquid yield (47 wt% organics) from poplar wood. The oil yield from a larger unit (28 kg/h) was lower (54 wt%) possibly because of a different feed (wood and bark).

Considering the above information we can state that there are reasonably well developed technologies to convert biomass into liquid organic material. The pyrolytic approach has potential for production of hydrogen, provided the pyrolysis oils can be efficiently converted to hydrogen and carbon oxides. Therefore, our main effort is directed to developing a catalytic steam reforming process for pyrolysis oils.

Catalytic Steam Reforming of Oxygenates

a. Background

The literature on steam reforming of oxygenates is limited to those of simple alcohols (methanol and ethanol) and oxygenated aromatic compounds (cresols). Our studies of the extensive literature on steam reforming of methane and heavier hydrocarbon feedstocks suggest that the biocrude, even though a complex mixture, can be steam reformed using known catalyst preparations. Little is known, however, about the optimal experimental conditions that will lead to long-term catalyst activity. To address these issues, we need a better understanding of mechanisms of both the thermal-only decomposition and catalytic steam reforming reactions of oxygenates, which are shown below:

- steam reforming: $$C_nH_mO_k + (n-k)H_2O = nCO + (n+\frac{m}{2}-k)H_2 \quad (1)$$

- thermal decomposition: $C_nH_mO_k \xrightarrow{H_2O} C_xH_yO_z + gas\,(H_2, CO, CO_2, \ldots) + coke$ (2)

  (or cracking)

Few of the primary pyrolysis products of biomass are thermally stable at the typical temperature of a reformer. The catalytic reforming reactions (eq. 1) will be in competition with thermal decomposition reactions (eq. 2). A literature search has been pursued to examine and document previous work on thermal decomposition of model oxygen-containing compounds in the gas phase. Some discussion on the stability of oxygen-containing compounds has been presented in a related review on the chemistry of catalytic hydrodeoxygenation by Furimsky (1983). The nature of vapor phase cracking products from biomass has been described in previous work from this laboratory (Evans and Milne, 1987). It was found that at lower cracking severity (a measure of residence time and temperature), the primary pyrolysis products are converted to CO, CO_2, light hydrocarbons, furans, and phenolics, while stable aromatic compounds, such as benzene, naphthalene and polynuclear aromatics, dominate the spectrum of products formed at high cracking severity. It has also been suggested that the polymerization of low molecular weight hydrocarbons leads to the formation of condensed aromatics. However, a complete understanding of the complex chemistry involved in the thermal cracking of biomass pyrolysis products would be difficult due to the large number of primary and secondary pyrolysis products induced by the many different pathways available to the highly functionalized molecules. One such example is coniferyl alcohol (a lignin-derived molecule) which decomposes to form several major products (Evans and Milne, 1986).

Pyrolysis of *o*-, *m*-, and *p*-hydroxy and methoxyanisoles has been studied in connection with coal liquefaction (Vuori, 1986). The thermal decomposition of substituted benzaldehydes and benzyl alcohols were also investigated as they were found to be main products in pyrolysis of *o*- and *p*-hydroxy and methoxyanisoles. Suryan *et al* (1989) have determined the rates of decomposition of a few methoxy- and ethoxy-substituted benzenes and phenols by very low pressure pyrolysis, and found that the O-methyl bond homolysis is the predominant dissociation process. Substituent effects on the O–CH_3 bond energy in anisole were inferred from differences in the measured rates. Ortho and para-substitutions by hydroxy and methoxy groups can weaken the O–CH_3 bond by 10-30 kJ/mol (2-7 kcal/mol), while substitution at the meta position has only slight influence on the bond dissociation energy (BDE). The thermal decomposition of 2,3-dihydro-1,4-benzodioxin and 1,2-dimethoxybenzene has also been studied (Schraa *et al*, 1994). Rajadurai (1994) has recently reviewed thermal decomposition of carboxylic acids on transition metal oxides.

In this section, we report experimental studies on steam reforming reactions of oxygen-containing model compounds present as major components in the pyrolysis oil. By examining the reaction pathways and relative reactivity of these model compounds, we are trying to understand whether a single catalyst formulation can reform both the complex and simple oxygenates present in the biocrude while limiting undesirable side reactions which will lower the yields of hydrogen. We will present results of thermal decomposition and steam reforming reactions of model oxygenated compounds obtained under conditions of low to incomplete conversions. These results will be discussed with respect to reaction mechanisms and their impact on the overall process of biocrude reforming to hydrogen. Three types of model compounds that represent major components of the biocrude were examined. Ketones and aldehydes were represented by acetic acid, acetone, and hydroxyacetaldehyde. The phenolic series included phenol, anisole, *o*-cresol, resorcinol, 2,6-dimethylphenol, guaiacol, and syringol. The furan family of model compounds consisted of furan,

2-methylfuran, 2,5-dimethylfuran, 2-furfuraldehyde, furfuryl alcohol, 5-methylfurfural, and 5-hydroxymethylfurfural.

Table 1 lists the stoichiometric yields of hydrogen from complete steam reforming reactions of model compounds studied in this work. Also shown are percentage yields by weight, *i.e.*, grams of hydrogen produced per gram of the compound being reformed. In general, the lignin portion of the biomass yields more hydrogen than the carbohydrates (cellulose and hemicellulose), in terms of either weight or mole, i.e., the oxygenated aromatics such as furans and phenolics produces higher yields of hydrogen than anhydrosugars and other carbohydrate-derived products.

In reality, the yield of hydrogen is somewhat off from the stoichiometric maximum shown above, since there are two undesirable products, CO and CH_4. One mole of hydrogen is missing in every remaining mole of CO and four for methane. High steam-to-carbon ratios shift these two reactions toward the side of hydrogen production, but the economics may become less favorable. The steam reforming of methane is kinetically favored under higher temperature conditions. However, those conditions also increase the formation of CO, which may be converted to CO_2 and H_2 in a second water-gas shift reactor operating at low temperatures. The formation of carbonaceus deposits (coke) could account for other missing hydrogen as well. Coking is well known for nickel-based catalysts and it leads to catalyst deactivation and decreased thermal efficiency on a reactor wall. Some of the oxygenate products derived from the carbohydrate component of biomass, especially anhydrosugars, are known to dehydrate rapidly and completely to form carbon. These types of carbon deposition will result in lower yields of hydrogen, for two moles of hydrogen per every missing mole of carbon. Furthermore, less hydrogen will be produced if there is incomplete conversion as a result of coke deposition on the catalyst and the reactor wall.

b. Microscale Laboratory Studies Using MBMS

All of the experimental work for this section were carried out in a vertical, dual bed quartz reactor interfaced with a molecular beam mass spectrometer (MBMS) for real time analysis of products (Figure 1). The details of this experimental setup have been described previously. The reactor is housed in a tubular furnace with four independently controlled temperature zones. The dual bed configuration of this reactor is used to study the effects of thermolysis and catalysis or to compare performances of two catalyst beds under the same temperature conditions. An outer flow is allowed for calibration purpose as well as for the dilution of samples with helium gas that is typically fed at a flow rate of 3.0 STP $L \cdot min^{-1}$ to obtain a better molecular beam and less noise. Steam was generated in the reactor by vaporizing water injected with syringe pumps (SAGE model 355 syringe pumps) through the bottom inlet or a special injection inlet in the side arm. Similarly, model liquid compounds were introduced into the reactor. The vapors are swept by a low flow of preheated gas such as helium. Solid samples were fed in batches through the side inlets and pyrolyzed in preheated helium and steam fed through the bottom inlet, which also carry the pyrolysis vapor upward. All samples were obtained from commercial sources and were used as supplied without further purification.

Mass spectra in the *m/z* range of 1-350 were obtained for pyrolysis and catalysis products with the

MBMS instrument under 25 eV electron impact ionization conditions. This apparatus has been described in previous publications from this laboratory (Evans and Milne, 1987). The MBMS sampling system has the advantage of simultaneously detecting, in real-time, all reactants and products, including any changes that may occur in the feed composition due to thermal reactions prior to reaching the catalyst bed. Any secondary reactions of products after existing the reactor prior to being detected in the mass spectrometer are prevented by sufficient cooling achieved during supersonic, free-jet expansion to form a molecular beam. The detection limit of the MBMS instrument corresponded to conversions of approximately 99.95% for most of the samples, *i.e.*, from the sample signal without catalyst at more than 1.0×10^6 cps to less than the instrument limit of 500 cps (noise = ±250 cps) with catalyst.

All catalysts were ground and sieved before testing and the size range of +60/−25 mesh (20-710 μm) was selected. The nickel-based catalyst was reduced at 600°C and the Cu/Zn shift catalyst at 350°C, with 20% hydrogen in helium for an extended period (over 24 hours). The desired amount of the reduced catalyst was weighted out and either used directly or mixed with pure quartz chips of +60/-45 mesh (250-355 μm) if the amount of catalyst was lower than 0.25 g. Quartz wool was placed at both ends of the bed for packing the catalyst in the tube. A K-type thermocouple was placed just inside the catalyst layer of the bed from above for monitoring catalyst temperature. The reactor was then heated to about 20°C above the desired operating temperature at which the catalyst was reduced again with 50% hydrogen in helium for 2 hours. The pressure drop through the catalyst bed was typically 0.5-3 psi at the highest reactant flow rates and catalyst temperatures. Thermal cracking reactions were carried in either a blank quartz tube or one packed with quartz chips.

For the quantitative analysis of hydrogen, the signal at *m/z* 2 is used directly since there is no significant interference from other molecules present in the steam reforming reactions. The calibration for hydrogen is repeated as often as possible throughout the day. The measured hydrogen yield is reported as the percentage of theoretical maximum according to the stoichiometry of the reaction, and it is estimated to be accurate to within ±3%. The main source of error is due to drifts in the MBMS instrument that limits its reproducibility for quantitative analysis.

Qualitative product mass spectra were obtained by subtracting the mass spectrum of the reactant (assumed to be unconverted under vaporization conditions of the low temperature and short residence time) from that of the reactant converted by pyrolysis or reforming reactions. Product assignments are based on a user library of mass spectral data collected for pure compounds in separate experiments.

c. Rapid Screening Tests

The first part of our experimental studies on steam reforming of pyrolysis oils for hydrogen production included rapid screening of model oxygen-containing compounds, catalysts and operating conditions. A series of model compounds as well as pyrolysis vapors and oils of, and also the major components (lignin, cellulose, and hemicellulose) in biomass were steam reformed with UCI G-90C catalyst under conditions of 600°C,M_{C1}HSV (defined as moles of carbon in feed per hour per cm^3 of catalyst) =0.0014-0.075, τ=0.25s, S/C=10-13, and results are summarized in Table 2. Several of the

model compounds selected are the major components in the pyrolysis oil, such as hydroxyacetaldehyde (HAA, 10%), acetic acid (7%), and levoglucosan (1.5%), while others represent well products derived from lignin pyrolysis. The UCI G-90C catalyst was very active and complete conversions of all samples studied were observed. However, hydrogen yields were far from stoichiometric values in a few cases, partly due to problems with sample feeding in addition to the factors mentioned earlier. A better feeding mechanism is needed for the bench scale, continuous flow reformer in order to vaporize the pyrolysis oils without char formation, such as using an atomizer.

All catalysts selected for screening experiments are listed in Table 3 and we have completed testing except for one (ICI 46-6) that we have not received yet from the manufacturer. The low temperature shift catalyst (UCI C18HC, containing $CuO/ZnO/Al_2O_3/C$) only worked for methanol but failed to show appreciable steam reforming activity for all the other model compounds studied. The other catalysts were tested under conditions of 700°C, S/C=5, high space velocity ($M_{Cl}HSV$=0.3 $mol_{carbon} \cdot mL_{catalyst}^{-1} \cdot h^{-1}$, *ca.* 0.25 cm^3 catalyst) and short residence time (τ=0.025s). These conditions were chosen in order to observe significant differences among the catalysts, since they are expected to work well. Methanol and three other model compounds, acetic acid, HAA, and 4-allyl-2,6-dimethoxyphenol (ADP), were reacted on each of these catalysts. Three of the six catalysts have been tested more than once to check on the reproducibility of screening results.

Table 4 lists the percent conversions for these screening tests of six catalysts and four model compounds. High conversions (>99%) were observed with all catalysts. In the steam reforming of the ADP/MeOH mixture, the conversion of ADP was always no better than that of methanol. The ICI 46-1 catalyst had the lowest conversion for ADP, reaching only about 97%. The H_2 yields for all catalysts and model compounds were high, averaging 89.5% (±5.3%). Within our experimental error limit, there is no clear indication of one catalyst being better than the others. The yields were reproduced very well for catalysts C and D (within 2-3%) but slightly worse for catalyst B (±5.5%). Among the different model compounds, we do observe that methanol and HAA yield slightly more hydrogen than acetic acid and ADP.

Effects of operating conditions were studied by varying the following parameters in a systematic manner: temperature, residence time, steam-to-carbon ratio, and space velocity. Their effects on the catalyst performance were measured by conversion, yields of H_2, CO_2, CO and CH_4. Three model compounds were chosen to represent the pyrolysis oil: hydroxyacetaldehye, acetic acid and 4-allyl-2,6-dimethoxyphenol, in addition to methanol used for checking possible catalyst deactivation. Temperature has the most profound effect on steam reforming reactions. The three small molecules, methanol, acetic acid and HAA, were all reformed in high conversions (>99.95%) at 421°C and above. The lignin model compound, ADP, was more strenuous to reform with steam, and higher temperatures at above 600°C were required for complete conversion. At the lower temperatures of 421, 500, and 600°C, the conversions were 21%, 81%, and 99.7%. The results on effects of temperature were compounded by catalyst deactivation as indicated by the decreased yields of hydrogen obtained from repeated experiments with the used catalyst at the end.

Within experimental error limits, varying residence time from 0.1 to 0.4 s and increasing S/C from 4.5 to 7.5 did not show significant effects on the yield of hydrogen under the conditions of 600°C and

$M_{CI}HSV = 0.075\ mol_{carbon} \cdot mL_{catalyst}^{-1} \cdot h^{-1}$ (UCI G-90C catalyst), which resulted in almost complete conversions of all four model compounds (methanol, acetic acid, HAA and ADP). Interestingly, methane formation showed significant dependence on residence time and S/C. As the residence time increased from 0.1 to 0.4 s, acetic acid and HAA showed a decrease in methane formation but both methanol and ADP/MeOH produced more methane. As expected, less steam also favored the formation of methane. At 700°C, there was no significant change in the yield of hydrogen when S/C is increased from 4.5 to 7.5. Methanol and acetic acid showed slight improvement at higher S/C, but the differences were still close to our experimental error limit.

d. Mechanistic Studies

We have carried out experimental studies on thermal decomposition and steam reforming reactions of oxygen-containing model compounds present as major components in the pyrolysis oil. Three types of model compounds that represent major components of the biocrude are being examined. Small amounts (ca. 10 mg) of solid samples were placed in quartz boats and fed into the reactor in pulses. Liquid samples were injected using syringe pumps. The absence of any organic solvent removes the possibility of ambiguity in the product origin. Steam reforming experiments were carried out with a small bed (0.25g) of the UCI G-90C catalyst at 400°C (low conversion) and 600°C (incomplete conversion). The steam-to-carbon ratios were kept low (<5); exact values were a little uncertain due to the pulse feeding of samples.

Acetic acid readily decomposes at 600°C to produce mainly ketene, and small amounts of acetone and CO_2. At 700°C, the main pyrolysis products are CO_2, CO, methanol, methane, and ketene. The ketonization reaction probably involves the reactor wall, which is made of quartz (SiO_2). This reaction was found to take place more rapidly and to completion on the shift catalyst and on catalyst support materials such as Al_2O_3. Acetone is rather stable and it only undergoes some aldol condensation reactions under catalytic conditions to form 2-methyl-2-pentenone and 1,3,5-trimethylbenzene. Hydroxyacetaldehyde (HAA) decomposes more readily than acetic acid. It undergoes self-condensation reactions to form many higher molecular weight species and forms char. At 700°C, HAA is converted to mainly methane, CO, formaldehyde, ketene, acetaldehyde and CO_2.

With the G-90C catalyst at above 400°C, no intermediates were found in steam reforming reactions of acetic acid, acetone and HAA. All three compounds were completely reacted and HAA is more easily reformed than acetic acid, probably due to the higher stability of acetic acid. Under the same operating conditions, yields of H_2 and CO_2 from HAA are higher than from acetic acid and more methane formation was observed from acetic acid than from HAA.

One interesting observation was that acetic acid reforming usually resulted in serious tailings in the formation of H_2 and CO_2. The reforming of hydroxyacetaldehyde and methanol did not show such delayed formation of H_2 and CO_2. This suggests that acetic acid forms significant amounts of carbon on the catalyst during steam reforming. It was such carbon deposits that was converted to H_2 and CO_2 by steam when there was no more feeding of acetic acid over the catalyst. Acetic acid has been shown to form adsorbed acetate species at low temperatures on clean metal surfaces such as Rh(111) (Li and Bowker, 1993) and Pd(111) (Aas and Bowker, 1993), and the acetate species decomposes

to yield H_2 and CO_2, leaving adsorbed carbon on the surface. We have also observed formation of carbon films on walls of reactors made of nickel alloys during our experiments on the bench scale reformer.

Furan, 2-methylfuran and 2,5-dimethylfuran showed negligible decomposition at 600°C. They are readily reformed by steam on the G90-C catalyst. Conversions are close to completion even at 400°C, with only small amounts of benzene and toluene remaining as the intermediates (but not at 600°C). Furan also formed detectable amounts of acetylene, ethylene, and propylene at 400°C over the catalyst, while some formation of acetone was also observed for 2-methylfuran. These results suggest that complete bond fission of the furans to adsorbed CH_x species takes place on the catalyst with some C_2 and C_3 units remaining intact as a result of ring opening, which fuse to form benzene. Dealkylation of substituted furans to furan is not important under the conditions used here.

Several stable intermediate products (acetone, furan, methylfuran, benzene, toluene and naphthalene) were observed in the steam reforming reaction of 2-furfuraldehyde at 400°C, while at 600°C only furan and benzene in trace amounts were still detected. 2-Furfuryl alcohol formed the following major intermediates (under partial steam reforming conditions at 400 and 600°C): acetone, furan, methyl and dimethylfurans, benzene and toluene, while it thermally decomposed to only acetone, furan and methylfuran at 600°C. The pathway by which 5-methylfurfural pyrolyzes is similar to that of 2-furfuraldehyde, namely by an initial homolysis of the aldehyde C–H bond. Methylfuran and CO were observed as the two major products and other identified products included di(5-methylfuryl). Catalytic reforming reactions of 5-methylfurfural at 400°C produced methylfuran, dimethylfuran, acetone, furfuryl alcohol and small amounts of furan, benzene, and toluene while only trace amounts of methyl and dimethylfurans remained at 600°C. The major pyrolysis product of 5-hydroxymethyl-furfural is 2-furfuraldehyde, which may derive from the cleavage of the H–O bond, followed by the loss of formaldehyde. These observations indicate that all three reaction pathways (total degradation, dealkylation/deformylation, and ring opening) are all operating under the employed conditions.

No intermediate was detected during the catalytic steam reforming of phenol above 400°C, whether as pure phenol or in a methanol solution. Phenol was the only intermediate detected at both 400 and 600°C when *o*-cresol was steam reformed over the G-90C catalyst, while significant amounts of cresols, phenol, benzene, toluene were observed from thermolysis of *o*-cresol at both 400 and 600°C. The results obtained for guaiacol and syringol are consistent with the fact that substitutions by a methoxy group facilitates both thermal decomposition and steam reforming reactions of phenolic compounds. When anisole is compared with *o*-cresol, the weak O–CH_3 bond in the former (BDE=272 kJ/mol) also has a much lower activation energy than that required for *o*-cresol. We could estimate BDE=351 kJ/mol for 2-MeC_6H_4O–H, from BDE=362 kJ/mol for PhO–H and a weakening substitution effect of -11 kJ/mol by a methyl group at the ortho position, similar to the value obtained this effect on the O–CH_3 bond strength in anisole (Suryan et al, 1989). This makes anisole much easier to undergo thermolysis and steam reforming reactions. Similarly, the decomposition and reforming reactions of syringol take place dramatically faster than phenol. In fact, syringol steam reforming is almost as facile as that of methanol.

The above results suggest that both thermal decomposition and catalytic reforming reactions take

place during the steam reforming of oxygenates found in pyrolysis oils. Thermal decomposition of the labile oxygenates competes with the catalytic steam reforming reactions of both the starting material and its secondary cracking products in the bed. The thermal cracking reaction may be facilitated by the reactor walls as well as the catalyst support. Only a few compounds are stable enough to reach the catalyst bed without thermal cracking. However, a highly active catalyst, such as the UCI G-90C catalyst used here, can effectively steam reform all compounds, including the secondary cracking products, into H_2 and CO_2. The remaining issues are how to effectively feed the pyrolysis oil into the reactor, and which catalyst will maintain high enough activity for a long time.

Fixed Bed Steam Reforming Reactor

A flow diagram of the installation is shown on Figure 2. The reactor is constructed in a 1.65 cm i.d x 42.6 cm length stainless steel tube. The reactor body is mounted inside an electrically-heated tubular furnace (MELLEN SC12-3x24V-32). The furnace incorporates three independent heating blocks, which allow the operation of the reactor under non-isothermal conditions if desired. The temperature in each heater zone is controlled by an analog controller (T-16, T-17 and T-18). The steam required for the reforming process is generated by a 3 kW electric boiler (SUSSMAN MBA6), capable of supplying up to 8.2 kg/h of saturated steam at 0.69 MPa. The boiler uses water from a 4 L stainless steel vessel pressurized with nitrogen. The steam flow is overheated to 155°C by an electric cartridge heater (E-1) and it is regulated using a manual needle valve, V-1. The steam flow-rate is measured by an orifice plate coupled to a differential pressure transducer. The steam is then mixed, if required, with CO_2, CO and/or N_2, and the mixture is directed to the reactor via a thermostated line (E-2), and overheated up to 700-850°C in a second cartridge heater (E-3) prior to the oil vaporizer. The flow rates of the different gases are adjusted by independent mass flow controllers, FC-2, 3 and 4 (MKS MFC-1100). The flow rate of pyrolysis oil or model compound solution is adjusted by a diaphragm metering pump, P-1 (PROMINENT G/4a 1601TT1), and the liquid is dispersed into the overheated gas mixture at the top of the reactor chamber by a gas-atomizing nozzle. Temperature in the catalyst bed is measured at the bed entrance (T-4), at one third of the bed length from the entrance (T-5), and at the bed outlet (T-6), using K-type thermocouples placed inside a 1/8 inch o.d. thermowell mounted at the center of the bed. The gaseous products resulting from the reforming process are removed from the bottom of the reactor and directed to a vertical double-pipe heat exchanger (E-5), in which the excess water and the fraction of non-reacted compounds are condensed and measured. Propylene glycol, flowing in a closed circuit from a refrigerated recirculator (NESLAB CFT-75D), is used as cooling fluid in the heat exchanger unit. The flow of dry gas is then measured with a dry test volumetric meter (AMERICAN DTM 325), and a fraction of the flow is split to an on-line infrared gas analyzer (ANARD AR600R) for determination of the CO_2 and CO contents, and to a gas chromatograph (MTI-QUAD) to measure the contents of H_2, CH_4 and other light hydrocarbons.

One of the commercial nickel-based catalyst for steam reforming (United Catalysts G-90C) was selected for the initial study. A sample of the catalyst was crushed and sieved. The fraction smaller than 4.00 mm (mesh 5) and retained in the 2.36 mm sieve (mesh 8) was used in this set of experiments. From 82 to 85 g of catalyst were normally used to pack the reactor tube. After packing the reactor, the catalyst was heated to 600°C and reduced during 5 h using hydrogen at a flow rate of 500 sccm.

Two compounds representative of the pyrolysis oil have been selected for the initial set of experiments: acetic acid and syringol. Selection of the reforming conditions were based on the results obtained with the microreactor as described in the previous section and on the industrial conditions used for the steam-reforming of naphtha. Conventional steam reforming of naphtha for hydrogen production is a well established process that is performed in fixed bed tubular reactors using nickel-based catalysts. In normal operation conditions, the mixture of naphtha and steam enters the catalyst bed at a temperature around 450 - 500°C and the products leave the reactor at 820 to 850°C. Steam to carbon molar ratios range from 2.5 to 6.5, depending on the final product of interest (hydrogen, ammonia, or town gas). If hydrogen is the desired final product, steam to carbon ratios higher than 5 are used. Gas hourly space velocity (GHSV) for naphtha reforming typically ranges from 700 to 2000 h^{-1} (Rostrup-Nielsen, 1977).

The experimental conditions used for each model compound and the main results are presented in Table 5. A first series of duplicate experiments was performed with acetic acid at constant steam to carbon ratio and space velocity, which were maintained around 5.9 (mol/mol) and 0.067 ($mol_{carbon} \cdot mL_{catalyst}^{-1} \cdot h^{-1}$) respectively, to determine the effect of the temperature profile along the catalyst bed. All experiments were completed using the same catalyst bed. Run# indicates the order in which they were executed, from run# 23 to run# 34. The duration of the experiments varied from 45 to 90 minutes. Carbon was formed on the catalyst bed in all the experiments, but the extent of its formation was strongly dependent on the temperature profile. Around 500°C (run# 29 and 34) only 70% of the carbon in the feed was recovered in the gas products, and a significant amount of char was formed during the experiment. Part of this char was entrained from the bed by the gas stream and was collected with water in the condenser. The accumulation of char in the bed caused the pressure at the reactor entrance to increase continuously during the experiment. In spite of char formation the catalyst did not lose any activity and the composition of the gas remained unchanged during run time. The char was reactive enough to be largely gasified by steam when the acetic acid feed was interrupted, even at this mild temperature. The course of char gasification was monitored by the presence of CO_2 in the steam at the reactor exit and also by the decrease of the pressure drop along the catalyst bed, which recovered the original value for the fresh catalyst. An increase in the temperature at the bed exit to 600°C (run# 25 and 26) improved the recovery of carbon in the gas products to 80% of the feed, and although char was also formed it was not entrained by the gas. Char formation was minimal when the exit temperature was raised to 710°C (run# 32 and 33). At this temperature the carbon recovery of 98% and the pressure drop along the catalyst bed was stable during all the experiment (90 min). Gas composition is also dependent on temperature. Since less carbon is lost in char-forming reactions, rising the catalyst temperature increases the hydrogen yield and also increases the relative amount of carbon monoxide with respect to the amount of carbon dioxide and methane.

Steam reforming of syringol (run# 38) was studied at the temperature profile, steam to carbon ratio and space velocity, that gave the best results for acetic acid. Syringol was dissolved in methanol at a concentration of 40:60 (w/w), which corresponds to a mixture in which 53% of the carbon is provided by syringol. Methanol was selected since it was verified that this solvent was easily reformed at these conditions without forming any appreciable amount of char on the catalyst surface. Syringol does not react as well as acetic acid at these conditions. Carbon conversion to gas products was

94.7% of the feed, which corresponds to only 90% conversion for syringol if methanol is assumed to be completely converted. Increasing the steam to carbon ratio to a value of 10 resulted in a higher carbon conversion (run# 42 and 43) and lower char formation, but further rising this parameter to 14.4 (run# 44) did not improve the results. In fact the catalyst experienced some lost of activity which caused a carbon conversion of only 96.2 of the feed and the detection of a significant amount of ethylene in the exit gas. Since these three experiments were carried out using the same catalyst bed, this result suggests that syringol causes significant deactivation of the catalyst after a certain time of operation. This is consistent with the experience on steam reforming of naphtha in which the aromatic content of the feedstock naphtha has to be low enough to ensure long-long term catalyst survival. Rising the catalyst temperature while maintaining a similar steam to carbon ratio to that of run# 38 resulted in a better carbon conversion, but still some increase in the pressure drop along the catalyst bed due to char accumulation was observed (run# 46-a). The char accumulated in the bed can also be gasified by CO_2 if the temperature is maintained above 800°C. After 90 minutes of operation (run# 46-a), the feed of steam and syringol/methanol solution was interrupted and 750 sccm of CO_2 were feed to the reactor and the temperature maintained at 830°C in all the bed. After 60 min, the char retained on the catalyst surface was completely gasified since no CO was detected on the outlet gas. Then, the CO_2 feed was interrupted and the same reforming experiment repeated (run# 46-b). The results show a perfect duplicate of run# 46-a, which indicate that no loss of catalytic activity was produced during the CO_2 gasification of the char.

Conclusions

Our experimental research effort has provided new insight into the H_2 production via Fast Pyrolysis followed by Catalytic Steam Reforming of the pyrolysis oils. The significant conclusions derived from our work are as follows:

- The compounds present in the pyrolysis oils (acetic acid, linear aldehydes, sugar related alcohols, furans and phenolic derivatives), can be steam reformed using Ni-based catalysts. Our microreactor screening results prove unequivocally this point.
- A mechanistic understanding of the catalytic steam reformed process of oxygenates is being achieved. It involves gas-phase thermal decomposition reactions competing with surface-driven catalysis in dual sites (Ni crystallites and alumina).
- The initial experiments on the bench scale fixed bed tubular reactor suggest that the control of coke formation is a key aspect of the catalytic steam reforming of oxygenates. The coke formation is difficult to prevent even by careful choice of the temperature profiles and steam/carbon ratio. Thus loss of activity after a few hours on stream will force periodic regeneration of the catalyst. We have proven that CO_2 available from the pressure swing adsorption operation, can effectively regenerate the catalyst.

The next stage of the project is to begin tests with the entire pyrolysis oils and study the longevity of the catalyst and its regeneration using the CO_2 removed by pressure swing adsorption.

Technoeconomic analysis has been conducted in parallel with this work and are reported in a paper by Mann (1995) as part of these proceedings.

References

Aas, N. and Bowker, M. "Adsorption and Autocatalytic Decomposition of Acetic Acid", *J. Chem. Soc., Faraday Trans.* 89 (1993), 1249.

Diebold, J.P., and Scahill, J. "Production of Primary Pyrolysis Oils in a Vortex Reactor", in *Pyrolysis Oils from Biomass,* E.J. Soltes and T.A. Milne, Eds., American Chemical Society, Washington, D.C. (1988), 31-40.

Elliott, D.C. "Relation of Reaction Time and Temperature to Chemical Composition of Pyrolysis Oils", in *Pyrolysis Oils from Biomass: Producing, Analyzing and Upgrading*, Soltes, E.J. and Milne, T.A., eds., ACS Symposium Series 376, ACS, Washington, D.C. (1988), 55.

Evans, R.J. and Milne, T.A. "Applied Mechanistic Studies of Biomass Pyrolysis", In *Proceedings of the 1986 Biomass Thermochemical Conversion Contractors' Meeting*, PNL-SA-13571, CONF-8510167; NTIS: Springfield, VA, (1986), 57-79.

Evans, R.J. and Milne, T.A. "Molecular Characterization of the Pyrolysis of Biomass. 1. Fundamentals", *Energy and Fuels* 1 (1987), 123, and "Molecular Characterization of the Pyrolysis of Biomass. 2. Applications", *Energy and Fuels* 1 (1987), 311.

Evans, R.J., Knight, R.A., Onischak, M., and Babu, S.P. "Process Performance and Environmental Assessment of Renugas Process", in *Proceedings of Energy from Biomass and Wastes X,* D.L. Klass, Ed., pp. 677-696, Institute of Gas Technology, Chicago, Illinois, (1988), 677-696.

Furimsky, E. "Chemistry of Catalytic Hydrodeoxygenation", *Catal. Rev.- Sci. Eng.* 25 (1983), 421-458.

Graham, R.G., Freel, B.A., and Bergoungou, M.A. "The Production of Pyrolytic Liquids, Gas and Char from Wood and Cellulose by Fast Pyrolysis" in *Research in Thermochemical Biomass Conversion,* A.V. Bridgwater and J.L. Kuester, Eds., Elsevier Applied Science, London and New York, (1988), 629-641.

Kovac, R.J., Gordon, C.W., and O'Neil, D.J. "Entrained Flow Pyrolysis of Biomass", in *Thermochemical Conversion Program Annual Meeting",* Solar Energy Research Institute, Golden, CO, (1988), 5-20.

Li, Y. and Bowker, M. "Acetate Formation, Stabilization and Surface Explosion on Rh(111)", *Surf. Sci.* 285 (1993), 219.

Mann, M., "Technoeconomic Analysis", Proc. at the 1995 DOE/NREL, Hydrogen Program Review, April 19-21, 1995 Coral Gables, Florida (in press).

Piskorz, J., Scott, D.S., and Radlein, D., "Composition of Oils Obtained by Fast Pyrolysis of Different

Woods", in *Pyrolysis Oils from Biomass*, E.J. Soltes and T.A. Milne, Eds. American Chemical Society, Washington, D.C. (1988), 167-178.

Radlein, D.; Piskorz, J.; and Scott, D.S. *J. Anal. Appl Pyrolysis* 19 (1991), 41.

Rajadurai, S. "Pathways for Carboxylic Acid Decomposition on Transition Metal Oxides", *Catal. Rev.-Sci. Eng.* 36 (1994), 385-403.

Rostrup-Nielsen, J. "Hydrogen via Steam Reforming of Naphtha", *Chem. Eng. Prog.* 73 (1977), 87-92.

Roy, C., de Caumia, B., Blanchette, D., Lemieux, R., Kaliaguine, S. "Development of a Biomass Vacuum Pyrolysis Process for the Production of Liquid Fuels and Chemicals", in *Energy from Biomass and Wastes IX*, D.L. Klass, Ed., Institute of Gas Technology, Chicago, Illinois, (1987), 1085-1102.

Schraa, G.-J.; Arends, I.W.C.E. and Mulder, P. "Thermal Decomposition of 2,3-Dihydro-1,4-benzodioxin and 1,2-Dimethyoxybenzene", *J. Chem. Soc. Perkin Trans. II* (1994), 189.

Scott, D.S., Piskorz, J., and Radlein, D. *Ind. Eng. Chem., Proc. Des. Dev.* 24 (1985) 581.

Suryan, M.M.; Kafafi, S.A. and Stein, S.E. "The Thermal Decomposition of Hydroxy- and Methoxy-Substituted Anisoles", *J. Amer. Chem. Soc.* 111 (1989), 1423, and "Dissociation of Substituted Anisoles: Substituent Effects on Bond Stengths", *J. Amer. Chem. Soc.* 111 (1989), 4594.

Vuori, A. "Pyrolysis Studies of Some Simple Coal Related AromaticMethyl Ethers", *Fuel* 65 (1986), 1575-1583.

Table 1. Stoichiometric Yields of Hydrogen from Complete Steam Reforming Reactions

Sample	Formula	MW	% Hydrogen Yield	
			(by mole C)[a]	(by weight)[b]
methane	CH_4	16.04	400%	50.3%
methanol	CH_4O	32.04	300%	18.9%
acetone	C_3H_6O	58.08	267%	27.8%
dimethylfuran	C_6H_8O	96.13	250%	31.5%
anisole, cresol	C_7H_8O	108.14	243%	31.7%
methylfuran	C_5H_6O	82.10	240%	29.5%
ADP[c]	$C_{11}H_{14}O_3$	194.23	236%	27.0%
phenol	C_6H_6O	94.11	233%	30.0%
guaiacol	$C_7H_8O_2$	124.14	229%	26.0%
furan	C_4H_4O	68.08	225%	23.5%
syringol	$C_8H_{10}O_3$	154.17	225%	23.5%
lignin	$C_7H_9O_3$	141.15	221%	22.1%
resorcinol, methylfurfural	$C_6H_6O_2$	110.11	217%	23.8%
poplar oil	$C_6H_{7.98}O_{3.18}$	130.99	214%	19.7%
aspen	$C_6H_{8.79}O_{3.62}$	138.84	213%	18.5%
poplar	$C_6H_{8.82}O_{4.02}$	145.27	207%	17.2%
oakwood oil	$C_6H_{9.14}O_{4.53}$	153.76	201%	15.8%
5-HMF[d]	$C_5H_4O_2$	96.09	200%	21.0%
xylan	$C_5H_8O_4$	132.12	200%	15.3%
cellulose	$(C_6H_{10}O_5)_n$	180.16	200%	14.9%
cellobiose	$C_{11}H_{22}O_{11}$	330.29	200%	13.4%
glucose	$C_6H_{12}O_6$	180.16	200%	13.4%
acetic acid, HAA[e]	$C_2H_4O_2$	60.05	200%	13.4%
formic acid	CH_2O_2	46.03	100%	4.4%

a Moles of hydrogen produced per mole of carbon in the reactant being reformed.
b The amount of hydrogen formed divided by the sample molecular weight.
c 4-Allyl-2,6-dimethoxyphenol.
d 5-Hydroxymethylfurfural.
e Hydroxyacetaldehyde.

Table 2. Catalytic Steam Reforming of Model Compounds, Biomass and Related Materials[a]

Sample	$M_{C1}HSV$	Conversion[b]	H_2 yield	CO_2 yield	$\frac{I_{m/z\ 28}}{I_{m/z\ 44}}$
methanol	0.015	> 99.95%	95%	93%	8%
acetic acid	0.0081	> 99.95%	86%	90%	5%
HAA (20 wt% in H_2O)	0.0081	> 99.95%	96%	103%	5%
phenol (20 wt% in MeOH)	0.013	> 99.95%	99%	98%	6%
syringol (20 wt% in MeOH)	0.013	> 99.95%	100%	100%	6%
ADP (41 wt% in MeOH)[c]	0.075	99.7%	69%	47%	12%
xylan[d]	≈0.03	> 99.95%	100%	93%	5%
levoglucosan[d]	≈0.03	> 99.95%	100%	87%	3%
cellulose[d]	≈0.03	> 99.95%	102%	98%	3%
cellobiose (18 wt% in H_2O)	0.0014	> 99.95%	83%	85%	5%
aspen[d]	≈0.06	> 99.95%	62%	60%	3%
lignin[d]	≈0.06	> 99.95%	41%	35%	3%

a Averaged results from triplicates. Reaction conditions were 600°C, τ=0.25s, S/C=10-13. Catalyst used: UCI G-90C.

b Limited by the detection capability of the MBMS instrument. Also see discussion in text.

c S/C=4.5.

d Samples pyrolyzed in batches of 5-10 mg at 600°C, residence time before reaching the catalyst bed was about 0.5s.

Table 3. Catalyst Properties

ID	(Name)	Manufacturer (shape and size)	Composition	Commercial Use
A		Sherbrooke Univ. (pellets; OD=2mm, length=2-5mm)	NiO Al_2O_3 Cr_2O_3 La_2O_3 MgO	NA (Research catalyst for steam reforming - high MW aromatics)
B	(UCI G-90C)	United Catalysts Inc. (rings; OD=⅝", ID=5/16", length=⅝")	15% Ni Ceramic carrier (70-76% Al_2O_3 5-8% CaO)	Steam reforming - more difficult service (low S/C ratios, C_3+ C_4 hydrocarbons etc.)
C	(ICI 25-4M)	Imperial Chemical Industries (4-hole shape; OD=11.5mm, length=13.8mm, hole diam.=3.0mm)	15% NiO 70% Al_2O_3 13% CaO 1.5% K_2O promoted	Steam reforming - natural gas and other low MW hydrocarbons
D	(ICI 46-1)	Imperial Chemical Industries (ring pellets; OD=17mm, ID=7mm, length=17mm)	10-25% NiO Refractory carrier 1.5% K_2O promoted	Steam reforming - high MW naphtha (b.p. up to 235°C, containing up to 25% aromatics)
E	(UCI G-90B)	United Catalysts Inc. (tablets; ¼"×¼")	11% Ni Ceramic carrier (76-82% Al_2O_3 6-9% CaO)	Steam reforming - more difficult service (low S/C ratios, C_3+ C_4 hydrocarbons etc.)
F	(UCI C18HC)	United Catalysts Inc. (tablets; 3/16"×3/32")	42% CuO 47% ZnO 10% Al_2O_3	Low temperature (200-260°C) shift conversion
G	(BASF G1-25S)	BASF (rings: OD=⅝", ID=⅜", length=⅜")	15% Ni Ceramic carrier	Steam reforming: natural gas (high activity & mechanical strength, easy reduction)
H	(ICI 46-6)	Imperial Chemical Industries	NiO CaO, Al_2O_3, ZrO_2	Steam reform: used with ICI 46-1 for removing C_2/C_3 intermediates

Table 4. Conversions of Model Compounds by Catalytic Steam Reforming[a]

Catalyst ID	MeOH	HAc	HAA	ADP/MeOH		MeOH, repeat
				ADP	MeOH	
A	≥99.95%	99.85%	≥99.95%	≥99.95%	99.7%	≥99.95%
E	≥99.95%	≥99.95%	99.8%	99.6%	99.7%	99.92%
G	99.91%	99.95%	≥99.95%	99.7%	99.95%	99.8%
D, #1	≥99.95%	≥99.95%	≥99.95%	98.0%	99.4%	≥99.95%
D, #2	≥99.95%	≥99.95%	99.95%	95.9%	98.3%	99.88%
C, #1	≥99.95%	≥99.95%	≥99.95%	≥99.95%	≥99.95%	≥99.95%
C, #2	99.5%	99.9%	99.7%	99.3%	99.5%	99.5%
B, #1	≥99.95%	≥99.95%	≥99.95%	≥99.95%	≥99.95%	≥99.95%
B, #2	≥99.95%	≥99.95%	99.90%	99.8%	≥99.95%	≥99.95%
B, #3	≥99.95%	≥99.95%				

a Experimental conditions: 700°C, S/C=5, $M_{C1}HSV$=0.3 $mol_{carbon} \cdot mL_{catalyst}^{-1} \cdot h^{-1}$ (*ca.* 0.25 cm^3 catalyst), and residence time = 0.025s.

Table 5. Steam Reforming of Model Compounds Using a Commercial Reforming Catalyst (UCI G-90C): Experimental Conditions, Carbon Balance and Hydrogen Yield

Compound	run#	S/C molar ratio	Space velocity[1] M_{Cl}HSV	Space velocity[1] GHSV	Temp. (°C) T-4	Temp. (°C) T-5	Temp. (°C) T-6	Carbon[2] balance (%)	H_2 yield (%)	mol of gas/100 mol of carbon feed H_2	CO_2	CO	CH_4	C_2H_4
Acetic acid	29	5.9	0.069	2710	476	487	511	73.6	60.8	121.6	60.5	9.2	3.9	0.06
	34	5.8	0.069	2721	497	498	520	68.2	57.3	114.7	56.3	9.5	2.3	0.06
	25	5.6	0.067	2614	507	535	599	80.1	64.7	129.5	59.9	17.2	2.9	-
	26	5.8	0.067	2614	505	533	594	80.8	65.5	131.0	61.0	17.0	2.8	-
	24	5.8	0.067	2606	504	547	661	83.9	68.5	137.0	59.0	23.6	1.3	-
	27	5.8	0.067	2627	508	547	658	87.3	70.5	140.9	60.9	24.9	1.5	-
	23	6.0	0.064	2509	510	560	708	88.3	70.9	141.7	59.3	32.4	0.5	-
	28	6.0	0.067	2632	510	558	706	88.6	70.9	141.8	58.1	29.9	0.6	-
	30	5.7	0.068	2646	548	610	709	91.9	72.0	144.0	58.6	32.8	0.6	-
	31	6.1	0.068	2646	555	615	708	94.8	74.8	149.6	59.8	34.4	0.7	-
	32	6.0	0.066	2602	608	667	710	97.9	75.6	151.2	58.3	38.9	0.7	-
	33	6.0	0.066	2602	617	661	709	97.9	74.0	148.1	56.7	42.5	0.9	-
Syringol and methanol mixture 40:60 (w/w)	38	6.1	0.069	2688	609	670	708	94.7	74.6	194.4	52.3	40.3	2.1	-
	42	10.0	0.058	2288	521	617	705	97.5	77.6	202.3	59.0	36.4	2.1	-
	43	10.0	0.059	2313	519	626	703	99.7	79.5	207.4	62.4	35.3	2.0	-
	44	14.4	0.059	2313	513	616	702	96.2	78.2	203.1	61.3	32.6	2.2	0.13
	46-a	7.4	0.056	2205	667	755	829	98.5	75.9	197.1	49.3	49.1	0.1	-
	46-b	6.9	0.056	2205	667	757	829	98.3	76.5	198.9	49.7	48.5	0.1	-

[1] M_{Cl}HSV in ($mol_{carbon} \cdot mL_{catalyst}^{-1} \cdot h^{-1}$); GHSV: methane equivalent gas hourly space velocity in (h^{-1}).

[2] Carbon recovered in the gas-phase products.

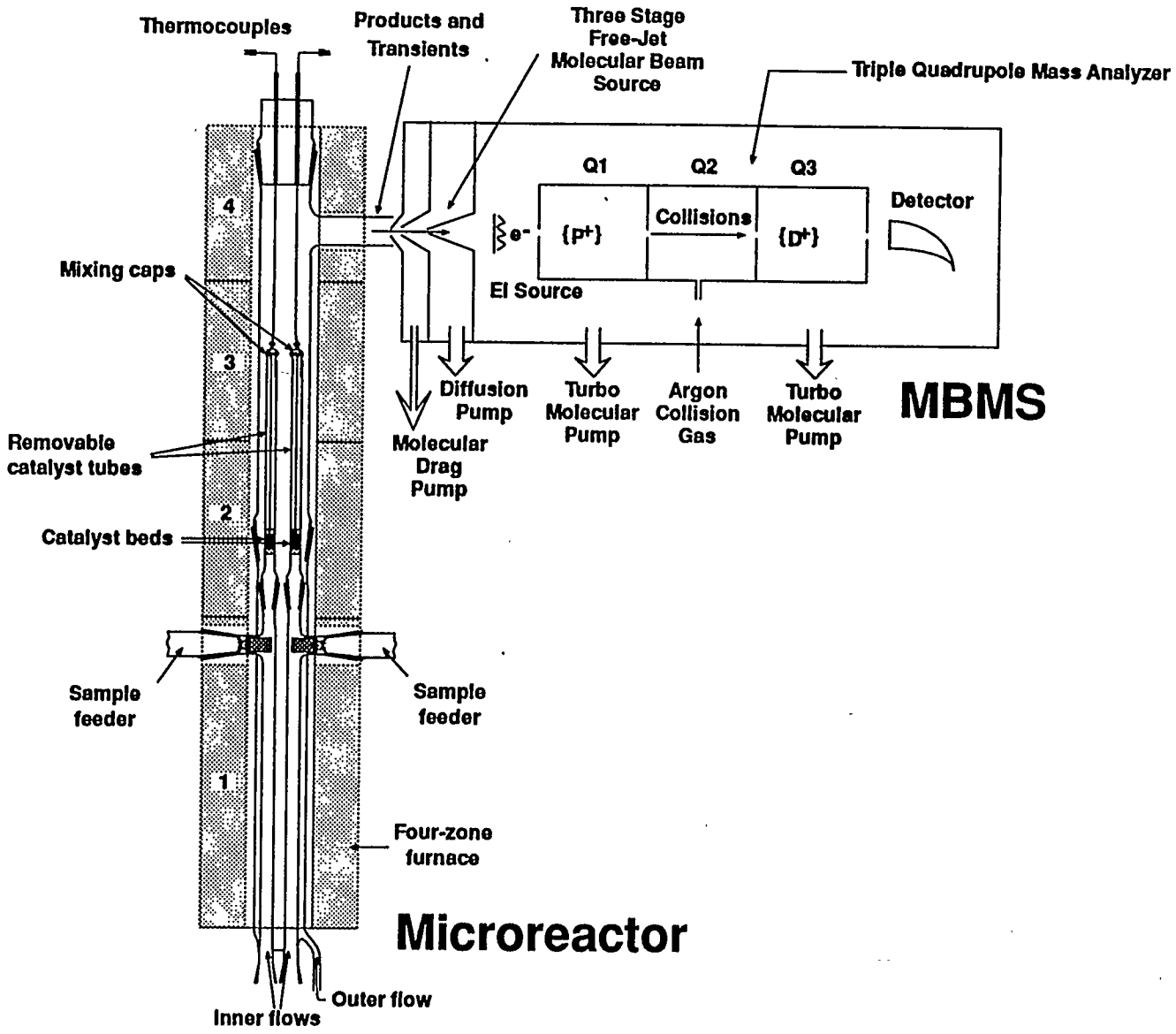

Figure 1. A schematic diagram of the vertical, dual catalyst bed, quartz reactor interfaced with the molecular beam mass spectrometric sampling system.

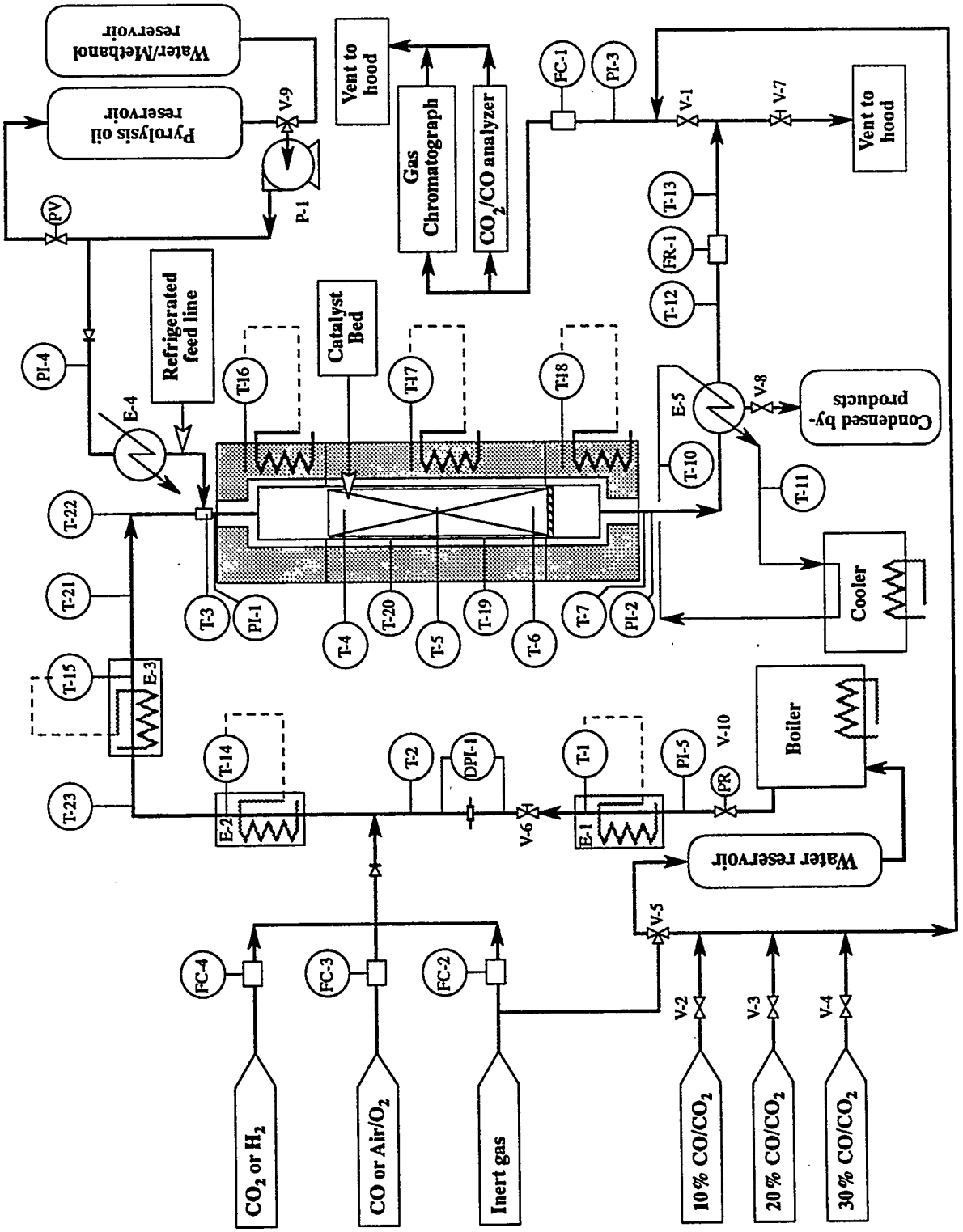

Figure 2. P&I of the fixed-bed catalytic reactor setup.

CONVERSION OF MUNICIPAL SOLID WASTE TO HYDROGEN

J. H. Richardson, R. S. Rogers, C. B. Thorsness and P. H. Wallman
Lawrence Livermore National Laboratory
Livermore, CA 94551

T.F. Leininger, G. N. Richter, A. M. Robin, H.C. Wiese and J. K. Wolfenbarger
Montebello Research Laboratory
Texaco Inc
Montebello, CA 90640

Abstract

LLNL and Texaco are cooperatively developing a physical and chemical treatment method for the conversion of municipal solid waste (MSW) to hydrogen via the steps of hydrothermal pretreatment, gasification and purification. LLNL's focus has been on hydrothermal pretreatment of MSW in order to prepare a slurry of suitable viscosity and heating value to allow efficient and economical gasification and hydrogen production. The project has evolved along 3 parallel paths: laboratory scale experiments, pilot scale processing, and process modeling. Initial laboratory-scale MSW treatment results (e.g., viscosity, slurry solids content) over a range of temperatures and times with newspaper and plastics will be presented. Viscosity measurements have been correlated with results obtained at MRL. A hydrothermal treatment pilot facility has been rented from Texaco and is being reconfigured at LLNL; the status of that facility and plans for initial runs will be described. Several different operational scenarios have been modeled. Steady state processes have been modeled with ASPEN PLUS; consideration of steam injection in a batch mode was handled using continuous process modules. A transient model derived from a general purpose packed bed model is being developed which can examine the aspects of steam heating inside the hydrothermal reactor vessel. These models have been applied to pilot and commercial scale scenarios as a function of MSW input parameters and have been used to outline initial overall economic trends. Part of the modeling, an overview of the MSW gasification process and the modeling of the MSW as a process material, was

completed by a DOE SERS (Science and Engineering Research Semester) student. The ultimate programmatic goal is the technical demonstration of the gasification of MSW to hydrogen at the laboratory and pilot scale and the economic analysis of the commercial feasibility of such a process.

Introduction

Municipal Solid Waste (MSW) is a large, growing, and little-used by-product resource of the United States. Approximately 200 million tons of MSW are produced annually in the United States, and the vast majority of this eventually winds up in landfills (Khan, 1993). Environmental concern over air pollution and the ash by-product has limited incineration as a disposal method, current landfills are becoming full, and concern over water pollution makes siting of future landfills difficult and expensive.

MSW is predominantly composed of carbon, hydrogen and oxygen, and as such is a potential energy source (Rogers, 1994). Thus, development of the technology necessary for gasification of MSW to hydrogen has the potential to address a number of economic, environmental, societal and resource issues. A path for the conversion of MSW to hydrogen has the potential to be economically advantageous because management and disposal of MSW is expensive, and the fees otherwise required to dispose of MSW become a credit against the cost of the produced hydrogen. The economics of MSW to hydrogen conversion relative to other sources will depend on tipping fees, the cost of alternate feed stocks such as coal or natural gas, and the differential processing costs. Conversion of MSW to hydrogen has the environmental advantage of decreasing the number of future landfills needed with the concomitant decrease in the associated water pollution issues. Furthermore, as gasification of MSW involves recycling of what is predominantly biomass, it introduces virtually no new carbon into the atmosphere. Finally, the energy content of one ton of MSW is comparable to a barrel of oil. Recovery of that energy through gasification would eliminate importing approximately 200 million barrels of oil, or ≈ 3-4 B$. Thus, even recovery of only a substantial fraction of the energy in MSW would have significant environmental and fiscal impact on the United States.

This report describes work done jointly between Lawrence Livermore National Laboratory (LLNL) and Texaco. The objective of this work is to generate hydrogen from MSW to capitalize on the proven gasifier technology developed and marketed by Texaco. The primary technical problem is the pretreatment of MSW into a form suitable to use as a feed stock to the Texaco gasifier. LLNL is focusing its efforts on the effects of MSW pretreatment on the heating value and viscosity properties of slurries suitable for injection into the gasifier. Supplemental feed stocks would be considered as needed (e.g., coal; heavy oils, which are of particular interest in California). The scope of this project does not include initial MSW classification; hence and as appropriate, additional industrial partnerships in the realm of MSW classification would be explored in order to address as fully as possible all the technical and economic issues. Initial results have been documented elsewhere (Pasternak, et. al., 1994).

The Texaco gasifier has been successfully developed and commercially employed for gasification of

coal, heavy oils, and petroleum coke with subsequent shift and hydrogen separation. The Texaco gasifier has many advantages: 1) oxygen can be utilized as the oxidant, resulting in no dilution and few nitrogen impurities; 2) hazardous metals are sequestered by the slag; 3) the high temperatures insure the complete destruction of hazardous organics; 4) the Texaco gasifier represents proven technology. Texaco will perform laboratory gasification runs of MSW feed stocks prepared by LLNL during the initial phase of pretreatment parameter optimization. Texaco and LLNL will jointly perform a system analysis of the feed preparation/gasification process in order to allow process tradeoffs to be evaluated on an economic as well as a technical basis. Slagging is both a proven asset and potential issue with respect to gasification of MSW. Consequently, another goal of this project is the development of a measurement/control system to ensure continuous ash slagging conditions despite variations in the ash compositions of for the MSW feed. Finally, it is intended that the project will conclude with the demonstration of MSW slurrying and subsequent gasification at the pilot scale size.

Subsequent work may deal with alternate biomass and waste feed stocks which potentially represent major energy resources; e.g., there are approximately 7 million tons of dry sewage sludge produced daily in the United States (Khan, 1993). MSW in particular and biomass/waste in general are predicted to have the greatest potential for annualized growth of electricity generation and displacement among renewable energy resources during the next 20 years (US Department of Energy, 1991). The development of technically and economically successful pretreatment processes for biomass waste suitable for subsequent gasification and hydrogen separation will make a major contribution towards the realization of this major renewable resource.

Discussion

Laboratory Scale Experiments

Objectives

The objective of the bench-scale laboratory work has been to establish operating conditions for a hydrothermal pre-processing scheme for municipal solid waste (MSW) that produces a good slurry product for conversion in a Texaco gasifier. "Good" in this context means a slurry that can be pumped and atomized in the gasifier feed injector, and that has a high Btu content leading to a high yield of hydrogen relative to the CO_2 byproduct. Pumpability and Btu content for raw MSW are contradictory requirements: high water content favors pumpability, i.e. lowers the viscosity of the slurry but also lowers the Btu content. However, hydrothermal treatment (Khan, 1993) results in partial dissolution of the solid and leaves an altered solid product that is more carbon-like in nature, and less water absorbing due to an altered pore structure. Both dissolution and reduced porosity lead to a lower viscosity of a slurry of given MSW content.

A more specific objective of the bench-scale work has been to study the kinetics of the hydrothermal reaction, i.e. the hydrolysis of the MSW, for the purpose of guiding the 1 ton/day pilot plant work. This work has mostly been carried out with model components of the MSW, namely several types

of paper, wood and paper/plastic mixtures. The kinetics work encompasses yield determinations for the three products, solubles, solids and gas, as well as rheological characterization of slurry products as a function of organic content. These results have been more completely documented elsewhere (Wallman, 1995).

Experimental Approach

The bench-scale work was carried out in batch autoclaves of three different sizes. The goal was isothermal experiments with preset reaction times. However, isothermal conditions were obtained only approximately because of the slow heat transfer between the oven atmosphere and the reactor wall. Gas yield was determined by allowing the product gas to fill an evacuated 1-liter volume at room temperature and recording the final pressure (at ambient temperature). Gas composition was determined by mass spectrometry. Slurries were prepared from either the wet filter cake (containing water and solubles) or from the dried cake by adding back the separated water, and shearing the resulting mixture. Slurry rheograms were determined on a Haake RV30 viscometer at Texaco's Montebello Research Laboratory. This viscometer uses a rotating spindle with a narrow gap between the spindle and the stationary wall. Some samples, particularly "thin" slurries, showed thixotropic behavior, i.e. thinning of the sample during the measurement. "Thick" samples showed separation upon loading the sample and could therefore not be run at all.

Cellulosic Yield and Viscosity Results

Table 1. Product yields (wt% feed)

Feed Material	Treatment	Solids	Solubles	Gas (mostly CO_2)	Water (difference)
Newspaper	320 C, 30 min	55	23	12	10
	275 C, 2 hours	67	10	11	12
Wood	310 C, 30 min	47	30	11	12
Paper dunnage	260 C, 30 min	61	16	12	11
	275 C, 30 min	55	17	12	16
	310 C, 30 min	48	17	17	18
	320 C, 30 min	50	16	16	18
	275 C, 2 hours	52	22	14	12

The yield results are summarized in Table 1 for a newspaper, a coniferous wood and a paper dunnage sample. The source of the newspaper sample was the laboratory bi-weekly newspaper which is printed on high-grade paper while the paper dunnage which is composed of tailings from paper mills came from an industrial packaging company. The wood was in the form of saw dust.

The experiments in Table 1 were conducted at a water/feed ratio of 2 except for the last row which

is the average of five experiments conducted with ratios 1, 2, 3, 4, and 10. The interpretation of this result is that a water/feed ratio of 1 is sufficient to "wet" the solid reactant and that any extra water merely acts as a diluent. This is important because a ratio of one produces a relatively thick slurry without any separation of excess water. It is, therefore, quite possible that a process can be designed without any excess waste water that would be expensive to treat. It is also noteworthy that no improvement was observed by starting with 0.1N acid instead of pure water. Using a base to force the cooking solution to be alkaline was deemed to be too expensive for a practical process.

In viscometer tests (Wallman, 1995) the paper dunnage produced acceptable slurries at higher concentrations than the newspaper did. This important result is also reflected in a yield difference between the two materials: The paper dunnage produces less solid product and more water. However, the soluble yield results in Table 1 leave uncertainty about the true trends because the two comparisons produce contradictory findings. Paper dunnage is expected to produce more solubles, but this must be confirmed in future work.

Figure 1 shows the first results on the effects of treatment severity on the paper dunnage that will be used for the pilot plant work. With severe treatment (310°C or 320°C for 30 minutes, or 275°C for 2 hours) the paper dunnage produces a slurry of 55% organic content at 1000 mPa·s apparent viscosity. Figure 1 also shows that the slurry quality degrades quickly as the hydrothermal treatment becomes less severe. Further work will be required to derive kinetic expressions to be used for reactor design calculations. The preliminary finding that 310°C with a 30 minute residence is equivalent to 275°C with a 2 hour residence time translates to very different reactors because the pressure requirement is very sensitive to operating temperature.

Results with Plastic Containing Feed

A breakdown of the plastic components of "typical" MSW was obtained from the San Marcos facility (Worell, 1994) and indicated that the dominant component was low density polyethylene. Thus, polyethylene (PE) garbage bags were used in the initial laboratory work as representative of the main plastic component of MSW.

Batch hydrothermal treatment experiments of 90 % paper with 10 % PE have simply shown that the paper produces the usual slurry, whereas the PE component is largely unaltered by the process. PE melts at treatment conditions to a very viscous liquid and then re-solidifies during cooling. A small amount of paper-derived product "sticks" to the plastic pieces in the re-solidification but this is only of the order 10 % of the plastic and therefore negligible in terms of paper loss (paper and other cellulosic material are the main slurry-forming vehicles). However, the plastic pieces remaining after the cook were found to be so resilient that no comminution occurred upon shearing. Because of the difficulties encountered in pulverizing the plastic component after the hydrothermal treatment, several alternatives addressing treatment of plastics were investigated in the bench-scale work. Some success was achieved with the 90-10 paper/PE feed in a reactor provided with a hot blow-down valve. Although only the water and part of the molten PE flowed through the valve, the plastic component appeared to have been atomized in the process. The valve was apparently too small to allow the paper component to flow through. However, the approach of using a hot blow-down valve to

disperse the plastic component warrants further study on a larger scale.

Process Modeling

A series of process models (Thorsness, 1994, 1995a, 1995b) have been developed to allow evaluation of conceptual large scale process configurations and possible operating scenarios for our pilot scale facility. Two of the models are steady-state models constructed using the ASPEN PLUS simulator and a third solves transient equations associated with operation of our pilot scale facility. These models provide a means of evaluating the overall process with respect to major inputs and outputs and changes in operating strategies. The ASPEN PLUS modeling is primarily directed toward a commercial scale operation, although it has also been used to look at possible operating strategies for our pilot work. In the ASPEN modeling the conceptual process is broken down into the discrete modules summarized in Figure 2: pretreatment, gasification, quench, shift, cleanup and separation.

Although the entire operation is dealt with in the ASPEN PLUS modeling, the primary focus has been on the pretreatment step where a high solids content slurry is formed from MSW using hydrothermal treatment. To date, two distinctly different hydrothermal pretreamtent conceptual process models have been translated into working ASPEN PLUS models. The first is an indirect heating option and the other is a direct steam heat option. The results presented below were obtained during the past year and the assumptions used represent our best estimates at the time. As work continues better estimates of process physics and chemistry will become available and the models will be used to make updated estimates.

In the modeling, a simplified method of dealing with the composition and the stoichiometry of the reactions has been employed. The raw input MSW is assumed to be composed of an organic composite material characteristic of biomass derived constituents, a plastic component, an ash component (inorganic constituents) and moisture or water. All but the water components are treated as nonconventional solids. At this point in the modeling process it has been assumed that the organic component undergoes chemical change in the process while the ash and plastic passes through chemically unchanged. Information to date also indicates that most of the plastic will probably not be chemically altered in the hydrothermal process at the temperatures currently under consideration.

In addition to the nonconventional solids used to specify the incoming MSW, one other nonconventional solid is defined. This solid is used to represent the solid product of the hydrothermal decomposition of the organic composite material in the MSW. Each of the nonconventional solids has been given a component name for use in the simulation. These names are:

ORG - The composite organic material of the incoming MSW
PLS - The plastic component of the MSW
ASH - The ash, inorganic, component of the MSW
GORG - The solid organic product of the hydrothermal decomposition of MSW

The decomposition of ORG (biomass related component of MSW) in the current models is handled by assuming the overall reaction can be adequately described by the following

$$CH_AO_B\ (ORG) \Rightarrow CH_a\ O_b\ (GORG) + \alpha CO_2 + \beta CO + \delta H_2 + \phi H_2O + \gamma CH_4$$

In this overall reaction methane is used to approximate all hydrocarbon type gaseous products. For simplicity, the N, S and Cl have been omitted from the simplified reaction description. Currently these species are all carried along with the GORG component.

The assumed MSW composition and decomposition stoichiometry values used are given in Tables 2 and 3. In the process modeling results it is assumed that the PLS component does not change in the hydrothermal treatment units and that the ORG component decomposes according to the stoichiometry given in Table 3. The energetics of the assumed ORG decomposition are given in the second part of the table. Notice for this choice of parameters the heat of reaction for the decomposition at 25 C is small and all the heating value of the MSW is available in the solid product.

Table 2. Assumed Raw MSW Component Composition.

Component	Weight %
H2O	25.0
ORG	48.6
PLS	8.3
ASH	18.1

Table 3. Stoichiometry and Energetics used in Defining MSW Related Components.

	Feed	Feed		Solid Product	Dry Gas Mole %					H2O Product /Feed	Dry Gas Product /Feed
	H/C	O/C	H/C	O/C	CO2	CO	H2	CH4	(kg/kg)	(kg/kg)	(kg/kg)
ORG	1.49	0.66	1	0.33	80	4	7	9	0.72	0.19	0.09
PLS	1.71	0.24	1.71	0.24	0	0	0	0	1	0	0
	1.52	0.60	1.10	0.32	80	4	7	9	0.76	0.16	0.08

	Feed Heating Value	Solid Product Heating Value	Heat Reaction	Solid Product / Feed Heating Value
	(MJ/kg)	(MJ/kg)	(MJ/kg)	
ORG	17.9	24.7	0.26	1.0
PLS	30.6	30.6	0	1.0
ORG + PLS	19.8	25.6	0.22	1.0

Indirect Heating Option

A process flowsheet for the indirect hydrothermal pretreatment option is shown in Figure 3. The incoming raw MSW is mixed with recycled water and shredded. A classification by weight is then done removing some of the heavier components. An ad hoc assumption that 50% of the incoming ash will be removed in this separation has been made. This yields a material with an ash content similar to that of RDF. This initial processing occurs at atmospheric pressure. The dilute slurry mixture is then raised to the desired reaction pressure using a high pressure pump. It then passes through a countercurrent heat exchanger system; the final reaction temperature is reached by addition of steam and indirect heating. After passing through the reactor vessel and the heat exchanger any free gas is separated from the liquid slurry. After a pressure letdown/flash, the slurry passes to a filter, or thickener, which establishes the desired solids content of the product slurry. The filtrate is then further flashed to drop the temperature so that the water can be recycled to the atmospheric operations. The flashed vapors are mixed with the separated gas and passed through a condenser. The condensate is added to the recycle stream. The recycle stream flow rate is controlled to give the desired ratio of raw MSW to water.

A topical report has been written (Thorsness, 1994) which outlines details of the model and discusses a variety of computed results, for both the hydrothermal process area and the overall plant. Selected results from the report are outlined here.

This model has been used to compute a best estimate base case for a process utilizing 30 kg/s (2600 tonne/day) of raw MSW feed. The processing scheme employed for the pretreatment of the MSW

was aimed at producing a water fuel slurry suitable for gasification in a Texaco slurry fed gasifier. For the base case 0.672 kmol/s of hydrogen are produced (equivalent to 192 MW of thermal energy based on hydrogen's higher heating value).

The process modeled was arranged so that all effluents from the MSW hydrothermal pretreatment are fed to the gasifier thus avoiding production of foul water and gases. The introduction of effluent gases from the pretreatment step degrades the gasifier performance since the gases have CO_2 as a major constituent. However, because of the relatively low flow rate it is calculated that oxygen input to the gasifier would have to be increased by less than 2%, and this would lead to production of essentially the same amount of hydrogen.

Two process modifications were identified which have the potential to materially increase the process performance by increasing the gasification efficiency. One is the removal of a larger fraction of the ash (inert) material present in the MSW. If nearly all the ash could be removed the gasifier efficiency would improve by more than 15%. Also, the addition of an auxiliary feedstock, heavy oil, would increase gasifier efficiency and probably be very attractive economically. Probably the largest potential for degradation in process efficiency from that computed for the base case would be a result of a lower solids content of the processed slurry. The base case assumes a content of 55%, which is an optimistic guess at the upper end of that achievable. However, a reduction in solid content could be compensated for by a decrease in ash content, the presence of dissolved organic matter and the use of auxiliary liquid feedstock.

Direct Steam Heat Option

In the indirect processing scheme, a large heat exchanger to heat the MSW slurry to reaction temperatures is employed. The heat exchanger allows heat to be transferred between the hot reacted slurry and the cold raw slurry. In this way only modest amounts of energy are required to heat the raw slurry to the desired reaction temperature. In order for this scheme to work, the raw slurry must have a low enough effective viscosity to allow it to be successfully heated in the heat exchanger. This means a raw solid loading of between 5-15 wt. %. This loading is far less then what is needed for an economically viable gasification process. Consequently, the reacted slurry in this scheme must be concentrated prior to its introduction into the gasifier.

In addition, the relatively low solid concentration of the incoming slurry means that a very large heat exchanger is required. Further, it may be that fouling would be a real problem in prolonged operation of such a unit. For these reasons and others the option of heating the MSW to the required temperature using direct heating with high pressure steam was considered.

The simplest means of utilizing direct steam heating of MSW would involve a batch process scheme. The shredded and classified raw MSW would be loaded into a pressure vessel and steam would be introduced. After maintaining the system at reaction temperature for the desired length of time the pressure would be gradually reduced, turning part of the water to steam which would cool the vessel contents. After reaching atmospheric pressure, the reactor would be unloaded and the hydrothermally altered MSW slurry would be ready to be fed to the gasification unit.

Schematically this process is shown in Figure 4. The raw MSW is shredded and classified and then loaded into a reactor vessel. The batch operation is depicted in the figure as if it were continuous. The various stages of operation of the reactor vessel are labeled stage 1-3. Stage 1 (not labeled in the figure) is the atmospheric loading of the classified MSW into the vessel. Stage 2 is the steam heating of the MSW feed with high pressure steam and stage 3 is the pressure letdown/cooling phase. The gas and steam from stage 2 and stage 3 operations are sent to a condenser. The water collected in the condenser is shown being fed back into the process during the stage 3 operation. This water could also be mixed after the cool down process.

The process scheme shown assumes that all the water entering the process will be present in the product slurry. One of the primary purposes of the modeling is to determine the final water content of the product slurry using this assumption. In theory, the final product slurry water content could be adjusted by addition or removal of water. However, if water removal is necessary then the processing would have to deal with a waste water stream.

The scheme represented in Figure 4 is the simplest process for using steam to heat the raw MSW. However, it is not the most thermally efficient because the hot steam and gases which emerge from the reactor are simply sent to the condenser. Clearly, a more energy efficient process would involve recovering some of this waste heat. Such a modification requires additional pressure vessels and effective staging of the flow of treated MSW. Each pressure letdown stage would have a companion preheat bed which would effectively capture the heat energy in the steam released during the pressure letdown operation. Any number of stages could be envisioned. In Figure 5 a clockwise time sequence for operation with one preheat bed is shown. Four vessels are shown, one each for the four major stages of operation, loading, preheating, heating/reacting and pressure letdown. Assuming times for each operation are similar, all four vessels would be participating in one of the operations at all times and a load of product slurry would be produced every Δt time internal. Additional vessels can be added to optimize heat recovery.

A topical report has been written which describes all of these additional conceptual process ramifications for direct steam heating in more detail (Thorsness, 1995a). Selected results are as follows. The product slurry produced by the process, based on recombining the condensate with the final product, has a solid content of 33 wt. %. If the condensate is not recombined with the final product then the product slurry would have a solid content of 52 wt %. It is interesting that these levels correspond very closely with desired values of 35-55 wt. % solids for a pumpable slurry product.

The use of the term solid content needs some clarification. This term is meant to represent all the nonwater portion of the slurry. In the model described here all the solid and liquid products of decomposition are represented by the nonconventional species GORG, and in the model GORG is treated like a solid. In reality, however, the products of decomposition would involve some liquid and some soluble components. These components are included here in what is referred to as solid.

Calculations done for the two preheat bed case indicate that there is an optimum pressure for the operation of the intermediate beds. At the optimum intermediate pressure, equal to 2.6 MPa, the

computed results show considerable improvement in process performance compared to the zero preheat bed case. The injection steam flow is 11.1 kg/s compared to 21.2 kg/s, the solid content is 42.5 wt.% compared to 33.5 wt.% and the required cooling is 18.7 MW compared to 43.6 MW. Thus, a conceptual hydrothermal process in which direct steam heating is used to raise MSW to the required reaction temperature is capable of producing product slurries in the range of interest for gasification, 35-55 wt.% solids. Computations indicate that slurries at the lower end of this range can be produced with no waste water cleanup since all condensate is added back to the product. At the higher end, some waste water treatment would be needed, although no net water would be produced. In this mode of operation condensate from the cooling operation could be cleaned sufficiently to supply water for the steam generator.

It appears that the use of multiple pressure vessels working together to recover waste heat would be the most efficient arrangement for direct steam heating of MSW in a hydrothermal processing scheme. Although a more complete design and accompanying economic evaluation is needed, it appears that a system in which two preheat stages are used is probably near the optimum. Furthermore, for systems in which preheat beds are used to capture waste heat there is an optimum pressure for operation of the companion intermediate pressure letdown stages. It is advantageous to operate the reaction stage somewhat above the minimum pressure which would maintain the water phase. This reduces the steam requirements at the expense of operating at a slightly higher pressure. Operating the reaction stage 1.5-2 MPa above the vapor pressure of water at the desired reaction temperature appears to be a good compromise between steam savings and increased operating pressure.

The efficiency of the heat recovery using preheat beds is a very weak function of pressure difference between gas source beds and preheat beds. Pressure drop within vessels and potential entrainment is a concern. The most severe conditions are present in the final pressure letdown stage of the process. Velocities in this vessel have the potential of entraining particles 100 microns or less in size.

Interchange of heat between vessel walls and interior would reduce the efficiency of the process. For the two preheat bed case the difference between complete adiabatic operation and complete equilibration of vessel contents and wall results in an increase of steam requirements of 40%. The manner in which heat would move from vessel contents to wall is fairly complicated and additional work is needed to determine the exact impact of the vessel walls on the process efficiency.

The wetter the MSW feed the less efficient the process. For the same operating conditions increasing the MSW feed water content from 25 to 35 wt.% increases the steam requirement by about 15 %.

Using heavy oil, or other low cost fuel, as an additional feedstock to increase the efficiency of the gasification of the product slurry should be considered. A slurry containing 42.3 wt.% solids can be produced assuming adiabatic operation of a two preheat bed system needing no waste water treatment. Gasifying this slurry on its own would produce 0.49 kmol/s of hydrogen from 30 kg/s of raw MSW, with a produced hydrogen to consumed oxygen mole ratio of 0.9. Adding 16 kg/s of heavy oil feedstock to the gasifier along with the 37 kg/s of slurry would result in the production of 2.6 kmol/s of hydrogen with a hydrogen/oxygen ratio of 2.6.

Continuous Flow Direct Steam Heat Option

The main advantage of the direct steam heat option is that heat transfer surfaces are not needed and the water content can conceivable be controlled so that no filtering operation is needed to set the desired high solids content of the final slurry. The primary drawback is that large amounts of expensive steam are needed or alternatively multiple high pressure vessels are needed to allow energy recovery at more modest steam requirements.

On the other hand, the primary advantage of the continuous operation is that it is continuous and thus concerns over cycling of condensers, steam generators and fired heaters is eliminated. Its primary drawback is the fact that it relies on a large heat exchanger to move heat from the reacted slurry to the raw incoming slurry. It is not clear that the fouling of the heat exchange surfaces could be controlled to acceptable levels. Another drawback is that the direct product of the process is a low solids concentration slurry which needs to be concentrated by filtering of the product.

A third process can be visualized which combines the direct steam heat and continuous operation. This process is like the batch-direct-steam-heat process in that no heat exchange surfaces are used, but at the same time it is continuous. The process involves starting with a pumpable raw slurry, on the order of 10 wt.% solids. The raw slurry is heated to near the required reaction temperature through a series of stages. Between each stage the pressure is increased by means of a pump. Heating occurs in each stage by introduction of steam from a companion flash operation. The flash operations occur as the slurry leaving the primary reactor vessel is sent through a series of flash drums in which the pressure is reduced. The pressures of the flash operations are kept slightly above the pressure of the heat stage so that the steam flows freely from the flash to the heat vessels. The final trim of the temperature to the desired reaction temperature is obtained by injection of high pressure steam.

Clearly, in this continuous-direct-steam-heat process there is a tradeoff between the number of stages and the amount of high pressure steam needed to achieve the desired reaction temperature. To determine the steam requirements as a function of number of stages a series of preliminary computations has been done assuming the slurry had the properties of water. Since the fluid has a relatively low solids concentration this simplification probably does not lead to serious error.

The choice of the number of heat recovery stages would be made based on an economic evaluation. Decrease in steam requirements comes at the expense of more vessels and pumps and an increase in process complexity. In related processes, such as multi-effect evaporation five to seven stages often turns out to be the most economical.

This continuous-direct-steam-heat process will work in principle. From an operational point of view possible failure modes include excessive frothing and resulting difficulty in pressure control during the pressure letdown operations. However, this difficulty would appear much less than the potential difficulty of fouled of heat exchanger surfaces faced by the indirect-continuos process.

Transient Model of Pilot Direct Steam Heat Operation

As a first step in investigating a steam heat option for preparing a suitable slurry from MSW some pilot scale experiments using shredded newspaper as a surrogate for MSW are planned. The planned pilot facility is shown schematically in Figure 6. The processing will be accomplished in a batch mode. First the newspaper will be loaded into the reactor vessel. The vessel will then be sealed and steam introduced into the reactor. As the temperature increases the pressure in the system will increase. At some point the upper pressure limit for the system will be reached. At this point the steam injection will be reduced and gas and steam will begin to exit through the pressure control back pressure control valve. After a suitable reaction time steam injection will be terminated and the system pressure will gradually be relieved by gradually opening of the pressure control valve. During the reaction and blow down phase, water vapor will be produced from the system and pass through a downstream condenser. After the pressure letdown some water will also remain in the reactor and the dropout vessels. Scrubber and charcoal filter units in the downstream line insure that the noncondensable gas, primarily carbon dioxide, is suitable for discharge to the atmosphere.

A transient model was formulated to allow estimates of the time history of the reactor and dropout vessels and their contents to be made. The system modeled consists of the two vessels connected together . Gas can exit Vessel 2 depending on the position of the control valve. Steam is introduced into the main reactor, Vessel 1. Heat can flow to/from the vessel walls and the environment or the vessel contents. An initial charge of newspaper is assumed to be present in the main reactor Vessel 1. Air is assumed to initially fill the void space in each vessel.

Material and energy balances are written for the two vessels and energy balances for the vessel walls. It is assumed that the newspaper present in Vessel 1 undergoes a first order reaction to produce solid product, noncondensable gases and water. Three gas phase species, one liquid and two solid species are assumed present in the system. The gases are assumed to consist of air, noncondensable gas products from the decomposition and water vapor or steam. The only liquid species considered is water and the solids are newspaper and the solid product of the hydrothermal decomposition reaction. An overall decomposition reaction,

$$\text{Newspaper} \rightarrow \alpha_s(\text{Solid Product}) + \alpha_w(\text{Water}) + \alpha_G(\text{Noncondesable Gas})$$

is assumed, where 's are the stoichiometric coefficients for the assumed overall reaction. The solid product coefficient is assumed to be expressed on a weight per weight of newspaper basis while the water and gas coefficients are assumed to be expressed on a mole per weight of newspaper basis.

The transient model was used to explore many operating options and assumptions about the nature of the processes which would actually occur during a pilot run. Details of the results are presented in a topical report (Thorsness, 1995b). It was found that using a flow of 2 mol/s steam and a programmed reduction of pressure in the blowdown phase would yield modest velocities within the

reactor system. The model indicates that because of the high heat capacity of the vessel walls it would be advantageous to preheat the walls of the primary reactor vessel externally to reduce the total amount of water which would be present in the vessel at the end of the process. At the same time to adequately cool the material and vessel walls after the decomposition external cooling of the reactor walls would be useful. Calculations indicate that forced air cooling using 6 mol/s (300 scfm) of air should be adequate to cool the system in a reasonable time.

Calculations indicate that there is no need to insulate the knockout vessel. Uncertainties in the energetics of the decomposition reaction translate into uncertainties in computed estimates of the amount of water accumulating in the reactor vessel for a given set of conditions. The computed results indicate that for a doubling of the assume 0.39 MJ/kg heat of reaction the amount of water in the reactor vessel at the end of the process would increase by about 50%.

The model results indicate that the total amount of condensate, resulting from a run, per unit newspaper declines as the amount of newspaper processed increases. For typical conditions an increase of 50% in the newspaper processed was found to decrease the final slurry product by 7 wt.% water, when the final product is assumed to contain all the condensate from a run.

The manner in which heat transfer occurs between the reactor vessel walls and the interior can have a substantial influence of the final water content of the reactor vessel. Model calculations indicate that the amount of water remaining in the reactor can change by a factor of two depending on the assumed heat transfer coupling between wall and contents. A drying front model was developed and incorporated into the model to try to address the heat transfer coupling issue. Computed results indicate that the actual system, in the absence of water movement within the reactor, will probably exhibit poor heat transfer between wall and reactor interior during the cool down period.

Based on the calculations performed an operating strategy and scenario was developed for the first pilot test. This test would use an uninsulated knockout vessel and a reactor insulated with its walls preheated to 150 C, but providing a means to externally air cool the walls during the cool down period. A maximum reactor pressure of 6.3 MPa is assumed. Model results for this case using a 2 mol/s steam flow during the heatup phase indicate that the heatup time would be 113 minutes, the maximum temperature 269 C and the final contents of Vessel 1 would contain 43 wt.% solids (57 wt % water). After a 48 hour cool down period the contents of the reactor should have cooled to 39 C while the reactor walls will have cooled to 31 C. This initial experiment is tailored to insure a relatively high water content in the reactor during the decomposition of the newspaper. A feed which has a water to dry newspaper ratio of 0.5 was assumed in the calculations. This leads to a computed water content of about 70 wt.% during the reaction phase.

Pilot Scale Processing

Lawrence Livermore National Laboratory is renting from Texaco a 6 ton/day hydrothermal treatment facility. This facility, mostly mounted on two trailers, was transported from Texaco MRL to LLNL in January 1995, following negotiations and is currently undergoing modification to permit batch processing. The Texaco plant was originally built to continuously process sewer sludges and requires

modification for use in MSW testing. All necessary permits have been obtained, and it is anticipated that initial shake-down will occur during early summer of 1995. Initial hot runs will be with approximately 200 kg of newspaper heated by direct steam injection to a temperature of 275 C. Figure 7 depicts the currently envisiaged layout of this facility.

Conclusions

Slurry viscosity at a given solids content was found to be strongly correlated both with the source material, and with the temperature and time of the hydrothermal treatment (Wallman, 1995). As expected, more severe conditions yielded better results. Treatment temperature could be lowered by a compensating increase in residence time. Quite unexpectedly, different paper grades produced different results with low-quality paper forming better slurries than high-quality papers. This finding points to the need for more exact feed characterization. Polyethylene plastic was not affected favorably by the batch hydrothermal treatment used in the bench-scale work. Hot blow down as part of hydrotreatment is proposed as a suitable treatment for the plastics. This will be investigated in future work in conjunction with expansion to other types of plastics.

MSW has been modeled as a process materials for the production of hydrogen (Rogers, 1994). A series of process models have been development to allow evaluation of conceptual large scale process configurations and possible operating scenarios for a pilot scale facility (Thorsness, 1994, 1995a, 1995b). Two of the models are steady-state models constructed using the ASPEN PLUS simulator and a third solves transient equations associated with operation of our pilot scale facility. These models provide a means of evaluating the overall process with respect to major inputs and outputs and changes in operating strategies. Advantages have been described with respect to direct steam injection as opposed to the extensive use of heat exchangers, and a conceptual process modeled for either a batch or continuous process stream. Economic considerations and experience from pilot scale-up are needed before a final decision can be made as to the optimal process configuration and parameters. A transient model has been developed to guide our initial pilot plant scale-up of MSW hydrothermal treatment.

Because of the lower costs of implementing the direct steam heat option at the pilot scale, versus the indirect option, our initial pilot scale work will used the direct steam option to produce pilot scale quantities of slurry for initial pumping and gasification tests at Texaco MRL. LLNL is modifying a hydrothermal treatment facility obtained from Texaco in order to provide sufficient material for these subsequent tests. Initial runs will be made with newspaper; based on computed results we currently plan for the first pilot experiment to use a dampened feed material containing a water-to-dry newspaper ratio of 0.5 to 1. The transient model predicts that this will result in a slurry product in the reactor vessel after cooldown containing 43 wt.% solids.

Future Work

The main activity for the remainder of FY95 will be modification and operation of the Texaco-built hydrothermal preprocessing pilot plant and experimental testing at LLNL. The initial experimental testing will be conducted with newspaper as surrogate MSW. Steam heating will be the initial processing option. The nominal capacity of the hydrothermal pilot plant will be 1 ton/day (dry weight), but experimental runs will typically be limited to about 8 h. The objective is to demonstrate that the high-Btu-content slurry preparation process based on hydrothermal treatment works with an idealized MSW feedstock. Guidance will be gleaned from the appropriate modeling simulations. Information for our system study will also be gathered.

Pumping tests of the produced slurry will be started at Montebello using feed slurry prepared from newspaper. Later gasification testing will be undertaken at the laboratory scale. We intend to quickly move into a demonstration of the ability to handle the plastic components of MSW. The primary plastic component present in MSW is polyethylene and preliminary testing has shown that this plastic melts but does not decompose during hydrothermal treatment. The dispersal of this and other plastics into solid particles no larger than 1 mm is essential to allow the produced slurry to be successfully fed to the gasifier. Options to deal with the dispersal of plastic include the use of post or preprocessing mechanical shearing, hydrodynamic shearing during processing and shearing during pressure letdown. This later option is related to steam explosion used in the manufacture of masonite from wood byproducts. Each of these options is most appropriately addressed at the pilot scale.

In addition, we plan to address the problem of the amount of raw MSW size reduction necessary prior to the hydrothermal treatment process. The amount of size reduction is tied closely to the particular process option contemplated. The indirect heating option, where heat exchangers are to be used, demands the greatest amount of initial size reduction. In this mode of operation a raw slurry capable of being successfully pumped through a heat exchanger is required. In the direct steam heat options this is not the case and larger particle sizes and higher initial slurry solid contents can be tolerated. Testing will be undertaken to determine the maximum particle size of which can be successfully treated with direct steam heating.

Depending on the results of surrogate testing extension to real MSW feedstock may begin in the later portions of FY96. The plan for FY97 calls for working towards testing of real MSW and integrated MSW-to-hydrogen tests at Montebello. Second iterations on the slurry test loop and gasification operation would be completed, with various pretreated MSW surrogates, components, and representative samples being supplied by LLNL. The hydrothermal pretreatment unit which is built on trailers will be transported to Montebello for continuous / batch test runs towards the conclusion of the year. One objective of these tests are to determine product qualities (including ash byproduct) in the face of varying feed quality (MSW is inherently more variable than other fuel feedstocks) and augmented, as necessary, with supplemental feed. Another objective for this year is to gather data for scale up of the process towards commercial size. A more-detailed economics study, including

operational costs and potential initial market applications, will be initiated once the details of the processing had been narrowed in scope.

Acknowledgements

This work was performed under the auspices of the U. S. Department of Energy by Lawrence Livermore National Laboratory under contract No. W-7405-Eng-48.

References

Khan, M. R. 1993. *Clean Energy from Waste and Coal. ACS Symposium Series 515*. Washington, D.C.: American Chemical Society.

Pasternak, A.D., J.H. Richardson, R.S. Rogers, C.B. Thorsness, G.N. Richter, J.K. Wolfenbarger, 1994. *MSW to Hydrogen* , UCRL-JC-116421. Lawrence Livermore National Laboratory, Livermore, CA.

Rogers, R. 1994. *Hydrogen Production by Gasification of Muncipal Solid Waste* , UCRL-ID-117603. Lawrence Livermore National Laboratory, Livermore, CA.

Thorsness, C.B. 1994. *Process Modeling of Hydrogen Production from Municipal Solid Waste* UCRL-ID-119231. Lawrence Livermore National Laboratory, Livermore CA.

Thorsness, C.B. 1995a. *A Direct Steam Heat Option For Hydrothermal Treatment of Municipal Solid Waste,* UCRL-ID-120283. Lawrence Livermore National Laboratory, Livermore CA.

Thorsness, C.B. 1995b. *Process Modeling of Hydrothermal Treatment of Municipal Solid Waste to Form High Solids Slurries in a Pilot Scale System,* UCRL-ID-119685. Lawrence Livermore National Laboratory, Livermore CA.

US Department of Energy, 1991. Energy Information Administration/Annual Energy Outlook.

Wallman, P. H. 1995. *Laboratory Studies of a Hydrothermal Pretreatment Process for Municipal Solid Waste*, UCRL-ID-120296. Lawrence Livermore National Laboratory, Livermore, CA.

Worell, B. 1994. Private communication. North County Resource Recovery Associates, San Marcos, CA.

Figure Captions

Figure 1 Effect of treatment severity on slurry viscosity using paper dunnage as the feedstock.

Figure 2 Overall MSW to Hydrogen conceptual process model showing all major material and energy streams entering and leaving the overall process.

Figure 3 The indirectlty heated continuous hydrothermal conceptual process.

Figure 4 Hydrothermal conceptual process using high pressure direct steam heating.

Figure 5 Process schematic for single preheat vessel case showing operation in each of four configurations (a-d). The sequence is repeated after 4Dt time units.

Figure 6 Schematic of pilot process.

Figure 7 Approximate configuration of pilot scale hydrothermal treatment unit, rented from Texaco MRL and undergoing modifications at LLNL.

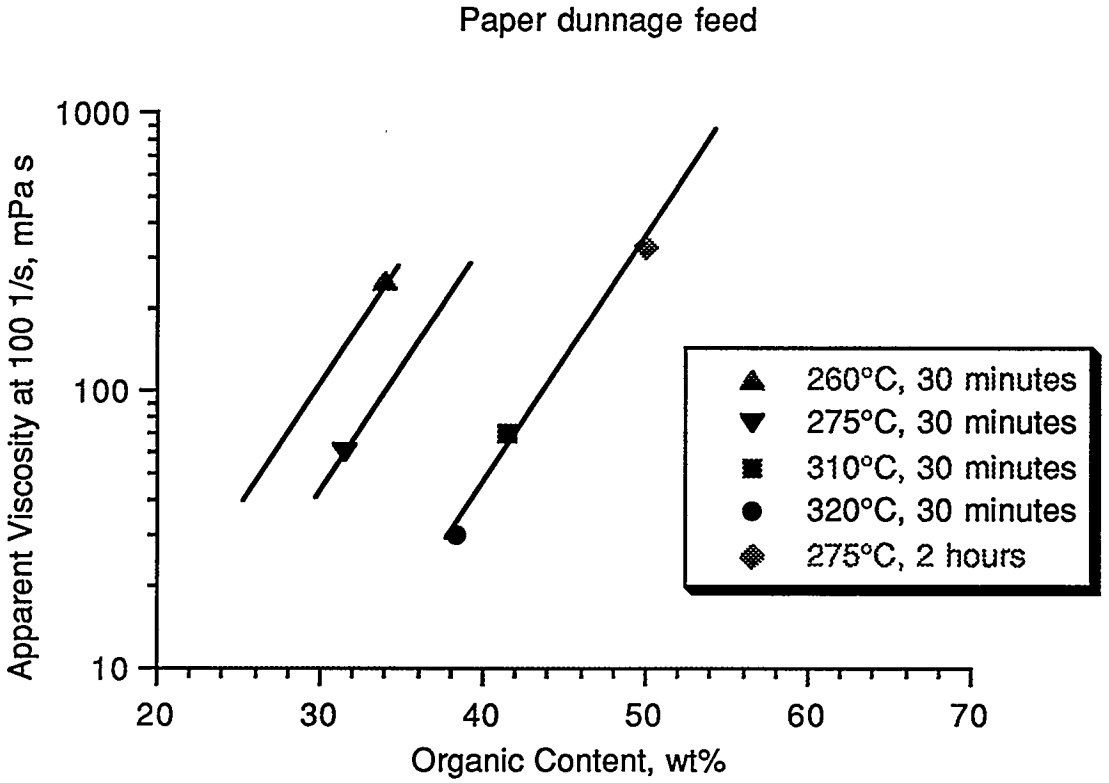
Paper dunnage feed
Apparent Viscosity at 100 1/s, mPa s
1000
100
10
20
30
40
50
60
70
Organic Content, wt%
260°C, 30 minutes
275°C, 30 minutes
310°C, 30 minutes
320°C, 30 minutes
275°C, 2 hours

Figure 1

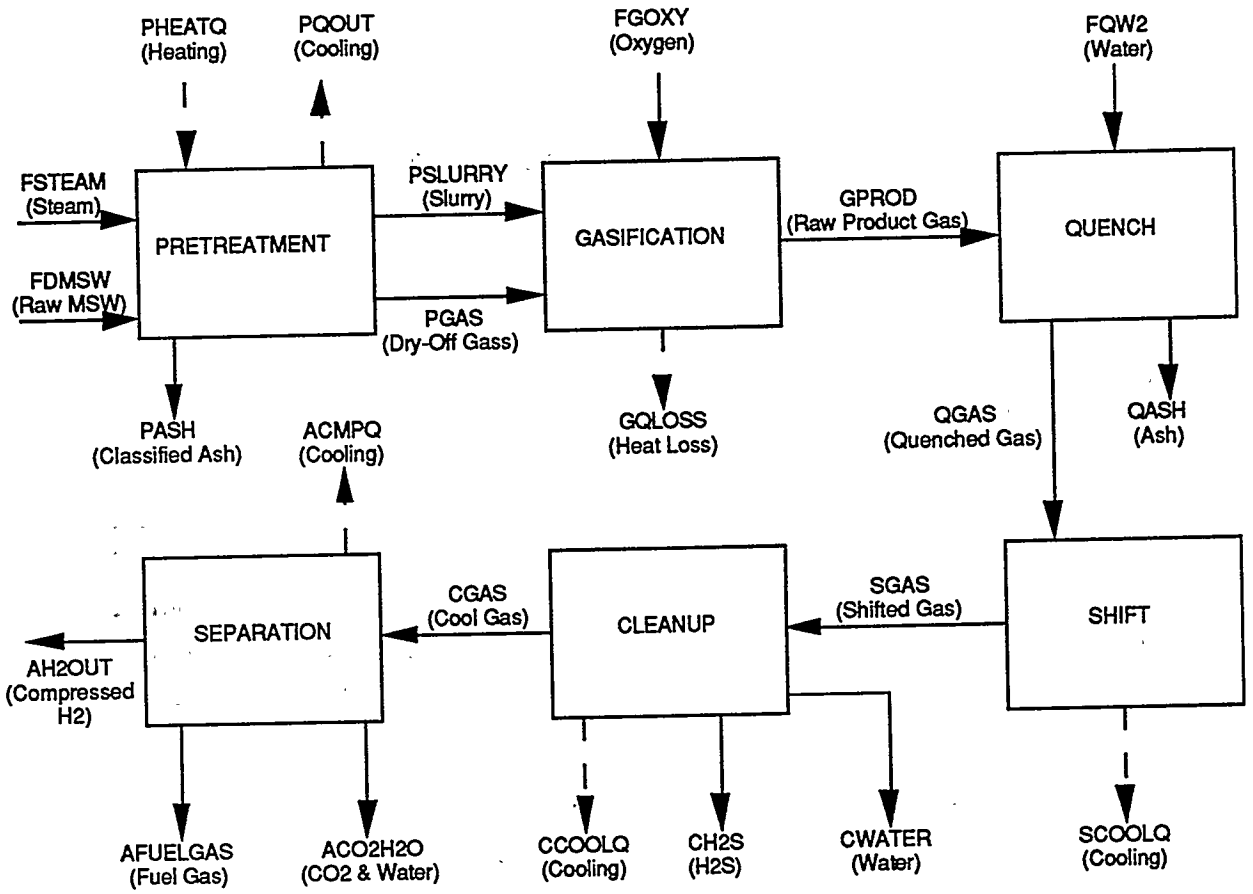
PHEATQ
(Heating)
PQOUT
(Cooling)
FGOXY
(Oxygen)
FQW2
(Water)
FSTEAM
(Steam)
FDMSW
(Raw MSW)
PRETREATMENT
PSLURRY
(Slurry)
PGAS
(Dry-Off Gass)
GASIFICATION
GPROD
(Raw Product Gas)
QUENCH
PASH
(Classified Ash)
ACMPQ
(Cooling)
GQLOSS
(Heat Loss)
QGAS
(Quenched Gas)
QASH
(Ash)
SEPARATION
CGAS
(Cool Gas)
CLEANUP
SGAS
(Shifted Gas)
SHIFT
AH2OUT
(Compressed
H2)
AFUELGAS
(Fuel Gas)
ACO2H2O
(CO2 & Water)
CCOOLQ
(Cooling)
CH2S
(H2S)
CWATER
(Water)
SCOOLQ
(Cooling)

Figure 2

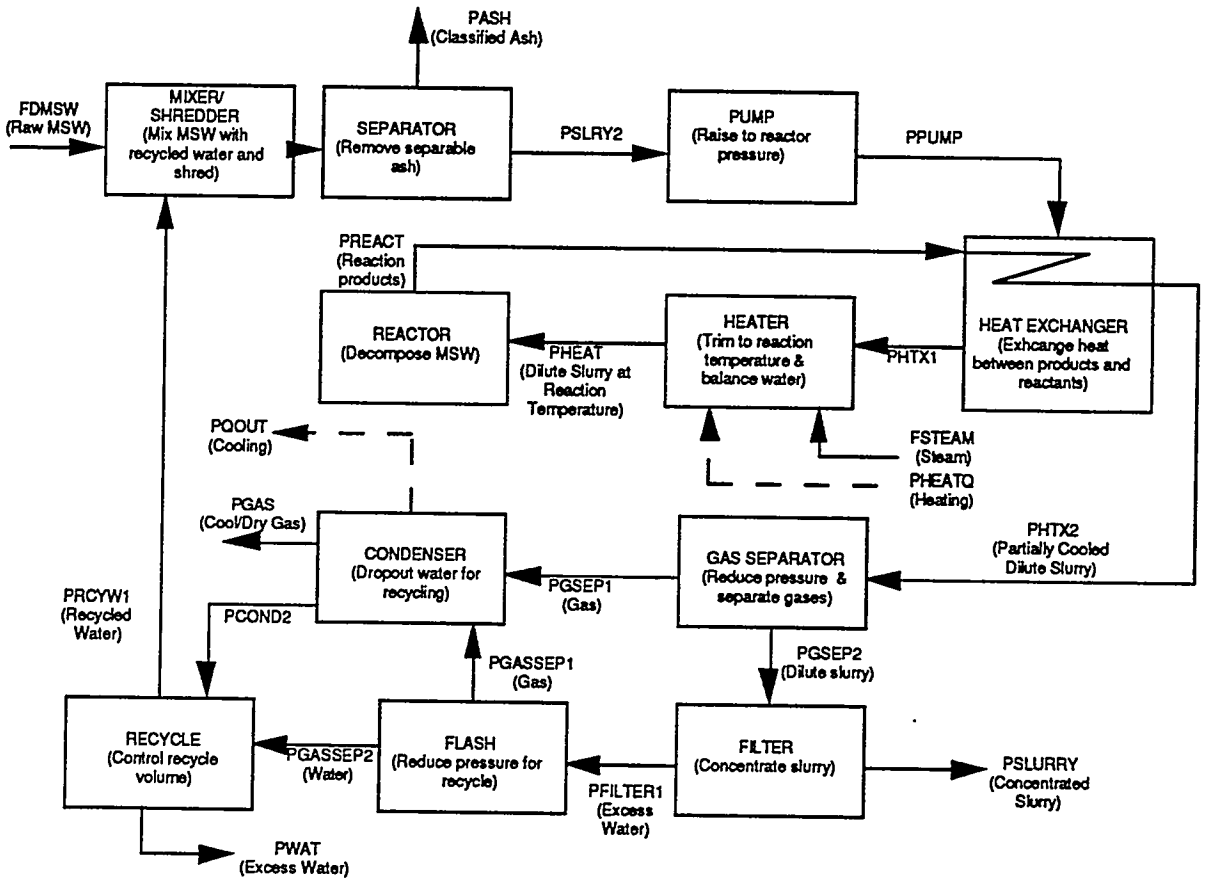
PASH
(Classified Ash)
FDMSW
(Raw MSW)
MIXER/
SHREDDER
(Mix MSW with
recycled water and
shred)
SEPARATOR
(Remove separable
ash)
PSLRY2
PUMP
(Raise to reactor
pressure)
PPUMP
PREACT
(Reaction
products)
REACTOR
(Decompose MSW)
PHEAT
(Dilute Slurry at
Reaction
Temperature)
HEATER
(Trim to reaction
temperature &
balance water)
PHTX1
HEAT EXCHANGER
(Exhcange heat
between products and
reactants)
POOUT
(Cooling)
FSTEAM
(Steam)
PHEATQ
(Heating)
PGAS
(Cool/Dry Gas)
CONDENSER
(Dropout water for
recycling)
PGSEP1
(Gas)
GAS SEPARATOR
(Reduce pressure &
separate gases)
PHTX2
(Partially Cooled
Dilute Slurry)
PRCYW1
(Recycled
Water)
PCOND2
PGASSEP1
(Gas)
PGSEP2
(Dilute slurry)
RECYCLE
(Control recycle
volume)
PGASSEP2
(Water)
FLASH
(Reduce pressure for
recycle)
PFILTER1
(Excess
Water)
FILTER
(Concentrate slurry)
PSLURRY
(Concentrated
Slurry)
PWAT
(Excess Water)

Figure 3

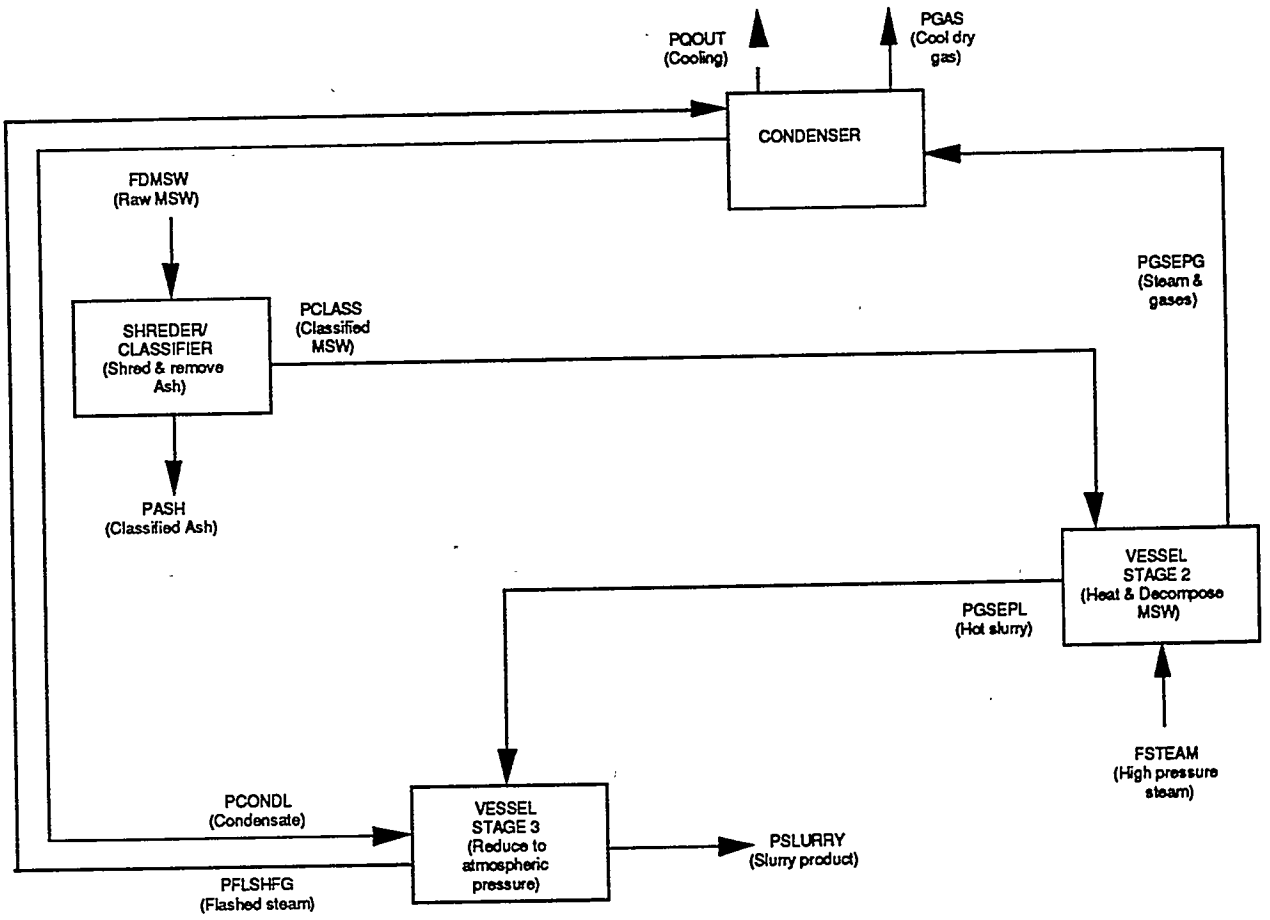
PQOUT
(Cooling)
PGAS
(Cool dry
gas)
CONDENSER
FDMSW
(Raw MSW)
PGSEPG
(Steam &
gases)
SHREDER/
CLASSIFIER
(Shred & remove
Ash)
PCLASS
(Classified
MSW)
PASH
(Classified Ash)
VESSEL
STAGE 2
(Heat & Decompose
MSW)
PGSEPL
(Hot slurry)
FSTEAM
(High pressure
steam)
PCONDL
(Condensate)
VESSEL
STAGE 3
(Reduce to
atmospheric
pressure)
PSLURRY
(Slurry product)
PFLSHFG
(Flashed steam)

Figure 4

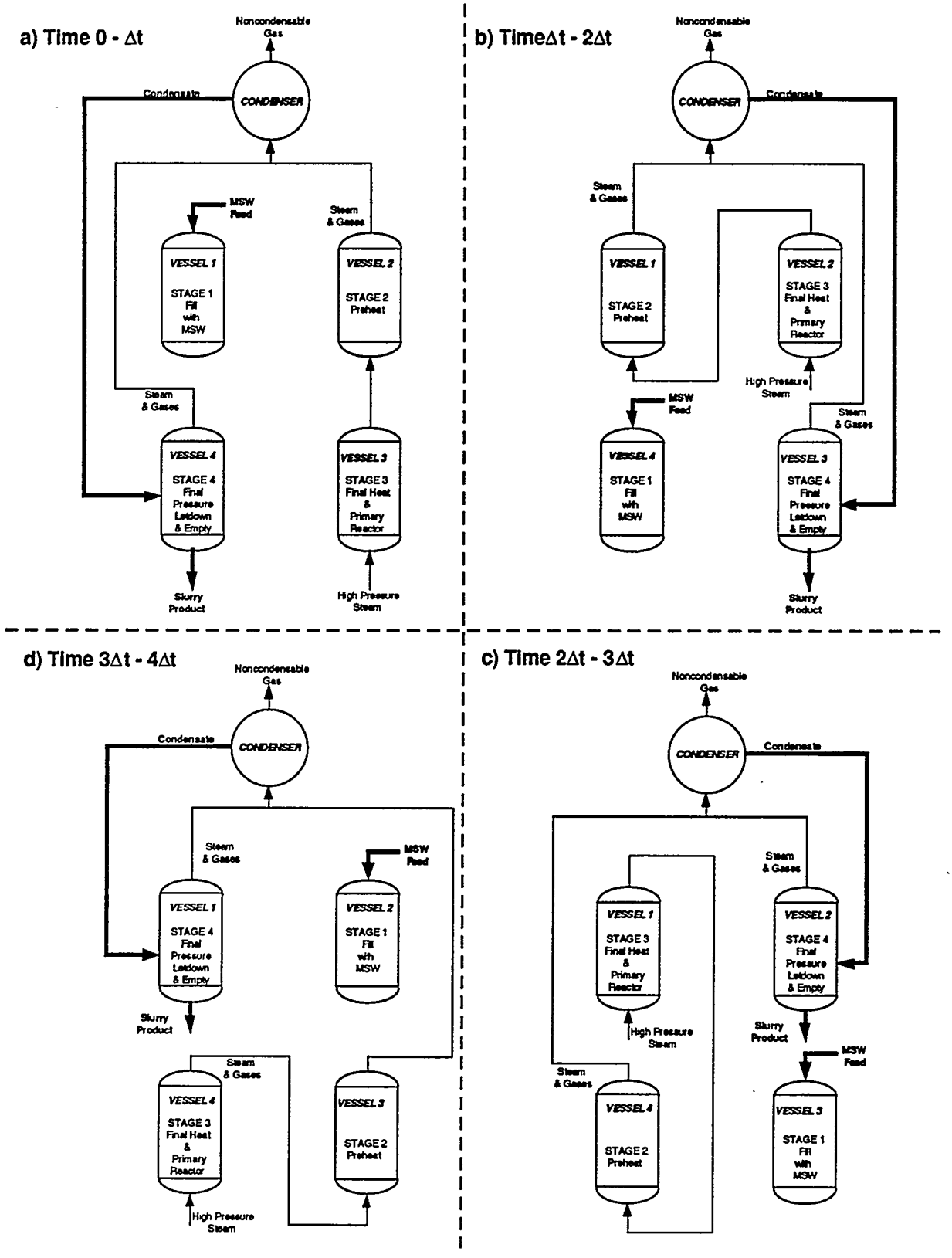
a) Time 0 - Δt
Noncondensable Gas
CONDENSER
Condensate
MSW Feed
Steam & Gases
VESSEL 1
STAGE 1 Fill with MSW
VESSEL 2
STAGE 2 Preheat
Steam & Gases
VESSEL 4
STAGE 4 Final Pressure Letdown & Empty
VESSEL 3
STAGE 3 Final Heat & Primary Reactor
Slurry Product
High Pressure Steam
b) TimeΔt - 2Δt
Noncondensable Gas
CONDENSER
Condensate
Steam & Gases
VESSEL 1
STAGE 2 Preheat
VESSEL 2
STAGE 3 Final Heat & Primary Reactor
High Pressure Steam
MSW Feed
Steam & Gases
VESSEL 4
STAGE 1 Fill with MSW
VESSEL 3
STAGE 4 Final Pressure Letdown & Empty
Slurry Product
d) Time 3Δt - 4Δt
Noncondensable Gas
CONDENSER
Condensate
Steam & Gases
MSW Feed
VESSEL 1
STAGE 4 Final Pressure Letdown & Empty
VESSEL 2
STAGE 1 Fill with MSW
Slurry Product
Steam & Gases
VESSEL 4
STAGE 3 Final Heat & Primary Reactor
VESSEL 3
STAGE 2 Preheat
High Pressure Steam
c) Time 2Δt - 3Δt
Noncondensable Gas
CONDENSER
Condensate
Steam & Gases
VESSEL 1
STAGE 3 Final Heat & Primary Reactor
VESSEL 2
STAGE 4 Final Pressure Letdown & Empty
High Pressure Steam
Slurry Product
MSW Feed
Steam & Gases
VESSEL 4
STAGE 2 Preheat
VESSEL 3
STAGE 1 Fill with MSW

Figure 5

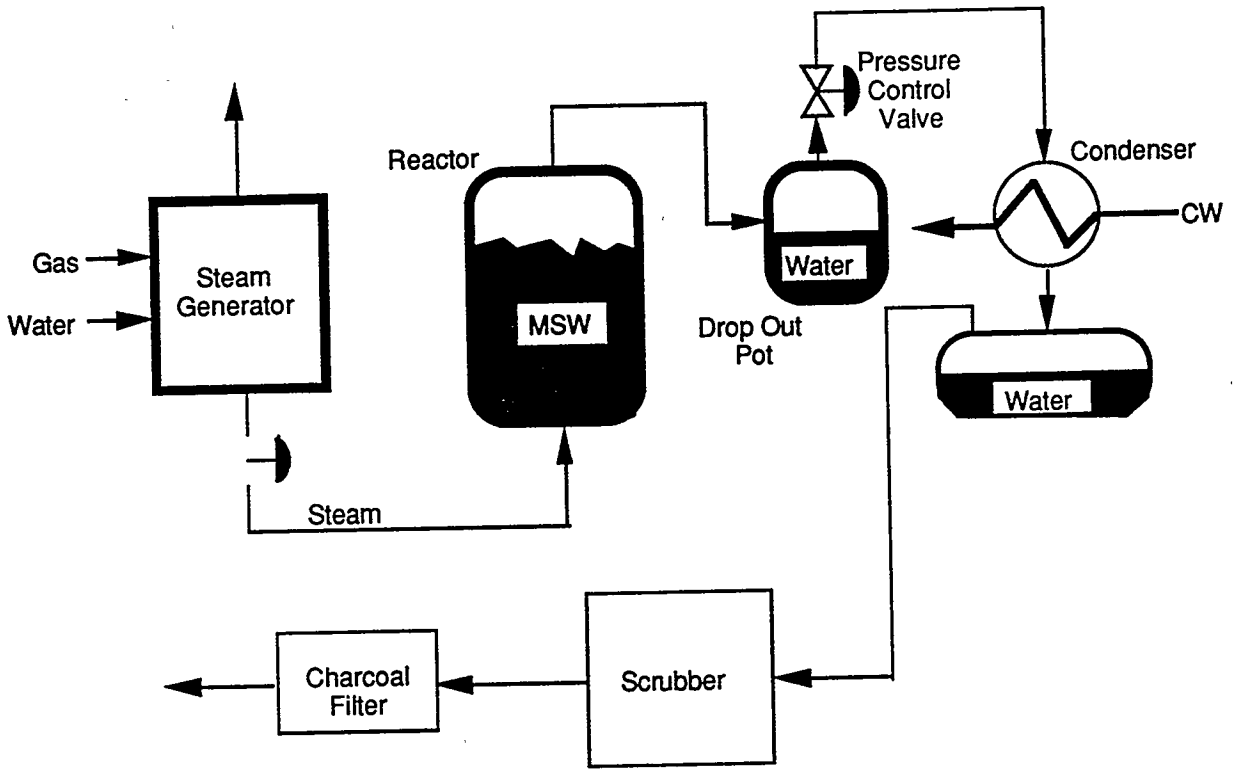
Pressure
Control
Valve
Condenser
Reactor
CW
Gas
Steam
Generator
Water
MSW
Water
Drop Out
Pot
Water
Steam
Charcoal
Filter
Scrubber

Figure 6

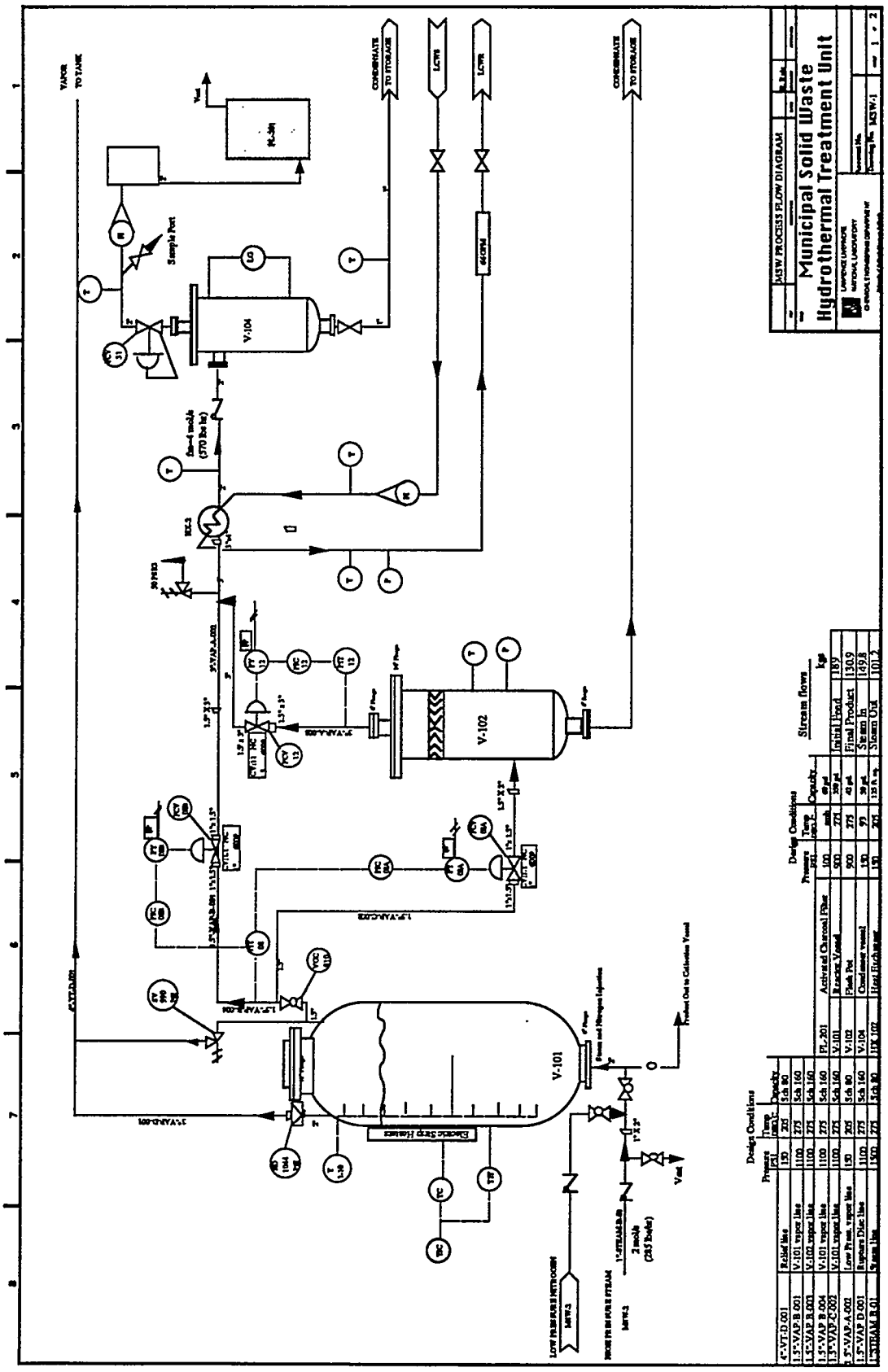
MSW PROCESS FLOW DIAGRAM
Municipal Solid Waste
Hydrothermal Treatment Unit
V-101
V-102
V-104
Design Conditions
Stream flows
Activated Charcoal Filter
Flash Pot
Condensate vessel
Heat Exchanger
Initial Heat
Final Product
Steam In
Steam Out
VAPOR TO TANK
CONDENSATE TO STORAGE
LCWR
Sample Port
Vent
Product Out to Celebration Vessel
Electric Strip Heaters
LOW PRESSURE STEAM
HIGH PRESSURE STEAM
2 inch (285 lbs/hr)

Figure 7

HYDROGEN PRODUCTION FROM HIGH-MOISTURE CONTENT BIOMASS IN SUPERCRITICAL WATER

Michael J. Antal, Jr., Yukihiko Matsumura, Michael T. Onuma, and Xiaodong Xu
Hawaii Natural Energy Institute
School of Ocean and Earth Science and Technology
University of Hawaii
Honolulu, HI 96822

Abstract

Wet biomass (water hyacinth, banana trees, cattails, green algae, kelp, etc.) grows rapidly and abundantly around the world. For example, water hyacinth produces over 100 tons/ha/yr of dry organic matter. However, wet biomass is not regarded as a promising feedstock for conventional thermochemical conversion processes because the cost of drying the material is too high. Our research seeks to address this problem by employing water as the gasification medium. Prior work has shown that low concentrations of glucose (a model compound for whole biomass) and various wet biomass species (water hyacinth, algae) can be completely gasified in supercritical water at 600°C and 34.5 MPa after a 30 s residence time. But higher concentrations of glucose evidenced incomplete conversion. For this reason, flow reactors were fabricated which could accommodate packed beds of catalyst, and studies were initiated of the steam reforming (gasification) reactions in the presence of various candidate heterogeneous catalysts. The goal is to identify active catalysts for steam reforming biomass slurries in supercritical water. The gaseous products (primarily hydrogen, carbon dioxide, and methane) phase separate from the water upon cooling at the exit of the reactor, and thereafter are available for storage or further processing at a pressure of 34.5 MPa (5,000 psi). Soon after tests began, a suitable class of carbon-based catalysts was discovered. These catalysts effect complete (>99%) conversion of high-concentration glucose (up to 22% by weight) to a hydrogen-rich synthesis gas. High space velocities are realized [>20 (g/hr)/g], and the catalyst is stable over a period of several hours. The carbon catalyst is not expensive, and exists in a wide variety of forms and compositions. After this discovery, work has focused on four interrelated tasks: (1) tests to identify the most active form and composition of the catalyst; (2) tests employing the preferred

catalyst to study the effect of feedstock composition on carbon conversion and gas composition; (3) studies of catalyst deactivation and subsequent reactivation, including the in-house synthesis of bifunctional catalysts which incorporate promoters and stabilizers; and (4)the design and fabrication of a larger, new reactor with a slurry feeder intended to handle high-concentration, wet biomass feeds.

Introduction

As detailed in this report, carbonaceous materials (such as charcoal and activated carbon) show great promise as catalysts for the complete gasification (steam reforming) of a wide variety of organic compounds in supercritical water. This is not a completely unexpected result: prior to World War I, biomass down-draft gasification reactors realized a tar-free gas product by passing the tar-laden pyrolysis vapors through a red-hot charcoal bed. The surprising discovery of our work is the ability of carbon to completely gasify many organic compounds in supercritical water at temperatures as low as 600°C. The following sections detail our progress during the year that has passed since the catalytic activity of these materials was first demonstrated.

Apparatus and Experimental Procedures

A schematic drawing of the reactor system is presented in Figure 1. The reactor is made of Inconel 625 tubing with a 0.375" OD and 0.187" ID. The temperature of the reactant flow is abruptly brought up to a desired value by an entry heater (ARi Industries)/cooling water jacket combination. The reactor is maintained at isothermal conditions by a furnace (Mellen Company) and a down-stream heater (ARi Industries)/cooling water jacket combination. To improve the heat transfer from the heaters to the fluids inside the reactor, the heaters are coiled on stainless steel rods which are in direct contact with the Inconel reactor. A unique feature of this reactor is that different sizes of annuli (made of Inconel 625) can be easily installed, giving different residence times. Moreover, different amounts of solid catalyst can be packed inside the reactor, giving desired WHSV (weight hourly space velocity). For the experiments reported in this paper, about two-thirds of the heated zone of the reactor was packed with catalyst. The axial temperature profile along the reactor's functional length of approximately 0.48 m is measured with 15 fixed, type K thermocouples. Furthermore, a movable type K thermocouple inside the annulus (Inconel 625) provides a temperature profile inside the reactor. Pressure in the reactor system is measured using an Omega PX302 pressure transducer. A Grove Mity-Mite Model 91 back pressure regulator (Grove Valve and Regulator Company) reduces the working pressure from 34.5 MPa to atmospheric pressure. After passing through the back pressure regulator, the reactor effluent passes through an in-house fabricated glass gas-liquid separator. The gas flow rate is measured using a Wet Test Meter (Precision Scientific).

Currently, a balloon feeding system is employed to feed the wet biomass slurry into the reactor. Wet biomass is first ground with a Speed Blender (Hamilton Beach, Inc.) and then with a Brinkmann Homogenizer (Brinkmann Instruments, Inc.). The heterogeneous biomass slurry fills the 500 ml high pressure/temperature vessel (Series 4570/80) equipped with a A1120HC magnetic drive (Parr

Instrument Company). A 10-gram Weather Measure meteorological balloon (Weather Measure Corp.) is placed in the vessel together with the biomass slurry. Water is pumped into the balloon, and as the balloon expands the biomass slurry is forced into the reactor.

The analysis of the gaseous products is accomplished on a Hewlett-Packard GC (Model 5890) equipped with flame ionization and thermal conductivity detectors. A 800/100 mesh Carbosphere molecular sieve packed column is used, operating at 35°C for 4.2 min, followed by a 15°C/min ramp to 227°C, a 70°C/min ramp to 350°C, and a 5.3 min hold at 350°C. A standard gas mixture used for calibration is obtained from AIRCO.

Results and Discussion

Catalytic Properties of Various Carbon Substrates

Table 1 displays the catalytic effects of various carbon substrates on the gasification of 1.2 M glucose in water. In all cases the tar yield was very low and the carbon gasification efficiency was high. Nevertheless, the coconut shell activated carbon catalyst produced a water effluent whose pH was almost identical to that of pure tap water in Hawaii, and its gas yield was the highest of the four carbons. Since this carbon is commercially available, bulk samples of the material are homogeneous, reproducible, and well characterized. Consequently, we decided to employ it in our subsequent work. The fact that other less expensive carbons were essentially as effective as the coconut shell activated carbon should not be overlooked.

Performance of Coconut Shell Activated Carbon

Catalyst Performance with Glucose

Results given in Table 2 demonstrate the need for heterogeneous catalysis if complete gasification of a concentrated organic feed is desired. As established in our earlier work, a carbon gasification efficiency of only 80% is realized without a catalyst. Note that the catalyst dramatically reduces the CO content of the gaseous products, evidently by enhancing the rates of both the water-gas shift reaction and the methanation reactions. Table 3 shows that temperatures near 600°C are required to achieve high carbon gasification efficiencies. Likewise, Table 4 reveals that pressures well in excess of critical pressure improve the gasification efficiency. Table 5 demonstrates the ability of the catalyst to accommodate increasing flows of feedstock. Some trends are visible, such as increasing yields of hydrogen and carbon monoxide, and decreasing yields of carbon dioxide with increasing flow. However, the most important conclusion is that the carbon gasification efficiency remains high over a wide range of WHSV. A classical test for mass transfer limitations in heterogeneous catalysis is to increase the amount of catalyst present while at the same time proportionately increasing the flow rate; thereby maintaining constant WHSV. If mass transfer is unimportant, few changes in the product spectrum should be observed. Table 6 displays such a test with 1.2 M glucose as feed. Although a large increase in the CO yield and a related decrease in the CO_2 yield are evident, accompanied by smaller decreases in the yields of hydrogen and methane, the carbon gasification

efficiency remains high.

Tables 7 and 8 examine deactivation of the catalyst as a function of time-on-stream. In Table 7, the gasification efficiency for 1.2 M glucose remains high for 4 hours or more, but the TOC analysis of the effluent shows an increase as early as the 1.77 hour sample. Because the TOC analysis is both expensive and somewhat unreliable, it is not available for the run with cellobiose whose data are displayed in Table 8. Evidently, cellobiose gasification is more demanding than glucose because the carbon gasification efficiency falls dramatically after about 4 hours. Note that cellobiose is only partially soluble in water; hence the WHSV is significantly lower in Table 8 than in Table 7. Clearly, some means of re-activating the catalyst will be necessary for commercial development of this process. A subsequent section of this report focuses on re-activation.

Catalyst Performance with Other Feeds

Tables 9, 10, and 11 display gasification results for various dilute, whole biomass feeds. Note that the gas yields in these three tables are expressed as mass fractions: gram of gas per gram of feed. In Table 9, the depithed bagasse liquid extract is rich in hemicelluloses and lignin. Effectively complete gasification of this feed is realized. Likewise, water hyacinth in low concentrations is easily gasified (see Table 10). The high total gas yield for water hyacinth evidences the participation of water in the gasification chemistry. Perhaps our most impressive result is given in Table 11, which shows that the catalytic gasification process can realize a 99% conversion of sewage sludge to a hydrogen- and methane-rich synthesis gas. Note that the TOC analysis of the water effluent is consistent with the gas yield measurement.

Glycerol is a by-product of biodiesel fuel production. Increasing demand for biodiesel promises to create a glut of glycerol, which should become available as a feedstock at low or negative cost. Table 12 shows that glycerol is easily and completely gasified to hydrogen in supercritical water *without* catalyst. The presence of the catalyst has little effect on the gas composition. Glycerol is evidently a perfect feedstock for hydrogen production.

The destruction of hazardous wastes is an important societal problem. Because of the large negative cost associated with their disposal, hazardous wastes could be a profitable feedstock for hydrogen production. Tables 13 and 14 portray the ability of the activated carbon catalyst to gasify various organic waste streams in supercritical water. In Table 13, data for the destruction of four representative Navy wastes are presented. Complete destruction of acetic acid and ethylene glycol is easily achieved. Methyl ethyl ketone (MEK) and methanol are somewhat less reactive; nevertheless, only 2.2% of the MEK and 6.8% of the methanol survived the reactor. The difference between the carbon gasification efficiency and the unconverted reactant for MEK is probably carbon deposited on the catalyst. In all cases, the gaseous product was rich in hydrogen and methane. As shown in Table 14, phenol is only partially converted to gases by the carbon catalyst, and benzene is a by-product of the reaction. Considering the stability of the aromatic ring, this is not a surprising result.

Deactivation and Regeneration of Coconut Shell Activated Carbon

Regeneration of the Spent Activated Carbon

Carbon gasification efficiency and composition of the generated gas during glucose decomposition shown in Table 7 clearly indicate the deactivation of the catalyst. After 5.2 hours, carbon gasification efficiency decreased and carbon monoxide concentration increased, showing insufficiency in the gasification and the water-gas shift reaction. The same tendency was observed in the cellobiose decomposition shown in Table 8. Judging from the observation that a carbonaceous film deposit was formed on the reactor wall after the experiment, deactivation may have been caused by the deposit of carbon on the surface of the activated carbon, thus covering the available active sites. Regeneration of the spent activated carbon by gasifying the deposited carbon is needed for long-term operation.

Usually, granular industrial activated carbon is regenerated for repetitive use (Clark and Lykins 1989). A typical regeneration system includes removal of the activated carbon from the activated carbon vessel and transportation to the regeneration plant. In the regeneration plant, spent activated carbon is treated under high temperature to release the adsorbed materials. This system requires a dynamic processing of the activated carbon. Here, a static regeneration with no removal or transportation of the activated carbon was examined. After the catalyst was deactivated, supercritical water without organic compounds was sent into the reactor. Deposited carbon reacts with water vapor to produce hydrogen, carbon monoxide, carbon dioxide, or methane. Regeneration is attained just by switching the feed without taking the activated carbon out of the reactor. The regeneration characteristics obtained here can also be used for estimating the regeneration of activated carbon which occurs side-by-side with deactivation. A proper condition may be found where deactivation and regeneration take place at the same rate so that no deactivation will proceed during the gasification.

An experiment was conducted using 0.235 M cellobiose solution to increase the rate of deactivation of the activated carbon. The run continued for 4 hours at 600°C, 34.5 MPa, producing spent activated carbon. Then supercritical water was sent for 6 hours into the reactor at 600°C, 34.5 MPa to regenerate the activated carbon. After the regeneration operation, cellobiose solution was fed to the reactor for 4 hours under the same condition as the first decomposition to measure the gasification characteristics of the regenerated activated carbon. The same apparatus and procedure used in the gasification work described in the preceding section were used.

A comparison of the effectiveness of the regenerated activated carbon to that of the virgin activated carbon is shown in Table 15. Good agreement was obtained. In both cases, gasification efficiency falls from complete gasification to 90% after 4 hours. The product gas composition shown in Table 16 was almost the same for gasification with the virgin and regenerated activated carbon. These facts indicate that regeneration using supercritical water is effective.

The gas generation rate was almost stable during regeneration. The typical composition of the product gas was hydrogen, 59%; carbon dioxide, 30%; carbon monoxide, 4%; and methane, 7%. The composition just after switching the cellobiose to supercritical water showed excess hydrogen,

which may be from hydrogen adsorbed during gasification. Blank experiment with no catalyst showed hydrogen generation by the wall corrosion, but the amount was too low to explain the hydrogen produced in excess. It is well known that hydrogen is adsorbed strongly onto the active sites of carbon, thus inhibiting gasification and being the cause of methane production. The amount of the excess hydrogen decreased as time passed, and was small for the gasification of virgin activated carbon shown later. These facts support the idea that excess hydrogen arises from the adsorbed hydrogen during the gasification. Carbon gasification rate based on the initial carbon weight, calculated from the gas generation rate and the composition, is shown in Figure 2. Average carbon gasification rate was 1.72×10^{-6} s^{-1}. Regeneration using oxygen in low concentration will be tried under supercritical water condition in the near future.

Change in iodine number through the gasification of cellobiose and regeneration is shown in Table 17. After the first gasification, a large decrease in the iodine number was observed. This may be caused by the carbonaceous deposit, which fills the pores. Following regeneration, the iodine number of the activated carbon recovers almost to its initial value. After the second gasification, however, the iodine number increased to a value much higher than before gasification. Experiments are currently underway to determine why this very high surface area, activated carbon was not an effective catalyst.

Carbon Gasification

To determine the regeneration characteristics of spent activated carbon, the gasification rate of graphite in supercritical water was measured. Reaction of carbon with water was studied in relation to the carbon gasification and activated carbon generation (Johnson 1981). It is known that carbon reacts with water vapor as:

$$C + H_2O \rightleftharpoons CO + H_2 \quad (1)$$

$$CO + H_2O \rightleftharpoons CO_2 + H_2 \quad (2)$$

A reaction mechanism which considered the competitive adsorption of water and hydrogen molecules to the same active sites was proposed (Gadsby et al. 1946; Strickland-Constable and Phil 1947; Long and Sykes 1948):

$$H_2O \ (OH)(H) \ (O)(H_2) \quad (3)$$

$$H_2 \ (H_2) \quad (4)$$

$$C + (O) \ CO \quad (5)$$

in which parentheses indicate the absorbed species. They assumed a steady state for the adsorbed molecules and succeeded in explaining their results for subatmospheric conditions. The rate equation they obtained had the form:

$$r = k_1 p_{H2O}/(1 + k_2 p_{H2} + k_3 p_{H2O}) \quad (6)$$

where k_1, k_2, and k_3 denote reaction rate constants, and p_{H2O} and p_{H2} express the partial pressure of water and hydrogen, respectively. This equation correctly predicts inhibition by the hydrogen molecules observed in the experiment. At elevated pressures, generation of methane becomes more important. Gasification at higher pressures was conducted by Blackwood and McGrory (1958), and the generation of methane in proportion to the steam vapor pressure was observed. They used a steam pressure as high as 4.7 MPa. They included a reaction step for methane formation:

$$C(H_2) + H_2O \rightarrow CH_4 + (O) \quad (7)$$

together with the reaction mechanism shown by Equations 3-5 to obtain the following rate equations:

$$r = (k_1 p_{H2O} + k_4 p_{H2} p_{H2O} + k_5 p_{H2O}^2)/(1 + k_2 p_{H2} + k_3 p_{H2O}) \quad (8)$$

$$r_{CH4} = (k_2/k_4) p_{H2O} \quad (9)$$

where r_{CH4} denotes the methane generation rate. Subsequent studies of the effect of hydrogen resulted in some modifications to Equation 6 (Huttinger 1989).

Various changes in the gasification rate in relation to the conversion were reported (for example, see DeGroot and Richards 1989; Taylor and Bowen 1976; Johnson 1974; Adschiri and Furusawa 1987). Explanations for this dependence of gasification rate on conversion include variations in the remaining amount of carbon, change in the surface area with gasification, or change in the characteristics of the carbon itself, but quantitative modeling of the behavior has not been established. A decrease in the gasification rate, which was observed in some of the results of steam gasification, was also reported in gasification with carbon dioxide and oxygen. In this case, the reactive surface area, determined by using the adsorption of oxygen on the carbon materials, is found to be a good measure of the reactivity (Laine et al. 1963; Tong et al. 1982; Radovic et al., 1983; Radovic 1991). However, for gasification using water vapor, where the reaction is much more complicated, this approach is not commonly utilized.

In spite of this accumulation of reaction data, no measurements of the gasification rate in supercritical water have been carried out. To understand the behavior of activated carbon during regeneration by supercritical water with pressures as high as 34.5 MPa, gas generation characteristics of activated carbon in the supercritical water should be investigated.

For regeneration of the spent activated carbon, gasification with development of porous structure may be important. The development of micropores requires fast mass transfer of reactant or product molecules through the porous structure compared to the consumption or generation of these molecules by the reaction. Virgin activated carbon was gasified at various temperatures and pressures to learn more about how gasification in supercritical water affects the pore structure.

Experiments were conducted by packing virgin activated carbon in the reactor used for the

decomposition work and feeding water using an HPLC pump, keeping the bed temperature and pressure under supercritical conditions. The same procedure and gas analysis used in the decomposition work were employed. After the experiment, the activated carbon was collected and the weight change was measured. Iodine tests (ASME D4607) were also conducted. Insofar as the amount of the activated carbon loaded in the reactor was no more than 3.6 g, one-tenth of the standard samples with one-tenth of the standard reagents were used in the iodine test. The iodine numbers measured by the standard method and the one-tenth method agreed within 13% error. The activated carbon used in this study was a granular activated carbon based on coconut shell (Barnebey & Sutcliffe, Type PE). Iodine number of this activated carbon was 1050.

The gas generation rate decreased slightly during the run. The effluent gas was composed of hydrogen, carbon dioxide, and a small amount of methane. The typical composition was hydrogen, 66%; carbon dioxide, 31%; and methane, 3%. The ratio of hydrogen to carbon dioxide was close to 2, which is expected from the reactions shown in Equations 1 and 2. This composition did not change during gasification.

The effect of mass transfer should be considered for the reaction of granular materials. In supercritical water, the pressure of water is so high that the mass transfer of the reactant through the boundary layer around the activated carbon particle and the porous structure does not influence the overall rate. However, as one can find from the rate Equation 6, the gasification of carbon using water is severely inhibited by the hydrogen product. Mass transfer of generated hydrogen through the pore and the boundary layer was estimated. For the mass transfer through the porous structure, a grain model was applied and the hydrogen concentration profile inside an activated carbon particle was calculated. The concentration profile within the porous solid was flat and the mass transfer rate was found to be fast enough not to affect the reaction rate. Mass transfer of the generated hydrogen from the surface of the particle to the bulk liquid was calculated using the equation of Thoenes and Kramers (1958). The result showed that the gasification rate was not affected by the mass transfer through the boundary layer. Thus the reaction rate measured in this experiment can be treated as an intrinsic reaction rate between carbon and supercritical water. Also the conversion of the water calculated from gas generation rate and composition is no more than 0.1% so that the condition required for the differential reactor is satisfied, and the inhibition of the gasification by the generated hydrogen can be neglected.

From the gas generation rate and gas composition, the carbon gasification rate was calculated based on the initial carbon amount. The carbon gasification rate, as well as the gas generation rate, decreased during the run. Here, the gasification rate at the point of 2 hours after the beginning of the experiment was taken as a representative value for the reaction rate analysis in relation to the pressure and temperature change.

Influence of pressure on the carbon gasification rate for the activated carbon treatment is shown in Figure 3. In this research, pressure was varied from 25.5 MPa to 34.5 MPa. No clear dependence on the pressure was found, which is in agreement with Equation 6. On the other hand, the gasification of coconut carbon by Blackwood and McGrory (1958), shown in Equation 8, predicts a 20% increase in reaction rate with the pressure change from 25.5 to 34.5 MPa at 600°C and

mis-predicts the effect of pressure within this pressure range. In our work, the composition of the generated gas was not influenced by the change in reaction pressure. The predicted mole fraction of methane using the rate coefficients determined by Blackwood and McGrory (1958) was 0.03%, which is much lower than the 3% observed in this work.

The effect of temperature is shown in Figure 4 in the form of an Arrhenius plot. The carbon gasification rate at 34.5 MPa calculated by the previous rate equations is also shown in the figure. Results from Long and Sykes (1948) show almost the same reaction rate as our result in spite of the large surface area of the activated carbon. From the results of this work, the activation energy was found to be 165 kJ/mol. The apparent activation energy of coconut char measured by Long and Sykes (1948) was 176 kJ/mol and in good agreement with the value obtained in this study. The prediction using the rate equation by Blackwood and McGrory (1958) presents a quite different dependence of the reaction rate on temperature. Their reaction rate equation added the effect of methane generation to the mechanism proposed by Long and Sykes (1948). This large difference between prediction and measurement indicates that for the gasification of the activated carbon in this work, the mechanism of methane generation proposed by Blackwood and McGrory (1958) may be erroneous. However, the coincidence between the activation energies of Long and Sykes (1948) and this work suggests that the fundamental mechanism of gasification does not change under a high pressure such as the supercritical condition. The modification of the hydrogen inhibition mechanism by Huttinger (1989) was not considered here because the effect of hydrogen can be neglected in this work. The carbon gasification rate at 600°C, 34.5 MPa, was in good agreement with the gasification rate observed in the regeneration experiment.

It is known that the shapes of carbon burn-off versus time plots are similar for most coal-derived chars in air, carbon dioxide, and steam, and often can be expressed by a single cubic equation in the normalized dimensionless plot using reduced time based on the time to attain a fraction burn-off to 0.5 and the carbon burn-off (Walker 1985). Though activated carbon is a partly gasified carbonaceous material and the initial conversion is unknown, the normalized plot was drawn using the conversion based on the initial activated carbon weight. Conversion obtained from weight change was considered as the final conversion, and time change of the conversion was calculated backward using the gas generation rate and the gas composition. In this work, the highest conversion is 0.25. Thus the normalized plot was drawn using the reduced time based on the time needed for increasing conversion from 0.075 to 0.1. Extrapolation was used in case of necessity. The plot shown in Figure 5 shows good agreement in burnoff curves for all gasification experiments. This agreement indicates the possibility of expressing the reaction rate change during the gasification using a single cubic equation.

Iodine number is utilized to represent the surface area of an activated carbon and thus its capacity for adsorption. A large increase in the iodine number of the activated carbon was found after treatment with supercritical water. Figure 6 shows the iodine number change with time at 600°C and 34.5 MPa. The iodine number increased with time toward a maximum value of about 1400. The influence of pressure on the iodine number after 6-hour treatment is shown in Figure 7. No significant effect was observed. The relation between the iodine number and the conversion (see Figure 8) shows an increase in the iodine number at the beginning, then maximum iodine number, and finally a decrease

in the iodine number at conversions above 0.2. The first increase in the surface area is because of gasification accompanied with the development of the pore size distribution and the decrease at high conversion is because of the burn-off of the wall between the pores. It is remarkable that the activated carbon used here is one of the granular activated carbons with the highest obtainable iodine number. Treatment in supercritical water is effective in developing a porous structure to a higher extent than that for the usual activated carbon.

Design of New Reactor and Associated Slurry Feeder

Currently, the reactor that is used in our work has a very small diameter and as a result it cannot process a high-concentration biomass slurry. We propose to build a new reactor to accommodate the use of concentrated biomass slurry as a feed material. The new reactor will operate in the same manner as the old, except the new reactor will have a larger diameter and an auger to help drive the viscous slurry down the reaction region.

Before the new reactor is built, a model will be assembled to show how it will work. Because the model will be made of Plexiglas, it will show how feed material will be flowing through the reactor and allow us to fix any problems that could occur. The Plexiglas portion of the model will include a piece that will represent the current Parr pressure vessel and another piece that will represent the new reactor. The feed material will be placed into the Plexiglas model of the Parr pressure vessel and the agitator and auger will be driven by a 1/12 hp motor. The agitator will stir and mix the feed material while the auger will facilitate the flow of the feed material down through the new reactor. Although calculations have shown that the motor should deliver enough power to drive the auger, the model will demonstrate if the motor can actually deliver enough power to drive the agitator, auger, and feed material.

The new reactor will be larger than the one that is presently being used. Calculations were done to determine a safe wall thickness for the new reactor, and after a long search, two companies were found that carry a pipe heavy enough to construct a safe reactor. The new reactor is made from a 1 IPS ^{x} sch.160 Hastelloy-276 pipe. The exact dimensions are 1.315" OD, 0.815" ID, and 0.25" wall thickness. According to calculations, the maximum inner diameter that the new reactor should have, to be designed to code, is 0.82". This calculation is based on an assumption that the internal pressure is 5,250 psi and the maximum allowable stress is 12,000 psi. The drawback to this reactor is the wall temperature cannot exceed 620°C because the maximum allowable stress decreases dramatically as the temperature increases above this point. As a result, a longer entrance heating zone is required to raise the reaction temperature to 600°C, while still maintaining wall temperatures to less than 620°C. The reason the Hastelloy-276 was selected is that it has excellent corrosion resistance properties.

The new reactor will use an auger that would drive viscous or liquid-solid feed material through the reactor. At the outlet point on the new reactor, there will be a cooling jacket, similar to the one on the current reactor, to help control the temperature profile. There will be an entrance heater at the inlet and a guard heater preceding the outlet cooling jacket. The section of pipe between the entrance

and guard heaters will be enclosed within a 3-zone furnace to keep the reactor at isothermal conditions. Finally, the new reactor will be attached to the Parr pressure vessel with the use of a pipe adapter.

The cost of the new reactor and feeder system is kept low by using as much as possible of our existing equipment. However, some new items need to be purchased. Table 18 shows the proposed budget to construct the new reactor. Almost half the cost is for the furnace and heaters. The required furnace and heaters are available from suppliers such as Applied Test Systems, Inc. and ARi Industries. The Hastelloy pipe is another expensive item because a schedule 160 Hastelloy pipe is very rare. Fortunately, Corrosion Metals and McSweeney Steel Co. stock the pipe that we need. Lastly, the 1/8 hp DC motor is an optional item, its purchase depending if more power is required to drive the agitator, auger, and feed material.

Conclusions

Activated carbon is an effective catalyst for gasification of biomass material and hazardous waste materials. Glucose solutions with concentrations as high as 1.2 M can be completely gasified to a hydrogen-rich gas with activated carbon at a weight hourly space velocity as high as 22.2 (g/hr)/g in supercritical water at 600°C, 34.5 MPa. Complete conversions of whole biomass feeds, including water hyacinth, depithed bagasse liquid extract were achieved. High destruction efficiency for waste and hazardous materials was also achieved. Deactivation of the gasification catalyst was observed after 6 hours, but regeneration was possible by treating the spent catalyst with supercritical water for 6 hours. Gasification of carbon in supercritical water showed the same activation energy as that measured at lower pressures, indicating the same reaction mechanism. Higher iodine number than conventional granular activated carbon was attained by supercritical water treatment.

Future Work

An economic study of this process by F.S. Frenduto of Air Products Corp. dated 17 March 1992 projected economic feasibility if complete gasification of 18% by weight biomass in water could be achieved. We realized this goal using glucose as a representative feedstock over a year ago. Our new goal is to demonstrate the process with a concentrated (>18% by weight) biomass slurry. This demonstration will require a new reactor with a slurry feeding system, and may also require an ability to regenerate the catalyst during long duration runs. We have completed the design for the feed system and will test the design soon. If the design functions as planned, and money is available to fabricate the equipment, we project a successful bench-scale demonstration of the process in about 18 months.

The Office of Technology Transfer and Economic Development (OTTED) of the University of Hawaii has agreed to invest about $15,000 to seek a patent on the invention described above. By the time of our presentation, the patent will have been filed and we will be able to freely discuss our work. Depending on the level of industrial interest, the University may seek world-wide patent

coverage. OTTED has already begun to solicit industrial interest in the commercialization of our work. We are anxious to cooperate with industry and seek industrial involvement in the scale- up activities which are currently ongoing.

References

Adschiri, T., and T. Furusawa. 1987. "Characterization of Coal Char Reactivity in Fluidized Bed Gasifier." *Fuel Processing Tech.*, 15:135-144.

Blackwood, J.D., and F. McGrory. 1958. "The Carbon-Steam Reaction at High Pressure." *Aust. J. Chem.*, 11:16-33.

Clark, R.M., and B.W. Lykins, Jr. 1989. *Granular Activated Carbon: Design, Operation, and Cost.* Chelsea: Lewis Publishers.

DeGroot, W.F., and G.N. Richards. 1989. "Relative Rates of Carbon Gasification in Oxygen, Steam, and Carbon Dioxide." *Carbon*, 27:247-252.

Gadsby, J., C.N. Hinshelwood, and K.W. Sykes. 1946. "The Kinetics of the Reactions of the Steam-Carbon System." *Proc. R. Soc.*, A187:129-151. London.

Hüttinger, K.J. 1989. "Mechanisms of Steam Gasification and the Role of Hydrogen Inhibition." *Am. Chem. Soc. Div. Fuel Chem.*, 34:56-62.

Johnson, J.L. 1974. "Kinetics of Bituminous Coal Char Gasification with Gases Containing Steam and Hydrogen." *Coal Gasification*, 145-178, L.G. Massey (ed.), Am. Chem. Soc. Adv. Chem. Ser. 131.

Johnson, J.L. 1981. "Fundamentals of Coal Gasification." Chemistry of Coal Utilization, 2nd Suppl. Vol., 1491-1598, M.A. Elliot (ed.), John Wiley & Sons, Inc.

Laine, N.R., F.J. Vastola, and P.L. Walker, Jr. 1963. "The Importance of Active Surface Area in the Carbon-Oxygen Reaction." *J. Phys. Chem.*, 67:2030-2034.

Long, F.J., and K.W. Sykes. 1948. "The Mechanism of the Steam-Carbon Reaction." *Proc. R. Soc.*, A193:377-399. London.

Radovic, L.R., P.L. Walker, Jr., and R.G. Jenkins. 1983. "Importance of Carbon Active Sites in the Gasification of Coal Chars." *Fuel*, 62:849-856.

Radovic, L.R. 1991. "Importance of Carbon Active Sites in Coal Char Gasification—Eight Years Later." *Carbon*, 29:809-811.

Strickland-Constable, R.F., and D. Phil. 1947. "Interaction of Steam and Charcoal at Low Pressures," *Proc. R. Soc.*, A189:1-10. London.

Taylor, R.W., and D.W. Bowen. 1976. *Rate of Reaction of Steam and Carbon Dioxide with Chars Produced from Subbituminous Coals*, Lawrence Livermore Laboratory Report UCRL-52002. Livermore, CA: University of California.

Thoenes, Jr., D., and H. Kramers. 1958. "Mass Transfer from Spheres in Various Regular Packings to a Flowing Fluid." *Chem. Eng. Sci.*, 8:271-283.

Tong, S.B., P. Pareja, and M.H. Back. 1982. "Correlation of the Reactivity, the Active Surface Area, and the Total Surface Area of Thin Films of Pyrolytic Carbon." *Carbon*, 20:191-194.

Walker, Jr., P.L. 1985. "Char Properties and Gasification." *Fundamentals of Thermochemical Biomass Conversion*, 485-510, R.P. Pverand, T.A. Milne, and L.K. Mudge (eds.). London: Elsevier.

Tables and Figures

Tables

Figures

Table 1. Effect of Various Carbon Catalysts on 1.2 M Glucose Gasification in Supercritical Water at 600°C, 34.5 MPa

Catalyst type	Coal activated carbon	Coconut shell activated carbon	Macadamia shell charcoal	Spruce wood charcoal
WHSV[a]	19.9 (g/hr)/g	22.2 (g/hr)/g	25.7 (g/hr)/g	17.6 (g/hr)/g
Product		**Gas yield[b]**		
H_2	1.48	2.24	2.71	1.61
CO	2.34	0.79	0.54	1.10
CO_2	1.45	3.09	1.09	2.66
CH_4	1.04	1.23	3.18	0.92
C_2H_4	0.002	0.0	0.002	0.01
C_2H_6	0.39	0.35	0.27	0.33
C_3H_6	0.002	0.0	0.003	0.01
C_3H_8	0.13	0.13	0.11	0.11
Carbon gasification efficiency[c]	97%	103%	95%	97%
		Liquid Product		
Tar yield[d]	0.066%	0.009%	0.046%	0.009%
pH of liquid sample	4	5	4	4

[a] WHSV = weight hourly space velocity
[b] Gas yield = mole of gas/mole of reactant
[c] Carbon gasification efficiency = mole of carbon in the gas/mole of carbon in the reactant
[d] Tar yield = gram of tar/gram of reactant

Table 2. Gasification of 1.2 M Glucose in Supercritical Water at 600°C, 34.5 MPa, with and without Coconut Shell Activated Carbon Catalyst

	0.60 g catalyst*	no catalyst**
	WHSV[a] = 22.2 (g/hr)/g	Res. time = 34 s
	Gas yield[b]	
H_2	2.24	0.56
CO	0.79	3.18
CO_2	3.09	0.29
CH_4	1.23	0.84
C_2H_4	0.00	0.03
C_2H_6	0.35	0.20
C_3H_6	0.00	0.00
C_3H_8	0.13	0.00
Carbon gasification efficiency[c]	103%	80%
	Liquid Product	
Tar yield[d]	0.008%	Not available

[a] WHSV = weight hourly space velocity
[b] Gas yield = mole of gas/mole of reactant
[c] Carbon gasification efficiency = mole of carbon in the gas/mole of carbon in the reactant
[d] Tar yield = gram of tar/gram of reactant

Note: * Experiment date: 4/18/94; ** Experiment date: 12/4/92

Table 3. Effect of Temperature on 1.0 M Glucose Gasification in Supercritical Water with Coconut Shell Activated Carbon Catalyst [WHSV[a] = 13.5 (g/hr)/g]

Temperature	600°C	550°C	500°C
Pressure	34.5 MPa	34.5 MPa	34.5 MPa
Product		**Gas yield[b]**	
H_2	1.97	0.62	0.46
CO	2.57	1.67	1.57
CO_2	1.54	0.73	0.85
CH_4	0.90	0.37	0.25
C_2H_4	0.008	0.01	0.016
C_2H_6	0.25	0.10	0.07
C_3H_6	0.009	0.03	0.04
C_3H_8	0.11	0.05	0.036
Carbon gasification efficiency[c]	98%	54%	51%
		Liquid product	
Tar yield[d]	0.1%	0.9%	1.3%

[a] WHSV = weight hourly space velocity
[b] Gas yield = mole of gas/mole of reactant
[c] Carbon gasification efficiency = mole of carbon in the gas/mole of carbon in the reactant
[d] Tar yield = gram of tar/gram of reactant

Note: Experiment date: 3/10/94

Table 4. Effect of Pressure on 1.0 M Glucose Gasification in Supercritical Water at 600°C with Coconut Shell Activated Carbon Catalyst

Pressure	34.5 MPa*	25.5 MPa**
WHSV[a]	3.7 (g/hr)/g	8.3 (g/hr)/g
Product	**Gas yield[b]**	
H_2	1.73	1.18
CO	1.32	2.47
CO_2	2.54	1.30
CH_4	1.10	0.86
C_2H_4	0.001	0.0081
C_2H_6	0.33	0.25
C_3H_6	0.005	0.014
C_3H_8	0.19	0.012
Carbon gasification efficiency[c]	103%	92%

[a] WHSV = weight hourly space velocity
[b] Gas yield = mole of gas/mole of reactant
[c] Carbon gasification efficiency = mole of carbon in the gas/mole of carbon in the reactant

Note: *Experiment date: 3/4/94; ** Experiment date: 3/16/94

Table 5. Effect of WHSV[a] on 1.0 M Glucose Gasification in Supercritical Water at 600°C, 34.5 MPa, with Coconut Shell Activated Carbon Catalyst

WHSV	3.7 (g/hr)/g	6.6 (g/hr)/g	13.5 (g/hr)/g
Product		**Gas yield[b]**	
H_2	1.73	1.57	1.97
CO	1.32	2.33	2.57
CO2	2.54	1.42	1.54
CH4	1.10	1.01	0.90
C2H4	0.001	0.003	0.008
C2H6	0.33	0.29	0.25
C3H6	0.005	0.001	0.009
C3H8 yield	0.19	0.14	0.11
Carbon gasification efficiency[c]	103%	96%	98%

a WHSV = weight hourly space velocity in g-glucose/hr g-catalyst
b Gas yield = mole of gas/mole of reactant
c Carbon gasification efficiency = mole of carbon in the gas/mole of carbon in the reactant

Table 6. Gasification of 1.2 M Glucose in Supercritical Water at 600°C, 34.5 MPa, with Coconut Shell Activated Carbon Catalyst

	0.60 g catalyst*	1.21 g catalyst**
Flow rate	1.0 ml/min	2.0 ml/min
WHSV[a]	22.2 (g/hr)/g	22.2 (g/hr)/g
Product	**Gas yield[b]**	
H_2	2.24	2.0
CO	0.79	2.99
CO_2	3.09	1.29
CH_4	1.23	0.88
C_2H_4	0.0	0.01
C_2H_6	0.35	0.23
C_3H_6	0.0	0.02
C_3H_8	0.13	0.09
Carbon gasification efficiency[c]	103%	100%
	Liquid Product	
Tar yield[d]	0.008%	0.09%

[a] WHSV = weight hourly space velocity
[b] Gas yield = mole of gas/mole of reactant
[c] Carbon gasification efficiency = mole of carbon in the gas/mole of carbon in the reactant
[d] Tar yield = gram of tar/gram of reactant

Note: * Experiment date: 4/18/94; ** Experiment date: 8/11/94

Table 7. Deactivation of Coconut Shell Activated Carbon Catalyst During 1.2 M Glucose Gasification in Supercritical Water at 600°C, 34.5 MPa [WHSV[a] = 19.9 (g/hr)/g]

Time on stream	0.7 hr	1.77 hr	3.92 hr	5.2 hr
Product		**Gas yield[b]**		
H_2	3.83	3.85	1.97	1.53
CO	0.79	0.63	2.41	2.71
CO_2	3.32	3.49	1.84	1.18
CH_4	0.95	0.94	0.93	0.83
C_2H_4	0.001	0.002	0.007	0.01
C_2H_6	0.26	0.26	0.25	0.21
C_3H_6	0.002	0.005	0.013	0.02
C_3H_8	0.15	0.13	0.11	0.09
Carbon gasification efficiency[c]	100%	100%	101%	91%
		Liquid Product		
Tar yield[d]	0.02%	0.03%	0.07%	0.16%
TOC yield[e]	1.4%	2.5%	5.4%	5.8%

[a] WHSV = weight hourly space velocity
[b] Gas yield = mole of gas/mole of reactant
[c] Carbon gasification efficiency = mole of carbon in the gas/mole of carbon in the reactant
[d] Tar yield = gram of tar/gram of reactant
[e] TOC yield = gram of organic carbon in the liquid effluent/gram of carbon in the reactant based on TOC analysis

Note: Experiment date: 5/4/94

Table 8. Deactivation of Coconut Shell Activated Carbon Catalyst During 0.235 M Cellobiose Gasification in Supercritical Water at 600°C, 34.5 MPa [WHSV[a] = 1.92 (g/hr)/g]

Time on stream	0.88 hr	3.2 hr	3.95 hr
Product	**Gas yield[b]**		
H_2	5.22	2.88	2.47
CO	1.59	1.83	1.49
CO_2	7.30	6.62	5.53
CH_4	1.87	1.96	1.40
C_2H_4	0.001	0.003	0.002
C_2H_6	0.47	0.48	0.34
C_3H_6	0	0	0
C_3H_8	0.19	0.20	0.12
Carbon gasification efficiency[c]	102%	100%	79%
	Liquid product		
Tar yield[d]	2.2%	2.3%	2.4%

[a] WHSV = weight hourly space velocity
[b] Gas yield = mole of gas/mole of reactant
[c] Carbon gasification efficiency = mole of carbon in the gas/mole of carbon in the reactant
[d] Tar yield =gram of tar/gram of reactant

Note: Experiment date: 1/18/95

Table 9. Gasification of Depithed Bagasse Liquid Extract in Supercritical Water at 600°C, 34.5 MPa, with Coconut Shell Activated Carbon Catalyst

Conc.	7.33 g/l	15.2 g/l	15.5 g/l
Catalyst	3.695 g	2.9 g	3.0 g
WHSV[a]	0.12 (g/hr)/g*	0.32 (g/hr)/g**	0.32 (g/hr)/g***
Product		**Gas yield[b]**	
H_2	4.2%	2.3%	2.3%
CO	0	0	1%
CO_2	96%	94%	83%
CH_4	7.2%	6.8%	7%
C_2H_4	0.02%	0.2%	0
C_2H_6	0.7%	1%	1.2%
C_3H_6	0	0	0
C_3H_8	1.1%	0%	0.3%
Total gas yield[c]	109.2%	104%	95%
		Liquid product	
Tar yield[d]	3.8%	0.6%	0.1%

[a] WHSV = weight hourly space velocity
[b] Gas yield = gram of gas/gram of reactant
[c] Total gas yield = gram of all gases/gram of reactant
[d] Tar yield = gram of tar/gram of reactant

Note: * Experiment date: 6/27/94
** Experiment date: 7/12/94
*** Experiment date: 1/20/95

Table 10. Gasification of 2.32 g/l Water Hyacinth in Supercritical Water at 600°C, 34.5 MPa, with Coconut Shell Activated Carbon Catalyst [WHSV[a] = 0.05 (g/hr)/g]

Product	Gas yield[b]	Mole fraction[c]
H_2	2.8%	22%
CO	45%	25%
CO_2	85%	31%
CH_4	16%	16%
C_2H_4	0	0
C_2H_6	8.7%	4.7%
C_3H_6	0	0
C_3H_8	4.5%	1.6%
Total gas yield[d]	162%	

[a] WHSV = weight hourly space velocity
[b] Gas yield = gram of gas/gram of reactant
[c] Mole fraction = mole of gas/total mole of gas in the effluent
[d] Total gas yield = gram of all gases/gram of reactant

Note: Experiment date: 2/24/94

Table 11. Gasification of 28 g/l Sewage Sludge in Supercritical Water at 600°C, 34.5 MPa, with Coconut Shell Activated Carbon Catalyst [WHSV[a] = 0.5 (g/hr)/g]

Product	Gas yield[b]	Mole fraction[c]
H_2	2.7%	33%
CO	3.5%	2.9%
CO_2	66.2%	36%
CH_4	16.3%	24%
C_2H_4	0.05%	0.04%
C_2H_6	7.7%	5.7%
C_3H_6	0.3%	0.15%
C_3H_8	1.7%	0.89%
Total gas yield[d]	98.4%	
Liquid product		
Tar yield[e]	0.99%	
TOC analysis	0.28 g of carbon/l	

[a] WHSV = weight hourly space velocity
[b] Gas yield = gram of gas/gram of reactant
[c] Mole fraction = mole of gas/total mole of gas in the effluent
[d] Total gas yield = gram of all gases/gram of reactant
[e] Tar yield = gram of tar/gram of reactant

Note: Experiment date: 6/22/94

Table 12. Gasification of 2.0 M Glycerol in Supercritical Water at 600°C, 34.5 MPa, with and without Coconut Shell Activated Carbon Catalyst

	no catalyst Res. time = 44 s*	3.12 g catalyst WHSV[a] = 4.36 (g/hr)/g**
Product	**Gas yield[b]**	
H_2	3.51	3.15
CO	0.13	0.14
CO_2	1.89	1.90
CH_4	0.86	0.86
C_2H_4	0.0	0.0
C_2H_6	0.07	0.04
C_3H_6	0.0	0.0
C_3H_8	0.0	0.0
Carbon gasification efficiency[c]	101%	99%

[a] WHSV = weight hourly space velocity
[b] Gas yield = mole of gas/mole of reactant
[c] Carbon gasification efficiency = mole of carbon in the gas/mole of carbon in the reactant

Note: * Experiment date: 2/16/95
** Experiment date: 2/3/95

Table 13. Catalytic Destruction of Representative Navy Wastes in Supercritical Water at 600°C, 34.5 MPa, with Coconut Shell Activated Carbon Catalyst

	Reactant			
	1.0 M Methanol	0.1M Methyl ethyl ketone	0.1M Ethylene glycol	0.1M Acetic acid
WHSV[a]	0.76 (g/hr)/g	0.17 (g/hr)/g	0.16 (g/hr)/g	0.14 (g/hr)/g
Product	**Gas yield[b]**			
H_2	1.61	2.97	1.27	1.08
CO	0.23	0.53	0.29	0.19
CO_2	0.42	0.61	0.78	0.96
CH_4	0.22	1.10	0.61	1.02
C_2H_4	0.0	0.0	0.0	0.0
C_2H_6	0.0	0.28	0.14	0.01
C_3H_6	0.0	0.0	0.0	0.0
C_3H_8	0.0	0.01	0.0	0.0
Carbon gasification efficiency[c]	88%	71%	98%	111%
	Liquid product			
Unconverted reactant	6.8%	2.2%	0	0

[a] WHSV = weight hourly space velocity
[b] Gas yield = mole of gas/mole of reactant
[c] Carbon gasification efficiency = mole of carbon in the gas/mole of carbon in the reactant

Note: Experiment date:12/15/94

Table 14. Catalytic Destruction of 0.025 M Phenol in Supercritical Water at 600°C, 34.5 MPa, with Coconut Shell Activated Carbon Catalyst

WHSV[a]	0.04 (g/hr)/g
Product	**Gas yield[b]**
H_2	2.50
CO	0.12
CO_2	1.45
CH_4	0.24
C_2H_4	0.0
C_2H_6	0.04
C_3H_6	0.0
C_3H_8	0.0
Carbon gasification efficiency[c]	32%
	Liquid product
Unconverted reactant	19.2%
Benzene	7.5%

[a] WHSV = weight hourly space velocity
[b] Gas yield = mole of gas/mole of reactant
[c] Carbon gasification efficiency = mole of carbon in the gas/mole of carbon in the reactant
[d] Benzene yield = mole of benzene/mole of reactant

Note: Experiment date: 7/14/94

Table 15. Gasification Results Using Virgin Activated Carbon and Regenerated Activated Carbon

	Virgin activated carbon		Regenerated activated carbon	
Time	Gas generation rate	Carbon gasification efficiency	Gas generation rate	Carbon gasification efficiency
[h]	[10^{-3} mol/min]	[-]	[10^{-3} mol/min]	[-]
1	5.77	1.04	5.47	0.95
2	5.28	-	5.68	0.96
3	5.30	-	5.16	-
4	4.89	0.90	4.99	0.91

Table 16. Composition of the Product Gas from Cellobiose Gasification Using Virgin Activated Carbon and Regenerated Activated Carbon

	Molar ratio	
Product gas	Virgin activated carbon	Regenerated activated carbon
H_2	0.50	0.51
CO	0.01	0.01
CO_2	0.38	0.37
CH_4	0.09	0.09
C_2H_6	0.02	0.02

Table 17. Change in Iodine Number of Deactivated and Regenerated Catalyst

	Iodine number
Virgin activated carbon	1050
After 1st deactivation	365
After regeneration	1125
After 2nd deactivation	1263

Table 18. Proposed Budget for the New Reactor

Item	Cost
Adapter fitting between stirring shaft and auger	$50
Agitator	50
Stainless steel tubing for cooling jacket, 2 in OD x 0.065 in wall x 10 ft @ $8.00/ft	80
Auger	500
Labor for machinists, welders, etc.	500
Fasteners	500
Heaters	950
Hastelloy piping, 1 IPS x sch. 160 x 20 ft @ $150/ft	3,000
Furnace and temperature controllers	7,500
Miscellaneous (thermocouples, tools, supplies, etc.)	400
1/8 hp DC motor (optional)	400
Sub-total (with optional motor)	$13,930
Contingency	1.20
Total (with motor)	**$16,716**

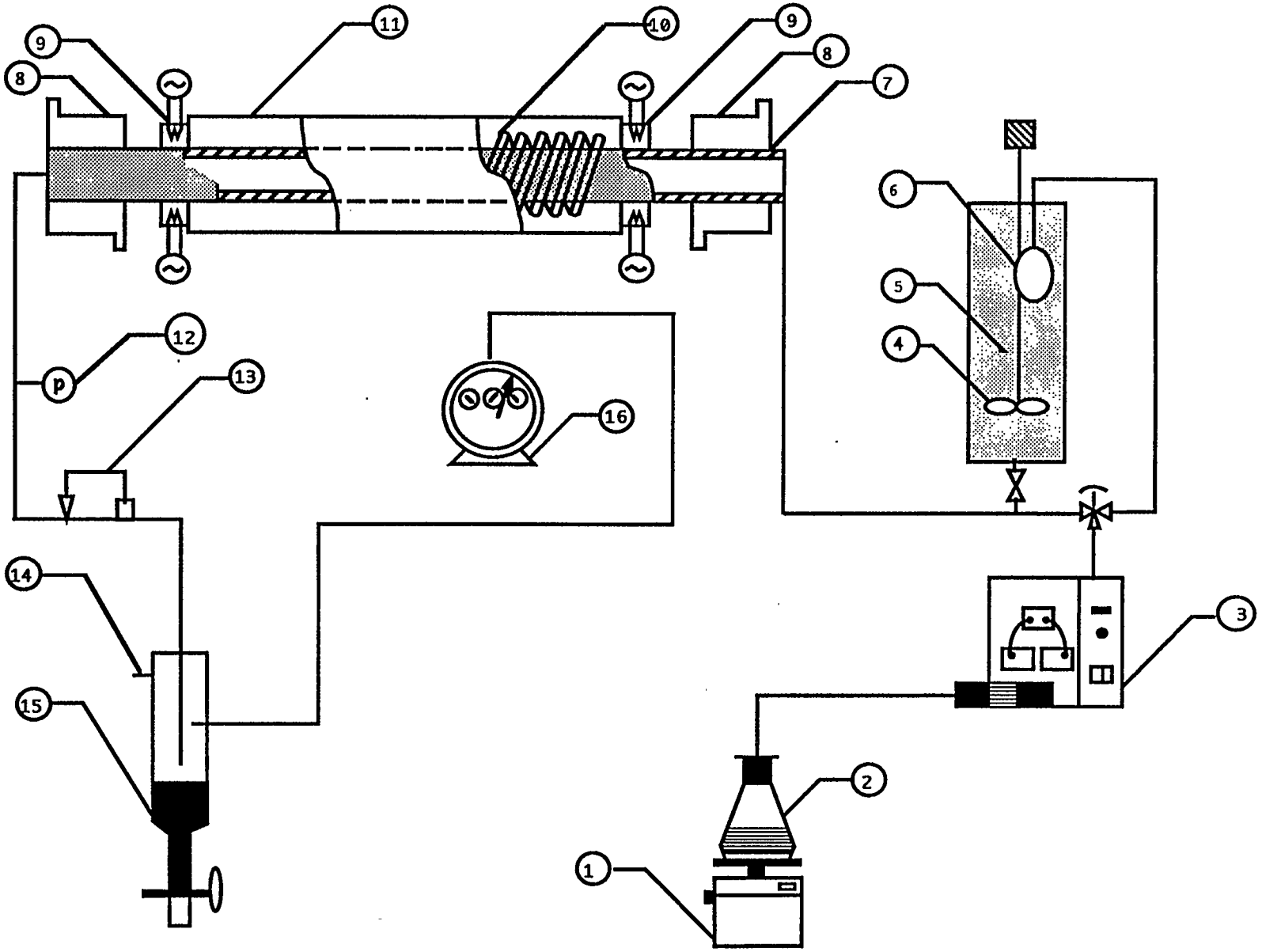

Figure 1. Supercritical Flow Reactor Scheme
1) Balance; 2) Flask with reactant; 3) HPLC pump; 4) Feeding vessel with agitator; 5) Wet-biomass slurry; 6) Balloon; 7) Inconel 625 tube; 8) Cooling jacket; 9) Heater; 10) Furnace; 11) Furnace shell; 12) Pressure transducer; 13) Back pressure regulator; 14) Gas sample outlet; 15) Liquid-gas separator; 16) Wet test meter

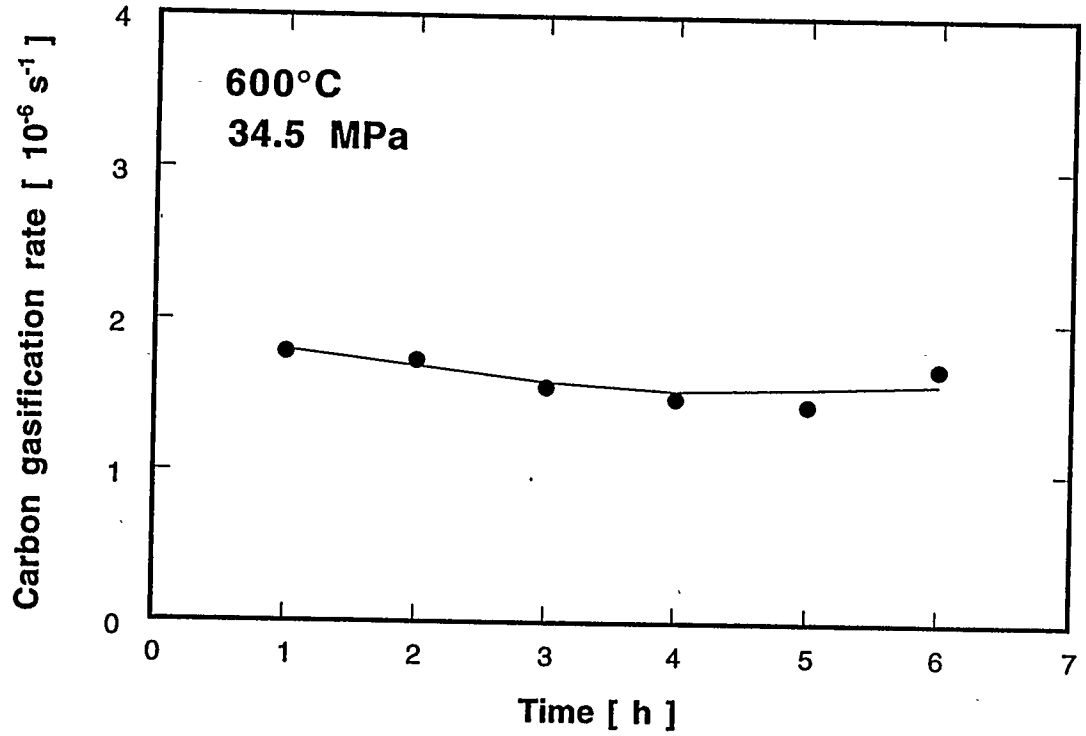

Figure 2. Carbon Gasification Rate During the Regeneration of Spent Activated Carbon

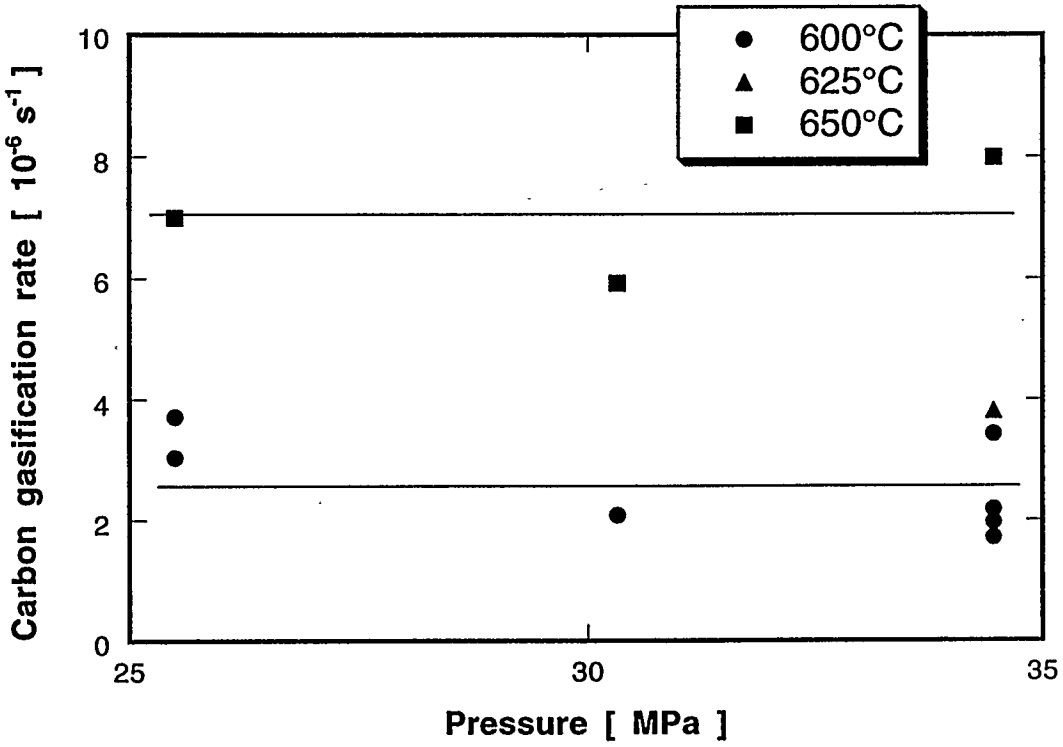

Figure 3. Pressure Effect on Carbon Gasification Rate Based on the Initial Weight

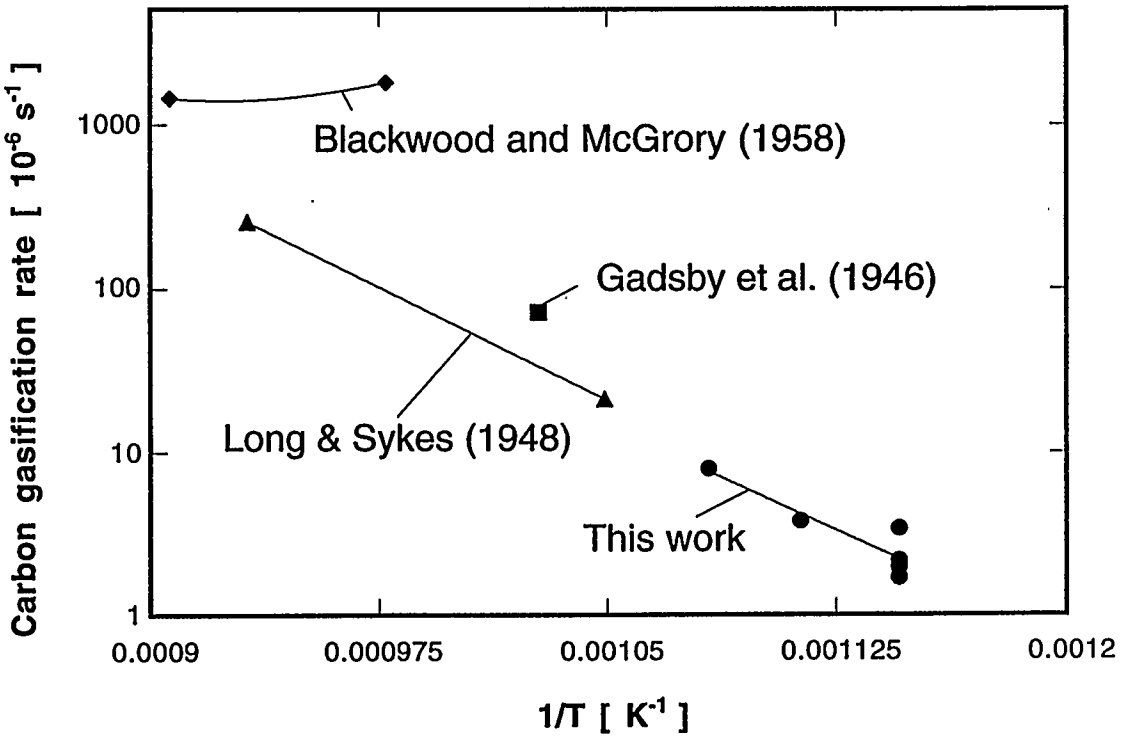

Figure 4. Arrhenius Plot for the Gasification Rate of Coconut Carbon in Water at 34.5 MPa

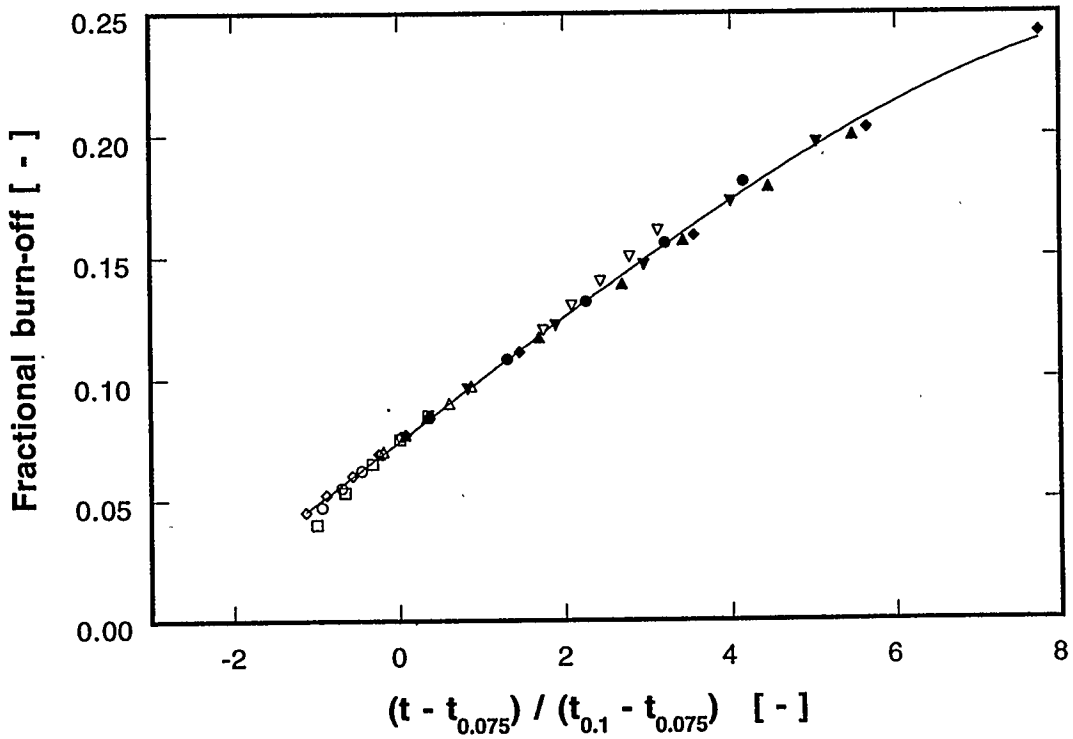

Figure 5. Normalized Plot for the Gasification of Activated Carbon in Supercritical Water

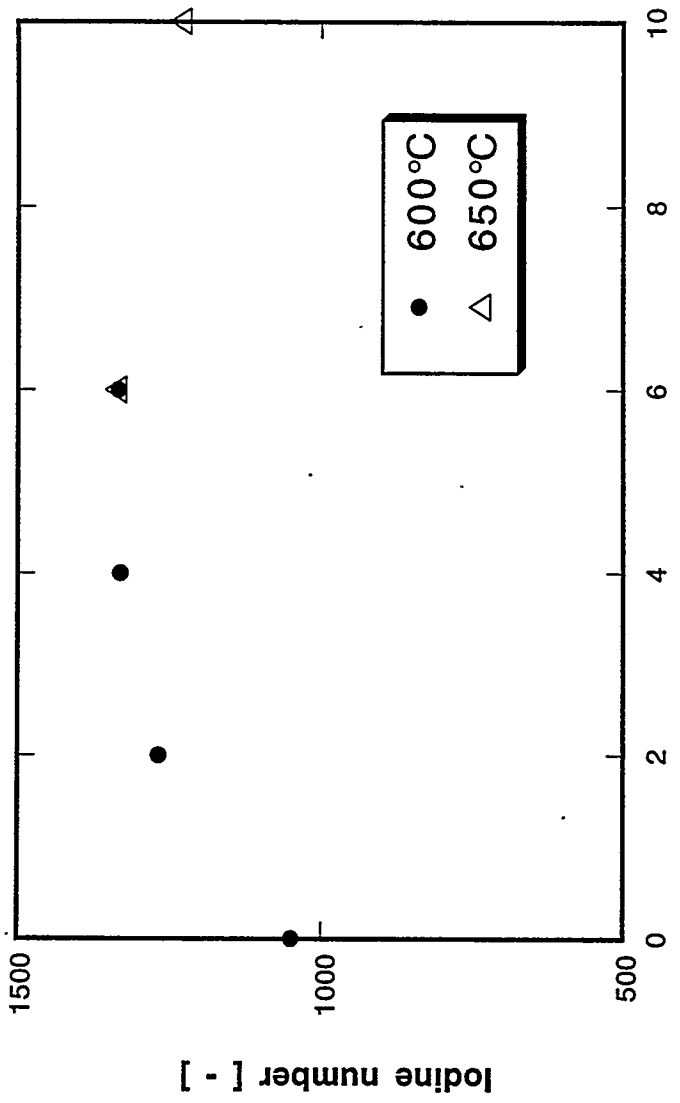

Figure 6. Change of Iodine Number with Time

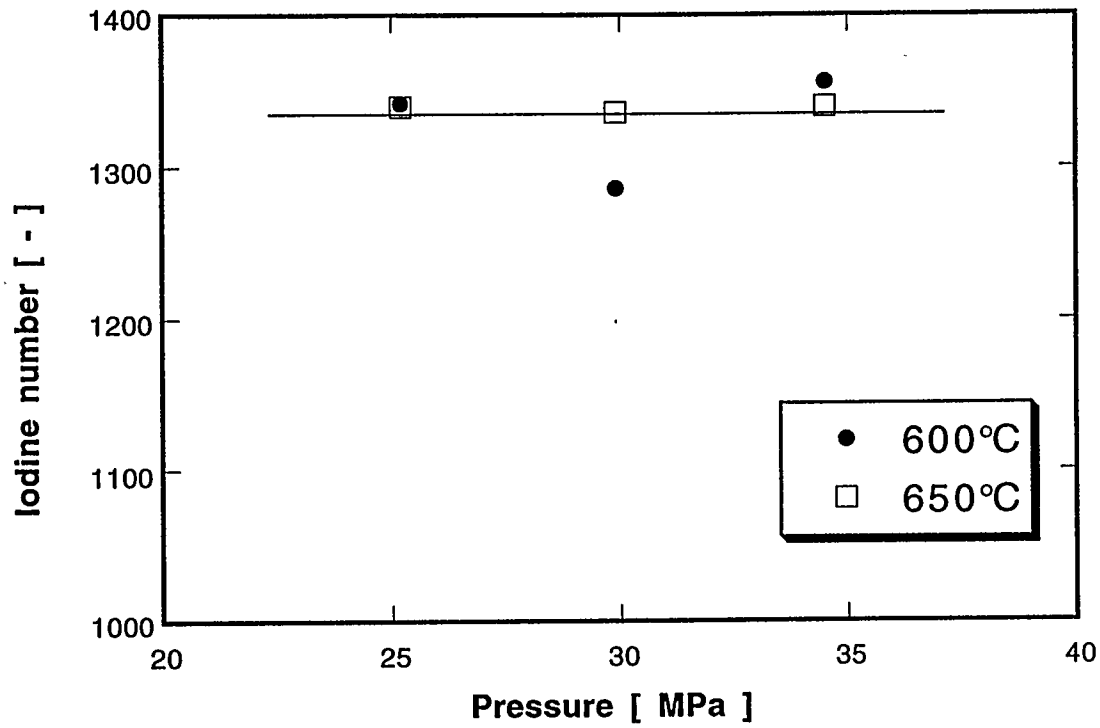

Figure 7. Pressure Influence on Iodine Number of Activated Carbon After 6-hour Treatment with Supercritical Water

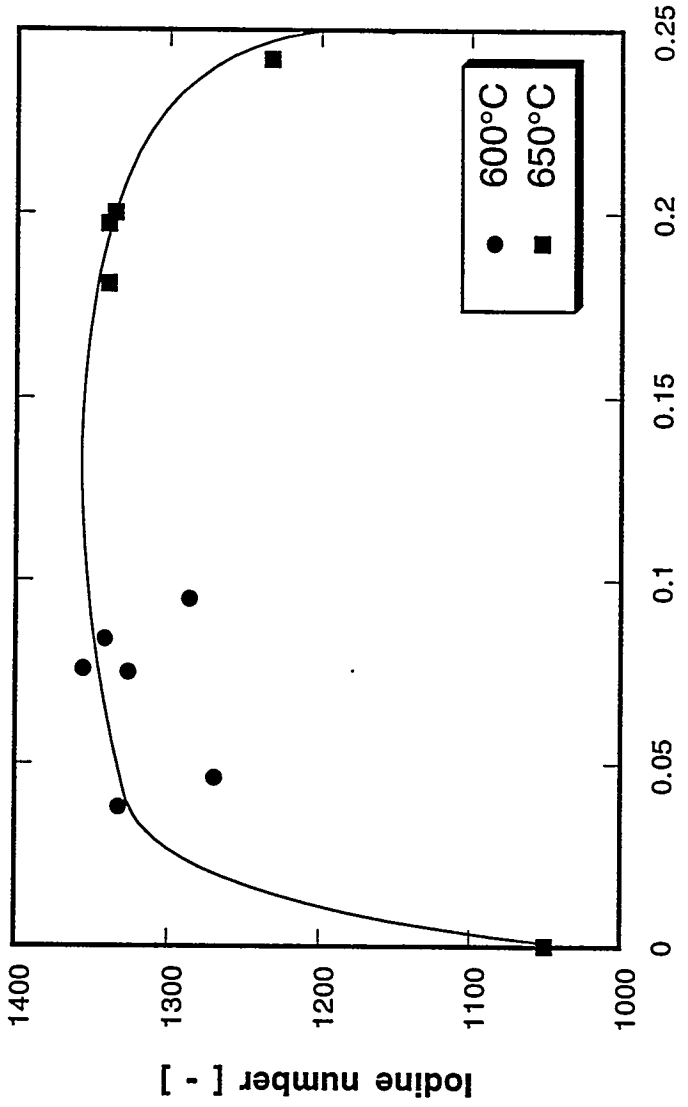

Figure 8. Relationship Between Conversion and Iodine Number

SOLAR PHOTOCATALYTIC H_2 PRODUCTION FROM WATER USING A DUAL BED PHOTOSYSTEM

Dr. Clovis A. Linkous
Florida Solar Energy Center
University of Central Florida
300 State Road 401
Cape Canaveral, FL 32920

Abstract

This work entails the use of photocatalytic particles in a dual bed configuration so as to effect the solar-driven decomposition of water to its constituent elements, particularly hydrogen. The system envisioned would consist of two modules, each consisting of a shallow, flat, sealed container, in which micron-sized photocatalytic particles are immobilized. An aqueous solution containing a redox mediator is pumped between the two chambers. Different photoparticles and catalysts are chosen for their respective modules so as to effect oxidative water-splitting in one vessel to evolve oxygen gas, and reductive water-splitting in the other to evolve hydrogen. This is a direct photoconversion scheme that breaks down the energetic requirement for water decomposition into a 2-photon process, and enables separate production of hydrogen and oxygen.

Various n-type and p-type semiconductors will be employed as photoparticles in the O_2- and H_2-evolving beds, respectively. Catalysts will also be evaluated to selectively promote the 4 half-cell reactions. On the microscopic level, there are many ways to configure the arrangement of catalyst and photoparticle. It is also important to determine whether the particles should be immobilized on an electronically conducting or insulating surface. Theoretical calculations of hydrogen production rates that include the energy band structure of free and immobilized particles are expected to provide guidance as to how the microstructure of the particles should be configured.

Introduction

In 1972 Fujishima and Honda pointed out that irradiation of wide band gap semiconductors such as TiO_2 could supply much of the energy required to electrolytically decompose water, evolving O_2 and generating protons that could be reduced at a dark electrode to produce hydrogen. This introduced photoelectrochemistry as a new approach to solar energy conversion. A flurry of activity began to develop semiconductor electrodes for use in photoelectrochemical cells.

Various problems arose as work progressed. One, the original wide band gap semiconductors, such as TiO_2 and SnO_2, required light energy well into the ultraviolet, making poor utilization of the solar spectrum; two, only highly crystalline, highly pure semiconductor specimens gave large photocurrents and quantum efficiencies, because of the limited lifetimes of the photogenerated charge carriers in the solid state; and three, semiconductors whose band gaps were better matched to the solar spectrum were subject to photoanodic corrosion, where the photogenerated hole could decay by dissolving a surface metal atom into the electrolyte.

It was also realized that the classic electrochemical configuration of two planar electrodes standing parallel to one another did not lend itself well to efficient use of the incoming solar photons. One either had to use an optically transparent counter electrode so that light could pass through it and the electrolyte to reach the semiconductor electrode, or deposit a thin film of semiconductor on glass and irradiate from the backside.

Since the essential feature of photoelectrochemical energy conversion was development of a barrier voltage at the semiconductor/electrolyte interface, it was realized that this could just as well be accomplished with the semiconductor in powder form. Conceptually this was a much simpler way to perform solar photoelectrolysis: just pour the semiconductor powder into water, expose the system to light, and H_2 and O_2 would bubble out.

New problems arose, however. The main one was separation of products. In an electrochemical cell, chemistry is performed by the occurrence of two half-cell reactions, each reaction proceeding at its own respective electrode. In the case of electrolyte-soluble products, an ion-conductive separator can also be included to ensure that the two chemical product streams do not mix with one another and back react. For the semiconductor particle system, the microscopic nature of the half-cell reaction surfaces causes H_2 and O_2 to be evolved essentially together. The gas stream released from the photoparticle slurry would be 66% H_2 by volume, the balance mostly O_2, well within the combustible range.

Our work to date has been geared toward understanding how photoparticle systems operate, and how a large scale reactor system might be configured. We have found that fixed bed arrays of particulates would make the most economic use of the solar energy-converting material. Furthermore, the loss in conversion efficiency compared to loose colloidal systems is compensated by the technical advantages of having a flow system that moves the dissolved products of reaction out the photoreactor, lessening the extent of back reaction.

Description of Concept

We plan to take the fixed particle bed approach and apply it to the photocatalytic water splitting problem. The intrinsic problem of gaseous product separation could be solved by employing 2 particle beds, one for oxidation of water to evolve O_2, the other for reduction of water to evolve H_2. Figure 1 depicts how the system would work.

The general chemical mechanism for a dual bed concept photosystem would be as follows:

Photoreactor 1, PC-R: $4H_2O + 4M^\circ \rightarrow 2H_2 + 4OH^- + 4M^+$

Photoreactor 2, PC-O: $\underline{4OH^- + 4M^+ \rightarrow O_2 + 2H_20 + 4M^\circ}$

net: $2H_2O \rightarrow 2H_2 + O_2$

where, PC-R: photocatalyst for the reductive stage of the process
PC-O: photocatalyst for the oxidative stage of the process
M: redox mediator

The immediate task is to identify photoactive materials that could be used for either H_2 or O_2 evolution, and devise ways to immobilize them on a surface. Much of the work done over the years in photoelectrochemical work can be built on for this task. As for O_2 evolution, one can identify 6 metal oxides that have achieved some measure of success as photoanodes: TiO_2, ZnO, SnO_2, WO_3, MoO_3, and Fe_2O_3. We will be using TiO_2 initially.

As for hydrogen evolution, comparably fewer materials have been identified. This is partly due to difficulties in p-type doping of materials that are stable in water, and also due to the use of Pt and other noble metals as rapid H_2-evolving electrodes that work in the dark while the anode is illuminated. Even so, a number of metal phosphides, such as InP and GaP, have been studied.

Also, a redox equivalent transfer agent or mediator should be identified to provide an anodic half-cell reaction in the H_2-evolving reactor and the cathodic half-cell back reaction in the O_2-evolving reactor. Charge transfer kinetics with the respective semiconductor powders should be reasonably rapid in order to make use of the photogenerated electrons and holes, but not so fast that the reverse reaction proceeds with equal facility. The respective back reactions between O_2 and M in one chamber and H_2 and M^+ in the other also represent an efficiency loss that should be accounted for.

The band characteristics of PC-R and PC-O will limit what redox agents could possibly serve as mediator in the dual particle bed system. As shown in Figure 2, the positive limit of redox potential is determined by the valence band edge of the p-type, H_2-evolving photocatalyst, while the negative limit is determined by the conduction band edge of the n-type, O_2-evolving photocatalyst. As band edges are difficult to determine, researchers frequently approximate them by measuring the flat band potential, V_{fb}.

To give an example, let PC-O be n-TiO_2. At pH 9, V_{fb} is calculated to be -0.375 V vs NHE, based on -0.7 V at pH 13. The previously mentioned approximation for n-type semiconductors is that $E_{cb} = V_{fb}$, and so -0.375 is the negative limit. Also let PC-R be p-InP. At the same pH, V_{fb} = +0.7 V, which approximates the InP valence band position. That enables a 0.7 - (-.375) = 1.07 volt range to work with.

Various iron complexes, quinones, and other reasonably rapid charge transfer agents within the optimum redox potential range would be examined. These components would be put together to make a proof-of-concept cell.

In summary, the advantages of the dual bed concept are:

- separate evolution of H_2 and O_2
- the efficiency of solar energy conversion is potentially higher (since the 2 light absorbers may be able to use more abundant, lower energy photons)
- flexibility (solar-thermal stages conceptually also could be involved in scheme)
- potentiality to use cheap reagents, photocatalysts and materials for construction

Disadvantages:

- more complex than a single bed system
- additional energy for the transportation of reagents is consumed
- the two photoredox modules are competing for the same photons (this aspect motivates development of a photovoltaic tandem cell equivalent of the photoparticle bed)

Results

Theory: Band Structure of Catalyst/Photoparticle Configurations

On the microscopic level, there are many ways to configure the arrangement of catalyst and photoparticle. Certainly they must be in close proximity to each other, so that the photogenerated charge can flow from semiconductor to catalyst phase without recombination or other loss mechanisms. One normally thinks of a catalyst as precious material, dispersed as fine particles on an inert support. In our case, the catalyst would be deposited on a semiconductor powder, which is certainly not inert. The optimum size of a catalyst deposit, both in terms of its absolute size and size relative to the semiconductor particle that supports it, needs to be determined. Also, the proximity of one catalyst island to another is important, because too much catalyst could block the incoming light that is to be absorbed by the semiconductor.

If the catalyst is not too expensive, one could just as well consider depositing the semiconductor on the catalyst, or better still, deposit both semiconductor and catalyst on an inexpensive, but

electronically conductive, substrate. That way, islands of semiconductor and catalyst could be placed side by side. This would cause some segregation of the respective oxidation and reduction reactions in each module, and would enable maximum light absorption by the photoparticle. It is intended to establish a theoretical basis for this approach.

Potential Distribution for a Flat, Infinite Semiconductor Surface

The model for the potential field in a semiconductor immersed in an electrolytic solution assumes a flat infinite semiconductor surface. A potential will develop according to Poisson's equation as follows:

$$\nabla^2 V(x) = \frac{-4\pi}{\epsilon_1}\rho \ , \tag{1}$$

which states that the potential is a function of the charge density, ρ, and semiconductor dielectric constant, ϵ_1. The charge density can be written in terms of concentrations of electron, holes, donor levels, and acceptor levels as follows (n,p,N_D,N_A respectively):

$$\rho = e(-n+p+N_D-N_A) \ . \tag{2}$$

Assuming complete ionization of donors and acceptors, free carrier concentration in the electric field can be determined by a Boltzmann distribution. Thus,

$$n(x) = n^{\circ}\exp^{\frac{e(V-V_b)}{kt}} ; \qquad p(x) = p^0\exp^{-\frac{e(V-V_b)}{kT}} \ , \tag{3}$$

Where n_0, p_0, and V_b are concentrations of electrons, holes and the potential at the bulk of the semiconductor, k is the Boltzmann constant, and T is temperature. Substituting this result into equation (2) yields

$$\rho = e\left(-n^0 e^{\frac{e(V-V_b)}{kT}} + p^0 e^{-\frac{e(V-V_b)}{kT}} + N_D - N_A\right) \ . \tag{4}$$

Substituting this into (1) results in

$$\nabla^2 V = -\frac{4\pi}{\varepsilon_1} e(-n^0 e^{\frac{e(V-V_b)}{kT}} + p^0 e^{-\frac{e(V-V_b)}{kT}} + N_D - N_A) \ . \tag{5}$$

For an n-type semiconductor for which $N_D >> N_A$ and $n^0 >> p^0$ equation (5) can be simplified to

$$\nabla^2 V = -\frac{4\pi}{\varepsilon_1} e(-n^0 e^{\frac{e(V-V_b)}{kT}} + N_D) \ . \tag{6}$$

Using only the first term of the series expansion of the exponential, equation (6) further simplifies to

$$\nabla^2 V = -\frac{4\pi}{\varepsilon_1} e\left(-n^0\left(1+\frac{e(V-V_b)}{KT}\right) + N_D\right) \ . \tag{7}$$

Because there is no space charge in the bulk of the semiconductor, $-n^0 + N_D \approx 0$. Taking this into account,

$$\nabla^2 V = \frac{4\pi n^0 e^2}{\varepsilon_1 kT}(V - V_b) \quad . \tag{8}$$

Asserting that V_b is the reference potential, hence equal zero, the solution to the flat infinite surface is:

$$V(x) = (V_0 - V_b)\, e^{-\frac{x}{L}} - V_b \quad , \tag{9}$$

where L is the Debye length defined as

$$L = \sqrt{\frac{\varepsilon_1 kT}{4\pi e^2 n^0}} \quad . \tag{10}$$

Free Semiconductor Particle

Expanding on this general development, a spherical semiconductor particle immersed in an electrolytic solution will be considered. The form of Poisson's equation is shown below after simplifications of the same nature as those above have been applied. Additionally, V_b=0 is assumed.

$$\frac{1}{r^2}\frac{\partial}{\partial r}\left(r^2 \frac{\partial V}{\partial r}\right) = \frac{1}{L^2} V \tag{11}$$

Equation (11) is of the form of a modified spherical bessel function as generally shown below:

$$z^2 w'' + 2zw' - [z^2 + n(n+1)] = 0 \quad . \tag{12}$$

Because the potential at the center of the particle must be finite ($V|_{r=0}$=constant), rejection of all solutions except the i-type bessel functions is possible. Also because our initial equation restricts n to 0 or -1 we can consider the case of n=0. Because $i_0(r)=\sinh(r)/r$ the appropriate solution is:

$$V = \frac{r_0 V_o}{r} * \frac{\sinh\left(\frac{r}{L}\right)}{\sinh\left(\frac{r_0}{L}\right)} \tag{13}$$

for the boundary for the boundary conditions $V=1|_{r=r_0}$ and $V=\text{constant}|_{r=0}$.

Potential Distribution for Interstitial Catalyst System

The potential for a semi-spherical semiconductor particle interfaced to a conductive substrate on the flat side and immersed in an electrolytic solution is in the following.

It is assumed that symmetry exists in the θ direction. Thus equation (1) takes the form below in 2 dimensional spherical coordinates.

$$\frac{1}{r^2}\frac{\partial}{\partial r}\left(r^2\frac{\partial V}{\partial r}\right)+\frac{1}{r^2\sin\phi}\frac{\partial}{\partial\phi}\left(\sin\phi\frac{\partial V}{\partial\phi}\right)=\frac{-4\pi}{\varepsilon_1}\rho(r,\phi) \tag{14}$$

Applying the same assumptions as in the first section equation (8) is as follows:

$$\frac{1}{r^2}\frac{\partial}{\partial r}\left(r^2\frac{\partial V}{\partial r}\right)+\frac{1}{r^2\sin\phi}\frac{\partial}{\partial\phi}\left(\sin\phi\frac{\partial V}{\partial\phi}\right)=\frac{1}{L^2}(V-V_b) \tag{15}$$

Substituting u=cos ϕ, and again asserting that V_b is the reference potential (V_b=0) this becomes

$$\frac{1}{r^2}\frac{\partial}{\partial r}\left(r^2\frac{\partial V}{\partial r}\right)-\frac{1}{r^2}\frac{\partial}{\partial u}\left((1-u^2)\frac{\partial V}{\partial u}\right)=\frac{1}{L^2}V \tag{16}$$

Utilizing separation of variables, it is assumed that the solution takes the form:

$$V(r,\phi)=R(r)M(u)\ , \tag{17}$$

which leads to

$$\frac{1}{R}\frac{\partial}{\partial r}\left(r^2\frac{\partial R}{\partial r}\right)-\frac{1}{L^2}r^2=\frac{1}{M}\frac{\partial}{\partial u}\left((1-u^2)\frac{\partial M}{\partial u}\right) \tag{18}$$

Because functions of r are equal to functions of u the two sides of equation (18) must be equal to an arbitrary constant λ. Thus,

$$\frac{1}{R}\frac{\partial}{\partial r}\left(r^2\frac{\partial R}{\partial r}\right)-Kr^2=\lambda \tag{19a}$$

$$\frac{1}{M}\frac{\partial}{\partial U}\left((1-U^2)\frac{\partial M}{\partial u}\right)=\lambda\ , \tag{19b}$$

Where equation (19a) is recognizable as a Bessel equation, equation (19b) is of the form of Legendre's equation and λ is a positive integer and separation parameter.

The solution to equation (19b) is the well known Legendre polynomial expressed as

$$M(u)=A_nP_n(u)\ , \tag{20}$$

where

$$P_n(x)=\sum_{m=0}^{\frac{n}{2}}(-1)^m\frac{(2n-2m)!}{2^n m!\,(n-m)!\,(n-2m)!}x^{n-2m}\ . \tag{21}$$

The solutions of equation (19a) are the spherically modified bessel function $i_n(x)$ and $k_n(x)$. Because the potential must be finite at r=0 only the i function is possible. Thus, the solution is of the form:

$$R(r)=D_n\, i_n\left(\frac{1}{L}r\right) , \tag{22}$$

where

$$i_n\left(\frac{r}{L}\right)=2^{-(n+1)}\sqrt{\Pi}\left(\frac{r}{L}\right)^n \sum_{k=0}^{\infty} \frac{\left(-\frac{re^{\frac{ni}{2}}}{4L}\right)^k}{k!\Gamma(n+.5+k+1)} . \tag{23}$$

Finally, substituting equations (20) and (22) into equation (17) results in the general form of the solution.

$$V(r,\phi)=\sum_{n=1}^{\infty} A_n D_n J_n\left(\frac{1}{L}r\right) P_n(\cos\phi) \tag{24}$$

Letting $a_n=A_nD_n$,

$$V(r,\theta)=\sum_{n=1}^{\infty} a_n i_n\left(\frac{1}{L}r\right) p_n(\cos\theta) . \tag{25}$$

The coefficient a_n is readily obtained by applying B.C. V=1 at $r=r_0$ and the condition of orthogonality to the Legendre polynomial.

$$a_n=\frac{(2n+1)k}{2i_n\left(\frac{r_0}{L}\right)}\int_0^{\frac{\pi}{2}} P_n(\cos(\phi))\sin(\phi)\, d\phi \tag{26}$$

Thus, the complete solution is

$$V(r,\phi)=\sum_{n=1}^{\infty}\left(\left(\frac{(2n+1)k}{2i_n\left(\frac{r_0}{L}\right)}\int_0^{\frac{\pi}{2}}\sin(\phi)\cdot P_n(\cos(\phi))\, d\phi\right) i_n\left(\frac{r}{L}\right) P_n(\cos(\phi))\right) . \tag{27}$$

At this point, the particular solution awaits imposition of additional boundary conditions. Discontinuities are found at the edges the semiconductor particle where it contacts both the

electrolyte and the conductive substrate. Finite element analysis may be necessary to define the potential distribution.

The milestones for the first year's effort are:

a) Provide a theoretical foundation supporting various catalyst/photoparticle configurations in terms of efficiency of charge separation/recombination.

b) Begin to perform oxidative photochemistry using light wavelengths better matched to the solar spectrum.

c) Reduce charge carrier recombination losses due to slow electron transfer kinetics.

Future Work

The various sources of performance losses need to be quantified and ranked with respect to one another. Thus we will estimate efficiency loss due to back reaction as a function of photoparticle/catalyst configuration

Also, as dye sensitizers are developed, the catalytic activity of O_2 system chromophores toward water splitting will be determined.

Chromophore/photoconductor systems for H_2 evolution must also be developed.

It will also be necessary to:

a) Determine level of sophistication needed for redox mediator.

b) Balance light absorptive and catalytic activity of the chromophore

c) Consider whether the H_2 cell would benefit from the dye sensitization approach.

Finally, we will need to

1. on the theoretical work, incorporate reverse chemical reaction kinetics into steady state equation

2. use supersensitizers in conjunction with base chromophore

3. catalysts for redox mediator oxidation and reduction

milestones:

a) Weigh the efficiency loss due to back reaction versus solid state processes; better match with theoretical and experimental results.

b) Improve overall kinetics by dividing water-splitting and light absorptive functions between different molecular species.

c) Increase rate of charge transfer between the redox mediator and the photoparticle without increasing its reactivity toward O_2 and H_2.

Acknowledgement

The author would like to thank Beverly Austin, Tom McCaige, and Darlene Slattery for their technical assistance on this work. The financial support of the Department of Energy, Office of Advanced Utility Systems, is gratefully acknowledged.

Figure Captions

Figure 1. Schematic of the dual photoparticle bed concept for water-splitting.

Figure 2. Energy band diagram showing range of possible mediator redox potentials.

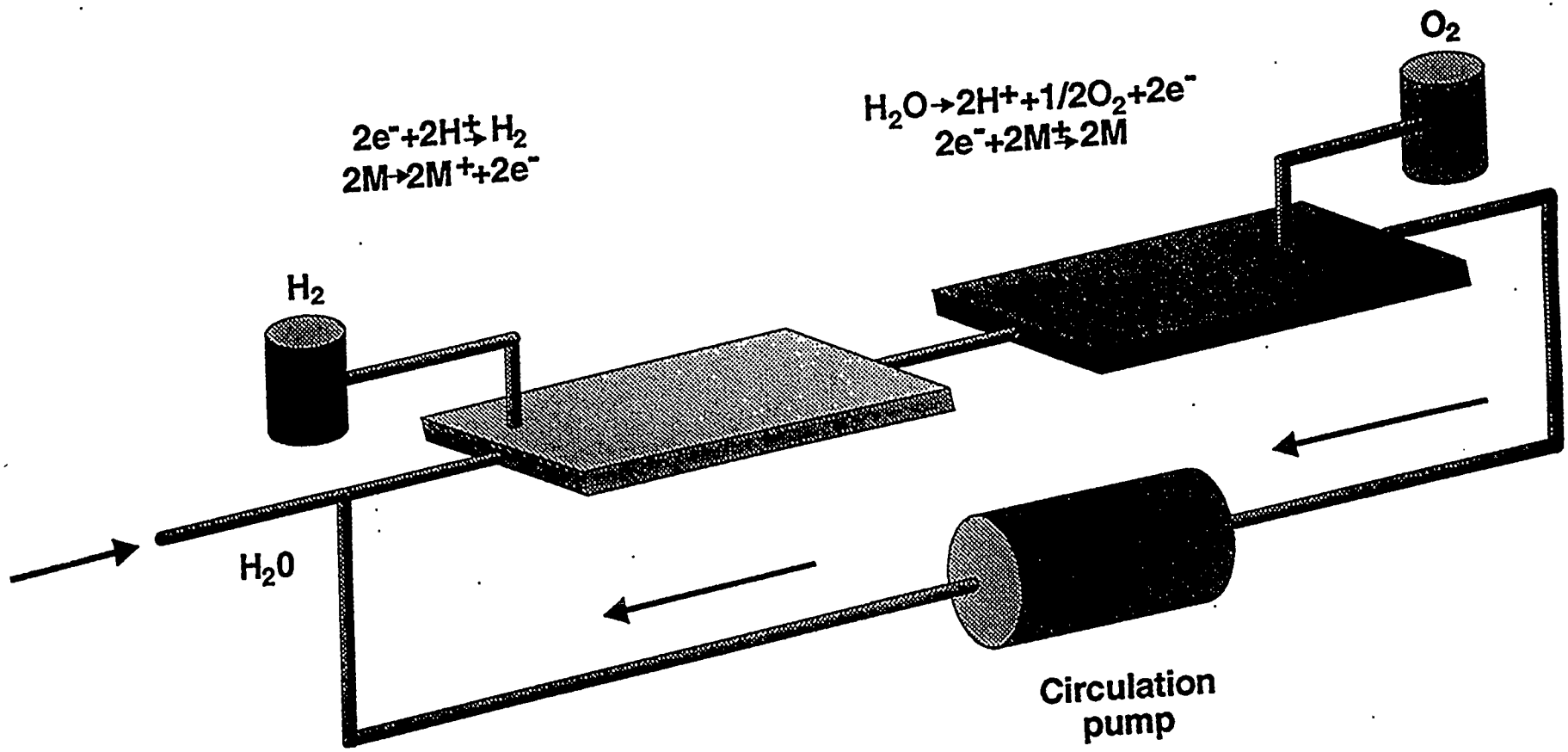
$2e^- + 2H^+ \rightleftharpoons H_2$
$2M \rightarrow 2M^+ + 2e^-$
$H_2O \rightarrow 2H^+ + 1/2O_2 + 2e^-$
$2e^- + 2M^+ \rightleftharpoons 2M$
O_2
H_2
H_2O
Circulation pump

807.a

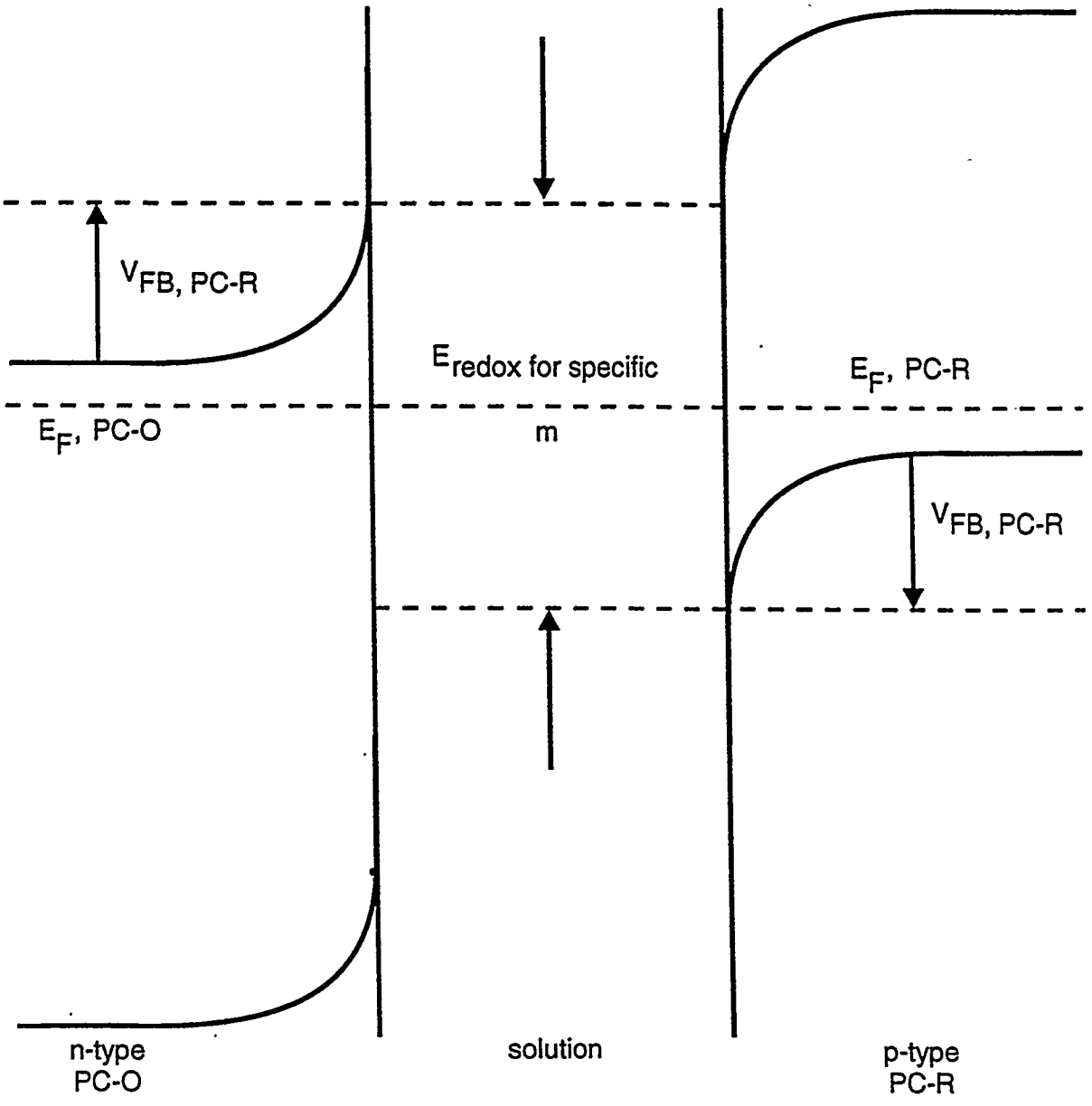
$V_{FB, PC-R}$
$E_{redox\ for\ specific}$
m
E_F, PC-R
E_F, PC-O
$V_{FB, PC-R}$
n-type
PC-O
solution
p-type
PC-R

PHOTOBIOLOGICAL PRODUCTION OF HYDROGEN USING CYANOBACTERIA

Dulal Borthakur, Kelton R. McKinley, and Edward J. Bylina
University of Hawaii
Honolulu, HI 96822

Abstract

Cyanobacteria are capable of generating hydrogen using sunlight and water. In both *Spirulina* and *Anabaena*, there is a soluble reversible hydrogenase that is involved in hydrogen evolution under anaerobic conditions in the dark. In addition, the nitrogen-fixing cyanobacterium *Anabaena* produces hydrogen as a by-product of nitrogen fixation. Most of this hydrogen is recaptured by a membrane-bound uptake hydrogenase present in *Anabaena* cells. Experiments have continued to develop a gene transfer system in *Spirulina* in preparation for improved hydrogen production via genetic manipulation of the reversible hydrogenase. We have identified and characterized four restriction enzymes in *Spirulina* and cloned the genes for two methylases that protect their own DNA from cleavage by restriction enzymes. We have also cloned and sequenced parts of *hupB* and *hupM* genes involved in the synthesis of uptake hydrogenase in *Anabaena*. Successful cloning of these *hup* genes represents an important and necessary step in our project because this will enable us to construct *Anabaena* strains with enhanced hydrogen production ability by disrupting the *hup* genes involved in hydrogen uptake. We are also setting up a bio-reactor to determine the amount of hydrogen released by different *Spirulina* and *Anabaena* strains under different physiological conditions.

Introduction

Cyanobacteria are a diverse group of organisms, living under a wide variety of environmental conditions. These organisms are able to generate their own source of organic substrates using light energy and using water as the ultimate source of reductant. Moreover, some cyanobacteria have

nitrogen-fixing ability and thereby convert atmospheric nitrogen into ammonia. Cyanobacteria also represent an important group of model organisms for the direct production of molecular hydrogen with water as the electron donor and for the production of hydrogen from photosynthate (Houchins 1981). They enzymatically convert solar energy to hydrogen, which we can use as a source of energy. Our goal is to enhance the production of hydrogen. Optimization of hydrogen production also entails systems designs to ensure efficient transfers of light energy and the capture of any hydrogen so produced. In order to achieve these goals, it is necessary to understand the hydrogen cycle within this subset of organisms and gain a measure of control over the physiological function of the organisms, either by selection or genetic manipulation of strains.

Our focus is the function and capacity for hydrogen production of the cyanobacteria *Spirulina* and *Anabaena*. Three basic enzyme systems are involved in hydrogen metabolism in cyanobacteria: reversible hydrogenase, nitrogenase, and uptake hydrogenase. Both *Anabaena* and *Spirulina* contain a soluble hydrogenase which is responsible for hydrogen evolution under anaerobic conditions in the dark. This reversible hydrogenase is expressed independently of the nitrogen metabolism, but is activated only under anaerobic conditions. In addition, the nitrogen-fixing cyanobacterium *Anabaena* produces hydrogen as a by-product of nitrogen fixation. Most of the hydrogen produced is recaptured by a membrane-bound uptake hydrogenase present in *Anabaena* cells, reducing the net yield of molecular hydrogen available, but conserving chemical energy within the *Anabaena* cells. Greater hydrogen availability can come as the result of increased hydrogen production and/or reduced recapture within cells. Techniques of molecular biology have been used to characterize the genetic make-up of these two filamentous cyanobacteria and to improve our understanding of their hydrogen cycles, with the target of increased net hydrogen production and capture.

Spirulina is a cyanobacterium that can be readily grown at commercial scales. The target of this large-scale commercial production, however, is not hydrogen. Enhanced hydrogen production requires manipulation of the hydrogenase systems. Soluble hydrogenases involved in hydrogen production have been partially purified from several species (Gu and Zhou 1987), but the genes encoding these enzymes have neither been cloned nor characterized. Moreover, a gene transfer system for *Spirulina* has not yet been developed. We need, therefore, to develop a genetic system for transferring genes within *Spirulina* and for mutagenesis. A complication in developing these tools for *Spirulina* is the fact that *Spirulina* produces several restriction enzymes that cleave any foreign DNA whenever an attempt is made to transfer it into *Spirulina*. It was therefore necessary to identify and characterize the restriction enzymes produced by *Spirulina* before proceeding to influence the production of hydrogen. We have now successfully completed the characterization of the restriction enzymes present in *Spirulina pacifica*.

For the nitrogen-fixing filamentous cyanobacterium *Anabaena*, hydrogen is evolved during nitrogen fixation within specialized cells, called heterocysts. This hydrogen is recaptured in most strains by an uptake hydrogenase during the normal course of the nitrogen fixation process. Manipulation of the uptake hydrogenase is essential to improved net hydrogen production. In various nitrogen-fixing bacteria, at least 20 *hup* genes involved in the hydrogen uptake activity have been cloned. Previous attempts to clone *hup* genes from *Anabaena* using cloned DNA from other nitrogen-fixing bacteria

have been unsuccessful because there is probably very little homology between *hup* genes of *Anabaena* and other bacteria. Our approach is more direct. Using a combination of several methods, including polymerase chain reaction (PCR), we have cloned *hup* genes from *Anabaena*.

Results

Development of a Genetic System for *Spirulina pacifica* in Preparation for Improved Hydrogen Production via Genetic Manipulation of Reversible Hydrogenases

Spirulina pacifica is a filamentous marine cyanobacterium that produces hydrogen under anaerobic conditions in the dark. We identified and characterized four restriction enzymes in the *Spirulina pacifica* cells. These are isoschizomers of Tth111I, PvuI, PvuII, and HindIII. We isolated these restriction enzymes from *Spirulina*, evaluated their assay conditions, and compared them with commercially available isoschizomers. The *Spirulina* enzyme SpaI, which is an isoschizomer of Tth111I, shows high activity at 37° C, compared to 65° C for Tth111I from *Thermus thermophilus* 111 (New England Biolab, MA). SpaI is inactivated quickly at 65° C. This enzyme shows high activity under conditions of 100 mM NaCl and at a pH of 7.0. SpaI may be the dominant restriction enzyme present in *Spirulina* and its extraction is relatively simple. The other three restriction enzymes isolated from *Spirulina*, namely SpaII, SpaIII, and SpaIV, are isoschizomers of PvuI, PvuII, and HindIII, respectively. These three endonucleases showed higher activity when the NaCl in the reaction is replaced with 100 mM KCl. These three enzymes showed maximum activity at pH 7.5.

Spirulina's own DNA is protected in the presence of these restriction enzymes because of the presence of various methylases. We also cloned the genes for Tth111I and PvuII methylases from *Spirulina* (data not shown). These cloned methylase genes will permit us to construct a vector for transferring DNA to *Spirulina*, a step which is essential for the genetic manipulation of *Spirulina* strains toward improved hydrogen production.

Cloning of the *hupB* Gene of *Anabaena* sp. Strain 7120 in Preparation for Improved Hydrogen Availability via Reduction of Uptake Hydrogenase Activity

The *hupB* gene product may be involved in the processing of hydrogenases into their mature, active forms. The *hupB* mutant in *Azotobacter* did not show hydrogenase activity (Tibelius et al. 1993). We found that *hup* genes of other nitrogen-fixing organisms, such as *Rhizobium* and *Bradyrhizobium* , do not show strong hybridization with *Anabaena* DNA. This is likely the result of insufficient similarity between hydrogenase genes of *Anabaena* and other organisms. However, we hypothesized that there must be small stretches of homologous sequences in the conserved regions of the *hup* genes in various organisms. Known *hup* gene sequences from several bacteria were compared and two conserved regions approximately 300 bp apart within *hupB* sequence were selected. Based on these conserved sequences, two primers for PCR were constructed and used to amplify DNA from the *Anabaena* sp. strain 7120. As expected, a 334-bp PCR fragment was generated, which was inserted in a cloning vector. Sequencing confirmed the presence of the *Anabaena hupB* gene. This cloned

fragment was used as a probe to *Anabaena* genomic DNA digested with EcoRI and HindIII. A 6.0-kb EcoRI fragment and 2.0-kb HindIII fragment hybridized with the probe suggested that the *hupB* sequences of *Anabaena* 7120 are located on this fragment.

Cloning of a 1.8-kb Region Containing *hupM* Gene from *Anabaena* 7120

HupM is a 30-kDa polypeptide in *Rhodobacter capsulatus* required for hydrogen uptake and autotrophic growth (Colbeau et al. 1993). This polypeptide is encoded by *hupM* gene in *Rhodobacter* and *hupC* gene in *Azotobacter chroococcum* (Tibelius et al. 1993). As in the case of *Rhodobacter* and *Azotobacter*, *hupM* gene in *Anabaena* 7120 is expected to be located between *hupL* and *hupD* genes. By constructing two PCR primers from the conserved region of *hupL* and *hupD* sequences of *R. capsulatus* and *A. chroococcum*, we generated a PCR 1.8-kb fragment from abaena 7120. We cloned this fragment and sequenced a part of it. Preliminary sequence data suggest that we have cloned the *hupM* gene and a part of the *hupL* gene of *Anabaena* 7120.

Discussion

In both *Spirulina* and *Anabaena*, there is a soluble reversible hydrogenase that is involved in hydrogen evolution (Houchins and Burns 1981; Gu and Wang 1984; Ewart and Smith 1989). It was suggested that in these organisms this hydrogenase is constitutively expressed but remains inactive in the presence of oxygen (Gogotov and Kosyak 1976). It is activated under anaerobic condition in the dark when there is no oxygen evolution due to photosynthesis. Hydrogen evolution in these cyanobacteria can be enhanced by genetically engineering this soluble hydrogenase. *Spirulina pacifica* is an important marine cyanobacterium which is now grown commercially and used for human consumption. We are working toward developing a genetic system in *Spirulina* by characterizing the restriction enzymes present in this organism. We have shown that there are at least four restriction enzymes in this organism. Understanding the restriction enzymes of *Spirulina* will help us to develop a suitable plasmid vector for this organism using genes for methylases. We have also identified two DNA fragments containing SpaI and SpaII methylases.

Besides the soluble hydrogenase in the vegetative cells, *Anabaena* has an uptake hydrogenase in the heterocysts, which are very specialized nitrogen-fixing cells. The function of this uptake hydrogenase is to recycle hydrogen evolved during nitrogen fixation. Therefore, another way to enhance hydrogen evolution in *Anabaena* is to disrupt the *hup* genes involved in hydrogen uptake. This will require cloning and characterizing of the various *Anabaena hup* genes and constructing mutations in these genes. In *R. capsulatus* and *A. chroococcum*, at least 20 potential genes involved in hydrogen uptake have been identified. We hypothesized at the onset of this project that some of these genes will be found in *Anabaena* 7120 also. We used the PCR method to clone parts of *hupB*, *hupM*, and *hupL* genes from *Anabaena* 7120. Successful cloning of these *hup* genes represents an important and necessary step in our project because this now opens the possibility of the engineering of *Anabaena* for increased hydrogen production. We are now directing our efforts toward the cloning of the complete *hupB* sequence and other related *hup* genes. New *Anabaena* strains will now be constructed by altering/disrupting the *hup* genes. These engineered strains, containing no or reduced

levels of uptake hydrogenases, are expected to permit a greater proportion of hydrogen produced as a result of nitrogen fixation to be captured for man's uses. Because *Anabaena* is a heterocystous cyanobacterium, hydrogen production can continue during active photosynthetic growth and in the presence of oxygen.

Future Work

The goals of our future work are: (1) cloning and sequencing of the complete *Anabaena hupB* gene; (2) sequencing and characterizing *hupM* and other genes cloned in the 1.8-kb PCR fragment; (3) cloning of *hupS*, *hupL*, and *hupH* genes, (4) isolating site-directed mutants of various cloned *hup* genes in *Anabaena*; (5) testing of these mutants for their hydrogen-production ability; (6) producing hydrogen from cyanobacteria using a bio-reactor; and (7) determining the optimum physiological conditions for maximum hydrogen production by *Anabaena*.

Acknowledgments

This work was supported by a grant (DE-FG04-94AL85804) to the Hawaii Natural Energy Institute from the U.S. Department of Energy via the National Renewable Energy Laboratory. We would like to thank Vincenz Tragut, Jyothirmai Gubili, and Jin Ronguan for their contributions to the work described in this report.

References

Colbeau, A., P. Richaud, B. Toussaint, F.J. Caballero, C. Elster, C. Delphin, R.L. Smith, J. Chabert, and P.M. Vignais. 1993. "Organization of the Genes Necessary for Hydrogenase Expression in *Rhodobacter capsulatus*; Sequence Analysis and Identification of Two *hyp* Requlatory Mutants." *Molecular Microbiology*, 8:15-29.

Ewart, G.C., and G.D. Smith. 1989. "Purification and Properties of Soluble Hydrogenase from Cyanobacterium *Anabaena cylindrica*." *Arch. Biochem. Biophys.*, 268:327.

Gogotov, I.N., and A.V. Kosyak. 1976. "Hydrogen Metabolism by *Anabaena variabilis* in the Dark." *Microbiologiya*, 45:586-591.

Grant, R.L., and G. Smith. 1981. "The Hydrogen Metabolism of Cyanobacteria." *Biology Review*, 56:589-660.

Gu, T., and F. Wang. 1984. "Studies of H_2 Evolution by *Spirulina platensis*." *Hydrobiologia*, 116/117:467-470.

Gu, T., and P. Zhou. 1987. "Isolation and Characterization of Hydrogenase from *Spirulina*

platensis." *Hydrobiologia*, 151/152:557-561.

Houchins, J.P. 1984. "The Physiology and Biochemistry of Hydrogen Metabolism in Cyanobacteria." *Biochim. Biophys. Acta.*, 768:227-255.

Houchins, J.P., and R.H. Burns. 1981. "Comparative Characterization of Two Distinct Hydrogenases from *Anabaena* sp. Strain 7120." *Journal of Bacteriology*, 146:215-221.

Tibelius, K.H., L. Du, D. Tito, and F. Stejskal. 1993. "The *Azotobacter chroococcum* Hydrogenase Gene Cluster: Sequences and Genetic Analysis of Four Accessory Genes, *hupA*, *hupB*, *hupY*, and *hupC*." *Gene*, 127:53-61.

SORPTION ENHANCED REACTION PROCESS (SERP) FOR PRODUCTION OF HYDROGEN

Shivaji Sircar, Madhu Anand, Brian Carvill, Jeff Hufton,
Steve Mayorga, Bob Miller
Air Products and Chemicals, Inc.
Allentown, PA 18195

Abstract

Sorption Enhanced Reaction (SER) is a novel process that is being developed for the production of lower cost hydrogen by steam-methane reforming (SMR). In this process, the reaction of methane with steam is carried out in the presence of an admixture of a catalyst and a selective adsorbent for carbon dioxide. The consequences of SER are: (I) reformation reaction at a significantly lower temperature (300-500°C) than conventional SMR (800-1100°C), while achieving the same conversion of methane to hydrogen, (ii) the product hydrogen is obtained at reactor pressure (200-400 psig) and at 99+% purity directly from the reactor (compared to only 70-75% H_2 from conventional SMR reactor), (iii) downstream hydrogen purification step is either eliminated or significantly reduced in size. The early focus of the program will be on the identification of an adsorbent/chemisorbent for CO_2 and on the demonstration of the SER concept for SMR in our state-of-the-art bench scale process. In the latter stages, a pilot plant will be built to scale-up the technology and to develop engineering data. The program has just been initiated and no significant results for SMR will be reported. However, results demonstrating the basic principles and process schemes of SER technology will be presented for reverse water gas shift reaction as the model reaction. If successful, this technology will be commercialized by Air Products and Chemicals, Inc. (APCI) and used in its existing hydrogen business. APCI is the world leader in merchant hydrogen production for a wide range of industrial applications.

This program fits well with DOE's hydrogen program's near term objective of increasing the efficiency of H_2 production by SMR and reducing the CO_2 emissions. The SER process to be developed in this program will be highly beneficial for installation of small low cost plants

thus facilitating the growth of hydrogen delivery and service infrastructures. The effort in the projects' first 2 years will be 4.5 man-years for each year. The development effort will be ramped up significantly in the subsequent years as the technology is demonstrated.

Introduction

Novel SER Process

Sorption enhanced reaction process (SERP) is a new process being developed for increasing the conversion of equilibrium limited reactions by combining reaction with separation in the same reactor. The reactants are fed into a reactor containing a physical mixture of a catalyst and an adsorbent that selectively removes one of the reaction products. This allows increased forward reaction for a reversible reaction and hence a higher conversion toward the less selectively adsorbed product in the reactor. The system consists of two reactor-sorbers which operate in a sequential cyclic manner. When the first reactor-sorber is saturated with the adsorbed product, the feed is diverted to the second reactor-sorber and the adsorbed product from the first reactor-sorber is desorbed by depressurization and purge. The reactor-sorber is thus regenerated for use in the next cycle. An extraneous purge gas is used to carry out a part of the desorption process. The reactor-sorber is then pressurized to the reaction pressure using the less selectively adsorbed reaction product. Some of the advantages of such a process are: (i) lowering the temperature of the reaction for an endothermic reaction while maintaining the high conversion, (ii) lowering the cost of the reactor, (iii) recovering an essentially pure product from the reactor, (iv) reducing or eliminating downstream separations, (v) reduction in energy costs and (vi) reducing or eliminating side reactions.

Background

The sorption enhanced reaction process has been demonstrated in our laboratories for the reverse water-gas shift (RWGS) reaction shown below for the production of carbon monoxide :

$$CO_2 + H_2 \quad CO + H_2O \qquad \ldots. \quad (1)$$

The basic principles for SERP have been developed for the RWGS reaction and will be discussed in some detail in this paper.

The SER process scheme developed for RWGS will be extended to steam-methane reforming (SMR) for the production of hydrogen. Two simultaneous reactions shown below occur in SMR :

(a) $CH_4 + H_2O \quad CO + 3\,H_2$ ..... (2) Reforming reaction
(b) $CO + H_2O \quad CO_2 + H_2$ ..... (3) Water gas shift reaction

In the proposed SER process, the reactants, steam and methane, are fed at 300-500°C and 200-400 psig into a reactor containing a mixture of reforming catalyst and an adsorbent for removing one of the reaction products (carbon dioxide) and producing a reactor effluent consisting of essentially pure hydrogen (98+%). The key benefits of producing H_2 by SERP are: (i) reformation at a significantly lower temperature (300-500°C) than conventional SMR (800-1000°C), while achieving the same conversion of methane to hydrogen, (ii) significantly lower capital cost, (iii) the product hydrogen is obtained at reactor pressure (200-400 psig) and at 98+% purity directly from the reactor, (iv) downstream hydrogen purification steps are either eliminated or significantly reduced in size, (v) reduction/elimination of CO as a by-product, (vi) minimizing side reactions like coking, (vii) reduction of excess steam used in conventional SMR.

The concept of removing a product from the reaction zone to increase the conversion for an equilibrium limited reaction has been known for a long time. Several researchers have proposed combining reaction and separation in the same unit operation where the separation is carried out by adsorption or in a membrane reactor. However, it is only recently that researchers have started to understand the processes involved in such hybrid systems. Table 1

Table 1. Literature Survey of Enhanced Conversion for Gas Phase Equilibrium Controlled Reactions

Ref Author	Year	Reaction Studied	Product	Process
1. Vaporciyan and Kadlec	1987	general, mathematical models	conceptual, mixed gas	no specific process
2. Westerterp et al.	1988	$CO+H_2$ CH_3OH	adsorbed methanol	separate reactor and cyclic methanol separation
3. Goto et al.	1993	C_6H_{12} $C_6H_6+3H_2$	benzene	H_2 adsorbed on $CaNi_5$; regeneration by vacuum/He purge
4. Han and Harrison	1994	$CO+H_2O$ CO_2+H_2	hydrogen in N_2; feed: coal gasification syn gas in N_2; dolomite as chemisorbent	eliminate need for shift catalyst; 99+% conversion; no process
5. Kirby et al.	1994	general, mathematical models	conceptual; gas mixture	4-bed conceptual PSR process

summarizes some of the recent efforts in the literature for increasing the conversion of gas phase equilibrium controlled reactions by combining reaction and separation by adsorption. The

purpose of this work is to develop an efficient process for H_2 production which has high conversion, low reaction temperature and high product purity straight from the reactor.

Objectives

The key objectives of this paper are to:
(i) Experimentally demonstrate SERP with the reverse water gas shift reaction for the production of CO,
(ii) Outline an SERP scheme for the production of H_2 by SMR,
(iii)Outline the development program with key milestones.

Project Rationale

This program fits well with near term objectives of the DOE hydrogen program; namely, increasing the efficiency of H_2 production by SMR and reducing the CO_2 emissions. The SER process to be developed in this program will be highly beneficial for installation of small, low cost H_2 plants, thus facilitating the growth of hydrogen delivery and service infrastructures.

Experimental

An apparatus has been built to perform RWGS reaction and SMR in a tubular reactor, the schematic for which is shown in Figure1. The system has an on-line GC-MS for analyzing the feed or the product streams. For RWGS, the reactor-sorber is filled with 500 g of a 1:1 mixture (by weight) of copper-zinc low temperature shift catalyst (BASF K3-111 LTS) and NaX zeolite (LINDE 13X) particles. The NaX zeolite selectively removes water from the reaction zone. The ratio of LTS:NaX was varied in some experiments.

Catalyst and Adsorbent Activation Procedures :

The reactor-sorber is first purged with nitrogen to remove oxygen followed by heating at 1°C/min to 180°C in nitrogen. A mixture of 1% H_2 in N_2 is then introduced at atmospheric pressure to start the catalyst activation procedure (exothermic reduction of CuO to Cu). The use of a low concentration of H_2 keeps the exotherm to within 20°C. Once the exotherm has moved through the bed, the H_2 concentration is incrementally increased to 100% at 180°C. Finally, the temperature is raised to 250°C to complete the reduction process. The bed is then dried by purging overnight with dry nitrogen.

Experimental SERP for RWGSR :

After the drying procedure, the reactor-sorber is prepared for reaction by purging and pressurizing to reaction pressure (50-100 psig) with H_2 or CO_2 or CO. A 1:1 molar mixture

of H_2 and CO_2 is fed at 200 cc/min into the reactor-sorber; the reactor effluent composition and flow rate are continuously monitored. The reaction is continued until a desired CO concentration in the effluent is attained at which point the feed is stopped and the regeneration procedure started. Regeneration is carried out countercurrent to the feed flow direction by decreasing the pressure in the reactor-sorber and purging with N_2 or CH_4. Once the bed is dry, the reactor is purged and pressurized with H_2 or CO_2 or CO. Now the reactor is ready for reaction again.

Results and Discussion

Production of CO by Reverse Water Gas Shift Reaction :

Figure 2 shows the composition and flow rate of effluent from the reactor-sorber for RWGS carried out at 250°C and 50 psig and 200 cc/min flow rate when the reactor is initially filled with the reactant H_2. The data show that :

(I) The reactor effluent initially contains a low concentration of CO which rises to about 85% and then falls below 15% after 160 minutes of reaction.

(ii) The flow rate of the effluent fluctuates initially, decreases to about 120 cc/min and then climbs back to about 180 cc/min.

(iii)Operation in this mode will not permit the production of CO at a high concentration. Moreover, the product flow rates and concentration vary significantly with time.

Figure 3 shows the composition and flow rate of effluent for the SER system at the same conditions as above except that the reactor is initially filled with the reactant CO_2. In this mode of operation, as in the previous case, the process produces a product CO stream which continuously varies in composition and flow rate and hence would not constitute a desirable process.

Figure 4 illustrates results for the same experimental conditions except that the reactor is initially filled with the less adsorbable product CO. The following observations can be made from Figure 4 :

(i) The initial effluent is pure CO which is displaced from the reactor void volume by the feed reactants (shown as cross-hatched area).

(ii) For the first ~80 min, the effluent flow rate is constant at about 100 cc/min.

(iii)During the first ~80 min the CO concentration is constant and above 95%.

Thus filling the bed with the less adsorbing product gas CO leads to a process which produces essentially pure product at a constant flow rate. The reaction step may be stopped once the effluent reaches a specified average CO purity. The effective conversion of CO_2 to CO was calculated to be 46.0% at an average purity of 99% CO and 56.0% at 98% purity. The CO recoveries were relatively low because of the small laboratory reactor and the relatively large size of the reaction-mass transfer zone (RMTZ) in the reactor. It is estimated that in a larger

commercial reactor, the CO conversion would be in excess of 90% because of the relatively smaller size of the RMTZ.

It is significant to compare the operating conditions and conversions for SERP-RWGS with conventional RWGS. The conversions for conventional RWGS were calculated from literature values of thermodynamic equilibrium constants [6]. These data are summarized in Table 2.

Table 2. SERP-RWGSR versus Conventional RWGSR for CO Production
53 cm long laboratory column
(3:1 LINDE NaX : BASF LTS)
(1:1 CO_2:H_2 feed gas)

	SERP-RWGSR	Conventional RWGSR
Operating Temperature	275°C	1000°C
CO_2 to CO Conversion	55%**	55%*
Product Composition	99+% CO	29.0%CO+35.5% CO_2+ 35.5% H_2 (DRY BASIS)
Reactor Effluent Pressure	50 psig	50 psig
Product Pressure	50 psig	5 psig

* CO conversion at 275°C is 12%
** CO conversion of >90% in commercial unit

The data in Table 2 show the following advantages of the SERP-RWGS versus conventional RWGS :

(i) A significantly lower temperature (275°C vs >1000°C) for the SERP to achieve comparable conversion.
(ii) Significant separation of the product stream must be carried out to obtain a pure CO product from conventional RWGSR. On the other hand, if 98% CO purity is acceptable, SERP-RWGSR would produce CO from the reactor directly without further separation. The separation system for SERP-RWGSR would be significantly smaller (vs conventional RWGSR) if higher CO purity is desired.
(iii) CO is recovered from the reactor at reaction pressure.

A process cycle has been developed for producing CO by this route and is shown in Figure 5.

The key steps for SERP are:

(1) Feed CO_2 and H_2 into reactor/sorber and collect product to a predetermined CO purity; water is selectively adsorbed in the reactor-sorber.
(2) Countercurrently depressurize to remove a part of the void gas, and same desorbed H_2O.
(3) Countercurrently purge with weakly adsorbing gas such as CH_4 to desorb H_2O from the bed.
(4) Countercurrently purge with product gas CO to purge CH_4 from the bed.
(5) Pressurize bed to reaction pressure with product CO.

The same cycle will be used for H_2 production by steam methane reforming except that CO will be replaced by H_2 for purging and pressurization steps.

Production of Hydrogen by SERP-SMR :

The conventional method for H_2 production by SMR and the proposed SER-SMR process are shown schematically in Figure 6. The figure shows that: (i) the catalytic reformer and shift reactors for conventional SMR are replaced by a single integrated reactor-sorber system for SERP-SMR, (ii) the large PSA separation system for conventional SMR is replaced by a significantly smaller PSA to obtain 99.99+% H_2 purity, (iii) the reaction is carried out at about 1000°C for conventional SMR compared to 300-500°C for SERP-SMR.

The methodology proposed for performing SERP-SMR for the following reaction is outlined below.

$$CH_4 + 2H_2O \quad CO_2 + 4H_2$$

This reaction will be carried out in a reactor-sorber containing a high temperature sorbent for CO_2. Preliminary screening of various sorbents suggests the use of MgO as a possible chemisorbent for CO_2. Adsorption isotherms were measured for MgO with 180 m^2/g surface area (Figure 7). The data show that the MgO has significant capacity at 300-500 C. Effort will be made to increase the CO_2 adsorption capacity further by increasing the surface area of the MgO. It should be noted that only one mole of CO_2 needs to be adsorbed for four moles of product from this reaction.

The process cycle for SERP-SMR is analogous to the one for SERP-RWGSR and is shown in Figure 8. The key differences are: (i) CH_4 and water are fed as reactants, CO is selectively adsorbed in the reactor-sorber; (ii) the weakly adsorbing purge gas CH_4 is purged by H_2 and the reactor is pressurized with H_2 prior to introduction of the reactants. The advantages of SERP-SMR vs conventional SMR are summarized in Table 3.

Table 3. SERP-SMR vs Conventional SMR for H_2 Production

	Conventional	SER Goals
Operating Temperature	800-1000°C	300-500°C
CH_4 to H_2 Conversion	80-85%	90+%
Reactor Product Composition	73.7% H_2+9.4% CO_2+ 12.0% CO+4.8% CH_4 (Dry Basis)	98+% H_2
Product Pressure	200-400 psig	200-400 psig

Proposed Future Work

The work proposed in this program is summarized in Table 4 along with the key milestones.

Table 4. Program Goals and Milestones

Program Goals	Milestones
Sorbent Development	1995-1996
SERP Development	1995-1997
Economic Evaluation	1996-1997
Process Development Unit Test	1997-1998

The key developments that need to occur in the first phase of the program (1995-1997) are :

(i) Development of an adsorbent for CO_2 which is stable in the presence of steam and maintains desired capacity under cyclic conditions.
(ii) Modification of the existing experimental system for performing SERP-SMR.
(iii)Demonstration of the SERP-SMR concept in the lab apparatus.

This technology will be commercialized by Air Products and Chemicals, Inc.

References

1. Vaporciyan, G.G. and R.H. Kadlec, AICHE J., 33 (8), p1334 (1987).
2. Westerterp, K.R., T.N. Bodewes, M.S.A. Vrijland and M. Kuczynski, Hydrocarbon Processing, p69 (1989).
3. Goto, S., T. Tagawa, T. Omiya, Chemical Engineering Essays (Japan), Vol. 19, No. 6 (1993).
4. Han, C. and D.P. Harrison, Chemical Engineering Science, Vol. 49, No. 24B, p5875 (1994).
5. Chatsiriwech, D., E. Alpay, L.S. Kershenbaum, C.P. Hull and N.F. Kirkby, Catalysis Today, 20, p351 (1994).
6. Catalyst Handbook, Ed. Martyn V. Twigg, Wolfe Publishing Ltd., p543 (1989).

List of Figures

Reactor Schematic

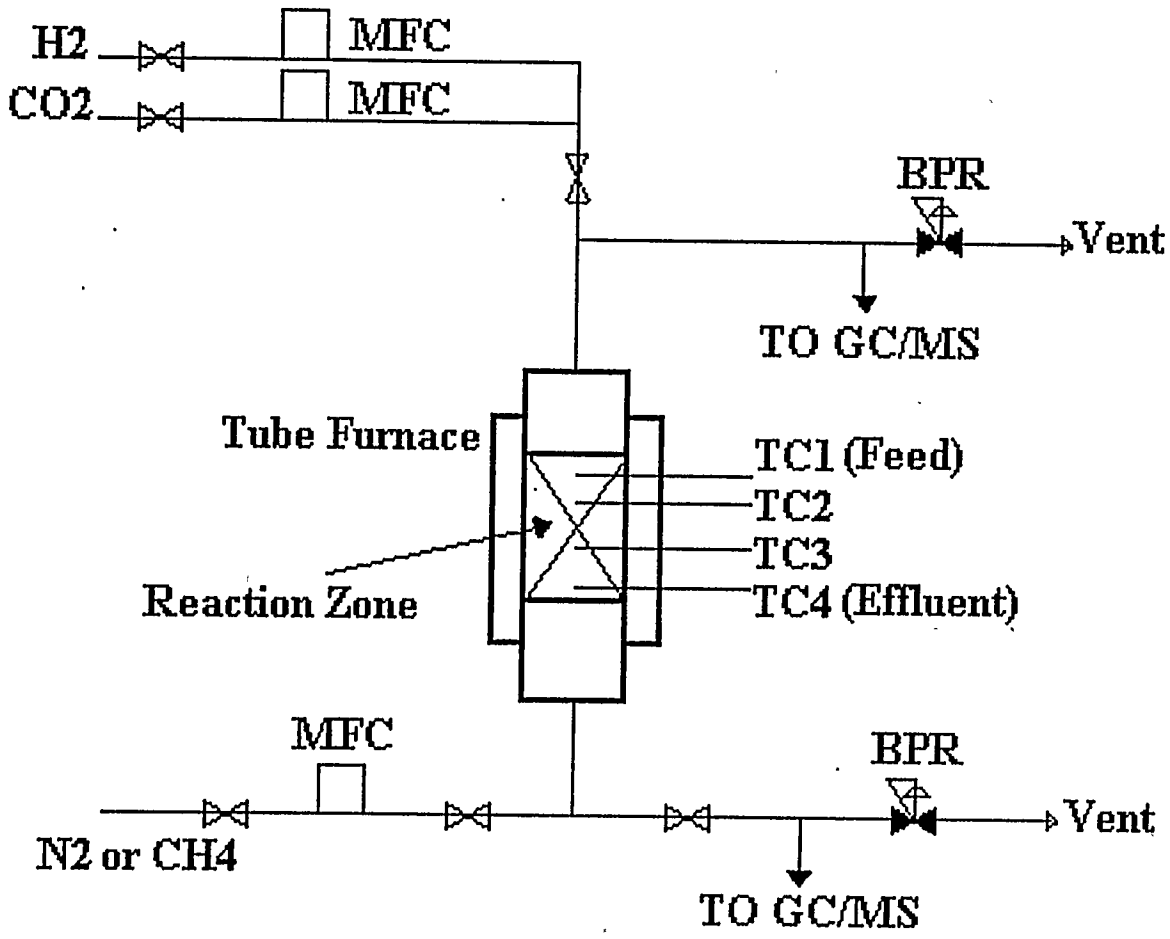

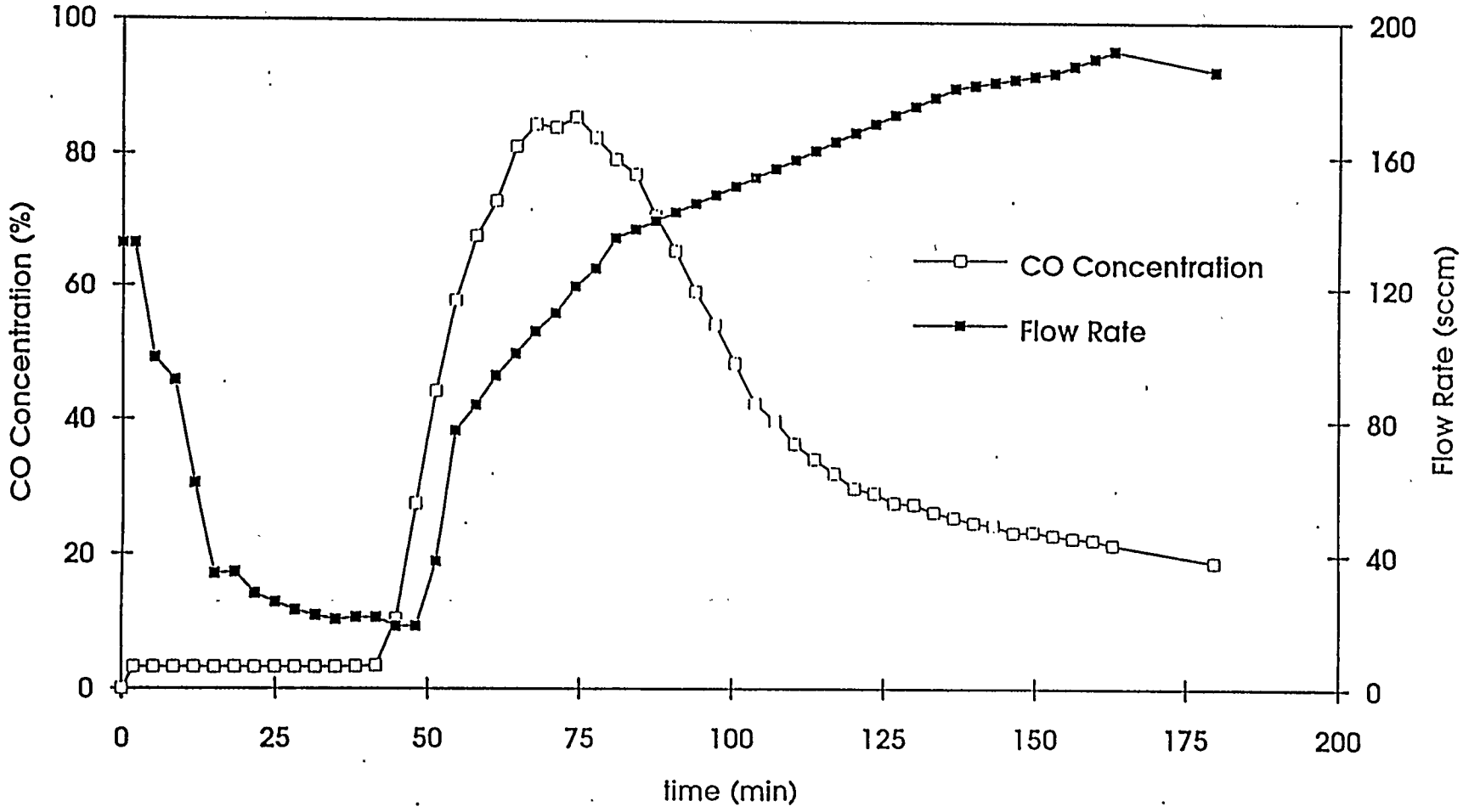
100
80
60
40
20
0
CO Concentration (%)
200
160
120
80
40
0
Flow Rate (sccm)
0
25
50
75
100
125
150
175
200
time (min)
CO Concentration
Flow Rate

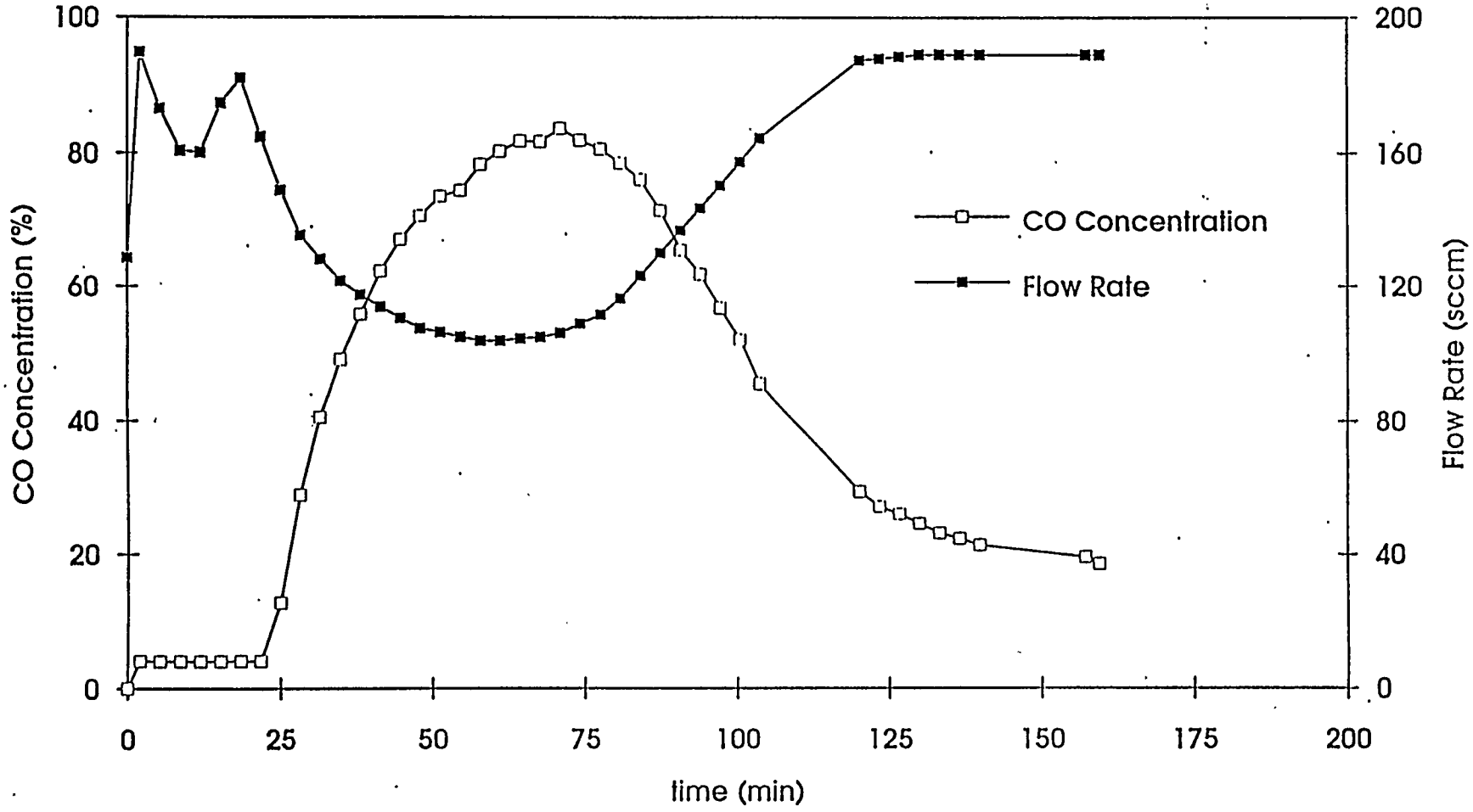
100
80
60
40
20
0
CO Concentration (%)
200
160
120
80
40
0
Flow Rate (sccm)
0
25
50
75
100
125
150
175
200
time (min)
CO Concentration
Flow Rate

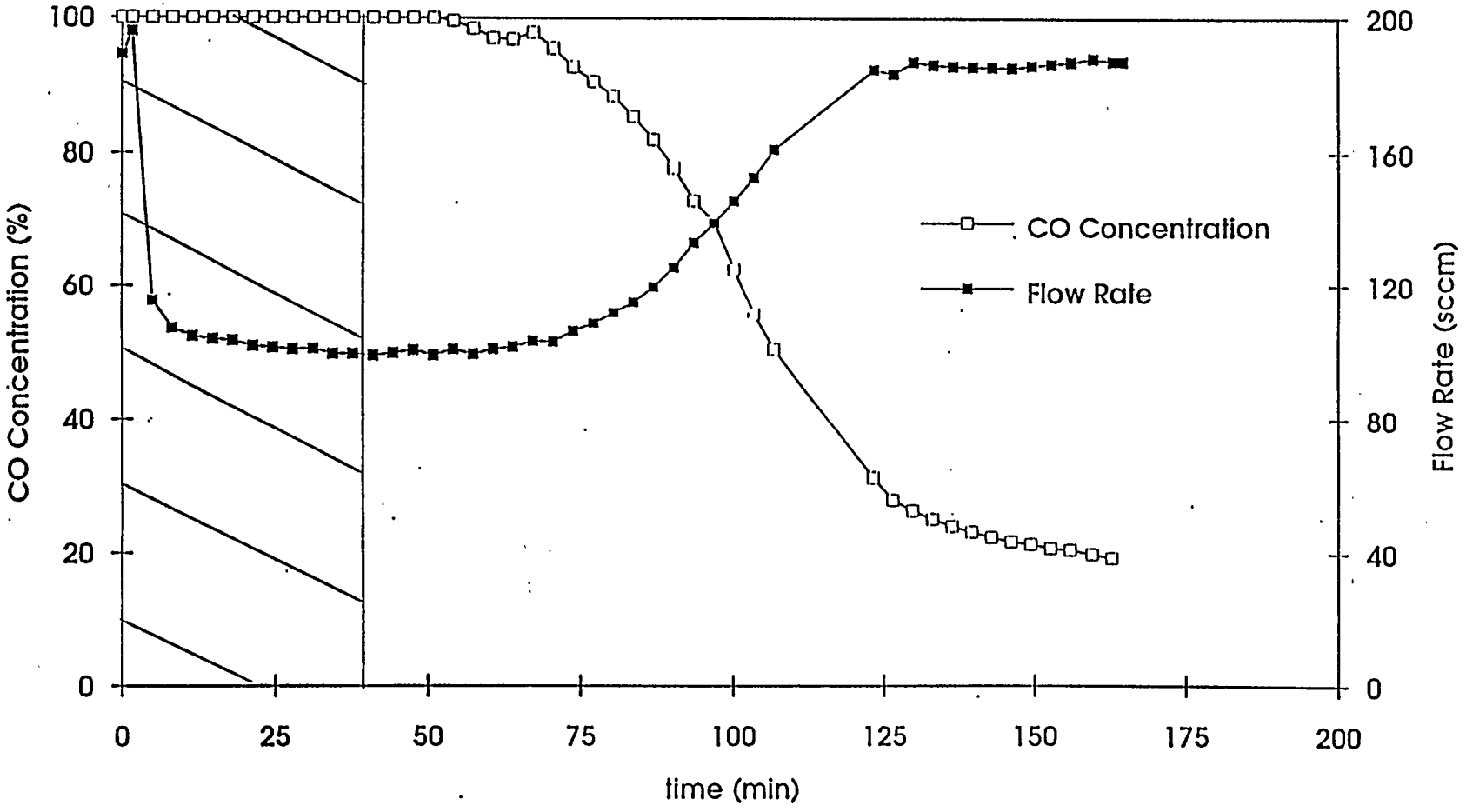
CO Concentration (%)
Flow Rate (sccm)
time (min)
CO Concentration
Flow Rate
0
20
40
60
80
100
0
40
80
120
160
200
0
25
50
75
100
125
150
175
200

SCHEMATIC OF SER PROCESS

CO PRODUCTION

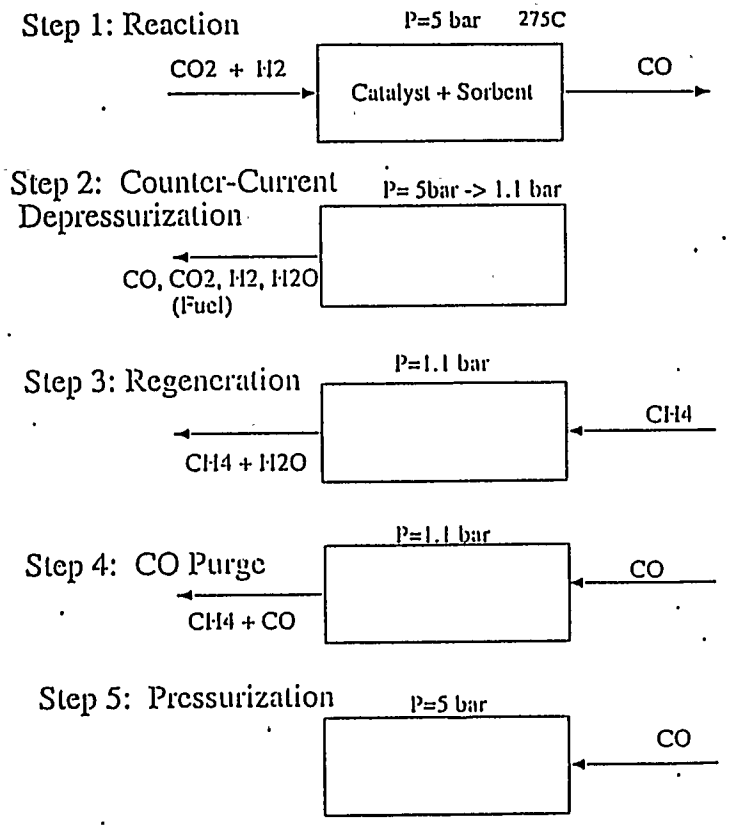

STEAM METHANE REFORMATION FOR PRODUCTION OF H_2

CONVENTIONAL

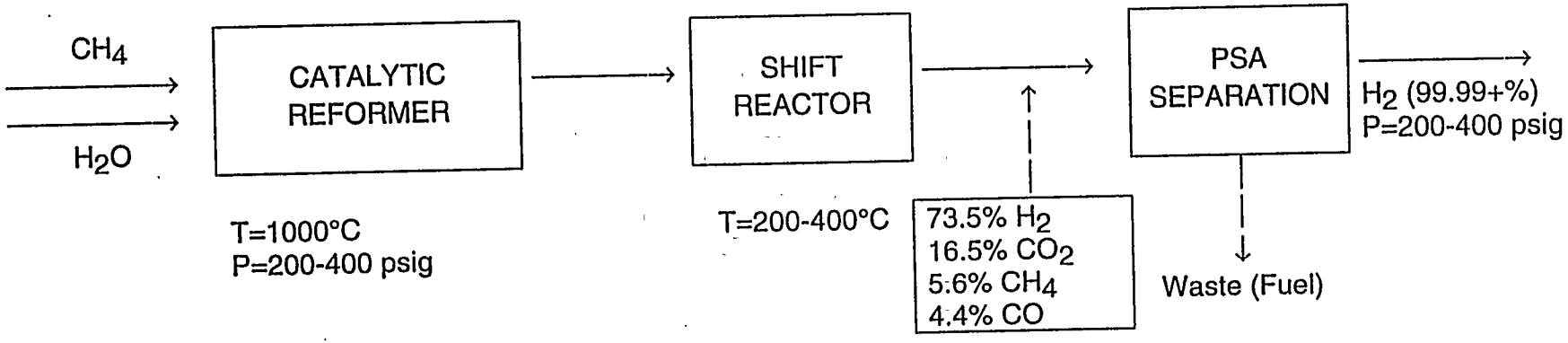

SER CONCEPT

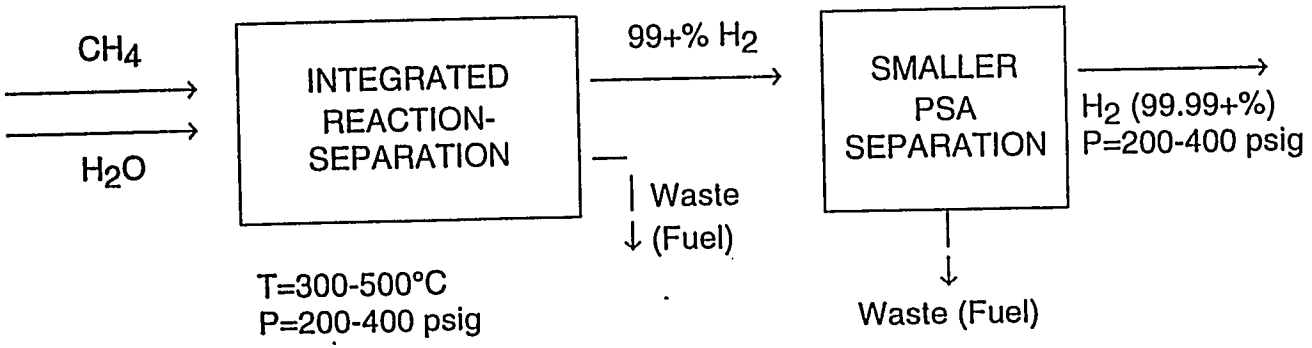

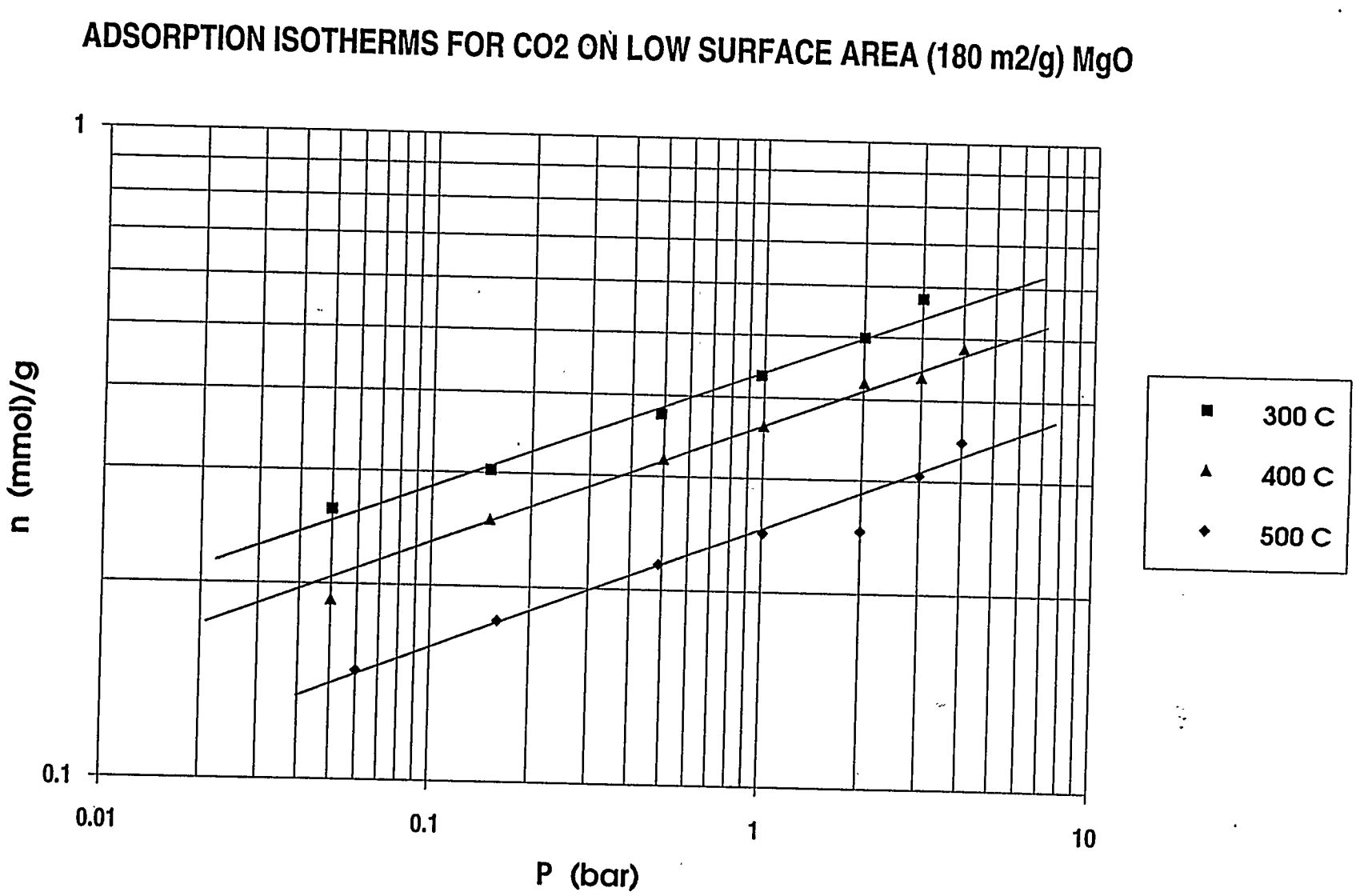
ADSORPTION ISOTHERMS FOR CO2 ON LOW SURFACE AREA (180 m2/g) MgO
n (mmol)/g
1
0.1
0.01
0.1
1
10
P (bar)
300 C
400 C
500 C

SCHEMATIC OF SER PROCESS

H_2 PRODUCTION

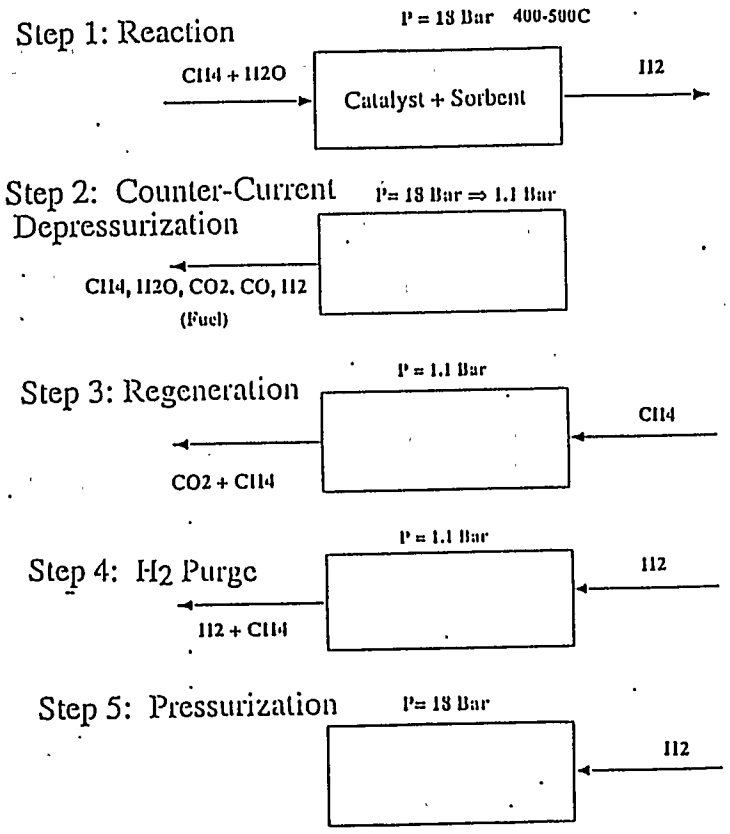

ENZYMATIC PRODUCTION OF HYDROGEN FROM GLUCOSE[1]

Jonathan Woodward and Susan M. Mattingly[2]
Chemical Technology Division
Oak Ridge National Laboratory[3]
Oak Ridge, Tennessee, 37831-6194

Abstract

The objective of this research is to optimize conditions for the enzymatic production of hydrogen gas from biomass-derived glucose. This new project is funded at 0.5 PY level of effort for FY 1995. The rationale for the work is that cellulose is, potentially, a vast source of hydrogen and that enzymes offer a specific and efficient method for its extraction with minimal environmental impact. This work is related to the overall hydrogen program goal of technology development and validation. The approach is based on knowledge that glucose is oxidized by the *NADP*$^+$ requiring enzyme glucose dehydrogenase (GDH) and that the resulting *NADPH* can donate its electrons to hydrogenase (H_2ase) which catalyzes the evolution of H_2. Thus hydrogen production from glucose was achieved using calf liver GDH and *Pyrococcus furiosus* H_2ase yielding 17% of theoretical maximum expected. The cofactor *NADP*$^+$ for this reaction was regenerated and recycled. Current and future work includes understanding the rate limiting steps of this process and the stabilization/ immobilization of the enzymes for long term hydrogen production. Cooperative interactions with the Universities of Georgia and Bath for obtaining thermally stable enzymes are underway.

---

[1] Research sponsored by the Office of Utility Technologies, Advanced Utility Concepts Division, U.S. Department of Energy.

[2] Oak Ridge Science and Engineering Student from Eastern Kentucky University.

[3] Managed by Martin Marietta Energy Systems, Inc. for the U.S. Department of Energy under contract DE-AC05-84OR21400

Introduction

Cellulose represents a vast supply of reducing power and, although non-reducing, the individual glucose molecules of the cellulose polymer can be oxidized using the enzyme glucose dehydrogenase (GDH). GDH, first described in 1931, catalyzes the oxidation of glucose and hexose-6-phosphates using both nicotinamide adenine dinucleotide *(NAD^+)* and nicotinamide adenine dinucleotide phosphate *($NADP^+$)* as cofactors (Tranulis *et al.*, 1994). The reduction potential (E'_0) for the half-reaction for the reduction of *$NADP^+$* is -320 mV which is too high for the reaction of *NADPH* with most soluble hydrogenases for H_2 evolution (Greenbaum, 1980). However, two hydrogenases have been shown to be capable of interacting with reduced nicotinamide nucleotides with concomitant hydrogen evolution. These are the soluble hydrogenases of *Alcaligenes eutrophus* (Egerer *et al.*, 1982) and *Pyrococcus furiosus* (Ma *et al.*, 1994). Since cellulose is an abundant primary and secondary resource that can be enzymatically degraded to glucose (Woodward, 1987) development of an enzymatic process for the generation of hydrogen from cellulose is feasible (Fig. 1).

It was the objective of this current work to demonstrate and optimize hydrogen production using this system (initially starting from glucose) and the results obtained so far are presented in this report.

Experimental Procedures

Materials

β-Glucose was purchased from Calbiochem. Glucose dehydrogenase (GDH) from calf liver and β-*$NADP^+$* were purchased from Sigma Chemical Company. Hydrogenase (H_2ase) from *Pyrococcus furiosus* was purchased from Dr. Michael Adams, University of Georgia.

Apparatus: Hydrogen Detection

A continuous flow system was constructed to measure the production of hydrogen as shown in Fig. 2. The system was continuously purged with helium and calibrated with an inline electrolysis cell and Faraday's law of electrochemical equivalence connected in tandem with the hydrogen detection system. The latter consisted of a combustible gas analyzer (Bio-Gas Detector Corporation, Okemos, MI) consisting of a Figaro semiconductor tin oxide gas sensor. A voltage increase occurs across the sensor when a combustible gas comes into contact with the sensor surface due to a decrease in the sensor resistance and this was measured by a Keithley Model 2000 multimeter. Current was measured with a Keithley Model 485 picoammeter. Data was analyzed using ASYST™ Technologies, Inc., 4.0 Analysis Software.

Enzyme Assay and Hydrogen Production

The activity of GDH was measured in a 1.0 ml reaction mixture containing 10 µmol glucose, 1 µmol *$NADP^+$* and 0.75 mg GDH in 50 mM sodium phosphate buffer, pH 7.5 at room temperature (23°C). The production of *NADPH* was monitored at 340 nm in a Carey 219 spectrophotometer. One unit

of activity is defined as that amount of enzyme which produces 1 µmol *NADPH* min^{-1} under the conditions of the assay. H_2ase was assayed in the flow system described above by measuring its *NADPH*-dependent H_2 evolution activity at room temperature (Ma *et al.*, 1994). The reaction mixture contained 0.4 mM *NADPH* and 0.1 ml H_2ase in 50 mM sodium phosphate buffer, pH 8.0. One unit of activity is defined as the production of 1 µmol H_2 min^{-1} under the assay conditions. A typical reaction mixture for the generation of hydrogen from glucose contained 10 µmol glucose, 1 µmol *NADP*$^+$, 1.0 mg GDH, 0.1 ml H_2ase all in 50 mM sodium phosphate buffer at a given pH. The reaction was run at room temperature.

Results and Discussion

The activity of calf liver GDH was calculated to be 2.0m units/mg at 23°C and its K_m and V_{max} determined to be 59 mM and 0.02 µmol min^{-1} with respect to glucose. The K_m with respect to *NADP*$^+$ was estimated to be 10 µM. The activity of H_2ase was calculated to be approximately 0.011 units ml^{-1} at 23° C. According to Ma *et al.*(1994) the K_m of H_2ase for *NADPH* is 200 µM. The enzymatic generation of hydrogen gas from glucose (and ultimately cellulosic materials) requires that the properties of GDH and H_2ase be compatible with respect to pH and temperature optimum/stability. Both enzymes are active between pH 7.0 and 9.0 with a respective optimum of pH 7.5 for GDH and pH 8.0 for H_2ase (Fig. 3). A comparison of the effect of temperature on the activity of GDH and H_2ase showed the difference between these two enzymes (Fig. 4) with respect to their temperature optimum. This is expected since *P. furiosus* is an hyperthermophile that grows optimally at 100°C (Ma *et al.*, 1993). It can be seen that there is little difference in the rate of *NADPH*-dependent hydrogen evolution between room temperature (23°C) and 60°C; however above 70°C the rate does increase over two-fold in agreement with the data of Ma *et al.* (1994) that showed less than a two-fold rise in activity from 60-80°C using *NADPH* (1.5 mM) as the electron donor. In our experiments a concentration of 0.2 mM *NADPH* was used.

The stability of *NADPH* at pH 8.0 was determined by measuring the yields of hydrogen from 0.2 mM *NADPH* at several temperatures. The data in Fig. 5 indicate that the yields obtained were close to theoretical maximum at both 60°C and 80°C. The major difference in these two sets of data is that it took over 12 h to reach theoretical maximum at 60°C unlike 2.5 h at 80 C. This would be explained by the difference in H_2ase activity between the two temperatures but also suggests that *NADPH* is stable under these experimental conditions. Clearly compatibility in the thermal stability of GDH and H_2ase is necessary for long-term hydrogen production at the fastest rates. Calf liver GDH is stable at 40°C for at least 5 h but above this temperature the rate of *NADPH* production becomes non-linear after 1 h suggesting instability above 40°C (Fig. 6).

Hydrogen was generated from the reaction mixture containing glucose, GDH, H_2ase and *NADP*$^+$ (Fig. 7). As far as is known, this is the first demonstration of the enzymatic conversion of glucose to hydrogen by such an *in vitro* system. The two experimental runs shown, were conducted at pH 7.0 and pH 8.0. At pH 8.0 the rate of H_2 evolution rose to a maximum after 6 h and then declined to zero after 20 h. The percentage of the theoretical yield of H_2 was 17%. At pH 7.0 the time to reach the maximum rate of H_2 evolution was 20 h at which time the yield of$_2$H was 16% of theoretical

maximum. At this point the experiment was stopped (by the addition of hydrogen peroxide; 0.025% final concentration in the reaction mixture) and so the maximum yield was not determined. It was also evident from these data that the co-factor *$NADP^+$* was regenerated and reused during the course of the reaction. Recently, we have shown that at pH 7.0, yields of H_2 at 30 h can be obtained close to theoretical maximum. Furthermore injection of another 10 µmol of glucose yields a further 10 µmol H_2 after 10 h. These data (not shown) are particularly exciting because they demonstrate: 1. the theoretical maximum yield of H_2 is obtainable, 2. the system had long term stability, at least at 23°C and, 3. the co-factor was recycled 20 times.

Future work will focus on obtaining maximum yields of H_2 in shorter reaction times. This will be achieved by increasing the rate of glucose oxidation and hydrogen evolution by increasing the reaction temperature. A thermally-stable glucose dehydrogenase from *Thermoplasma acidophilum* has been expressed in *Escherichia coli* from which it can be extracted and purified (M. Danson, University of Bath, personal communication). A sample of this GDH will be obtained from Dr. Danson's laboratory and will be used in our system. Ultimately, GDH and H_2 ase will be immobilized in order to recover them from the reaction mixture and for their subsequent reuse. It should also be pointed out that the other product of this reaction, gluconic acid, is a valuable commodity used as a sequestering agent and in the dairy and brewing industries (Szmant, 1986). Such a reaction may also have advantages for the manufacture of gluconic acid over fermentation methods currently used (Godfrey and Reichelt, 1983).

Acknowledgements

We would like to thank Steve Blankinship for his continuing assistance with the experimental apparatus for this project, Eli Greenbaum, Barbara Evans and Lynette Stephan for useful technical discussions. We are also grateful to the Office of Utility Technologies, Advanced Utility Concepts Division, U.S. Department of Energy for financial support.

References

Egerer, P., H. Gunther, and H. Simon. 1982. "On the Hydrogen-Deuterium Exchange Reaction Catalyzed by the Soluble Hydrogenase from *Alcaligenes eutrophus* H16 in the Free and Immobilized State". *Biochim. Biophys. Acta*, 703:149-157.

Godfrey, T., and J. Reichelt. 1983. *Industrial Enzymology-The Application of Enzymes in Industry.* New York: The Nature Press.

Greenbaum, E. 1980. "Simultaneous Photoproduction of Hydrogen and Oxygen by Photosynthesis". *Biotechnol. Bioeng. Symp.*, No.10:1-13.

Ma, K., R.N. Schicho, R.M. Kelly, and M.W.W. Adams. 1993. "Hydrogenase of the Hyperthermophile *Pyrococcus furiosus* is an Elemental Sulfur Reductase or Sulfhydrogenase:

Evidence for a Sulfur-Reducing Hydrogenase Ancestor". *Proc. Natl. Acad. Sci. USA*, 90:5341-5344.

Ma, K., Z.H. Zhou and M.W.W. Adams. 1994. "Hydrogen Production from Pyruvate by Enzymes Purified from the Hyperthermophilic Archaeon, *Pyrococcus furiosus*: A Key Role for NADPH". *FEMS Microbiol. Lett.*, 122:245-250.

Szmant, H.H. 1986. *Industrial Utilization of Renewable Resources.* Lancaster: Technomic Publishing Company.

Tranulis, M.A., B. Christophersen, and B. Borrebaek. 1994. "Glucose dehydrogenase in beef (*Bos taurus*) and rainbow trout (*Oncorhynchus mykiss*) liver: a comparative study". *Comp. Biochem. Physiol.*, 109B:427-435.

Woodward, J. 1987. "Utilization of Cellulose as a Fermentation Substrate: Problems and Potential". In *Carbon Substrates in Biotechnology*, 45-65. Oxford: IRL Press, Ltd.

Legend to Figures

Figure 1 - Reaction pathway for the conversion of cellulose (glucose) to hydrogen.

Figure 2 - Schematic illustration of the reaction system and detection apparatus used in the enzymatic conversion of glucose to hydrogen. The data for hydrogenase was taken from Ma et al., 1994.

Figure 3 - Activity of glucose dehydrogenase and hydrogenase as a function of pH.

Figure 4 - Activity of glucose dehydrogenase and hydrogenase as a function of temperature.

Figure 5 - NADPH-dependent evolution of hydrogen by hydrogenase as a function of temperature.

Figure 6- Stability of glucose dehydrogenase as a function of temperature.

Figure 7- Enzymatic conversion of glucose to hydrogen gas.

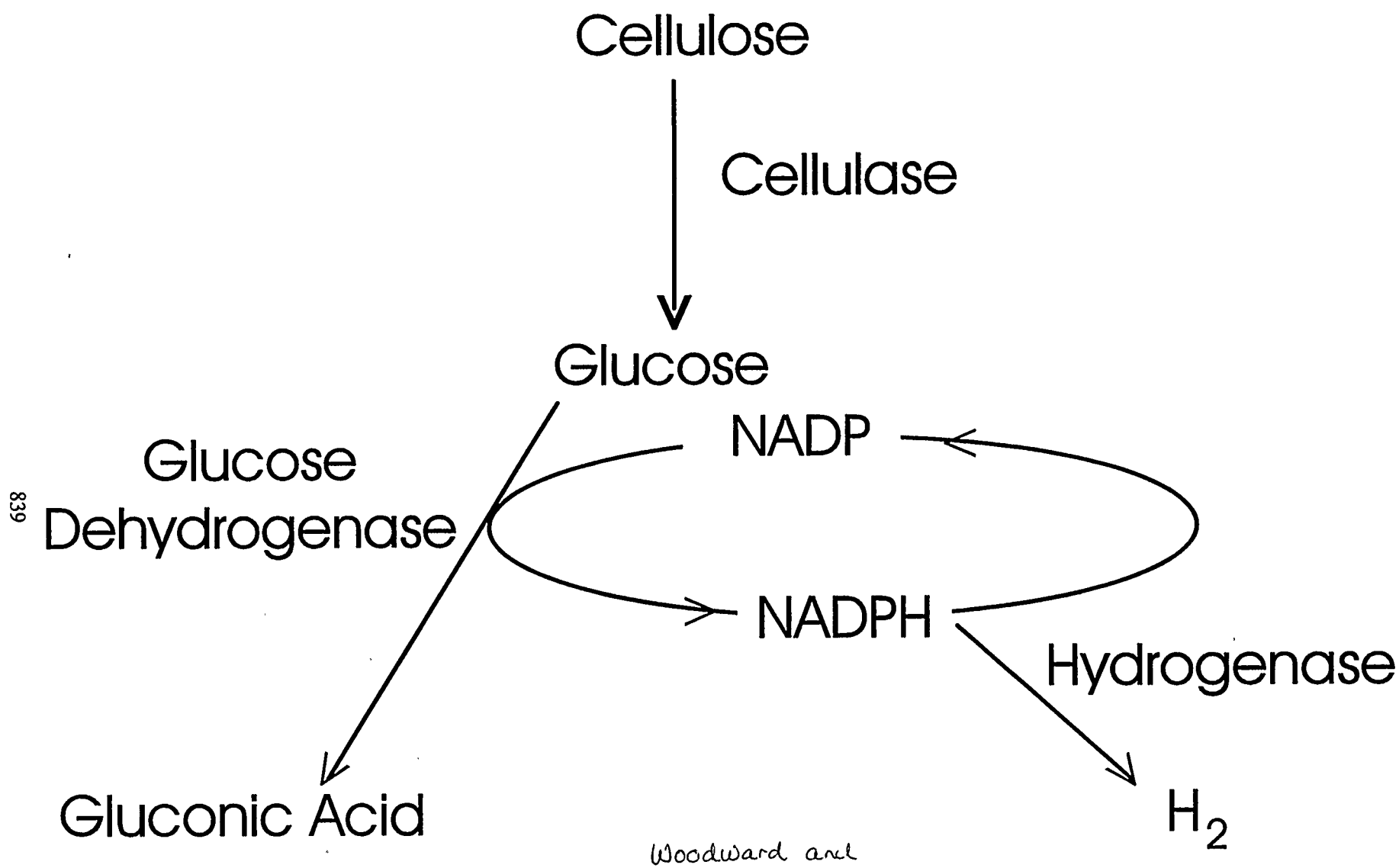

Woodward and Mattingly

Fig. 1

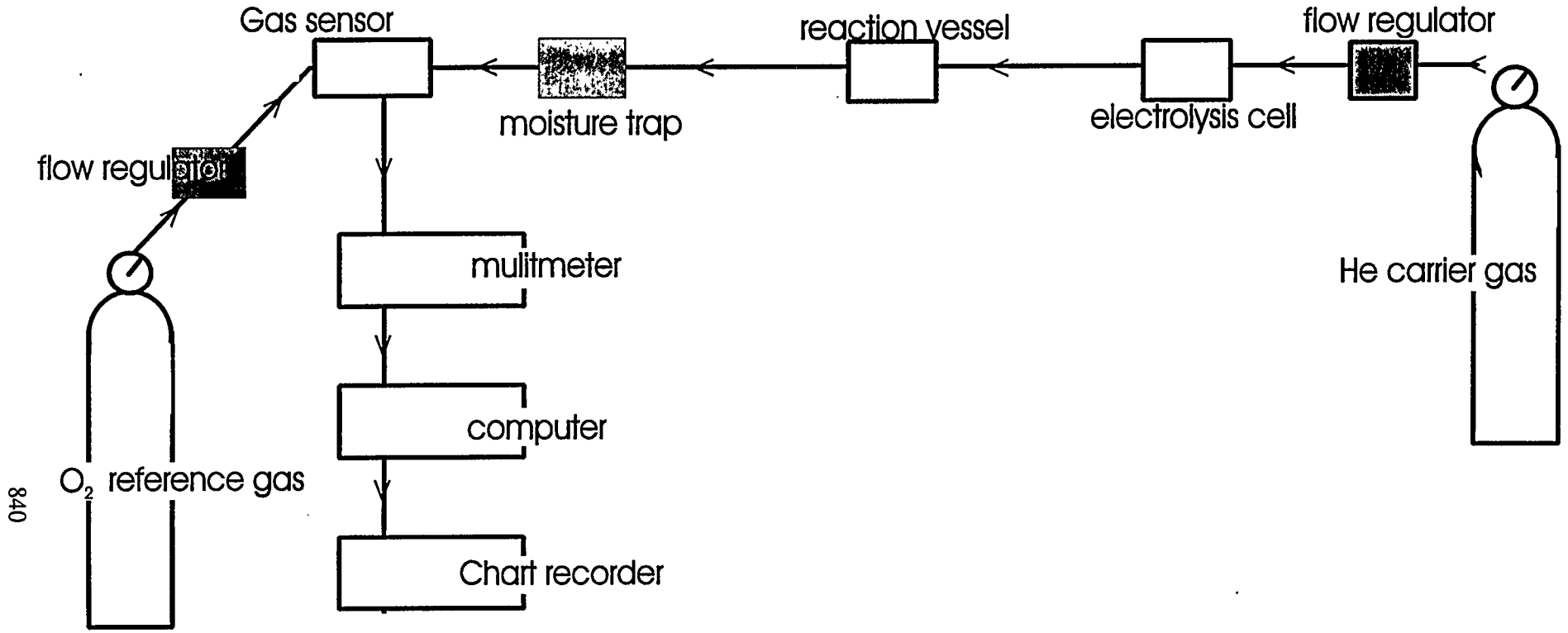

840

Woodward and Mattingly

Fig. 2

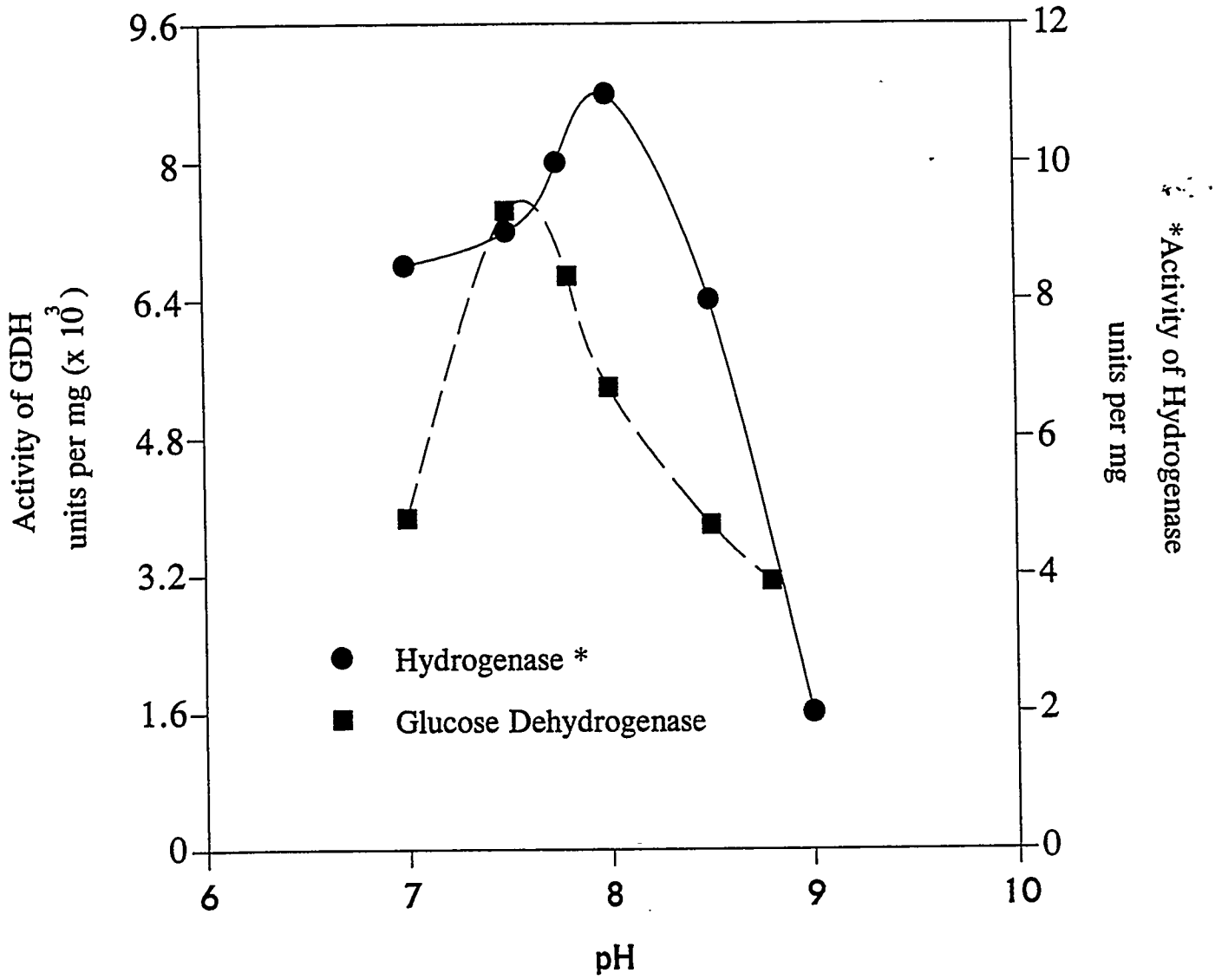

Woodward and
Mattingly

Fig. 3

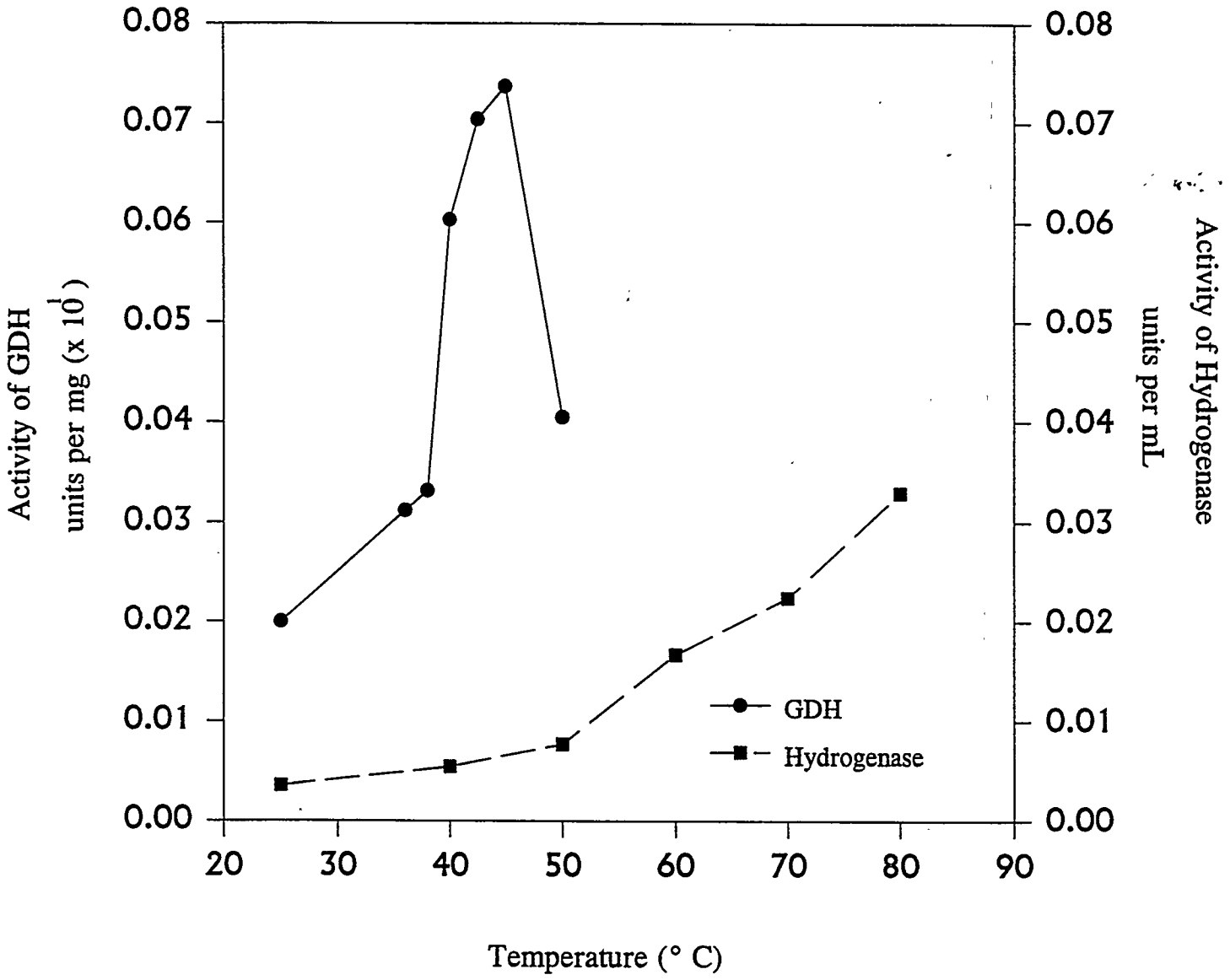

Woodward and
Mattingly
Fig. 4

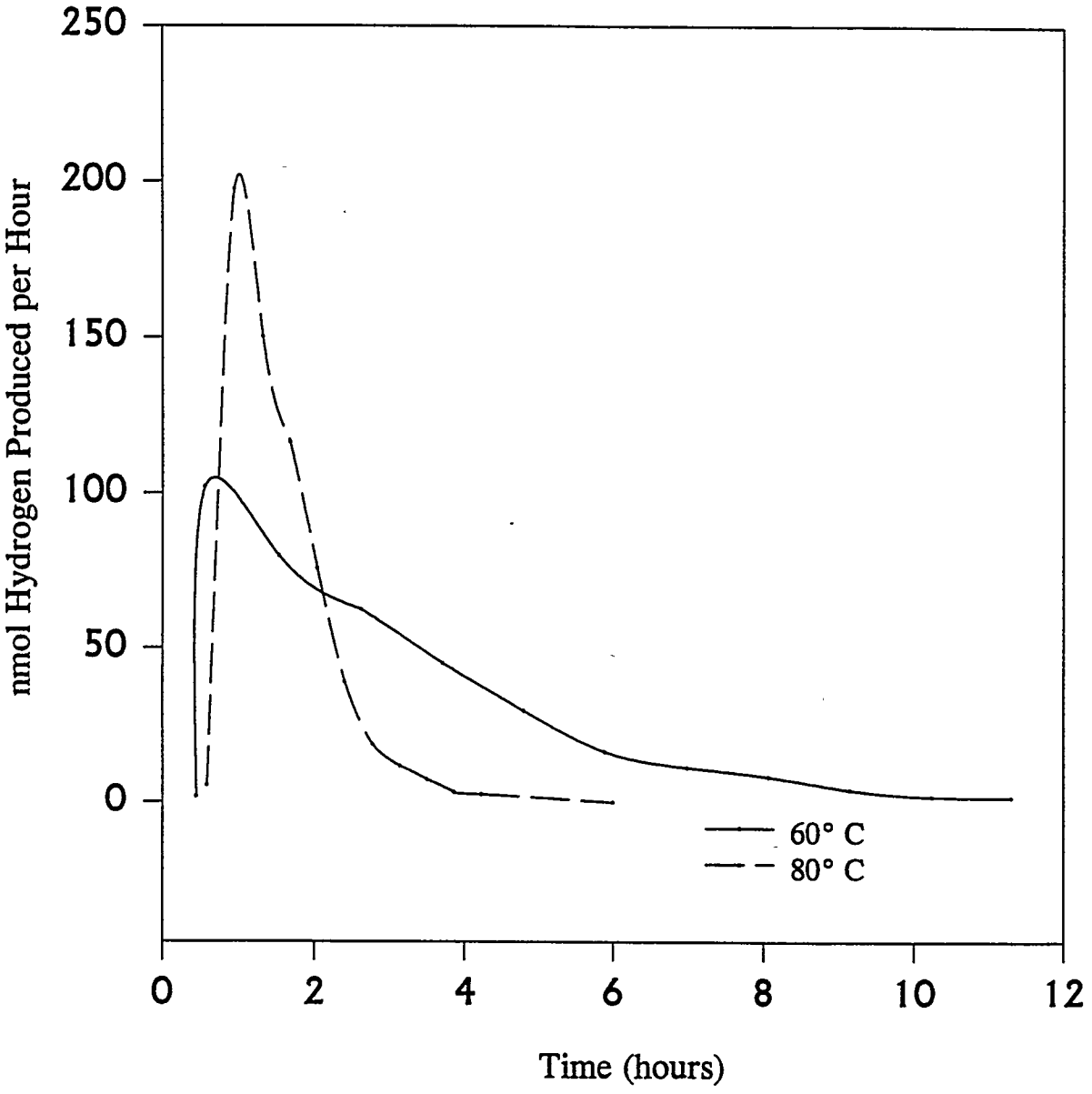

Woodward and
Mattingly
Fig 5

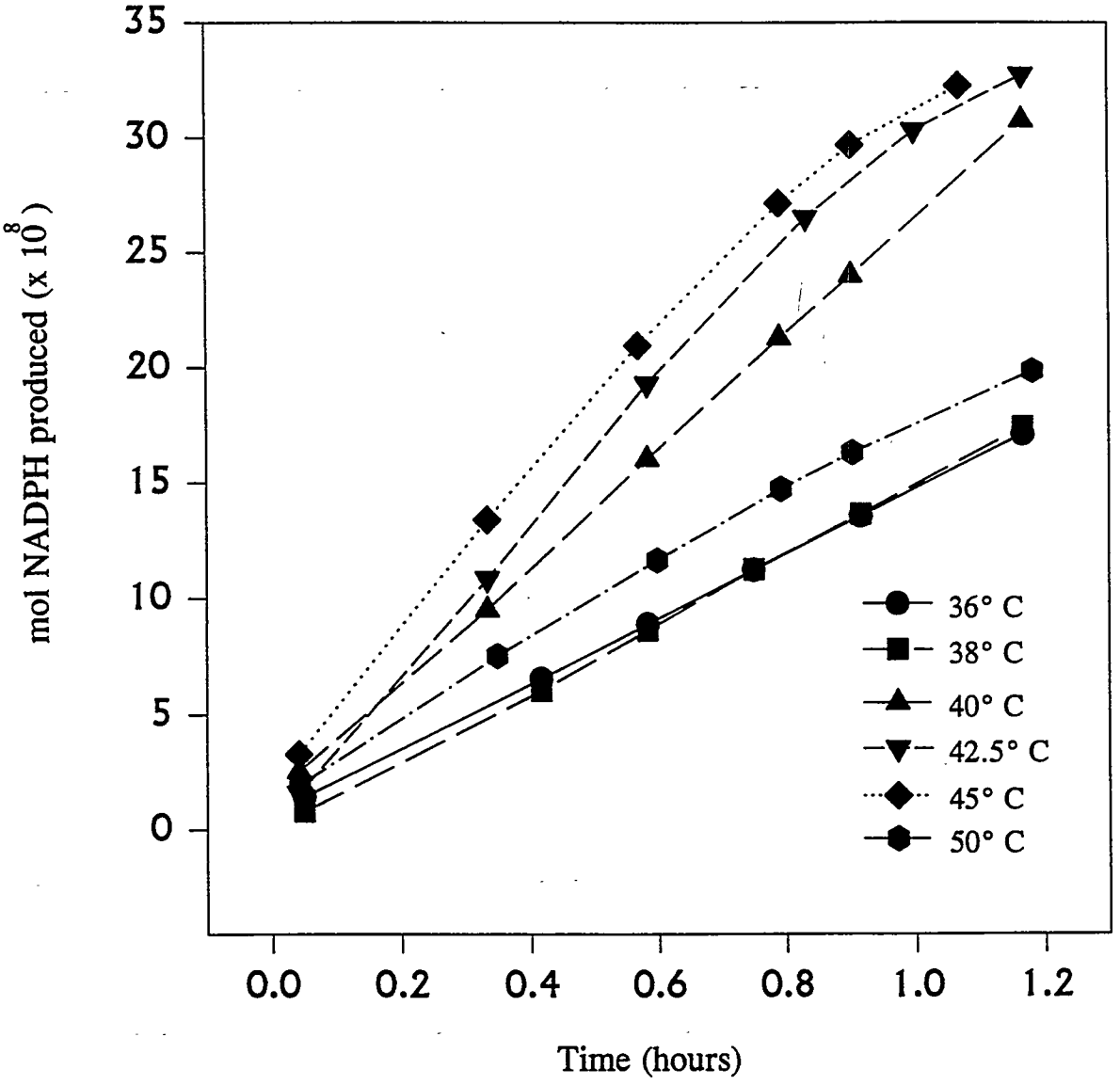

Woodward and Mattingly Fig. 6

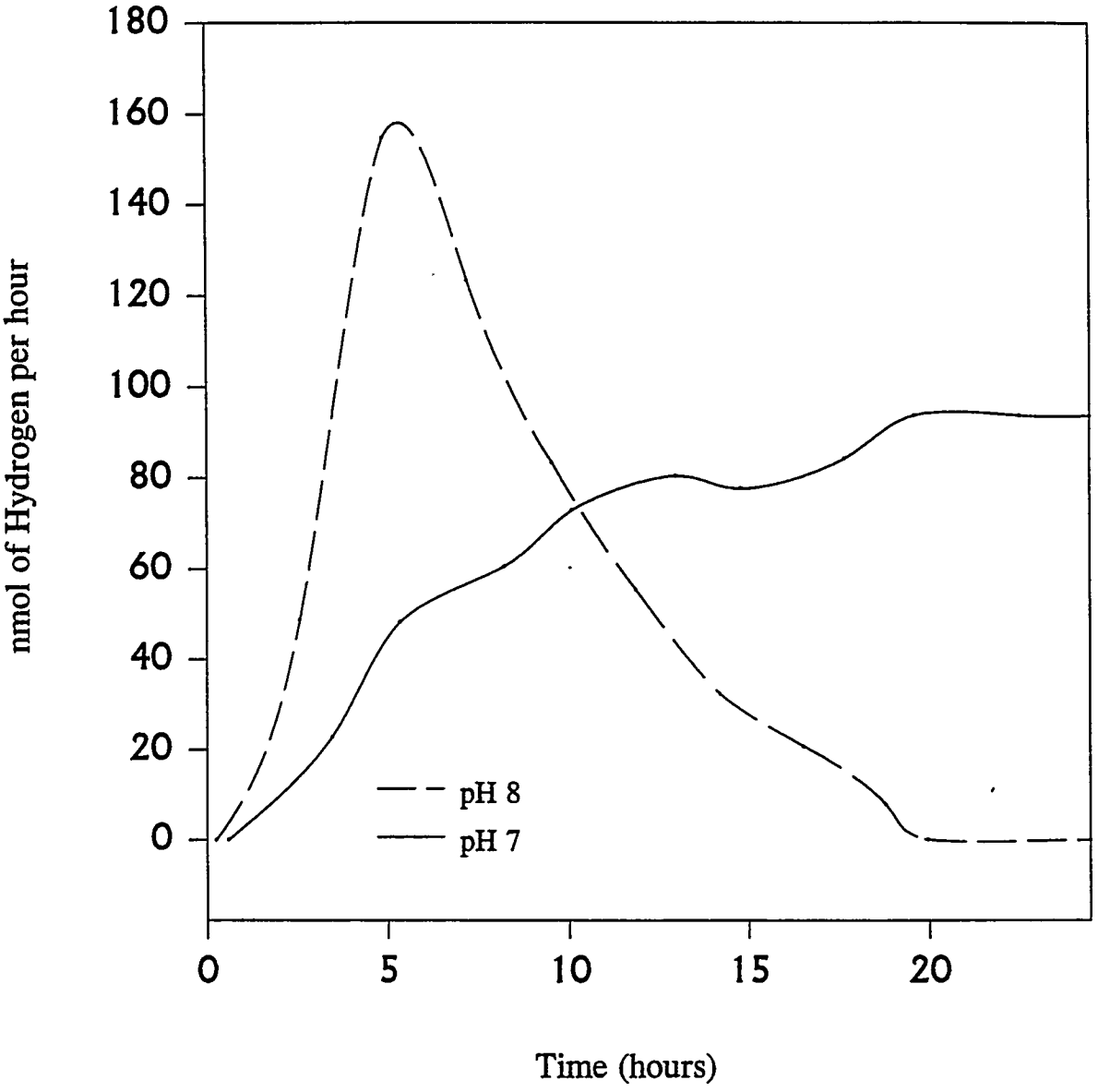

Woodward and Mattingly

Fig. 7

PRODUCTION OF HYDROGEN BY THERMOCATALYTIC CRACKING OF NATURAL GAS

Nazim Z. Muradov
Florida Solar Energy Center, University of Central Florida
300 State Road 401, Cape Canaveral, FL 32920

Abstract

It is universally accepted that in the next few decades hydrogen production will continue to rely on fossil fuels (primarily, natural gas). On the other hand, the conventional methods of hydrogen production from natural gas (for example, steam reforming) are complex multi-step processes. These processes also result in the emission of large quantities of CO_2 into the atmosphere that produce adverse ecological effects. One alternative is the one-step thermocatalytic cracking (TCC) (or decomposition) of natural gas into hydrogen and carbon. Preliminary analysis indicates that the cost of hydrogen produced by thermal decomposition of natural gas is somewhat lower than the conventional processes after by-product carbon credit is taken. In the short term, this process can be used for on-site production of hydrogen-methane mixtures in gas-filling stations and for CO_x-free production of hydrogen for fuel cell driven prime movers. The experimental data on the thermocatalytic cracking of methane over various catalysts and supports in a wide range of temperatures (500-900°C) are presented in this paper. Two types of reactors were designed and built at FSEC: continuous flow and pulse fix bed catalytic reactors. The temperature dependence of the hydrogen production yield using oxide type catalysts was studied. Alumina-supported Ni- and Fe-catalysts demonstrated relatively high efficiency in the methane cracking reaction at moderate temperatures (600-800°C). Kinetic curves of hydrogen production over metal and metal oxide catalysts at different temperatures are presented in the paper. Fe-catalyst demonstrated good stability (for several hours), whereas alumina-supported Pt-catalyst rapidly lost its catalytic activity.

Introduction

Energy systems based on hydrogen as an energy carrier coupled with renewable energy resources are considered as ultimate long term option. Natural gas appears to be a viable near term option. According to Marchetti (1979) and Nakicenovic (1990), natural gas will become, globally, the major source of energy during the next century. It is widely accepted that in the short- to medium-term hydrogen production will continue to rely on natural gas. On the other hand, the use of natural gas as a chemical feedstock and a fuel for the conventional processes of hydrogen production, for example, steam reforming (SR) or partial oxidation (PO), results in the emission of large quantities of CO_2 that produce adverse ecological effects. SR of natural gas is a complex process consisting of four processing steps:

1) feedstock purification

2) steam reforming of methane to hydrogen and carbon monoxide:

$$CH_4 + H_2O \rightarrow CO + 3H_2 + 206\ kJ \qquad (1)$$

3) water-gas shift reaction:

$$CO + H_2O \rightarrow CO_2 + H_2 - 41\ kJ \qquad (2)$$

4) gas purification (CO_2 removal)

The reforming reaction is a strongly endothermic, high temperature (800-900°C) process. To ensure a maximum conversion of CH_4 into the products , the process generally employs an excess of steam (steam/carbon ratio 3-5). The process thermal efficiency of the steam reformer is seldom greater than 50% (Cromarty 1992). Because of the energy intensive stages of SR process the usage of natural gas as a fuel is almost equal to its usage as a chemical feedstock. As a result the production of every cubic meter of hydrogen is accompanied by the emission of 0.5 cubic meter of CO_2. CO_2 can be removed from flue gases by several methods (*e.g.* adsorption by molecular sieves, cryogenic separation, membrane separation, etc.) which are energy and investment intensive processes. However the real problem is what to do with accumulating volumes of CO_2 that are not released into the atmosphere. Simple calculations indicate that the amounts of CO_2 generated by reforming/scrubbing process would be truly enormous: the disposal of 10 millions tons of CO_2 would be the price to pay for each million ton of hydrogen produced. Although several proposals have been reported in literature (for example, Cheng and Steinberg 1986) on CO_2 disposal in natural underground reservoirs, depleted natural gas fields, the deep ocean, etc., concern was expressed by some experts on the possible ecological effects of high concentrations of CO_2 in the ocean or other disposal sites on the local biosphere (Nakicenovic 1993).

Thermal Cracking of Methane

One alternative to SR is a single-step thermal cracking (TC) of natural gas into hydrogen and carbon:

$$CH_4 \rightarrow C + 2H_2 + 75.6\ kJ \qquad (3)$$

The energy requirement per mole of hydrogen produced for TC is somewhat less than that for SR reaction: 37.8 and 41.2 kJ/mole H_2, respectively. The process is slightly endothermic, so only an insignificant amount of hydrogen produced could be used as a source of the thermal energy for the process. The H_2/CH_4 ratio for both TC and SR processes is approximately 2 (considering fuel usage of methane). In addition to hydrogen as a major product, the process produces a very important by-product: clean carbon.

A comparative assessment of hydrogen production processes by TC and SR of natural gas yields the following conclusions:

1) The energy and feedstock consumption per unit of hydrogen produced for the processes are comparable.

2) TC of natural gas is a technologically simple one-step process without energy and material intensive gas separation stages, while SR is a multi-step process.

3) The maximum temperature of the SR process is still high (815 °C) despite many decades of intensive operation and improvement. This leaves a very low probability for further reductions in the reaction temperature. In contrast, the TC process has a great potential for decreasing the maximum temperature of the process (by several hundred degrees centigrade) by using effective catalysts.

4) There is a very valuable by-product of TC process: pure carbon, while SR produces no useful by-products.

5) TC produces practically no CO_2 emissions.

It was shown (Steinberg and Cheng 1988) that the cost of hydrogen produced by TC of natural gas is somewhat lower than that for the conventional processes and is equal to \$1.64 per 10^3 SCF after by-product carbon credit is taken.

Thermocatalytic Decomposition of Methane

The thermodynamic data show that the methane decomposition can be realized at relatively moderate temperatures. Thus, the use of catalysts is needed for the realization of thermal decomposition of methane at comparatively low temperatures. Attempts have been made to use catalysts for the cracking of methane and light hydrocarbons. For example, authors used alumina, silica-alumina, silica-magnesia, etc. at 800-1000°C (Pohleny and Scott 1966) and Co, Cr, Ni, Pt-based catalysts at 895-1100°C (Callahan 1974). The carbon produced was then burned off the surface of the catalyst. In this regard, these processes exhibit no significant advantages over conventional processes (for example, SR) because of high operational temperatures and large CO_2

emissions.

Our approach is based on the selection of the active catalysts for the methane decomposition operating at moderate temperatures (650-850°C) and carbon recovery. It is more attractive from technical and ecological points of view to store carbon rather than CO_2. Since TCC of natural gas does not produce CO_2 emissions it can be considered as a transition process linking the fossil fuel and the renewable energy resource-based economies. In the short-term, this process can be used for on-site production of hydrogen-methane mixtures in gas-filling stations and for CO_2-free production of hydrogen for fuel cell driven prime movers.

Experimental

We have used two types of thermocatalytic systems, namely: continuous flow (CF) and pulse reactors. The schematic diagram of the catalytic system with CF reactor is given in Figure 1. The experimental set-up consists of 3 subsystems: fixed bed catalytic reactor, gas introduction and sampling subsystem and analytical subsystem. The catalytic reactor (volume 58.4 mL) is made out of quartz and contains 6 g of catalyst. The reactor is placed in a temperature-controlled (Love Controls Corp.) oven. The methane (Bitec, 99.0%) and nitrogen (Bitec, 99.999%) enter the reactor alternately at flow rates of 50 mL/min. The yield of hydrogen production is determined by a gas-chromatograph (SRI 8610) using a thermal conductivity detector (TCD) and Hysep D_B and silicagele columns. Figure 2 depicts the schematic diagram of the catalytic system with pulse reactor which consists of a microreactor (volume 3.2 mL) with a catalyst (0.5 g), 6-port sampling valve with 1 mL sampling loop and gas chromatograph. Pulses (1 mL each) of methane are injected into the microreactor and the methane cracking products enter GC.

Results and Discussion

We studied thermocatalytic decomposition of methane over various catalysts and contacts. It was observed that the hydrogen production rate is a function of the temperature. Figure 3 depicts the temperature dependence of the hydrogen concentration (% vol) in the effluent gas using different catalysts and refractory materials including the reactor material: quartz. It was found that quartz as well as graphite and alumina showed no or insignificant activity in the methane decomposition reaction at temperatures below 700°C. Alumina-supported Ni- and Fe-catalysts demonstrated high catalytic activity in the range of 650-800°C and 800-900°C, respectively. It should be noted that in some cases we observed a decline in the hydrogen yield as the run proceeded due to the carbon build-up on the catalyst surface. Therefore, only maximum values of hydrogen yields were considered in plotting the temperature dependence of the methane decomposition reaction.

It was observed that the shape of the kinetic curve for hydrogen production is mostly determined by the chemical composition of the contact. For example, alumina-supported Pt-catalyst demonstrated high catalytic activity only during first several minutes and then the rate of the methane decomposition drastically dropped and reached the stationary level which corresponds

to the hydrogen concentration in the effluent gas equal to approximately 20% vol. (Figure 4). In case of oxide type catalysts the maximum yield of hydrogen is reached after the induction period corresponding to the catalyst reduction to its metallic state. Figure 5 depicts the time dependence of H_2 concentration in the product of the methane decomposition in presence of alumina-supported Fe-catalyst. After a relatively long induction period, the stationary process of methane decomposition over the catalyst surface with the formation of gas (95% vol. H_2) was observed. It should be noted that in this experiment the hydrogen production rate did not decline for at least two hours. Another behavior was demonstrated by the alumina-supported Ni-catalyst. The maximum hydrogen yield was reached after a short induction period (5 min) followed by slow decrease in the catalytic activity. The kinetic curves of the hydrogen and carbon oxides production in presence of Ni-catalyst are shown in Figure 6. Unfortunately, the continuous flow reactor does not allow accurate measurements of the maximum yields of hydrogen production primarily because of short induction time and the longevity of GC analysis. The best solution for this purpose is to use pulse reactor, such as that in Figure 2. 1 mL pulses of CH_4 at regular intervals are injected into the catalytic microreactor and the reaction products enter the GC analyzer. In a typical experiment we conducted 90 such injections. Figure 7 depicts the dependance: the methane decomposition products yields *vs* the number of 1 mL methane injections. First injections result in a deep oxidation of the methane into the carbon oxides and the reduction of the catalyst to its reduced (probably, metallic) form. We observed the onset of the hydrogen formation after 13 injections with the maximum hydrogen yield corresponding to 25-40 injections. Beginning from the 30th injection hydrogen was the only product of the methane decomposition. The most important result of this series of experiments is that the maximum concentration of hydrogen in the effluent gas is fairly close to its equilibrium (*i.e.* theoretical) value which is an indication of an active catalyst.

Conclusion

Natural gas will dominate as a hydrogen source in the near- to medium-term future. All conventional methods of hydrogen production from hydrocarbon feedstock are multi-step processes accompanied with CO_2 emission. Recovery and disposal of CO_2 produced from fossil fuels is economically unattractive and there are some ecological uncertainties of storing CO_2 in large quantities. It is more attractive from technical and ecological points of view to store carbon rather than CO_2. Thus, the environmentally optimum way of hydrogen production from natural gas is its catalytic cracking into hydrogen and carbon. Thermocatalytic cracking of the methane over various catalysts and contacts was studied in this paper. Catalyst activity and stability tests were conducted using two types of thermocatalytic systems: fixed bed continuous flow and pulse reactors. Alumina-supported Fe- and Ni-catalysts demonstrated high catalytic activity at 800 and 650°C, respectively. Fe-catalyst also revealed a good stability in the methane cracking reaction. The concentration of hydrogen in the effluent gas reached 95% (900°C) and 80% vol. (790°C) using alumina-supported Fe- and Ni-catalysts, respectively.

Future Work

Future work will focus on the following areas:

1. The optimization of the catalyst for the methane catalytic decomposition. Studies on the effect of the catalyst surface area and the size and shape of the catalyst pellets on its catalytic activity. The effect of the catalyst composition on the non-stationary and stationary phases of the thermocatalytic process. The problems of thermal stability of the catalysts.

2. Catalyst activity measurements on a specially designed gradientless reactor with well mixed conditions. The temperature dependence and the activation energy of the catalytic conversion of the methane. The effect of the methane partial pressure on the rate of its catalytic decomposition.

3. Effect of the carbon deposition on the methane decomposition rate. Physico-chemical and crystallographic characteristics of the carbon formed on the catalyst surface at different temperatures. The problems of long term stability and the catalyst deactivation and regeneration.

References

Callahan, M. 1974. "Catalytic Pyrolysis of Methane and Other Hydrocarbons". In *Proceedings of 26th Power Sources Symposium,* 181-184. Red Bank, N.J.

Marchetti, C. and N. Nakicenovic. 1979. *The Dynamics of Energy Systems and the Logistics Substitution Model,* IIASA, RR-79-13, Laxenburg, Austria.

Nakicenovic, N. 1993. *Energy Gases: The Methane Age and Beyond,* IIASA Working Paper WP-93-033, Laxenburg, Austria.

Pohleny, J. and N. Scott. 1966. U.S.Patent No 3,284,161 (UOP).

Steinberg, M. and H. Cheng. 1988. "Modern and Perspective Technologies for Hydrogen Production from Fossil Fuels". In *Proceedings of 7th World Hydrogen Energy Conference,* 699-730. Moscow, USSR.

Figure Captions

Figure 1. Schematic Diagram of Continuous Flow Thermocatalytic System for CH_4 Cracking. Reactor Volume: 58.4 mL. Catalyst: 6 g.

Figure 2. Pulse Reactor System for the Methane Thermocatalytic Cracking. Reactor Volume: 3.2 mL. Catalyst: 0.5 g.

Figure 3. Temperature Dependence of Hydrogen Concentration in the Effluent Gas Using Various Catalysts and Contacts

Figure 4. Time Dependence of Hydrogen Concentration in the Effluent Gas in the Presence of Alumina-Supported Pt-Catalyst. Temperature: 900°C.

Figure 5. Time Dependence of Hydrogen Concentration in the Effluent Gas in the Presence of Alumina-Supported Fe-Catalyst. Temperature: 900°C.

Figure 6. Time Dependence of Methane Decomposition Products Concentrations in the Effluent Gas Using Alumina-Supported Ni-Catalyst. Temperature: 650°C.

Figure 7. Methane Decomposition Products Concentrations in the Effluent Gas as a Function of the Number of Methane (1 mL) Injections into Pulse Reactor. Alumina-Supported Ni-Catalyst. Temperature: 650°C.

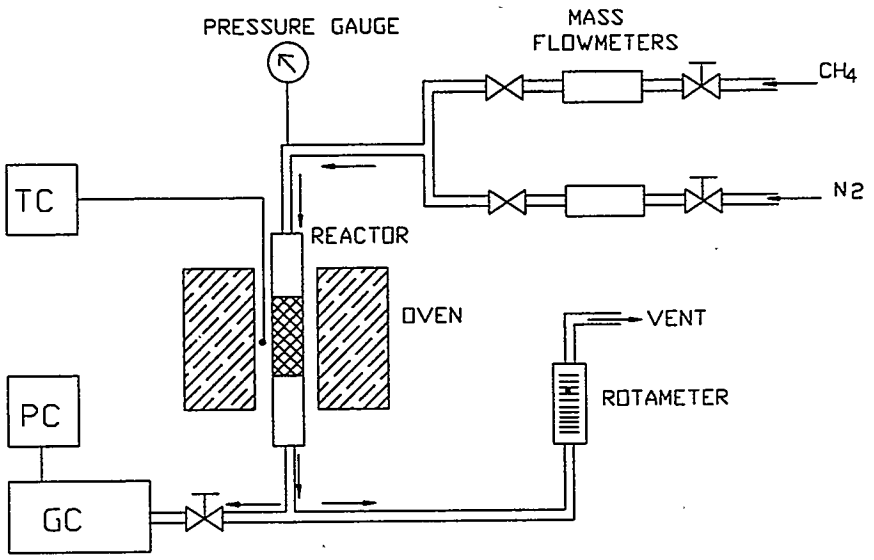
PRESSURE GAUGE
MASS
FLOWMETERS
CH4
N2
TC
REACTOR
OVEN
VENT
ROTAMETER
PC
GC

Figure 1.

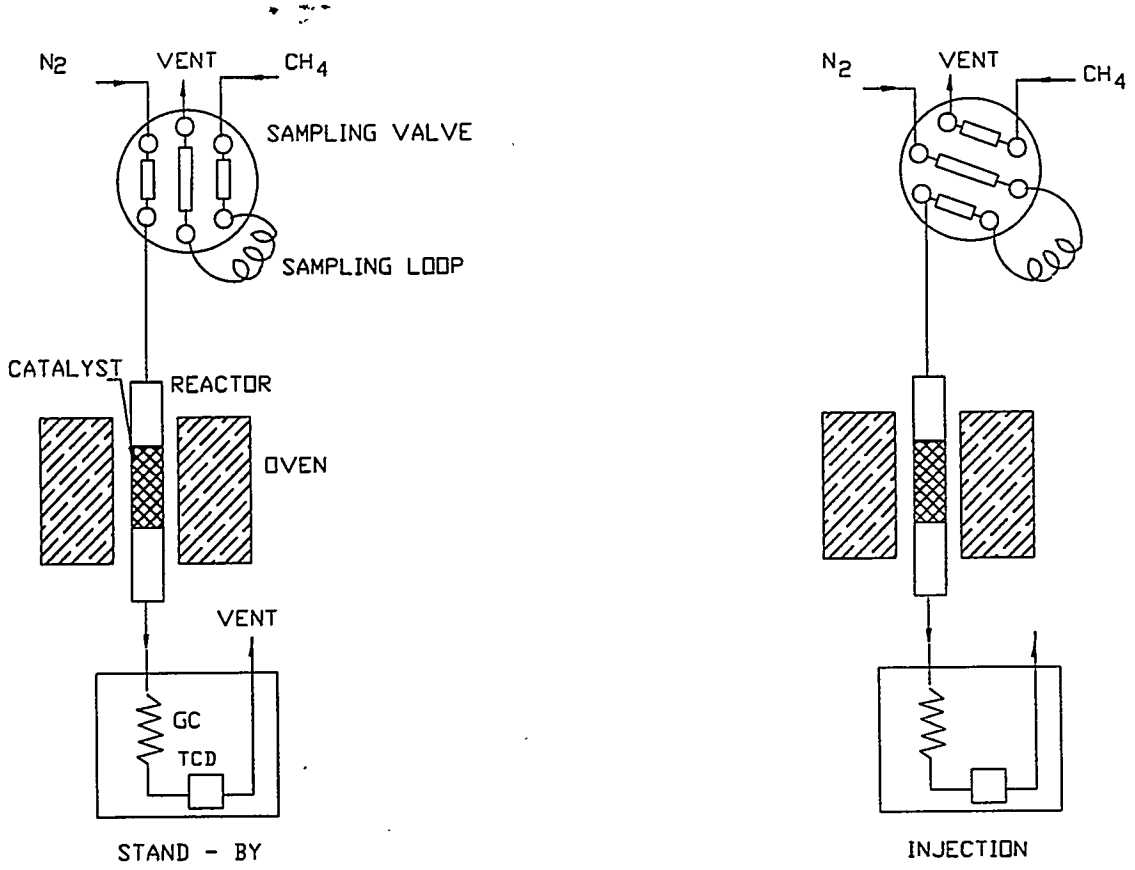
N2
VENT
CH4
SAMPLING VALVE
SAMPLING LOOP
CATALYST
REACTOR
OVEN
VENT
GC
TCD
STAND - BY
N2
VENT
CH4
INJECTION

Figure 2.

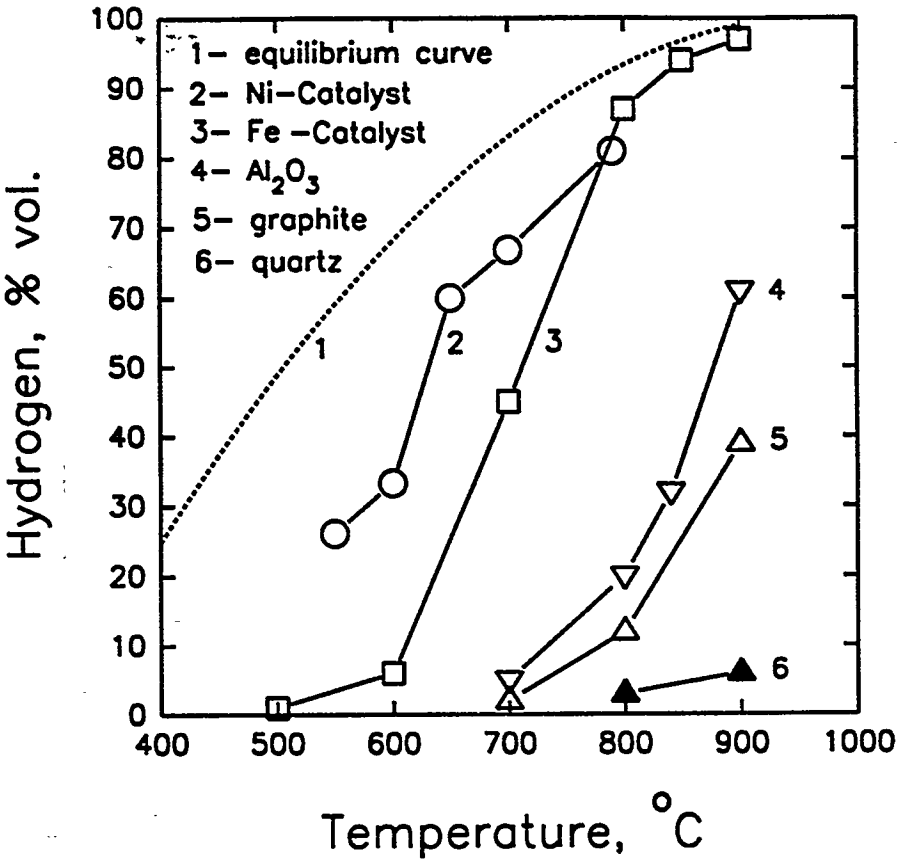
1– equilibrium curve
2– Ni–Catalyst
3– Fe –Catalyst
4– Al_2O_3
5– graphite
6– quartz
Hydrogen, % vol.
Temperature, °C
100
90
80
70
60
50
40
30
20
10
0
400
500
600
700
800
900
1000
1
2
3
4
5
6

Figure 3.

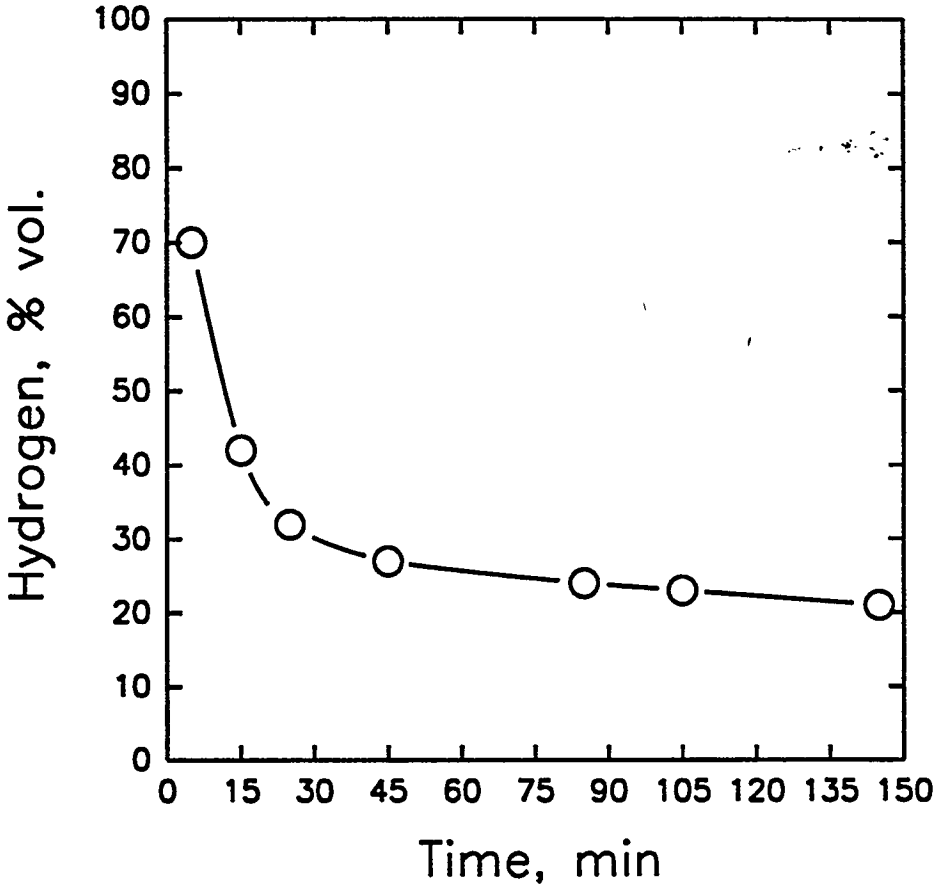
Hydrogen, % vol.
100
90
80
70
60
50
40
30
20
10
0
0 15 30 45 60 75 90 105 120 135 150
Time, min

Figure 4.

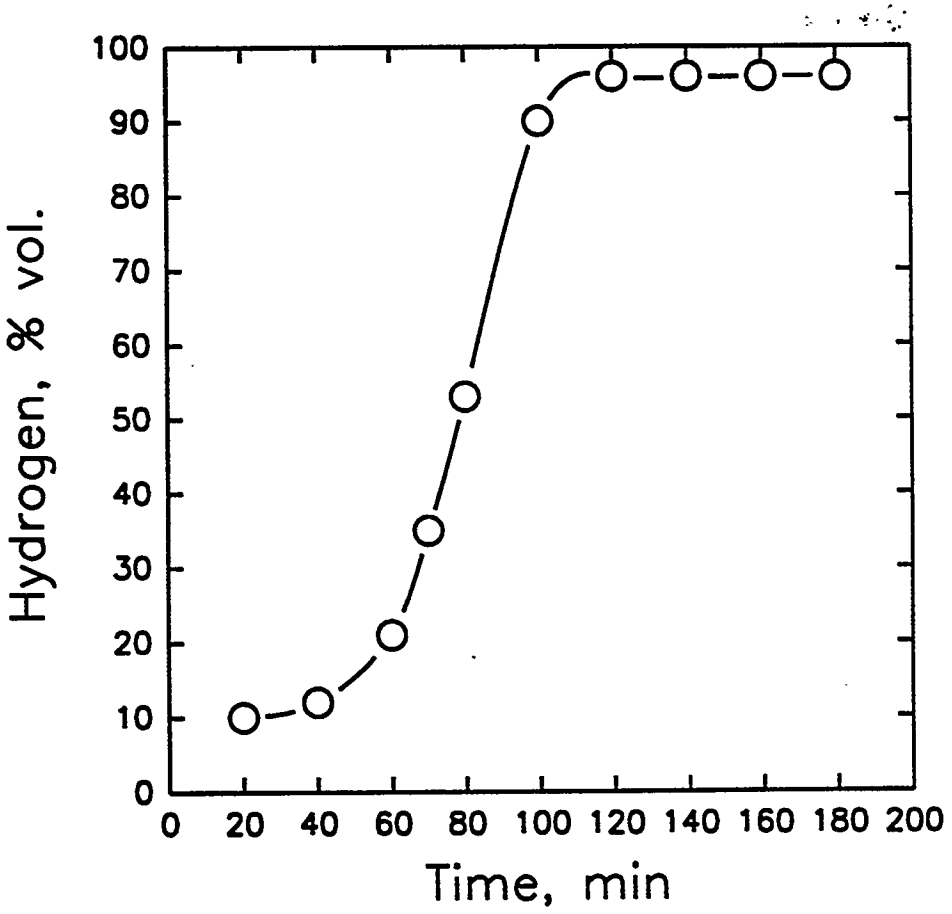
Hydrogen, % vol.
100
90
80
70
60
50
40
30
20
10
0
0 20 40 60 80 100 120 140 160 180 200
Time, min

Figure 5.

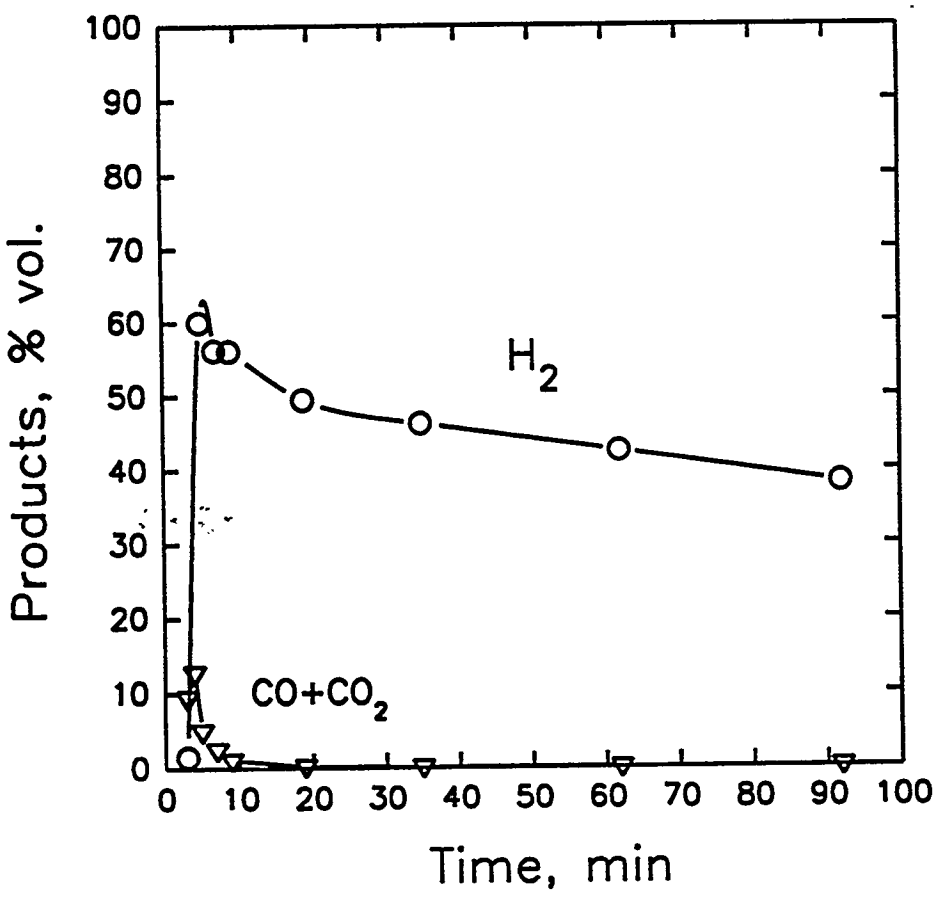
Products, % vol.
100
90
80
70
60
50
40
30
20
10
0
0
10
20
30
40
50
60
70
80
90
100
Time, min
H2
CO+CO2

Figure 6.

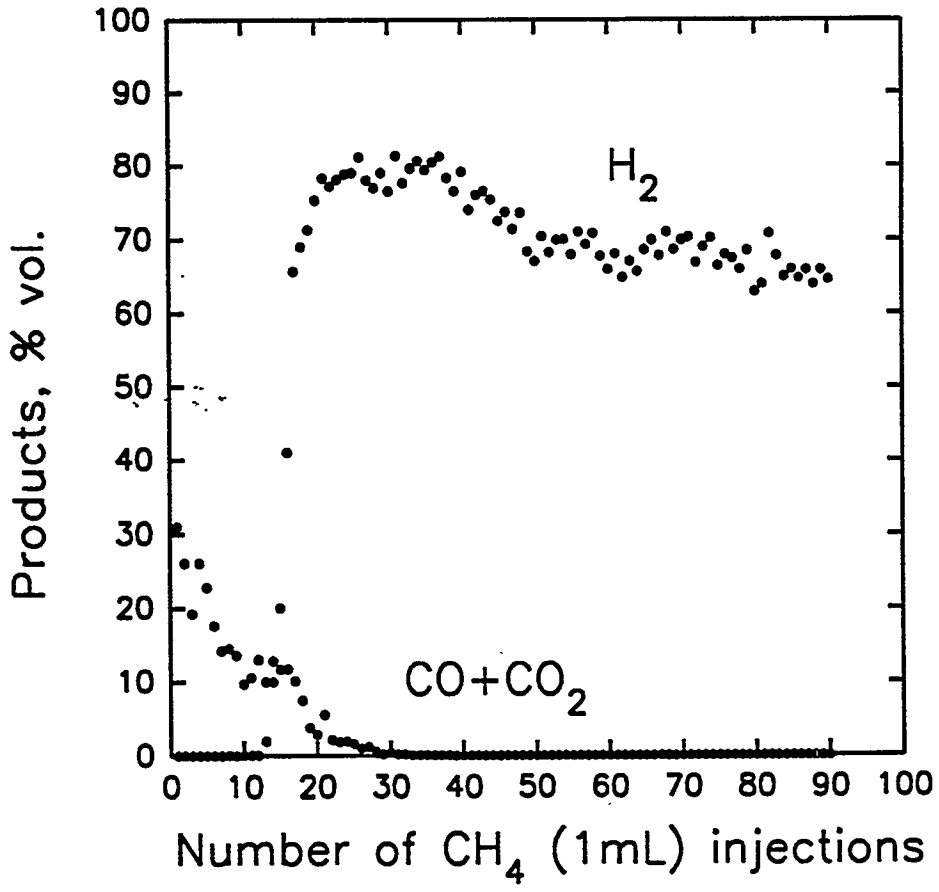
Products, % vol.
100
90
80
70
60
50
40
30
20
10
0
0 10 20 30 40 50 60 70 80 90 100
Number of CH4 (1mL) injections
H2
CO+CO2

Figure 7.

H_2 FROM BIOSYNGAS VIA IRON REDUCTION AND OXIDATION

John Straus and Peter Terry
H Power Corp.
Belleville, NJ, 07109

Abstract

The production of hydrogen from the steam-oxidation of iron is a long-known phenomenon. The rise in interest in the production and storage of hydrogen justifies the examination of this process (and of the reverse process, the reduction of iron oxide) for commercial use. Under NREL subcontract ZAR-4-13294-02, a process simulation program was developed and used as a design tool to analyze various configurations of the iron-hydrogen purification/storage scheme. Specifically, analyses were performed to determine the effectiveness of this scheme in conjunction with biomass-derived gasified fuel streams (biosyngas). The results of the computer simulations led to a selection of a two-stage iron oxide reduction process incorporating interstage water and CO_2 removal.

Thermal analysis shows that the iron-hydrogen process would yield essentially the same quantity of clean hydrogen per unit of biomass as the conventional route. The iron-hydrogen process benefits from the excellent match potentially achievable between the otherwise-unusable energy fraction in the off-gas of the reduction reactor and the parasitic thermal, mechanical and electrical energy needs of some typical gasifier systems. The program simulations and economic analysis suggest that clean hydrogen from biomass feedstock could cost about 20% less via the iron-hydrogen method than by conventional methods of purification (using the same feedstock). Cost analyses show that lower capital costs would be incurred in generating clean hydrogen by utilizing this approach, especially in response to the fluctuating demand profile of a utility.

Introduction

This study addresses a multi-faceted need that could potentially be met by a single concept. The need is for the conversion of low-grade fuel streams typical of gasified biomass into a high-grade fuel stream, the inexpensive storage of the biomass-derived chemical energy, and the safe and inexpensive transportability of the stored energy. The concept that potentially meets these needs is a process employing the cyclical oxidation and reduction of porous iron or "sponge iron."

Typical biosyngas compositions are usually high in carbon monoxide, which is generally incompatible with fuel cells, especially P.E.M. fuel cells where even small CO residues are unacceptable. Because the oxidation of iron by steam, the hydrogen producing reaction, is decoupled from the reduction process, which utilizes energy in the biosyngas, high-CO-content or other low-grade fuels may be used for the reduction of iron. The only product of the overall process is pure hydrogen (which carries some unreacted H_2O, a desirable entity, with it to the fuel cell).

A scheme that could simultaneously purify, store, and transport what starts out as biosyngas and ultimately ends up as clean hydrogen could well enhance the prospects of generating electricity from biomass via fuel cells or via clean hydrogen heat engines. Other systems requiring clean hydrogen for chemical processes could also benefit.

H Power's iron-hydrogen approach and the theoretical and experimental work so far performed in its pursuit suggest that advances toward such goals may well ensue from further work on this scheme. Conceptually, this cyclic scheme is straightforward. It alternately stores "latent" hydrogen as iron metal and returns it as hydrogen gas.

Storage

Hydrogen, pure or impure, at atmospheric (or elevated) pressure reacts with an iron oxide (typically Fe_3O_4; i.e., magnetite rust) to form iron metal and steam. If the hydrogen comes mixed with carbon monoxide (as in reformed natural gas or water gas), the overall reaction may also convert some of the CO to CO_2, forming additional iron metal. These reactions, which are highly reversible, can generally be described as follows:

$$4\,H_2 + Fe_3O_4 \longrightarrow 3\,Fe + 4\,H_2O$$
$$4\,CO + Fe_3O_4 \longrightarrow 3\,Fe + 4\,CO_2$$

The H_2O and CO_2 are discarded and the metallic iron, generally in the form of porous, brittle pellets, is saved for later use as a source of hydrogen. If pure or nearly pure hydrogen is the reactant used in the oxide-reducing process, then only water vapor will be emitted to the atmosphere.

Discharge

Metallic iron particles react with steam to generate hydrogen gas and (generally) magnetite (rust), thus reversing the storage reaction:

$$3\,Fe + 4\,H_2O \longrightarrow Fe_3O_4 + 4\,H_2$$

The Fe_3O_4 is saved for later recycling back to metallic iron, using either pure hydrogen or a reducing mixture of hydrogen, other reducing gases, and inert gases. The iron is then ready to resume the cycle by once again generating hydrogen from steam.

Hydrogen Purification/Storage from Biomass

The system in which hydrogen is produced from biomass can be identified as three separate processes: (1) biomass preparation, (2) gasification, and (3) hydrogen purification. Initially, the biomass must be harvested or collected and possibly dried and pelletized as preparation for input into the gasifier. The gasifier reduces the biomass into lighter-weight hydrocarbon gases (biosyngas). These gases are then reduced to hydrogen through the purifier. As part of the purification process, the composition of the biosyngas can, if necessary, be chemically altered to increase the concentration of hydrogen. The hydrogen can then be removed either by conventional means, such as through a pressure swing adsorption unit, or by the proposed method of purification using the iron-hydrogen process.

Approach

The objective was to study the conversion of suitable types of biomass into hydrogen using the iron-hydrogen process. The study was basically addressed as two separate stages: (1) the analysis of the iron oxide reduction process and (2) the incorporation of this process and the iron oxidation process into the overall biomass-to-hydrogen system.

The reduction of iron oxide using biosyngas and the steam-oxidation of iron to produce hydrogen were examined via thermodynamic computer models. The final process configuration selected was based upon the effects of four design parameters on the performance of the iron oxide reduction system. These parameters were feed gas composition, reactor temperature, CO_2 removal, and the number of reactor stages.

A thermal and economic analysis was then performed on the overall biomass-to-hydrogen system incorporating the iron-hydrogen purification/storage process. These studies were then compared with that of a biomass-to-hydrogen system using a conventional purification process (based on pressure swing adsorption).

Simulation Program

The simulation program used was designed to easily accept changes of the system configuration. It could therefore be used to quickly and accurately determine the performance and assess the advantages and disadvantages of many different configurations. To this end, the simulation program was developed to be used as a design tool. To accomplish this, the simulation program was structured around a modular format. Each module or subroutine was, in general, designed to perform

a single function, sometimes calling upon other modules to achieve the desired task.

Assumptions and Methodology

No attempt was made to model the fuel processor (gasifer). Instead, available experimental data on gasifier product gases were used as inputs to the simulation program. Other assumptions made were as follows:

1. Reactors operate isothermally
2. Heat exchangers are adiabatic (no losses)
3. All processes are at constant pressure (atmospheric)
4. Losses involved with minor mechanical equipment are negligible
5. MEA-based CO_2 scrubber removes equal amounts of CO_2 and H_2O.

JANAF tables of enthalpy were included for the iron/iron-oxide reduction and oxidation beds. JANAF tables were also used for all Gibbs function data. Specific heats were integrated over temperature to determine the enthalpy changes for each of the components in the process stream.

The only oxide of iron assumed present was Fe_3O_4. (Depending on whether the kinetics actually allow the formation of the intermediate compound $Fe_{0.947}O$, which is somewhat doubtful, the above equations may be a simplification. However, the practical effect would be relatively small.) Process stream gases could include O_2, H_2, CO, CO_2, H_2O, N_2, and CH_4.

Key Results

Iron Oxide Reduction System

Many variations on the design parameters were explored before arriving at the final configuration. The effect of these parameters on the conversion efficiency (heating value of H_2 produced to heating value of biosyngas fed) of the iron oxide reduction system are summarized in Table 1. The final configuration selected for the detailed design is a two-stage reactor employing CO_2 removal (Figure 1). The reducer at each stage operates at 1400K providing for favorable conditions for the reduction of the iron oxide.

A Shell-type gasifier was used as the biomass processor because its product syngas contained low concentrations of methane. This was desired because it lowered the potential need for a methane steam reformer. The molar composition of the product biosyngas is:

O_2- 0 %
H_2- 30.67 %
CO- 39.04 %
CO_2- 11.77 %
H_2O- 18.36 %

N_2- 0.05 %
CH_4 - 0.11 %.

The driving force behind the selection of the two-stage system was the energy requirements of the overall biomass-to-hydrogen system, which includes the biomass processor. A single-stage design would have a low conversion efficiency and surplus waste heat at the reducer's exhaust. A three- or four-stage system would have a considerably higher conversion efficiency; however, excess energy would be required to compensate for the gasifier's endothermic reaction. The two-stage system allows for a good conversion efficiency and a good overall system thermal efficiency.

Carbon fouling within the reducers was also examined through the use of a C-H-O diagram. The relative percentages of C, H, and O atoms of the gas stream were determined at the inlet and exit of both reducers and plotted on the C-H-O diagram. As the reaction in the reducers proceeds towards equilibrium, the tendency for carbon deposition lowers. Since the conditions for carbon deposition at the inlets of each reducer are not highly favorable, the potential for carbon fouling within the reducer beds is small.

Biomass-to-Hydrogen System

The iron-hydrogen purification/storage process was incorporated into the overall biomass-to-hydrogen system and compared with a similar system based on a conventional purification process. The biomass-to-hydrogen systems based on both the conventional and the iron-hydrogen process are shown in Figures 2a and 2b, respectively. Efficiency and cost data for the conventional purification system were taken from Katofsky. This system was based on the use of a pressure swing adsorption unit. For both systems, the product syngas of the gasifier is directed into the hydrogen purifier. For the iron-hydrogen based process, Figure 2b shows simplistically how the elemental iron stored in a bin is deliverable on demand to the hydrogen generator. Likewise, the iron consumed in the hydrogen generator (iron oxide) is sent to a separate storage bin to be later reprocessed in the iron oxide reduction unit.

Process Concepts

Although simulation results were sufficient for finalizing the reduction process and determining the conversion efficiency, they did not address the handling of Fe and Fe_3O_4. Figure 3 pictorially shows the process by which the iron and iron oxide are handled. As seen in the figure, three separate two-stage reactors are proposed for the present design. While the iron oxide beds in one reactor set are being reduced by biosyngas, the other two reactor sets are exchanging heat with each other (the iron/iron-oxide preheat/precool process). As implied in Figure 3, both the iron and iron oxide require supplemental heat transfer. The iron, prior to storage, is further cooled to ambient temperature. The iron-oxide requires additional heating to be brought up to the operating temperature of the reducer. When the reduction and heat exchange processes are complete, the three reactor sets are effectively rotated (cycled) and the process repeated. Once the cooled iron is unloaded into the iron storage bin, the reactor sets are rotated and new Fe_3O_4 is loaded from its storage bin into the empty reactor set. The iron oxide product of the hydrogen generation reaction is stored in the iron oxide bin.

Thermal Analysis

An energy balance diagram of the proposed biomass-to-hydrogen system is given in Figure 4. This figure summarizes how the available heat from the iron oxide reduction process is used in all the subsystems of the biomass-to-hydrogen system. The two sources of heat from the iron oxide reduction process are the trim cooler and the burner (Figure 1). The available process heat from the burner is shown under four separate temperature regimes. This process heat reflects excess energy available after the reduction process endothermic reaction requirements have been accounted for. The high quality heat, available down to 1400K, is used to both heat the iron oxide to 1400K prior to being fed into the reactors (supplements the iron/iron-oxide preheat/precool process) and supply a portion of the gasifier endothermic reaction heat. The heat available down to 673K is used to generate electricity for the gasifier.

The remaining energy from the burner, with the exception of that used to provide steam for the gasifier, is not usable by the overall system. (The heat required by the MEA CO_2 absorber can use some of this low-grade heat waste heat.) The second of the two sources of heat is represented by the trim coolers. The process heat available from the trim coolers is used to dry the biomass from 45% to 11% moisture content (a requirement of the gasifier). This requires approximately 63 MW.

It is noted that the biosyngas-to-hydrogen conversion efficiency in the conventional biomass-to-hydrogen system is substantially higher than that in the system based on iron-hydrogen purification (97% vs. 68%). However, the former conversion is heat-deficient while the latter entails excess heat availability in conjunction with overall system ancillary loads. The associated reduction of supplemental biomass energy requirements for the iron-hydrogen system results in essentially equal thermal efficiencies for the two systems (60%).

Economic Analysis

The capital costs of the iron/iron-oxide process based biomass-to-hydrogen conversion system were developed. The iron/iron-oxide process has the ability to easily store energy in the form of reduced iron. This process is therefore ideally suited to systems with varying hydrogen demands. The reduction of iron oxide can be conducted at a rate equal to the average demand of the overall system. The reduced iron can, on demand, be used to produce hydrogen at a rate limited only by the hydrogen generator portion of the system. Referring to Figure 2b, all process components to the left of the hydrogen generator can be sized for the average hydrogen demand, while only the hydrogen generator itself must be sized to meet the peak hydrogen flow rate. Storage of the reduced iron and the iron oxide is easily accomplished at normal environmental conditions.

For this analysis, a duty cycle that would take advantage of the storage abilities of the iron/iron-oxide process was assumed. An average hydrogen demand of 75 MW (HHV) with a peak hydrogen demand of 300 MW (HHV) was used. Referring again to Figure 2b, the dryer, gasifier, and iron oxide reduction system were sized for 75 MW hydrogen production. The hydrogen generation system, although operating at an average of 75 MW hydrogen production, was sized for 300 MW.

Capital costs for the iron/iron-oxide process were developed by using published chemical industry cost estimates for individual process components. The costs for the biomass processing and gasification equipment were assumed to be the same regardless of post-gasification treatment. Costs for that portion of the overall system were therefore taken from studies dealing directly with biomass processing. These costs are presented in Tables 2, 3, and 4.

Table 5 shows the capital costs of the iron-based biomass-to-hydrogen system as compared to the estimates of that using the conventional purifier. Capital costs for the conventional system were scaled from Katofsky's data to the 300 MW rate. Both systems were assumed to operate at an average rate of 75 MW with a 300 MW peak capacity. Because the conventional purification system lacks the means to store energy, its gasifier and purifier (Figure 2a) was sized and costed to meet the 300 MW peak requirement. The oxygen plant listed is required for the gasifier. Since O_2 can be stored, this unit was sized for the 75 MW rate. However, an allowance of $3 million was added to the oxygen plant costs for storage. Table 5 shows that, for the hydrogen-demand profile assumed, the total capital cost of the iron-based biomass-to-hydrogen systems is nearly half that of that using the conventional purifier.

Table 6 presents a breakdown of the levelized costs for both biomass-to-hydrogen schemes. The total cost of the iron-based system per GJ of energy is shown to be nearly 30% less than that for the conventional system. This is due in most part to the lower capital costs of the iron-hydrogen purification/storage system per GJ throughput. An entry on purchased energy is included to account for energy required of the gasifier in the conventional process. Most of this energy is supplied by the burner gases in the iron-based system. The purchased energy for the iron-based system is therefore negligible; however, higher feedstock costs reflect the corresponding increase in feedstock consumption.

Conclusions

A thermal and economic analysis of the biomass-to-hydrogen system using the iron-hydrogen purification/storage process was performed. The results of these analyses indicate that the proposed system can purify low-quality fuel streams into high-quality hydrogen for roughly 20% less cost than by a conventional purification scheme assuming a fluctuating demand profile of a utility. Thermal efficiencies of both systems were determined to be almost identical. Cost analyses indicate considerably lower capital investments for the iron-hydrogen system.

Future Work

This study has demonstrated that the iron-hydrogen system offers economic and operational advantages for the conversion of biosyngas to hydrogen. The ability of this system to store energy, as reduced iron, and to provide high-quality hydrogen make it attractive for further development.

Reaction kinetics, the effects of methane and other hydrocarbons in the biosyngas, and the effects of

trace impurities should be evaluated in subscale test reactors. Upon completion of this testing, the construction of a pilot plant should be evaluated.

References

Katofsky, Ryan E., "The Production of Fluid Fuels from Biomass," Master's Thesis, Princeton University, June 1993.

Marks' Standard Handbook for Mechanical Engineers, 9th Edition.

Table 1. Iron-Hydrogen Purification/Storage System Analysis Summary[6]

System Description	g Fe_3O_4 Reduced / Feed LHV (kJ)	g H_2[5] / Feed LHV (kJ)	LHV H_2[5] / Feed LHV
CH_4 Reformate: 2-Stage, 1400K Reactor (Baseline)	0.1469	0.00512	61.4%
CH_4 Reformate: 3-Stage, 1400K Reactor	0.1690	0.00589	70.6%
CH_4 Reformate: 2-Stage, 1400K Reactor. CO_2 removal[1]	0.1654	0.00576	69.1%
CH_4 Reformate: 2-Stage, 1255K Reactor. CO_2 removal[1]	0.1347	0.00469	56.3%
CH_4 Reformate: 2-Stage, 1033K Reactor. CO_2 removal[1]	0.1045	0.00364	43.7%
Typical Biosyngas[2]: 2-Stage, 1400K Reactor	0.0861	0.00300	36.0%
Typical Biosyngas[2]: 2-Stage, 1400K Reactor, CO_2 removal[1] (Final)	0.1359	0.00473	56.7%
Typical Biosyngas[2] 2-Stage, 1200K Reactor, CO_2 removal[1]	0.1289	0.00449	53.9%
Typical Biosyngas[2]: 2-Stage, 1400K/1200K[3] Reactor, CO_2 removal[1]	0.1323	0.00461	55.3%
Typical Biosyngas[2]: 2-Stage, 1400K/900K[3] Reactor, CO_2 removal[1]	0.1232	0.00429	51.5%
Typical Biosyngas[2]: 3-Stage, 1400K Reactor	0.096	0.0033	40.0%
Typical Biosyngas[2]: 3-Stage, 1400-1400-900K Reactors	0.097	0.0034	40.4%
Typical Biosyngas[2]: 3-Stage, 1400K Reactor, CO_2 removal[1]	0.1666	0.00580	69.6%
Typical Biosyngas[2]: 3-Stage, 1400-1400-900K Reactors, CO_2 removal[1]	0.159	0.0055	66.6%
ElectroFarm biomass Steam Reformate, 2-Stage, 1400K Reactors, CO_2 removal[1]	0.118	0.0041	49.4%
Typ. Producer Gas[4]: 2-Stage, 1400K Reactor, CO_2 removal[1]	0.0891	0.00310	37.2%

(1) At condenser.
(2) Katofsky, Ryan E., "The Production of Fluid Fuels from Biomass," Master's Thesis, Princeton University, June 1993.
(3) First-stage/second-stage operating temperatures.
(4) Marks' Standard Handbook for Mechanical Engineers, 9th Edition.
(5) H_2 recoverable via subsequent iron H_2O-oxidation.
(6) Copied from preliminary findings.

Table 2. Capital Costs - Iron Oxide Reduction System
75 Megawatt (HHV) Hydrogen Throughput

COMPONENT	COMMENTS	COST
1st Stage		
Recuperative heat exchanger	12,500 ft^2 Area, Stainless steel tube sheet, Internally insulated vessel	$144,000
Condenser		
-Heat exchanger	16,000 ft^2 Area, Plate construction, Mild steel	$130,000
-Air blower	35,000 SCFM, 20 hp	$5,000
-Knock out drum		$1,500
MEA scrubber	Packed columns, Fiberglass w/ packing, 2 Req. @ $50,000 ea.	$100,000
-Pumps (2)	750 GPM, 15 hp, $3,000 ea.	$6,000
-Heat exchangers		
-Regenerative		$10,000
-Water cooled		$10,000
-Piping and frame		$50,000
-Controls		$10,000
Trim heat exchanger	790 ft^2, U Tube construction, Stainless steel	$22,000
Iron oxide reduction vessel	503 ft^3 Capacity, 30,000 ft^2 Internal heat transfer area, Stainless steel, 3 Req. @ $220,000	$660,000
Pelletized iron	190,000 lbs. @$0.07/lb.	$13,300
2nd Stage		
Recuperative heat exchanger	8,750 ft^2 Area, Stainless steel tube sheet, Internally insulated vessel	$115,000
Condenser		
-Heat exchanger	11,000 ft^2 Area, Plate construction, Mild steel	$130,000
-Air blower	35,000 SCFM, 20 hp	$5,000
-Knock out drum		$1,500
MEA scrubber		$150,000
Trim heat exchanger	550 ft^2, U Tube construction, Stainless steel	$17,500
Iron oxide reduction vessel	191 ft^3 Capacity, 12,000 ft^2 Internal heat transfer area, Stainless steel, 3 Req. @ $130,000	$390,000
Pelletized iron	72,000 lbs. @$0.07/lb.	$5,040
TOTAL	w/out piping and support	$1,975,840

Table 3. Capital Costs - Hydrogen Generation System
300 Mw (HHV) Peak Hydrogen Production

COMPONENT	COMMENTS	COST
Iron oxidation reactor	2%/ min. Fe_3O_4 Conversion 2,300 ft^3 volume, SS construction, Internal preheat coil, External insulation	$134,000
Feed water pump	350 gpm	$2,000
Circulating water pump	1,000 gpm	$3,000
Separator	5 min. residence time	$ 22,000
Waste heat exchanger	2100 ft^2	$34,000
Lock hopper	2800 ft^3/hr	$15,000
Pelletized iron	1 hour supply 316,000 lbs @$0.07/lb	$ 22,120
TOTAL		$232,120

Table 4. Equipment Cost Totals For Iron-Hydrogen System

ITEM	COMMENTS	COST
Iron Oxide Reduction System	75 MW Rate, See Table 2	$1,975,840
Hydrogen Generator	300 MW Rate, See Table 3	$232,120
Piping & Support	Estimate	$1,000,000
Fe/Fe_3O_4 Handling	Estimate, Includes storage and conveying	$1,000,000
TOTAL		$4,207,960

Table 5. Capital Cost Comparison
Iron-Hydrogen System/Conventional*

Process Item	Iron-Hydrogen Purification	Conventional Purification
Feed Preparation	$14.7**	$14.7
Gasifier	11.3	28.23
Oxygen Plant	22	25
Purification	4.2	29.4
Utilities/Auxiliaries	13.05	24.33
TOTAL	$65.25	$121.66

* Conventional plant costs adjusted for 300MW peak, 75MW average duty cycle.

** All dollars in millions.

Table 6. Levelized Cost Comparison

Cost Breakdown ($/GJ)	Iron-Hydrogen Purification	Conventional Purification
Capital Cost	6.68	12.48
Labor and Maintenance	5.84	5.84
Purchased Energy	0.06	1.24
Feedstock	3.35	2.53
Total	15.93	22.09

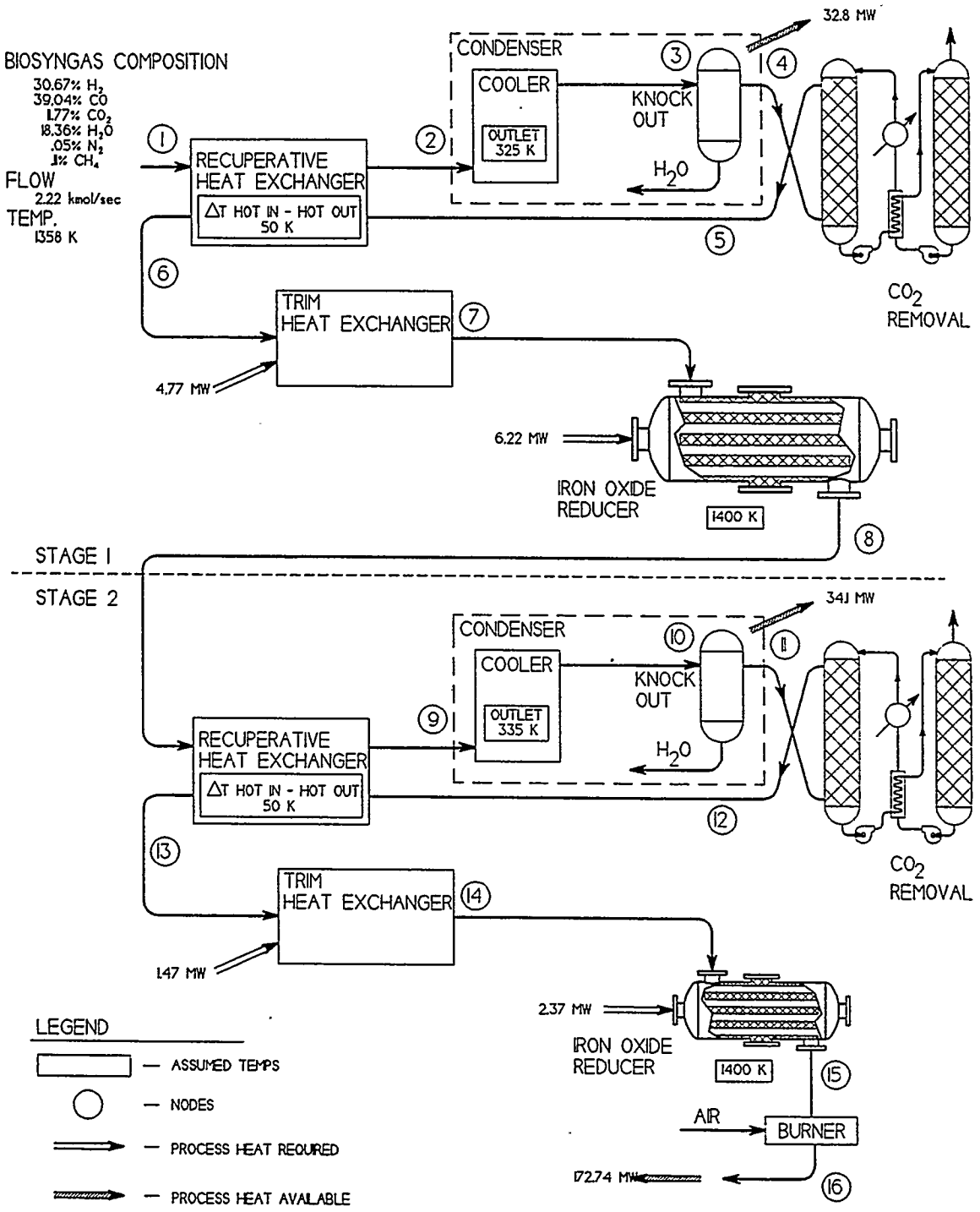

— IRON OXIDE REDUCTION PROCESS USING BIOSYNGAS —

— Figure 1 —

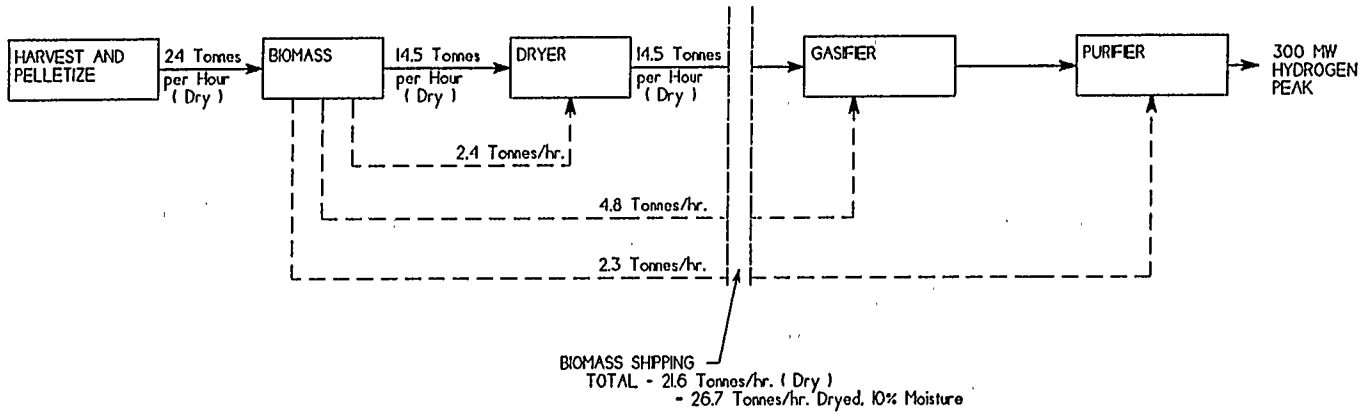

(a) Conventional

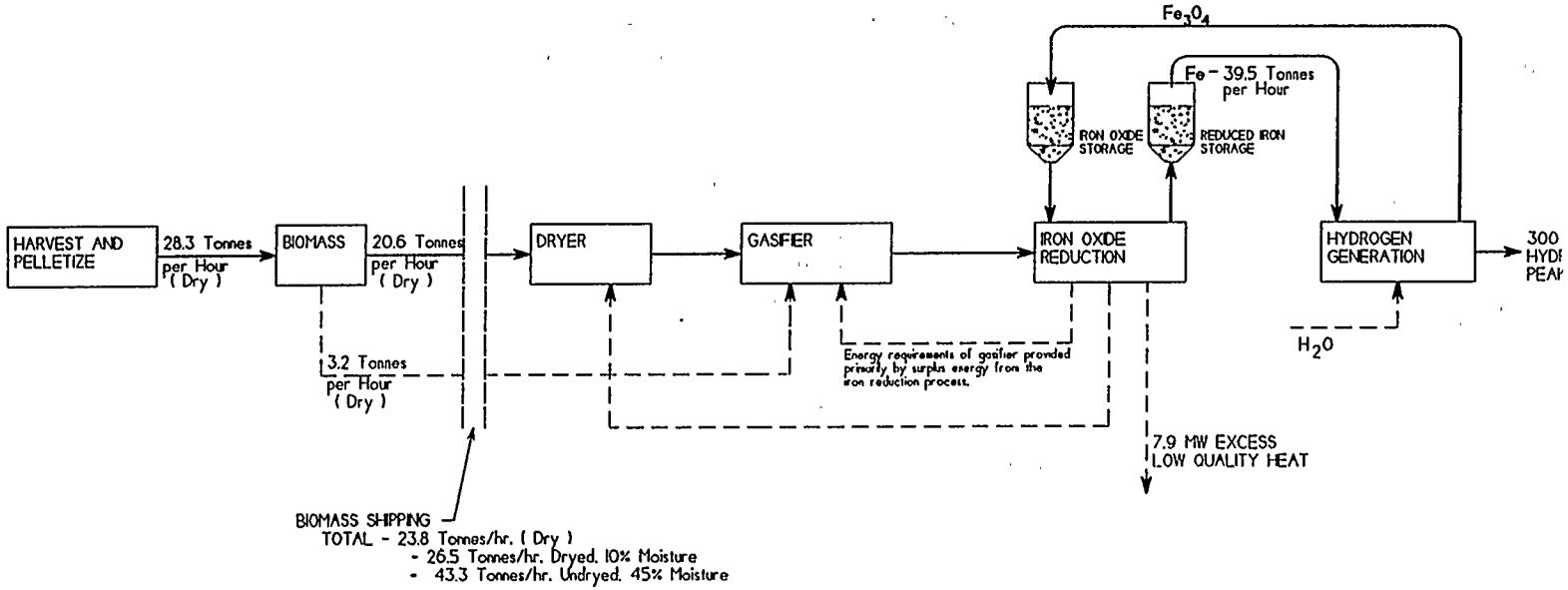

(b) Iron - Hydrogen

BIOMASS TO HYDROGEN SYSTEMS

— Figure 2 —

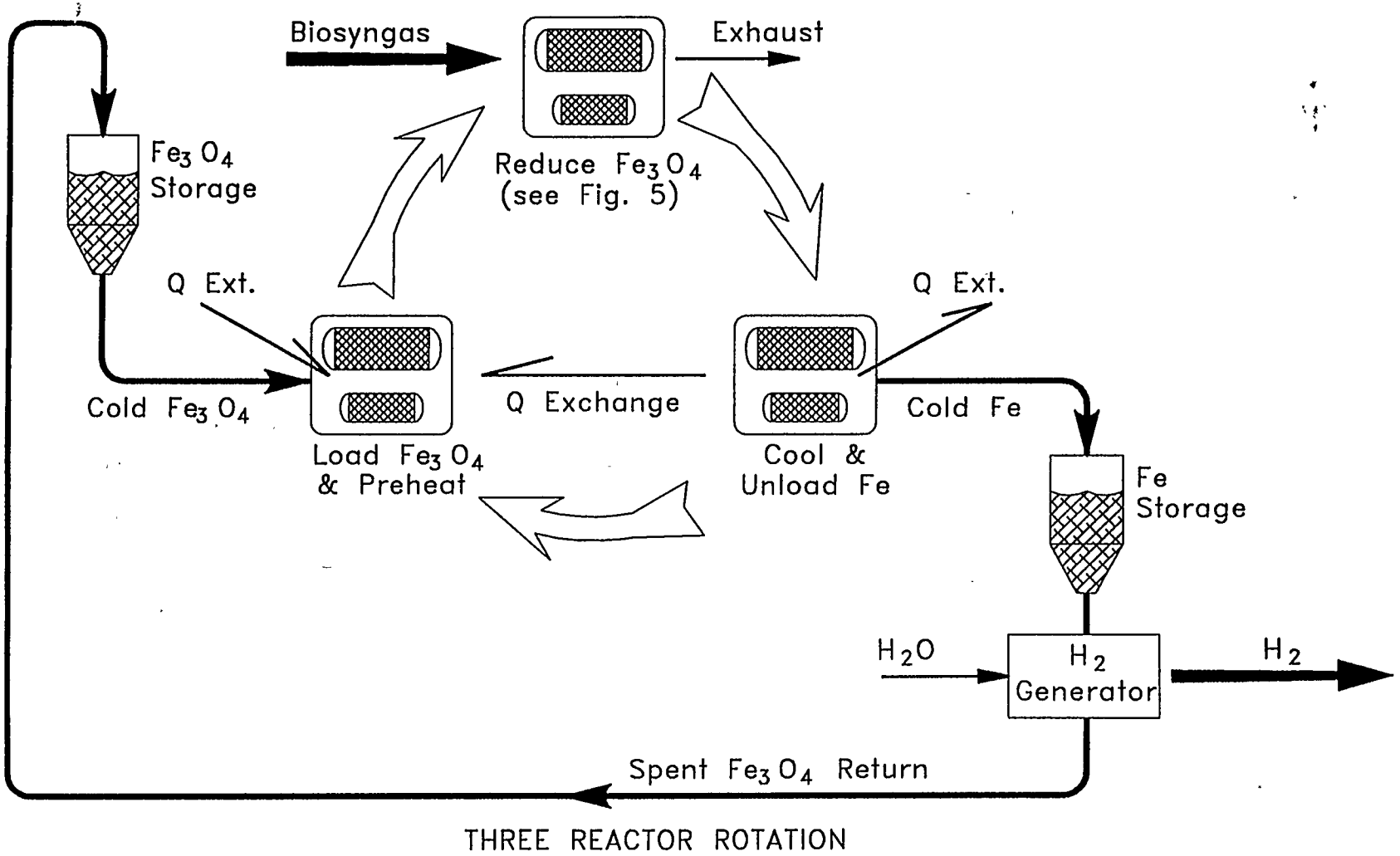

THREE REACTOR ROTATION

Figure 3

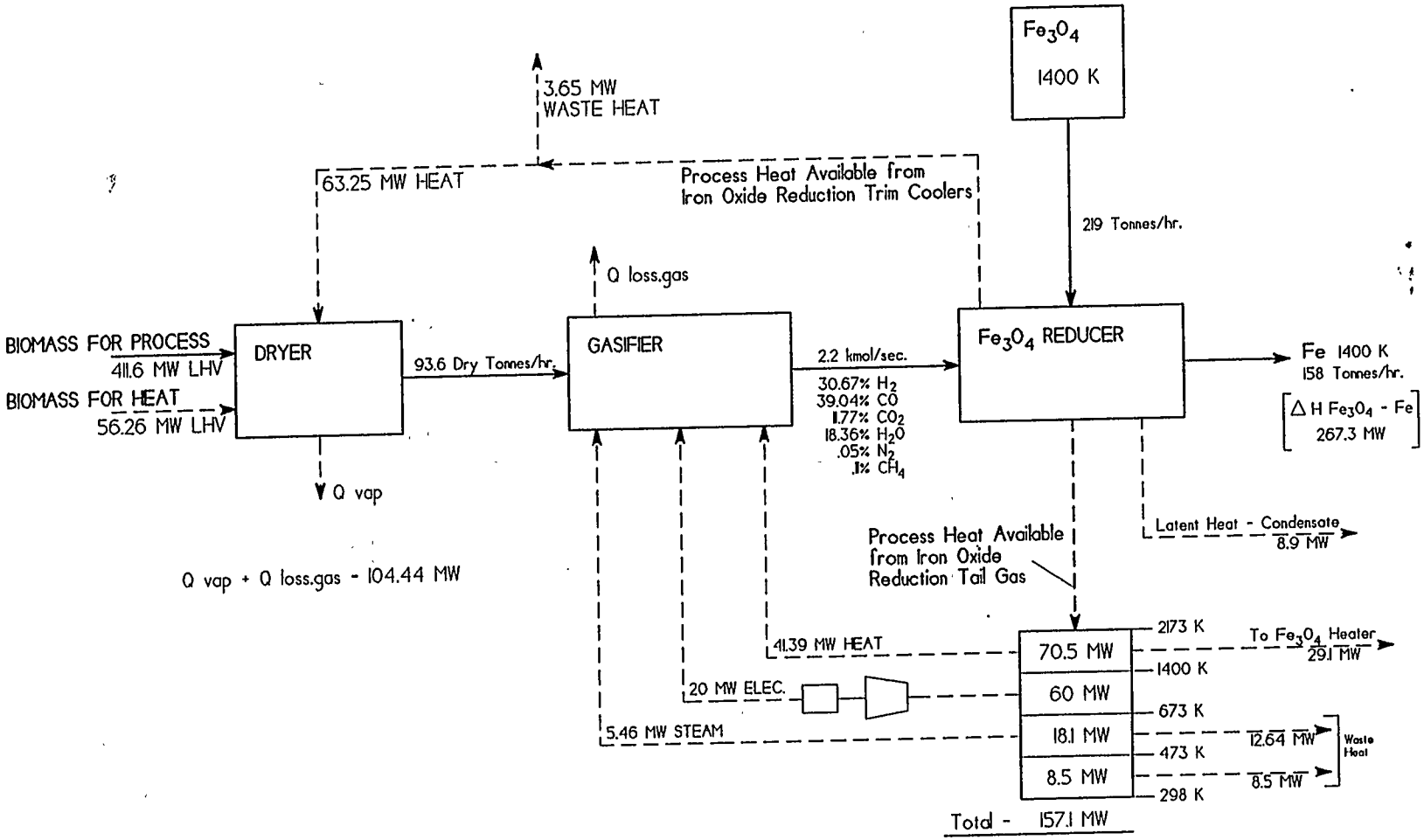

BIOMASS TO HYDROGEN ENERGY BALANCE

— Figure 4 —